Proceedings of the International RILEM Conference

Materials, Systems and Structures in Civil Engineering 2016
Segment on

Service Life of Cement-Based Materials and Structures

Vol. 2

Edited by
Miguel Azenha, Ivan Gabrijel, Dirk Schlicke, Terje Kanstad
and Ole Mejlhede Jensen

Proceedings
PRO 109

cost
EUROPEAN COOPERATION
IN SCIENCE AND TECHNOLOGY

rilem

International RILEM Conference on

Materials, Systems and Structures in Civil Engineering 2016

segment on

Service Life of Cement-Based Materials and Structures

Vol. 2

International RILEM Conference on Materials, Systems and Structures in Civil Engineering
Conference segment on Service Life of Cement-Based Materials and Structures
22-24 August 2016, Technical University of Denmark, Lyngby, Denmark

Published by RILEM Publications S.A.R.L.
4 avenue du Recteur Poincaré 75016 Paris - France
Tel : + 33 1 42 24 64 46 Fax : + 33 9 70 29 51 20
http://www.rilem.net E-mail: dg@rilem.net
 ISBN Vol. 1: 978-2-35158-170-4
Vol. 2: 978-2-35158-171-4 Vol. 1&2: 978-2-35158-172-8 e-ISBN : 978-2-35158-173-5
Printed by Praxis – Nyt Teknisk Forlag, Ny Vestergade 17, 1471 København K, Denmark
Photo 1st cover page: Øresund Bridge seen from below the deck. Credit: Antony McAulay (Adobe Stock, boutik.pt)

RILEM, The International Union of Laboratories and Experts in Construction Materials, Systems and Structures, is a non profit-making, non-governmental technical association whose vocation is to contribute to progress in the construction sciences, techniques and industries, essentially by means of the communication it fosters between research and practice. RILEM's activity therefore aims at developing the knowledge of properties of materials and performance of structures, at defining the means for their assessment in laboratory and service conditions and at unifying measurement and testing methods used with this objective.

RILEM was founded in 1947, and has a membership of over 900 in some 70 countries. It forms an institutional framework for co-operation by experts to:

- optimise and harmonise test methods for measuring properties and performance of building and civil engineering materials and structures under laboratory and service environments,
- prepare technical recommendations for testing methods,
- prepare state-of-the-art reports to identify further research needs,
- collaborate with national or international associations in realising these objectives.

RILEM members include the leading building research and testing laboratories around the world, industrial research, manufacturing and contracting interests, as well as a significant number of individual members from industry and universities. RILEM's focus is on construction materials and their use in building and civil engineering structures, covering all phases of the building process from manufacture to use and recycling of materials.

RILEM meets these objectives through the work of its technical committees. Symposia, workshops and seminars are organised to facilitate the exchange of information and dissemination of knowledge. RILEM's primary output consists of technical recommendations. RILEM also publishes the journal *Materials and Structures* which provides a further avenue for reporting the work of its committees. Many other publications, in the form of reports, monographs, symposia and workshop proceedings are produced.

International RILEM Conference on Materials, Systems and Structures in Civil Engineering
Conference segment on Service Life of Cement-Based Materials and Structures
22-24 August 2016, Technical University of Denmark, Lyngby, Denmark

International RILEM Conference on

Materials, Systems and Structures in Civil Engineering 2016

Segment on
Service Life of Cement-Based Materials and Structures
Vol. 2

Lyngby, Denmark

August 22-24, 2016

Edited by
Miguel Azenha, Ivan Gabrijel, Dirk Schlicke, Terje Kanstad and Ole Mejlhede Jensen

RILEM Publications S.A.R.L.

Sponsors:

CITY OF COPENHAGEN

Knud Højgaards Foundation

Larsen & Nielsen foundation

Ingeborg og Leo Dannis Legat for Videnskabelig Forskning

Hosted by:

Technical University of Denmark

Department of Civil Engineering

DANISH
TECHNOLOGICAL
INSTITUTE

International Organization by:

- Miguel Azenha (University of Minho, Portugal)
- Ole Mejlhede Jensen (Technical University of Denmark)
- Dirk Schlicke (Graz University of Technology, Austria)
- Terje Kanstad (Norwegian University of Science and Technology)

Scientific Committee:

Ivan Gabrijel (chair)	Croatia
Miguel Azenha	Portugal
Farid Benboudjema	France
Violeta Bokan Bosiljkov	Slovenia
Matthieu Briffaut	France
Laurie Buffo-Lacarrière	France
Paulo Cachim	Portugal
Robby Caspeele	Belgium
Özlem Cizer	Belgium
Cyrille Dunant	Switzerland
Rui Faria	Portugal
Erez Gal	Israel
Dariusz Gawin	Poland
Max Hendriks	Norway
Wibke Hermerschmidt	Germany
Ole Mejlhede Jensen	Denmark
Terje Kanstad	Norway
Agnieszka Knoppik-Wróbel	Poland
Katalin Kopecskó	Hungary
Tang Luping	Sweden
Enrico Masoero	United Kingdom
Theodore Matikas	Greece
Sreejith Nanukuttan	United Kingdom
Ivan Paric	Germany
Bernhard Pichler	Austria
Vlastimir Radonjanin	Serbia
Emmanuel Rozière	France
Aljoša Šajna	Slovenia
Dirk Schlicke	Austria
Wolfram Schmidt	Germany
Marijana Serdar	Croatia
Vít Šmilauer	Czech Republic
Tayfun Altuğ Söylev	Turkey
Stéphanie Staquet	Belgium
François Toutlemonde	France
Gregor Trtnik	Slovenia
Neven Ukrainczyk	Germany
Jörg F. Unger	Germany
Mateusz Wyrzykowski	Switzerland
Guang Ye	Netherlands
Yibing Zuo	Netherlands

RILEM Publications

The following list presents the latest offer of RILEM Publications, sorted by series. Each publication is available in printed version and/or in online version.

RILEM PROCEEDINGS (PRO)

PRO 94 (online version): HPFRCC-7 - 7th RILEM conference on High performance fiber reinforced cement composites, e-ISBN: 978-2-35158-146-9, *Eds. H.W. Reinhardt, G.J. Parra-Montesinos, H. Garrecht*
PRO 95: International RILEM Conference on Application of superabsorbent polymers and other new admixtures in concrete construction, ISBN: 978-2-35158-147-6; e-ISBN: 978-2-35158-148-3, *Eds. Viktor Mechtcherine, Christof Schroefl*
PRO 96 (online version): XIII DBMC: XIII International Conference on Durability of Building Materials and Components, e-ISBN: 978-2-35158-149-0, *Eds. M. Quattrone, V.M. John*
PRO 97: SHCC3 – 3rd International RILEM Conference on Strain Hardening Cementitious Composites, ISBN: 978-2-35158-150-6; e-ISBN: 978-2-35158-151-3, *Eds. E. Schlangen, M.G. Sierra Beltran, M. Lukovic, G. Ye*
PRO 98: FERRO-11 – 11th International Symposium on Ferrocement and 3rd ICTRC - International Conference on Textile Reinforced Concrete, ISBN: 978-2-35158-152-0;
e-ISBN: 978-2-35158-153-7, *Ed. W. Brameshuber*
PRO 99 (online version): ICBBM 2015 - 1st International Conference on Bio-Based Building Materials, e-ISBN: 978-2-35158-154-4, *Eds. S. Amziane, M. Sonebi*
PRO 100: SCC16 - RILEM Self-Consolidating Concrete Conference**,** ISBN: 978-2-35158-156-8; e-ISBN: 978-2-35158-157-5
PRO 101 (online version): III Progress of Recycling in the Built Environment, e-ISBN: 978-2-35158-158-2, *Eds I. Martins, C. Ulsen and S. C. Angulo*
PRO 102 (online version): RILEM Conference on Microorganisms-Cementitious Materials Interactions, e-ISBN: 978-2-35158-160-5, *Eds. Alexandra Bertron, Henk Jonkers, Virginie Wiktor*

In relation to the International RILEM Conference on Materials, Systems and Structures in Civil Engineering, MSSCE 2016 which the present proceedings belongs to, the following RILEM proceedings will be issued:

PRO 108: Innovation of Teaching in Materials and Structures
PRO 109 (two volumes): Service life of Cement-Based Materials and Structures
PRO 110: Historical Masonry
PRO 111: Electrochemistry in Civil Engineering
PRO 112: Moisture in Materials and Structures
PRO 113: Concrete with Supplementary Cementitious materials
PRO 114: Frost Action in Concrete
PRO 155: Fresh Concrete

RILEM REPORTS (REP)

Report 45: Repair Mortars for Historic Masonry - State-of-the-Art Report of RILEM Technical Committee TC 203-RHM, e-ISBN: 978-2-35158-163-6, *Ed. Paul Maurenbrecher and Caspar Groot*

International RILEM Conference on Materials, Systems and Structures in Civil Engineering
Conference segment on Service Life of Cement-Based Materials and Structures
22-24 August 2016, Technical University of Denmark, Lyngby, Denmark

Contents

Preface

The conference "Materials, Systems and Structures in Civil Engineering – MSSCE 2016" is part of the RILEM week 2016, which consists of a series of parallel and consecutive conference and doctoral course segments on different topics as well as technical and administrative meetings in several scientific organizations. The event is hosted by the Department of Civil Engineering at the Technical University of Denmark and the Danish Technological Institute and it is held at the Lyngby campus of the Technical University of Denmark 15-29 August 2016.

This volume contains the proceedings of the MSSCE 2016 conference segment on "Service Life of Cement-Based Materials and Structures", which is organized by COST Action TU1404 (www.tu1404.eu). This COST Action is entitled: "Towards the next generation of standards for service life of cement-based materials and structures", dedicated to assist deepening knowledge regarding the service life behaviour of cement-based materials and structures. The main purpose of this Action is to bring together relevant stakeholders (experimental and numerical researchers, standardization offices, manufacturers, designers, contractors, owners and authorities) in order to reflect today's state of knowledge in new guidelines/recommendations, introduce new products and technologies to the market, and promote international and inter-speciality exchange of new information, creating avenues for new developments. The COST Action is basically divided in three main workgroups targeted to this purpose:

WG1 – Testing of cement-based materials and RRT+
WG 2 – Modelling and benchmarking
WG 3 – Recommendations and products

The activities of TU1404 started in November 2014 with a kick-off meeting in Brussels. Since then, three major meetings have taken place, as to promote networking and scientific discussions among participants: April 2015 in Ljubljana, Slovenia; September 2015 in Vienna, Austria; March 2016 in Zagreb, Croatia.

Also, two important instruments of the Action are now under way: the Extended Round Robin Testing Program (RRT^+), and the numerical benchmarking. The RRT^+ is currently involving 43 laboratories and has involved shipment of more than 100 tons of raw materials. An initial phase of testing has been finished already, and laboratories are shifting focus to the main experiments of this extended program. The numerical benchmarking program has also begun and will soon interact with the RRT^+ program and even extend beyond it.

The present conference segment deals with a wide breadth of topics related to the service life of concrete, comprising aspects related to the 3 Workgroups mentioned above. The conference segment is attended by 80 presenters from university, industry and practice representing more than 30 different countries. All contributions have been peer reviewed.

It should be mentioned, that these proceedings do not contain all the papers that have been submitted in the scope of COST TU1404 in MSSCE2016. Due to scheduling and organization issues, as well as affinity with topics of other segments, some of the papers were moved. A separate set of electronic proceedings shall be prepared to include all papers related to COST TU1404, and will be made available in the website of the Action (www.tu1404.eu).

Miguel Azenha Ivan Gabrijel Dirk Schlicke Terje Kanstad Ole Mejlhede Jensen

August 2016, Lyngby, Denmark

Acknowledgements

This publication is based upon work from COST Action TU1404 'Towards the next generation of standards for service life of cement-based materials and structures', supported by COST (European Cooperation in Science and Technology).

COST (European Cooperation in Science and Technology) is a pan-European intergovernmental framework. Its mission is to enable break-through scientific and technological developments leading to new concepts and products and thereby contribute to strengthening Europe's research and innovation capacities. It allows researchers, engineers and scholars to jointly develop their own ideas and take new initiatives across all fields of science and technology, while promoting multi- and interdisciplinary approaches. COST aims at fostering a better integration of less research intensive countries to the knowledge hubs of the European Research Area. The COST Association, an International not-for-profit Association under Belgian Law, integrates all management, governing and administrative functions necessary for the operation of the framework. The COST Association has currently 36 Member Countries.

cost
EUROPEAN COOPERATION
IN SCIENCE AND TECHNOLOGY

COST is supported
by the EU Framework
Programme Horizon 2020

Welcome

Were you aware that a part of your daily language is likely to be in Danish? A thousand years ago the Danish word "*Vindue*" came along with the Vikings to England. Several hundred years later it reached North America, and from there – just two to three decades ago – almost every person in the world learned to understand and pronounce this word: "*Windows*", which etymologically means "an eye to the wind".

As a child your career as construction professional may have started with *LEGO*, and before you went to bed, your mother told you the unforgettable fairytales of *H.C.Andersen*. You may have grown up with the delicious taste of *Lurpak* butter on your bread, and though you might find it strange that "God plays dice with the Universe", hopefully your school teacher told you that on this topic Einstein was flat out wrong and *Niels Bohr* was right. Right now you may prefer to be sitting in the sun with a chilled *Carlsberg* beer in your hand, enjoying the iconic view of the *Sydney Opera House*. All of it is Danish made, and many things around you at home, if not made in Denmark, were probably brought to you by *Maersk*, the world's largest shipping company, the modern Danish Viking fleet.

Though Denmark is one of the world's smallest countries, yet it stands – along with your country – among the greatest. On top of a thousand years of outreach from Denmark, your visit to the Danes is most welcome. On your approach to Copenhagen airport you had a view to *wind turbines* harvesting green energy, you saw record breaking *bridges*, and perhaps you got a glimpse of the island Ven where the nobleman *Tycho Brahe* literally speaking changed our view of the world through perfection of astronomical observations with his naked eye. In Copenhagen you may appreciate a walk in the fairytale amusement park *TIVOLI*, and in the Copenhagen harbour you may have a rendezvous with a *Little Mermaid*.

Of all things in Denmark you will surely enjoy the conference and doctoral courses *Materials, Systems and Structures in Civil Engineering, MSSCE 2016* which are held in conjunction with the *70th annual RILEM week*. On this occasion RILEM celebrates its 70 years birthday and thus maintains generations of experience. However, new activities and the in-built diversity keep RILEM fresh and dynamic like a teenager.

The event takes place in northern Copenhagen, Lyngby, at the campus of the Technical University of Denmark, 15-29 August 2016. MSSCE 2016 aims at extending the borders of the RILEM week by including doctoral courses, by involving a palette of RILEM topics in the conference and workshop activities, and by collaborating with other scientific organizations. The insight and outlook provided by this event make it RILEM's technical and educational activity window.

It is a pleasure to share with you what is unique to RILEM and Denmark!

Ole Mejlhede Jensen, Technical University of Denmark
Honorary president of RILEM 2016, Chairman of MSSCE 2016

International RILEM Conference on Materials, Systems and Structures in Civil Engineering
Conference segment on Service Life of Cement-Based Materials and Structures
22-24 August 2016, Technical University of Denmark, Lyngby, Denmark

EFFECT OF RECYCLED AGGREGATE CONCRETE ON EARLY AGE BEHAVIOR

Ahmed Z. Bendimerad[(1)], Brice Delsaute[(2)], Emmanuel Roziere[(1)], Stéphanie Staquet[(2)], Ahmed Loukili[(1)]

(1) Ecole Centrale de Nantes, Civil engineering and Mechanics research Institute (GeM) – UMR CNRS 6183, Nantes
(2) Service BATir, Université Libre de Bruxelles, Belgium.

Abstract
This paper presents the results of experimental research on recycled aggregate concrete at early age. The influence of recycled gravel (RG) and recycled sand (RS) on plastic shrinkage and cracking sensitivity was investigated. The concrete mixtures were designed using 30% and 100% of recycled gravel, and 30% of recycled sand. The total water was kept constant for all the mixtures during the mixing process. The gravel/sand ratios were adjusted to keep the Maximum Paste Thickness (MPT) constant. To understand the evolution of early age parameters, a timeline was established and the analyses showed correlations between the evolution of plastic shrinkage and other properties at early age. A stress/strength approach based on experimentally assessed parameters was used to compare the cracking sensitivity of different concretes with recycled aggregates. A high rate of substitution of recycled gravel or sand affected the early age properties of the recycled concrete and the cracking sensitivity especially when natural sand was replaced by recycled concrete sand

1. Introduction

In many urban areas, a critical shortage of natural aggregates is detected. At the same time, increasing quantities of demolished concrete from old structures are generated as waste material in these same areas. Sustainable development has become a strategic issue and affects construction materials in terms of CO_2 emission, energy consumption and the use of natural raw materials. The use of construction and demolition waste obtained from building demolition as recycled aggregates for the production of new concrete has become more common for the last decade. However, the influence of aggregates on short-term and long-term behaviour of concrete is significant [1], [2].
Many studies regarding the recycled concrete aggregates can be found in literature. These focus mostly on the effect of replacing natural aggregates by recycled aggregates on long-term properties (strength, creep and drying shrinkage) [3], [4].

Early age cracking of horizontal concrete elements is likely to appear a few hours after it is cast, during setting and early hardening of concrete. Plastic shrinkage may occur when the evaporation rate exceeds the bleeding rate [5]. Two methods can be found in literature for analyzing the cracking sensitivity. The first one is based on the strain capacity [6], [7] and the second on stress criteria [8], [9]. If the tensile strength is lower than the stress level caused by restrained shrinkage, plastic shrinkage cracking occurs [9]. The tensile strength of concrete made of recycled aggregates is generally lower than the strength of natural aggregate concrete. However it is not easy to conclude on the effect of replacing natural aggregates with recycled aggregates on restrained shrinkage cracking, as the parameters act in opposite ways, for instance drying shrinkage and elastic modulus.
The aim of the present experimental study is to quantify the cracking sensitivity of recycled concrete at early age, based on the monitoring of plastic shrinkage and mechanical properties. The experimental approach based on stress criteria is applied to concrete mixtures. The water absorption and the saturation rates of the recycled aggregates used in this study were determined by combining experimental methods [10]. Plastic shrinkage measurements were associated with other experimental techniques to understand the evolution of plastic shrinkage and the influence of recycled aggregates. An approach based on direct tensile testing and calculated elastic stresses is then used to assess the cracking sensitivity. The results obtained for all the concrete mixtures of recycled aggregates are presented, analysed and discussed.

2. Experimental program

The experimental program focuses on the effect of substitution rate of natural aggregates with recycled aggregates, all (gravel and sand) being at the saturated surface dry state. Four mixtures were designed in this study (Table 1). The concrete designation 0RS-30RG means that 0% (in mass) of recycled sand (i.e. there is only natural sand) and 30% (in mass) of gravel used is recycled.
The plastic shrinkage development was measured using two identical steel moulds (70x70x280) mm^3 covered on the inside by Teflon, limiting friction between concrete and the mould. The concrete was cast in a plastic sheet between two PVC plates. Their displacement was measured without contact by two laser sensors [11]. To understand the plastic shrinkage evolution several experimental techniques were associated to this test: Elastic modulus, capillary pressure, Vicat setting, and hydration degree.
The evolution of elastic properties of concrete at early age was assessed by the FreshCon system through the monitoring of the velocity of ultrasonic pressure and shear waves [12]. The capillary pressure was measured using a porous ceramic cup placed horizontally in the middle of a cylinder [13] and connected to a pressure sensor. The Vicat test was used to monitor initial and final setting time according to the European standard EN 196-3 [14]. An isothermal calorimeter TAM air was used [15] to determine the hydration degree. The tensile strength was assessed using a direct tensile test [16].

Table 1: Admixture of natural and recycled aggregates concrete.

	0RS-0RG	**30RS-0RG**	**0RS-30RG**	**0RS-100RG**
NG 6,3/20 (kg/m^3)	820	829	462	
RG 10/20 (kg/m^3)			296	701
NG 4/10 (kg/m^3)	267	190	228	
RG 4/10 (kg/m^3)				163
NS 0/4 (kg/m^3)	780	549	813	806
RS 0/4 (kg/m^3)		235		
Cement, C (kg/m^3)	270	276	276	282
Limestone, L (kg/m^3)	45	31	31	31
Superplasticizer SP (kg/m^3)	0.747	0.798	0.861	0.798
W_{eff} (kg/m^3)	180	185	185	189
W_{tot} (kg/m^3)	194.6	221.4	212.3	241
W_{eff}/B_{eq} (kg/m^3)	0.64	0.65	0.65	0.65
Volume of paste (l/m^3)	285	287	287	293
Slump (mm)	195	204	193	195
Packing density g*	0.785	0.79	0.781	0.777
MPT (mm)	0.80	0.86	0.82	0.89

3. Results and discussion

3.1 Analysis of early age behaviour

Several interesting time points were defined on each curve to understand the phenomena occurring during the plastic shrinkage development.

The derivative of the shrinkage deformation actually gives two minima (Figure 1). The first minimum generally occurs during the first two hours. Before this point, the plastic shrinkage rate is high and decreases rapidly. It corresponds to the thermal deformation, as the temperature of fresh concrete after mixing is different from the temperature in the plastic shrinkage moulds (20°C). All the following curves of plastic shrinkage are initialized at the first minimum of derived deformation, noted (Initial def). It has no consequence of stress development as the Young modulus is still relatively low (Figure 3). The second point is noted as (2nd min derived def). The third point corresponds to 95% of the maximum deformation. Between (Initial def) and (2nd min derived def) the rate of plastic shrinkage increases then decreases until a minimum. At the end of this stage, initial setting has not occurred, the capillary pressure has not developed, and the elastic modulus is still relatively low. Thus shrinkage observed during this stage is likely to be caused by chemical shrinkage of cement paste.

The hydration process is also characterized by several stages [17]. Three times, corresponding to the points where this derivative equals zero, were defined as initial heat flow, 1st max heat flow and 2nd max heat flow (Figure 2). The initial heat flow corresponds to the dormant period and concurs quite well with the time of (2nd min derived def). The period before 1st max heat flow is related to the acceleration period and this time actually showed a good correlation with time of final setting (Figure 3).

The characteristic time corresponding to (2nd min derived def) coincided well with the point corresponding to the start of the heat flow (Figure 2). These two points showed good correlation (Figure 3). The acceleration phase of the plastic shrinkage is controlled by the onset of hydration.

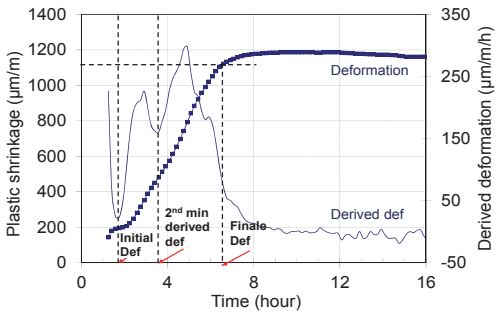

Figure 1. Plastic shrinkage and its derivative.

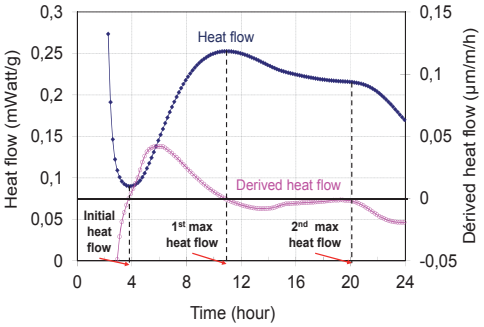

Figure 2. Heat flow evolution and its derivative.

Other characteristics times were defined from curve of Vicat test and capillary pressure noted: Initial and final setting and pressure development. At initial setting time the value of shear modulus was 0.3 GPa (Figure 4). As long as cement paste remains fluid, autogenous deformation is equal to chemical shrinkage. Then, as the stiffness of the paste increases, the hydration of cement causes cavitation and the creation of voids in the cement matrix. The time characterized by capillary pressure development (Pressure development), shown in Figure 4, matches the appearance of menisci in the pores and between the cement matrix and the ceramic porous sensor [18], [19]. Capillary pores were initially filled with water. As water is consumed by the hydration of cement, voids appear and liquid-vapour menisci are created in the pores. The maximum plastic shrinkage rate was observed between (2nd min derived def) and time noted (Final def) (Figure 1). During this stage capillary pressure significantly increased. Shrinkage is actually caused by capillary depression caused by self-desiccation shrinkage and external drying. But in the same time elastic and shear modulus significantly increase, which finally prevents concrete from shrinking.

For all the mixtures, the shear modulus G starts to increase when the first hydration products are formed, filling up the pore space and creating a denser structure. Thus, an increase in shear modulus will cause an increase in the S-wave velocity but not in penetration resistance (G=0.05GPa). Only after some time, when the cement particles are connected, the shear modulus and thus the penetration resistance start to develop [20]. This time corresponds to pressure development and the initial setting (G=0.33GPa) (Figure 3). The final setting determined with Vicat test related quite well with the time of 1st max heat flow and it corresponds to G=2.7GPa (Figure 4).

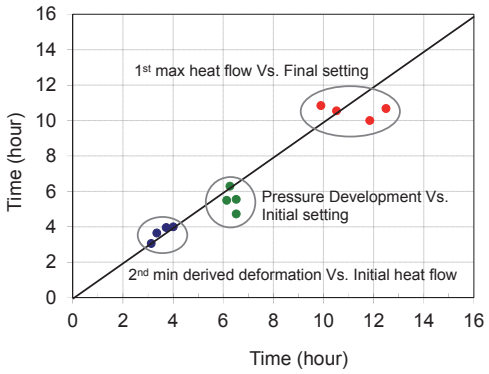

Figure 3. Correlation between different parameters.

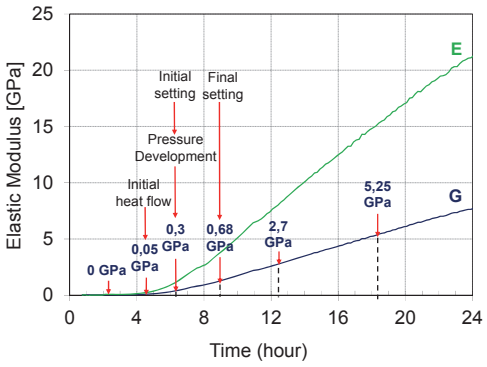

Figure 4. Evolution of elastic properties at early age.

3.2 Effect of substitution rate on plastic shrinkage

The graphs (Figure 5) show the influence of substitution rate of recycled aggregate (gravel or sand) on plastic shrinkage. After 8 hours a 31% difference could be observed between the concrete with recycled sand and conventional concrete.

The plastic shrinkage of 30%RG and 100%RG concretes were close. If the conventional concrete (0RS-0RG) is chosen as a reference, the difference is significant but lower than 10%. This can be explained by a physical parameter called Maximal Paste Thickness (MPT). The MPT corresponds to the distance between two coarse aggregates [21]. The MPT was calculated for the four mixtures (Table 1) and found almost constant, knowing that the shrinkage of concrete mainly comes from free shrinkage of cement paste in MPT.

The recycled concrete 0RS-100RG has the highest value of MPT (0.89 mm) but it showed lower plastic shrinkage than the other recycled concrete 0RS-30RG. This concrete mixture has lower MPT (0.82) but lower total water content (Table 1), thus lower potential self-curing provided by porous recycled aggregates.

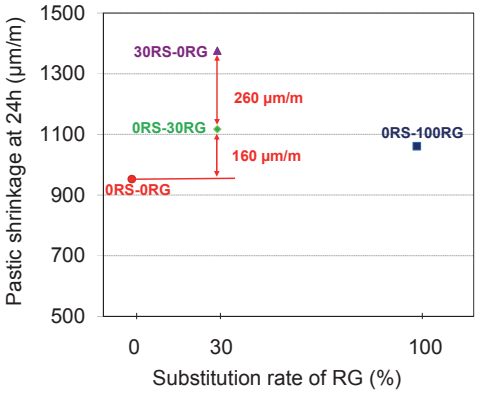

Figure 5. Effect of substitution rate on plastic shrinkage.

The highest plastic shrinkage magnitude concerned concrete with recycled sand (Figure 5). Recycled sand had the highest coefficient of absorption and percentage of fines. As a consequence, the effective water intended for the cement paste is attracted and kept in the menisci created by the recycled fines. Therefore, the bleeding water is lower than in the control mix and the risk of plastic shrinkage related to insufficient curing increases.

3.3 Early age cracking risk

The experimental study was designed to compare the shrinkage-induced cracking sensitivity of different conventional and recycled concretes at early age, based on monitoring of the evolution of stress and strength [8], [9]. The evolution of plastic shrinkage and tensile strength has been experimentally assessed using specific tests. The approach was based on an elastic model and the time evolutions of the properties of concrete (Eq. 1):

$$\sigma(t) = \varepsilon(t) \times E(t) \quad (1)$$

Where: $\varepsilon(t)$ is plastic shrinkage deformation, $E(t)$ is Young modulus evolution and $\sigma(t)$ is the estimated stress produced by total restraint. The value of $\sigma(t)$ at 24 hours is noted S.
The concrete tensile strength, noted R, was experimentally assessed 24 hours after casting using direct tensile test. The S/R ratio of the different mixtures were assessed to quantify the cracking sensitivity of recycled concrete at early age.
The percentage of substitution of recycled gravel or sand significantly affected the elastic modulus and tensile strength (Figure 6), resulting in a higher cracking sensitivity of concrete mixtures with recycled aggregates. The 0RS-30RG and 30RS-0RG concretes were characterized by a higher stress development due of the increase in elastic modulus and plastic shrinkage respectively which implied higher S/R ratios. The effect of relaxation is not taken into account in this study and the concrete with 100% recycled gravel is likely to show lower cracking sensitivity than concrete with 30% recycled gravel and 30% recycled sand (Figure 7).

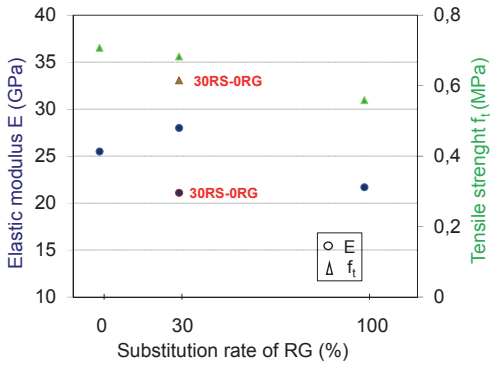

Figure 6. Influence of substitution rate of RG on early age properties.

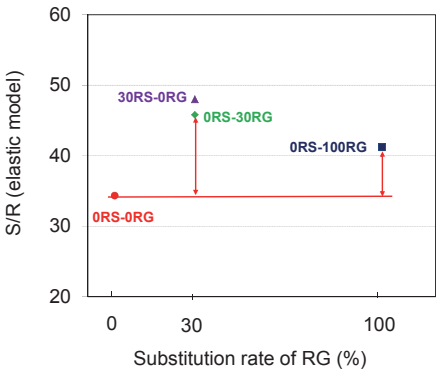

Figure 7. Influence of substitution rate on cracking sensitivity.

4. Conclusions

The study presented in this paper focused on the plastic shrinkage and cracking sensitivity of concrete at early age. An estimation of a potential early age cracking sensitivity based on a stress/strength elastic approach was also developed, focusing on the evolution of elastic properties and plastic shrinkage. Based on the results presented in this paper the following conclusions can be drawn:

- A timeline was established for a better understanding of the evolution of plastic shrinkage by showing correlations with the evolution of other properties at early age, such as heat flow, setting, and elastic modulus.
- The rate of substitution of recycled gravel had a relatively low influence on plastic shrinkage. The concrete mixtures were actually designed keeping the maximum paste thickness (MPT) constant.
- The concrete with 30% recycled sand showed the highest plastic shrinkage. Recycled sand actually develops a significant surface area, especially at the level of fines. The effective water intended for the cement paste is attracted and kept by the recycled fines, which results in higher plastic shrinkage related to insufficient curing.
- The cracking sensitivity at early age was assessed according to an experimental approach. This was based on experimentally assessed tensile strength and stresses calculated from plastic shrinkage and elastic modulus. The concrete mixtures with 30% recycled gravel and sand were characterized by a highest stress levels due to the increase in elastic modulus and plastic shrinkage. The cracking sensitivity was not proportional to the recycled aggregate content.

Acknowledgments

Support from the *Agence Nationale de la Recherche* (National Research Agency, France) is acknowledged (*ECOREB* project). The authors would like to thank *UNPG* (National Association of Aggregate Producers, France) for providing some of the aggregates.

References

[1] R. Landgren, "Water-Vapor Adsorption-Desorption Characteristics of Selected Lightweight Concrete Aggregates," in *Proceedings of the American Society for Testing and Materials, Philadelphia*, 1964, pp. 830–845.

[2] P. B. Bamforth, "Rapport CIRIA: Early-age thermal crack control in concrete." p. 112, 2007.

[3] A. Katz, "Properties of concrete made with recycled aggregate from partially hydrated old concrete," *Cem. Concr. Res.*, vol. 33, pp. 703–711, 2003.

[4] a. Domingo-Cabo, C. Lázaro, F. López-Gayarre, M. a. Serrano-López, P. Serna, and J. O. Castaño-Tabares, "Creep and shrinkage of recycled aggregate concrete," *Constr. Build. Mater.*, vol. 23, no. 7, pp. 2545–2553, 2009.

[5] T. . Powers, *Properties of Fresh Concrete*, John Wiley. London, 1968.

[6] Z. Bayasi and M. McIntyre, "Application of fibrillated polypropylene fibers for restraint of plastic shrinkage cracking in silica fume concrete," *ACI Mater. J.*, vol. 99, no. 4, pp. 337–344, 2002.
[7] S. Swaddiwudhipong, H. R. Lu, and T. H. Wee, "Direct tension test and tensile strain capacity of concrete at early age," *Cem. Concr. Res.*, vol. 33, no. 12, pp. 2077–2084, 2003.
[8] T. A. Hammer, K. T. Fossa, and Ø. Bjøntegaard, "Cracking tendency of HSC : Tensile strength and self generated stress in the period of setting and early hardening," *Mater. Struct.*, vol. 40, pp. 319–324, 2007.
[9] D. Ravina and R. Shalon, "Plastic Shrinkage Cracking," *ACI J.*, vol. 65, no. 4, pp. 282–294, 1968.
[10] A. Z. Bendimerad, E. Roziere, and A. Loukili, "Combined experimental methods to assess absorption rate of natural and recycled aggregates," *Mater. Struct.*, vol. 48, no. 11, pp. 3557–3569, 2015.
[11] P. Turcry and A. Loukili, "Evaluation of Plastic Shrinkage Cracking of Self-Consolidating Concrete," *ACI Mater. J.*, vol. 103, no. 4, pp. 272–279, 2006.
[12] H. W. Reinhardt and C. U. Grosse, "Continuous monitoring of setting and hardening of mortar and concrete," *Constr. Build. Mater.*, vol. 18, no. 3, pp. 145–154, 2004.
[13] A. Radocea, "Autogenous volume change of concrete at very early age," *Mag. Concr. Res.*, vol. 50, no. 2, pp. 107–113, 1998.
[14] EN NF196-3, "Méthodes d'essais des ciments, Partie 3 : Détermination du temps de prise et de la stabilité," 2009.
[15] TA Instruments, "Introduction à la Calorimétrie et au TAM Air," 2013.
[16] E. Roziere, R. Cortas, and A. Loukili, "Tensile behaviour of early age concrete : New methods of investigation," *Cem. Concr. Compos.*, vol. 55, pp. 153–161, 2015.
[17] J. K. Young, "Hydration of Portland cement in 'Instructional modulus in cement science,'" . Roy, Materials education Council. Materials Research Laboratory, University Park, PA. USA, 1985.
[18] F. H. Wittmann, "On the action of capillary pressure in fresh concrete," *Cem. Concr. Res.*, vol. 6, pp. 49–56, 1976.
[19] V. Slowik, M. Schmidt, and R. Fritzsch, "Capillary pressure in fresh cement-based materials and identification of the air entry value," *Cem. Concr. Compos.*, vol. 30, no. 7, pp. 557–565, 2008.
[20] T. Voigt, C. U. Grosse, Z. Sun, S. P. Shah, and H. W. Reinhardt, "Comparison of ultrasonic wave transmission and reflection measurements with P- and S-waves on early age mortar and concrete," *Mater. Struct.*, vol. 38, no. 8, pp. 729–738, 2005.
[21] F. de Larrard and T. Sedran, "Optimization of ultra-high-performance concrete by the use of a packing model," *Cem. Concr. Res.*, vol. 24, no. 6, pp. 997–1009, 1994.

International RILEM Conference on Materials, Systems and Structures in Civil Engineering
Conference segment on Service Life of Cement-Based Materials and Structures
22-24 August 2016, Technical University of Denmark, Lyngby, Denmark

MECHANICAL ACTIVATION OF SUPPLEMENTARY CEMENTITIOUS MATERIALS IN ORDER TO USE AS HYDRAULIC BINDER

Gábor Mucsi [(1)], Ákos Debreczeni [(1)], Viktor Török[(1)]

(1) University of Miskolc, Miskolc, Hungary

Abstract
Stirred media mill today is a widely applied device due to its good efficiency in the very fine (submicron) size range. In spite of this, only few results are reported recently with this mill in the cement industry. Present paper deals with the investigation of F class fly ash (FA) and granulated blast furnace slag (GBFS). Mechanical activation experiment of both raw materials was carried out in a stirred media mill separately for various time.
Ground sample was tested with laser particle size analyzer (LPSA) to determine and calculate the material fineness (PSD and SSA). Hydraulic binder paste was prepared using ground FA and GBFS in various portions (0, 25, 50, 75 and 100 %) with lime addition under specific water/cement ratio. Cubic specimens were produced from paste and uniaxial compressive strength was measured at the age of 7, 28 and 56 days.
The results of the experiments show the effect of FA and GBFS fineness on the compressive strength of the resulted binder. Relationships between grinding fineness, FA/GBFS ratio, material structure and strength were revealed.

1. Introduction

Coal fired power station fly ash and granulated blast furnace slag are two of the most important industrial by-products generated in huge amount worldwide. On the other hand, they might be valuable raw materials in a wide range of applications, mainly in the construction industry due to their high alumino-silicate content. However, their quality is very heterogeneous. Namely, the reactive ones are of great importance in the cement and other allied industries. Nevertheless, the less valuable by-products are landfilled. The low reactivity of such secondary raw materials can be improved by mechanical activation [1-3]. There are several states of mechanical activation and the following situations can be distinguished: i) mechanical dispersion, ii) surface activation and iii) mechano-chemical (structural) activation [4]. It has been reported that the application of high energy density mills (planetary ball mill,

vibratory mill, stirred media mill) allow dramatic change of the structure and surface properties of minerals [5].
Based on these facts the goal of our research is to investigate the effect of mechanical activation (MA) of fly ash and granulated blast furnace slag on their reactivity, to determine their optimal fineness in order to develop a hydraulic binder.

2. Materials and methods

Two industrial by-products were chosen for the experimental investigation, power plant fly ash (FA) and granulated blast furnace slag (GBFS) from Hungary.

2.1 Materials

Class F fly ash (FA) was generated in a brown coal fired power plant (Tiszaújváros, Hungary) and landfilled decades ago, while the granulated blast furnace slag (GBFS) was sampled in Dunaújváros (ISD Dunaferr PLC.). The main physicochemical properties of FA and GBFS can be found in Table 1.

Table 1. Main physical properties of FA and GBFS.

Property	FA	GBFS
Particle density	1.66 g cm^{-3}	2.72 g cm^{-3}
Bulk density	0.73 g cm^{-3}	0.96 g cm^{-3}
Moisture content	12.11%	6.63%
Median particle size	81 µm	1.9 mm

The chemical composition of the samples, measured by X-ray Fluorescence method (Rigaku Supermini 200), can be found in Table 2.

Table 2. Chemical Composition of FA and GBFS.

Constituent	FA, %	GBFS, %
SiO_2	60.90	36.80
Fe_2O_3	4.98	0.25
Al_2O_3	27.10	6.00
CaO	1.55	28.80
MgO	0.94	7.27
Na_2O	1.03	0.36
K_2O	1.38	0.85
SO_3	0.07	-
L.O.I.	2.17	-

Main mineral phases of fly ash identified using XRD (Bruker D8 Advance 2) apparatus were quartz, mullite, cristoballite, quartz, maghemite, anhydrite and albite while those of the GBFS were as follows: merwinite, akermanite, calcite, calcite-magnezian and diopside. The amorphous content of the fly ash and the granulated blast furnace slag were 70% and 59% respectively.

2.2 Methods

The mechanical activation was performed in a laboratory scale high energy density mill, namely a stirred media mill equipped with ceramic liners and discs. The cooling system of the mill consists of a double walled cooling jacket. Effective volume of the mill chamber is 530 cm^3, the used filling ratio (φ_{gm}) of grinding beads (Ø 0.8-1.0 mm Zirconium silicate balls) was 70%. The material filling ratio (φ_m) was 80%. Control of the rotor speed (5 m/s) was realized by a frequency control unit. The residence time of grinding was 1, 3, 5, 10, 20 and 30 (60) min. Additionally, the GBFS sample having coarser particles (up to 20 mm) was preground in a rolls crusher and a tumbling ball mill prior to stirred ball milling.

The particle size distribution (PSD) of the raw and the ground material was measured by HORIBA LA-950V2 laser diffraction particle size analyzer in wet mode using distilled water as dispersing media and sodium-pyrophosphate as dispersing agent applying the Mie-theory as evaluation method, which is more accurate in the fine size (< 20 micron) particles. The geometric specific surface area (SSA) was calculated using PSD data by the laser sizer software, using the shape factor 1.0 (spherical shape).

For our investigation of hydraulic activity CK HSZ 4706-2 standard [6] was used by lime addition and lime absorption. During the experiments 1 g of fly ash is sampled from the differently ground material than it is put to a graduated cylinder of 100 ml, than 100 ml saturated lime solution is added and shaked well. During the test the cylinder has to be shaked every day, and every second day 50 ml is sampled and titrated. Finally another fresh 50 ml saturated lime solution is put to the pregnant solution.

Uniaxial compressive strength of the specimens containing fly ash and granulated blast furnace slag was measured by a Universal tester.

3. Results and discussion

3.1. Mechanical Activation by Grinding

Fly Ash

Figure 1 shows the particle size distribution curves of the raw and ground fly ash samples. Continuous size reduction can be seen until 30 min grinding time concerning median particle size. However, agglomeration of the submicron particles (moreover <600 nm) appeared from 20 min residence time. On the other hand, the ratio of “coarse” fraction (>6 μm) increased significantly due to agglomeration of fines to the surface of the coarser particles.

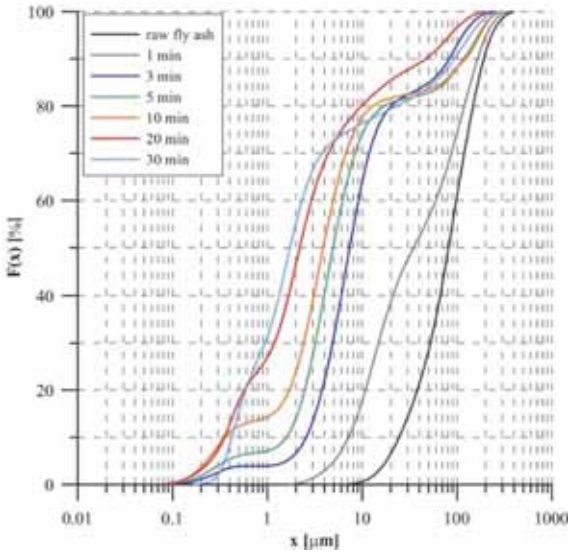

Figure 1. Cumulated particle size distribution of the raw and mechanically activated fly ash.

Beside the particle size distribution, the specific surface area of the ground fly ash was calculated from the PSD data and illustrated [7]. The SSA results are plotted as a function of grinding time in Figure 2. The maximum fineness reached 85000 cm^2/g after 20 min residence time. After it the specific surface area dropped down significantly to 73000 cm^2/g.

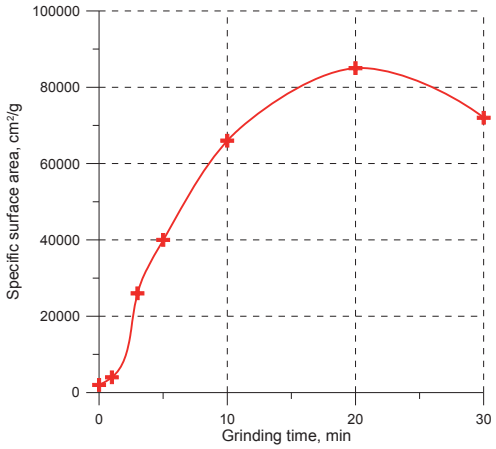

Figure 2. Specific surface area of the raw and mechanically activated fly ash as a function of grinding time.

The above described behavior (Figure 2) is in strong correspondence with the well known grinding phenomena which has three stages, namely (1) Rittinger section until 10 min, (2) aggregation from 10 to 20 min and (3) agglomeration section after 20 min. The only one difference is the reduction of the aggregation stage compared with that of the low energy density mills.

Granulated Blast Furnace Slag

Particle size distribution curves of the ground granulated blast furnace slag are demonstrated in Figure 3 which shows a moderate decrease in median particle size from ~20 µm down to ~10 µm.

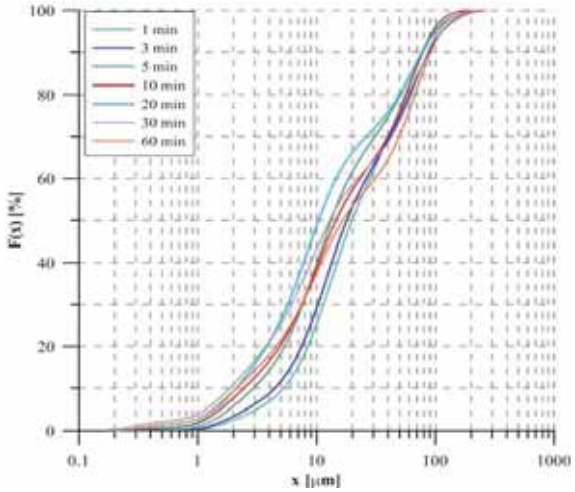

Figure 3. Particle size distribution of the mechanically activated granulated blast furnace slag.

However, it is important to note that this sample was pregroung in a ball mill to have appropriate fineness for stirred milling. On the other hand it can be stated that remarkable coarsening was found from 30 min grinding time due to the agglomeration. Furthermore, the maximum particle size remains almost the same during grinding steps from 1 to 60 min.
The characteristic curve of SSA change of granulated blast furnace slag as a function of time can be seen in Figure 4. The shape of the curve was similar to that of the SSA variation of fly ash shown in Figure 2.

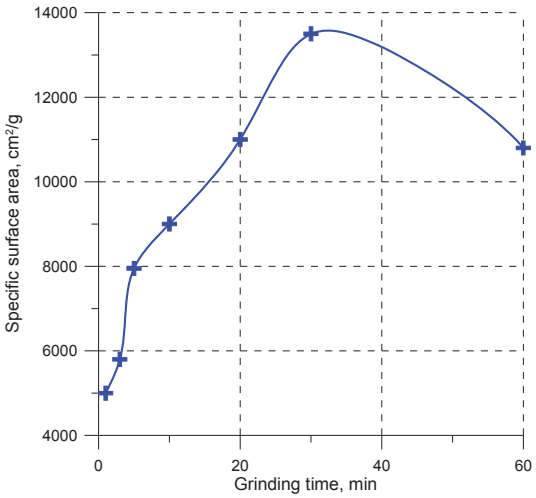

Figure 4. Variation of specific surface aree of GBFS as function of grinding time.

Rittinger section ends at 20 min where the SSA increases in proportion with grinding time, the aggregation is between 20 min and 30 min, and agglomeration starts at 30 min where the GBFS starts to coarsen. The highest specific surface area of GBFS was reached after 30 min residence time 13418 cm^2/g which was significantly lower than that of FA.

3.2. Hydraulic Binder

Hydraulic activity of fly ash

The lime adsorption capacity of the raw and mechanically activated fly ash can be seen in Figure 5. It can be observed that the highest cumulative lime adsorption capacity was achieved in the case of fly ash with 5 min grinding time, namely 125 mg/g was reached after 30 days. This is a 229% increase compared to the results of the raw fly ash. Until this point a continuous increase was found. However, after 5 min residence time the cumulated capacity decreased and started to fluctuate. On the other hand all of the mechanically activated fly ash curves can be described using linear functions. Contrary to this, the reactivity of the raw fly ash has shown a slower increase until about 14 days.

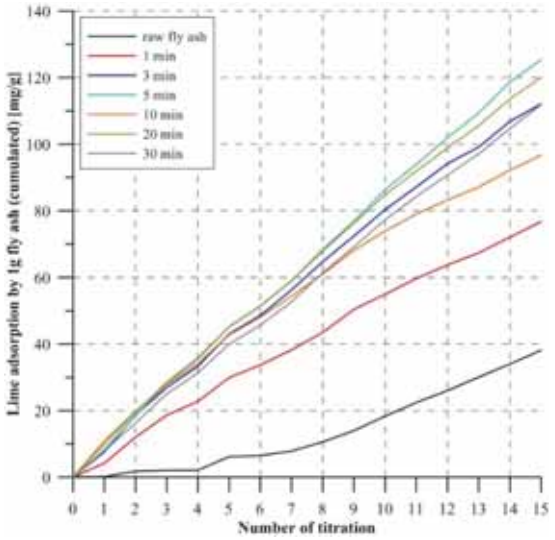

Figure 5. Lime adsorption capacity of the raw and mechanically activated fly ash as a function of number of titration (15 titrations = 30 days).

Uniaxial compressive strength of fly ash-lime binder

After the lime adsorption measurement, the reactivity of the fly ash was determined by compressive strength test of the binder specimens made of the mechanically activated fly ash and lime (as chemical activator). The goal of this test is to find correlation between the results of the chemical and mechanical tests. In this case 10m/m% CaO was added to the treated fly ash to prepare the paste, water/cement ratio was 0.5. The size of the cubic specimens was 20x20x20 mm. We decided to use these relatively small specimen size, beacuse a laboratory scale stirred media mill was applied for the mechanical activation test of the raw materials with a small grinding chamber. Therefore, it was practical to reduce the size of specimen.

Three parallel measurements were carried out for each composition and average was calculated. The maximum lime adsorption capacity and the compressive strength results at 7 and 28 days are plotted as function of grinding time in Figure 6.

It can be seen from Figure 6 that the maximum values of each curve were found at 5 min grinding time. Furthermore, it can be established that the compressive strength of binder containing 1 min and 3 min mechanically activated fly ash increased very moderately compared to that of the raw fly ash. However, the strength of binder made of 5 min ground fly ash was remarkably higher than the other cases. It reached 7.7 MPa and 12.8 MPa compressive strength after 7 and 28 days aging respectively. After this maximum both the strength and the lime adsorption capacity decreased on spite of the higher specific surface area. Additionally, the highest rate of strength increase was found in the case of 5 min activated fly ash, which proved the lime adsorption results. Based on the above presented results 5 min activated fly ash was used for the following experiments.

In the next step the effect of CaO dosage (5, 10, 15, 20, 25, és 30 m/m%) to the ground fly ash was investigated in order to determine the optimal CaO content. The compressive strength

results are found in Figure 7. The aging of these specimens was carried out under normal laboratory conditions, so circumstances (humidity, temperature) were varied.

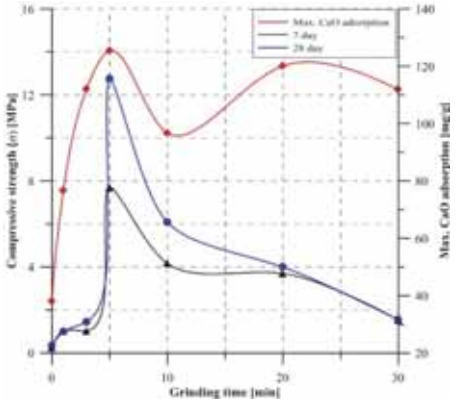

Figure 6. Relationship between lime adsorption of fly ash and strength values of fly ash based binder.

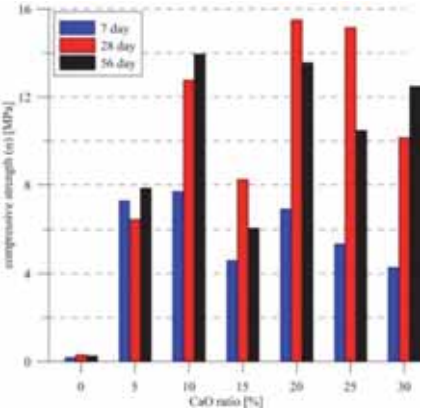

Figure 7. Compressive strength of fly ash-lime based biner at various lime dosage at different age (aging in normal conditions).

It can be seen that there is an increase in the strength of specimen as function of lime addition until 20%, then it decreased if we ignore 15% CaO content which is probably an accidental measuring mistake. Strength decrease might be explained with CaO hydration to $Ca(OH)_2$, which caused volume change (expansion) and increased heat generation leading to shrinkage cracks. The specimens without lime addition were very weak (< 0.5 MPa) as expected. At the age of 7 days the highest compressive strength was found in the case of 10 % CaO dosage. The absolute maximum strength reached after 28 days with 20% lime addition (15.6 MPa). It is important that the strength started to decrease at 56 days in almost every case. Probably it can be explained with the changing aging conditions, mainly humidity variation. Since the water evaporated from the binder resulted in insignificant amount of water for the hydration reaction which obstructed the C-S-H formation. Based on the above results 20% CaO was added to the alumino-silicate phase in the following tests.

Effect of GBFS on the fly ash – lime binder

In these experimental series a given proportion of fly ash (25, 50, 75 and 100 m/m%) was replaced with GBFS ground for 5 min (~8000 cm^2/g). Additionally, 20m/m% $Ca(OH)_2$ was added to the paste as chemical activator. (The previously tested CaO was changed to $Ca(OH)_2$ in order to decrease heat generation). The compressive strength results are shown in Figure 8 and 9. The aging of these specimens was carried out under normal laboratory conditions too, so circumstances were varied (humidity, temperature).

It can be seen clearly in Figure 8 that the strength decreased when GBFS was added to the fly ash –lime based paste when 15.5 MPa was detected after 28 days.

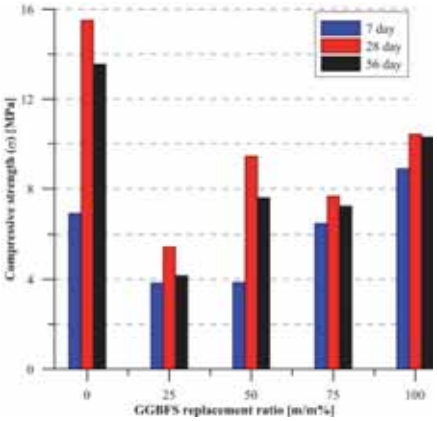

Figure 8. Compressive strength of fly ash-lime binder as a function of GBFS content (aging in normal conditions).

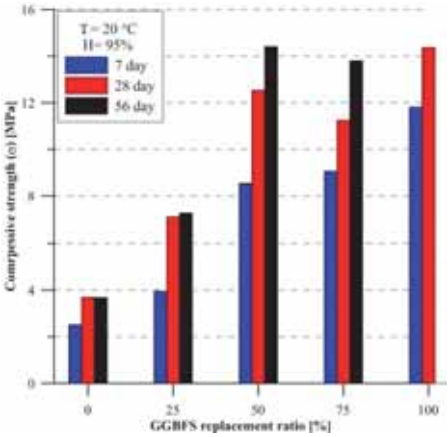

Figure 9. Compressive strength of fly ash-lime binder as a function of GBFS content (aging in humidity chamber).

On the other hand the strength increased continuously as function of GBFS content from 25% up to 100% (11.7 MPa). A similar phenomenon was appeared as experienced before, namely water evaporated from binder during aging after 28 days being unsatisfied amount of water for pozzolanic reaction. Normal conditions of aging were 20 ^{o}C temperaute and 50...60% rel. humidity.

To avoid this side effect of changing conditions the following aging was performed in a humidity chamber. In this way the appropriate humidity for hydration could be satisfied, namely 20 ^{o}C and 95% rel. humidity. The compressive strength results are found in Figure 9.

The compressive strength of specimen consisting of only fly ash and lime aged in humidity chamber reduced compared to that of aged at the normal conditions. However, the strength of GBFS bearing specimens (25, 50, 75 and 100%) increased due to the appropriate conditions for hydration, i.e. high humidity and constant temperature. Additionally, in the case of the specimens aged at normal conditions the strength decreased at 56 days, while that of the aged in humidity chamber increased. The highest strength of specimen reached 14.4 MPa made of 50% fly ash. The specimen prepared from only GBFS and lime were disintegrated probably due to the shrinkage.

4. Conclusions

Based on the results of the experimental investigation the following conclusions can be drawn. Mechanical activation in stirred media mill increased significantly the reactivity of fly ash. However, there is no correlation between material fineness and reactivity. Strong correlation was found between lime adsorption capacity of mechanically activated fly ash and compressive strength made of it. Optimal lime and GBFS content was determined. Maximum compressive strength was 15.6 MPa.

5. Acknowledgments

The research work was supported by the János Bolyai Research Scholarship of the Hungarian Academy of Sciences (MTA) performed in the Centre of Excellence in Sustainable Natural Resource Management at the Faculty of Earth Science and Engineering, University of Miskolc. The authors greatly appreciate the mineralogical investigation for the Institute of Mineralogy and Geology.

References

[1] Kumar, R., Kumar, S., Mehrotra S. P., Towards sustainable solutions for fly ash through mechanical activation. Resources, Conservation and Recycling 52 (2007) 157-159.
[2] Kumar, R., Kumar, S., Badjena, S., Mehrotra, S. P., Hydration of Mechanically Activated Granulated Blast Furnace Slag, Metallurgical and Materials Transactions B 36 (2005) 873-883.
[3] Mucsi, G., Csőke, B., Gál, A., Szabó, M., Mechanical activation of lignite fly ash and brown coal fly ash and their use as constituents in binders. Cement International 7 (2009) 76-85.
[4] Juhász, A. Z., Opoczky, L., Mechanical Activation of Minerals by Grinding. Ellis-Horwood Ltd. Publishers. Budapest – Chichester, 1990
[5] Baláz, P., Extractive metallurgy of activated minerals, Elsevier, Amsterdam, 2000, p. 278.
[6] Mucsi, G., Gombkötő, I., Molnár, Z., Török, V., Móricz, F., Mechanical activation by grinding and classification of fly ash to enhance its reactivity. Balkan Mineral Processing Congress. Belgrade, Serbia, (2015) 931-937.
[7] CK HSZ 4706-2 Standard. Cement additives. Natural pozzolic materials (trasses). (In Hungarian)

International RILEM Conference on Materials, Systems and Structures in Civil Engineering
Conference segment on Service Life of Cement-Based Materials and Structures
22-24 August 2016, Technical University of Denmark, Lyngby, Denmark

MODELLING OF AGEING OF LOW-PH CONCRETES

Laurie Buffo-Lacarrière [(1)], Youssef El Bitouri [(1)], Alain Sellier [(1)], Xavier Bourbon [(2)]

(1) Université de Toulouse, UPS, LMDC (Laboratoire Matériaux et Durabilité des Constructions), France
(2) ANDRA, Châtenay-Malabry, France

Abstract
A model of chemo-mechanical evolution of new cementitious materials such as low-pH cements is described. The proposed phenomenological model, usable at structure scale, is based at early age on a multiphasic hydration developed for blended cements. At higher ages, the evolution of mechanical properties of such binder with high silica content cannot be explained by pozzolanic reaction (because portlandite is entirely consumed at early ages). At these ages, mineralogy analyses showed that the hydration of remaining anhydrous silica oxide is still developing by consumption of calcium from hydrates with high C/S ratios (for instance C-S-H produced by clinker hydration at early age). These chemical evolutions are modeled taking into account chemical equilibrium of solution and solid phases in terms of calcium concentration. The impact on mechanical properties is then also predicted. Finally the chemo-mechanical model is applied on the prediction of mechanical behavior of nuclear waste storage structures casted with low pH based concrete.

1. Introduction

One of the main concerns in the context of deep geological disposal of radioactive waste is that all elements of the storage structure (clay barrier and concrete) should maintain their confinement properties. To meet this requirement, the concrete used must satisfy certain criteria. For example, in order to reduce chemical interactions with clay, the pH of the pore solution of the concrete must not exceed 11 [1]. These requirements have led to the use of special binders called low-pH cements [2,3,4]. The principle of formulating these binders is based on a "key" parameter. To obtain a pH less than 11, it is necessary for the total equivalent silica content of the binder to exceed 50% by mass [5]. After the initial fast hydration process, the surplus silica progressively reacts with the high calcium C–S–H to form more low calcium C–S–H [6]. The stoichiometry of hydrates will therefore vary depending on the reaction of the silicate in the anhydrous phases.

For a better prediction of the chemical and then mechanical properties of these ternary binder based concrete, modelling of the stoichiometry variation during hydration was needed.
In this paper, a phenomenological approach is used and hydration development and its consequences are predicted using a two-step model. At early age, an existing multiphase hydration model is used [7,8]. This model is well suited to the prediction of early age chemo-mechanical behaviour because it takes account of coupling between hydration development and water and temperature variations (which are needed to predict the strains that develop at early age in concrete in endogenous conditions). But this model assumes fixed stoichiometry for the hydrates produced by clinker and pozzolanic additions (such as silica fume). Consequently, it is not able to reproduce the long-term chemical evolutions observed in low-pH cement (hydration of silica fume and variation of C/S ratio in C-S-H). This is why, after 28 days (an arbitrarily chosen time, short enough for chemical evolutions to be considered as still negligible but long enough for the short-term reactions of hydration to be considered as relatively stabilized), a new model is proposed, which takes the long-term stoichiometry variation into account.

2. Chemical evolution model after 28 days

2.1 Presentation of chemical evolution model

The model assumes that the evolution of calcium concentration alone in the liquid phase describes the chemical evolution of cement-based materials in the context of external calcium exchange (decalcification) [9-12] or of internal calcium exchange between the solid phases.

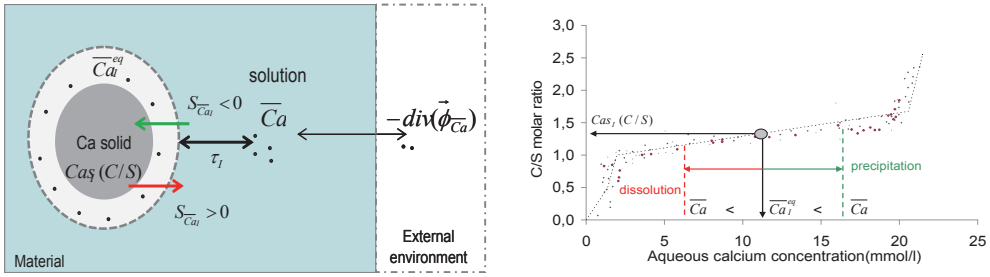

Fig. 1 : Principle of the internal reequilibrium of calcium

Local internal calcium exchange is due to a disequilibrium between the calcium content of the interstitial solution just around the solid phase $\overline{Ca}_I^{eq}$ (which is equilibrated with the solid phase following the local equilibrium diagram) and the calcium in the pore solution $\overline{Ca}$. These local exchanges are represented, at macroscopic scale, in the mass balance equation (eq. 1) by a source of calcium for each solid phase I (given in the following equation)

$$\frac{\partial(w\overline{Ca})}{\partial t} = -div(\vec{\phi}_{\overline{Ca}}) + \sum_I S_{\overline{Ca}_I} \quad (1)$$

In eq (1), w is the water content and $\vec{\phi}_{\overline{Ca}}$ is the macroscopic calcium flow (in the case of a concentration gradient at macroscopic level).

The sink term $S_{\overline{Ca}_I}$ is calculated for each solid phase following the kinetics of dissolution/precipitation induced by local disequilibrium in the aqueous calcium content which occurs when the global calcium concentration in solution is lower than the equilibrium concentration.

$$S_{\overline{Ca}_I} = \frac{1}{\tau_I}\left(\overline{Ca}_I^{eq} - \overline{Ca}\right) \tag{2}$$

The equilibrium concentration $\overline{Ca}_I^{eq}$ is controlled by the equilibrium diagram for silicate phases such as C-S-H and depends on the C/S of the phase. For calcium oxide in the anhydrous clinker and slag, and in portlandite, it occurs if the calcium concentration is less than 22 mmol/l. For aluminates (AFm and AFt), we assume that the dissolution of their solid calcium occurs progressively between 19 and 2 mmol/l.

The characteristic time τ_I describes the delay of dissolution/precipitation reactions due to the micro-diffusion of calcium [13]. This micro-diffusion, like diffusion at macro scale, is affected by the water content and the temperature. But it is also affected by the ability of calcium and water to move through the hydrates to reach anhydrous phases. The characteristic time is thus defined as follows:

$$\tau_I(t) = \tau_{28} \cdot g(w) \cdot h(T) \cdot f_I^i\left(\frac{C}{S}\right) \tag{3}$$

In this equation, τ_{28} is a characteristic time calculated analytically in order to respect the continuity of the hydration kinetics at 28 days (given by the multiphase short-term hydration model).

The function g(w) and h (T) reflect the influence of water content and temperature on micro-diffusion process (related to the kinetic at 28 days).

$$\mathrm{g(w)} = \frac{\mathrm{w}_{28}}{\mathrm{w}} \text{ and } h(T) = \exp\left(\frac{\mathrm{E_d^a}}{\mathrm{R}}\left(\frac{1}{T} - \frac{1}{T_{28}}\right)\right) \tag{4}$$

The function f describes the water accessibility to anhydrous material (clinker or slag). In fact, this accessibility can be affected by the formation of a new layer of hydrates surrounding the anhydrous phases.

$$f_I^i\left(\frac{C}{S}\right) = \exp\left(\mathrm{k_0^i} \times \int \frac{\partial}{\partial t}\left(\frac{C}{S}\right)\, dt\right) \tag{5}$$

For anhydrous phases (clinker and slag), this function, initially equal to 1, increases progressively as the connection to the pore solution of new layers of hydrates created on the surface is reduced. On the other hand, for hydrates (present at 28 days), it is assumed that this new layer does not change their initial accessibility significantly and keeping the function f equal to 1 is therefore an acceptable approximation. Reactions of anhydrous phases are thus delayed by the effect of this new layer, except for the silica fume, for which the function f is also kept equal to 1. As its specific surface area is higher than that of clinker and slag, the silica fume, if it is well dispersed, is mixed with hydrates. We consequently consider that the function f concerns only residual anhydrous components of clinker and slag.

To take the effect of the new layer of hydrates (formation of C-S-H) into account, the function f evolves according to the increase of the progressive hydration of silicate present in the

clinker and slag remaining at 28 days. As the water accessibility is managed by diffusion, an exponential function is chosen [7,8]. As the hydration progresses with the quantity of calcium bound in the new C-S-H created, the function is expressed according to the C/S ratio of new C-S-H (with a fitting parameter k for each phase).

2.2 Definition of a mean degree of hydration for mechanical property evolution

In the case of blended cements, it is impossible to separate the contribution of the cement clinker and the additions to the development of mechanical properties, because they react together. A simplified approach consists of modelling the evolution of the mechanical properties with empirical laws by using a global variable for hydration. It should be noted that a homogenization approach [14,15] is also suitable for predicting the evolution of mechanical properties during hydration but it is not easy to implement in the case of binder with low cement content because the mechanical properties of the great variety of hydrates created during the long-term chemical evolution are not known. So, the approach based on empirical laws [16] has the advantage of simplicity.

Concerning ternary binders, the definition of a global degree of hydration is needed. The chemical evolution model predicts the formation of new C-S-H by the progressive calcification of the unhydrated silicate and the decalcification of hydrates present at 28 days. The new C-S-H formed after 28 days will contribute to the densification of the material and increase its cohesion. On the other hand, for the sake of simplicity, the moderate decalcification of phases having a high C/S ratio at 28 days is assumed not to affect the mechanical performance significantly (because, even with a low C/S, C-S-H remains a cohesion factor [9]). To take these considerations into account, a mean degree of hydration($\overline{\alpha}$) is defined as follows (eq. 5):

$$\frac{\partial \overline{\alpha}}{\partial t} = \frac{1}{Ca^{total}} \sum_J \frac{\partial Ca_{S_J}}{\partial t} \quad \text{and} \quad \frac{\partial Ca_{S_J}}{\partial t} = \underbrace{\frac{C}{S_J} \frac{\partial S_J}{\partial t}}_{a} + \underbrace{S_J \frac{\partial}{\partial t}\left(\frac{C}{S_J}\right)^+}_{b} \tag{5}$$

where:

- Ca^{total} is the total calcium content of the binder (mol/m3 of material),
- Ca_{S_J} is the calcium content of the hydrated siliceous phases J (C-S-H) (mol/m3 mat.).
- S_J is the molar content of hydrated siliceous phases (C-S-H) or unhydrated siliceous phase (remaining anhydrous silica fume for instance) (mol/m3 of material),
- $\frac{C}{S_J}$ is the C/S molar ratio of the siliceous phase J (C/S starts >0 for C-S-H present at 28 days and from 0 for anhydrous silicate which will become the new C-S-H after 28 days),
- The symbol + means that only the calcification of the silicate is taken into account.

3. Application to a low pH cement

3.1 Evolution of mineral composition of hydrates

An experimental programme was carried out on a ternary binder (formulated to obtain a low pH in the interstitial solution) named T^L containing 20% of Portland cement, 33% of silica fume and 47% of blast furnace slag [13] (Table 1).

Table 1: Chemical composition (% weight) for the main oxides of binder constituents

	CaO	SiO_2	Al_2O_3	Fe_2O_3	MgO
CEM I	67.3	22.1	3.19	2.27	0.6
Silica fume	0.5	95	<0.2	0.1	<0.2
Blast furnace slag	44	36.4	10.7	0.41	7.25

The characteristic time τ_{28} is calculated analytically in order to respect the continuity of the hydration kinetics at 28 days and the parameter k_0^i , which controls the long-term kinetics, is estimated from the evolution of the aqueous calcium concentration.
The result of the fitting is presented in Fig. 10, where the triangles represent experimental results found by Bach [9] and the curve in red is the calibration result for fitting parameters k0 (slag and clinker). The other curves highlight the influence of the fitting parameter k0 for slag. The characteristic time at 28 days is directly identified using the results of the hydration model in order to ensure kinetic continuity between the two models. The only fitting parameters are k0 for clinker and slag (Fig. 2). The water content and the temperature at 28 days are also given by the hydration model.

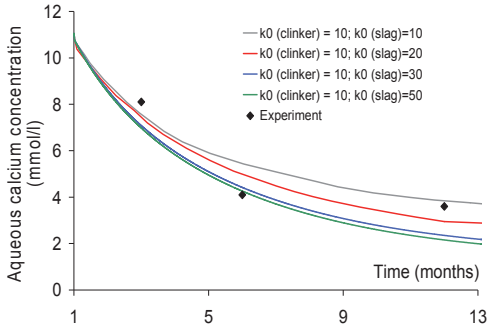

Parameters identified to ensure continuity with hydration model		
w_{28}	T_{28}	τ_{28}
0.46 m^3/m^3	293 K	11 hours

Fitting parameters	
k_0 *(clinker)*	k_0 *(slag)*
10	20

Fig. 2 : Evolution of aqueous calcium concentration (mmol/l) for low pH cement TL and model parameters

The main variable of the chemical evolution model is the calcium bound in solid phases. It is the variable used to characterize the mechanical evolution of the binder with time in the model, but, for comparison with the histograms obtained experimentally, the results can also be expressed in terms of evolution of C/S ratios of siliceous solid phases. In the model, for hydrates of each silicate, we considered only the mean C/S ratio of the total quantity of the phase. To ease comparison with the histogram envelope identified in section 2, we distributed this mean C/S using normal laws. For each group (for TL binder we managed 6 silicate phases: 3 C-S-H produced by short term hydration of clinker, silica fume and slag, and 3 new C-S-H produced by complementary hydration of silicate in the remaining anhydrous phases), a standard variation around 0.05 was used. The mode weight associated with each mean C/S was the fraction of the corresponding solid phase calculated by the model. The histogram envelopes obtained are compared with the experimental ones in figure 2.
The model qualitatively reproduces the mineralogical evolution of paste between 3 and 9 months. A small proportion of the differences between experimental and model results can be

explained by the fact that silicate anhydrous phases in clinker and slag are artificially separated in the model into pure calcium (with infinite C/S) and pure silica (with C/S of zero at 28 days). A part of the phases included in group 1 for model results is thus seen in group 2 for experimental results (slag particles with a mean C/S around 1.2).
But the main cause of the difference is the smoothing of the distribution by the experimental procedure (volume interaction of EDS and incapacity to "see" pure silica fume due to its small size). The experimental distribution covers a lower range of C/S and exhibits larger modes (because the result of 1 measurement is the mean of several species).
Thus a quantitative validation of EDS analyses is not possible. As the chemical evolution model is designed to predict the evolution of the mechanical properties of these specific binders, the quantitative validation was performed on the mechanical properties.

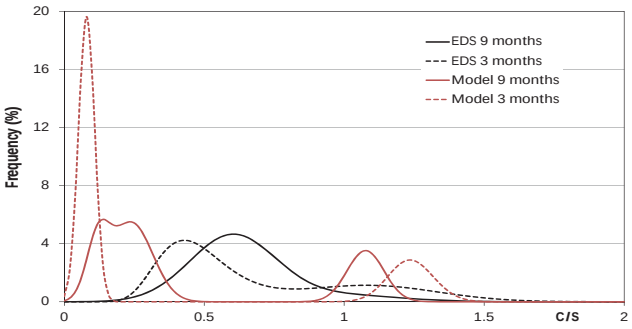

Fig. 3 : Distribution of C/S ratio at 3 and 9 months (model ad EDS results)

3.2 Evolution of mechanical properties

To determine how the mechanical properties changed during chemical evolution (short-term hydration and complementary hydration after 28 days), the following empirical laws proposed in [16] were used:

$$X_i(\bar{\alpha}) = X_{ith}\left(\frac{\bar{\alpha}(t)-\bar{\alpha}_p}{1-\bar{\alpha}_p}\right)^{k_i} \quad (6)$$

- $\bar{\alpha}$ is the mean degree of hydration previously defined according to the calcium content of solid phases by equation 5,
- R_{cth}, R_{tth} and E_{th} are, respectively, the theoretical compressive strength, tensile strength and Young modulus reached if $\bar{\alpha}=1$,
- $\bar{\alpha}_p$ is the mean degree of hydration that corresponds to the mechanical threshold for percolation (calibration parameter identical for all mechanical properties considered),
- k_c, k_t and k_e are the calibration parameters identified using the mechanical experiments performed by Leun Pah Hang et al. [17] from casting to 28 days.

Table 2: Parameters of De Schutter laws identified from 0 to 28 days.

	Xith	ki	$\bar{\alpha}_p$
R_c	130 MPa	1	
R_t	7.2 MPa	1	0.13
E_t	55 GPa	0.5	

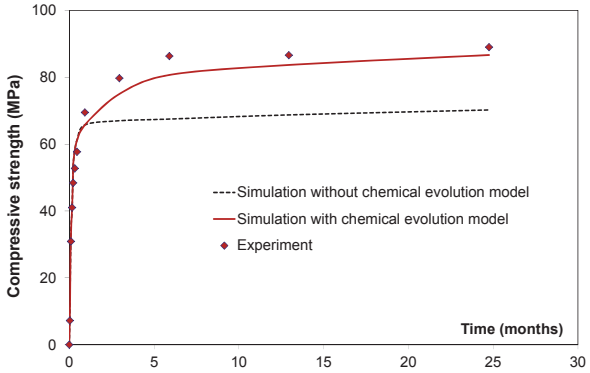

Fig. 4 : Evolution of compressive strength along hydration from (0 to 2 years)

In order to validate the chemical evolution model, we simulated the evolution of compressive strength after 28 days using the parameters identified up to 28 days. Figure 3 clearly shows that the chemical evolution model (used instead of the short-term hydration model after 28 days) allows the evolution of mechanical properties to be better taken into account by predicting a higher hydration degree after 28 days (even with mechanical parameters fitted only on the 28 first days). The knowledge of how the mechanical properties of the ternary concrete T^L change during chemical evolution was subsequently used to calculate the risk of a structure element cracking during the first three months after casting.

3.3 Applicability at structural scale (radioactive waste storage structure)

The models presented were used to assess the risk of cracking of a massive structure. The cracking risk studied was due to the temperature rise during the hydration. The structure studied was the sealing system of the nuclear waste disposal structure (figure 4).

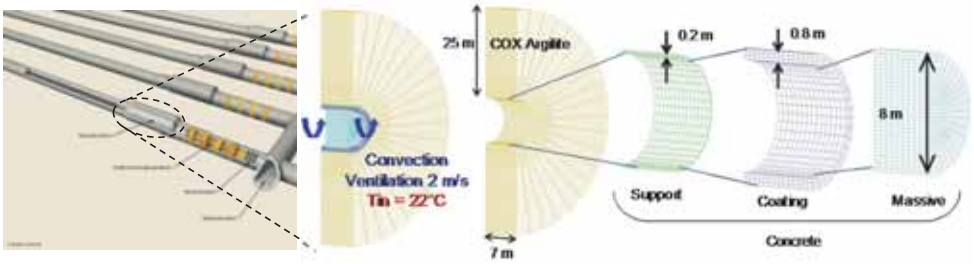

Fig. 5 : The nuclear waste disposal structure (sealing system)

The storage structure is located 500 m deep in Callovo Oxfordian argillite. It consists of a 20-cm-thick support wall implemented just after excavation, an 80-cm-thick coating wall implemented 6 months after excavation, and a massive containment wall implemented 100 years after excavation. Given the massive nature of the latter, the technical implementation could have a significant impact on the temperatures developed during hydration, and hence

the thermal strains induced at early age. The option considered here is progressive vertical casting (from bottom to top) in 24 hours. To forecast the temperature in the structure, not only the concrete but also the soil had to be modelled, as heat transfers by conduction are allowed between the two materials and can significantly modify the temperature field. The concrete used to cast this massive structure was chosen, among other reasons, for its low heat release. It is based on the ternary cement studied in the previous sections.

Table 3: Formulation of concrete used in the sealing system concrete structures

	CEM I	SF	Slag	Gravel	Sand	Effective water
Content (kg/m3)	76	123	180	949	855	152

To simulate the behaviour of the structure, the timing of the implementation of the various elements (support, coating and containment) was taken into account using a latency time.
This latency time, defined previously by Kolani [18] to represent the delay effect induced by certain super-plasticizers (retarders) on cement hydration, was used as a numerical tool to delay casting in this study. The idea was to block the hydration of the element, as the latter had not been set up. This avoided having to resort to a complex mesh of the structure.
For the calculation of the storage structure, the "short-term" hydration model and the "long-term" chemical evolution model were used to predict the development of the concrete hydration. Then, using the chemo-mechanical coupling, a mechanical model was used to assess the risk of cracking due to the consequences of chemical evolution (heat release and variations in mechanical properties).The mechanical model previously developed by Sellier et al. [19,20] was used. This model consists of a rheological model for delayed strains (creep, shrinkage) coupled with an orthotropic damage model. The calculations on the structure were performed by implementing the model in the 3D finite element code CASTEM2012 [21].

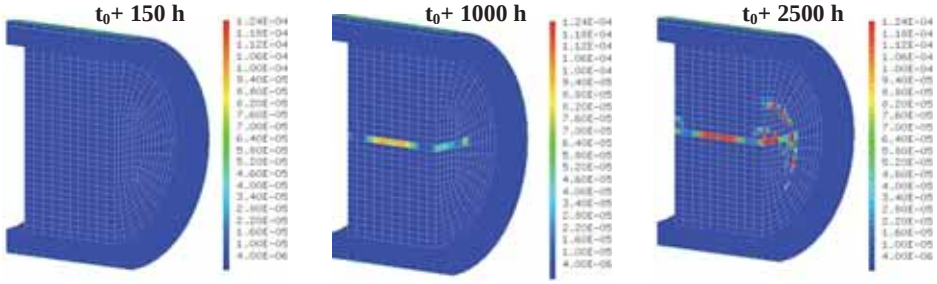

Fig. 6 : Temperature variations for different points of the structure

Figure 6 shows the crack opening field. During the temperature rise phase, the dilation of the core of the massive wall is blocked by the boundary conditions. This leads to a system of stresses characterized by compressive stresses on the core of the massive block, and tensile stresses on the surfaces. But, as shown on figure 6 at 150h, these stress system does not lead to the occurrence of opened cracks. In contrast, the stress distribution is reversed during the cooling phase, when the contraction of the core of the massive block is blocked by the edges. Such blocking of the contraction of the core of the massive block could lead to the initiation

of a localized crack as shown in figure 6 at 1000h. The crack first occurred at core around 100 hours after casting (with a maximal crack opening of 100 microns). A way to avoid this crack would be to optimize the casting process, in order to limit the temperature rise and so prevent thermal shrinkage gradients. This optimization could be performed by Andra using the proposed models.
The crack is then slowly evolving (it reaches 120 microns 2500 hours after casting). This justifies the necessity of a good prediction of the mechanical properties of such specific binders after 28 days (672 hours), because even if the temperature does not evolves too much in this period, the evolution of mechanical properties is not negligible and drives the evolution of crack opening during this period.

4. Conclusions

A model predicting the hydration development of low-pH cements has been proposed. It assumes that the micro-diffusion of calcium plays a major role in explaining how the different C/S ratios of initial C-S-H all tend towards a medium stabilized value. This model predicts the long-term hydration development. It is used beyond 28 days, and before that instant, the short-term hydration development is predicted by the multiphase hydration model previously proposed by Buffo-Lacarrière et al. [7]. The proposed complementary model can predict the residual silicate hydration observed with the EDS-analysis. A hydration degree adapted to this type of cement was then defined. This variable was useful to consider the evolution of mechanical properties during hydration from short (<28 days in our case) term to long term. The prediction of the evolution of mechanical properties after 28 days shows that the chemical evolution model is needed for this kind of highly substituted binders, which exhibit a significant increase of mechanical properties at higher ages than clinker cement based concretes.

Acknowledgements
The authors acknowledge the technical and financial support of ANDRA (Agence Nationale pour la gestion des Déchets RadioActifs).

References

[1] ANDRA, 2005 Report on Clay—Evaluating the Feasibility of a Geological Repository in Clay Formation, ISBN: 2-951-0108-8-5, 2005, p. 238.
[2] Codina M., Cau-dit-Coumes C., Le Bescop P., Verdier J., Ollivier J.P., Design and characterization of low-heat and low-alkalinity cements. Cement and Concrete Research 38 (2008), 437-448.
[3] Gray M.N., Shenton B.S., For better concrete, take out some of the cement, Proc. 6th ACI/CANMET Symposium on the Durability of Concrete, Bangkok, Thailand, May 31 to June 5 (1998).
[4] Fries T., Weber H., Wetzig V., Low-pH shotcrete field tests on apalinus clay samples. R&D on low-pH cement for a geological repository, 3rd workshop Paris, June (2007), 13-14.

[5] Cau-Dit-Coumes C., Courtois S., Nectoux D., Leclercq S., Bourbon X., Formulating a low-alkalinity, high-resistance and low-heat concrete for radioactive waste repositories, Cement and Concrete Research 36 (2006), 2152-2163.
[6] Lothenbach B., Scrivener K., Hooton R.D, Supplementary cementitious marterials, Cement and Concrete Research 41 (2011), pp. 1244-1256.
[7] Buffo-Lacarrière L., Sellier A., Escadeillas G., Turatsinze A., Multiphasic finite element modeling of concrete hydration, Cement and Concrete Research 37 (2007), pp. 131-138.
[8] Kolani B., Buffo-Lacarrière L., Sellier A., Escadeillas G., Boutillon L., Linger L., Hydration of slag-blended cements, Cem. and Conc. Comp. 34 (2012), pp 1009-1018.
[9] Gérard B., Contribution des couplages mécanique-chimie-transfert dans la tenue à long terme des ouvrages de stockage de déchets radioactifs, PhD thesis, ENS Cachan, Paris, France, and Université de Laval, Québec, Canada (1996), 373p.
[10] Mainguy M., Tognazzi C., Torrenti J. M., Adenot F., Modelling of leaching in pure cement paste and mortar, Cement and Concrete Research 30 (2000), pp. 83–90.
[11] Gawin D., Pesavento F., Schrefler B., Modeling deterioration of cementitious materials exposed to calcium leaching in non-isothermal conditions, Computer Methods in Applied Mechanics and Engineering 198 (DOI :10.1016/j.cma.2009.05.005) (2009), 3051–3083.
[12] Buffo-Lacarrière L., Sellier A., Chemo-mechanical modeling requirements for the assessment of concrete structure service life, Journal of Engineering Mechanics 137, American Society of Civil Engineers (2011), N°9, pp. 625-633.
[13] El Bitouri Y., Buffo-Lacarrière L., Sellier A., Modelling of chemo-mechanical behaviour of low pH concretes, Cement and Concrete Research 80 (2016), pp. 70-80.
[14] Bernard O., Ulm F.J., Lemarchand E., A multiscale micromechanics-hydration model for the early age elastic properties of cement-based materials, Cement and Concrete Research 33 (2003), pp. 1293-1309.
[15] Torrenti J.M., Benboudjema F., Mechanical threshold of cementitious materials at early age, Materials and Structures 38, n°277 (2005), pp. 299-304.
[16] De Schutter G., Taerwe L., Degree of hydration based description of mechanical properties of early age concrete, Materials and Structures 29 (1996), pp. 335-344.
[17] Leung Pah Hang T., Verdier J., Vidal T., Buffo-Lacarrière L., Bourbon X., Hydration and properties of low pH concrete.Consec13, Nanjing, China (2013)
[18] Kolani B., Comportement au jeune âge des structures en béton armé à base de liants composés aux laitiers, PhD thesis, Université de Toulouse, France (2012), 282 p.
[19] Sellier A., Multon S., Buffo-Lacarrière L., Vidal T., Bourbon X., Camps G., 2016, Concrete creep modelling for structural applications: non-linearity, multi-axiality, hydration, temperature and drying effects. Cem. and Conc. Res., Vol. 79, pp. 301-315
[20] Sellier A., Casaux-Ginestet G., Buffo-Lacarrière L., Bourbon X., Orthotropic damage coupled with localized crack reclosure processing, Part I: Constitutive laws, Engineering Fracture Mechanics 97 (2013), pp. 148-167.
[21] Commissariat à l'Energie Atomique CEA, web page: http://www-cast3m.cea.fr/

International RILEM Conference on Materials, Systems and Structures in Civil Engineering
Conference segment on Service Life of Cement-Based Materials and Structures
22-24 August 2016, Technical University of Denmark, Lyngby, Denmark

CHLORIDE PENETRATION COEFFICIENT AND FREEZE-THAW DURABILITY OF WASTE METAKAOLIN CONTAINING HIGH STRENGTH SELF-COMPACTING CONCRETE

Girts Bumanis [(1)], Diana Bajare [(1)]

(1) Riga Technical University, Department of Building Materials and Products, Institute of Materials and Structures, Latvia

Abstract
Traditional ordinary concrete testing methods are still applied to characterize self-compacting concrete (SCC). This allows comparing properties of two types of concrete, however, the efficiency of such testing methods is still under question due to superior properties of SCC. In the present research high strength SCC using metakaolin containing waste as partial cement replacement was created and its durability characterized. Constant amount of water was used in all mixtures and workability (>600 mm by cone flow) was ensured by changing the amount of superplasticizer. The compressive strength was tested at the age of 7, 28 and 180 days. The chloride penetration was tested according to NT BUILD 492 and freeze-thaw test was performed according to LVS 156-1:2009 annex C respectively. The compressive strength of SCC at the age of 28 days was from 68-70 MPa. The results indicate that the chloride penetration test method NT BUILD 492 is a fast and progressive test method which could effectively characterize SCC, while freeze-thaw resistance test of SCC could take up to 6 months to reach 150 freeze-thaw cycles using 5% NaCl solution as de-icing solution for concrete specimens and more rapid and reliable testing method should be used instead.

1. Introduction

Chloride penetration coefficient and freeze-thaw resistance of concrete could affect service life of concrete structures which are exposed to marine environment as well as in road infrastructure, where salty water is present and together with freezing and thawing could cause significant deterioration of the concrete [1]. Industries working under such conditions are continuously demanding improved construction durability in these conditions. Well known ordinary concrete (OC) has proved that durability of such concrete provides an average performance; therefore new concrete types and production methods are introduced [2]. Chicker et. al. indicated that W/C and silica fume content are the main parameters affecting the durability results of chloride penetration depth of the ordinary and self-

compacting concrete (SCC) and in general SCC mixes presented better durability results compared to OC [3]. This gives significant advantage of using SCC instead of OC not only because of high durability results but also due to the fact that improved workability of SCC reduces construction costs. SCC is associated with high binder and chemical admixture volumetric content; therefore there have been attempts to produce SCC with high volumes of supplementary cementitious materials such as silica fume or metakaolin to make SCC cost-effective and more durable [4]. Ganesh et. al has detected that rapid chloride penetration, water sorptivity and water absorption durability of high strength concrete can be improved by replacing cement with nanosilica by up to 2wt.% [5]. Using metakaolin high performance concrete can be obtained having higher resistance to sulphuric acid comparing to the reference mix [6].

In addition, metakaolin proves to be one of the most effective among available natural pozzolanic materials because metakaolin reactivity is 1050 mg $Ca(OH)_2$/g pozzolan compared to 427 g of silica fume and 875 g of fly ash respectively [7]. The incorporation of metakaolin in concrete mixture usually reduces workability of conventional concrete; however, if it is compared to silica fume additive, metakaolin requires from 25 to 35% less superplasticizers [8]. Ouyang et al. has reported that optimal amount of cement replacement with metakaolin was 15% and this could lead to 20% improvement of compressive strength; however, superplasticizers must be used to ensure workability of mortar replacing cement by metakaolin [9].

Metakaolin can be obtained by the endothermic reaction of kaolin as dihydroxylation of kaolin begins at 450 °C and continues up to 900 °C and amorphous metakaolin $Al_2Si_2O_7$ is obtained when exceeding 925 to 950 °C. The metakaolin transforms to spinel $Si_3Al_4O_{12}$ and mullite at 1050 °C [10]. Not only metakaolin derived from naturally occurring minerals can be successfully used in concrete. An artificial kaolinite can be obtained by utilizing paper sludge coming from paper industry. By burning paper sludge at 700 to 800 °C metakaolin and calcium hydroxide can be produced which exhibit pozzolanic reactivity similar to commercially available metakaolin [11]. Metakaolin can also be derived from coal mining wastes which can contain up to 30% kaolinite and after its treating at high temperatures highly pozzolanic product can be obtained [12]. Radonjanin et al has reported that replacement of ordinary Portland cement with metakaolin by 10 wt.% gives compressive strength increase by 13% at 28 days and 9% at 90 days [13].

Metakaolin greatly affects the pore structure of concrete reducing the permeability and diffusion rates of harmful ions [14]. This factor could increase the durability of concrete. In cement pastes blended with 10 and 20% metakaolin reduced Cl^- concentration in pore solution was detected [15]. The incorporation of metakaolin in concrete mixture composition reduces the expansion of concrete maintained in 5% sodium sulfate solution [16]. The freeze-thaw resistance of cement mortar can be increased more than two times for mortar containing waste paper sludge metakaolin from 10 to 20 wt.% of cement compared to reference sample [17]. Metakaolin also turns out to be an alternative pozzolanic additive in ultra high performance concrete effectively replacing silica fume [18].

There is a wide range of tests for concrete evaluation under freeze-thaw initiated damage. Some of them are used to measure scaling from the concrete surface during rapid freeze-thaw cycles (2 cycles per 24h) but does not give any evaluation of concrete compressive strength change or cracking [19]. Other test methods measures concrete strength change during freeze-thaw cycles by testing sample compressive strength, mass changes or ultrasonic pulse velocity

(LVS 156-1:2009, annex C). Also solutions, where concrete samples during freeze-thaw cycles are stored, could be different, beginning from deionized water and ending up to 5% NaCl solution. The freezing temperature of test methods could be starting from -18 °C and reach -50 °C. These conditions determine number of cycles necessary to obtain concrete freeze-thaw resistance at standard conditions [20].
The chloride penetration of concrete structures could be detected by various testing methods. The most popular among them are: Salt Ponding Test, Bulk Diffusion Test, Rapid Chloride Permeability Test, Electrical Migration Techniques, Rapid Migration Test, Resistivity Techniques, Pressure Penetration Techniques, Indirect Measurement Techniques, Sorptivity and others. The rapid testing method should be used for testing durability of high performance SCC in order to perform test in short term and provide reliable results. If long term testing methods usually applied for OC will be adapted for SCC then the test duration could increase to unacceptably long period of time or give inadequate results.
In the present research durability of the high strength SCC with metakaolin containing waste was tested. Compressive strength, chloride migration coefficient and freeze-thaw durability were obtained.

2. Materials and methods

Self-compacting concrete (SCC) mixture composition was designed from locally available cement, gravel and sand. Cement CEM I 42.5 N produced by Cemex Ltd (Latvia) with Blaine fineness of 3787 cm^2/g was used. Natural washed gravel with fraction 4/12 mm was used as coarse filler and natural sand with fraction 0/4 mm was used as fine filler. Quartz sand with fraction 0/0.3 mm was used as microfiller to improve workability of SCC and avoid segregation of fresh mixture.
In the present research metakaolin containing waste by-product (MKW) from foam glass granule production plant "JSC Stikloporas" Ltd. (Lithuania) with fraction <0.355 mm was studied as pozzolanic material in SCC partially replacing cement. The MKW comes from foam glass granule production process where kaolin clay is used as a substance for anti-agglutination in the final stage of granule production. During production MKW was calcined at 850 °C for about 40-50 minutes. The X-ray diffraction (XRD) analysis of MKW is given in Fig. 1. A halo of amorphous metakaolin was detected in 2θ region from 15 to 30° and quartz (Q) was detected in XRD as impurity present in MKW. Also unreacted kaolin (K) was detected in the structure of MKW and small illite (I) and microcline (M) peaks were detected.
SCC mixture series were created with different amount of MKW as partial cement replacement, and mixture compositions are given in Table 1. Reference (Ref) mixture composition with cement content 500 kg/m^3 was created. Then cement was replaced from 5 to 15 wt.% with MKW (5%MKW, 10%MKW and 15%MKW). The water to cement and pozzolan (MKW) ratio (W/(C+P) was constant for all mixture compositions being 0.38. The workability of SCC remained constant by changing the amount of superplasticizer and SCC with cone flow remained >600 mm by adding additional amount of superplasticizer.

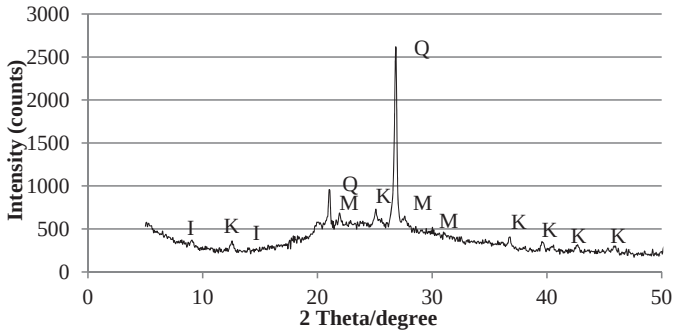

Figure 1. XRD pattern of metakaolin containing waste by-product (MKW). M – microcline, I – illite, K – kaolin, Q – quartz.

Table 1. Mixture composition of self-compacting concrete.

Compound	Amount (kg/m^3)			
	REF	5%MKW	10%MKW	15%MKW
Cement CEM I 42.5 N (Cemex)	500	475	450	425
Sand 0/4 mm	700	700	700	700
Quartz sand 0/0.3 mm	118	118	118	118
Gravel 4/12mm	908	908	908	908
Water	190	190	190	190
Superplasticizer Sikament 56	4.0	4.0	4.6	4.8
Metakaolin containing waste	0	25	50	75
W/C	0.38	0.40	0.42	0.45
W/(C+P)	0.38	0.38	0.38	0.38

The mixing procedure of SCC was carried out in a planetary drum mixer and included the following stages: all dry components were mixed together for 120 s to obtain homogenous mixture of dry components. Then half of the calculated amount water was added and mixing was continued for another 120 s. Then rest of water with superplasticizer was added and mixing was continued for additional120 s. Then density of fresh concrete was measured according to LVS EN 12350-6 and workability of SCC was tested according to LVS EN 12350-8. Samples were casted in 100x100x100 mm and 40x40x160 mm moulds for further investigations. Compressive strength was determined according to LVS EN 12390-3. Three specimens at every age were tested and average value with deviation calculated. Water absorption was tested by immersing the prismatic SCC specimens in water for 72h. The specimens were weighed and then dried in an oven at 80 °C to a constant weight for the following measurement of water absorption.

Durability of the chloride penetration for SCC was performed according to NT BUILD 492 (Fig. 2). Three specimens with Ø100 mm and height of 50 mm were created and tested.

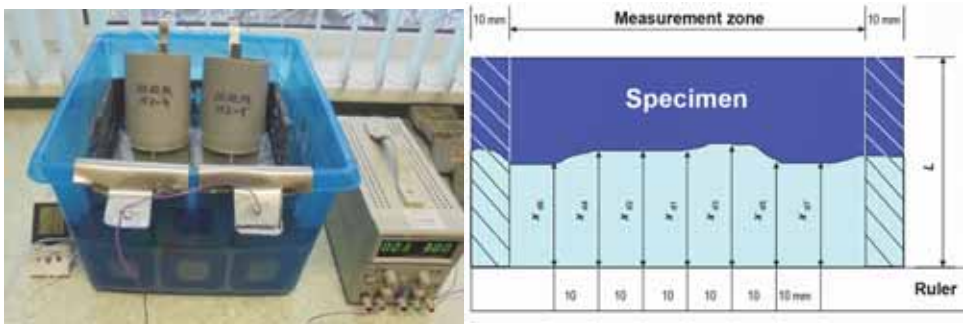

Figure 2. The experimental setup of the test to determine the depth of chloride migration coefficient and the illustration of measurement for chloride penetration depths.

The freeze-thaw test was performed according to Standard LVS 156-1:2009 annex C [20]. Six specimens of each series were tested. 5 % NaCl solution was used as deicing solution. All specimens were tested after 150 freeze-thaw cycles which is equal to 500 standard freeze-thaw cycles in deionized water. Strength reduction was calculated and the obtained result evaluated according to the Standard [20].

3. Results and Discussion

The properties of fresh SCC containing different amount of MKW as partial cement replacement are given in Table 2. The decrease of fresh SCC density was observed: from 2428 kg/m^3 for Ref to 2394 kg/m^3 for mixture composition with 15% of MKW as partial cement replacement (15%MKW). The partial cement substitution with MKW reduced workability to the level corresponding to data available in literature sources; therefore additional amount of superplasticizer should be used to retain the workability properties of SCC (see Table 1). Up to 20% more superplasticizer must be used to ensure workability >600 mm for SCC with 15% MKW as partial cement replacement. The flow time of fresh SCC increased from 25 to 34 seconds.

Table 2. Fresh self-compacting concrete properties.

Mixture design	Fresh concrete density, (kg/m^3)	Flow time, (s)	Cone flow diameter, (mm)
Ref	2430	25	630
5%MKW	2410	25	600
10%MKW	2400	23	680
15%MKW	2390	34	670

The compressive strength results of SCC are given in Fig. 3. The results indicate that SCC strength at 7 days was 56 MPa for Ref mixture and remained the same for 5% MKW and 10%

MKW (56 and 57 MPa) and reduced to 53 MPa for 15% MKW. The improvement of SCC particle packing provided by MKW and superplasticizer could retain the same strength at early age even replacing cement up to 10%, while the early age strength reduction is associated with slow rate of pozzolanic reactions and reduced amount of initial content of cement which lead to reduced compressive strength. At the age of 28 days compressive strength for Ref was 68 MPa while for mixture composition 15% MKW it increased to 70 MPa and for 5% MKW and 10% MKW it was 63 and 66 MPa respectively. Strength increase for SCC with MKW could be referred to the pozzolanic reactions. The increased amount of MKW provided higher compressive strength for SCC at the age of 28 days. The long term curing (180 days) lead to further strength increase. For Ref it was 79 MPa while for SCC with MKW it was from 71 to 74 MPa. The limitation of further strength increase was detected for SCC with MKW. This could be contributed to the reduced amount of cement in mixture composition and the pozzolanic reaction could be limited due to rapid strength increase at the age of 28 days.

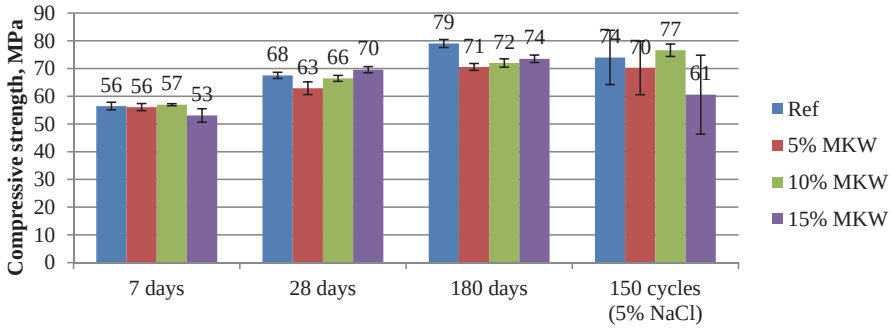

Figure 3. Compressive strength of self-compacting concrete with metakaolin containing waste as partial cement replacement at different ages and after 150 freeze-thaw cycles in 5% NaCl.

The durability of SCC was affected by the MKW content in the mixture composition. The freeze-thaw test indicates that 5% NaCl saturated SCC with 10% MKW can withstand up to 150 freeze-thaw cycles without mechanical or physical damage to the specimens. It was indicated that samples saturated with 5% NaCl after 150 freeze-thaw cycles reduced compressive strength for samples Ref, 5%MKW and 15%MKW (Fig. 3). The only series which retained the same strength and even gained strength was 10%MKW. The compressive strength increased to 77 MPa with acceptable standard deviation, while for other samples the strength deviation was not acceptable according to the Standard [20].
The chloride penetration test results are given in Table 3. Non-steady-state migration coefficient (D_{nssm}) indicates that incorporation of MKW in the mixture composition reduced D_{nssm} by 3.7 times compared to Ref. The test results indicate that SCC mixture composition 15%MKW could be evaluated as “very good” (D_{nssm} $<2\cdot10^{-12}m^2/s$) regarding to the resistance to chloride ingress while SCC with D_{nssm} $<8\cdot10^{-12}m^2/s$ has been evaluated as “good” resistance against chloride ingress [21]. The results for specimens Ref and 15%MKW after chloride penetration test are given in Fig. 4. The water absorption was from 3.3 to 3.5 wt.%

and open porosity from 7.6 to 8.2% and both slightly decreased by replacing cement with MKW, which could reduce the permeability of SCC and increase the durability.

Table 3. Chloride penetration test results of SCC (non-steady-state migration coefficient).

Mixture design	D_{nssm} [$10^{-12}m^2/s$]	Standard deviation
Ref	7.70	0.37
5%MKW	5.41	0.11
10%MKW	3.63	0.12
15%MKW	2.08	0.03

a) b)

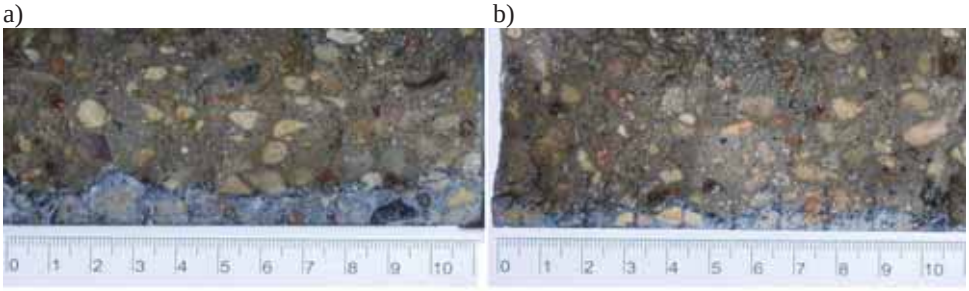

Figure 4. The depth of chloride migration according to NT BUILT 492 in reference (a) and SCC containing 15% metakaolin containing waste as partial cement replacement (b).

4. Conclusions

The reduction of workability should be taken into account if metakaolin containing waste products (MKW) are incorporated in self-compacting concrete (SCC) as partial cement replacement. By replacing cement with MKW from 5 to 15 wt.%, the amount of superplasticizer must be increased from 15 to 20% to ensure the proper mix flow. The strength index of SCC with MKW at the age of 28 days was from 93 to 103% compared to reference SCC (63 to 70 MPa). The durability against chloride penetration was increased more than 3.7 times which was detected by calculating non-steady-state migration coefficient (D_{nssm}7.70 $10^{-12}m^2/s$ for reference mix reduced to 2.08 for mixture with 15% MKW as partial cement replacement). Therefore NT BUILD 492 test method proved to be effective for testing and evaluating SCC chloride penetration durability. The freeze-thaw test results indicated that SCC durability up to 500 freeze-thaw cycles could be obtained by incorporating 10% of MKW as partial cement replacement. Using 5% NaCl solution as deicing fluid, according to Standard LVS 156:2009 annex C, the required number of freeze-thaw cycles could be reduced to 150 cycles which still takes a long period of time for performing this test due to capacity of 1 cycle per 24 h.

Acknowledgement

The research leading to these results has received the funding from the Latvian state research program under grant agreement "Innovative Materials and Smart Technologies for Environmental Safety, IMATEH" and COST Action TU1404 "Towards the next generation of standards for service life of cement-based materials and structures".

References

[1] Zhang, H. et al., Chloride penetration in concrete under marine atmospheric environment – analysis of the influencing factors, Struct Infrastruct Eng (2016), 1-11
[2] Bajare, D. et al., Coal Combustion Bottom Ash as Microfiller with Pozzolanic Properties for Traditional Concrete, Proc Eng 57 (2013), 149-158
[3] Chiker, T. et al., Sodium sulfate and alternative combined sulfate/chloride action on ordinary and self-consolidating PLC-based concretes, Constr Build Mater 106 (2016), 342-348
[4] Güneyisi, E. et al., Eco-Efficient Concrete. A volume in Woodhead Publishing Series in Civil and Structural Engineering (2013), 218-240
[5] Ganesh, P. et al., Effect of nanosilica on durability and mechanical properties of high-strength concrete, Mag Concr Res 68 (2016), 229-236
[6] Azevedo, F. et al., Properties and durability of HPC with tyre rubber wastes, Constr Build Mater 34 (2012), 186-191
[7] Asbridge, A. H. et al., Ternary Blended Concretes - OPC/ggbfs/metakaolin, Denmark Concr Accross Borders (1994), 547-557
[8] Caldarone, M. A. et al., High-Reactivity Metakaolin: A New Generation Mineral Admixture, Concr Int 16, (1994), 37-40
[9] Ouyang, D. et al., Increasing mortar strength with the use of activated kaolin by-products from paper industry, Constr Build Mater 25 (2011), 1537-1545
[10] Bellotto, M. et al., Kinetic study of the kaolinite-mullite reaction sequence. Part I: Kaolinite dehydroxylation, Phys Chem Miner 22 (1995)
[11] Pera, J. and Amrouz, A., Development of Highly Reactive Metakaolin from Paper Sludge, Adv Cem Based Mater. 7 (1998), 49-56
[12] Vigil De La Villa, R. et al., Use of coal mining waste as pozzolanic material in new blended cement matrixes in 16th European Conference on Composite Materials, ECCM (2014)
[13] Radonjanin, V. et al, Green recycled aggregate concrete, Con Build Mat 47 (2013) 1503-1511
[14] Sabir, B. et al., Metakaolin and calcined clays as pozzolans for concrete: a review, Cem Concr Compos 23 (2001), 441-454
[15] Coleman, N. J. and Page, C. L., Aspects of the pore solution chemistry of hydrated cement pastes containing metakaolin, Cem Concr Res. 27 (1997), 147-154
[16] Khatib, J. and Wild, S., Sulphate Resistance of Metakaolin Mortar, C.C. Res 28 (1998), 83-92
[17] Vegas, I. et al., Freeze–thaw resistance of blended cements containing calcined paper sludge, Constr Build Mater 23 (2009), 2862-2868
[18] Tafraoui, A. et al., Metakaolin in the formulation of UHPC, Con Bui Mat 23 (2009), 669-674
[19] Setzer, M. J. et al., TC 117-FDC: Freeze-Thaw and Deicing Resistance of Concrete (1995)
[20] LVS 156-1:2009 – Concrete, National annex of Latvian standard to European standard EN 206-1 - Part 1: Requirements for classification and attestation of conformity, Latvia (2009)
[21] Edvardsen, C. and Jepsen, M. T., Chloride migration coefficients from non-steady-state migration experiments at environment-friendly 'green' concrete," 2nd Int. Rilem Work. Test. Model. Chloride Ingress into Concr., 19 (2000). 203–209

International RILEM Conference on Materials, Systems and Structures in Civil Engineering
Conference segment on Service Life of Cement-Based Materials and Structures
22-24 August 2016, Technical University of Denmark, Lyngby, Denmark

AN INVESTIGATION ON USABILITY OF BASALT FIBRE IN CEMENT-BASED COMPOSITES

Şükrü Özkan[(1)], Emre Sancak[(1)], Fuat Demir[(1)]

(1) Suleyman Demirel University, Isparta

Abstract

In this work, instead of polivinyl (alcohol) (PVA) fibers, 9 different ECC samples were prepared by using basalt fibers in the range of 2% -6% by weight. Furthermore, ECC reference samples for comparison (M45) were manufactured. In the scope of this study, it was aimed to define the mechanical properties of the samples by performing flexural and compressive strength tests. According to mechanical testing results, it was observed that by increasing the amount of basalt fibers addition to a certain level while keeping the amount of other minerals and additives constant, the bending rigidity and compression strength capacity can be enhanced. It was also recorded that ECC materials containing a varying ratios of basalt fibers, 4%, 4.5%, 5%, 5.5%, and 6%, displayed much better compression strength values than PVA included ECC materials. A cost effective, promising green and sustainable construction material was achieved by the introduction of basalt fibers into composite mixtures.

1. Introduction

In European Design Codes, public buildings constructed using concrete are required to have a service life of over 75 years [1]. However, experiences have demonstrated that many concrete infrastructures begin to deteriorate after just 20 or 30 years when the effects of mechanical stresses and environmental conditions are combined [2]. The short lifecycle of infrastructures in which Portland cement concrete is used has a significant effect due to the vehicle emission and fuel consumption related to traffic congestion during material production for the replacement or repair of deteriorated infrastructures. The weakness in the durability of concrete cracks reinforced with Portland cement is one of the main reasons for the short lifecycle of concrete infrastructures [3]. Cracks are generally the result of various physical, chemical and mechanical interactions between the concrete and environmental conditions, and they may occur at different stages throughout the life cycle of the building. The structure of the cracks in traditional brittle concrete without crack width control is primarily responsible for the two extraordinary damages. These damages are the decrease in

the strength and rigidity of the concrete and the acceleration of the entrance of harmful chemicals that lead to other types of concrete deterioration such as corrosion, alkali-silica reactions, freeze-thaw damages and sulfate attack [3, 4]. Therefore, durability is extremely important for all concrete structures, and this feature is substantially related to the brittle nature of the concrete.

The development of a composite material with cement based high-ductility in structural applications has been needed due to these reasons. The high-performance fiber reinforced cementitious composites (by their patented name Engineered Cementitious Composites – ECC) that show strain hardening and are designed micromechanically, and are a new type of high-performance fiber reinforced cementitious composites, are the ductile fiber reinforced cementitious composites designed micromechanically to show high damage tolerance under heavy loads and high durability under normal service conditions [5, 6, 7]. The most important feature of ECC that distinguishes it from traditional and fiber reinforced concretes (FRC) is the fact that it has an axial tensile strain capacity ranging from 3% to 5% depending on the mixture. This capacity is related to the formation of very tightly spaced micro cracks. ECC has more strain capacity than 300 times that of normal concrete. These cracks that can carry higher loads after the formation of the cracks allow the material to show strain hardening similar to ductile metals.

In this study, the mechanical properties of designed cementitious composites (ECC) especially reinforced with non-metallic fibers such as PVA and basalt fiber (BF) were determined. The use of selected basalt fibers in concrete [8] was preferred since they have a good tensile strength and similar properties with expensive carbon fiber and glass fibers, and they are less costly than carbon fibers. However, PVA fibers are more included in the literature and have been recently used in cementitious composites designed, and these fibers are observed to have better properties.

In their studies in which Ayub et al. (2015) investigated the compressive strength, splitting tensile strength and the elastic modulus of high strength concrete samples containing PVA fiber and basalt fiber in terms of mechanical properties, they prepared high strength concrete mixtures using basalt fiber in three mixtures, 1%, 2% and 3% concrete volume of which contained PVA fiber, and in other three mixtures at a similar ratio and dose as in PVA fiber. According to the experimental results, they found out that basalt and PVA fiber increased the compressive strength in a 1% volume fraction which is the optimum dosage up to 9% and 17%, respectively [9].

In their study carried out on fiber reinforced concrete with high ductility and sufficient durability properties having an extensive usage, Jiang et al. (2014) analyzed the effects of basalt fiber length and volume fraction on mechanical properties of fiber reinforced concrete (FRC). The results demonstrated that although tensile strength, flexural strength, and toughness index significantly improved with the addition of basalt fiber, there was no increase in compressive strength. Furthermore, they stated that the basalt fiber length had an effect on mechanical properties, it raised the compressive strength, splitting tensile strength and flexural strength of 12 mm basalt fiber reinforced concrete to 0.18-4.68%, 14.08-24.34%, and 6.30-9.58%, respectively, compared to normal concrete, and the related increase in strength was 0.55-5.72%, 14.96-25.51% and 7.35-10.37% when the basalt fiber length was raised to 22 mm [10].

2. Materials, Specimen Preparation and Test methods

2.1. Materials

The standard CEM I 42.5R type Portland cement (C) produced by Göltaş Cement Plant was used within the scope of this study. The specific gravity of cement is 3.06 gr/cm^3, and the Blaine specific surface is 3250 cm^2/gr. The chemical properties of the cement are presented in Table 2.1.

According to ASTM C 618 standard, F-class fly ash (FA) was obtained from Sugözü Thermal plant to be used in this study. The specific gravity of Sugözü fly ash is 2.31 gr/cm^3, and the Blaine specific surface is 2900 cm^2/gr. The chemical properties of the fly ash are given in Table 2.1.

In the production of specimens, fine quartz sand with an average particle size of about 150 μm and 200 μm and with a specific gravity of 2.60 gr/cm^3 and a water absorption capacity of 0.3% was used as an aggregate. The chemical properties of quartz sand are given in Table 2.1.

The modified polycarboxylate-based polymer type superplasticizer additive (SA) called Sika ViscoCrete-SF 18 was used to increase the workability of ECC mixtures. The SA additive used in experimental studies is an additive in liquid form with 3-7 pH value and specific gravity of about 1.10±0.02 kg/l. Attention was paid for the amount of SA additive to have the consistency that would ensure the homogenous distribution in the matrix of fibers, the resistance against decomposition, and the performance of the additive during mixture.

Table 2.1: Chemical properties of Portland cement, fly ash and quartz

Chemical properties	**Cement**	**Fly ash**	**Quartz**
CaO (%)	63.65	1.16	0.02
SiO_2 (%)	19.87	61.72	99.79
Al_2O_3 (%)	4.11	20.13	0.06
Fe_2O_3 (%)	3.44	7.46	0.02
MgO (%)	1.61	1.80	0.01
SO_3 (%)	2.68	0.22	-
K_2O (%)	0.48	1.88	0.01
Na_2O (%)	0.12	2.57	0.02
Loss on ignition (%)	2.20	2.99	0.07
SiO_2+Al_2O_3+Fe_2O_3	27.42	89.31	-

12 mm long BFs which are used in different percentages by weight were obtained from Spinteks firm in the production of ECCs in the study. PVA fibers specifically produced for ECCs were used to obtain reference samples. The feature of these fibers is that their surface is covered with a special hydrophobic (water repellent) oil in the ratio of 1.2% by weight. The physical, mechanical and geometric properties of PVA and BFs used in this study are given in Table 2.2.

Table 2.2: Some physical, mechanical and geometric properties of fibers used in the study

Fiber variety	Tensile strength (MPa)	Diameter (μm)	Length (mm)	Modulus of elastic (GPa)	Elongation at break (%)	Density
PVA	1620	39	8	42.8	6.0	1.30
BF	2500	13-20	10-14	89	3.15	2.8

2.2 Specimen preparation

As a result of the experimental mixtures performed with the fixed amounts of cement, fly ash, water, PVA fiber and sand within the scope of this study, the most appropriate ratios were calculated as follows: the water/total binder material (W/BM) ratio as 0.26, the fly ash-cement ratios as 1.20, and the sand/binder (S/BM) ratio as 0.36. The polypropylene, plastic, basalt and some textile factory wastes were tested in the investigations of the use of some fibers produced around the world in ECC production, and the expected behaviour in terms of the mechanical aspect could not be achieved [11]. The consistent and high ductility could be achieved in the use of PVA fibers [12].
The most important factor that increases the cost of the ECC composite material is the PVA fiber among the components. In the reference mixtures produced (M45) [13], PVA fiber in the ratio of 26 kg/m^3 (2% by volume) which was determined by the micromechanical design approach was used. For a better analysis of the effect of the change in basalt fiber amount on mechanical properties in the study, 9 different ratios of basalt fibers (42, 52, 63, 73, 84, 94, 105, 115 and 125 kg/m3) (by volume 2.00, 2.50, 3, 3.5, 4, 4.5, 5, 5.5 and 6.00%) were used provided that all other mixture parameters were the same, and the mixtures were prepared again (Table 2.3).
In coding the specimens used in this study, the initial letter B represents the basalt fiber and the number in front it indicates the ratio of the BF amount by weight. For instance, the specimen coded with B2 mixture indicates the mixture formed by adding 2% basalt fiber.

All mixtures were prepared using a Hobart type mixer with a 20-liter capacity. Cement, FA, and crushed silica sand were firstly mixed for 2 minutes at 100 rev/min speed as dry. Then, the mixture was mixed for a total of 3 minutes at 100 rev/min speed until it got a homogenous dough consistency by adding water, and SA additive was added in the duration of 20 seconds at the same speed. Afterwards, the mixing process continued for 2 minutes at 100 rev/min speed. Approximately a 2-liter specimen was taken before adding fiber to ECC matrix prepared, and the fresh and rheological properties of the matrix (flow diameter with the mini-slump cone, plastic viscosity, and threshold stress with Marsh cone flow time and viscometer) were determined by being repeated at least twice. Immediately after having taken samples, PVA fibers were added to the matrix and the mixing process continued for 2 minutes at 200 rev/min speed in the mixer. Experiments on the matrix were performed while the fiber+matrix mixing process was going on.

Table 2.3: Material amounts of ECC mixtures

Mix ID	W/BM	Q/BM	FA/C	C	PVA fiber	Basalt fiber	SP
M45	0.26	0.36	2.2	1	26	-	4.9
B2	0.26	0.36	2.2	1	-	42	6.4
B2.5	0.26	0.36	2.2	1	-	52	6.7
B3	0.26	0.36	2.2	1	-	63	6.8
B3.5	0.26	0.36	2.2	1	-	73	7.2
B4	0.26	0.36	2.2	1	-	84	7.6
B4.5	0.26	0.36	2.2	1	-	94	8.0
B5	0.26	0.36	2.2	1	-	105	8.5
B5.5	0.26	0.36	2.2	1	-	115	8.9
B6	0.26	0.36	2.2	1	-	125	9.3

2.3 Test Methods

For the determination of flexural strengths of the hardened specimens, four-point flexural strength test was applied to beam specimens of 360x75x50 mm^3 in size in the universal testing device. Flexural tests were performed as strain controlled (at a speed of 2 mm/second) using an electromechanical testing device. During the experiment, the deflection occurring in the center and the corresponding load were recorded precisely and automatically as 10 data per second with computer software.

For the determination of the compressive strengths of ECCs produced with BF and NF combination, 6 cube specimens of 50 x 50 x 50 mm^3 in size from each ECC mixture were cured for 28 days in water with an average temperature of 20 ± 2 °C. The compressive strength test was performed on specimens that were cured for 28 days in the universal testing device with a 25-ton capacity in accordance with ASTM C39 standard.

The four-point flexural strength values of ECC specimens were calculated according to the following formula;

$$\mathbf{F_{cf}:}\ (F_{max}*L_s)/(b*h^2) \quad (1)$$

Where:
F_{cf}: Flexural Strength (N/mm^2)
F_{max}: Maximum Load (N)
L_s: Effective span (clear span) (mm)
b: Specimen width (mm)
h: Specimen height (mm)

The compressive strength values of ECC specimens were calculated according to the following equation;

$$\mathbf{F_c = (F/A_c)}\ (N/mm^2) \quad (2)$$

where:
F_c: Compressive strength of ECC specimen
F: Breaking Load (N)
A_c=(b*h): average cross-sectional area of the test specimen perpendicular to the application direction (mm^2)

3. Results and discussion

3.1. Mid-span deflection, flexural strength, and compressive strength

The changes of beam midpoint deflection, flexural and compressive strengths of ECCs produced with basalt fiber depending on the basalt fiber combination ratios by weight are shown in Table 3.1.

Table 3.1: Mechanical properties of ECC mixtures

Mix ID	Maximum deflection (mm)	Flexural strength (MPa)	Compressive strength (MPa)
M45	4.27	12.73	46.95
B2	1.43	8.77	34.97
B2.5	1.42	8.83	41.76
B3	1.67	9.01	42.88
B3.5	1.83	9.57	46.42
B4	1.87	9.65	48.65
B4.5	1.83	10.93	48.99
B5	1.95	10.99	54.28
B5.5	2.11	11.39	55.09
B6	2.18	12.22	55.92

Furthermore, the change of beam midpoint deflection capacity and flexural strength depending on the fiber ratio are shown in Figure 3.2 and Figure 3.3, respectively. As it is seen from Figure 3.2, the optimum fiber ratio in terms of beam midpoint deflection capacity was achieved in ECC coded B6 and containing 6% basalt fiber (2.18 mm). Although the beam midpoint deflection capacities increased linearly by increasing the BF ratio from 2% to 6%, the amount of increase in 6% basalt fiber reinforced specimens with the highest amount of deflection was 78% compared to 2.5% basalt fiber reinforced specimens with the lowest amount of deflection. As it is seen from Table 3.1, flexural strength values in BF reinforced specimens varied between 8.77 and 12.22 MPa. It is seen from Figure 3.3 that there was an increase in the flexural strength values in parallel with the increase in fiber ratio in BF reinforced specimens.

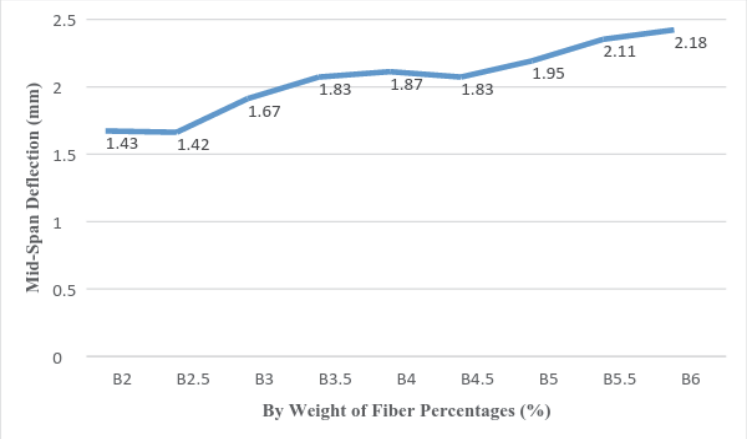

Fig. 3.2: Deflection capacities of ECC mixtures with basalt fiber

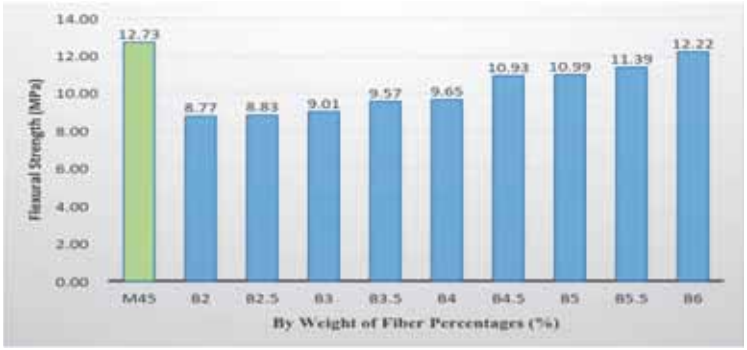

Fig: 3.3. Flexural strength values of ECC mixtures with basalt fiber

The compressive strength tests were performed on the 28th day on cube specimens produced from ECCs with basalt fiber. The compressive strength results obtained with the use of BF amount in the ratios of 2%, 2.5%, 3% and 3.5% by weight in ECC mixtures were lower than an M45 specimen with PVA fiber, which was the reference specimen. However, high results were achieved from the reference value (M45) in specimens reinforced with 4%, 4.5%, 5%, 5.5% and 6% basalt fiber (48.65, 48.99, 54.28, 55.09 and 55.92 MPa, respectively). In the specimens with BF, although the proportional increase of BF amount increased the strengths in the specimens formed with BF in the range of 4%-6%, it formed a decreasing trend in the compressive strengths of the specimens in the samples, in which BF ratio varied between 2%-4%. Furthermore, it ensures the homogeneous distribution of cement particles in the cement matrix due to the adsorption of chemical additive molecules on the surface of cement particles in the mixtures in which the dosage of the additive was determined in a way that the modified V-cone flow time would be between ~30 seconds in this study. Therefore, this adsorption process increased the workability of the mixtures, decreased the water need and, thereby,

created a positive effect on the compressive strength [13]. Data on the compressive strengths are presented in Figure 3.4.

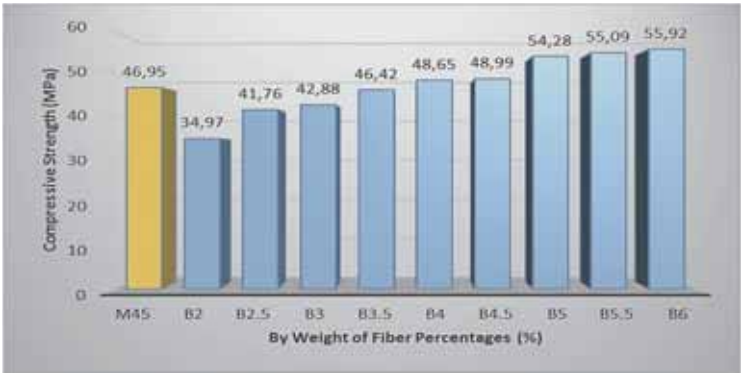

Fig. 3.4: Compressive strength values of basalt fiber reinforced ECC mixtures

4. Conclusions

In this study, the effects of the use of BF in ECC mixtures by increasing its amount by 0.5% in each mixture provided that other mixture parameters were kept fixed on mechanical properties (compressive strength, flexural strength, beam midpoint deflection capacity) were investigated. Consequently:

- The optimum ratio of basalt fiber was determined to be 6% in ECC samples containing BF in terms of beam midpoint deflection capacity. Although the beam midpoint deflection capacities increased with the increase of BF ratio in general, they showed a very small amount of a decreasing trend in the samples formed by adding 2.5% BF and 4.5% BF compared to the previous sample, namely the specimens with 2% and 4% basalt fiber additive.
- Flexural strengths are increased in direct proportion to BF increase in BF reinforced samples. The percentage decrease of lower flexural strength is about 4 value was obtained in 6% BF reinforced samples compared to the reference sample.
- Regarding the compressive strengths, better results were achieved in 6% BF reinforced samples in terms of strength values. It can be said that the use of BF amount in the range of 4%-6% by weight in the mixture can be beneficial to the compressive strength of BF-ECCs.
- While the compressive strength value was 48.65 MPa in B4 sample, this amount was 48.99 MPa in the samples coded B4.5 with the increase of about 0.7%, and approximately a 10.8% strength increase was observed in the samples coded B5. The strength increase was approximately 1.49% and 1.50%, respectively, in the samples containing 5.5% and 6% BF. Consequently, the increase of basalt fiber amount is resulted by increased compression values in the ECC samples.

- It is useful to conduct studies in which clipped basalt fibers and other types of fibers are used together as a hybrid for the development of sustainable, more economical and high-performance ECC composites.

Acknowledgement

The authors acknowledge TUBITAK-The Scientific and Technological Research Council of Turkey (project # 214M344) for funding the research.

References

[1] Alexander, M.G. and Stanish K., Durability design and specification of reinforced concrete structures using a multi-factored approach, CONMAT'05, Canada (2005), 1- 10.
[2] Mehta P.K. and Burrows R.W., Building durable structures in the 21st century. Conc Int, 23(3), (2001), 57-63.
[3] Mindess S. and Young J.F., Concrete, Prentice Hall, New Jersey, 1981; 2nd Ed. in Darwin D., Prentice Hall, NJ, (2002).
[4] Li, M. and Li, V. C., Durability of HES-ECC repair under mechanical and environmental loading conditions, High Performance Fiber Reinforced Cement Composites, Germany (2007), 399-408.
[5] Mehta P.K., Concrete technology at the crossroads — problems and opportunities. ACI SP-144, (1994), 1-30.
[6] Emmons P. and Vaysburd A., Performance criteria for selection of repair materials, Phase I. Tech Report, (1995)
[7] Mather B. and Warner J., Why do concrete repairs fail. http://aec.engr.wisc.edu/resources/rsrc07.html, (2016)
[8] Meng, L.J.Y.Y.Y. and Yan, Z,. Experimental research on the mechaniccal behaviour of chopped basalt fiber reinforced concrete. Ind. Construct. 6 (2) (2007).
[9] Ayub, T., Nasir, S., Nuruddin, M. F., Khan, S. U., Mechanical Properties of High-Strength Concrete Reinforced with PVA and Basalt Fibres. Proceedings of the International Civil and Infrastructure Engineering Conference, Springer Singapore (2014), 567-575.
[10] Jiang, C. et al, Experimental Study on the Mechanical Properties and Microstructure of Chopped Basalt Fibre reinforced Concrete. Materials and Design, 58 (2014), 187–193.
[11] H. Said, S. and Abdul Razak, H., The effect of synthetic polyethylene fiber on the strain hardening behaviour of engineered cementitious composite (ECC), Materials and Design, 86 (2015), 447–457
[12] Tosun-Felekoglu, K., Felekoglu, B., Effects of fibre hybridization on multiple cracking potential of cement-based composites under flexural loading. Construction and Building Materials, 41 (2013), 15–20
[13] Yıldırım, et al, A review of intrinsic self-healing capability of engineered cementitious composites: Recovery of transport and mechanical properties, Construction and Building Materials, 101 (2015), 2-10

International RILEM Conference on Materials, Systems and Structures in Civil Engineering
Conference segment on Service Life of Cement-Based Materials and Structures
22-24 August 2016, Technical University of Denmark, Lyngby, Denmark

EFFECTS OF CURING TEMPERATURE ON CHLORIDE MIGRATION AND ELECTRICAL RESISTIVITY OF CONCRETE

Utkan Çorbacıoğlu [(1)], Egemen Kesler [(2)], T. Alper Yıkıcı [(3)], Yılmaz Akkaya [(2)]

(1) Dogus Insaat AS, İstanbul, Turkey
(2) Istanbul Technical University, Istanbul, Turkey
(3) MEF University, İstanbul, Turkey

Abstract
Durability and service life of reinforced concrete structures are affected by microstructure and permeability of concrete. Parameters, including cementitious materials, mixture design and maturity influence the hydration rate and pore structure of the binder phase, and thus development of microstructure and permeability of concrete. This study compares the results obtained by chloride migration and electrical resistivity tests of several concrete mixtures cast with supplementary cementitious materials, cured under different temperatures. The correlation between the results of the two test methods were investigated with respect to development of capillary porosity, calculated based on degree of hydration by Powers model. Trends observed with concretes, cast with blast furnace slag, fly ash and microsilica, were further investigated by thin section analysis of the microstructures. Development of the capillary pore system of the concrete was monitored through thin section microscopy at different curing temperatures. Capillary porosity of the concrete mixtures was compared with the light intensity measurements from thin section analysis. It was found that microcracks, observed in thin section analysis of concrete containing blast furnace slag, affect the chloride migration and electrical resistivity test results. Test results from construction site were also obtained and compared with the trends evaluated from laboratory testing. Type of cementitious materials, curing conditions and testing methods are found to be important factors in determination of the permeability, due to their effects on maturity and microstructural development of concrete.

1. Introduction

Deterioration of public infrastructure is a growing concern since service life is often used as a concept in design of such structures. Particularly reinforced concrete structures exposed to harsh environments which experience damages such as cracking and spalling that can result in

loss of strength and durability of the reinforced concrete members. One of the common damage mechanisms is corrosion of reinforcing steel due to chlorides. Consequently, concrete resistance to chloride penetration needs to be increased in order to minimize the risk of corrosion induced deterioration. Improving durability and long term mechanical performance of infrastructure facilities, while minimizing maintenance cost, can be achieved by low permeability concrete with dense microstructure, containing binary or ternary blends of Portland cement and mineral admixtures [1].

Chloride permeability of concrete can be determined using various experimental procedures, such as bulk diffusion tests [2-3], non-steady-state migration tests [4-5-6], steady-state migration tests [7-8-9] and electrical indication of chloride penetration test [10-11]. Additionally, chloride permeability can also be evaluated via non-destructive test methods by measuring the concrete's electrical resistivity [12-13-14-15].

In this study, effect of curing temperature on chloride migration coefficient and electrical resistivity of concrete specimens were investigated. Non-steady state chloride migration coefficients (D_{nssm}) were determined according to NT BUILD 492 and electrical resistivity was measured using a Wenner Probe technique in accordance with AASHTO TP 95. Additionally, development of the concrete microstructure and capillary porosity were evaluated through fluorescent thin section analysis. Capillary porosities were estimated following Powers model and the degree of hydration of concrete was calculated from semi-adiabatic calorimeter test results.

Results have shown that chloride migration coefficients and resistivity values of concrete samples are sensitive to development of hydration, porosity and microstructure as well as curing temperatures. Therefore, while verifying concrete quality with respect to service life calculations, based on chloride penetration, temperature history and the microstructure of the concrete should also be taken into account.

2. Experimental Study

For this study five different concrete mixtures were investigated with different types of cement and cementitious materials, and equivalent water to cement ratios with 0.38 and 0.40. Compressive strength class and the workability class of all mixtures were C40/50 and S5, respectively. Each concrete mixture design was specifically developed to satisfy structural service life requirement of minimum 100 years, by using CEM III B cement or combining CEM I cement with Class F fly ash, micro silica and ground granulated blast furnace slag (GGBFS) as mineral admixtures. Siliceous natural sand and crushed limestone sand were used as fine aggregates, and two crushed limestone aggregates with nominal maximum sizes of 10 mm and 20 mm were used as coarse aggregates. Concrete mixture design proportions are given in Table 1.
Accordingly, concrete mixtures were produced in the laboratory and, 100 mm by 200 mm cylinders were cast for chloride migration, resistivity and microstructural evaluations. Specimens were kept in molds for the first 24 hours and then placed in lime water baths at 10°C, 20°C, 35°C and 50°C. Moreover, semi-adiabatic calorimetry tests were conducted in

accordance with NT BUILT 388 [16]. Additionally, in-situ electrical resistivity readings were taken on a structure and core samples were extracted to perform chloride migration tests.

Table 1: Concrete Mix Designs.

	Mix 1	**Mix 2**	**Mix 3**	**Mix 4**
Eq.w/c	0.38	0.38	0.40	0.38
Cement Type	CEM III B 32,5 N	CEM I 42,5N	CEM I 42,5N	CEM I 42,5 R
Cement, kg	360	360	300	135
Fly Ash, kg	-	60	80	-
Micro Silica, kg	-	20	-	-
GGBFS, kg	-	-	-	265
Natural Sand, kg	444	425	417	502
Crushed Sand, kg	426	408	419	380
Coarse Agg. No. I, kg	481	425	479	437
Coarse Agg No. II, kg	500	442	511	570

2.1 Chloride migration

Chloride migration tests were performed according to NT Build 492 (Figure 1). Specimens were cured in lime-water baths at different temperatures until the day of testing and test results are given in Figure 2. It can be observed, that the calculated D_{nssm} values of concrete samples cured at 20°C, decreased by 79%, 78%, 66% and 68% from 7 days to 28 days, for Mix 1, Mix 2, Mix 3 and Mix 4, respectively. It can also be observed that, there is a significant difference between D_{nssm} values obtained from specimens cured in different temperatures. The differences between chloride migration coefficients, measured from specimens, cured in 10°C and 50°C at 28 days, were calculated as 95%, 87% 74% and 81% for Mix 1, Mix 2, Mix 3 and Mix 4, respectively.

Figure 1: Chloride migration test set up.

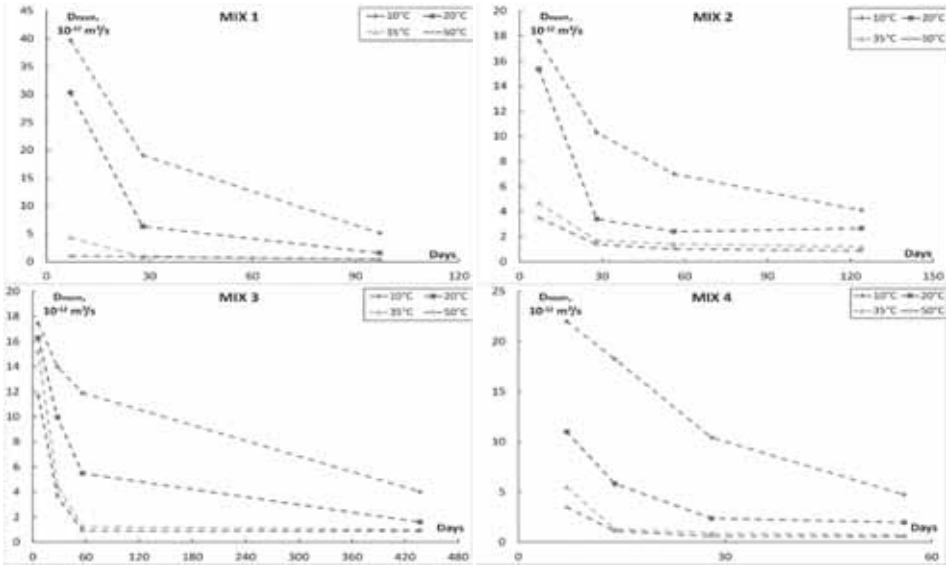

Figure 2: Chloride migration coefficient vs time under various curing temperatures for Mix 1, Mix 2, Mix 3 and Mix 4.

At 7 days, the D_{nssm} of Mix 1 sample cured at 50°C is 98% lower compared to the sample cured at 10°C, whereas the difference between D_{nssm} values of Mix 3 samples cured at 10°C and 50°C is only about 33%. Results indicated that Mix 1 with CEMIII B cement which contains 65% GGBFS, was very sensitive to changes in curing temperature compared to Mix 3, which contains 20% fly ash.

2.2 Resistivity

Electrical resistivity was measured using a Wenner method according to AASHTO TP 95. All specimens were placed in 20± 1°C lime-water baths for 2 hours, before taking any measurements. It can be observed from Figure 3 that the electrical resistivity of concretes varied with different mixture proportions and curing temperatures. According to the readings from Mix 1, Mix 2, Mix 3 and Mix 4, concrete samples cured at 20°C, values increased by 77%, 70%, 47% and 75% from 7 days to 28 days, respectively. Besides, the differences in electrical resistivities of samples cured at 10°C and 50°C for 28 days were about 90% for all concrete mixtures.

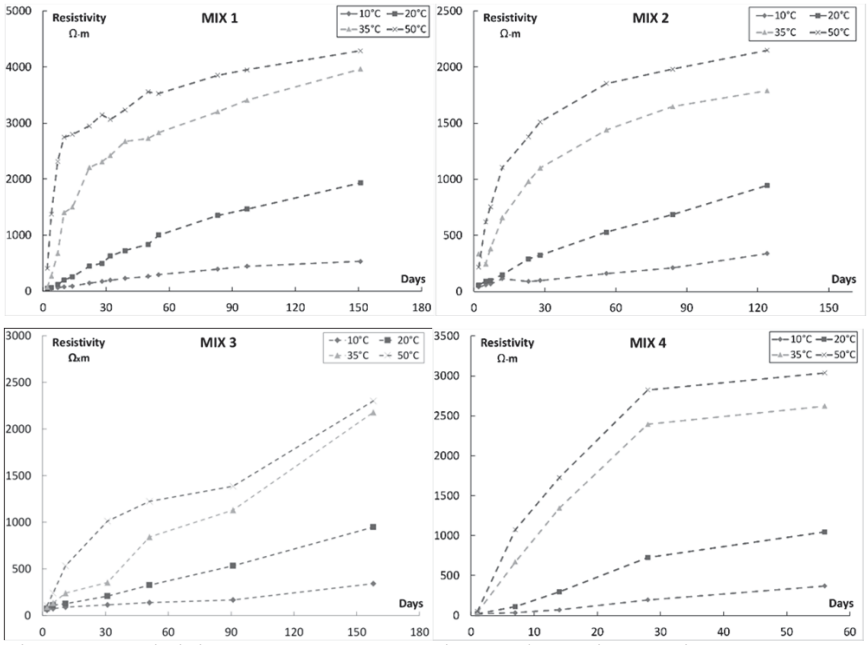

Figure 3: Resistivity measurements vs Time under various curing temperatures for Mix 1, Mix 2, Mix 3 and Mix 4.

Results indicate that, electrical resistivity of Mix 1 and Mix 4, cured at 10°C, did not reach 500 Ω-m, where samples cured at 50°C exceeded 3000 Ω-m at 60 days.

To compare the laboratory test results with actual field performance, a concrete structure cast with Mix 3 was investigated. In order to minimize the effect of maturity, a two-year old structure was selected for investigation. Resistivity readings were taken on seven locations where surfaces were in saturated condition. Additionally, core samples with 10 cm in diameter were taken from the structure, and chloride migration tests were performed. Results are presented in Figure 4 along with the laboratory test results for comparison.

3. Discussion of test results

To represent temperature dependence of the specimen age, Arrhenius equation was employed and equivalent age of the concrete samples cured in 10°C, 20°C and 50°C were calculated at the time of testing. The reference temperature was taken to be 20°C and the activation energy values (E) for each concrete mixture were determined following TI-B 103 procedure [17], using compressive strength values. E values for curing temperatures higher than 20°C were calculated as 26, 34, 33 kJ/mol for Mix 1, Mix 2 and Mix 3, respectively. For curing temperatures lower than 20°C, E values were calculated as 43, 46, 49 kJ/mol for Mix 1, Mix 2 and Mix 3, respectively. Since the amount of GGBFS in Mix 1 (with CEM III B) and Mix 4

were similar, the activation energy test and further analysis were performed only for Mix 1, Mix 2 and Mix 3.

Development of electrical resistivity vs. chloride migration coefficients is presented in Figure 4. It can be observed that the correlation between the two measurements can be established based on the concrete mixture design. As the maturity of the samples increases the D_{nssm} converges to a minimum value where resistivity values continue to increase. It can also be observed that the field test results are in compliance with the trends evaluated from the laboratory tests as indicated by the circular mark on Figure 4 (right).

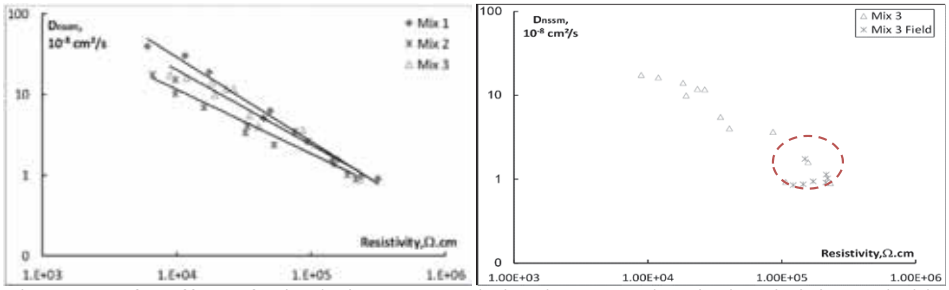

Figure 4 Left: Effect of mix design on correlation between electrical resistivity and chloride migration. Right: Comparison of laboratory vs. field measurements (inside the circular mark).

The correlations between D_{nssm} and conductivity (1/ρ) were calculated and plotted in Figure 5. The slopes (k) are found to be in accordance with the earlier reported results [18]. Concrete containing CEM III B (Mix 1) exhibited higher slope compared to concrete containing fly ash and microsilica (Mix 2) and concrete containing fly ash (Mix 3). Differences can be attributed to the pore solution chemistry, as well as connectivity and size of the capillary pore system.

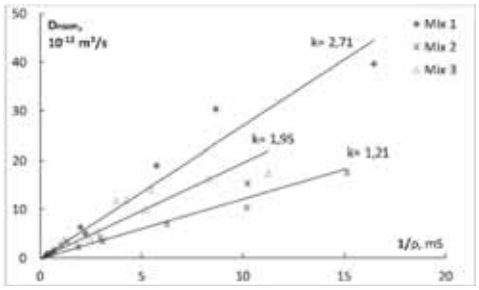

Figure 5: Correlation between D_{nssm} and conductivity (1/ρ).

According to Powers and Brownyard, hardened cement paste is composed of unhydrated cement grains, hydration products and capillary pores. The total volume of capillary pores can be estimated following Powers model, in case water to cement ratio, hydration degree and the specific volume of the binder is known [19]. The hydration degree of the concrete mixtures was calculated using the heat development obtained experimentally from semi-adiabatic calorimeter tests [16,20]. The development of the capillary porosity was calculated

based on Powers model, and its relation to chloride migration and electrical resistivity test results are presented in Figure 6.

As it can be observed from Figure 6, trend of concrete with CEM III B (Mix 1) considerably differs from concrete containing fly ash and microsilica (Mix 2), and concrete containing fly ash (Mix 3). Therefore, Mix 1 and Mix 2 were selected for further investigation in terms of microstructure.

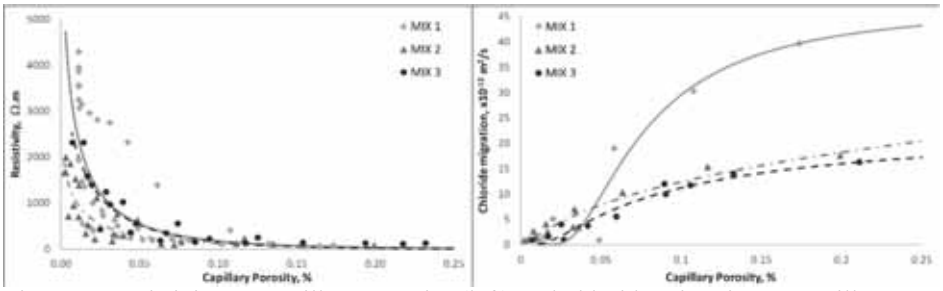

Figure 6: Resistivity vs. capillary porosity (left) and chloride migration vs capillary porosity (right).

4. Microstructural analysis

In order to investigate concrete microstructure, epoxy with fluorescent dye was impregnated into Mix 1 and Mix 2 concrete samples, extracted from cylinder specimens cured at 10°C, 20°C and 50°C and thin sections of approximately 30 microns thickness were produced according to DS.423.40 [21]. Thin sections were photographed by a UV-light polarization microscope where aggregate particles appear in dark, voids and cracks appear in light color, and cement paste can be observed in between, depending on the volume of capillary porosity.

Samples of microstructure images from thin sections of Mix 1, cured at 10°C and 50°C are presented in Figure 7 and Figure 8. As it can be seen from the thin section analysis, curing at higher temperatures increased hydration and decreased capillary porosity, and thus, darker images were obtained.

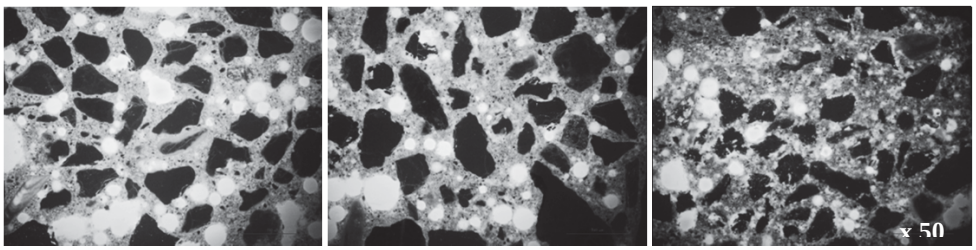

Figure 7: Microstructure at 10°C, Mix 1 (Left: 14 days, Middle: 28 days, Right: 56 days).

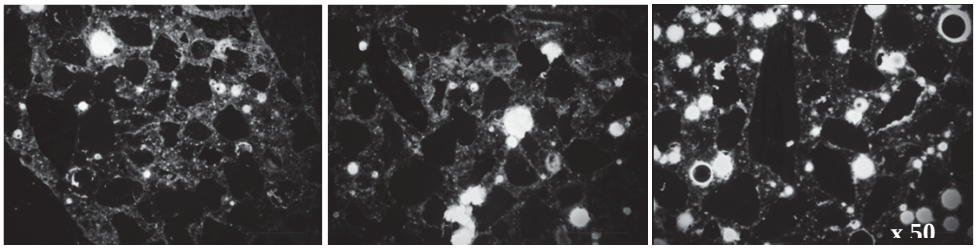

Figure 8: Microstructure at 50°C, Mix 1 (Left: 14 days, Middle: 28 days, Right: 56 days).

In order to quantify the capillary porosity by the level of light intensity of the cement paste, the fluorescence level was measured through image analysis [22]. Readings were then normalized and plotted against capillary porosity in Figure 9. It can be observed that light intensities measured from thin section analysis are consistent with capillary porosity calculated from Powers model.

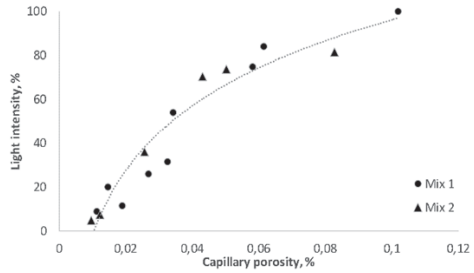

Figure 9: Light intensity vs. capillary porosity relationship.

Microcracks at paste and at the interfaces between paste and aggregates were observed in concrete with CEMIII B (Mix 1). High amount of calcium hydroxide (CH) was observed in the air voids (Figure 10, right), indicating lower reactivity of the slag at 10°C. Moreover, high capillary porosity around the microcracks (Figure 10, left-top), suggested high degree of connectivity of the microcrack system. However, at 50°C, porosity around microcracks was less due to increased degree of reactivity (Figure 10, left-bottom).

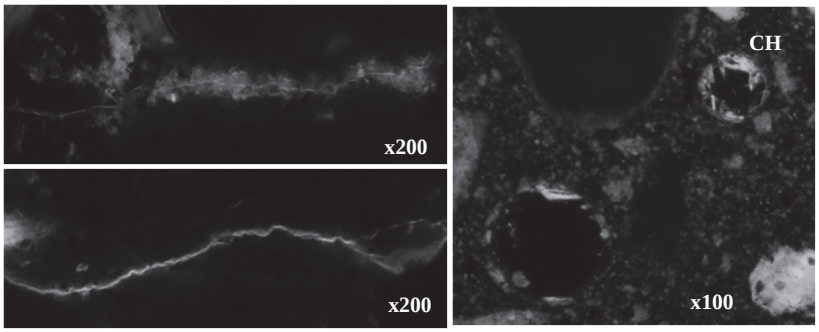

Figure 10 Left: Microcracks at 10°C (top) and 50°C (bottom), Right: CH deposits in air voids.

Additionally, number of paste and bond microcracks of widths less than 10 microns were counted at 10 locations with x50 magnification (corresponding to an area analyzed approximately 180 mm^2), on each thin section and results are presented in Table 2. The differences observed in the capillary porosity vs. chloride migration and capillary porosity vs. resistivity measurements of Mix 1 in Figure 6 can be attributed to the presence of microcracks and the degree of their connectivity in the system.

Table 2: Number of microcracks.

Curing temperature	10°C		50°C	
Crack location	Paste	Bond	Paste	Bond
Number of microcracks	24	14	31	17

5. Conclusion

Test results indicated that chloride migration and electrical resistivity measurements are sensitive to the type of binder used in concrete as well as concrete maturity at testing. Therefore, correlation between the two test methods depends on the development of capillary porosity, calculated based on degree of hydration. As the capillary porosity of the concrete decreases, D_{nssm} converges to a minimum value, where electrical resistivity values continue to increase.

Moreover, microstructural analysis indicated that the different trends observed in capillary porosity vs. chloride migration and electrical resistivity of concrete mixtures with GGBFS and fly ash can be attributed to the presence of microcracks and their degree of connectivity. It was also observed that light intensity measured from thin section analysis was consistent with capillary porosity calculated from Powers model.

Verification of the field quality of concrete based on chloride migration and electrical resistivity depends not only on maturity but also on microstructure of concrete. It was also observed that the field test results were in compliance with the trends evaluated from the laboratory tests.

References

[1] Mehta P.K., Monteiro, P.J.M, Concrete: Microstructure, properties, and materials, McGraw-Hill Publishing (2014)
[2] NT BUILD 443, Concrete, hardened: Accelerated chloride penetration, NORDTEST, Espoo, Finland, (1995)
[3] ASTM C1556-04, Standard test method for determining the apparent chloride diffusion coefficient of cementitious mixtures by bulk diffusion, ASTM International, West Conshohocken, PA, (2004)

[4] NT BUILD 492, Concrete, mortar and cement-based repair materials: Chloride migration coefficient from non-steady-state migration experiments, NORDTEST, Espoo, Finland, (1999)
[5] Tang, L. and Nilsson, L. O., Rapid determination of the chloride diffusivity in concrete by applying an electrical field, ACI Mater J 89 (1992), 49-53.
[6] Andrade, C., Sanjuán M. A., Recuero A., and Rio O., Calculation of chloride diffusivity in concrete from migration experiments, in non-steady-state conditions, Cem Conc Res 24 (1994), 1214-1228.
[7] NT BUILD 355, Concrete, mortar and cement based repair materials: Chloride diffusion coefficient from migration cell experiments, NORDTEST, Espoo, Finland, (1997)
[8] Li, Z., Peng, J., and Ma, B., Investigation of chloride diffusion for high-performance concrete containing fly ash, microsilica and chemical admixtures, ACI Mater J 96 (1999), 391-396.
[9] Yang, C.C., and Chiang S.C., A rapid method for determination of the chloride migration coefficient in concrete using electrical field. J ASTM Int 5 (2008), 1-13.
[10] Whiting, D., Rapid measurements of chloride permeability of concrete, Public Works 45 (1981), 101-112.
[11] ASTM C1202, Standard test method for electrical indication of concrete's ability to resist chloride ion penetration, American Society for Testing and Materials, USA (1997)
[12] Millard, S.G. and Gowers K.R., Resistivity assessment of in-situ concrete: The influence of conductive and resistive surface layers. Proc Inst Civil Eng Struct Build 94 (992), 389-396.
[13] AASHTO TP 95-11, Standard method of test for surface resistivity indication of concrete's ability to resist chloride ion penetration, American Association of State Highway and Transportation Officials, Washington, DC, (2011)
[14] Sengul, O. and Gjørv, O. E., Electrical resistivity measurement for quality control during concrete construction. ACI Mater J 105 (2008), 541-547
[15] Andrade, C., d'Andrea, R. and Rebolledo, N., Chloride ion penetration in concrete: The reaction factor in the electrical resistivity model, Cem Conc Comp 47 (2014), 41-46.
[16] NT BUILT 388, Concrete: Heat development, NORDTEST, Espoo, Finland, (1992)
[17] TI-B 103, Activation energy for the maturity method, Danish Technological Institute Building Technology, Denmark, (1996)
[18] Chlortest, Resistance of concrete to chloride ingress- From laboratory test to in-field performance-Guidelines for practical use of methods for testing the resistance of concrete to chloride ingress (G6RD-CT-2002-00855), (2006).
[19] T.C. Powers and T.L. Brownyard, Proc. Am. Concrete Inst., 1947, 41, part 1: 101-132, part 2: 249-336, part 3: 469-504, part 4: 549-602, part 5: 669-712, part 6: 845-880, part 7: 933-992; reprinted as PCA Bulletin, 1948, 22, with original pagination.
[20] De Schutter, G.,Hydration and temperature development of concrete made with blast-furnace slag cement. Cem Conc Res 29.1 (1999), 143-149.
[21] DS 423.40 Testing of concrete - Hardened concrete - Producing fluorescence impregnated thin sections, Danish Standard, Denmark, (2002)
[22] McCloy, R. A., Rogers, S., Caldon, C. E., Lorca, T., Castro, A., and Burgess, A., Partial inhibition of Cdk1 in G2 phase overrides the SAC and decouples mitotic events. Cell Cycle 13 (2014), 1400-1412.

International RILEM Conference on Materials, Systems and Structures in Civil Engineering
Conference segment on Service Life of Cement-Based Materials and Structures
22-24 August 2016, Technical University of Denmark, Lyngby, Denmark

CONTEMP – A VIRTUAL THERMO-MECHANICAL SIMULATOR FOR HYDRATING REINFORCED CONCRETE BLOCKS WITH EXTENSION TO SERVICE LIFE

Vít Šmilauer[(1)], Luis Baquerizo[(2)], Thomas Matschei[(3)], Petr Havlásek[(1)], Wilson Ricardo Leal da Silva[(4)], Karolina Hájková[(1)]

(1) Czech Technical University in Prague, Faculty of Civil Engineering, Czech Republic
(2) LafargeHolcim R&D, St Quentin Fallavier, France
(3) LafargeHolcim, Building segment, Holderbank, Switzerland
(4) Danish Technological Institute, Taastrup, Denmark

Abstract
Concrete is the single most widely used material in the world. Its performance is strongly affected by mix design, thermal boundary conditions, its evolving mechanical properties, and internal/external restraints with consequences to possible cracking with impaired durability. A virtual simulator, namely ConTemp uses a staggered multiscale thermo-mechanical approach that is able to capture relevant properties and boundary conditions for predicting temperature, strains, stresses or cracking in concrete structures. The mechanical part uses the B3/B4 model for concrete creep and shrinkage with isotropic damage model for cracking. ConTemp validation on several massive concrete blocks over the world shows excellent temperature predictions. Likewise, strain validation demonstrates good predictions on a restrained reinforced concrete wall. Induction time for carbonation and chloride ingress is evaluated *a posteriori,* based on computed crack width, reinforcement cover and environmental conditions.

1. Introduction

Concrete is the most man-made material in the world, exceeding 3.5 tons per capita a year. Its performance depends on a large extent on early-age curing which is influenced by thermal and mechanical boundary conditions, reinforcement, and/or mix design.

Mass concrete describes concrete members where high thermal gradients may lead to cracking. Binder content and initial concrete temperature belong to the most critical factors; even concrete members that are only 0.5 m in thickness may be susceptible to thermal cracking [1]. Significant tensile stresses may develop, leading to early-age thermal cracking, compromising concrete durability [2].

Models for stand-alone temperature prediction in hardening concrete belong to the most traditional concrete models. They consider either adiabatic temperature rise or general thermal boundary conditions [3]-[5]. Humidity transport plays no major role in massive concrete elements; hence only temperature field can be calculated. Thermal models can be widened for multiscale formulation, recognizing the role of cement paste for hydration [3]. Precise results can be obtained by fitting hydration models to semi-adiabatic measurements on small samples and upscaling to a structural scale [6],[7].

Several complex thermo-chemo-mechanical models were formulated during the last decades. They include prediction of stress, often including concrete creep, autogeneous shrinkage, drying shrinkage and they may predict early-age cracking and crack width [8],[9]. The number of input parameters presents the bottleneck of simulations, varying broadly over cements, their types, local practices and boundary conditions.

Another bottleneck stems from a practical point of view – designers, consultants and/or technologists require a quick tool to obtain trial results. A standard procedure, using a modeller and a mesh generator, takes time and is rather unnecessary for simpler structures. The philosophy behind ConTemp is to provide a user-friendly tool where relevant material properties and boundary conditions are easy to handle. ConTemp uses only a prismatic block, simplifying the whole thermo-mechanical analysis and data interpretation.

2. Design and description of ConTemp

ConTemp is a virtual thermo-mechanical simulator for hydrating reinforced concrete blocks with a graphical user interface (GUI), see Figure 1. Such tool has been under development since 2012 and is currently owned by LafargeHolcim. Qt4 framework in C++ creates ConTemp's GUI. Two external codes are called from the GUI, namely finite element software OOFEM [10] and postprocessor ParaView-4.2.0.

The thermal simulation part in ConTemp can solve heat transfer problems with various boundary conditions. A four-parametric affinity hydration model predicts hydration heat.

The mechanical simulation part in ConTemp captures creep, autogeneous shrinkage and possible damage. In massive structures the drying shrinkage can be neglected. The mechanical model is capable of predicting stresses, strains, crack orientation or crack width using underlying constitutive material laws. Creep model includes extended microprestress-solidification theory which captures transient thermal creep [11]. The main features of ConTemp are listed as follows:

- Simple geometry of a concrete block specified by three orthogonal dimensions.
- Arbitrary orthogonal reinforcement and/or constant reinforcement ratio.
- Concrete mix design, including cement, SCM, aggregate content, and ice.
- Database of 10 commonly used Portland and blended cements and their kinetics.
- Thermal boundary condition as free, fixed, convection or day-night convection.

- Mechanical boundary conditions as free, fixed, master-slave, or spring, defined in each orthogonal direction on each side.
- Autogeneous shrinkage according to fib ModelCode2010 [15] or B4 model [16].
- Adaptive time driver for optimal computation speed.

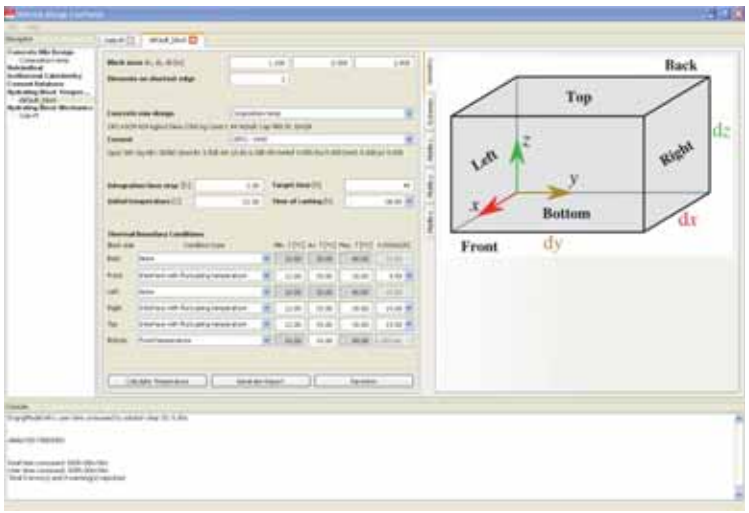

Figure 1: ConTemp's main GUI

2.1 Thermal part

Temperature field on a block is predicted from heat balance equation

$$-\nabla^T q(\mathbf{x}) + \overline{Q}(\mathbf{x},t) = \rho(\mathbf{x})\, c_V(\mathbf{x}) \frac{\partial T(\mathbf{x},t)}{\partial t} \tag{1}$$

using further Fourier's law on an isotropic material

$$q(\mathbf{x}) = -\lambda(\mathbf{x}) \nabla \mathrm{T}(\mathbf{x}) \tag{2}$$

where $\overline{Q}$ is heat power from hydrating cement (W/m^3), ρ concrete density (kg/m^3), c_V concrete thermal capacity (J/kg/K) and λ heat conduction (W/m/K). Equation (1) can be further complemented with initial conditions and several other boundary conditions including convection. ConTemp neglects thermal radiation.

The heat power $\overline{Q}$ originates from hydrating cement paste according to Figure 2. The figure defines material scale with an affinity hydration model that captures reaction kinetics. Since the affinity model depends strongly on temperature, coupling with structural scale needs to be carried out. ConTemp uses a strong coupling with a predictor-corrector scheme to achieve balance on both scales.

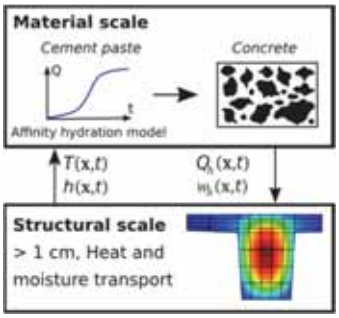

Figure 2: Multiscale hydration model with material and structural scales

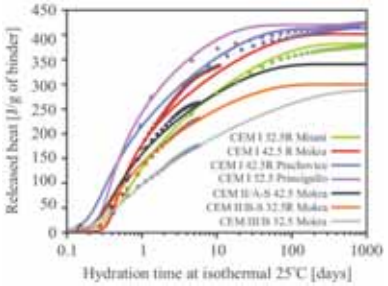

Figure 3: Performance of affinity hydration model on selected cements

Affinity hydration model is the heart of the multiscale formulation. The evolution of hydration is approximated with a four parametric function

$$\tilde{A}_{25} = B_1\left(\frac{B_2}{\alpha_\infty}+\alpha\right)(\alpha_\infty-\alpha)\exp\left(-\bar{\eta}\frac{\alpha}{\alpha_\infty}\right) \tag{3}$$

where $\tilde{A}_{25}$ is the affinity at isothermal temperature 25°C, and B_1, B_2, α_∞, η are the four parameters for calibration. Isothermal calorimetry is a perfect method how to obtain these parameters and Figure 3 shows released heat of common cements [6]. As described in Figure 2, temperature influences hydration rate and vice versa. Temperature-dependent kinetics is approximated with Arrhenius equation

$$\frac{1}{Q_{h,pot}}\frac{\partial Q_h}{\partial t} = \frac{\partial \alpha}{\partial t} = \tilde{A}_{25}\exp\left[\frac{E_a}{R}\left(\frac{1}{T_{25}}-\frac{1}{T}\right)\right] \tag{4}$$

where $Q_{h,pot}$ is the potential hydration heat (J/g), E_a the activation energy and R the universal gas constant. This multiscale heat transfer model has been used several times for validation with excellent results on structures from 0.01 m^3 up to 1050 m^3 [6].

2.2 Mechanical part

The mechanical part combines extended B3 creep model [11] with isotropic damage model. The incremental constitutive equation reads

$$\Delta\sigma_{eff} = \bar{E}\mathbf{D}_\mathbf{V}(\Delta\varepsilon-\Delta\varepsilon''-\Delta\varepsilon_{sh,aut}-\Delta\varepsilon_T) \tag{5}$$

where $\Delta\sigma_{eff}$ is an increment of effective stress, $\bar{E}$ incremental elastic modulus, $\Delta\varepsilon$ strain increment, $\Delta\varepsilon''$ strain increment due to creep, $\Delta\varepsilon_{sh,aut}$ an increment of autogeneous shrinkage, $\Delta\varepsilon_T$ thermal strain increment [11],[16]. $\mathbf{D}_\mathbf{V}$ stands for a unit elastic stiffness matrix. The nominal stress is computed from damage mechanics as

$$\sigma = (1-\omega)\sigma_{eff} \tag{6}$$

where ω is damage. Damage is initiated when the effective principal tensile stress exceeds the tensile strength of concrete. Exponential softening is assumed with a crack-band approach to maintain objectivity with respect to the mesh size [10]. Evolution of compressive strength, tensile strength and fracture energy is adopted from ModelCode 2010 [15] and a user can directly enter concrete strength at 28 days. Autogeneous shrinkage is controlled by maximum asymptotic value and the evolution can be specified according to ModelCode 2010 [15] or B4 model [16]. The crack width *w* is evaluated as

$$w = L_{ch}\omega\varepsilon_{1,red} \tag{7}$$

where L_{ch} stands for element length projected from first principal stress and $\varepsilon_{1,red}$ is the first principal strain decreased by thermal and autogeneous strain.

A staggered approach is adopted such that thermal part passes temperatures to the mechanical part. A user can set the end of setting time (4 hours by default) and beginning of mechanical analysis (8 hours by default).

3. Thermo-mechanical validation

3.1 Temperatures on Sri Lanka's foundation caps

A new commertial/residential building Access Tower II with 28 floors has been constructed during 2014-2016. There has been several pile cap foundations, the biggest one with dimensions of 16.0 x 8.0 x 2.5m. Technical standards specified maximum concrete temperature of 70°C with compressive strength over 45 MPa at 28 days. After concrete mix optimization, 395 kg/m^3 of fly ash cement was used. A pile cap with dimensions of 7.15 x 7.15 x 2.5 m was validated via gage T3 which is located 125 mm from the concrete surface as showed in Figure 4. The maximum measured temperature in T1 was of 70.1^{o}C while ConTemp predicted 72.7^{o}C. Thermal gages served also in other two pile caps with slightly different dimensions, yielding maximum temperature differences 2.2 and 1.6^{o}C.

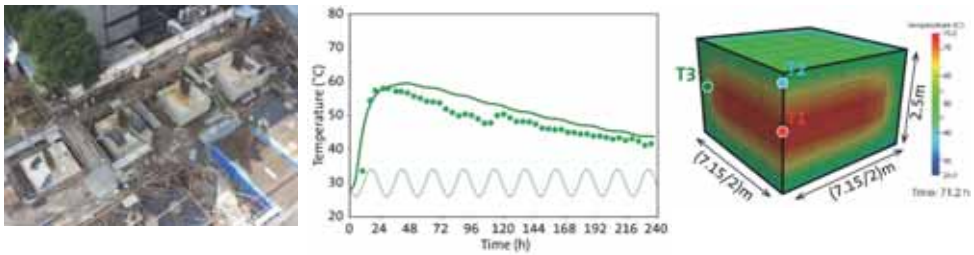

Figure 4: Top view of foundation caps, temperature validation in gage T3 and temperature field in a characteristic cap

3.2 Gas turbine foundation in Ecuador

A massive concrete slab for a gas turbine foundation in Ecuador was cast in 2014. Outer dimensions were approximately 20.0 x 6.0 m with slab thickness of 2.0 and 2.8 m as showed in Figure 5. The concrete mix initial design considered 403 kg/m^3 of cement which yielded simulated temperature 85.5^{o}C, too high to be accepted.

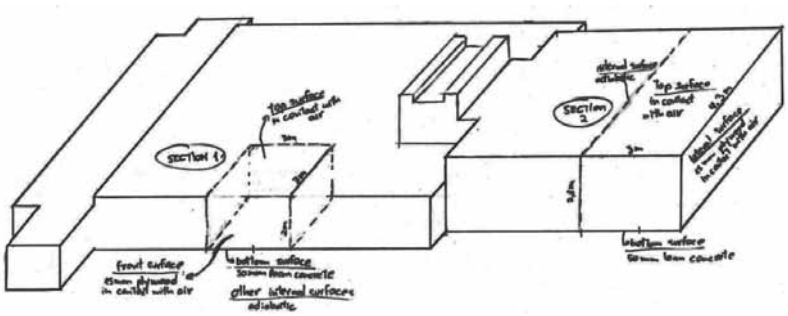

Figure 5: A sketch of a gas turbine foundation in Ecuador

Based on this result, the amount of cement was decreased to 350 kg/m^3 and water was replaced with ice in the amount of 175 kg/m^3. As a result, ConTemp predictions indicate that the mix temperature being cast dropped to 22.5^{o}C instead of 27^{o}C. The maximum temperature in the block reached 71^{o}C which is in agreement with the measured data, see Figure 6.

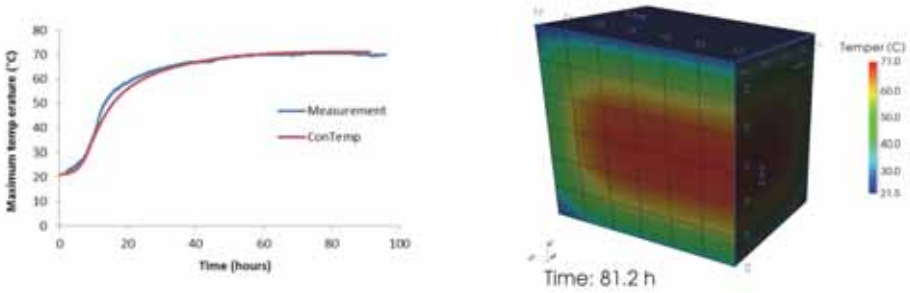

Figure 6: Validation of maximum core temperature and temperature field at maximum temperature

3.3 Thermo-chemo-mechanical simulation of Oslo's restrained wall

The Norwegian Public Roads Administration developed a "low-heat" concrete with a minimal risk of early-age cracking with a forerunner experiment for Bjørvika submerged tunnel project running between 2005 and 2012. A reference concrete SV 40 with CEM I 52.5 404 kg/m^3 and silica fume 20 kg/m^3 was tested from a series of small-scale lab tests to a restrained wall [17]. The first test was a small semi-adiabatic calorimeter using a concrete cube with 247 mm edge wrapped in EPS foam. The cement used in this test had slightly higher initial kinetics than that of similar cement in ConTemp database; hence, the kinetic was slightly increased to match core temperature in the adiabatic calorimeter, see Figure 7. A restrained wall with the

same concrete composition was built in Oslo, see Figure 8. In particular, the right wall utilized low-heat concrete with a minimal risk of early-are cracking and high water tightness, whereas the left wall utilized SV40 concrete for reference. Both walls were cast on a hardened raft concrete slab [17]. The left wall is validated using thermo-chemo-mechanical model in ConTemp.

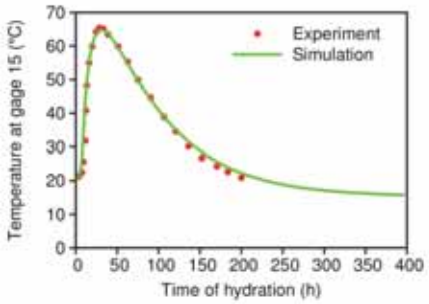

Figure 7: Core concrete temperature is a semi-adiabatic calorimeter

Figure 8: A restrained wall in Oslo [17]

Thermal simulation is carried out on a wall with a cross section of 1.0 x 2.0 m. The length was shortened to 6.5 m to decrease computing time. The next reduction came from symmetry so the modeled block size shrank to 0.5 x 2.0 x 3.25 m.

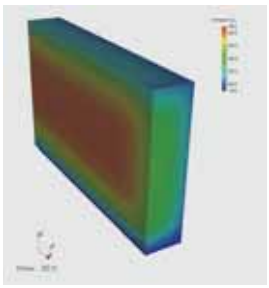

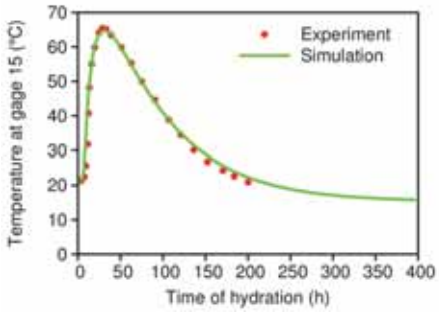

Figure 9: Temperature field during maximum temperature at 30 hours and validation

A fixed temperature of 15^{o}C was assigned to the bottom and fluctuating ambient temperature ranging 12-18^{o}C was prescribed to other surfaces. Heat transfer coefficients set at 4.50 W/m^2/K acted on vertical surfaces covered with a formwork while the top was covered with a foil yielding a heat transfer coefficient of 13.50 W/m^2/K. Figure 9 shows temperature validation in gage 15, located in the middle of the wall and 1.2 m from the bottom. Formwork was removed after 216 hours from mixing time and formwork stripping down was neglected in the simulation.

The mechanical part in ConTemp used B3 creep model for concrete with microprestress-solidification extension [11]. A mean compressive concrete strength was set at 77 MPa,

ultimate autogeneous shrinkage -180 με, and the coefficient of thermal expansion taken $10 \cdot 10^{-6}\,K^{-1}$ as the average [17]. Reinforcement ratio was estimated as 0.002 which had small effect on mechanical behavior and improved convergence. It was assumed that the hardened concrete fully restrained the bottom of the simulated wall.

The simulation shows that first cracks on the surface appeared already in 12 hours but they closed at 60 hours due to surface cooling. The majority of the cracks appeared after 70 hours on the interface with the hardened concrete base where a high shear stress leads to tension on inclined planes. Figure 10 shows cracks and principal stress at t=300 h, where the widest cracks attain width of 0.58 mm. The validation of horizontal strain measured by vibrating wire strain gage is in agreement with experimental data, see Figure 10.

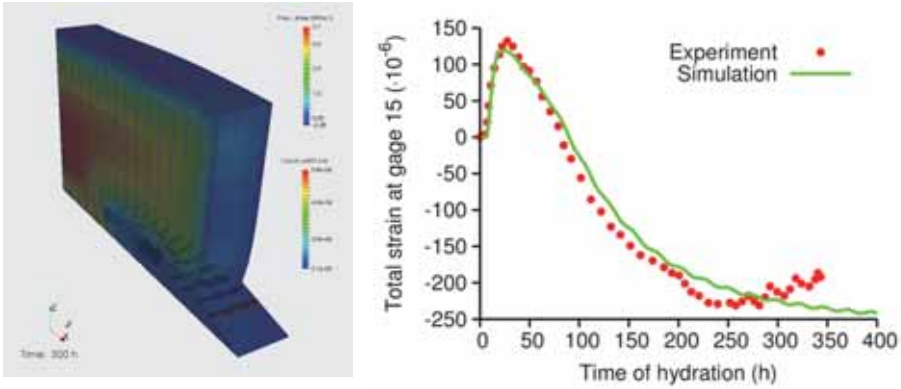

Figure 10: First principal stress and cracks at 300 hours. Validation of horizontal strain

4. Extension for durability

The presence of cracks accelerates both carbonation and chloride ingress. Carbonation depth can be computed from Papadakis and Tsimas's model [18], which reads

$$x_c = \sqrt{\frac{2D_{e,CO2}CO_2}{0.218(C+kP)}}\sqrt{t} = A_1\sqrt{t} \tag{8}$$

and the acceleration due to crack width can be computed with Kwon and Na's model [19]

$$x_c(t) = (2.816\sqrt{w}+1)A_1\sqrt{t} \tag{9}$$

where w is the crack width (mm). Note that the presence of a 0.3 mm wide crack increases carbonation depth by a factor of 2.54. This also means that induction time is 6.46 times shorter compared to a sound concrete.

The model for chloride ingress is based on Kwon et al. [19] as 1D transient problem with initially free chloride content

$$C(x,t) = C_S\left[1 - erf\left(\frac{x}{2\sqrt{D_m(t)\,f(w)t}}\right)\right] \tag{10}$$

where C_S is the chloride content at surface (kg·m^{-3}), D_m is the averaged diffusion coefficient at time t (mm^{2}s^{-1}), x is the position from the surface in mm and $f(w)$ gives the acceleration by cracking (equals to one for a crack-free concrete). Based on recent results, the following scaling function is proposed (Kwon, Na et al. 2009)

$$f(w) = 31.61w^2 + 4.73w + 1 \tag{11}$$

where w stands for crack width (mm). The presence of a 0.3 mm crack increases the mean diffusion coefficient by a factor of 5.26. In reality, crack width evolves and incremental solution needs to be formulated. Several examples for carbonation and chloride ingress were already presented in [20].

5. Conclusions

ConTemp is a valuable tool for predicting thermo-mechanical behaviour of reinforced massive concrete blocks. Current experience and validation concludes that

1. ConTemp's performance is highly reliable for temperature predictions under various boundary conditions.
2. ConTemp's mechanical part shows good validation in a few tested examples. Further validations run currently on other benchmarks.
3. Predicted crack width serves for models of carbonation and chloride ingress. A crack width of 0.3 mm decreases induction time approximately six fold for both phenomena.

We gratefully acknowledge the financial support from the Technology Agency of the Czech Republic TAČR under the projects TA04031458 (durability) and TE01020168 (optimization). We thank Czech Technical University in Prague for further support during SGS12/116/OHK1/2T/11 project.

References

[1] Neville, A.M.: Properties of Concrete, 4th edn. Wiley, London, UK (1997)
[2] Weiss, W., Yang, W., Shah, S.: Factors influencing durability and early-age cracking in high strength concrete structures. In: High Performance Concrete: Research to Practice, Farmington Hills, MI (1999) 387–409
[3] Bentz, D. P., Waller, V., and de Larrard, F. Prediction of Adiabatic Temperature Rise in Conventional and High-Performance Concretes Using a 3-D Microstructural Model. Cem. Concr. Res. 28 (1998) 285–297
[4] Estrada, C. F., Godoy, L. A., and Prato, T. Thermo-mechanical behavior of a thin concrete shell during its early age. Thin-Walled Struct. 44 (2006) 483–495

[5] Park, K.-B., Jee, N.-Y., Yoon, I.-S., and Lee, H.-S. Prediction of Temperature Distribution in High-Strength Concrete Using Hydration Model. ACI Mater. J. 105 (2008) 180–186
[6] Leal Da Silva, W., Šmilauer, V., Štemberk, P.: Upscaling semi-adiabatic measurements for simulating temperature evolution of mass concrete structures. Materials and Structures 48 (2015) 1031-1041
[7] Briffaut, M., Benboudjema, F., Torrenti, J-M, Nahas, G.: Analysis of semi-adiabiatic tests for the prediction of early-age behaviour of massive concrete structures, Cement and Concrete Composites 34 (2012) 634–641
[8] Gawin, D., Pesavento, F., Schrefler, B.A.: Hygro-thermo-chemo-mechanical modelling of concrete at early ages and beyond. Part I: hydration and hygro-thermal phenomena. International Journal for Numerical Methods in Engineering 67 (2006) 299–331
[9] Gawin, D., Pesavento, F., Schrefler, B.A.: Hygro-thermo-chemo-mechanical modelling of concrete at early ages and beyond. Part II: shrinkage and creep of concrete. International Journal for Numerical Methods in Engineering 67 (2006) 332–363
[10] Patzák, B.: OOFEM - an object-oriented simulation tool for advanced modeling of materials and structures. Acta Polytechnica, 52 (2012) 59–66
[11] Jirásek, M. and Havlásek, P.: Microprestress-solidification theory of concrete creep: Reformulation and improvement. Cement and Concrete Research 60 (2014) 51–62
[12] Hellmich, C., Mang, H.A., Ulm, F. J.: Hybrid method for quantification of stress states in shotcrete tunnel shells: combination of 3D in situ displacement measurements and thermochemoplastic material law. Computers & Structures 79 (2001) 2103–2115
[13] Jendele, L., Šmilauer, V., Červenka, J.: Multiscale hydro-thermo-mechanical model for early-age and mature concrete structures. Advances in Engineering Software 72 (2014) 134-146
[14] Ulm, F.J., Coussy, O.: Couplings in early-age concrete: From material modeling to structural design. International Journal of Solids and Structures 35 (1998) 4295–4311
[15] Fédération Internationale du Béton. Model Code 2010. Vol. 55 in fib Bulletin. International Federation for Structural Concrete (fib), 2010
[16] RILEM Technical Committee TC-242-MDC (Z. P. Bažant, chair): Model B4 for creep, drying shrinkage and autogenous shrinkage of normal and high-strength concretes with multi-decade applicability. Materials and Structures, 48 (2015) 753–770
[17] Ji, G.: Cracking risk of concrete structures in the hardening phase: Experiments, material modeling and finite element analysis, Ph.D. thesis, NTNU, 2008
[18] Papadakis, V. G. and S. Tsimas: Supplementary Cementing Materials in Concrete. Part I: Efficiency and Design. Cement and Concrete Research 32 (2002) 1525–1532
[19] Kwon, S. J., U. J. Na, et al.: Service Life Prediction of Concrete Wharves with Early-aged Crack: Probabilistic Approach for Chloride Diffusion. Structural Safety 31 (2009) 75-83
[20] Šmilauer, V., Jendele, L., Červenka, J.: Prediction of Carbonation and Chloride Ingress in Cracked Concrete Structures. In Proceedings of the Fourteenth International Conference on Civil, Structural and Environmental Engineering Computing. Stirling: Civil-Comp Press Ltd (2013), 1-12

International RILEM Conference on Materials, Systems and Structures in Civil Engineering
Conference segment on Service Life of Cement-Based Materials and Structures
22-24 August 2016, Technical University of Denmark, Lyngby, Denmark

MECHANICAL PROPERTIES OF ULTRA HIGH PERFORMANCE FIBRE REINFORCED CONCRETE

Radoslav Sovják [(1)]

(1) Czech Technical University in Prague, Czech Republic

Abstract
Ultra-high performance fiber reinforced concrete is a composite material with a high cement and silica fume content, a low water-binder ratio, and aggregates smaller than 4 mm. It has outstanding material characteristics such as self-consolidating workability, very high mechanical properties and low permeability, which results in excellent environmental resistance. Typical strengths are 100 to 200 MPa in uniaxial compression and 6 to 15 MPa in uniaxial tension. Moreover, these materials exhibit strain hardening under tension and a significant energy absorption capacity. In addition, the author describes a formulation process for ultra-high performance fiber reinforced concrete that has been developed without using heat treatment, pressure, or a special mixer. Only ordinary materials available commercially in the Czech Republic were utilized throughout the material design process.

1. Introduction

UHPFRC can be characterized as a cementitous composite containing large volume of steel fibres, low water-binder ratio, high microsilica and cement content and absence of coarse aggregate i.e. larger than 4 mm [1]. Typical strengths are 150 to 200 MPa in compression and 7 to 15 MPa in uniaxial tension [2]. Moreover, these materials exhibit strain hardening under tension [3,4] and high energy absorption capacity [5,6]. It is well known that traditional fibre reinforced concrete with normal strength matrix has large capacity to absorb energy [7]. However, several authors suggest that UHPFRC has much greater capability to absorb energy [8–10].

The UHPFRC can be also characterized by very low porosity which makes the material predestined to be highly durable [11] in any possible conditions including chemically-based degradation processes or freeze/thaw cycles. UHPFRC has very low permeability which is the

first line of defence against any of the physio-chemical deterioration processes [11] and results in excellent environmental resistance [12–14]. Regularly, a service lifetime of 75+ years is expected from expensive public works [15]. However, concrete often undergoes significant alternations that often have significant adverse consequences on its engineering properties while interacting with its service environment [16]. Nowadays, normal strength concretes are gradually replaced by the high-strength concretes and ultra-high performance concretes, especially in structures exposed to the severe environment [16]. Through the use of UHPFRC, which displays significantly higher impermeability, durability problems may be solved. Several researchers stated that UHPFRC has the potential to address the poor condition of the ageing infrastructure [17].

This study focuses on an evaluation of mechanical properties of ultra-high performance fiber reinforced concrete developed in the Czech Republic from local materials. Experimental techniques as well as results for compressive strength, bending strength, direct tensile strength, fracture energy, modulus of elasticity and triaxial compressive strength are described in this paper. In addition a brief mixing procedure as well as sample preparation is presented. This paper presents results on a broad variety of mechanical properties where fiber content was selected as the main variable.

The first mixture was designed following the proportions of cement : silica fume : glass powder recommended by Wille [1] as 1 : 0.25 : 0.25 with a water-binder ratio of 0.2. Subsequent changes in the most important parameters such as high-range water reducer, water content, amount of aggregate, silica fume, and glass powder led to an optimized cementitious matrix in terms of compressive strength and workability. From the 24 tested mixtures, the best performing composition was chosen (Table 1). High particle packing density is a key property of ultra-high compressive strength of concrete. Therefore, the mixture design was based on optimizing the particle packing density of sand, silica fume, glass powder, and cement. Improving particle packing was achieved mainly by changing the matrix composition and proportions and by selecting ranges of particles for sand.

Table 1: Mixture design including various fiber contents

Type of component	Proportions by weight			
	UHPC	UHPFRC		
Cement CEM I 52,5R	1	1	1	1
Silica fume	0.25	0.25	0.25	0.25
Glass powder	0.25	0.25	0.25	0.25
Water	0.22	0.22	0.22	0.22
(HRWR) Sika SVC 20 Gold	0.031	0.031	0.031	0.031
(HRWR) Sika ViscoCrete 20He	0.019	0.019	0.019	0.019
Fine sand 0.1/0.6 mm	0.42	0.42	0.42	0.42
Fine sand 0.3/0.8 mm	1.0	0.9	0.8	0.7
Water/binder ratio	0.2	0.2	0.2	0.2
Fibers	-	0.1	0.2	0.3

The UHPFRC was mixed in the conventional mixers and the specimens were cured in water tanks under ambient temperature (20°C). The UHPFRC was produced using high cement and silica fume contents, a low water-binder ratio and aggregates smaller than 1 mm. The content of the cement in the UHPFRC mixture used in this study according to the Table 1 was 700 kg/m^3. Straight steel micro fibers were used in the UHPFRC mixture in order to improve ductility of the material. The fibers were 13 mm in length and 0.14 mm in diameter.

During the mixing of UHPFRC, it is very important to achieve good workability, particle distribution and packing density. The densest hardened cement paste could only be obtained when the packing density is high enough while the space among particles is fully filled up by hydrates [18]. In comparison with normal strength concrete, UHPFRC contains more constituents and finer particles. Several researchers have recommended mixing all fine dry particles first before adding water and high-range water reducers [1,3]. This is because the small particles tend to agglomerate, and it is easier to break these chunks when the particles are dry. The specific mixing procedure was as follows: In the first step, both types of aggregate and silica fume were mixed for five minutes. In the second step, cement and glass powder were mixed for another five minutes. At the end of the procedure, water and high-range water reducers were added gradually. The mixture became fully workable after another five more minutes.

Straight steel fibres were added up to 3% of volume in replacement of the equivalent volume of coarser sand to the best performing mixture. Straight fibres were used because it is known that they provide a good trade-off between tensile properties and workability of the composite. The tensile strength of the fibres was 2800 MPa, as specified by the manufacturer. The fibres were added at the end of the mixing procedure to the fully workable mixture and the fibres were mixed with the mixture for another five minutes. Thus, the mixing time for mixture containing fibres was 20 minutes.

2. Mechanical Properties

Compressive strength and secant modulus of elasticity were measured on cylinders with a diameter of 100 mm and height of 200 mm. The strength of the best available capping material (100 MPa) is significantly lower than expected UHPFRC strength values. Consequently, the tops of the cylinders were cut off and ground. Compressive strength was measured on cylinders by monotonic increments of pressure with an average rate of 36 MPa/min up to 70% of the expected compressive strength. At this point loading was switched to deformation controlled loading with a rate of 0.48 mm/min for about 2 minutes in order to measure peak and post peak behavior. In the softening branch, the loading rate was increased to 1.2 mm/min.

Modulus of elasticity was measured using two strain gauges (with a measurement length amounting to 100 mm) attached to the lateral surface of the cylindrical specimens. A hydraulic loading machine DSM2500-100 was used and the loading procedure was stress controlled. In the first step, the specimens were loaded to 1/3 of the expected compressive strength – in this case 50 MPa – for 60 seconds. Afterwards, the specimens were unloaded to

5 MPa. This procedure was repeated three times. The secant modulus of elasticity was calculated from the third unloading branch. In the second step, the specimens were loaded until failure and compressive strength was determined.

Direct tensile tests were carried out on "dog-bone" shaped specimens without a notch. The direct tensile tests were performed on MTS loading machine. The specimens were mounted into specially developed grips. The extension in the elastic region was measured with two strain gauges glued on both narrow sides. After the localization of a crack, the extension was measured with two LVDTs mounted with a special frame to the dog-bone specimens. The loading rate was 0.2 mm/min.

Flexural strength was determined in three-point-bending tests on $100 \times 100 \times 400$ mm^3 large beams with a clear span of 300 mm. The loading rate was set to 0.2 mm/min. Fracture energy was determined on $100 \times 100 \times 550$ mm^3 large beams with a 30 mm deep notch and clear span of 500 mm. During each test, the deflection in the mid-span of the specimen was recorded. The fracture energy was determined based on the load-deflection curve as specified by RILEM recommendations [19,20].

The triaxial compressive strength was determined simultaneously on cylinder and cubes made of UHPC. The cylinders were 200 mm in height and 100 mm in diameter; the sides of the cube were 100 mm long. The cylinders were tested in a triaxial chamber, where the confinement pressure was provided by mineral oil. A waterproof coating was provided for all cylinders in order to avoid the ingress of mineral oil into the UHPC structure. It was verified experimentally that this kind of coating has no influence on the uniaxial compressive strength. At first, the cylinders were prestressed by the crossbeam of the hydraulic loading machine. Afterwards, the chamber with the UHPC cylinder was flooded by the mineral oil, which was subsequently pressurized to the prescribed confinement pressure.

The cubes were tested in a triaxial hydraulic loading machine, in which each side of the cube was pushed by the loading plate with dimensions 95×95 mm^2. The cubes were placed in the hydraulic loading machine, and all the loading plates applied the compressive stress simultaneously until the prescribed confinement pressure was reached. At this point, two directions were fixed to the confinement stress, while the stress in the third direction was further increased until failure of the UHPC cube. A further detailed description of the testing device and the testing procedure can be found in the work of Hampel et al. [21]. In both cases, i.e. cylinders and cubes, the loading was controlled by the increments of the deformation. The loading speed was 0.48 mm/min.

3. Results and discussion

Table 2 shows determined compressive, flexural, and tensile strength, as well as secant modulus of elasticity and effective fracture energy of the investigated material, as a function of the fiber content. The values presented in the Table 2 are averages from five samples. It can be seen that the average highest compressive strength of 151.7 MPa was achieved for 2 % volumetric content of fibers. In correspondence with that, the highest average secant modulus

of elasticity of 56.9 GPa was measured for 2% fiber volume content. The highest fracture energy, flexural, and direct tensile strength was achieved for samples containing 3% of fibers by volume.

Table 2: Mechanical properties of the UHPC and UHPFRC mixtures

	UHPC	UHPFRC		
Fiber content [%]	0	1	2	3
Workability – spread [mm]	200	220	225	190
Compressive strength [MPa]	132.4	148.5	151.7	148.1
Flexural strength [MPa]	9.9	27.0	40.1	47.5
Direct tensile strength [MPa]	6.6	7.8	9.9	10.9
Modulus of elasticity [GPa]	41.1	45.1	56.9	51.5
Effective fracture energy [kJ/m^2]	0.35	12.0	17.9	25.3
Density [kg/m^3]	2270	2310	2360	2410

The results of the uniaxial tensile tests on specimens containing 0, 1, 2 and 3 % of fibers respectively are presented in Figure 1. The figure is divided into two parts that are typical for UHPFRC behavior: a) linear-elastic and strain hardening part, which includes the linear-elastic stress rise and the strain hardening part of stress-strain diagram and b) the softening part in which the energy is dissipated in a localized crack at the crack surface.

Figure 1a) shows the stress-strain relationship in the strain hardening part of the curve. The stress is calculated by dividing the measured force by the reduced cross-section of the dog bone specimen (30 × 30 mm^2). Strain values were determined as the average strain measured by two strain gauges, which were glued on the side of the specimen. Figure 1b) provides the relation between stress and total crack width during softening. The total crack width was measured as an average from two LVDTs which spanned over the entire reduced cross-section of the specimen. The average apparent strain at the end of strain hardening region was 154 µm/m for samples with 1% of fibers, 1105 µm/m for samples with 2% of fibers and 1081 µm/m for samples containing 3% of fibers. Wuest [22] used similar types of fibers

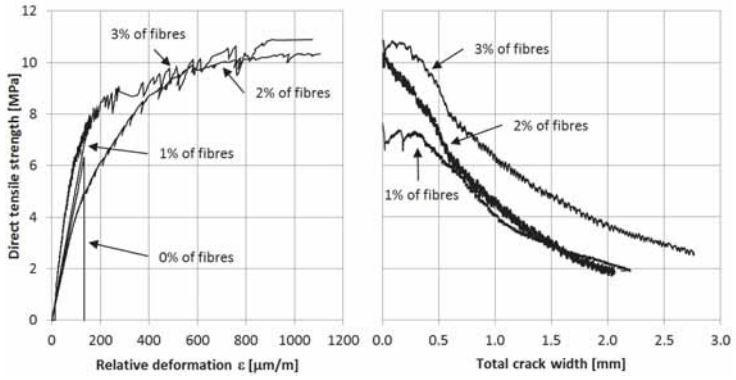

Figure 1: Tensile behavior of UHPC and UHPFRC

(2.5% vol.) and measured 2400 μm/m at the end of strain hardening region at a tensile strength of 14.2 MPa which is more than observed in this study where the average direct tensile strength was 7.7 MPa, 10.3 MPa, and 10.9 MPa, respectively.

The experimental results shown in this study showed that an increase in the fiber volume fraction resulted in an increase in the effective fracture energy (Figure 2). A closer examination of the fracture surface revealed fibre pull-out from the matrix, which is more energy-expensive than fibre rupture (Figure 3). Data obtained by other researchers dealing with UHPFRC with straight steel micro-fibres subjected to flexure using notched specimen were examined in order to verify the results derived from this study. Kang et al. [23] tested UHPFRC using a notched 3-point bending test, where the fibre volume fraction varied from 1% to 5%. The UHPFRC used in their study was mixed using a *w/b* ratio of 0.2 and steel fibres with an aspect ratio of 65 (13×0.2 mm). The tensile strength of the fibres was specified to be 2500 MPa. The beams were 400 mm in length (300 mm clear span) with a notch 30 mm in height. The effective fracture energy derived from their study increased approximately linearly with an increasing fibre volume fraction until 5%. A linear increase in G_f was also observed in the work conducted by Yoo et al. [24]. Yoo et al. tested UHPFRC up to 4% of the fibre volume fraction, and the effective fracture energy values tended to increase as the fibre volume increased. Yoo et al. also tested smooth steel fibres with an aspect ratio of 65 (13×0.2 mm) and with tensile strength of 2500 MPa. The beams were 400 mm in length with a 300 mm-long clear span, and the notch was 10 mm in height. The average compressive strength of the UHPFRC used by Yoo et al. ranged from 182 MPa to 207 MPa.

The energy absorption capacity is the main material property that benefits from fibre reinforcement. The effective fracture energy of a material is defined as the energy required to open a unit crack surface area. The fracture energy is primarily governed by the tensile mechanism of the material, and represents the amount of energy consumed when a crack propagates through a beam. The effective fracture energy is a key parameter for evaluating the ability of a material to withstand an impact or blast load and also to redistribute the load from the exposed structure to its surrounding parts. It can be stated that the resistance of civil infrastructure is strongly related to the energy absorption capacity. Such a material with certain properties and specifications is well suited for energy absorption facade panels and key elements of building structures that may be exposed to impacts or blast loads [25,26].

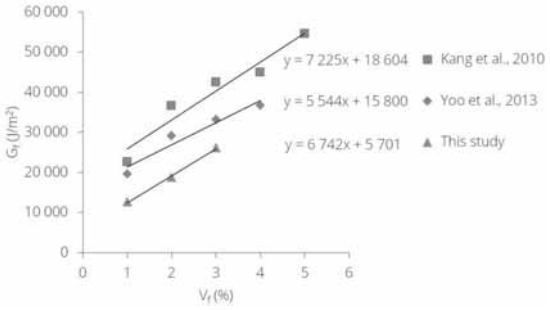

Figure 2: Effect of fiber volume fraction on the effective fracture energy of UHPFRC

Figure 3: Micro-fibers used in this study and pull-out failure mode

Triaxial loading better reflects the actual behavior of the material in construction than conventional uniaxial tests. The triaxial compressive strength was characterized using various samples and loading procedures. UHPC without fibers was used for the triaxial compressive strength tests, as it has been found that fibers have no effect on triaxial compressive strength [27]. The triaxial compressive strength was determined under confinement pressures amounting to 10, 20, 30 MPa for the cylinders, and to 15, 30, 60, 90 MPa for the cubes (Table 3). The triaxial compressive strength values determined under elevated confinement pressure were normalized by the uniaxial compressive strength, in order to obtain the first evaluating parameter. The ratio of the confinement pressure and the uniaxial compressive strength was used as a second parameter, in order to describe the strength of the UHPC in triaxial compression. As the confinement pressure increased, the UHPC compressive strength also increased. The best reliability, using the least square method, was achieved by fitting the development of UHPC triaxial strength by the power law function (Figure 4).

The dependence of the UHPC triaxial strength on confinement pressure can be fitted by a power-law regression function. Evaluating this regression function for a confinement pressure equal to the uniaxial compressive strength, it is estimated that the triaxial compressive strength is 381 MPa for cylinders and 548 MPa for cubes. Figure 4 also shows that the failure surface of UHPC falls below the failure surface of the conventional normal strength concrete [27,28], especially at higher confining pressures [29,30].

Table 3: Triaxial compressive strength of the UHPC

Confinement pressure [MPa]	Sample	
	Cylinder [MPa]	Cube [MPa]
0	123	148
10	178	-
15	-	231
20	209	-
30	231	280
60	-	362
90	-	432

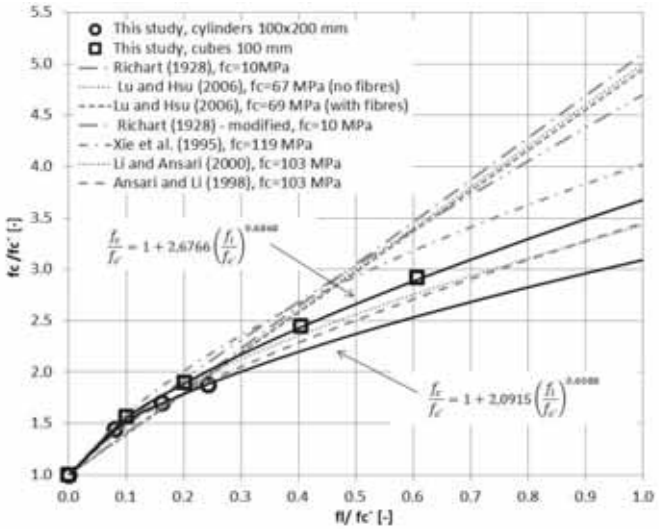

Figure 4: Development of triaxial compressive strength

4. Conclusions

A UHPFRC mixture was developed in this study to find the best-performing combination of constituents with respect to workability and strength. The experimental work described herein showed that it is relatively easy to create an UHPFRC with superior mechanical properties using standard mixing and curing techniques. With an increase in target mechanical parameters, UHPC and UHPFRC become more sensitive to quality of the components, the dispersion of the particles, mixing procedure, the specimen preparation, and curing. The brittle behavior of UHPC is greatly improved when short steel fibers are added into the mixture as a replacement of coarse aggregates. During the direct tensile tests, multiple evenly spaced cracking was observed at the sides of specimens made of UHPFRC, which indicates strain hardening behavior. The failure mode was observed by pull-out of the fibers which increases the capacity to absorb energy. The fracture energy of the UHPFRC is approximately five times higher than that of conventional fiber reinforced concrete. It is believed, that such type of material is the future of concrete industry, it will allow executing higher, more effective structures with excellent durability.

Acknowledgement

The author gratefully acknowledges the assistance given by the Experimental Centre at the Czech Technical University in Prague and also by the Otto-Mohr-Laboratory at the Technical University in Dresden.

References

[1] Wille K, Naaman AE, Parra-Montesinos GJ. Ultra-high performance concrete with compressive strength exceeding 150 MPa (22 ksi): a simpler way. ACI Materials Journal 2011;108:46–54. doi:10.14359/51664215.

[2] Nicolaides D, Kanellopoulos A, Petrou M, Savva P, Mina A. Development of a new Ultra High Performance Fibre Reinforced Cementitious Composite (UHPFRCC) for impact and blast protection of structures. Construction and Building Materials 2015;95:667–74. doi:10.1016/j.conbuildmat.2015.07.136.

[3] Habel K, Charron J-P, Braike S, Hooton RD, Gauvreau P, Massicotte B. Ultra-high performance fibre reinforced concrete mix design in central Canada. Canadian Journal of Civil Engineering 2008;35:217–24. doi:10.1139/L07-114.

[4] Rossi P, Arca A, Parant E, Fakhri P. Bending and compressive behaviours of a new cement composite. Cement and Concrete Research 2005;35:27–33.

[5] Habel K, Gauvreau P. Response of ultra-high performance fiber reinforced concrete (UHPFRC) to impact and static loading. Cement and Concrete Composites 2008;30:938–46.

[6] Bindiganavile V, Banthia N, Aarup B. Impact response of ultra-high-strength fiber-reinforced cement composite. ACI Materials Journal 2002;99.

[7] Wang N, Mindess S, Ko K. Fibre reinforced concrete beams under impact loading. Cement and Concrete Research 1996;26:363–76.

[8] Farnam Y, Mohammadi S, Shekarchi M. Experimental and numerical investigations of low velocity impact behavior of high-performance fiber-reinforced cement based composite. International Journal of Impact Engineering 2010;37:220–9.

[9] Maalej M, Quek ST, Zhang J. Behavior of hybrid-fiber engineered cementitious composites subjected to dynamic tensile loading and projectile impact. Journal of Materials in Civil Engineering 2005;17:143–52.

[10] Nicolaides D, Kanellopoulos A, Savva P, Petrou M. Experimental field investigation of impact and blast load resistance of Ultra High Performance Fibre Reinforced Cementitious Composites (UHPFRCCs). Construction and Building Materials 2015;95:566–74. doi:10.1016/j.conbuildmat.2015.07.141.

[11] Mehta PK. Concrete technology at the crossroads--problems and opportunities. ACI Special Publication 1994;144.

[12] Marchand J, Gagné R, Pigeon M, Jacobsen S, Sellevold EJ. The frost durability of high-performance concrete. Concrete Under Severe Conditions: Environmental and Loading 1995;1:273.

[13] Fagerlund G. Frost resistance of high performance concrete--some theoretical considerations: a contribution to RILEM-3C-Workshop“ Durability of high performance concrete”, Wien 14th-15th February, 1994. Report TVBM 1993.

[14] Pigeon M, Gagné R, Aïtcin P-C, Banthia N. Freezing and thawing tests of high-strength concretes. Cement and Concrete Research 1991;21:844–52. doi:10.1016/0008-8846(91)90179-L.

[15] Alexander MG, Stanish K. Durability design and specification of reinforced concrete structures using a multi-factor approach. Mindess Symposium, Third Int. Conference on Construction Materials, Vancouver, 2005.

[16] Chan SYN, Luo X, Sun W. Effect of high temperature and cooling regimes on the

compressive strength and pore properties of high performance concrete. Construction and Building Materials 2000;14:261–6. doi:10.1016/S0950-0618(00)00031-3.

[17] Wille K, Boisvert-Cotulio C. Material efficiency in the design of ultra-high performance concrete. Construction and Building Materials 2015;86:33–43. doi:10.1016/j.conbuildmat.2015.03.087.

[18] Ye G, Xin H, Bao-lin Z, Bao-guo M, Hong-bo Z. Method for calculating packing density of powder particles in paste with continuous particle size distribution. Powder Technology 2008;187:88–93. doi:10.1016/j.powtec.2008.01.026.

[19] Bažant ZP, Kazemi MT. Size dependence of concrete fracture energy determined by RILEM work-of-fracture method. International Journal of Fracture 1991;51:121–38. doi:10.1007/BF00033974.

[20] Hillerborg A. Concrete fracture energy tests performed by 9 laboratories according to a draft RILEM recommendation: Report to RILEM TC50-FMC. Report TVBM 1983.

[21] Hampel T, Speck K, Scheerer S, Ritter R, Curbach M. High-Performance Concrete under Biaxial and Triaxial Loads. Journal of Engineering Mechanics 2009;135:1274–80.

[22] Wuest J, Denarié E, Brühwiler E. Measurement and modelling of fibre distribution and orientation in UHPFRC. Proceedings, HPFRCC 2007;5.

[23] Kang S-T, Lee Y, Park Y-D, Kim J-K. Tensile fracture properties of an Ultra High Performance Fiber Reinforced Concrete (UHPFRC) with steel fiber. Composite Structures 2010;92:61–71. doi:10.1016/j.compstruct.2009.06.012.

[24] Yoo D-Y, Lee J-H, Yoon Y-S. Effect of fiber content on mechanical and fracture properties of ultra high performance fiber reinforced cementitious composites. Composite Structures 2013;106:742–53. doi:10.1016/j.compstruct.2013.07.033.

[25] Sovják R, Vavřiník T, Zatloukal J, Máca P, Mičunek T, Frydrýn M. Resistance of slim UHPFRC targets to projectile impact using in-service bullets. International Journal of Impact Engineering 2015;76:166–77. doi:10.1016/j.ijimpeng.2014.10.002.

[26] Máca P, Sovják R, Konvalinka P. Mix Design of UHPFRC and its Response to Projectile Impact. International Journal of Impact Engineering 2013. doi:10.1016/j.ijimpeng.2013.08.003.

[27] Lu X, Hsu C-TT. Behavior of high strength concrete with and without steel fiber reinforcement in triaxial compression. Cement and Concrete Research 2006;36:1679–85.

[28] Richart FE. A study of the failure of concrete under combined compressive stresses. University of Illinois Engineering Experiment Station Bulletin 1928;185.

[29] Li Q, Ansari F. High-strength concrete in triaxial compression by different sizes of specimens. ACI Materials Journal 2000;97.

[30] Ansari F, Li Q. High-strength concrete subjected to triaxial compression. ACI Materials Journal 1998;95.

International RILEM Conference on Materials, Systems and Structures in Civil Engineering
Conference segment on Service Life of Cement-Based Materials and Structures
22-24 August 2016, Technical University of Denmark, Lyngby, Denmark

DISCRETE MODELING OF SURFACE CRACKING OF DRYING CONCRETES AT DIFFERENT AGES: APPLICATION TO TU1404 RRT CONCRETE

Arnaud Delaplace [(1)], Clément Vert[(1)], Eric Brouard[(1)]

(1) LafargeHolcim Research Center, Saint Quentin Fallavier, France

Abstract
The drying process of concrete is a well-known phenomenon occurring at early age when the concrete is exposed to ambient conditions. The kinetics of drying is strongly linked to the concrete microstructure, as the water circulates into the paste porosity. In the same way, the induced drying shrinkage is also linked to the paste porosity through the capillary pressure developed in the pore network: the pore size distribution is key when dealing with drying process. This study focuses on the drying process using an analytical model allowing to take into account a gradient of properties due to the difference of hydration degree. In particular, the effect of the hydration gradient between the core and the surface of a concrete sample will be analysed, thanks to the results provided by Round Robin Test of the European action COST TU1404.

1. Introduction

Several studies have shown that the drying process of concrete depends on the time of exposure to drying, as the pore size distribution depends on the hydration degree (see for example [1-3]). Two main effects can be observed as the hydration degree increases:

- the size of the finest pores decreases, leading to a high level of capillary pressure and potentially to a high level of shrinkage
- the concrete Young modulus and the material strength increase.

These effects can be seen at the macroscopic level, through the evolution of the shrinkage vs. the mass loss. This measure is common and described in different international standards (ASTM C490-07, NF EN 680). Nevertheless, the procedure is usually performed starting at a fixed time exposure (after a 7-day curing for example). A single time exposure doesn't allow to deduce the effect of gradient of hydration degree on the shrinkage process.

We propose in the study to analyse the influence of the hydration degree on the drying process, by using experimental campaigns for which different times of drying have been used for the same mix-design, as proposed in the Round Robin Test of the COST TU1404 action. An analytical drying model is used to deduce the properties of the concrete, from the macroscopic response of shrinkage and mass loss. Although the model is very simple and is not applicable at very early age when hydrates properties evolve strongly with time, it represents accurately the shrinkage/mass loss evolution. In a second step, a discrete model is used to evaluate the risk of cracking for different drying conditions.

2. Drying model

2.1 Drying process

The drying process can be represented using different types of models [4]. Basically, drying is a diffusion process between the core of a sample and its external surface. In the case of concrete, it is usually expressed in terms of relative humidity *RH* or moisture content *C*. Considering the moisture content, the diffusion equation reads:

$$\frac{\partial C}{\partial t} - \mathrm{div}(D\ \mathrm{grad}\ C) = 0 \tag{1}$$

For concrete, the diffusion coefficient *D* depends on the moisture content, the hydration degree, the temperature *T*. Different assumptions can be done to simplify the expression of *D*. Solving for a 1D problem with convection boundary conditions, one can evaluate the evolution of moisture content with time. Figure 1 shows such an evolution.

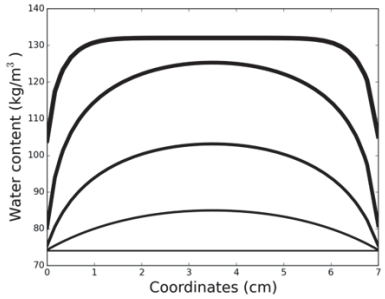

Figure 1: Example of a moisture content evolution solving equation (1) for a 1D problem with convection boundary conditions at x=0 and x=7 cm. The initial moisture content is 132 kg/m^3, the final one 74 kg/m^3. The typical time range between the initial state and the final one is one year for a 7x7x28 cm concrete prismatic sample.

At early age, the moisture content in external layer drops as the internal moisture content decreases slowly. Few days after the beginning of drying, the moisture content of the internal part decreases slowly until the equilibrium is reached.

We propose next to use a simple analytical model to describe this drying process. The main hypothesis is that the moisture content is assumed to be uniformed in the central part and in the external layer. Then, the drying process can be split in two parts [5, 6]:

- First stage: the external layer dries from an initial water content C_{ini} to a final water content C_{end}^{ext}. δ_1 is the final thickness of this external layer.

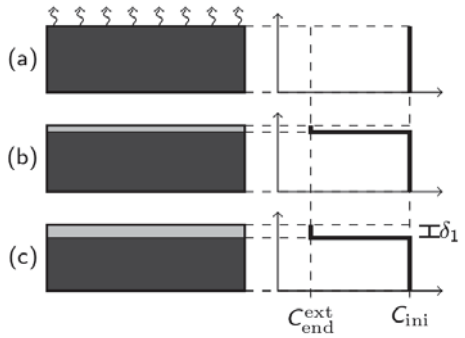

Figure 2: Moisture content for a 2D sample drying on top during first stage.

- Second stage: the internal part dries from the initial water content C_{ini} to a final water content C_{end}^{int}.

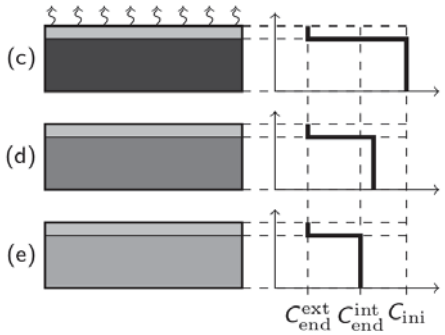

Figure 3: Moisture content for a 2D sample drying on top during second stage.

We consider two final water contents for the internal and external parts because the moisture content is linked to the hydration degree: depending on the initial time of drying, the hydration degree of the external part can be lower than the one of the central part.
From those evolutions, the mass loss μ reads:

$$\mu(\delta) = \frac{V_e(\delta)(C_{ini} - C_{end}^{ext})}{M_0} \text{ for stage 1} \quad (2)$$

where V_e is the volume of the external layer, δ the width of the drying layer and M_0 the initial mass of the sample, and:

$$\mu(C) = \frac{V_e(\delta_1)(C_{\text{ini}} - C_{\text{end}}^{\text{ext}}) - V_c(\delta_1)(C_{\text{ini}} - C)}{M_0} \text{ for stage 2} \quad (3)$$

where δ_1 is the final width of the external layer, V_c=V_{tot}-V_e the volume of the central part.

2.2 Shrinkage

The induced drying shrinkage is computed assuming a uniform distribution of the strain in the cross section, following the Euler-Bernoulli hypothesis. The general stress σ-strain ε relation reads:

$$\sigma = E(1 - D)\varepsilon_e \quad (4)$$

where E is the Young modulus, D is a variable that affects the Young modulus (typically due to cracking), ε_e the elastic strain expressed as ε_e=ε-ε_{sh}. The drying shrinkage ε_{sh} could be assumed to be proportional to the internal relative humidity. The use of the internal moisture can be done using the isotherm of the material. We assume next that for the considering range of relative humidity, a linear dependence is also obtained for the water content: ε_{sh}=κΔC with κ the shrinkage coefficient in m^3/kg.

The mechanical equilibrium requires that the sum of internal force resulted from strain gradient must equal to 0. It leads to the following equation:

$$\int_S E(x,y)\big(\varepsilon_{tot} - \varepsilon_{sh}(x,y)\big)dxdy = 0 \quad (5)$$

with S the cross section of the sample perpendicular to z axis. Using equation (5), and assuming a sample length l >> perpendicular section, the global shrinkage is:

$$\varepsilon_1(\delta) = \frac{(1-D)S_e(\delta)\kappa^{\text{ext}}(C_{\text{ini}} - C_{\text{end}}^{\text{ext}})}{(1-D)S_e + S_c} \text{ for stage 1} \quad (6)$$

and

$$\varepsilon_2(C) = \frac{(1-D)S_e(\delta)\kappa^{\text{ext}}(C_{\text{ini}} - C_{\text{end}}^{\text{ext}}) + S_c\kappa^{\text{int}}(C_{\text{ini}} - C)}{(1-D)S_e + S_c} \text{ for stage 2} \quad (7)$$

Again, a difference of the shrinkage coefficient between the central part and the external one is considered to take into account the dependence of the hydration degree. Note that the difference between the central and the external parts can be neglected if long curing is applied to the concrete. This model has been used to predict size effects as well as different curing conditions [7].

3. Application to 45 concretes

The model has been applied on 45 different concretes (water/cement ratio [0,45-0,65], binder content [220-400] kg/m^3, cement types [CEMI, CEMII, CEMIII, CEMIV, CEMV] and additions [limestone, fly ash, slag]). The curing of the concretes has been done at 100% relative humidity during 7 days. As a first approximation, we assume that the external and internal properties of the concrete are equivalent as the hydration degree is greater than 0.6 (note that this assumption is not verified for samples exposed to drying after one day). Then, $C_{end}^{int} = C_{end}^{ext}$ and $\kappa^{ext} = \kappa^{int}$ and the number of parameters is reduced to 4 (the final water content, the shrinkage coefficient, the thickness of the external layer, the stiffness reduction of the external layer). Figure 4 gives an example of model response for 5 different concretes.

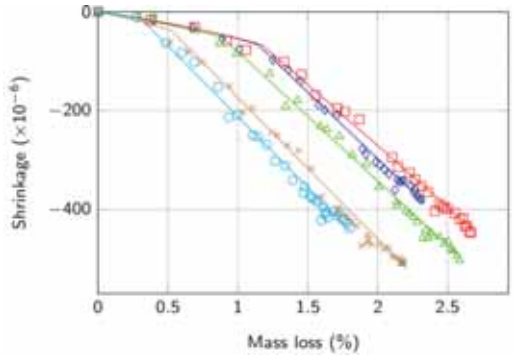

Figure 4: shrinkage vs. mass loss for 5 different concretes. The markers are experimental results, the continuous lines are the response of the model.

3.1 Identified parameters

The following graphs show the distribution of the parameters for the 45 concretes.

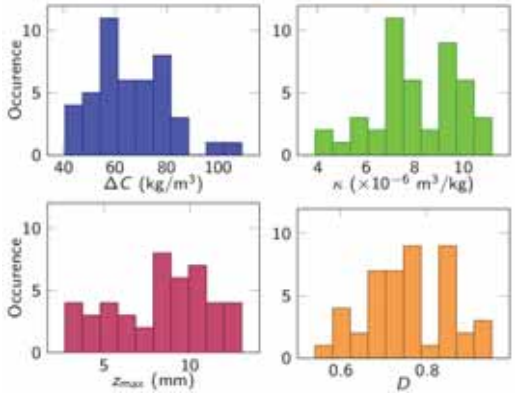

Figure 5: Distribution of the model parameters for the 45 concretes.

Some trends have been observed between the model parameters and the material physical properties (figure 6), except for the damage variable D: we can consider that the external layer is cracked, and the continuous approach of the damage variable is not adapted to described a cracked layer in this case.

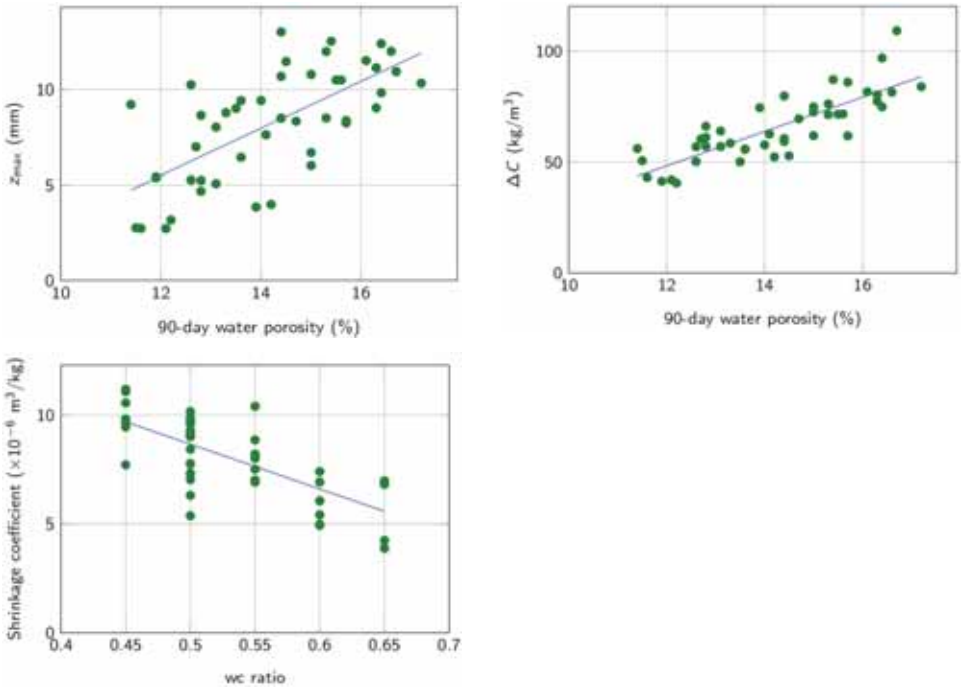

Figure 6: Correlation between the model parameters and material properties (external layer thickness $z_{max}=\delta_1$ vs. 90-day water porosity, moisture loss vs. 90-day water porosity, shrinkage coefficient vs. water/cement ratio).

The values obtained for ΔC and κ are in agreement with the numerous studies available in the literature. It's more difficult to obtain data on the thickness of the external drying layer because the direct measurement is not possible. An inverse analysis, based on the crack spacing, can be used to obtained this thickness [9, 10]. Such an analysis is shown in next section.

3.1 Cracking state

The cracking state of a drying sample is obtained using a discrete particle lattice model. The material is represented as an assembly of particles linked together by brittle Euler-Bernoulli beam. A failure criteria based on the strain state is introduced. Once the criteria is reached, beams break irreversibly (the details of the model can be found in [8]). The elastic parameters and the breaking threshold is assumed to be constant. An improvement is to consider the

evolution of these parameters with the hydration degree of the cement, and to introduce creep to avoid the overestimation of the stress state.

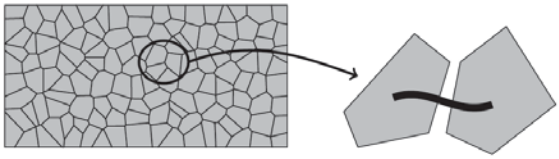

Figure 7: sketch of the discrete model, with the Voronoi particles and the representation of the beam linking two particles.

In this study, just the drying shrinkage is considered by affecting to each particle a shrinkage value computed from the drying model presented above. As the drying process is decoupled to the mechanical part, the drying strain is applied to the left-hand side of the global equilibrium equation:

$$\mathbf{Ku} = \boldsymbol{f_{ext}} + \boldsymbol{f_{sh}} \tag{8}$$

where **K** is the global stiffness matrix, **u** and $\boldsymbol{f_{ext}}$ (=**0** in our case) are respectively the displacement and external force vectors. The shrinkage force $\boldsymbol{f_{sh}}$ is the assembly of the local shrinkage induced forces. For two linked particles *i* and *j*, the local force is:

$$\boldsymbol{f_{sh}^{ij}} = \boldsymbol{K_{local}^{ij}}^{\boldsymbol{t}}(\boldsymbol{\varepsilon}_{sh}^{ij}, \boldsymbol{\varepsilon}_{sh}^{ij}, 0) \tag{9}$$

with $\boldsymbol{\varepsilon}_{sh}^{ij}$ the average of drying shrinkage between both particles and $\boldsymbol{K}_{local}^{\boldsymbol{ij}}$ a spring stiffness matrix.

Two cases are considered: cracking state without particles (homogeneous properties) and cracking state with aggregates (figure 8).

Figure 8: Discrete model with (left) and without (right) particles.

The cracking patterns obtained for different thicknesses (4, 8 and 12 mm) of external layer is shown in figure 9. The influence of the aggregates are obvious.

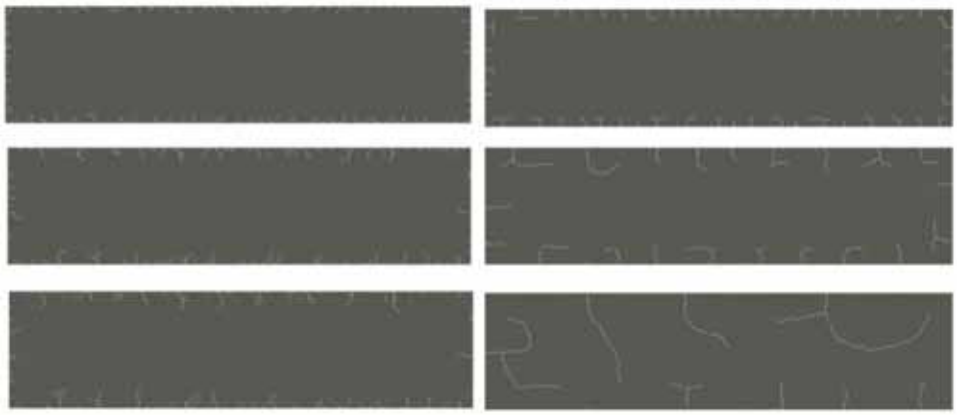

Figure 9: example of cracking patterns for δ_1=4, 8, 12 mm (top to bottom), with aggregates (left) and without aggregates (right).

From these patterns, we can plot the evolution of the thickness of the drying layer vs. the crack spacing.

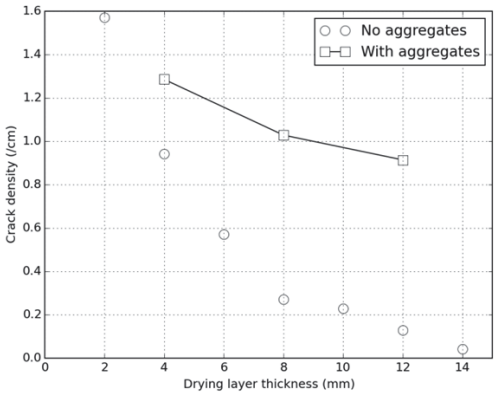

Figure 10: evolution of crack density vs. thickness of drying layer.

The proposed results are strongly dependent on the nature of aggregates (shape, size distribution, mineralogy) [11]. The curve with square markers in figure 10 is just an example and should be characterized for other type of aggregates.

4. Application to COST-TU1404 RRT concrete

The drying test is still under progress, and the final identification of model parameters will be proposed during the conference. However, the beginning of the shrinkage vs. mass loss for a 28-day cured 7x7x28 prismatic sample is shown next.

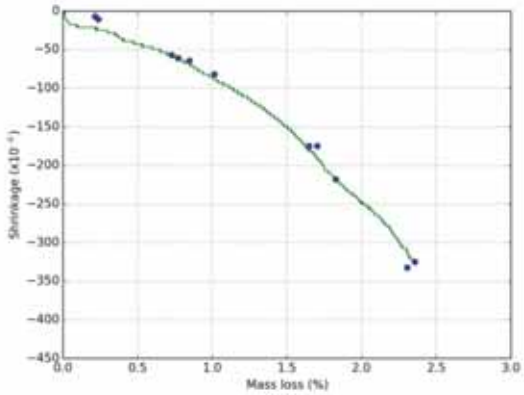

Figure 11: Drying shrinkage vs. mass loss for the RRT concrete, from 0 to 3 weeks.

Using the results of drying tests at different drying times provided during the Round Robin Test, we will propose the complete identification of the model parameter.

4. Conclusion

An analytical drying model is used to represent the drying evolution of concrete samples. The model is based on 4 or 6 parameters, depends on the hydration degree of the concrete at initial drying time. Even based on simplified hypothesis, the model gives accurate representation of the mass loss-shrinkage evolution. The model has been applied successfully to 45 different concretes, and to the concrete of the Round Robin Test of the European Action COST TU1404.

One of the model parameters is related to the thickness of the external damage drying layer, which is difficult to observe experimentally. Coupled with a cracking model, the influence of aggregates on cracking pattern could be analysed.

References

[1] Almudaiheem, J. A. and Hansen, W. Effect of specimen size and shape on drying shrinkage. ACI Materials Journal 84 (1987), 130–135
[2] Bazant Z.P. and Wittmann, F.H., Creep and Shrinkage in Concrete Structures. Chichester, John Wiley & Sons (2002)
[3] Torrenti J-M., Granger L., Diruy M. and Genin P. Modeling concrete shrinkage under variable ambient conditions. ACI Mater J 96 (1997), 35-39
[4] Hansen, W. Drying shrinkage mechanisms in portland cement paste. Journal of the American Ceramic Society 70 (1987), 323–328

[5] Bakhshi, M., Mobasher, B. and Soranakom, C. Moisture loss characteristics of cement-based materials under early-age drying and shrinkage conditions. Construction and Building Materials 30 (2012), 413–425
[6] Delaplace, A. and Noyalet, H.. A simple two-stage model for simulating drying shrinkage vs. mass-loss evolution of concrete. In J. Van Mier, G. Ruiz, C. Andrade, R. Yu, and X. Zhang (Eds.), VIII International Conference on Fracture Mechanics of Concrete and Concrete Structures, FraMCoS-8 (2013)
[7] Delaplace, A. and Noyalet, H. Drying cracking pattern analysis using a simple two-stage drying model and a discrete model, Computational Modelling of Concrete Structures, Edited by Nenad Bícanić, Herbert Mang, Günther Meschke and René de Borst, CRC Press (2014), 659-665
[8] Colina, H. and Acker, P. Drying cracks: Kinematics and scale laws. Materials and Structures 33 (2000), 101-107
[9] Bisschop, J. and Wittel, F. Contraction gradient induced microcracking in hardened cement paste. Cement & Concrete Composites 33 (2011), 466-473
[10] Delaplace, A. Tensile damage response from discrete element virtual testing. Geomechanics and Geoengineering: An International Journal 4 (2009), 79-89
[11] Bisschop, J. and van Mier, J.G.M. How to Study Drying Shrinkage Microcracking in Cement-based Materials using Optical and Scanning Electron Microscopy, Cement and Concrete Research 32 (2002), 279-287

International RILEM Conference on Materials, Systems and Structures in Civil Engineering
Conference segment on Service Life of Cement-Based Materials and Structures
22-24 August 2016, Technical University of Denmark, Lyngby, Denmark

IMPACT OF BIOGENIC SELF-HEALING ADDITIVE ON PERFORMANCE OF CEMENT-BASED MORTAR

Ali Amiri [(1)], Zeynep Basaran Bundur [(1)]

(1) Ozyegin University, Istanbul, Turkey

Abstract
Microcracks are one of the main reasons for a decrease in service life in concrete structures. Recent research in the field suggested that it might be possible to develop a cement-based material that is capable of remediate cracks by triggering biogenic calcium carbonate (CaCO3). This paper summarizes the study undertaken to investigate the application of vegetative *Sporosarcina pasteurii* (*S.pasteurii*) cells to remediate flexural cracks and impact of biogenic self-healing agent on composition and strength of cement-based materials. To develop biogenic self-healing agent, vegetative *S. pasteurii* cells were grown in urea- corn steep liquor (UCSL), and then mixed with cement and sand. Incorporation of cells as well as the nutrient media to the bacterial mortar did not affect the compressive strength negatively, however substantial retardation was observed in initial setting of samples prepared by UCSL medium and bacteria. The influence of superplasticizers and air entraining agents (AEA) on biogenic $CaCO_3$ precipitation was also investigated. The results indicated that use of industrial waste CSL and bacteria, resulted biogenic $CaCO_3$ are compatible with commercially used admixtures, which can be potentially used for self-healing applications in cement-based mortars.

1. Introduction

Recent research in the field of concrete materials suggested that it might be possible to develop a smart cement-based material that is capable of remediate cracks by triggering microbial induced calcium carbonate precipitation (MICCP) within the cracked regions[1–3]. MICCP is a biochemical process in which microorganisms stimulate the formation of calcium carbonate ($CaCO_3$) [4]. Recent studies showed that MICCP can be used to bind non-cohesive sand particles and improve their properties under shear [5,6]. Further, MICCP has been used

in cement-based materials to remediate microcracks, improve mechanical properties and reduce permeability [7–10].

An early approach was incorporation of *Shewenella* species in the mixing water of mortar [2]. It was found that the incorporation of these cells decreased the pore sizes and improved the compressive strength. Another approach was to suspend *Bacillus pseudofirmus* and *Bacillus cohnii* endospores in mixing water of mortar to provide self-healing of microcracks [11]. These endospores were found to be viable up to 4 months and were able to seal the surface microcracks; however these endospores with their nutrient sources reduced the compressive strength of mortar [11]. Then, concerns regarding the use of the endospores within the restrictive and high pH environment of cement-based materials led researchers to propose encapsulation for the endospores. Wiktor and Jonkers used lightweight expanded clay particles to encapsulate *Bacillus alkalinitriculus* endospores with calcium lactate [10]. With this approach, the researchers could extend the viability of the bacteria and provided self-healing of cracks, however of LWAs decreased the compressive strength of the material. Wang et al. [12] proposed a bio-compatible hydrogel encapsulation for *Bacillus sphaericus* endospores to remediate surface cracks in mortars. It has been shown that these hydrogels were able to seal cracks as large as 0.5 mm within 7 days.

Up-to-date, so called self-healing applications in cement-based materials targeted to remediate cracks induced after 28-days of casting, which can be considered as an early age application for cement-based materials. In such a case, it might not be necessary to encapsulate the microorganisms. A proper microbial selection and nutrient medium, 2% of the *S. pasteurii* cells were found viable 11 months after mortar mixing [13]. The inoculated *S. pasteurii* cells were able to improve the microstructure of the mortar samples after internal micro-cracks were induced [14]. However, Bundur et al. [15] has shown that incorporation of urea-yeast extract (UYE) medium significantly delayed the initial set of the cement-paste. Besides the fact that yeast extract induced a negative impact on setting, almost 60% of total operating cost of UYE medium is due to use of yeast extract [16]. Thus it is crucial to replace yeast extract with a cheaper alternative. Corn steep liquor (CSL), as being a waster product of corn industry, can be a cheaper alternative for yeast extract. Achal et al. [16] showed a significant reduction in total cost by using CSL as a carbon source for *S. pasteurii*. Moreover, it was found that use of CSL improved the urease activity and calcite production of *S. pasteurii* cells [16]. However, there is a very limited information regarding use of CSL for biomineralization applications in cement-based materials in terms of its impacts on setting, strength and chemical composition of cement-based materials.

This study evaluates the potential use of CSL as an alternative carbon source *for S. pasteurii*. We examined the influence of CSL on bacterial growth and in-vitro $CaCO_3$ precipitation; the impact of cells and their nutrient medium on setting and strength of cement-based mortar as well as their compatibility with superplasticizers and air entraining agents.

2. Materials and methods

2.1 Microorganism growth

Leibniz Institute- German Collection of Microorganisms and Cell Cultures: *S. pasteurii* (DSMZ 33) was grown in Urea-Corn Steep Liquor (UCSL) medium at pH 9. UCSL medium was obtained by adding tris base (0.13M), urea (10g) and CSL (15g) to a liter of DI water. CSL was provided in liquid form as a commercially available product from Sigma Aldrich. Twelve-grams of agar per liter were added to the media when solid medium was required. *S. pasteurii* cells were inoculated in 600 mL of UCSL medium and incubated aerobically with shaking conditions at 30°C. Sample aliquots were taken from these medium periodically and plated on agar plates. Samples for viable plate counts were serially diluted; and the cell concentration was obtained by viable plate counts and represented as colony forming units (CFU/mL). Bacterial growth curve was and this plot was used to estimate the time required to obtain required concentrations. Mid-exponential phase cells (10^7–10^8 CFU/mL) were used for the paste/mortar inocula.

2.2 Cement, aggregates and admixtures

CEM I 42.5R was used in this experiment. For mortar samples, sand was used as fine aggregates. ASTM C128-15 was used to determine the absorption coefficient of the sand [17] and ASTM C136-14 was used to determine the PSD of the sand [18] and average fineness modulus of the aggregates was determined 2.8. Absorption capacity for the sand was found as 0.67% and specific gravity was found as 2.56. To investigate the impacts of commerciallyty available superplasticizers and air entraining agents on biogenic $CaCO_3$ precipitation, BASF MasterGlenium 51 (by 1% of cement weight) and MasterAir 200 AEA (by 0.1% cement weight). It should be noted that these admixtures influenced both the flow and the setting of cement paste.

2.3 Preparation of cement paste and mortar mixes

For this study, 3 types of cement paste mixes were prepared. Neat paste was prepared by mixing tap water and cement. Bacterial paste was prepared by replacing the water of the cement paste with the bacterial culture and nutrient paste was prepared by replacing the water of the cement paste with UCSL medium (Table 1). The mass ratio of solution (water, UCSL medium or bacterial culture) to cement (s/c) in neat paste, bacterial paste and nutrient paste were kept at 0.45. Mortar samples were prepared by adding sand (*see* Section 2.2).

2.4 Experimental methods

In-vitro biogenic $CaCO_3$ precipitation:

To determine the influence of external $[Ca]^{+2}$ source and admixtures on MICCP 3 different compounds were used: Calcium nitrate - $Ca(NO_3)_2$ (28 g/L of nutrient medium) and Calcium chloride- $CaCl_2$ (16 g/L of nutrient medium) and Calcium lactate-$C_6H_{10}CaO_6$ (30 g/L of nutrient medium). To induce precipitation, *S. pasteurii* cells were incubated in UCSL medium and once the cells reach their exponential growth, $[Ca^{+2}]$ sources were added to media. To investigate the impacts of chemical admixtures, after 7 hours of incubation at 30°C, AEA (2.22 g/L of nutrient medium) and superplasticizer (22.2 g/L of nutrient medium) were added and the incubation process was continued for another 17 hours, then precipitates were collected by centrifuging (Nuve NF 800R, Ankara, Turkey). Collected biogenic precipitates

Table 1: Mix design for 2.6 liters of neat, nutrient and bacterial mortars. Bacterial culture contains 8 x 10^8 CFU/mL suspended in UCSL medium. *The dosages are given as percent mass ratio relative to cement content. SP: Superplasticizer; AEA: Air Entraining Admixture

	Cement (g)	**Water (g)**	**UCSL (g)**	**Bacterial Culture (g)**	**Sand (g)**	**SP* (%)**	**AEA* (%)**
Neat mortar	564	266.5	-	-	2059	-	-
Bacterial mortar	564	-	-	266.5	2059	-	-
Nut mortar	564	-	266.5	-	2059	-	-
Neat_SP	564	266.5	-	-	2059	1	-
Neat_AEA	564	266.5	-	-	2059	-	0.1
Nut_SP	564	-	266.5	-	2059	1	-
Nut_AEA	564	-	266.5	-	2059	-	0.1
Bac_SP	564	-	-	266.5	2059	1	-
Bac_AEA	564	-	-	266.5	2059	-	0.1

including the bacterial cells were gold coated and processed by JEOL Scanning Electron Microscope (SEM) (Freising, Germany). The accelerating voltage was kept at 5 kV while the working distance was held at 9-12 mm. To determine the crystal structure of biogenic $CaCO_3$ precipitated, a qualitative X-ray diffraction (XRD) analysis was conducted with BRUKER D8 Advance X-ray Diffractometer (Karlsruhe, Germany). In general, collected precipitates were kept in a drying chamber at 40°C for 24 hours prior to XRD analysis. Then, the samples were placed and compacted into a sample holder and analysis was conducted at angles from 10-90° 2θ at a step size of 0.02° 2θ.

Vicat Needle test

A modified Vicat Needle test was conducted to determine the setting time of the cement pastes. For the test, cement paste samples were prepared according to a modified ASTM C191-13 [19]. Instead of determining the w/c ratio that will yield a "normal consistency" paste, the s/c ratios were kept constant at 0.45 to be consistent with the ratios used throughout the other analysis conducted in the study. The bacterial concentration in the bacterial inoculum was found as 10^8 CFU/mL. Analyses were conducted according on triplicates of samples.

Compressive Strength test

For compressive strength testing, mortar samples were prepared (*see* Table 1) according to ASTM C305-14 [20]and the standard was modified by replacing the water content with UCSL medium or bacterial culture. The mortar samples were cast in 5 x 5 x 5 cm cubes and kept in humid environment at 22ºC for 24 hours. Then the molds were removed and the samples were further cured in UCSL medium until testing (22ºC). Compressive strength

testing was conducted according to ASTM C109-[21] at 3,7 and 28 days on triplicates of samples.

3. Results and discussion

3.1 In-vitro biogenic $CaCO_3$ mineral formation

Figure 1 and Figure 2 show the SEM images and X-Ray diffractograms for *in-vitro* biogenic $CaCO_3$ precipitation without any chemical admixtures. Use of $CaCl_2$ as a $[Ca^{+2}]$ source induced both biogenic rhombohedral calcite and spheroid vaterite precipitation in UCSL medium (pH 9). However, only spheroid vaterite precipitates were obtained from UCSL medium having $Ca(NO_3)_2$ as a calcium source. Incorporation of calcium lactate in a bacterial culture grown in UCSL medium resulted with mostly calcite crystals that do not have regular rhombohedral crystal structure.

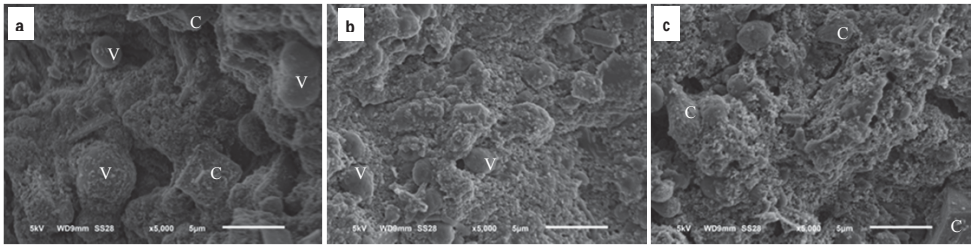

Figure 1: SEM images of *in-vitro* biogenic $CaCO_3$ induced by (a) *S. pasteurii* grown in UCSL medium + $CaCl_2$ (b) *S. pasteurii* grown in UCSL medium + Ca $(NO_3)_2$ (c) *S. pasteurii* grown in UCSL medium + Calcium Lactate C: Calcite, V: Vaterite

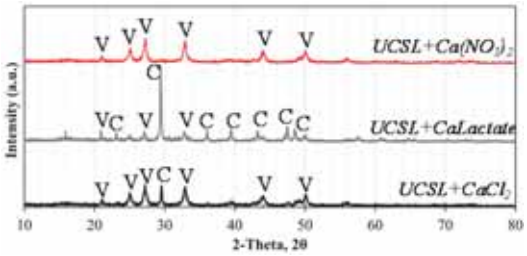

Figure 2: X-ray diffractograms of *in-vitro* biogenic $CaCO_3$ induced by (a) *S. pasteurii* grown in UCSL medium + Ca $(NO_3)_2$ (b) *S. pasteurii* grown in UCSL medium + Calcium Lactate (c) *S. pasteurii* grown in UCSL medium + $CaCl_2$; C: Calcite, V: Vaterite

Given the unique morphologies obtained from in vitro biogenic $CaCO_3$ precipitation, the type of $[Ca^{+2}]$ also effects the crystallization of $CaCO_3$. Even though the mass of $[Ca^{+2}]$ sources added to UCSL medium were determined in a certain range such that the 0.15M $[Ca^{+2}]$ ions could be provided in the solution. The difference in the $CaCO_3$ crystal morphology could be attributed to different solubility coefficients of these three compound, as calcium lactate being least soluble and $Ca(NO_3)_2$ having the highest solubility at room temperature. The least

soluble compound calcium lactate resulted in a more prominent calcite peaks while $Ca(NO_3)_2$ induced more prominent vaterite peaks. This might be attributed that different solubilities of these compounds might interfere with the morphology of $CaCO_3$ by affecting $[Ca^{+2}]$. Ogino et al.[24] suggested that an increase in $[Ca^{+2}]$ favored vaterite precipitation and inhibited the transformation of vaterite to calcite. Compounds with a higher solubility might lead to a higher $[Ca^{+2}]$ dissolved in the solution correspondingly increase the ionic strength, contained more vaterite and less calcite than the cultures supplemented with the compounds having lower solubility.

Incorporation of AEA and superplasticizer to *in-vitro* cultures influenced the morphology of biogenic $CaCO_3$ precipitates (see Figure 3). While only vaterite precipitates were obtained from UCSL medium having $Ca(NO_3)_2$ without any chemical admixtures, addition of AEA to the solution induced both calcite and vaterite precipitation and addition of superplasticizers induced only calcite precipitation (see Figure 4). It was also observed that the $CaCO_3$ crystals were irregular and bound together rather than forming individual rhombohedral crystals. For MICCP, bacterial surface charge is known to be substantially important [25–27]. Previous studies suggested that, *S. pasteurii* cells had a negative net surface charge because in neutral and alkaline environments, these bacterial cells showed a negative zeta potential [28,29]. Use of AEA and superplasticizers might interfere with the surface charge of the microorganisms and influence the nucleation of crystals.

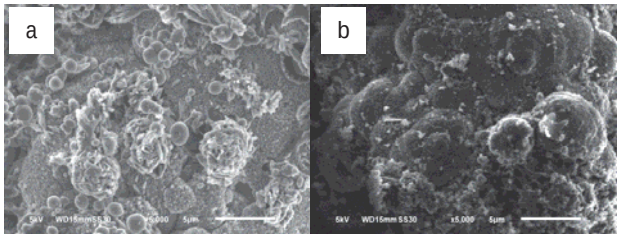

Figure 3: SEM images of *in-vitro* biogenic $CaCO_3$ induced by (a) *S. pasteurii* grown in UCSL medium + Ca $(NO_3)_2$ + AEA; (b) *S. pasteurii* grown in UCSL medium + Ca $(NO_3)_2$ + Superplasticizer

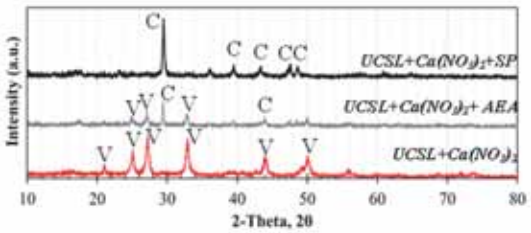

Figure 4: X-ray diffractograms of *in-vitro* biogenic $CaCO_3$ induced by (a) *S. pasteurii* grown in UCSL medium + Ca $(NO_3)_2$ + AEA; (b) *S. pasteurii* grown in UCSL medium + Ca $(NO_3)_2$ + Superplasticizer; C: Calcite, V: Vaterite

3.2 Effects of inoculated *S.pasteurii* on initial setting

Figure 5 represents the modified Vicat needle test results. The different initial setting times were evaluated by comparing them with the reference neat paste sample having an initial setting time of 5 hours. Previously Bundur et al.[15] showed that addition of UYE medium to cement paste extended the induction period for approximately to 13 hours, and this was due to addition of 1% yeast extract by weight of cement. Similar behavior was observed by Wang et al. [8], such that increasing yeast extract content from 0.35% to 0.85% by cement weight extended the delay in the end of induction period and decreased the degree of hydration in cement paste samples. The resulted delay in initial set was likely due to the presence of carbohydrates and sugars in yeast extract, where they are known to be good retarders [30]. Even though, incorporation UCSL also retarded the initial set for 8 hours, it was still significantly less than what it was found previously with the addition of UYE medium [8,15]. This might be attributed to very low sugar content of CSL compared to yeast extract [31]. Addition of *S. pasteurii* cells with UCSL medium exacerbated the delay initial setting. Since the microorganisms were grown in this media, there might be changes in UCSL medium due to the metabolic activity of cells. The changes in the nutrient medium induced by the metabolic activity of cells might influence the ionic concentration of the medium, thus affecting the initial set time.

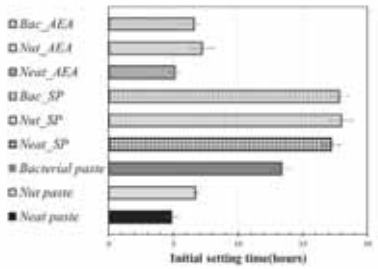

Figure 5: Modified ASTM C191-13 initial setting times of different cement paste mixes. The bars are representing the average initial setting time values based on triplicates of cement paste samples and error bars represent the one standard deviation. An s/c of 0.45 was used for all pastes.

Addition of superplastcizers significantly increased the initial setting for all paste types, which might be due to the dispersive effect of superplastcizers [32]. Addition of AEA has no adverse affect on initial setting of cement pastes. Thus it can be concluded that the chemical admixtures studied herein have no significant influence over initial setting time.

3.3 Effects of *S. pasteurii* cells on compressive strength of mortar

Figure 6 represents the compressive strength test results of mortar samples. At any day of testing, nutrient mortar samples exhibited a higher strength than the neat mortar samples. However, addition of *S. pasteurii* cells in bacterial mortar resulted with a lower strength compared to nutrient mortar but did not result with a strength decrease relative to neat mortar. This might be due to composition and by-products of consumed UCSL growth medium. CSL is a protein rich carbon source [33]. Ersan et al. [34] suggested compressive strength bacterial mortars could decrease due to the degradation of proteins at pH, which might induce

the formation of air bubbles. Even though, the proteins in CSL will also degrade in nutrient mortar due to high pH, incorporation of microorganism might induce a higher degree of protein decomposition in the growth media that might lead to a relatively lower strength compared to nutrient mortar.

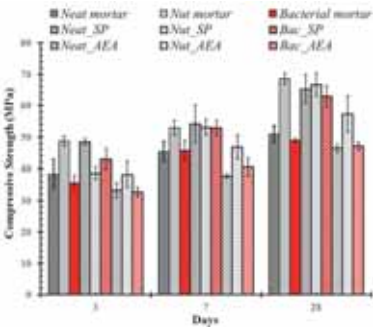

Figure 6: Influence of UCSL medium and *S. pasteurii* on compressive strength of mortar. An s/c of 0.45 was used. Bars show the average compressive strength based on the triplicates of samples and error bars represent one standard deviation.

Addition of superplastcizers slightly increased the compressive strength for all mortar types, which might be due to a higher degree of compaction of mortars due to their improved flowability [32]. Addition of AEA decreases the compressive strength for all mortar samples due to the presence of extra air bubble inside the mortar specimens. Since this is the sole purpose of adding air entrainment, the strength decrease was expected due to the nature of AEA admixtures. Thus it can be concluded that the chemical admixtures studied herein have no significant influence over the compressive strength for MICCP applications.

4. Conclusion

In the presented study, the impact of embedding vegetative *S. pasteurii* cells into cement-based materials was investigated. In-vitro MICCP studies revealed that morphology of $CaCO_3$ crystals was significantly affected by type of $[Ca^{+2}]$ source and presence of admixtures. Initial setting of cement paste was highly influenced by the presence of *S. pasteurii* cells, which might be attributed to the depletion of the UCSL nutrient medium components and accumulation of bacterial by-products in the medium. Even though, there was a significant change in the initial set the compressive strength of the bacterial mortar was similar to, and, in some cases, exceeded the neat mortar. In addition, it can be concluded that the chemical admixtures studied herein have no significant influence over the performance of the MICCP applications in cement-based materials. This suggests that biomineralization might be obtained within the cement paste matrix using a simple procedure that does not require encapsulation of the microorganisms in the cement paste matrix and CSL can be used as an effective carbon source for *S. pasteurii* growth and MICCP applications for cement-based materials. Further studies are being conducted to evaluate the interactions between admixtures and MICCP, as well as self-healing of surface flexural cracks in mortars.

Acknowledgment

This research was conducted by financial assistance of the Scientific and Technical Research Council (TUBITAK) of Turkey Project: MAG-114M308. The authors graciously acknowledge Prof. Mehmet Ali Gulgun for allowing the authors access to FENS laboratory facilities of Sabanci University, Istanbul for SEM and XRD analyses. The authors also acknowledge undergraduate research assistants Seyma Gurel and Cansu Acarturk for their help in experimental work.

References

[1] W. De Muynck, N. De Belie, W. Verstraete, Microbial carbonate precipitation in construction materials : A review, Ecol. Eng. 36 (2010) 118–136.
[2] P. Ghosh, S. Mandal, B.D. Chattopadhyay, S. Pal, Use of microorganism to improve the strength of cement mortar, Cem. Concr. Res. 35 (2005) 1980 – 1983.
[3] N. De Belie, Microorganisms versus stony materials: a love–hate relationship, Mater. Struct. 43 (2010) 1191–1202.
[4] S. Mann, Biomineralization: Principles and Concepts in Bioinorganic Materials Chemistry, Oxford, New York, 2001.
[5] J.T. Dejong, M.B. Fritzges, K. Nüsslein, Microbially induced cementation to control sand response to undrained shear, J. Geotech. Geoenvironmental Eng. (2006) 1381–1392.
[6] P. Taylor, V.S. Whiffin, L.A. Van Paassen, M.P. Harkes, Microbial carbonate precipitation as a soil improvement technique microbial carbonate precipitation as a soil improvement technique, Geomicrobiol. J. 24 (2007) 417–423.
[7] J.Y. Wang, N. De Belie, W. Verstraete, Diatomaceous earth as a protective vehicle for bacteria applied for self-healing concrete., J. Ind. Microbiol. Biotechnol. 39 (2012) 567–77.
[8] J.Y. Wang, H. Soens, W. Verstraete, N. De Belie, Self-healing concrete by use of microencapsulated bacterial spores, Cem. Concr. Res. 56 (2014) 139–152.
[9] H.M. Jonkers, E. Schlangen, Crack repair by concrete-immobilized bacteria, Civ. Eng. (2007) 1–7.
[10] V. Wiktor, H.M. Jonkers, Quantification of crack-healing in novel bacteria-based self-healing concrete, Cem. Concr. Compos. 33 (2011) 763–770.
[11] H.M. Jonkers, A. Thijssen, G. Muyzer, O. Copuroglu, E. Schlangen, Application of bacteria as self-healing agent for the development of sustainable concrete, Ecol. Eng. 36 (2010) 230–235.
[12] J.Y. Wang, D. Snoeck, S. Van Vlierberghe, W. Verstraete, N. De Belie, Application of hydrogel encapsulated carbonate precipitating bacteria for approaching a realistic self-healing in concrete, Constr. Build. Mater. 68 (2014) 110–119.
[13] Z. Basaran, Biomineralization in cement based materials: Inoculation of vegetative cells, University of Texas at Austin, 2013.
[14] S. Liu, Z.B. Bundur, J. Zhu, R.D. Ferron, Evaluation of self-healing of internal cracks in biomimetic mortar using coda wave interferometry, Cem. Concr. Res. Cem. Concr. Res. 83 (2016) 70-78.

[15] Z. Basaran Bundur, M.J. Kirisits, R.D. Ferron, Biomineralized cement-based materials: Impact of inoculating vegetative bacterial cells on hydration and strength, Cem. Concr. Res. 67 (2015) 237–245.
[16] V. Achal, A. Mukherjee, M.S. Reddy, Biocalcification by *Sporosarcina pasteurii* using corn steep liquor as the nutrient source, Orig. Reseacr Ind. Biotechnol. (2010) 170–174.
[17] ASTM International, ASTM-C 128-15: Standard Test Method for Density , Relative Density (Specific Gravity), and Absorption, West Conshohocken, 2015.
[18] ASTM International, ASTM C136/C136M-14 Standard Test Method for Sieve Analysis of Fine and Coarse Aggregates, West Conshohocken, 2014.
[19] ASTM International, ASTM C191-13 Standard Test Methods for Time of Setting of Hydraulic Cement by Vicat Needle, West Conshohocken, 2013.
[20] ASTM International, ASTM C305-14 Standard Practice for Mechanical Mixing of Hydraulic Cement Pastes andMortars of Plastic Consistency, West Conshohocken, 2014.
[21] ASTM International, ASTM C109/C109M-13e1 Standard Test Method for Compressive Strength of Hydraulic Cement Mortars (Using 2-in. or [50-mm] Cube Specimens), West Conshohocken, 2013.
[22] C. Rodriguez-Navarro, F. Jroundi, M. Schiro, E. Ruiz-Agudo, M.T. González-Muñoz, Influence of substrate mineralogy on bacterial mineralization of calcium carbonate: implications for stone conservation., Appl. Environ. Microbiol. 78 (2012) 4017–29.
[23] C.Y. Tai, F. Chen, Polymorphism of $CaCO_3$, precipitated in a constant-composition environment, AIChE J. 44 (1998) 1790–1798.
[24] T. Ogino, T. Suzuki, K. Sawada, The formation and transformation mechanism of calcium carbonate in water, Geochim. Cosmochim. Acta. 51 (1987) 2757–2767.
[25] V. Achal, A. Mukerjee, M. Sudhakara Reddy, Biogenic treatment improves the durability and remediates the cracks of concrete structures, Constr. Build. Mater. 48 (2013) 1–5.
[26] J. Dick, W. De Windt, B. De Graef, H. Saveyn, P. Van der Meeren, N. De Belie, et al., Bio-deposition of a calcium carbonate layer on degraded limestone by Bacillus species., Biodegradation. 17 (2006) 357–67.
[27] V. Achal, a Mukherjee, P.C. Basu, M.S. Reddy, Lactose mother liquor as an alternative nutrient source for microbial concrete production by Sporosarcina pasteurii., J. Ind. Microbiol. Biotechnol. 36 (2009) 433–8.
[28] M. Fletcher, Bacterial Adhesion: Molecular and Ecological Diversity, John Wiley & Sons, Inc., Hoboken, 1996.
[29] S.L. Williams, M.J. Kirisits, R.D. Ferron, Optimization of growth medium for Sporosarcina pasteurii in bio-based cement pastes to mitigate delay in hydration kinetics, J. Ind. Microbiol. Biotechnol. (2016) 1–9.
[30] V. Bolobova, V.I. Kondrashchenko, Use of yeast fermentation waste as a biomodifier of concrete (Review), Appl. Biochem. Microbiol. 36 (2000) 205–214.
[31] R.W. Liggett, H. Koffler, Corn steep liquor in microbiology, Bacteriol. Rev. 12 (1948) 297–311.
[32] A.M. Neville, Properties of Concrete, 5th Editio, Pearson, Essex, England, 2011.
[33] V. Achal, A. Mukherjee, S.M. Reddy, Effect of calcifying bacteria on permeation properties of concrete structures, J. Ind. Microbiol. (2010).
[34] Y.Ç. Erşan, F.B. Da Silva, N. Boon, W. Verstraete, N. De Belie, Screening of bacteria and concrete compatible protection materials, Constr. Build. Mater. 88 (2015) 196–203.

International RILEM Conference on Materials, Systems and Structures in Civil Engineering
Conference segment on Service Life of Cement-Based Materials and Structures
22-24 August 2016, Technical University of Denmark, Lyngby, Denmark

NON-DESTRUCTIVE EVALUATION OF ECO-FRIENDLY CEMENTITUOUS MATERIALS BY ULTRASOUND

Markus Krüger [(1)], Rok Bregar [(1)], Gheorghe Alexandru David [(1)], Joachim Juhart [(1)]

(1) Institute of Technology and Testing of Building Materials, Graz University of Technology, Austria

Abstract
Ultrasonic methods have been developed in the past to study properties of cement based materials in the fresh and hardening state. However, most of the methods only consider a certain type of ultrasonic waves. To derive elastic parameters of fresh concrete like the Poisson's ratio and elastic modules it is required to obtain shear waves as well as compressional waves. It is certainly much more difficult to establish a setup to transmit and record shear waves in a way that the onset of these slower waves (compared to compressional waves) can be detected as clear as necessary to calculate shear wave velocity values with the required accuracy. A test setup for testing cement paste with different ultrasonic waves is presented. Tests have been conducted that show reasonable ultrasonic compressional and shear wave transmission right after mixing. Thus ultrasound is found to be suited for the characterisation of paste mixtures and the determination of changes in the rheological properties already before setting. Test results from different cementitious mixes with a special focus on eco-pastes are presented. These eco-pastes show optimized packing density (using micro and eco fillers as replacement of Portland cement clinker).

1. Introduction

The properties of cement based materials in the fresh and hardening state are currently measured with rather conventional methods. Ultrasonic methods have been developed in the past using through-transmission techniques and analysing the whole waveform. Material properties as for example the workability are investigated based on parameters like the compressional wave velocity, the energy and the frequency content or even the derivative of the signals [1, 2 and 3]. Ultrasound is already accepted to be a very useful tool to investigate the setting and hardening process of cementitious materials. However, many investigations and signal interpretation strategies are more or less empirical and is applicable only on certain

type of mixes of similar composition. Especially new binder developments in the concrete sector and its investigation by ultrasound shows that the interpretation with empirical methods are sometimes insufficient.

It is for example not feasible to derive the Poisson's ratio of fresh concrete or to get information even on the elastic modules data based on compressional waves only if the mix to be investigated cannot be classified into a group of "standard" mixture proportions. This is for example the case for new mixes with reduced binder contend and optimized packing density using micro-filler made of inert materials that are more "eco-friendly". To study the setting and hardening process of such new binder compositions it useful to obtain also shear waves beneath compressional waves [4]. But it is certainly much more difficult to establish a setup to transmit and record shear waves in a way that the onset of these slower waves (compared to compressional waves) can be detected as clear as necessary to calculate shear velocity values with the required accuracy.

2. Materials

The main materials, used for this paper are CEM I 52.5 N-SR3, limestone filler of different grain size classes (so-called eco-filler 3 µm ≤ d50 ≤ 30 µm and micro-filler d50 < 3µm) [5]. Material properties of basic materials are presented in Table 1 and particle size distribution of the materials and the corresponding mixes is shown in Figure 1.

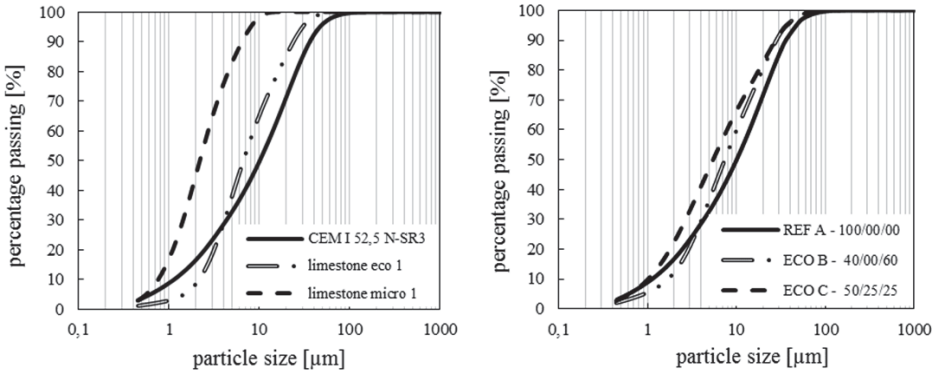

Figure 1: particle size distribution of materials (left) and mixtures (right).

The grain size distribution analysis were performed by laser diffraction (HELOS) and automatically generated with the device software WINDOX 5.6.0.0 from the detected laser diffraction pattern as a result report with average diameter, standard deviation and output. As complex indices of refraction of the different materials, the proposed values from the ISO 13320:2009 were used. The results of the average diameter are shown in Table 1.

Table 1: Properties of investigated materials

	type	true density ρ_0	mean diameter d_{50}	Blaine-value	water demand (at saturation) V_{ws}/V_p	water demand (for flowability f=170 mm) $V_{wf.\,170}/V_p$	GWP	PEI
		g/cm³	µm	cm²/g	-	-	$kgCO_2/t$	MJ/t
OPC 1	CEM I 52,5 N-SR3 PMCP2	3.17	10.5		0.71	1.13	831	4030
LE1	limestone eco 1	2.70	6.9	4032	0.65	0.68	25	717
LM1	limestone micro 1	2.73	2.2	9314	0.61	0.65	36	1006

Additionally, the amount of water to reach a certain workability of a water/powder-mix plays a major role. Table 1 shows properties of source materials covered in this paper. The values for water demand V_{ws}/V_p, which is the volume of water at saturation point and $V_{w,f,i}/V_p$, which is the volume of water for a certain flowability and V_p which is the volume of powder water-powder mixes, were determined by a new method presented by Juhart [5]. This new approach combines the so-called "mixing energy method (MEM)", cp. Marquardt [6] to determine the void content of a powder by its water demand at saturation point with the spread flow test (ST) according to the procedure of Okamura [7] for determining the flowability of pastes, therefore we call it MEM-ST. It can be used for a single material as well as a mix of granular materials. In the first step a certain volume of dry powder (V_p) is introduced into a mixer that is able to record changes in mixing energy input and power consumption Additionally the amount of water added is measured continuously with the help of a flow-meter. In the next step - while mixing with constant speed and continuously adding water - the saturation point of a granular material or mix is determined as the peak of the power consumption. At this point, immediately before saturation, capillary bridges between particles cause a maximum of shear resistance [8]. There the water demand (V_{ws}/V_p) corresponds to a minimum void content resulting in a maximum packing density; the mix appears to be "earth-moist". In the following phase additional water is added stepwise. At each step the spread flow (f,i) is determined on a dry glass plate with a Hägermann cone (according to EN 1015-3 [9] but without any shocks) - and the corresponding water demand ($V_{wf,i}/V_p$) is recorded [5].

For the following tests three different basic mixes were investigated with three different consistencies each. The consistency was adjusted by just modifying the added water (see table 2). While the reference mixes (REF) are based on CEM I cement only the ECO B mixes are modified in a way that 60% of CEM I was replaced by the ECO Filler (LE1), but without using the package density optimisation method. The ECO C mixes are mixture compositions with optimized packing density as described above.

Table 2: Composition and properties of the investigated mixtures.

		REF A1	**ECO B1**	**ECO C1**	**REF A2**	**ECO B2**	**ECO C2**	**REF A3**	**ECO B3**	**ECO C3**
flowability		standard consistency EN 196-3			ø = 190 mm			ø = 275 mm		
Cem I 52.5		100	40	50	100	40	50	100	40	50
$LIME_{ECO}$	[V-%]	0	60	25	0	60	25	0	60	25
$LIME_{MICRO}$		0	0	25	0	0	25	0	0	25
w/c		0.28	0.59	0.38	0.40	0.85	0.42	0.48	1.03	0.43
V_w/V_p		0.90	0.74	0.61	1.27	1.09	0.66	1.53	1.31	0.68
V_w/V_c	[-]	0.90	1.86	1.21	1.27	2.72	1.32	1.53	3.27	1.35
$V_{w,s}/V_{p\,(Vicat)}$		0.9**	0.74**	0.61	-	-	-	-	-	-
$V_{w,s}/V_{p\,(MEM\text{-}ST)}$		0.72	0.69	0.61	0.72	0.69	0.61	0.72	0.72	0.61
$f_{cm,1d}$		47.9	19.5	42.8	30	7.7	42.7	19.7	4	37.1
$f_{cm,7d}$	[N/mm²]	91.3	46.1	80.5	57.3	21.9	74.6	37.5	12.7	73.8
$f_{cm,28d}$		107	58.1	100.1	82.9	29.1	84.8	53.2	19.7	
density	[kg/m³]	2114	2023	2111	1949	1916	2136	1860	1841	2110
Vicat initial set	[h]	5:21	3:41	3:03	7:58	6:26	03:28	10:15	09:19	03:54
Vicat final set	[h]	6:52	4:31	4:13	8:58	8:04	04:25	10:55	10:17	05:32

3. Ultrasound experimental setup for simultaneous p- and s-wave measurements

Figure 2 shows the experimental test setup that is used for a combined p- and s-wave measurement. This test setup is similar to that proposed by a RILEM recommendation worked out by RILEM TC 218-SFC [11]. However, besides the usage of a container equipped with p-wave transducers with a center frequency of 500 kHz an additional container with two broadband s-wave transducers with a center frequency of 250 kHz are used. A sensor distance of 50 mm was found to be sufficient for both containers. The sensors are coupled by a thin polyimide film (d=25µm) directly through the mix to allow for best signal transmission. A detailed system description is given in Krüger [12].

One of the most crucial parts is to extract as accurate as possible the onset time (i.e. the arrival time) of the signal in relation to the trigger time. Therefore, onset of the signals has to be discriminated from noise. There are various possibilities to do this since there are threshold and energy based methods and auto-regressive processes [10, 12]. For the following tests a picking algorithm called AIC-Picker is used to detect the p-wave onset time. This picker is based on the Akaike Information Criterion (AIC) [13] and was adapted to ultrasonic signals by Kurz, Grosse and Reinhardt [10].

To determine the onset time of the shear wave, the time signal is transformed into a time-frequency domain by means of a continuous wavelet transform (for details see [14]).

To study the setting and hardening time at very early age in the following a test time of 24 hours was considered with a test interval of 5 minutes. In a post processing procedure the measurements were analysed and further elastic parameters were calculated. If it is assumed that the material to be tested is homogeneous and isotropic the dynamic elastic properties can be calculated from the shear wave velocity v_s, the compressional wave velocity v_p and the materials density ρ_c by using the following equations:

$$\sigma_{dyn} = \frac{\frac{1}{2} \cdot v_p^2 - v_s^2}{v_p^2 - v_s^2} \tag{1}$$

$$E_{dyn} = \frac{(1 + \sigma_{dyn}) \cdot (1 - 2\sigma_{dyn})}{(1 - \sigma_{dyn})} \cdot v_p^2 \cdot \rho_c = (2 + 2\sigma_{dyn}) \cdot v_s^2 \cdot \rho_c \tag{2}$$

$$G_{dyn} = \frac{E_{dyn}}{2 + 2\sigma_{dyn}} = v_s^2 \cdot \rho_c \tag{3}$$

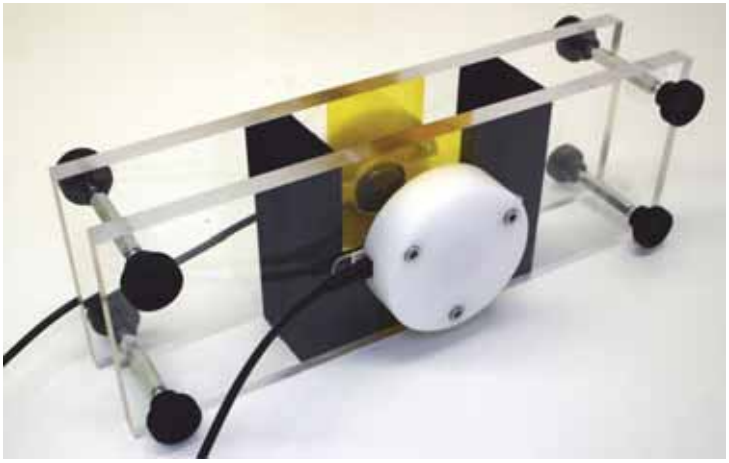

Figure 2. Test container for combined compressional and shear wave testing.

4. Test results and evaluation of the mixes

To study the setting and hardening process at very early age especially investigations were conducted within the first 24 hours of hydration at room temperature 20±2°C and relative humidity of 65%. One of the benefits of ultrasound is that within that time hydration processed can be studied permanently and non-destructive. An example of the change in compressional and shear wave velocity during hydration is given in Figure 3 (left). It can be seen that at very early age in the dormant period of the mix no significant change in wave velocity is obviously measureable and that during further hydration the wave velocities increase from very low velocities up to values of several thousand m/s after one day. From

that determined wave velocities dynamic elastic properties can be calculated like it is described in equations (1) to (3) and plotted in Figure 3 (right).

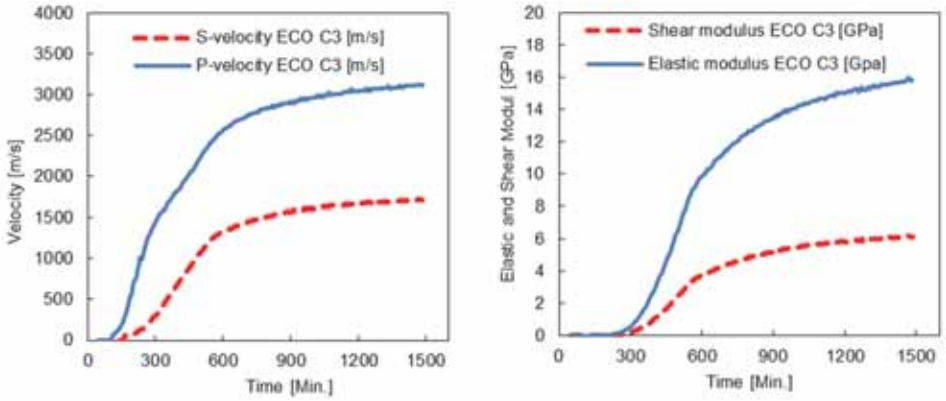

Figure 3: Evolution of compressional and shear velocity (left) and compressional and shear modulus (right) of ECO C3 mix.

One of the main advantages of analysing the dynamic elastic properties instead of the wave velocities only is that it is more feasible to correlate elastic properties with other mechanical values like strength or initial or final setting time according to Vicat, which is a penetration test that is itself strongly correlated with the shear strength and shear modulus. An additional advantage is that the calculated elastic properties also take into account the density of the material so it includes an additional and variable material parameter relevant to mechanical characteristics of the investigated materials.

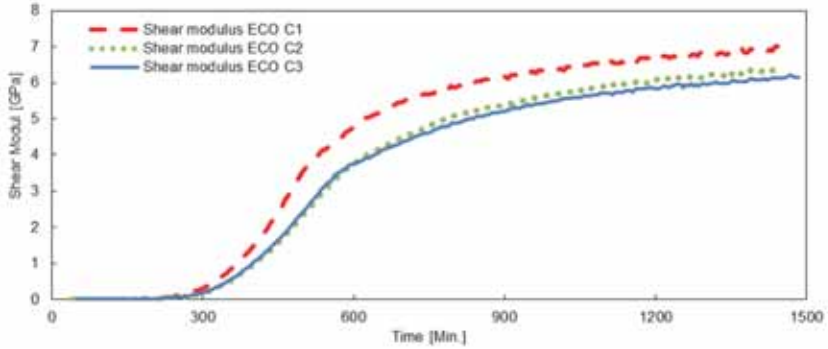

Figure 4: Evolution of compressional and shear modulus of the three ECO C3 mixes

To compare the results of the different tests conducted some values were extracted from the continuous ultrasound measurements, i.e. wave velocities and calculated elastic properties at the initial and final setting time according to the Vicat needle test for each mix and also values after 24 hours of hydration where also strength was determined (see table 3).

Table 3: Characteristic material properties of the tested mixtures.

		REF A1	**ECO B1**	**ECO C1**	**REF A2**	**ECO B2**	**ECO C2**	**REF A3**	**ECO B3**	**ECO C3**
vp, initial vicat	[m/s]	1177	614	667	1437	1353	1169	1483	1469	1023
vs, initial vicat	[m/s]	156	110	74	254	195	126	292	326	128
vp, final vicat	[m/s]	1519	1017	1291	1545	1516	1625	1520	1513	1579
vs, final vicat	[m/s]	373	207	220	406	335	406	362	383	418
E, initial vicat	[GPa]	0.15	0.07	0.03	0.37	0.22	0.10	0.47	0.58	0.10
G, Initial vicat	[GPa]	0.05	0.02	0.01	0.13	0.07	0.03	0.16	0.20	0.03
E, final vicat	[GPa]	0.86	0.26	0.30	0.94	0.63	1.03	0.72	0.79	1.08
G, final Vicat	[GPa]	0.29	0.09	0.10	0.32	0.22	0.35	0.24	0.27	0.37
vp, 24h	[m/s]	3167	2861	3262	2804	2317	3125	2540	1996	3105
vs, 24h	[m/s]	1750	1522	1820	1487	1163	1721	1294	896	1703
E, 24h	[GPa]	16.58	12.22	17.82	11.24	6.91	16.23	8.26	4.06	15.72
G, 24h	[GPa]	6.48	4.69	6.99	4.31	2.59	6.33	3.12	1.48	6.12

It has to be noted that the Vicat needle test is designed to be conducted with a standard consistency that guarantees a comparable plasticity at the beginning of the test. This means that Vicat setting times obtained from mixes with other consistency than the standard consistency might not be interpreted correctly to represent the initial setting time of the material. Especially if the water/binder ratio is changed and thus the particle density shows variation, the percolation process during hydration is expected to behave different. Finally, an increased capillary porosity can be expected during further hydration if the total water added to the mix is not needed for the hydration of the used binder. As can be seen from table 2 the mixes show different densities – mainly due to i) more or less optimisation of particle size distribution and thus the packing density and ii) adding additional water to vary the consistency – right after mixing and also very different strength after one day of hydration. It is clear that strength is not only dominated by the used binder but also strongly by the density of the matrix (see Fig. 7). The optimization of the packing density by the use of micro fillers is one of the concepts of developing eco-friendly cementitious matrices with reduced cement clinker content like it is presented here. It can be assumed that due to the higher packing density the mean distance between each particle is lower compared to that of mixes with lower packing density, either given by a non-optimized particle size distribution (see mixes REF A and ECO B) or even be adding additional water. This lower mean particle distance has also effect on the strength development dominated by the hydration of the cement. The different reactions during the hydration process are itself complex with its time dependent formation of hydration products, which is also influenced by the available pore space respectively particle distance. It can be assumed that the evolution of the viscoelastic properties of the matrix during hydration will depend on the mean particle distance and that also the viscous and the elastic properties will be altered in the same manner. This might be

the reason why the dynamic elastic shear modulus determined by the ultrasound shear wave velocities do not correlate at a constant value with the initial setting time given by the Vicat test, which is a destructive test providing a value that depends on the viscoelastic properties of the material, i.e. shear modulus and shear strength. Moreover, Fig. 6 (right) shows that higher shear moduli are to be expected at the individual initial setting time according to Vicat needle test if packing density is less. Having that assumptions in mind it is obviously not feasible to obtain an initial setting time just by analysing ultrasound values like the compressional or shear wave velocity without a former calibration on reference mixes (see Fig. 6 (left)). This is especially true for the analysis of the compressional wave velocity only, because this velocity is at early stage strongly influenced by the presence of air within the mix as well as the total water content [1, 15]. However, it is on the other hand not feasible to use the Vicat needle test on every mix composition to get an idea of initial setting because the test is not designed for variable initial consistencies, nor you will get an idea of the full hydration process and the evolution of mechanical material properties.

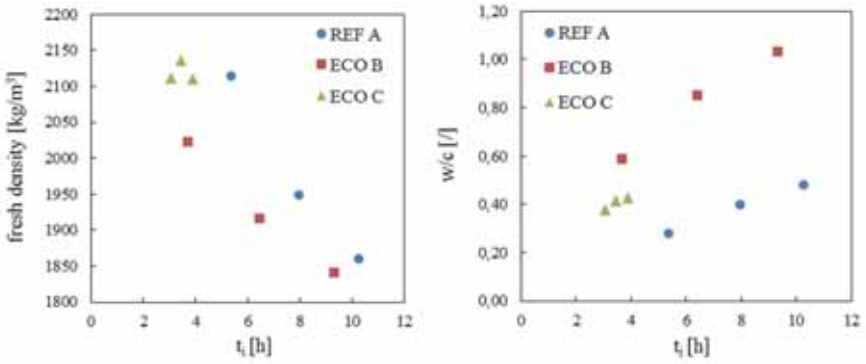

Figure 5: Density at fresh state (left) and water/cement ratio (right) versus setting time according to Vicat needle test.

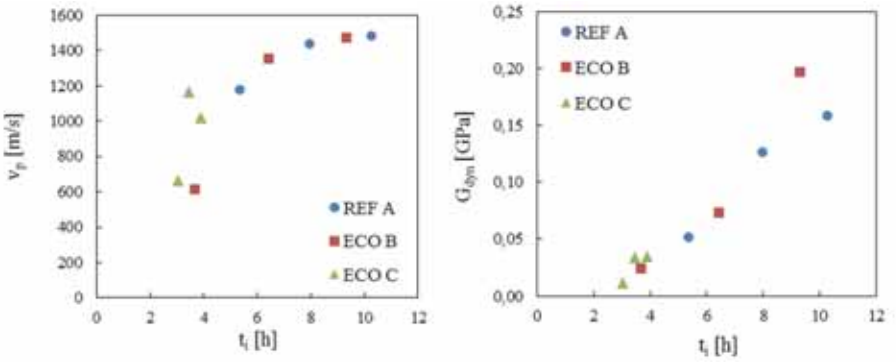

Figure 6: Compressional wave speed versus setting time (left) and shear modulus versus setting time according to Vicat needle test (right).

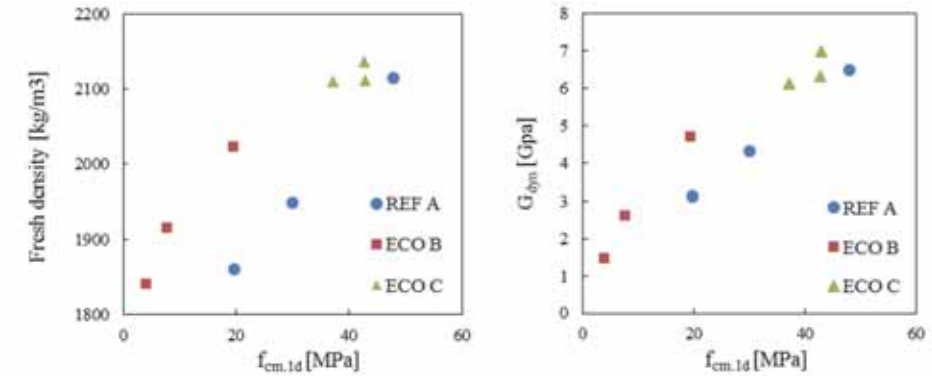

Figure 7: Density at fresh state versus strength (left) and shear modulus versus strength (right); 1 day values.

5. Conclusions

From the test series and the results presented in this paper several conclusions can be drawn:

- Ultrasound measurements are found to be very useful to characterize the setting and hardening behaviour of cement pastes as well as eco-friendly cementitious pastes with reduced cement clinker but optimized packing density.
- However, the use of compressional wave velocities only might result in misleading interpretation of the setting and hardening process especially if it will be correlated with initial and/or final setting times (according to Vicat) without former calibration. This is because the compressional wave speed at early stage is strongly influenced by the presence of air within the mix as well as the total water content resp. density of the mix.
- The dynamic elastic properties (dynamic elastic modulus and dynamic shear modulus) derived from the ultrasound compressional and shear wave velocities show good correlation with the strength development independently from the mixture composition. In addition to that, the dynamic elastic modules show also higher sensitivity on mechanical properties evolution compared to the wave velocities.
- Although Vicat needle test can be conducted with consistencies different from the standard consistency, the interpretation of such mixes with respect to the initial setting time is questionable as Vicat needle penetration is influenced by the total water amount and variable air presence within the mix. For this reason it is assumed that the evolution of shear modulus derived from the ultrasound measurements is a more reliable indicator for initial setting time of any mixture composition.

Acknowledgments

The work presented here is part of the Extended Round Robin Testing programme (RRT+) conducted in the context of the COST action TU1404 (http://www.tu1404.eu/, http://www.cost.eu/COST_Actions/tud/TU1404).

References

[1] Robeyst, N, Gruyaert, E., Grosse, C.U., De Belie, N., Monitoring the setting of concrete containing blast-furnace slag by measuring the ultrasonic p-wave velocity. Cem. Concr. Res., 38 (10) (2008), pp. 1169–1176
[2] Carette, J., Staquet, S., Monitoring the setting of mortars by ultrasonic P-wave and S-wave transmission velocity measurement, Constr. Build. Mater. 94 (2015) pp. 196-208.
[3] Carette, J., Staquet, S., Monitoring the setting process of eco-binders by ultrasonic P-wave and S-wave transmission velocity measurement: Mortar vs. concrete, Constr. Build. Mater.110 (2016) pp. 32-41.
[4] Reinhardt, H.-W., Grosse, C.U., (2005), Mechanical wave propagation – Basics. Chapter 4.1 in: Advances testing of cement based materials during setting and hardening. RILEM Report 31. Bagneux: 2005. pp. 83-96.
[5] Juhart, J., David, G.A., Nickel, C., Fischer, G., Mittermayr, F., A new combined filler concept for eco-concrete, Proc. of 14th International Congress on the Chemistry of Cement (ICCC 2015), Beijing (2015)
[6] Marquardt, I., Ein Mischungskonzept für selbstverdichtenden Beton auf der Basis der Volumenkenngrößen und Wasseransprüche der Ausgangsstoffe (in German), PhD thesis, Rostocker Berichte aus dem Fachbereich Bauingenieurwesen, Nr. 7, Rostock (2002)
[7] Okamura, H. et al, Self-compacting concrete. Journal of Advanced Concrete Technology, Japan Concrete Institute, Vol. 1, No. 1 (2003), 5-15
[8] Puntke W., Wasseranspruch von feinen Kornhaufwerken (in German), Beton, 52 (5) (2002), 242-248
[9] Standard EN 1015-3, Methods of test for mortar for masonry – Part 3: Determination of consistence of fresh mortar (by flow table), (2007)
[10] Kurz, J.H.; Grosse, C.U.; Reinhardt, H.W. (2005), Strategies for reliable automatic onset time picking of acoustic emissions and of ultrasound signals in concrete. Ultrasonics, vol. 43, pp. 538 - 546, 2005.
[11] Reinhardt, H.W., Krüger, M., Grosse. C.U., Testing of fresh concrete by ultrasound transmission. Technical Committee 218-SFC: Sonic methods for quality control of fresh cementituous materials, in preparation.
[12] Krüger, M., Lehmann, F. (2010), SmartPick – User Manual, Rev. 1.50. Smartmote.
[13] Akaike, H. (1974), A new look at the statistical model identification. IEEE transactions on automatic control, vol. AC-19, no. 6, 1974.
[14] Krüger, M., Grosse, C.U., Lehmann, F.: Automated shear-wave techniques to investigate the setting and hardening of concrete in through-transmission. International Symposium on Nondestructive Testing of Materials and Structures, May 15-18, 2011, Istanbul, Turkey, RILEM Bookseries, Springer, Dordrecht, The Netherlands, 2012.
[15] Harker, A.H., Temple, J.A.G., Velocity and attenuation of ultrasound in suspensions of particles in fluids, J. Phys. D, Appl. Phys. 21 (1988) pp. 1576-1588.

International RILEM Conference on Materials, Systems and Structures in Civil Engineering
Conference segment on Service Life of Cement-Based Materials and Structures
22-24 August 2016, Technical University of Denmark, Lyngby, Denmark

WASTE CERAMICS AS PARTIAL CEMENT AND AGGREGATE REPLACEMENTS IN SELF-COMPACTING CONCRETE

Paul Archbold [(1)], John Flattery [(1)]

(1) Department of Civil Engineering, Athlone Institute of Technology, Dublin Road, Athlone, Co. Westmeath, Ireland

Abstract
There is increasing demand for the replacement of virgin materials in large-scale production of construction materials. Similarly, there is a desire to reduce the amount of waste being sent to landfill. Both of these demands are derived from concerns about the environmental impacts of traditional methods of production and waste disposal. One approach to tackling both of these concerns is to use recycled material in concrete production – either as a supplementary cementitious material or as an aggregate replacement. This paper reports on preliminary testing carried out on two types of waste ceramics – ceramic foundry casts and ceramic waste sludge respectively, which have been examined as partial replacements for both the cementitious material and the fine aggregates in self compacting concrete. Properties assessed include rheology, compressive strength and durability. The impact of this partial replacement of materials is reported and benchmarked against other similar studies. The results are consistent with previously published values and indicate that the potential use of these waste materials is worthy of further investigation. They indicate that the substitution of ceramic materials in self-compacting concrete may improve the durability and performs in terms of compressive strength. However, the addition of ceramic materials in a mix reduces the passing/filling ability of the self-compacting concrete.

1. Introduction

Self-compacting concrete (SCC) was developed in Japan in the 1980's and is characterised by its ability to consolidate under its own weight. It has excellent deformability and high resistance to segregation. SCC's ability to flow makes it extremely suitable for placing in difficult conditions and sections with congested reinforcement and therefore is widely used in precast industries and large pours. The filling ability (the ability of SCC to flow into and fill completely all spaces within the formwork, under its own weight), passing ability (the ability

of SCC to flow through tight openings such as spaces between steel reinforcing bars without segregation or blocking) and stability of mixes (the ability of SCC to remain homogeneous in composition during transport and placing) can be considered the distinguishing properties of fresh SCC [1]. As such, specific tests (the slump flow test, V-funnel test and the filling box test) have been developed to assess such properties and characterise SCC, which are in addition to the standard concrete assessment methods [2].

In terms of composition, SCC mixes tend to have more powder content and smaller amounts of coarse aggregates than ordinary concrete mixes in order to deliver the improved filling ability and stability while limiting the blocking potential in the concrete. SCC mixes also incorporate more admixtures such as, water reducers to achieve excellent flow at low water contents and superplasticizers to reduce bleeding [3].

The production of concrete has well-established detrimental impacts on the environment. It has been claimed that the cement industry is the second largest CO_2 emitting industry behind power generation [4]. Moreover, traditional aggregates are a finite resource and will not alone be able to cope with the growing demand of the construction industry. There is, therefore, considerable motivation for discovering new sources of recycled aggregates to contribute to making concrete a more sustainable construction material [5].

1.1 Ceramic Waste Material as a Partial Replacement in Concrete

Ceramics have been described as a "refractory, inorganic and non-metallic material" Traditional ceramics consist of clay products, primarily silica, silicate glass and cement, whereas advanced ceramics consists of carbides (SiC), pure oxides (AI_2O_3), nitrides (Si_3N_4), non-silicates glasses and many others [6]. Ceramics are popular in manufacturing industries, but generally are sent to landfill once their primary use has been exploited.

Ceramic foundry sand is a by-product from the metal alloys casting industry and typically has a high silica content. The classification of foundry sands depend on the type of binder used in the metal casting - it may be either clay bonded sand or chemically bonded sand, with 85-95% and 93-99% silica content respectively [7]. As a result, the use of foundry sand may be a suitable aggregate for cement-based products and concrete products. However, the use of ceramic sand may be limited to 30% replacement of the fine aggregates due to the high percentage of fine material [8]. Foundry sand has been reported to have a higher absorption rate than natural sand and a higher void ratio. Further, it is reported that the increased addition of waste foundry sand as a fine aggregate replacement reduced the slump of concrete [9], [10], [11]. This was then further developed by Exteberria et al., who studied that chemical foundry sand gained a greater slump than clay bonded foundry sand, with values of 150mm and 75mm achieved respectively [12].

In terms of compressive strength, the literature is less conclusive. Some authors, reported a slight increase in compressive strength when waste foundry sand replaced fine aggregates [13], [14]. However, others have shown a slight decrease in compressive strength, particularly with high levels of aggregate replacement by ceramic materials [10], [15].

In addition, Hagy reports recycled ceramic aggregates show a much higher percentage of water absorption compared to stone aggregates. The percentage is so large that the ceramic aggregates must be pre-saturated before being used in the production of concrete [16]. Regarding concrete durability, it has been shown that the use of ceramics as partial replacements can lead to a reduction in the water absorption capability of concrete, while also reducing the air permeability and chloride ion diffusion [18], [15]. Equally, it has been reported that ceramic waste materials may contain pozzolanic constituents which may make them suitable as partial cement replacements [17]. The aim of this study is thus to examine the potential of waste ceramic material as partial replacements for aggregates and cement respectively in self-compacting concrete mixes.

2. Methodology

2.1 Materials

The ceramic sand used in this material was formed from waste foundry casts, used in the production of hip and knee replacements. The casts were crushed, cleaned and passed through a 4mm sieve to separate the fine and coarse aggregates. Further segregation of the finer material was required to remove wax deposits left from the manufacturing process.

Secondly, a ceramic sludge which is the residue left from polishing the ceramic casts was dried and mixed with a recycled lime material to form a clinker, which was then ground to the desired grading. The exact nature of the lime treatment is withheld for confidentiality reasons. For this experimental program the recycled ceramic sludge was to replace different percentages of limestone filler and also different percentages of cement in the concrete mix. The type of limestone filler used in these mixes is Betocarb made by Omya UK Ltd. Therefore the recycled ceramic sludge is passed through a 2mm sieve. The type of cement used is CEM I 42.5R (Appendix 1) produced by Irish Cement at their plant in Drogheda, Ireland. The grading for this cement type is <70μm.The ceramic sludge was then sieved through the 63μm to replace the cement in the mix.

Analysis of this material yielded a particle density of 2.7Mg/m^3 and a water absorption value of 2.1% for the ceramic sand. The density is similar to that of the conventional aggregate, while the water absorption is higher than the conventional aggregate value of just 0.21%. However, the value for the ceramic material is within the limit of 3% set by BS 8007 [19]. The values for the ceramic waste sludge (CWS) material, on the other hand were considerably lower at 1.17Mg/m^3 and 2.8% respectively – lower than average values for cement and lime filler.

2.2 Test Samples

In this study, two basic references - C50/60 SCC Rapid CEM I mix and C50/60 SCC Rapid CEM III/A – 50% GGBS mix – were employed. For each mix, the limestone filler was then replaced at 25%, 50% and 100% levels by the ground CWS material. Similarly, fine aggregate was replaced at 25%, 50% and 100% proportions by the ceramic sand. Finally, the cement was replaced by CWS at levels of 10%, 15% and 20%. This combination yielded 20 different mix compositions as detailed in Table 1.

For compressive strength testing, 100mm x 100mm cubes were cast, while for durability testing, 300mm x 300mm x 100mm samples were created.

Table 1. Mix Descriptions for Testing

Mix Reference	Description
C1R	CEM I Reference Mix
C1L25	CEM I 25% Lime Filler Replacement
C1L50	CEM I 50% Lime Filler Replacement
C1L100	CEM I 100% Lime Filler Replacement
C1S25	CEM I 25% Sand Replacement
C1S50	CEM I 50% Sand Replacement
C1S100	CEM I 100% Sand Replacement
C1C10	CEM I 10% Cement Replacement
C1C15	CEM I 15% Cement Replacement
C1C20	CEM I 20% Cement Replacement
C3R	CEM III/A
C3L25	CEM III/A 25% Lime Filler Replacement
C3L50	CEM III/A 50% Lime Filler Replacement
C3L100	CEM III/A 100% Lime Filler Replacement
C3S25	CEM III/A 25% Sand Replacement
C3S50	CEM III/A 50% Sand Replacement
C3S100	CEM III/A 100% Sand Replacement
C3C10	CEM III/A 10% Cement Replacement
C3C15	CEM III/A 15% Cement Replacement
C3C20	CEM III/A 20% Cement Replacement

2.3 Rheology Testing

Immediately after the mixing, the fresh SCC was tested for filling ability and passing ability. The Slump Flow test and the V-funnel test, according to standard EN 12350-8 and EN 12350-9 respectively, were used to measure the filling ability (viscosity) of the SCC. The Slump Flow measures the maximum uninterrupted flow width of SCC through a slump cone, whereas the V-funnel flow time measures the interval required for a mass of concrete to completely flow though the trap door of the funnel.

The passing ability of the fresh SCC was tested using J-ring test complying with standard EN 12350-12. The J-ring measures the blockage of concrete due to the presence of reinforcement bars (Figure 1) and was carried out by first holding a mass of concrete in a ‘slump cone’, placing the J-ring and then lifting the cone, thus allowing concrete to pass through the reinforcement. The slump flow and the average concrete height difference between the centre and outside of the ring (step height) was measured.

2.4 Compressive Strength

The strength of the concrete was determined by testing the compressive strength of the 100mm cubes created at the casting process, conforming to EN 12390-3. The compressive

strength was measured at 7, 28 and 56 days by testing 3 cubes from each mix at each time interval.

Figure 1. Measurement of blockage due to congested reinforcement on the J-ring

Figure 2. Measuring water permeability using GWT Apparatus

2.5 Durability

To determine the durability of the concrete mixes, the water permeability was measured using the commercially available Germann's Water Permeability Test (GWT) apparatus (Figure 2). The GWT measures the permeation of water into the test surface under an applied pressure. The procedure involves pressurising de-aired water on the surface of the concrete sample to a pressure of 1.2 Bar and allowing the water to be absorbed into the sample. The amount of water absorbed is determined and a concrete permeability coefficient is calculated.

3. Results

The results from each of the tests are shown in Table 2. Each result shown is the average of three tests on the particular sample.

4. Discussion

4.1 Rheology

Figure 3, Figure 4 and Figure 5 shows the results from the Slump Flow Test, the V-Funnel Test and the J-Ring Test respectively. Immediately apparent is that the CEMIII reference mix (C3R) exhibited a greater slump flow (by approximately 75%) and a shorter time interval (by almost 20%) in the V-funnel test than the CEMI reference mix (C1R). This is to be expected as the use of GGBS results in greater workability for consistent w/c ratios.

When the limestone filler was replaced by the CWS material (mixes C1L25, C1L50, C1L100, C3L25, C3L50, C3L100), the slump flow spread reduced, while the flow time increased, indicating a decrease in the filling ability of the concrete. This was the case for both the CEM I mixes and the CEMIII/A mixes. When the sand was replaced, the results followed a very similar trend. This is in general agreement with previously published values from other authors [10], [11], [12]. The results from the J-Ring test were less conclusive.

4.2 Compressive Strength

Figure 6 shows the results from the compressive strength tests on all samples. The 25% lime filler replacement mix (C1L25) achieved the greatest compressive strength for the CEM I mixes, with a considerable increase in strength after 56 days. This outcome is similar to that of Alves et al. [20] whom found that 20% replacement with ceramic aggregate achieved the optimum compressive strength. However this did not hold true for the CEM III mixes.

Table 2. Results from Rheology, Compressive Strength and Water Permeability Tests

	Slump Flow	**V-Funnel**	**J Ring**	**Compressive Strength,**			**Water Penetration**
Mix Reference	**SF Spread (mm)**	**Flow Time, t_v (s)**	**Flow Spread, PJ (mm)**	**f_{cu} (N/mm^2) 7 days**	**f_{cu} (N/mm^2) 28 days**	**f_{cu} (N/mm^2) 56 days**	**C_{cp} x 10^{-6} {mm/s}**
C1R	770	13.45	10	61.64	69.49	75.78	1880.94
C1L25	750	13.94	8	75.63	81.50	97.53	57.87
C1L50	710	14.12	15	59.34	70.82	84.30	1338.36
C1L100	640	15.70	13	54.09	68.94	75.78	1587.04
C1S25	750	17.81	10	71.35	85.72	88.50	1210.85
C1S50	690	20.11	10	61.13	66.65	72.91	661.04
C1S100	600	25.89	20	61.72	66.86	71.15	193.52
C1C10	770	8.63	10	59.32	63.54	79.90	1442.35
C1C15	760	14.15	10	61.99	71.81	73.62	1481.24
C1C20	740	16.05	8	62.40	73.33	74.03	1518.31
C3R	920	7.69	5	71.43	89.85	90.39	1433.31
C3L25	900	8.89	2.5	61.48	77.13	77.06	1426.98
C3L50	880	9.23	0	52.04	81.22	86.61	691.79
C3L100	860	9.89	5	57.20	81.46	85.20	343.63
C3S25	900	12.50	10	73.02	85.30	97.00	1057.12
C3S50	870	13.97	10	64.19	73.73	80.12	400.60
C3S100	700	18.64	20	39.19	56.68	63.04	1206.33
C3C10	930	7.04	0	68.97	73.13	88.23	1470.39
C3C15	930	8.61	10	58.91	84.41	99.20	1409.80
C3C20	900	11.30	0	64.76	75.00	84.81	1181.92

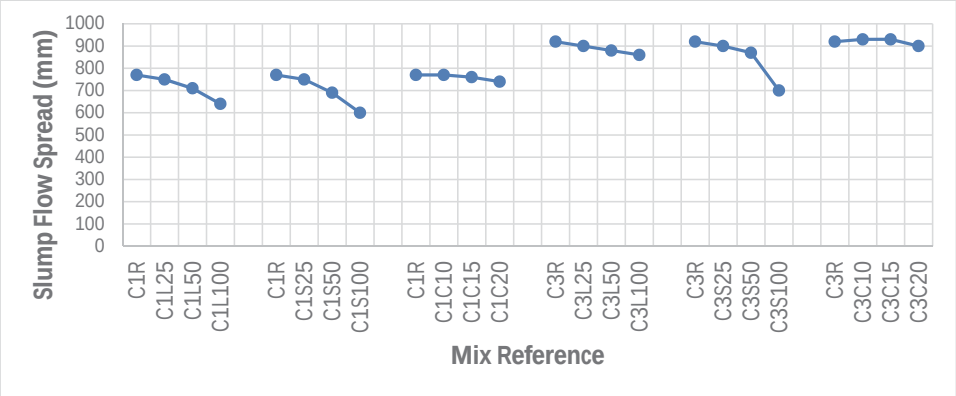

Figure 3. Results from Slump Flow Test

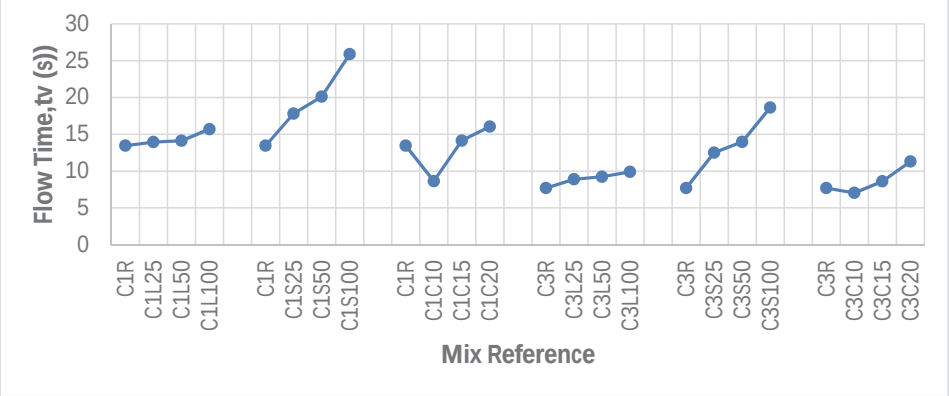

Figure 4. Results from V-Funnel Test

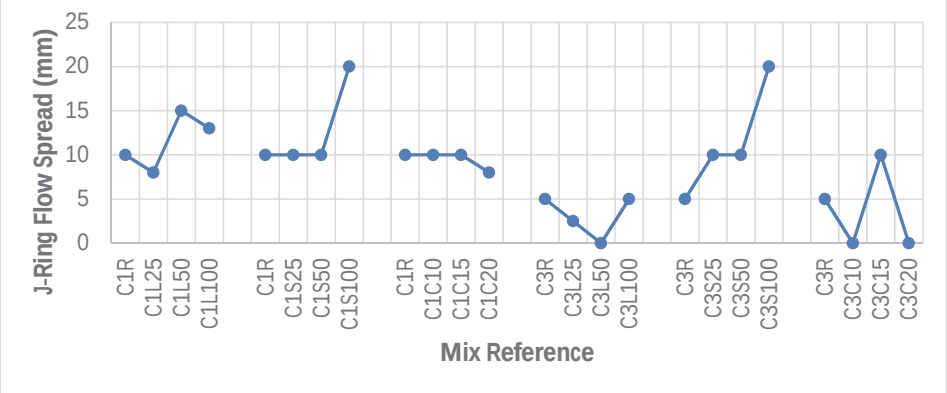

Figure 5. Results from J-Ring Test

To improve clarity, Figure 7 shows the relative compressive strength in terms of the reference mix for all of the CEM I mixes. When considering the sand replacement, for both the CEM I and the CEM III/A mixes, 25% sand replacement with ceramic sand yielded the maximum increases in compressive strength. For the cement replacement, there was a negligible effect on the compressive strength results.

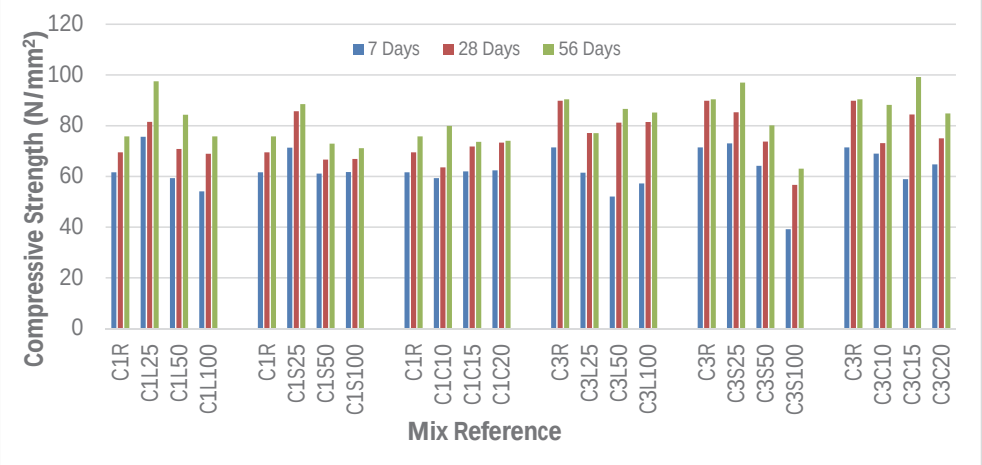

Figure 6. Compressive Strength Results

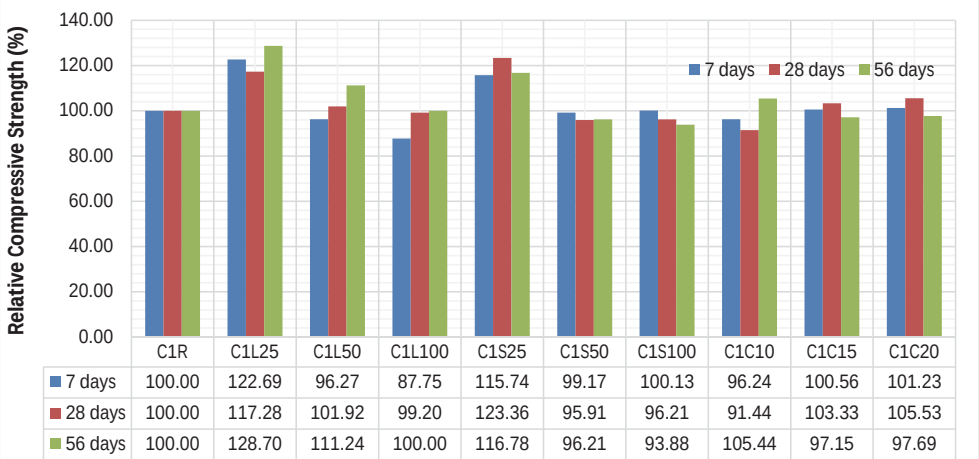

	C1R	C1L25	C1L50	C1L100	C1S25	C1S50	C1S100	C1C10	C1C15	C1C20
7 days	100.00	122.69	96.27	87.75	115.74	99.17	100.13	96.24	100.56	101.23
28 days	100.00	117.28	101.92	99.20	123.36	95.91	96.21	91.44	103.33	105.53
56 days	100.00	128.70	111.24	100.00	116.78	96.21	93.88	105.44	97.15	97.69

Figure 7. Relative Compressive Strength Results

4.3 Water Permeability

Figure 8 presents the results from the water permeability testing using the GWT apparatus. In each case, the water permeability reduced with the addition of ceramic waste – either as a

replacement for the lime or cement (CWS) or as a replacement for the fine aggregate (ceramic sand).

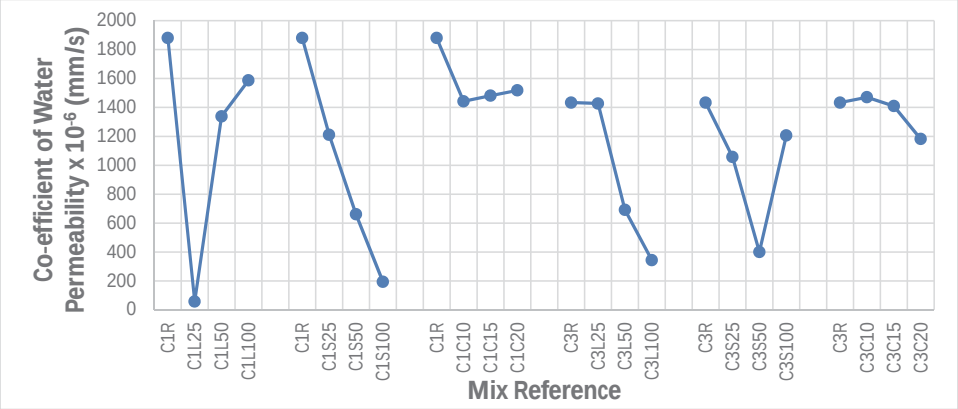

Figure 8 Results from the water permeability testing using the GWT apparatus.

Overall, 25% replacement in lime filler and sand and 15% replacement in cement were the optimum replacement percentages for the C50/60 SCC Rapid CEM I mix. Whereas 50%, 25% and 15% replacement in lime filler, sand and cement respectively were the optimum replacements in the C50/60 SCC Rapid CEM III/A – 50% GGBS mix.

5 Conclusions

Concrete production is environmentally onerous due to the manufacturing process, but also due to the heavy reliance on virgin natural materials to produce aggregates and cement. Equally, ceramics are used extensively in manufacturing industries, generally being sent to landfill once their primary use has been exhausted. However, previous studies suggest that ceramics may be suitable for use in concrete as partial replacements for either the fine aggregate or the cementitious material. This paper examined the possibility of using two types of waste ceramic (ceramic waste sludge and ceramic sand) as partial replacements in self-compacting concrete. Rheology, compressive strength and water permeability tests were carried out on two control mixes – a CEM I Portland cement mix; and a CEMIII/A Portland Cement/GGBS blended mix, together with mixes containing the waste ceramics as partial replacements for the sand, lime filler and cement respectively. The results have shown that these materials do offer potential for use and may even contribute to improving the mechanical properties of the hardened concrete, with optimum replacement levels identified.

Acknowledgements
The authors would like to thank Gannon Eco Ltd and Banagher Precast Concrete Ltd for supplying materials and test facilities for this study.

References

[1] EFNARC 'Specifications and Guidelines for SCC', EFNARC, Hampshire, UK (2001).
[2] Okamura, H. & Ouchi, M., 'Self-Compacting Concrete: Development, present use and future', Advance Concrete Technology, Vol. 1. (1999).
[3] Nehdi, M., 'Why some carbonate fillers cause rapid increases of viscosity in dispersed cement-based materials', Cement and Concrete Research, Vol. 30. (2000)
[4] Ambuja Cements, 'Environmental Impact', (Accessed: 15th October 2015), http://foundationsakc.com/process/environment-impact (2015)
[5] Kwan, W. H., Ramli, M., Kam, K. J. & Sulieman, M. Z., 'Influence of the amount of recycled coarse aggregate in concrete design and durability properties', Construction and Building Materials, Vol. 26. (2012)
[6] Baehr, G., Day, J., Dieshow, L., Faulise, D., Overocker, E. & Schwan, J., 'Ceramics – Windows to the future', Materials Science and Technology, Illinois (1995).
[7] Prabhu, G., Hyun, J.H. & Kim, Y.Y, 'Effect of used-foundry sand on the mechanical properties of concrete', Construction and Building Materials, Vol. 70. (2014)
[8] Naik, T.R. & Kumar, R., 'Recycled materials in concrete industry', University of Wisconsin, Milwaukee (2003).
[9] Guney, Y., Sari Y.D., Yalcin, M., Tuncan, A. & Donmez, S., 'Re-usage of waste foundry sand in high strength concrete', Waste Management, Vol. 30. (2010)
[10] Mansur, M.A., Wee T.H. & Cheran L.S., 'Crushed bricks as coarse aggregate for concrete', Construction and Building Materials, Vol. 96 (1999).
[11] Khatib, J.M., 'Properties of concrete incorporating fine recycled aggregate', Cement and Concrete Research, Vol. 35. (2005)
[12] Etxeberria, M., Pacheco, C., Meneses, J.M. & Berrid, I., 'Properties of concrete using metallurgical industrial by-products as aggregates', Construction and Building Material, Vol. 24. (2010).
[13] Siddique, R., Schutter, G. & Noumowec, A., 'Effect of used-foundry sand on the mechanical properties of concrete', Construction and Building Materials, Vol. 23 (2009).
[14] Medina, C., Rojas, M.I.S. & Frias, M., 'Reuse of sanitary ceramic wastes as coarse aggregate in eco-efficient concretes', Cement and Concrete Composites, Vol. 34 (2012).
[15] Senthamarai, R.M. & Manoharan, P.D., 'Concrete with ceramic waste aggregate', Cement and Concrete Composites, Vol. 25 (2005).
[16] Hagy, F.H., 'Structural Materials and Engineering', Nova Science Publishers, New York. (2009).
[17] Heidari, A., & Tavakoli, D., 'A study of the mechanical properties of ground ceramic powder concrete incorporating nano-SiO2 particles', Construction and Building Materials, Vol. 38 (2013).
[18] Pacheco-Torgal, F. & Julali S., 'Reusing ceramic wastes in concrete', Construction and Building Materials, Vol. 24 (2010).
[19] British Standards, 'Concrete – Complementary British Standard to BS EN 8007: Part 1: Code of practice for design of concrete structures for retaining aqueous liquids', British Standards Institution, London. (1987).
[20] Alves, A.V., Virira, T.F., De Brito, J. & Correia J.R., 'Mechanical properties of structural concrete with fine recycled ceramic aggregates', Construction and Building Materials, Vol. 64 (2014).

International RILEM Conference on Materials, Systems and Structures in Civil Engineering
Conference segment on Service Life of Cement-Based Materials and Structures
22-24 August 2016, Technical University of Denmark, Lyngby, Denmark

COMPARATIVE ANALYSIS OF COMPRESSIVE STRENGTH AND VOLUME CHANGE FOR DETERMINATION OF SULFATE RESISTANCE OF RAC

Vesna Bulatović[(1)], Vlastimir Radonjanin[(1)], Mirjana Malešev[(1)], Miroslava Radeka[(1)], Ivan Lukić[(1)]

(1) University of Novi Sad, Faculty of Technical Sciences, Department of Civil Engineering and Geodesy, Serbia

Abstract
Some results of the experimental investigation on the sulfate resistance of concrete with recycled concrete aggregate (RAC) immersed in 5% Na_2SO_4 and 5% $MgSO_4$ solutions for periods of 3 and 6 months are presented in the paper. For concrete production natural river fine aggregate and coarse recycled concrete aggregate were used. The effect of water to cement ratio and cement type on sulfate resistance of RAC were investigated. Two water to cement ratios were varied (0.38 and 0.55) and two types of common cement were used (CEM I 42,5R and CEM III 32,5N LH/SR). Sulfate resistance was monitored through change in compressive strength and volume change. Compressive strength was determined on cylinders ∅100x100mm, while length change was monitored on prisms 100mmx100mmx500mm. It was observed that both methods show results that lead to same assessment of sulfate resistance. Recycled aggregate concrete could achieve satisfactory sulfate resistance if appropriate type of cement and water to cement ratio are chosen.

1. Introduction

External sulfate attack is one of the durability problems associated with concrete. Sulfate attack has often been discussed in terms of the reaction between hydration products of cement and sulfate ions in solution. The source of sulfate ions are soil, groundwater, rivers, seawater, cooling towers, industrial wastes, in combination with cations such as sodium, potassium, magnesium and calcium ions [1].

It has been difficult to define the precise nature of the mechanisms of sulfate attack because of its complex behaviour [1]. The use of new and supplementary cementing materials in recent decades makes the picture of sulfate resistance more complicated because of the varied effects ranging from beneficial to deleterious [2]. The major problem in assessing materials is that

the form of attack in sulfate environments is variable [3]. The extent to which concrete is affected by sulfates depends on several factors such as permeability of concrete, water/cement ratio, type of cement, exposure conditions and the environment. Most testing is undertaken on mortar or cement paste samples, as concrete introduces additional variables and makes testing more labour intensive [3].

The expansion resulting from sulfate attack is generally attributed to the formation of ettringite and gypsum, although there is some controversy about the exact mechanisms causing expansion. In addition to this phenomenon, degradation of calcium silicate hydrate (CSH) may also occur [4].

In the case of sodium sulfate (Na_2SO_4) the main reactions are the reaction of Na_2SO_4 and CH to form gypsum and the reaction of the formed gypsum with CAH to form ettringite. In the case of magnesium sulfate ($MgSO_4$), it reacts with all cement compounds, including CSH, thus decomposing cement. Concrete deterioration due to $MgSO_4$ attack was attributed to the decalcification of CSH to form MSH, the formation of magnesium hydroxide (brucite) as well as the expansion caused by the formation of expansive salts.

Two main factors that control the resistance of a given concrete to sulfate attack are the chemistry of the cement and the permeability of the concrete. Lower w/c ratio and/or mineral additions (blast-furnace slag, fly ash, silica fume) as a partial replacement of ordinary cement are recommended. On this way, permeability and the amount of CH and C_3A are reduced. CH and C_3A are known to be responsible for the formation of ettringite and gypsum [5].

In most parts of the world, the construction industry consumes a huge amount of natural resources and generates large quantities of construction waste. The disposal of waste has become a severe social and environmental problem [6]. It is logical to use life cycle and sustainable engineering approaches to concrete mix design. This requires several elements: maximizing concrete durability, conservation of materials, use of waste and supplementary cementing materials (blast-furnace slag, fly ash, silica fume) and recycling of concrete. Waste and supplementary cementing materials can be used as partial replacements for portland cement. These materials can improve concrete durability, reduce the risk of thermal cracking in mass concrete and are less energy- and CO_2-intense than cement. Use of aggregate obtained from crushed concrete is an example of recycling and conservation of raw materials [7].

Most of the studies were focused on the mechanical or microstructural characteristics of concrete containing recycled aggregate (RA), while limited works were performed on the durability aspects of the RA [6]. In general, RCA are found to be weaker than corresponding virgin aggregate against mechanical, physical and chemical action [8]. In that way, aggressive external ions can more easily transport in RCA concrete, imposing the risk of chemical attack. Due to the weakness, the use of RCA is very limited especially in case that the concrete structure needs a high strength and/or a high durability [9]. Despite a perception that concrete made with RCA is inherently of inferior quality, research has shown that RCA has the potential to satisfy the mechanical and physical requirements for a range of applications [10]. From previous studies, it should be noted that the compressive strength and durability of

recycled aggregate concrete are worse than those of conventional concrete. Thus many researchers have attempted to improve the properties of recycled aggregate concrete by adding supplementary cementitious materials (fly ash, slag, silica fume, etc.) in the concrete mixture [11].

2. Experimental investigation

The objective of the research described in this paper was to assess resistance to sulfate attack of recycled aggregate concrete that combine both, type of cement and water to cement ratio. In order to investigate the effects of these parameters, ordinary (CEM I) and sulfate resisting (CEM III, according to EN 197-1) cements were used to prepare concrete mixture with two different w/c ratios (0.38 and 0.55) and different type of coarse aggregate (natural and recycled concrete). The sulfate exposure testing procedure was conducted by immersing concrete specimens after the specified initial curing in 5% sodium sulfate and 5% magnesium sulfate solutions. The sulfate solutions were changed every 3 months and samples were tested periodically. Lime-saturated water was used as the reference solution. All containers were covered to minimize carbonation. Eight concrete mixtures were prepared and the resistance of these concrete mixtures to sulfate attack was tested by measuring a compressive strength, capillary water absorption, length change, change in weight and analyzing SEM (Scanning Electron Microscope) and MIP (Mercury Intrusion Porosimetry) results.

The paper reports some results of this experiment like development of compressive strength and length change of four concrete mixtures with recycle concrete aggregate (RCA) which have been immersed in sulfate solutions 3 and 6 months.

2.1 Component materials and the composition of the tested concrete mixtures

To assess effects of water/cement ratio and chemical and mineralogical compositions of cement on the sulfate resistance of concrete with natural and coarse recycle concrete aggregate, the following component materials were used:

- Portland cement CEM I 42.5R (Lafarge-BFC Serbia, γ_{sc}=3100kg/m^3),
- Low heat/Sulfate resistance cement CEM III/B 32.5N LH/SR (Lafarge-BFC Serbia, γ_{sc}=2650kg/m^3),
- Fine aggregate (natural aggregate, river Drina, 0/4 mm, γ_{sa}=2650kg/m^3),
- Coarse aggregate (recycled concrete aggregate, 4/8 and 8/16mm, γ_{sa}=2340 kg/m^3),
- HRWRA ("Sika ViscoCrete 3070", "Sika"- Switzerland, γ_s=1090kg/m^3),
- Tap water.

The basic physical properties of Portland cement and Sulfate resistance cement were tested according to standards EN 196-1, EN 196-3 and EN 196-6.

Fig. 1 shows RCA before sieving and selected fractions, 4/8mm and 8/16mm. The particle density and water absorption of the RCA were measured in accordance with SRPS EN 1097-6

and obtained results are γ_{sa}=2340 kg/m^3 and $u_{v4/8}$=3.0%, $u_{v8/16}$=2.2%, respectively. The origin concrete mix design for recycled concrete aggregate was unknown.

Figure 1-a) RCA before sieving; b) fraction 4/8mm; c) fraction 8/16mm

The concrete mix was designed based on the following conditions:

- Absolute volume of cement and water, around 0.3 m^3,
- Maximum grain size, 16 mm,
- Two w/c ratios, 0.38 and 0.55,
- The amount of super-plasticizer, based on the need to achieve the required consistency,
- Air content, approximately 2%.
- Designed compositions of concrete mixtures are shown in Table 1.

Table 1: Labels and mix proportions of concrete in kg/m^3

Concrete type	$m_{c,}$ CEM I	$m_{c,}$ CEM III	m_v	$m_{v,ad}$	$m_{a,f}$	$m_{a,c}$	m_{spk}	w/c
RPC1	350	-	192.5	20.2	874	803	-	0.55
RPC2	425	-	162	20.5	880	813	3.4	0.38
RMC1	-	338	186	20.5	881	813	-	0.55
RMC2	-	414	157	20.5	881	814	3.3	0.38

2.2 Methods

For testing compressive strength and length change, the following types of concrete specimens were prepared from each mixture:

- 150mm cubes for compressive strength at age of 28 days
- 100mm diameter x 100mm height cylinders for compressive strength at 3 and 6 months
- 100mmx100mmx500mm prisms for measuring length change.

For testing of compressive strength at the age of 3 and 6 months cylinders 100mmx100mm were chosen, although in EN 206 the cubes 150mm are proposed. The reason for changing the shape and dimension of specimens is idea to faster sulfate deterioration. Also, testing a cylinder 100mmx100mm gives a strength value equivalent to the strength value of a 150mm cube (EN 13791). After casting and finishing, the molds for cubes and prisms were covered with plastic sheets and stored for 24h in a moist room. Cylinders stayed in closed cans for 7

days. After the initial curing period (one day or seven days), specimens were demoulded and cured in lime-saturated water at 20±2°C until 42 days (from preparing mixture) after that part of specimens were transferred to containers with a sulfate solutions. Specimens from each mixture have first letter in label "E" if they are in lime-saturated water solution, "N" if they are in 5% Na_2SO_4 solution or "M" if they are in 5% $MgSO_4$ solution stored. Testing of compressive strength was performed according to SRPS EN 12390-3 on specimens before were immersed in sulfate solutions and at 3 and 6 months holding there.

Length change of concrete specimens was determined by procedure given in UNI 11307. The samples were in horizontal position during measurement and their length was measured using digital length comparator with a precision of 0.001mm. For each mixture, three prisms were measured once per week. Expansion data are presented as differences between the length specimens at the time of measurement and the initial length.

2.3 Results and discussion

2.3.1 Compressive strength

The compressive strength computed as an average of three specimens. The results of concrete compressive strength after 3 and 6 months of immersion in magnesium sulfate, sodium sulfate and lime-saturated water, as well as 28 day strength, are shown in Table 2.

Table 2 - Compressive strength (MPa) of specimens at 28 days, 3 and 6 months

Concrete type	28 days	3 months	6 months	Concrete type	28 days	3 months	6 months
ERPC1		53.5	54.5	ERMC1		39.7	45.9
NRPC1	43.1	49.1	35.9	NRMC1	31.3	43.2	46.7
MRPC1		54.8	49.3	MRMC1		41.6	42.5
ERPC2		78.0	79.6	ERMC2		71.2	74.4
NRPC2	61.8	79.3	74.8	NRMC2	54.1	65.7	67.7
MRPC2		77.1	73.4	MRMC2		67.8	68.5

The type of cement and water to cement ratio have notable effect on concrete compressive strength, as it can be seen in Table 2. Concrete mixtures made with CEM I 42.5R have higher strength than corresponding concrete mixtures with CEM III 32.5N LH/SR (with same w/c ratio, and at the same age) regardless of the type of exposure (Na_2SO_4, $MgSO_4$, or lime-saturated water). A little deviation from this conclusion can be seen on specimens NRPC1-6 months and NRMC1-6 months. The similar conclusion can be made regarding to water to cement ratio. Concrete mixtures with lower w/c ratio have higher strength than corresponding concrete mixtures with higher w/c ratio.

Comparing the results of compressive strength of specimens that were exposed to Na_2SO_4 or $MgSO_4$ solutions during period of 3 and 6 months with corresponding 28-day compressive strength of reference samples (Table 2), it can be concluded that almost all concrete mixtures

showed an increase in compressive strength after these periods of exposure to sulfate solutions. The exception is concrete mixture with CEM I and w/c= 0.55 (NRPC1) that showed decrease in compressive strength of 17% after 6 months of exposure to Na_2SO_4 solution (Table 2).

Fig.2 illustrates the strength of the specimens subjected to sulfate solutions, relative to the corresponding compressive strength of the reference specimens of the same age. After 3 months of immersion, the concrete specimens with cement CEM I stored in Na_2SO_4 and $MgSO_4$ solutions did not show any significant difference in compressive strength compared to referent samples in lime-saturated water, except for samples NRPC1 (Fig. 2a, 2b). This concrete mixture showed decrease in compressive strength up to the 10% (Fig. 2a). After 6 months of immersion in sulfate solutions, all specimens with cement CEM I showed drop in strength compared to reference specimens (Fig. 2a, 2b). The concrete with w/c=0.55 and CEM I which was immersed in 5% Na_2SO_4 solution (NRPC1) had the greatest reduction of compressive strength (34%) (Fig. 2a).

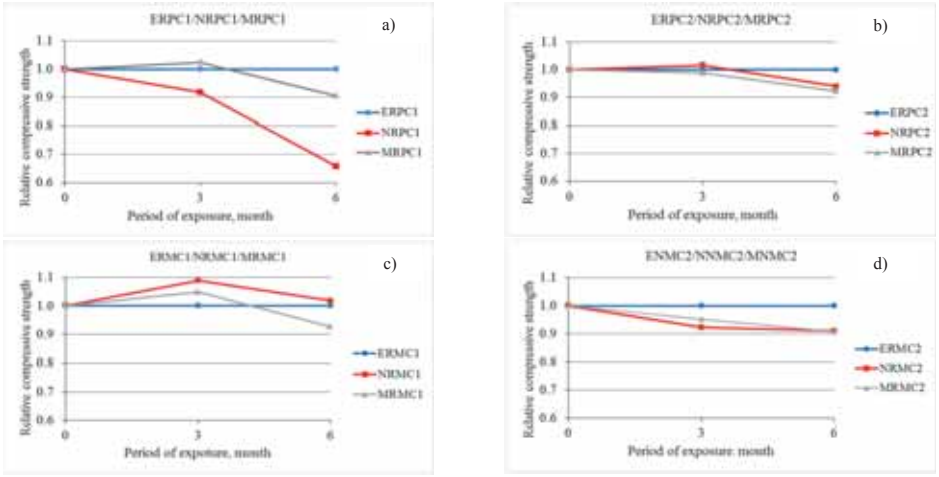

Figure 2: Changes of compressive strength of concretes exposed to sulfate solutions in relation to corresponding strength of control specimens (a - CEM I, w/c=0.55, b – CEM I, w/c=0.38, c – CEM III, w/c=0.55, d - CEM III, w/c=0.38)

The concrete specimens with cement CEM III LH/SR stored in both sulfate solutions showed difference in compressive strength at the age of 3 and 6 months compared to corresponding lime-saturated water stored samples (Fig. 2c, 2d). Obtained compressive strengths of specimens after 3 months of exposure to sulfate solutions were up to 10% higher or lower than corresponding referent value, depending on w/c ratio (Fig. 2c, 2d). After 6 months of immersion in sulfate solution specimens showed drop in strength up to the 10%, compared to corresponding referent value except for samples NRMC1 (Fig. 2c, 2d).

In order to evaluate sulfate resistance of tested concrete mixtures, the calculated values of compressive strength decrease were compared to strength loss limit given by Mehta [12], who

recommended 25% strength loss limit for sulfate resistance concrete. Based on that criteria only the concrete NRPC1, made with CEM I and with w/c=0.55 immersed six months in 5% Na_2SO_4 solution does not have satisfactory sulfate resistance.

2.3.2 Length change

The length changes of the concrete prisms subjected to 5% Na_2SO_4 and 5% $MgSO_4$ solutions, as well as the length change of control samples immersed in lime-saturated water, are shown in Fig. 3. Every one of four diagrams illustrates specimens' length change depending on the type of solutions and the time of exposure for one concrete mixture. From Fig. 3a, 3b, it can be easily noticed that the lower w/c ratio leads to reduction of the linear expansion of concrete samples with CEM I immersed in sulfate solutions. However, this effect is not seen for concrete with CEM III LH/SR (Fig. 3c, 3d).

The largest linear expansions has concrete mixture with CEM I and w/c=0.55 for both sulfate solutions (Fig. 3a) while the higher expansion is observed on specimens placed in Na_2SO_4 solution compared to those placed in $MgSO_4$ solution. By comparing the values of linear expansions of concrete specimens with CEM I and w/c=0.38 (Fig. 3b) stored in different solutions it is seen that there are no significant differences among them. The same conclusion can be derived from the results shown in Fig. 3c and 3d.

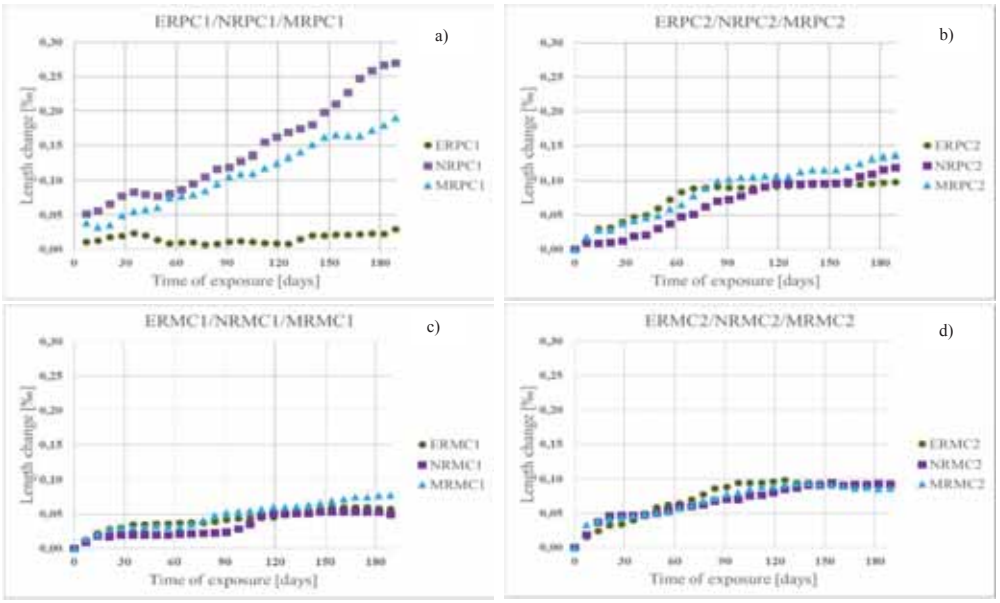

Figure 3: Length change of concretes exposed to sulfate solutions and lime saturated water (a - CEM I, w/c=0.55, b – CEM I, w/c=0.38, c – CEM III, w/c=0.55, d - CEM III, w/c=0.38)

In order to verify truthfulness of this conclusion (as a hypothesis) the statistical tests for comparing sample variances (S^2) and sample means ($\bar{x}$) of obtained length change results were applied. The length changes of specimens made of the same concrete type but immersed

in different sulfate solutions or in lime saturated water were compared mutually. Parameters for both statistical tests are presented in Table 3 and statistical test results are given in Table 4. Number of measured values for each set is n=27. Critical values F_0 (for sample variances) and t_0 (for sample means) are used for evaluation of posted hypothesis. For the testing sample variances the test statistic F_α (quantile of Snedecor's F distribution) for the chosen significance level (α=0.05) and number of freedom (ν=n-1=26) is 1.93. For the testing sample means, test statistic t_α (quantile of Student's t distribution) is 2.01 for same significance level and number of freedom of 52 ($\nu=n_1+n_2-2=52$).

Table 3: Parameters for testing sample variances and sample means

Par	ERPC2	NRPC2	MRPC2	ERMC1	NRMC1	MRMC1
$\bar{x}$	0.07786	0.06334	0.08309	0.04132	0.03277	0.04691
S^2	0.00109	0.00143	0.00155	0.00022	0.00029	0.00042
Par	ERMC2	NRMC2	MRMC2			
$\bar{x}$	0.07132	0.06650	0.06857			
S^2	0.00085	0.00059	0.00059			

Table 4: Results from statistical tests

Par.	ERPC2 NRPC2	ERPC2 MRPC2	ERMC1 NRMC1	ERMC1 MRMC1	ERMC2 NRMC2	ERMC2 MRMC2
F_0	1.309	1.420	1.304	1.902	1.438	1.438
$F_0>F_\alpha$	no	no	no	no	no	no
S	0.03484	0.03567	0.03877	0.01759	0.026	0.026
t_0	1.5310	0.5387	0.8110	1.1679	0.671	0.389
$t_0>t_\alpha$	no	no	no	no	no	no

From the test results it can be concluded that our hypothesis is accepted ($\sigma_1^2=\sigma_2^2$ and $\bar{x}_1 = \bar{x}_2$) and that observed sets analysed sets have same variances and mean values at 0.05 significance level. It means that concrete mixtures with CEM I, w/c=0.38 and with CEM III LH/SR, w/c=0.38 and w/c=0.55 immersed six months in 5% Na_2SO_4 or 5% $MgSO_4$ have the similar length changes like corresponding reference samples cured in lime saturated water. For evaluation of sulfate resistance of tested concrete mixtures, the calculated values of length changes were compared to expansion limit given by Miller and Manson [12]. They proposed a 0.2‰ of expansion as limit for sulfate resistance concrete. Based on that criteria only the concrete NRPC1, made with CEM I and with w/c=0.55 immersed six months in 5% Na_2SO_4 solution does not have satisfactory sulfate resistance.

3. Conclusion

Based on the performed experimental research and the analysis of obtained results, the following conclusions can be drown:

- The type of cement and water to cement ratio have notable effect on concrete compressive strength. Concrete mixtures with lower w/c ratio have higher strength than corresponding concrete mixtures with higher w/c ratio.
- Compressive strength of concretes after 6 months of exposure to sulfate solutions depends of cement type and w/c ratio. The concrete made with CEM I and with w/c=0.55 which was immersed in 5% Na2SO4 solution has the greatest decrease of compressive strength (34%), that exceed strength loss limit given by Mehta [12]. Other examined concretes showed changes in compressive strength up to 10% regardless of cement type, w/c ratio and sulfate solution type.
- Linear expansion of tested concretes after 6 months of exposure to sulfate solutions depends of cement type, w/c ratio and type of sulfate solution. The concrete made with CEM I and with w/c=0.55, immersed in 5% Na2SO4 solution, has the greatest linear expansion (0.27‰), that go beyond expansion limit given by Miller and Manson [12]. All other concretes have linear expansion below limit value of 0.20‰.
- Although, there is no universally accepted criterion for evaluating of concrete sulfate resistance, proposed criteria by Mehta [12] related to strength loss limit and by Miller and Manson [12] related to limit linear expansion give the similar sulfate resistance rating.
- The greatest influence on concrete sulfate resistance has cement type, i.e. chemical and mineralogical composition of cement. Water to cement ratio has negligible influence on sulfate resistance in concrete with cement CEM III LH/SR. However, in concrete with cement CEM I w/c ratio has significant influence on sulfate resistance.

Since all investigated concretes were made with recycled concrete aggregate main conclusion based on this research is that recycled aggregate concrete can be sulfate resistance.

Acknowledgements

The research work reported in this paper is a part of the investigation within the research project TR 36017 "Utilization of by-products and recycled waste materials in concrete composites in the scope of sustainable construction development in Serbia: investigation and environmental assessment of possible applications", supported by the Ministry of Education, Science and Technological Development of the Republic of Serbia. This support is gratefully acknowledged.

References

[1] Lee, S. T., Moon H.Y., Swamy, R. N., Sulfate attack and role of silica fume in resisting strength loss, Cement & Concrete Composites 27 (2005), 65-76

[2] Aimin, X., Ahmad, S., Pud, B., Test methods for sulfate resistance of concrete and mechanism of sulfate attack, Review Report 5 (1998)
[3] Chabrelie, A., Müler, U., Skrivener, K.L., Mechanism of Degradation of Concrete by External Sulfate Ions under Laboratory and Field Conditions, The 13th International Congress on the Chemistry of Cement, Madrid (3rd- 8th July 2011)
[4] Santhanam, M., Cohen, M. D., Olek, J., Mechanism of sulfate attack: A fresh look Part I:Summary of experimental results, Cement and Concrete Research 32 (2002), 915-921
[5] Sahmaran, M., Kasap, O., Duru K., Yaman, I.O., Effects of mix composition and water-cement ratio on the sulfate resistance of blended cements, Cement and Concrete Composites 29 (2007) 159-167
[6] Lee, S., Influence of recycled fine aggregates on the resistance of mortars to magnesium sulfate attack, Waste Management 29 (2009), 2385-2391
[7] Berndt, M.L, Properties of sustainable concrete containing fly ash, slag and recycled concrete aggregate, Cement and Building Materials 23 (2009), 2606-2613
[8] Parekh, D. N., Modhera, Dr. C. D., Characterization of recycled aggregate concrete, International Journal of Advanced Engineering Technology, Vol.II, Issue IV, October-December (2011), 321-330
[9] Hwang, J. P., Shim, H. B., Lim, S., Ann, K. Y., Enhancing the Durability Properties of Concrete Containing Recycled Aggregate by the Use of Pozzolanic Materials, Journal of Civil Engineering 17 (1) (2013), 155-163
[10] Abbas, A., Fathifazl, G., Fournier, B., Isgor, O. B., Zavadil, R., Razaqpur, A. G., Quantifacion of the residual mortar content in recycled concrete aggregates by image analysis, Materials Characterization 60 (2009), 716-728
[11] Radonjanin, V., Malešev, M., Marinković, S., Al Malty, A.: Green recycled aggregate concrete, Journal "Construction and Buliding Materials", Volume 47, (2013), pp. 1503–1511
[12] Ghafoori, N., Diawara, H., Beasley, S., Resistance to external sodium sulfate attack for early-opening-to-traffic Portland cement concrete, Cement & Concrete Composites 30 (2008) 444-454
[13] Tangchirapat,W., Khamklai, S., Jaturapitakkul, C., Use of ground palm oil fuel ash to improve strength, sulfate resistance, and water permeability of concrete containing high amount of recycled concrete aggregates, Materials and Design 41 (2012), 150-157
[14] Bulatović, V., Malešev, M., Radonjanin, V., Radeka, M., Lukić, I., Effect of concrete type and water to cement ratio on the sulfate resistance of concrete with RCA, Proceeding from The sixth international conference Civil engineering - science & practice, Montenegro (2016), 689-698
[15] SRPS EN 196, Methods of testing cement, Institute for standardization of Serbia, Serbia
[16] SRPS EN 197-1, Cement - Part 1: Composition, specifications and conformity criteria for common cements, Institute for standardization of Serbia, Serbia (2013)
[17] SRPS EN 12390-3, Testing hardened concrete- Part 3: Compressive strength of test specimens, Institute for standardization of Serbia, Serbia (2010)
[18] Italian Standard UNI 11307, Testing for Hardened Concrete – Shrinkage Determination (2008)
[19] SRPS EN 206-1, Concrete: Specification, performance, production & conformity, Institute for standardization of Serbia, Serbia (2011)

International RILEM Conference on Materials, Systems and Structures in Civil Engineering
Conference segment on Service Life of Cement-Based Materials and Structures
22-24 August 2016, Technical University of Denmark, Lyngby, Denmark

SENSITIVITY ANALYSIS FOR PREDICTION OF CORROSION INITIATION BY CARBONATION

Van-Loc TA [(1)], Stéphanie BONNET [(2)], Tristan SENGA KIESSE [(3)], Anne VENTURA [(1)]

(1) LUNAM Université, Université de Nantes, GeM, Institut de Recherche en Génie civil et Mécanique – CNRS UMR 6183 – Chaire Génie Civil Eco-construction, France
(2) LUNAM Université, Université de Nantes, GeM, Institut de Recherche en Génie civil et Mécanique – CNRS UMR 6183, France
(3) INRA, UMR 1069 Sol Agro et hydrosystème Spatialisation, Rennes, France

Abstract
Corrosion of reinforcement in concrete is the main cause for deterioration of reinforced concrete (RC) structures. In this paper, sensitivity analysis (SA) are carried out to determine the influence of input parameters involved in corrosion initiation model on the corrosion initiation time, t_{cor}^{i}. This method is applied to a RC structure with class C30/37 concrete using CEM I 32.5N exposed in class XC4. The concrete cover depth, initial curing period linked to technological parameters; cement content linked to concrete mixtures; ambient temperature linked to environmental exposure conditions. They are found to be most influential on the time t_{cor}^{i}; whereas, the physical and chemical characteristics of cement type CEM I 32.5N, sable, gravel contents and the maximum aggregate size used are found to be less influential on the time t_{cor}^{i}. In order to improve the durability of RC structures using CEM I 32.5N with regards to carbonation, the best choices are required for the concrete cover depth, the initial curing period, cement content and water to cement ratio.

1. Introduction

A reliable prediction of the corrosion initiation time (t_{cor}^{i}) of reinforced concrete (RC) structures exposed to CO_2 is critical for selecting the durable and cost-efficient design and for optimizing the inspection and maintenance of built structures. In that context, semi-empirical models are user-friendly format to civil engineers to predict the time t_{cor}^{i} of RC structures due to carbonation. The time t_{cor}^{i} can be defined as the time when the carbonated cement concrete front reaches the reinforced layer. Corrosion is likely to occur because steel bars are not passive anymore. It is clear that significant uncertainties can be associated with the time t_{cor}^{i}.
The aim of this paper is to answer the following questions: (i) which parameters have the greatest impact on t_{cor}^{i}; (ii) which parameters require more focus at the design stage to

increase the time t_{cor}^{i}; (iii) how to use these results for engineering purposes, to achieve effective design, inspection, and maintenance of RC structures.

Section 1 presents the theoretical corrosion initiation model, studied case and statistical governing parameters of the model. The parameters studied can be categorized as follows: (i) technological parameters: the concrete cover depth (d), the maximum aggregate size (S_max) and the initial curing period (t_c); (ii) concrete compositions: cement (C), water (W), sable (S) and gravel (G) content of concrete; (iii) physical and chemical composition of cement: the cement density (ρ_c), the clinker content of cement ($\varphi_{clinker}$), the amount of silicon oxide (SiO_2), aluminum oxide (Al_2O_3), iron oxide (Fe_2O_3), calcium oxide (CaO), and sulfur oxide (SO_3) per weight cement; (iv) environmental parameters: ambient temperature (T), relative external humidity (RH), and CO_2 concentration in the air (CO_2). Theoretical sensitivity analysis (SA) methods are presented in Section 3. Section 4 presents SA results of the time t_{cor}^{i} for RC structures exposed in class XC4, which use a class C30/37 concrete with CEM I 32.5N, to the governing parameters. The probabilistic corrosion initiation model, and the recommendations of the technological parameters are carried out in Section 5. The recommendations allow improving the durability of RC structures with regards to carbonation. Section 6 is the discussion on the obtained results.

2. Diffusion-based corrosion initiation model

Because carbonation is governed by the CO_2 diffusion within concrete, the square root of time formula is commonly used for carbonation depth modelling [1]:

$$x = A\sqrt{t} \tag{1}$$

where: x (m) is the carbonation depth, t (s) is the exposure time, A (m/s$^{1/2}$) is the carbonation coefficient.

Many factors influencing the coefficient A are found in the literature. Therefore, a new meta-model calculating the coefficient A built upon several already available specific models is presented. It is specifically developed to suit any situation by improving some of the former models. We write:

$$\begin{aligned} A = {} & f_1(S\_max, t_c) \times f_2(C, W, S, G) \\ & \times f_3\,(\rho_c, \varphi_{clinker}, SiO_2, Al_2O_3, Fe_2O_3, CaO, SO_3) \times f_4(T, RH, CO_2) \end{aligned} \tag{2}$$

where: f_1, f_2, f_3 and f_4 are the functions including the technological parameters; concrete mixtures; physical and chemical characteristics of cement type CEM I 32.5N; and environmental exposure conditions, respectively. All symbol parameters are detailed in the introduction's part.

The model is not fully detailed herein; it has been detailed in a separate article presently under submission. Since depassivation due to carbonation starts when the carbonation depth x equals the depth d [1], from Eq. (1) t becomes the time t_{cor}^{i} expressed as:

$$t_{cor}^{i} = \frac{d^2}{A^2} \tag{3}$$

It is widely known that the use of Portland cement is recommended for exposure condition referring to carbonation-induced corrosion [1]. Recent European standards NF EN 206-1 (2014) [2] provide recommendations for prescribing limiting values. Minimum strength class C30/37 concrete for RC structures is, for instance, required for the exposure class XC4 that RH can be ranged from 0.4 to 1 [1]. In this study, we follow these recommendations. Thus, statistical parameters (mean, coefficient of variation (COV), distribution law) for class C30/37 concrete are described in Tab. 1 [3]. The depth d is a design parameter varying with the severity of the environmental exposure conditions [4]. It also depends on the quality of workmanship and control during construction, its value can vary from 0.025 up to 0.08 m [5]. The environmental parameters are uncertain or random in nature, they are selected from the literature [6].

Table 1: Statistical description of random variables for class C30/37 using CEM I 32.5N (n.u. = no unit) for the exposition XC4

Symbol	Unit	Mean	Min-Max	COV	Distribution	Ref.
d	m		0.025-0.08		Uniform	[5]
S_max	mm		12-20		Uniform	[2]
t_c	days		1-3		Uniform	[7]
C	kg/m^3	370	325.6-414.4	0.03	Lognormal	[3]
W	kg/m^3	181	166.52-195.48	0.02	Lognormal	[3]
S	kg/m^3	644	566.72-721.28	0.03	Lognormal	[3]
G	kg/m^3	1187	1044.56-1329.44	0.03	Lognormal	[3]
ρ_c	kg/m^3	3100	2976-3224	0.01	Normal	[3]
$\varphi_{clinker}$	n.u.		0.95-1		Uniform	[8]
SiO_2	n.u.		0.1904-0.2292		Uniform	[9]
Al_2O_3	n.u.		0.035-0.0583		Uniform	[9]
Fe_2O_3	n.u.		0.0135-0.0658		Uniform	[9]
CaO	n.u.		0.6041-0.6591		Uniform	[9]
SO_3	n.u.		0.0234-0.0377		Uniform	[9]
T	K	283	274.06-291.94	5	Normal	[6]
RH	n.u.	0.65	0.52-0.78	0.05	Normal	[6]
CO_2	ppm	380	304.56-456.84	0.05	Normal	[6]

3. Sensitivity analysis methods

We use a model f, which links the time t_{cor}^{i} and the input parameters, in the form:

$$t_{cor}^{i} = f(d, S\_max, t_c, C, W, S, G, \rho_c, \varphi_{clinker}, SiO_2, Al_2O_3, Fe_2O_3, CaO, SO_3, T, RH, CO_2)$$
or
$$t_{cor}^{i} = f(X_1, X_2, X_3, X_4, X_5, X_6, X_7, X_8, X_9, X_{10}, X_{11}, X_{12}, X_{13}, X_{14}, X_{15}, X_{16}, X_{17}) \quad (4)$$

SA study combines Morris' local qualitative method [10] with Sobol's global quantitative method [11]. These two distinct SA methods are successively used. This is for two main reasons: (i) the Sobol's method provides the quantification of influences but it is time-consuming, whereas the Morris' method quickly allows identifying non-influential parameters; (ii) the Morris' method provides additional information compared to Sobol's one with regards to parameters' trends. Both methods thus provide complementary information to the decision-making process. They require that all input parameters are independent.

3.1 Morris qualitative sensitivity analysis

The Morris' method [10] aims at ranking influential parameters. It determines the sense of parameter variations. This method needs a local interval range (minimum and maximum values) of each input parameter as given in Tab. 1. It is a "one at a time" method which consists in varying one parameter and keep constant the others, over a certain number of repetitions r. The variation coefficient which is calculated for each input parameter X_i at each repetition k is called the elementary effect. We have:

$$EE_i^{(k)} \approx \frac{f(X_i + \Delta X_i) - f(X_i)}{\Delta X_i}, k = 1, 2, \dots, r \quad (5)$$

with ΔX_i is a fixed step.

The average μ_i and the standard deviation σ_i of all elementary effects $EE_i^{(k)}$ are calculated. They are considered as the sensitivity analysis criteria for each input parameter [10]. The mean of absolute value of the effect (μ_i^*) is also proposed as the third criterion to prevent the case where the average μ_i is closed to zero, due to $EE_i^{(k)}$ values having opposite signs in case of non-monotonic functions [12]. These three criteria provide the following sensitivity information: (i) the algebraic sign of μ_i indicates the increasing (i.e. $\mu_i > 0$) or decreasing ($\mu_i < 0$) trend of the indicator relative to the considered parameter; (ii) the higher both μ^*_i and σ_i, the more influential the interaction between X_i and the other parameters and/or the more nonlinear X_i effects [10]. This information can be complemented by the ratio σ/μ^*: (i) almost linear $\sigma/\mu^* \leq 1$; (ii) monotonic ($1 < \sigma/\mu^* \leq 0.5$); (iii) almost monotonic ($0.5 < \sigma/\mu^* \leq 1$); (iv) marked non-monotonic non-linearities or interactions with other parameters ($\sigma/\mu^* > 1$) [13].

3.2 Sobol quantitative sensitivity analysis

The Sobol method [11] evaluate the contribution of the variation of each input parameter to the total variation of model output. This method requires characterizing the probability density function (PDF) for each input parameter (Tab. 1) in order to run Monte Carlo

simulations. It consists in varying simultaneously all input parameters X_i according to their PDF and calculating the associated model outputs $Y = t_{cor}^{i}$. This method provides quantitative indices of the influence given by:

$$S_i = \frac{Var(\mathbb{E}[Y \mid X_i])}{Var(Y)} \tag{6}$$

where: S_i is the first order sensitivity index, $\mathrm{Var}(\mathbb{E}[\mathrm{Y} \mid \mathrm{X_i}])$ is the conditional variance of the output parameter Y produced due to the variation of the input parameter X_i, $Var(Y)$ is the total variance of the output parameter. The S_i of parameter X_i represent its individual effect. It quantifies the contribution to the output variance of the main effect of X_i. Similarly, indices of higher order $S_{i,j\neq i}$ can be calculated for evaluating the contribution of the interaction of X_i with the other parameters $X_{j\neq i}$. The total sensitivity index (S_{T_i}) is introduced by Homma and Saltelli [14]. It represents the sum of the individual influences in the S_i of parameters-added to all of its interactions with other parameters $X_{j\neq i}$ such as:

$$S_{T_i} = 1 - \frac{Var(\mathbb{E}[Y \mid X_{\neq i}])}{Var(Y)} \tag{7}$$

where $\mathrm{Var}(\mathbb{E}[\mathrm{Y} \mid \mathrm{X}_{\neq \mathrm{i}}])$ is the conditional variance of the output parameter Y produced due to the variation of all parameters except X_i. Sobol's indices can study quantitative or qualitative parameters [15]. The S_i and S_{T_i} indices can be interpreted as follow [16]: (i) if S_i is close to 0, the parameter are none influential on the model output; (ii) if the difference between S_{T_i} and S_i is high (in practice $S_{T_i} - S_i > 30\%$), the parameter has a considerable interaction influence. Then the second or more order indices should be calculated to quantify these interactions, until $S_{T_i} - \left(S_i + S_{i,j\neq i}\right)$ is close to zero.

4. Results of sensitivity analysis

SA results from Sobol's method with respect to S_i and S_{T_i} are shown in Fig. 1. It can be observed that d, C, t_c, T are the most influential variables on the corrosion initiation time t_{cor}^{i} of RC structures exposed in class XC4. Parameters d and t_c are categorised as controlable technological parameters, whereas, parameter C is categorised as non controlable material parameters linked to concrete mixtures in this study, and parameter T is categorised like non controlable linked to the environmental exposure conditions. Fig. 1 shows that almost all influential parameters have the ratio σ/μ^* within the interval [0.17 – 0.30]. It indicates that the effects between parameters are monotonic. With a maximum of value of the term $S_{T_i} - S_i$ below 10%, none of the parameters under study is found to have important interactions. We found a decreasing trend of the effects ($\mu < 0$) for the following parameters W, T, ρ_c, CO_2, Fe_2O_3, SO_3, S and G, meaning that if their values increase, the durability of RC structures with regards to carbonation will decrease. The other parameters are found to have an increasing trend.

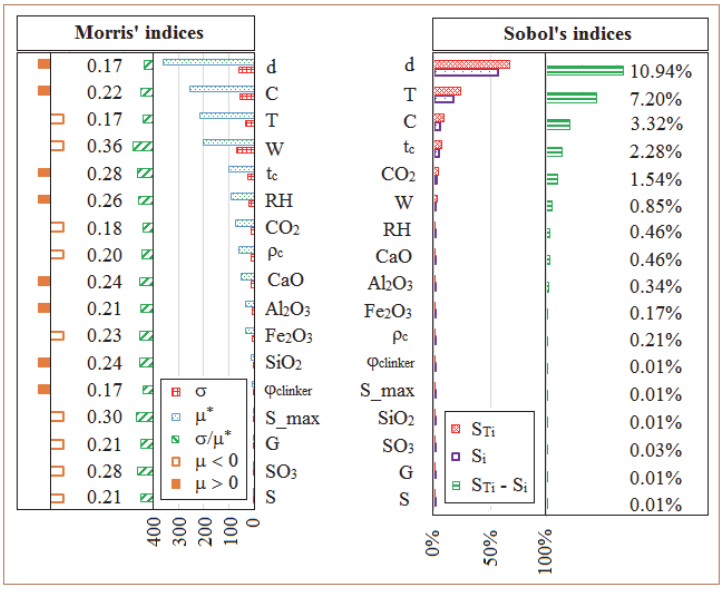

Figure 1: Importance of relative variables on the corrosion initiation time

5. Probabilistic simulation

Due to uncertainties of concrete mixtures, physical and chemical characteristics of cement type CEM I 32.5N and environmental conditions, it is not possible to predict accurately the corrosion initiation time t_{cor}^{i} of RC structures regarding carbonation. Therefore, it is thus useful to conduct a probabilistic analysis by treating input parameters like random variables or processes. A probabilistic analysis propagates the uncertainty and variability of these parameters and quantifies the variability of the final result. Monte Carlo simulations are used to determine the main descriptors (mean and coefficient of variation (COV)) for t_{cor}^{i}.

After identifying all key technological parameters as shown in Fig. 1, the time t_{cor}^{i} is predicted for four scenarios (Tab. 2) using Monte Carlo simulations with 100 000 generated values for each variable. They are predicted by setting the concrete cover depth, the maximum aggregate size and the initial curing period as given in Tab. 2. Other parameters set at their distribution law given in Tab. 1. A plot of the distributions of the time t_{cor}^{i} are shown in Fig. 2 for DS and FTS scenarios. The objective of the comparison between DS and FTS scenarios is to find out the improving durability of RC structures exposed to CO_2 associating with the favourable technological parameters. The results will be useful as a guide for the design of durable RC structures. Lognormal distributions for t_{cor}^{i} were obtained with a mean value around 99 and 305 years with both a COV = 0.41 for DS and FTS scenarios, respectively. The average corrosion initiation time t_{cor}^{i} is thus improved 3.1 times by comparing favourable to default scenarios with regards to technological parameters. However, uncertainties are

partially overlapping showing that concrete compositions and environmental conditions are influent and may thus reduce this improvement if they happen to be unfavourable.

We compared our results with existing recommendations. The minimum concrete cover depths for design working life of 50 and 100 years proposed by LNEC E464 [17] are 0.04 and 0.05 m, respectively (Tab. 2). Then, the service life of RC structures with regards to carbonation-induced corrosion of steel reinforcement can be predicted associating with these recommendations. The typical deterioration models distinguish two periods: initiation period and propagation period [18]. The service life can be calculated according to [5] as:

$$t_L = \frac{t_{cor}^{i}}{\gamma} + t_{cor}^{p} \tag{8}$$

where: t_L (years) is the service life, γ (n.u.) is the safety factor (γ = 2.3), t_{cor}^{p} (years) is the propagation period, its value ranges from 5 up to 15 years for the design working life 50-year and from 10 up to 20 years for the design working life 100-year. The average service life predictions range from 38 up to 48 years and from 52 up to 72 years for the 50 years and 100 years designed working life, respective. The recommendations are thus not enough to ensure the workability of RC structures exposed in class XC4.

Table 2: Design service life of RC structures exposed in class XC4 using class C30/37 concrete with CEM I 32.5N

Scenarios	d **(m)**	S_max **(mm)**	t_c **(days)**	t_L **(years) (min-max)**	
DF (with mean values)	0.05	16	2	48	63
FTS (with favourable values)	0.08	20	3	138	153
Design working life 50 years	0.04	20	3	38	48
Design working life 100 years	0.05	20	3	52	72

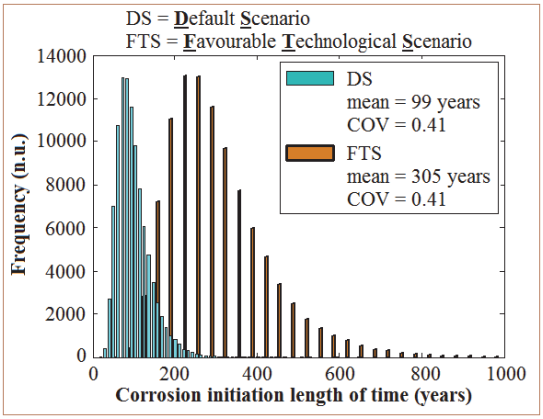

Figure 2. Impacts of the DS versus the FTS for corrosion initiation time

6. Discussion

SA results, as shown in Fig. 1, strongly agree with the literature.

For technological parameters: the concrete cover depth d is the greatest single factor that can influence the premature corrosion of reinforcement. The performance of the structure can be highly sensitive to defects in cover. However, higher d (e.g., d > 0.08 m) may favor cracking that will eventually lead to poor protection of steel bars. A short t_c will hinder hydration of cement and lead to high porosity, especially in the concrete cover, it will lead to increase the ingress of CO_2 gas through concrete [1]. Higher S_max provoke a decrease of the time t_{cor}^{i} [19], for several reasons: first, bigger aggregate results in larger inter-facial transition zone (ITZ) and second, internal bleeding water can take place. Thus, the standard limits the S_max to be used at 20 mm.

For concrete mixtures: the cement content C has been identified as major contributor to the time t_{cor}^{i}. By increasing C and decreasing W the durability of RC structures is improved [20]. However, the risk of cracking due to heat of hydration or drying shrinkage can be enhanced by increasing C significantly. Both S and G seem to have negligible effects on the time t_{cor}^{i} compared to C and W. They are found to have decreasing trends on the time t_{cor}^{i} [21].

For physical and chemical characteristics of cement type CEM I 32.5N: the more the amount of CaO, the less the rate carbonation because of chemical reaction between CO_2 and $Ca(OH)_2$ takes time [22]. Furthermore, cement chemical composition is a major contributor to concrete porosity during chemical reaction of hydration [23]. The effect of ρ_c had the same trend like $\varphi_{clinker}$, meaning RC structures is more durable with the increase of ρ_c and $\varphi_{clinker}$. However, according to our sensitivity analysis results, they are not found very influent compared to the other parameters. However, the simulation was only performed with CEM I 32.5N and the result may be different with other types of cements.

For environmental exposure conditions: ambient temperature (T) is found very influent. It increases on the rate at which CO_2 reacts with $Ca(OH)_2$ to form $CaCO_3$ (calcite), i. e. the CO_2 diffusion process increases as a result of an increase of T [24]. SA results indicate that the relative external humidity (RH) increases from 52% to 78%, the time t_{cor}^{i} increases too. This is consistent with the literature [25]. We assume that the relative internal humidity inside concrete is equivalent to the relative external humidity for natural carbonation. The CO_2 transport gas through concrete is slow due to waterlogging of pores, as a results of an increases in RH. Its influence is not found important on the time t_{cor}^{i} compared to the other parameters in the case study, because the varying interval of RH is as a plateau [26]. As aforementioned, the CO_2 diffusion through concrete is affected by both technological parameters, concrete mixtures and environmental exposure conditions. The influence of CO_2 is not found important to predict the time t_{cor}^{i} compared to the other parameters (d, t_c, T and C).

Recommendations: The predictions of service life of RC structures exposed in class XC4, which use the class C30/37 concrete with CEM I 32.5N, indicated that the minimum concrete cover depth requirements according to [17] are not enough to reach the intended working life

both 50 and 100 years. The recommendations may not be exhaustive of all the aspects related to design for the durability of RC structures (e.g. environmental conditions and quality to the execution process like the initial curing period).

7. Conclusion

Two different methods, Morris qualitative and Sobol quantitative SA, are used to determine the sensitivity of corrosion initiation time (t_{cor}^{i}) of class C30/37 concrete RC structures, which supposed to be exposed in class XC4, to the following parameters of model: (i) technological parameters; (ii) concrete mixtures; (iii) physical and chemical characteristics of cement type CEM I 32.5N; (iv) environmental exposure conditions. The results show that the time t_{cor}^{i} is highly sensitive to: (i) technological parameters: the concrete cover depth (d) and the initial curing period (t_c); (ii) material's composition parameters: cement content (C); (iii) environmental exposure conditions: the ambient temperature (T). These parameters should therefore be carefully considered in future research related to prediction of corrosion initiation time. They will also be incorporated into the numerical model.

The initiation corrosion time of class C30/37 concrete RC structures with regards to carbonation can be improved by setting technological parameters at favourable values, but uncertainties of concrete mixtures and environmental conditions are influent and may reduce this improvement. Reducing uncertainties about concrete composition could lead to a significate difference. The minimum depth d recommendations [17] for RC structures exposed in class XC4, which use class C30/37 concrete with CEM I 32.5N, are found out not enough to reach the intended working life both for 50-year and for 100-year designs. Actual recommendations thus have to be changed both for technological parameters and for concrete mixtures. A better prediction of the time t_{cor}^{i} in natural conditions with respect to carbonation provides effective decision support for the maintenance of RC structures, according to initiation design choices.

References

[1] fib CEB-FIP, Ed., *Model code for service life design*. Lausanne: fib, 2006.
[2] NF EN 206, "Béton: Spécification, performances, production et conformité." 2014.
[3] M. G. Stewart, B. Teply, and H. Kralova, "The effect of temporal and spatial variability of ambient carbon dioxide concentrations on carbonation of RC structures," in *9th International Conference on Durability of Building Materials and Components, CSIRO*, 2002.
[4] NF EN 1992-1-1/NA, "Eurocode 2: Calcul des structures en béton - Partie 1-1: Règles générales et règles pour les bâtiments," 2007.
[5] P. F. Marques and A. Costa, "Service life of RC structures: Carbonation induced corrosion. Prescriptive vs. performance-based methodologies," *Constr. Build. Mater.*, no. 24, pp. 258–265, 2010.
[6] IPCC, "Climate change 2013: The physical science basis. Contribution of working group I to the fifth assessment report of the intergovernmental panel on climate change," 2013.

[7] LNEC E465, "Concrete. Methodology for estimating the concrete performence properties allowing to comply with the design working life of the reinforced or pre-stressed concrete structures under environmental exposures XC and XS." Lisbon: LNEC, 2007.
[8] I. Galan, C. Andrade, P. Mora, and M. A. Sanjuan, "Sequestration of CO2 by concrete carbonation," *Environ. Sci. Technol.*, vol. 44, no. 8, pp. 3181–3186, 2010.
[9] VDZ Activity Report, "Performance of cement." 2005-2003.
[10] M. D. Morris, "Factorial Sampling Plans for Preliminary Computational Experiments," *Technometrics*, vol. 33, no. 2, p. 161, May 1991.
[11] I. M. Sobol, "Global sensitivity indices for nonlinear mathematical models and their Monte Carlo estimates," *Math. Comput. Simul.*, vol. 55, no. 1, pp. 271–280, 2001.
[12] F. Campolongo, J. Cariboni, and A. Saltelli, "An effective screening design for sensitivity analysis of large models," *Environ. Model. Softw.*, vol. 22, no. 10, pp. 1509–1518, Oct. 2007.
[13] D. Garcia Sanchez, B. Lacarrière, M. Musy, and B. Bourges, "Application of sensitivity analysis in building energy simulations: Combining first- and second-order elementary effects methods," *Energy Build.*, vol. 68, pp. 741–750, Jan. 2014.
[14] T. Homma and A. Saltelli, "Importance measures in global sensitivity analysis of nonlinear models," *Reliab. Eng. Syst. Saf.*, vol. 52, pp. 1–17, 1996.
[15] A. Saltelli, "Making best use of model evaluations to compute sensitivity indices," *Comput. Phys. Commun.*, vol. 145, pp. 280–297, 2002.
[16] I. Dimov, R. Georgieva, and T. Ostromsky, "Monte Carlo sensitivity analysis of an Eulerian large-scale air pollution model," *Reliab. Eng. Syst. Saf.*, vol. 107, pp. 23–28, Nov. 2012.
[17] LNEC E 464, "Concrete. Prescriptive methodology for a design working life of 50 and 100 years." 2007.
[18] K. Tuutti, "Corrosion of steel in concrete," *Swed. Cem. Concr. Res. Inst. Stockh.*, 1982.
[19] L. Basheer, P. A. M. Basheer, and A. E. Long, "Influence of coarse aggregate on the permeation, durability and the microstructure characteristics of ordinary Portland cement concrete," *Constr. Build. Mater.*, vol. 19, no. 9, pp. 682–690, Nov. 2005.
[20] Y. F. Houst and F. H. Wittmann, "Influence of porosity and water content on the diffusivity of CO2 and O2 through hydrated cement paste," *Cem. Concr. Res.*, vol. 24, no. 6, pp. 1165–1176, 1994.
[21] P. A. M. Basheer, F. R. Montgomery, A. E. Long, and others, "Factorial experimental design for concrete durability research," *Proc. ICE-Struct. Build.*, vol. 104, no. 4, pp. 449–462, 1994.
[22] V. G. Papadakis, "A reaction engineering approach to the problem of concrete carbonation," *AIChE J.*, vol. 35, no. 10, pp. 1639–1650, 1989.
[23] V. G. Papadakis, "Experimental investigation and theoretical modeling of silica fume activity in concrete," *Cem. Concr. Res.*, vol. 29, no. 1, pp. 79–86, 1999.
[24] M. A. Sanjuan and R. Muñoz-Martialay, "Influence of the water/cement ratio on the air permeability of concrete," *J. Mater. Sci.*, vol. 31, no. 11, pp. 2829–2832, 1996.
[25] S. K. Roy, K. B. Poh, and D. O. Northwood, "Durability of concrete-accelerated carbonation and weathering studies," *Build. Environ.*, vol. 34, pp. 597–606, 1999.
[26] B. G. Salvoldi, H. Beushausen, and M. G. Alexander, "Oxygen permeability of concrete and its relation to carbonation," *Constr. Build. Mater.*, vol. 85, pp. 30–37, Jun. 2015.

International RILEM Conference on Materials, Systems and Structures in Civil Engineering
Conference segment on Service Life of Cement-Based Materials and Structures
22-24 August 2016, Technical University of Denmark, Lyngby, Denmark

CHLORIDE DIFFUSION AND BINDING IN HARDENED CEMENT PASTE FROM MICROSCALE ANALYSES

Pietro Carrara [(1)], Laura De Lorenzis [(1)]

(1) Technische Universität Braunschweig - Institute of Applied Mechanics, Braunschweig, Germany

Abstract
Chloride ions in concrete constitute a primary issue for the durability of concrete structures because they can trigger the corrosion of the steel rebars. Chloride diffusion is strongly influenced by the heterogeneous nature of the hardened cement paste (HCP) microstructure, i.e. at a μm length scale. HCP can be composed of more than 30 phases and only some of them, typically AFm and CSH gel, can interact with chlorides influencing their diffusion (so-called binding effect). To date, the direct observation of the HCP 3D microstructure and phases arrangement is still a challenge. To overcome this problem, simulation codes such as CEMHYD3D were developed to simulate the HCP hydration and microstructure development making possible to distinguish between all the possible phases present. The chloride diffusion into HCP is here studied through a novel diffusion model. The Fick's theory is modified to account for the binding effect phase-wise. A homogenization technique is adopted to upscale the diffusivity at the mesoscale, namely where the HCP can be assumed homogeneous. Both real and simulated HCP microstructures are used and their properties compared and related to the chloride diffusive behavior. Also, comparisons between experimental and numerical results from the proposed model are presented.

1. Introduction

The penetration of chloride ions into the concrete cover can induce the corrosion of the steel reinforcement causing a variety of problems, e.g. steel rebars cross-sectional reduction and diffuse cracking of the cement matrix. Thus, the ability to predict the rate of penetration of chloride solutions (e.g., sea water or aqueous solution containing deicing salts) is of primary concern to schedule an efficient maintenance. While the effects of the chlorides presence show up at the meso- and macro-scale, their diffusion is strongly influenced by the microstructural arrangement of the hardened cement paste (HCP), i.e. at the μm length scale.

Different studies highlighted that, beside the extension and topology of the micropore network (constituting a preferential pathways for chlorides), the interaction between some hydration products and chloride ions can influence the diffusion rate [1-3], leading to the so-called binding effect [3,4]. On the other hand, the diffusivity of the HCP is usually assessed by means of specific tests [5-7] which cannot give direct information about the role of the microstructural arrangement because they are performed at a scale (i.e., *cm* scale) much larger than the microscale. This calls for numerical methods based on the multiscale decomposition of the problem [8,9], that thus can bridge the gap between that two scales.

To the purpose, a detailed description of the HCP phases at the microscale is needed. This can be achieved either through simulated microstructures whose characteristics are statistically similar to the real ones (e.g., using codes such as CEMHYD3D [10,11] or HYMOSTRUCT3D [12]), or pushing to the limit the resolution of imaging techniques such as computer tomography (CT). Although recently the latter method has been strongly improved, it still presents some limitations, mainly related to the CT scanners resolution available that, to date, is not sufficient to distinguish between each single phase in HCP [13,14].

Recently different authors studied the chloride diffusivity in concrete at different scales using numerical simulations. Zhang et al. [8] coupled lattice-Boltzmann and finite element methods to study the micro- and meso-scale diffusivity in simulated concrete samples. However, the local interaction among diffusive species and the HCP microstructure was accounted for only empirically. Differently, Bentz and Garboczi [15] studied the diffusion of chlorides during the hydration of the cement clinker at the micro-scale adopting an approach based on a random walk algorithm. This allowed to explicitly account for the binding effect.

In the present work, the chloride diffusion process into HCP is studied through a numerical model obtained modifying the Fick's equation of diffusion in order to account for the interaction between chloride ions and HCP phases at the microscale. The homogenized diffusivity of the HCP obtained through numerical simulation is compared with experimental results from the literature and the diffusivity of both simulated and real (i.e., from CT scan images) 3D HCP microstructures is studied along with their binding behavior.

2. Coupled diffusion and binding in HCP

In the following the numerical model adopted is briefly summarized. For more details and a more extended validation, please refer to [16].

2.1 Governing equations

The diffusion process in saturated porous media can be described by [2,8]

$$\frac{\partial C_{tot}}{\partial t} = -div(J) \tag{1}$$

where C_{tot} is the total concentration of the diffusive species in solution, t is the time and J is the diffusive species flux vector. Eq. (1) is usually referred to as the second Fick's law and is

directly inferred from the mass conservation condition. When dealing with chloride diffusion in HCP, not all the ions in solution are free to diffuse because part of them can interact chemically or physically with the hydration products, remaining bounded to them [1,2,4,5,8,16]. Hence, they do no longer influence the diffusion process. For this reason it is important here to distinguish between free and bound chloride ions, respectively C_f and C_b, which are related to the total chloride concentration by

$$C_{tot} = C_f + C_b \tag{2}$$

Since the driving force of the flux J is only related to the gradient of the free chloride ions concentration, the flux constitutive law (usually referred to as first Fick's law [1, 2, 8]) assumes the following form

$$J = -D_0 grad(C_f) \tag{3}$$

where D_0 is the free diffusivity coefficient of the diffusive species in saturated pores that depends on the temperature and on the topology of the pores. D_0 can range between different orders of magnitude depending on the extension and topology of the pore and micropore network [6, 16]. In HCP, for example, diffusivity in pores is much higher than in C-S-H gel [15], because this latter has very small micropores, condition that delays diffusion [16].
Using Eq. (2), C_f can be written as a function of C_{tot} and C_b, and then

$$grad(C_f) = grad(C_{tot} - C_b) = \left(1 - \frac{\partial C_b}{\partial C_{tot}}\right) grad(C_{tot}) \tag{4}$$

where

$$\mu_B = 1 - \frac{\partial C_b}{\partial C_{tot}} \tag{5}$$

is called binding activity coefficient and expresses the tendency of a species of being bounded by the material through which it diffuses. Substituting Eq. (4) in Eq. (3), and the result in Eq. (1) leads to

$$\frac{\partial C_{tot}}{\partial t} = div\left(\left(1 - \frac{\partial C_b}{\partial C_{tot}}\right) D_0 grad(C_{tot})\right) \tag{6}$$

where $D_{eff}=\mu_B D_0$ is the effective diffusivity coefficient, which is now also dependent on the concentration of the diffusive species. Hence, it is necessary to know the amount of chloride ions bounded by each phase present in the HCP to completely define the effective diffusion coefficient D_{eff}.

2.2 Binding isotherms

In the present work, the binding activity coefficients are obtained from the binding isotherms, as illustrated in the following. A binding isotherm is a relationship between the concentration of bound and free chlorides at a constant temperature for a given HCP phase [3]. Here, the isotherms proposed by Hirao et al. [4] are adopted. These relationships were directly calibrated by means of tests on pure AFm and C-S-H samples and then validated using a Portland cement similar to the one studied here. Different studies confirm that, among all the phases present in Portland HCP, C-S-H gel and AFm together are responsible for the almost entire chloride uptake [3,4]. For this reason, herein only the binding due to AFm and C-S-H is accounted for. For the AFm phase the following relationship is proposed [4]

$$C_b^{AFm} = K_{AFm} C_f^{\,0.58} \tag{7}$$

where K_{AFm} is equal to 12.30 when $\mu g/mm^3$ are used. Conversely, for the C-S-H gel Hirao et al. [4] suggested to adopt the following formula

$$C_b^{CSH} = K_{CSH} \frac{a_{CSH} C_f}{1 + a_{CSH} C_f} \tag{8}$$

where K_{CSH} and a_{CSH} are equal to 46.30 and $7.47 \cdot 10^{-2}$ when $\mu g/mm^3$ are used.

3. Numerical procedure

The chloride diffusion process at the microscale (HCP level) is simulated by applying the central finite difference method to Eq. (6) with the further steady state condition $\partial C_{tot}/\partial t=0$. Such assumption is justified considering that corrosion process is a slow process compared to diffusion. Furthermore, accounting for transient diffusion requires the binding reaction kinetics to be known, but there are no data available in the literature, to date. The voxelized 3D microstructures of the HCP (Figure 1) are obtained following two different approaches: X-ray CT of a real HCP (obtained from the Visible Cement Dataset – VCD – of NIST [13,14], Figure 1a) and the artificial generation of the 3D microstructure by means of the CEMHYD3D [10,11] code (Figure 1b-c). The former method is able to distinguish only between hydration, unhydrated and pores phases [13,14] (Figure 1a). Conversely, the CEMHYD3D [10,11] package reproduces, starting from a distribution of clinker particles geometrically approximated using spheres, the microstructural arrangement of a 3D HCP volume and is able to distinguish between more than 30 different hydrated and unhydrated chemical species (Figure 1b-c). Both approaches have the same resolution of 1 $\mu m^3/voxel$ and the volume analyzed here is a cube with dimensions of 100x100x100 μm^3 with one node per voxel.

3.1 HCP microstructures

For the real HCP (Figure 1a), the Portland cement termed *'Cement and Concrete Reference Laboratory cement 133'* or *CCRL133* [13] with a *w/c*=0.45 is chosen since it is one of the

most tested HCP and its composition is standard (i.e., no fly ashes, slag or additive are present). Also, a curing time t_{cur} of 124 *hours* is used because is the maximum curing time available in the VCD [13,14]. For the artificial structure, two types of HCPs are generated starting from the same *CCRL133* phases distribution: one is coherent with the real HCP described above (t_{cur}=124*h* and *w/c*=0.45, Figure 1b), while the other involves 8 fully cured ($t_{cur}\rightarrow\infty$) microstructures with *w/c* ratios ranging from 0.35 to 0.80 (e.g., Figure 1c). The fully cured condition is essential to compare the numerical results with the experimental tests available in the literature [4-7].

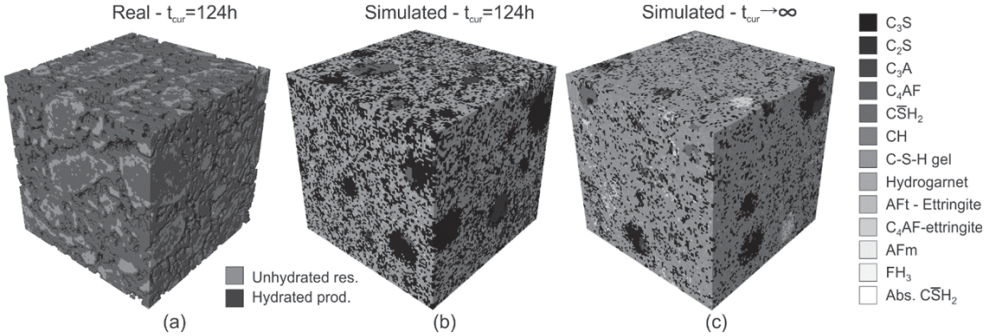

Figure 1: Voxel based meshes used for the numerical analyses: (a) real HCP from VCD [13,14], (b) artificial HCP simulating the real microstructure, (c) example of an artificial HCP with ideally infinite curing time.

3.2 Numerical homogeneization

In the following, the homogenized effective diffusivity D^H_{eff} of the HCP is found by means of the least square minimization of the following error objective function

$$\Pi := \left[\langle J\rangle - J^H\right]^2 = \left[\langle J\rangle + D^H_{eff}\langle grad(C_{tot})\rangle\right]^2 \rightarrow \min \tag{9}$$

where J^H is the flux of an ideally homogeneous material equivalent to the microscale heterogeneous ones which reads $J^H=-D^H_{eff}\langle grad(C_{tot})\rangle$. $\langle\bullet\rangle$ is the volume averaging operator, defined as

$$\langle\square\rangle = \frac{1}{V}\int_V \square\, dV \tag{10}$$

where V is the volume of the domain hosting the diffusion process. Solving Eq. (9) for D^H_{eff} gives

$$D^H_{eff} = \frac{\sum_{i=1}^{3}\left[\langle j\rangle_i \langle grad(C_{tot})\rangle_i\right]}{\sum_{i=1}^{3}\left[\left(\langle grad(C_{tot})\rangle_i\right)^2\right]} \tag{11}$$

where the subscript $i=1,2,3$ states the component of a vectorial quantity along the corresponding reference direction e_i, i.e. j_i is the scalar flux component in direction i. This minimization aims at defining a single equivalent diffusivity (upscaled) value that links and transfers the information from the heterogeneous microscale to the mesoscale, where the microstructural heterogeneities cannot be explicitly resolved and the cement paste is idealized as a homogeneous material.

4. Simulations of the diffusion test

The test simulated here, often referred to as diffusion test, involves the application of a chloride concentration gradient between two opposite faces of a prismatic sample, while all the other faces are considered sealed. This test is used to determine the average effective diffusivity D^H_{eff} of a HCP, as explained, for example, by Page et al. [5]. The experimental results of the diffusion tests from Page et al. [5] and Tang and Nilsson [7] are reproduced here. The setups used in both studies are very similar: a disc of HCP is placed in a diffusion cell and one of its circular faces (inlet face) is in contact with a chloride solution while the opposite is in contact with pure water (outlet face). The main difference between the two setups is the concentration of Cl^- at the inlet face C_{inlet}, Page et al. [5] used $C_{inlet}=1$ *mol/l* while Tang and Nilsson [7] $C_{inlet}=0.5$ *mol/l*.

4.1 Parameters used

For all the numerical simulations presented here a free diffusivity coefficient at room temperature (i.e., T=20°C) for the pores $D_{0,pores}=3.0\cdot10^{-4}$ mm^2/s is adopted which is very close to the values proposed by other authors [5] For the phases exhibiting binding behavior in HCP (AFm and C-S-H) the well accepted empirical formula $D_{0,AFm}=D_{0,CSH}=D_{0,pores}/400=7.5\cdot10^{-7}$ mm^2/s [15] is assumed. Also, since in the literature it is qualitatively reported that D_0 in all other phases is much lower than in AFm and C-S-H but no reliable estimations are available, here it is assumed that $D_{0,NObind}=0.1D_{0,AFm}=7.5\cdot10^{-8}$ mm^2/s. The latter value applies also to the unhydrated products in the real microstructure $D_{0,unhyd}= D_{0,NObind}$, while for the hydration products it is supposed that their composition in volume is equal to the simulated one – 59.5% and 1.0% of C-S-H and AFm respectively – and thus the free diffusivity is equal to the weighted average of the respective free diffusivities, i.e. $D_{0,hyd}=0.605D_{0,CSH}+0.395D_{0,NObind}=4.8\cdot10^{-7}$ mm^2/s. The same procedure is also applied to the binding isotherms, i.e. $C_b^{real}=0.595C_b^{CSH}+0.010C_b^{AFm}$. It is worth noting that no fine tuning of the parameters is performed to improve the comparison with the experimental results, but, rather, only mean values from the literature are adopted. Furthermore, it is evident how, to reliably evaluate the diffusivity and the binding isotherms of the real microstructure, a sufficiently precise estimation of the amount of phases exhibiting binding is needed.

4.2 Comparison between CT scan and simulated microstructures

Figures 2 and 3 report the contour maps of the analyses performed on real and artificial microstructures with $t_{cur}=124h$ and $w/c=0.45$ for the Page et al. [5] setup. The two images are qualitatively and quantitatively very similar, although the initial clinker particles in the artificial microstructure are spheres (Figures 1b and 2) while in reality they are irregular

(Figures 1a and 3). The homogenization procedure gives a value of the effective homogenized diffusivity of $13.1 \cdot 10^{-6}$ mm^2/s and $17.9 \cdot 10^{-6}$ mm^2/s for the artificial and real microstructure respectively and accounting for the binding effect. If binding is neglected the obtained values are $14.3 \cdot 10^{-6}$ mm^2/s for the artificial sample and $18.7 \cdot 10^{-6}$ mm^2/s for the real one. The limited difference between the results in both sets of values can be explained considering that the diffusivity adopted for the hydration products in real HCP is a volume average, constituting thus an upper bound (namely, a Voigt bound). Conversely, the modest effect of the binding observed is due, in this case, to the limited curing time of the samples, which allow only a limited production of hydration products.

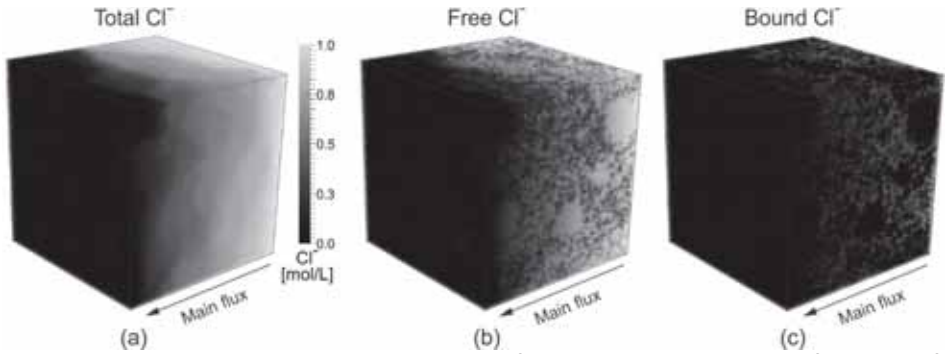

Figure 2: Steady state chloride concentrations from numerical simulation for the artificial HCP with t_{cur}=124h and w/c=0.45 reproducing the *CCRL133* [13,14] cement: (a) total concentration, (b) free chloride concentration, (c) bound chloride concentration.

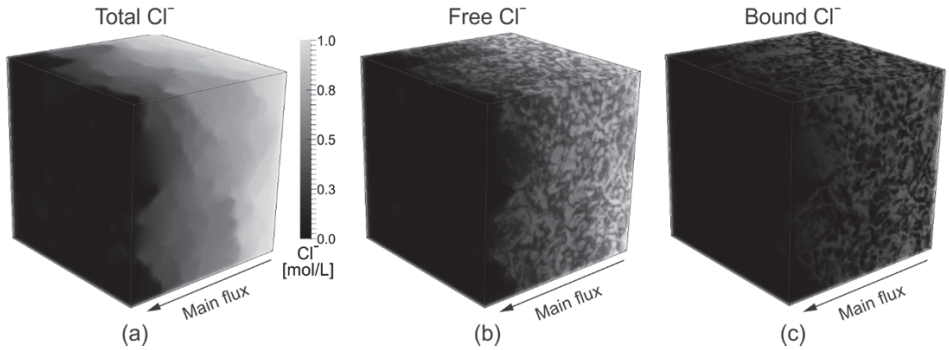

Figure 3: Steady state chloride concentrations from numerical simulation for the real *CCRL133* HCP [13,14] with t_{cur}=124h and w/c=0.45: (a) total concentration, (b) free chloride concentration, (c) bound chloride concentration.

4.3 Comparison with experimental results

Figure 4 shows the total, free and bound chloride concentrations for the artificial HCP with w/c=0.45 and t_{cur}=124h using the Page et al. setup [5]. A non-uniform distribution of the bounded Cl^- is evident as a result of the non-uniform distribution of the phases. Figure 5a-b

shows the curve relating the homogenized effective diffusivity D^{H}_{eff} and the *w/c* ratio for the Page et al. tests (Figure 5a) as well as for the Tang and Nilsson setup (Figure 5b). A good agreement between numerical and experimental results is observable, especially in the range of *w/c* ratios normally used in the practice (i.e., between 0.35 and 0.60). The overestimation of the diffusivity present for very high *w/c* ratios (Figure 5b) can be explained considering that such very porous HCPs have a microstructure characterized by large cavities that can introduce in the diffusive process a convective contribution, which is not accounted for in the Fick's theory.

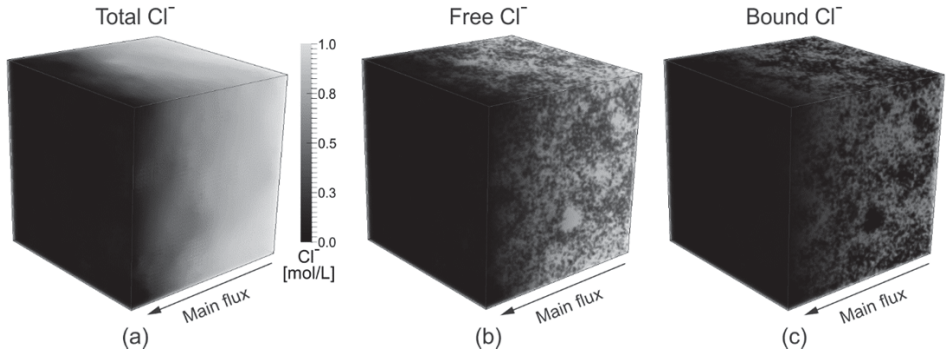

Figure 4: Steady state chloride concentrations from numerical simulation of the Page et al. test [5] for the artificial HCP with $t_{cur}\rightarrow\infty$ and *w/c*=0.45: (a) total concentration, (b) free chloride concentration, (c) bound chloride concentration.

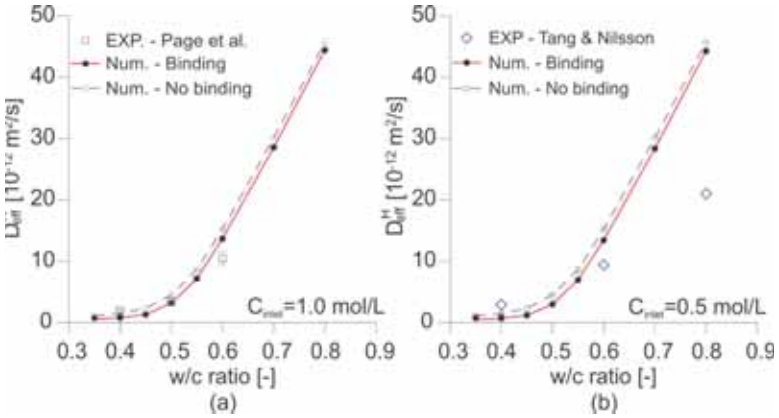

Figure 5: Results from numerical analyses: (a) homogenized diffusivity vs. *w/c* ratio for the test results of Page et al. [5], (b) homogenized diffusivity vs. *w/c* ratio for the test results of Tang and Nilsson [7].

Figure 6 shows the curve relating the *w/c* ratio with the coefficient ρ_D, which is used to assess the binding effect on the homogenized diffusivity. It is defined as

$$\rho_D = 1 - \frac{D^H_{eff}}{D^H_{eff,NObind}} \tag{10}$$

where $D^H_{eff,NObind}$ is the homogenized diffusivity calculated neglecting the binding behavior. Figure 6 shows that the binding effect reduces the homogenized diffusivity by up to the 60%. Also, the binding effect is relevant in the *w/c* ratio range between 0.35 and 0.60 and is much higher than the one obtained for the microstructures with $t_{cur}=124$ h.

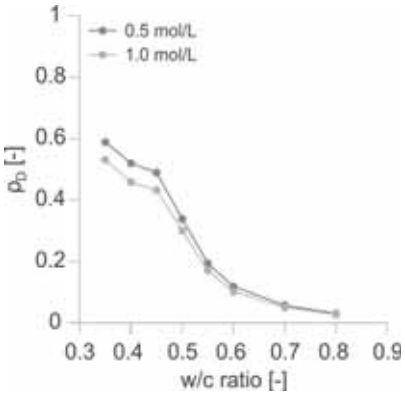

Figure 6: Influence of the binding effect on the homogenized diffusivity.

5. Summary and conclusions

A novel approach to simulate the chloride diffusion into the hardened cement paste accounting for the phase-wise uptake of chloride ions by the AFm and C-S-H phases is presented. The diffusion process is described by means of a modified version of the second Fick's law, where the concentration of total chloride ions is decomposed into bounded and free ions. The amount of chloride bounded by AFm and C-S-H phases is established using the binding isotherms suggested by Hirao et al. [4]. The governing equations are discretized and solved by means of the finite difference method. Different real and artificially generated HCP microstructures varying both *w/c* ratio and curing time are employed. The numerical analyses show a good agreement between real and artificially generated HCP. Also, the following conclusions can be drawn:

- comparisons between numerical evidence and results from the literature confirm the capability of the proposed approach to correctly reproduce the diffusion process of chloride ions into HCP;
- artificially generated and real HCP microstructures give similar results provided that a good estimation of the volume fractions of phases exhibiting binding is known, at least in terms of homogenized chloride diffusivity;

– neglecting the binding behavior leads to an overestimation of the homogenized diffusivity of the HCP by up to the 60 %, especially for cement pastes cured for long time;

References

[1] Bentz, D. P., and Garboczi, E. J. A Computer Model for the Diffusion and Binding of Chloride Ions in Portland Cement Paste, NISTIR 5125, (1993).
[2] Martìn-Pèrez, B., Zibara, H., Hooton, R. D., and Thomas, M.D.A. A Study of the Effect of Chloride Binding on Service Life Predictions, Cem Concr Res, 30, (2000), 1215-1223.
[3] Yuan, Q., Shi, C., De Schutter, G., Audenaert, K., and Deng, D. Chloride Binding of Cement-Based Materials Subjected to External Chloride Environment - A Review, Constr Build Mater, 29, No. 1, (2009), 1-13.
[4] Hirao, H., Yamada, K., Takahashi, H., and Zibara, H. Chloride Binding of Cement Estimated by Binding Isotherms of Hydrates, J Adv Concr Tech, 3, No. 1, (2005), 77–84.
[5] Page, C.L., Short, N.R. and A. El Tarras. Diffusion of Chloride Ions in Hardened Cement Pastes, Cem Concr Res, 11, (1981), 395-406.
[6] Yu, S.W., and Page, C.L. Diffusion in cementitious materials: 1. Comparative study of chloride and oxygen diffusion in hydrated cement pastes, Cem Concr Res, 21, (1991), 581–588.
[7] Tang, L., and Nilsson, L.-O. Chloride binding capacity and binding isotherms of OPC pastes and mortarts, Cem Concr Res, 23, (1993), 247–253.
[8] Zhang, M., Ye, G., and van Breugel, K. Multiscale Lattice Boltzmann-Finite Element Modelling of Chloride Diffusivity in Cementitious Materials. Part I: Algorithms and Implementation, Mech Res Com, 58, (2014), 53–63.
[9] Wu, T., and Wriggers, P. Multiscale Diffusion–thermal–mechanical Cohesive Zone Model for Concrete. Computational Mechanics, 55, No. 5, (2015), 999–1016.
[10] Bentz, D.P., Three-Dimensional Computer Simulation of Portland Cement Hydration and Microstructure Development, J Am Cer Soc, 80, No. 1, (1997), 3–21.
[11] Bentz, D.P., CEMHYD3D: A Three-Dimensional Cement Hydration and Microstructure Development Modelling Package. Version 3.0, NIST, (2005).
[12] van Breugel, K., Simulation of Hydration and Formation of Structure in Hardening Cement-Based Materials, PhD thesis, 1997 (2nd Edition), Delft University of Technology, Delft
[13] Bentz, D.P. et al., The Visible Cement Data Set, J Res NIST, (2002).
[14] Visible Cement Dataset [online], Available from: http://visiblecement.nist.gov
[15] Garboczi, E. J., and Bentz D. P., Computer Simulation of the Diffusivity of Cement-Based Materials, J Mat Sci, 27, No. 8, (1992), 2083–92.
[16] Carrara, P., De Lorenzis, L., Bentz, D.P., Chloride diffusivity in hardened cement paste from microscale analyses and accounting for binding, (2016), Submitted in revised form to Modelling Simul Mater Sci Eng

International RILEM Conference on Materials, Systems and Structures in Civil Engineering
Conference segment on Service Life of Cement-Based Materials and Structures
22-24 August 2016, Technical University of Denmark, Lyngby, Denmark

NON-DESTRUCTIVE EVALUATION OF STRENGTH DEVELOPMENT IN CONCRETE

Ivan Gabrijel [(1)], Dubravka Bjegović [(1)], Josip Kujek [(1)]

(1) University of Zagreb, Faculty of Civil Engineering, Zagreb, Croatia

Abstract
The research presented in this paper analyses the possibilities of acousto-ultrasonic (AU) method in monitoring of hardening process in concrete from the time when concrete is in plastic state. The measuring system which enables continuous acquisition of the transmitted waveform, is presented and its performance is evaluated through an experimental investigation. Analysis was performed on concrete mixtures made with different w/c ratios (0.4, 0.5 and 0.65) and two cement types: CEM I 42,5 R and CEM III/B 32,5. Simultaneously with the AU method compressive strength development was evaluated through destructive testing of concrete cubes. It was found that a strong linear correlation exist between the amplitude of the waveform transmitted through the concrete sample and the compressive strength development.

1. INTRODUCTION

Interests of monitoring strength development or to predict strength at a certain age of concrete can be very profound in a lot of different applications, usually as a tool for speeding up of construction or production process. Development of strength of concrete is a process controlled by a large number of variables. Curing temperature, cement properties, w/c ratio, aggregate properties etc, all govern the hardening process to some extent. The most important changes in the structure and properties of concrete and other cement based materials will happen in the first few days after mixing as a result of cement hydration process. During that period, the increase in quantity of hydration products formed is largest and increase of strength and rigidity of concrete are fastest. Because progress of hydration reflects as changes of chemical, physical, mechanical and electrical properties of concrete it can be monitored by measuring changes in chemical composition, enthalpy, ultrasonic wave velocity, volume, consistency or strength. A large number of different techniques and testing methods for

monitoring of hydration have been developed over the last 60 years, and global overviews of such methods can be found in the literature [1, 2, 3]. Most of the methods developed can be applied only at laboratory conditions but for practical application in civil engineering methods that can be applied in-situ are most important.

Prediction of compressive strength at a certain age requires understanding of hydration process and a means of monitoring it. Hydration is a continuous process and techniques which enable continuous measurement of a certain parameter like for example liberated heat of hydration or ultrasonic wave velocity can give real time information about the course of hydration. Probably the most widespread approach for monitoring of compressive strength of concrete in-situ is measuring of temperature history of concrete. According to Schindler, curing temperature is arguably the one variable that has the most significant effect on the rate of hydration [4]. From measured temperatures maturity of concrete is calculated and compressive strength is estimated upon a previously established strength-maturity relationship. A fundamental disadvantage of the maturity method is the fact that strength of concrete is not actually measured and therefore additional testing is required. Another disadvantage of maturity method is that it does not take into consideration effect of temperature on concrete strength but only on the speed of hydration reactions. This problem was noted from so-called crossover effect where concrete cured at higher temperature has lower final strength compared to concrete cured at lower temperature [5].

In ultrasonic testing of early-age concrete, deviations in the ultrasonic response caused by changes in the material properties are studied. Microstructural build-up during early ages gradually enables better transfer of ultrasonic wave energy which on the macro-level reflects as an increase of the wave velocity and increase in the quantity of wave energy transferred. Probably mostly used method for monitoring of strength development in concrete is ultrasonic pulse velocity. Although vide variety of strength-velocity correlations can be found in the literature Popovic states that parameters like composition of concrete, temperature, curing, and so on do not have the same effect on the concrete compressive strength development and on the ultrasonic wave velocity and this precludes setting up of a reliable regression model for estimation of compressive strength [6]. On the other hand shear wave reflection method was proven to have almost linear correlation with strength development of concrete [1, 7]. Another great advantage of this method is that it can be applied in-situ and only one side of element has to be available for testing.

This paper presents outcome of a laboratory investigation in which acousto-ultrasonic (AU) method was studied for monitoring of strength development of concrete. An AU testing set-up was designed and changes in the ultrasonic signals transmitted through concrete specimens during the first few days of hydration were analysed. In the following section AU principles, setup and experimental testing program are described.

2. EXPERIMENTAL WORK

Acousto-ultrasonic (AU) method is closely related to the acoustic emission. While acoustic emission normally requires loading in acousto-ultrasonics stress waves are generated

externally, usually by a transducer [8]. One of the main differences between ultrasonic and acousto-ultrasonic testing is in sensors used to collect signals. While in ultrasonics longitudinal or shear wave sensors are used, acoustic emission sensors are sensitive to both longitudinal and transversal motion of the surface. In AU measurements a parameter called stress wave factor (SWF) is determined from the ultrasonic signal. SWF is used to quantify AU signals for comparison with the mechanical properties variation or fracture resistance.

Philippidis and Aggelis had already shown that AU can be used for monitoring of changes during early age in mortar and concrete [9]. They reported linear strong linear correlation between compressive strength of concrete tested at ages of 2, 7, 28 and 90 days and corresponding energy of the transmitted signal. In this research continuous monitoring of waveform characteristics is applied from the time of casting up to the age of 7 days.

2.1 Description of AU testing setup

The scheme of the AU test setup is presented on Figure 1. Sensors are placed on the opposite sides of a specimen at the centre of the surface. Waveform generator produces a pulse of 10 V which excites one piezoelectric sensor. The stress wave propagates through the material and it excites another sensor of the same type, which is attached on the opposite surface. This signal is then processed and stored as a waveform. The equipment used consists of Physical Acoustics Corporation (PAC) components: arbitrary waveform generator ARB-1410-150, PAC 1220 preamplifiers with selectable gain of 0/20/40 dB, 16 bit PCI-8 data acquisition system and piezoelectric transducers type R6 which are sensitive in the range 20-120 kHz. Waveforms were recorded at a sampling rate of 1 MHz. The same sensors were used as pulser and receiver through the entire experimental work presented in order to avoid influence of different sensor characteristic on measurement results. During measurement, a pulse repetition frequency of 0,01 Hz was used which is equal to one pulse every 100 seconds.

a) b)

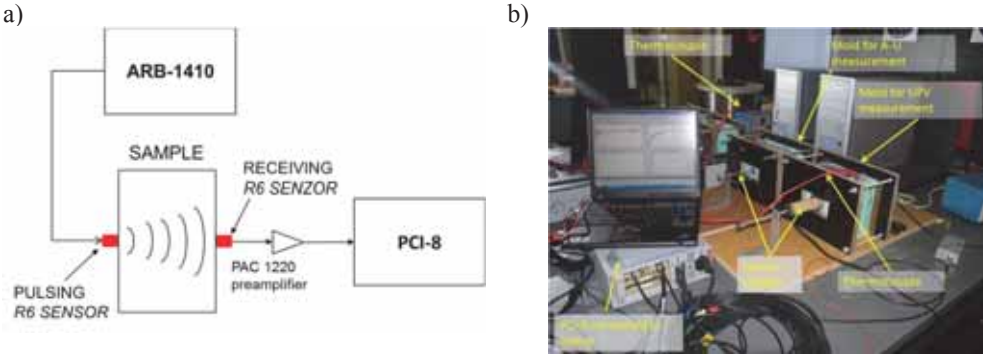

Figure 1: a) the scheme of AU setup; b) experimental setup during testing

AU measurements were started when concrete was still in the fresh state. In order to achieve that, an adequate mold had to be devised. The mold consisted of 2 cm thick extruded polystyrene and water resistant plywood frame connected with bolts. Dimension of the concrete specimens in the mold are 15x15x10cm^3. The distance between sending and receiving sensors was 10 cm. After mixing concrete was cast into mold and compacted by a

handheld vibrator because it was noted that compaction on vibrating table did not ensure satisfactory compaction probably due to the damping of vibrations caused by XPS. Before placing of concrete into mold, a PELD foil was placed in mould between concrete and XPS. This was made in order to prevent evaporation of water from concrete and shrinkage which can cause reduction of stress wave energy transmission between sensors and specimen. A layer of water was also placed on top of each specimen during AU measurement to prevent drying shrinkage which could cause the reduction of stress wave energy transfer between the sensor and the specimen. After compaction specimens were placed in a temperature controlled room with temperature 19 ± 2°C. Sensors were then mounted and slightly pressed against specimen through PELD foil. A layer of grease is applied in the sensor-foil interface to assure acoustical coupling.

2.2 Concrete mix design

Two types of cement were used for making concrete specimens: ordinary Portland cement CEM I 42,5 R (OPC) and blast furnace slag cement CEM III/B 32,5 N SR-LH (CEM III) in which 66-80% of Portland cement clinker is replaced by a ground granulates blast furnace slag. Slag cement is used during experimental work because slag has a large impact on the kinetics of hydration. Six concrete mix compositions were used during experimental work. Besides cement type w/c ratio was varied in the range form 0.4-0.65. Aggregates were dolomite. Three fractions were used for making concrete: 0-4 mm (35,6 %), 4-8 mm (24,0 %) and 8-16 mm (40,4 %). Concrete mix proportions are presented in Table 1. Mixtures are labelled according to cement type and w/c ratio of the mix. In Table 1 properties of fresh concrete are also listed.

Table 1: Concrete mix composition and properties

	Mixture label					
	CEM I 42,5 R			CEM III/B 32,5 N SR-LH		
Property	**BI-0.4**	**BI-0.5**	**BI-0.65**	**BIII-0.4**	**BIII-0.5**	**BIII-0.65**
w/c ratio	0,4	0,5	0,65	0,4	0,5	0,65
Water [kg]	190	190,0	190	190	190	190
Cement [kg]	475,0	380,0	292,3	475,0	380,0	292,3
Aggregate [kg]	1793,4	1879,1	1958,1	1764,3	1855,9	1940,3
Properties of concrete						
Fresh density [kg/m^3]	2490	2490	2480	2450	2470	2460
Slump [mm]	35	55	70	10	30	60
Temperature [°C]	23,8	22,6	22,4	23,5	22,1	22,3
Air content [%]	1,8	1,4	1,4	2,2	1,0	1,2

2.3 Mixing, curing and testing procedures

Approximately 24 hour prior to mixing all concrete components are stored at a temperature 20±2°C. Concrete strength was tested on standard cubes with 15 cm edge. Strength was tested at ages of 1, 2, 3, 7 and 28 days after mixing. For concrete made with cement type CEM I, the first strength test was made after 12 hours. After mixing cubes were compacted on a vibrating table and cured for the first 24 hours in the moulds covered with plastic sheet and then in the curing chamber afterwards at 20±2°C. Temperature was measured inside 2 cubes from each

mixture. Temperature was measured so that its influence on hydration, and strength development consequently, could be evaluated. AU measurements started approximately 1 hour after mixing. Changes in AU signals were continuously recorded up to the first 7 days of hydration.

3. RESULTS

The fundamental hypothesis of AU approach states that in brittle or quasi-brittle materials greater stress or strain energy flow corresponds to higher strength and fracture resistance so the purpose of AU testing is to evaluate relative efficiency of stress wave energy propagation [8]. This evaluation is done on the basis of stress wave factors (SWF) which are extracted from the waveform. The dominant effect measured in AU is relative attenuation and lower values of SWF generally correspond to regions of higher attenuation [8]. During this experiment AU measurements started approximately 1 hour after mixing. As an example waveforms recorded during measurement on concrete mix BI-0.4 after 6, 12 and 48 hours are presented on Figure 2a. From Figure 2a it is visible that amplitude of the waveform increases with increasing age of the specimen tested. Although there are several parameters that can be extracted from the waveform values of most of them depend on the shape of the entire waveform which contain ring-down and potential reflection components. It is therefore presumed here that amplitude is less influenced by these effects and accordingly will be more closely related to changes in concrete properties than other parameters.

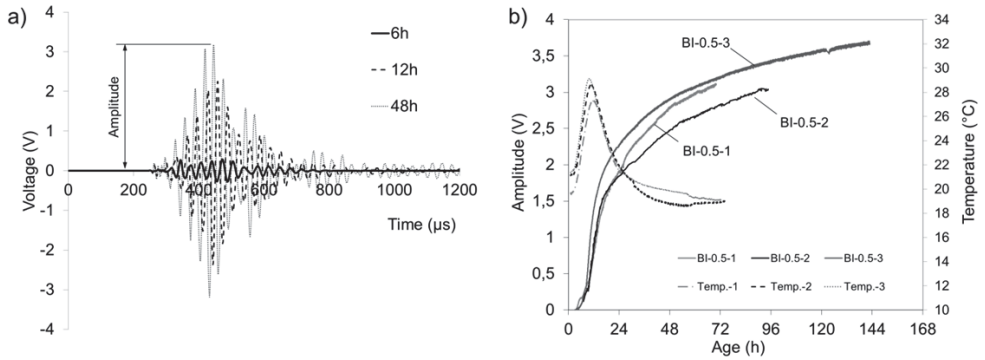

Figure 2: a) example of waveforms recorded at an age of concrete of 6h, 12h and 48h; b) Amplitude development for mixture BI-0.5

Measurement on the samples taken from mixture BI-0.5 was repeated 3 times and measured amplitude values are plotted in Figure 2b. Amplitude of the waveform increased continuously during measurement. On the same graph temperature measured inside samples during test is plotted. Figure shows that increase in temperature is followed by the increase in the amplitude.

Energy transfer of ultrasonic wave across interface is highly dependent on presence of microscopically sized air voids. Deviations in measured amplitude values in Figure 2b can be

partially attributed to that effect. To overcome or at least to reduce impact of this effect on interpretation of a measurement results a way to normalize amplitude is presented in the following.

3.1 Modelling of amplitude development

An exponential model is often used to describe degree of hydration evolution or compressive strength development [5, 10]. In equation 1 $A(t)$ is the value of the amplitude at age t, A_u is the ultimate amplitude, τ_A is time parameter and β_A is slope parameter.

$$A(t) = A_u \cdot e^{-\left(\frac{\tau_A}{t}\right)^{\beta_A}} \quad (1)$$

Examples of measured amplitude values fitted with exponential model are presented in Figure 3a. It can be seen that this model can describe amplitude evolution through entire measurement. Largest deviations between model and measured values are present in the initial period of amplitude evolution during which amplitude seems to follow some different trend of growth. Based on the model parameters 28 day (672 hours) value of amplitude (A_{28}) is calculated and then relative amplitude is expressed as $A_{rel} = A(t)/A_{28}$. That way relative amplitude represents percentage of the 28-day amplitude value (Figure 3b).

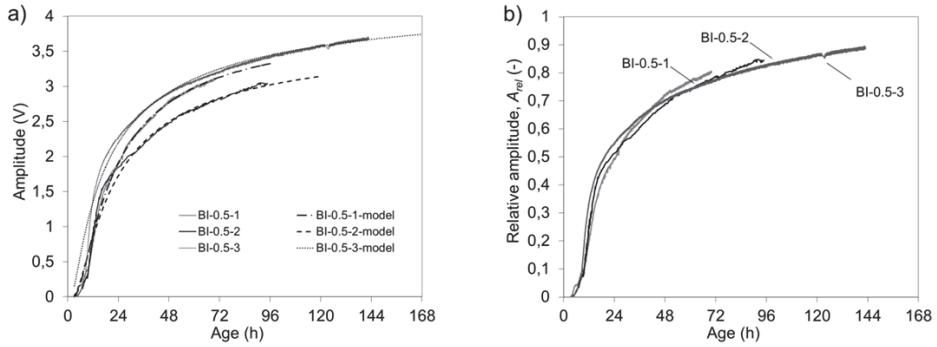

Figure 3: a) exponential model fitted into measured amplitude values for samples from mixture BI-0.5; b) relative amplitude plot for samples from mixture BI-0.5

3.2 Amplitude and compressive strength development

Plot of amplitude vs. age for all concrete mixture compositions is presented in Figure 4a. Amplitude of the waveform increases continuously during hydration. Start of the increase depends on concrete composition and it goes from 2,5 hour for sample from mixture BI-0.4 to 4,5 hour for sample from mixture BIII-0.65. In a mixture with lower w/c ratio distances between cement particles are smaller and the microstructure becomes better connected at a lower degree of hydration compared to higher w/c ratio mixtures [3]. Generally this results in a faster strength increase in mixtures with lower w/c ratio but in this case in a faster amplitude development.

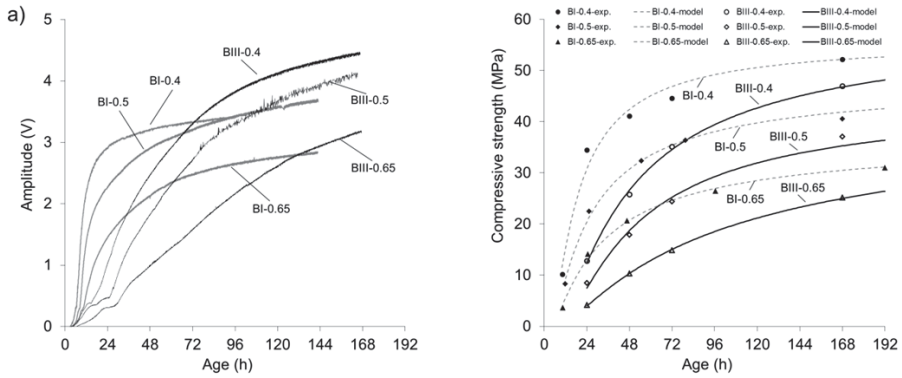

Figure 4: a) amplitude development measured on specimens from all mixtures; b) compressive strength development

It was found that amplitude measured on samples made with CEM III became larger than amplitude measured on samples made with OPC for mixtures with the same w/c ratio. This amplitude crossover effect was found for all w/c ratios. Strength development measured on concrete cubes is shown in Figure 4b. Strength development data in Figure 4b is fitted by 3-parameter exponential model. Compressive strength measured on concrete cubes was at all tested ages higher than in mixtures made with OPC.

Magnitude variations of AU signal primarily depend on material factors that govern attenuation which are microstructure, morphology, porosity and so on [8]. Therefore amplitude variations in concrete will be also governed by these effects. When slag cement is used in making concrete, microstructure of the cementitious matrix becomes less permeable, comparing to ordinary Portland cement mixtures [11, 12]. Pores in concrete that normally contain calcium hydroxide are, in part, filled with calcium silicate hydrates resulting from the hydration of the slag and this leads to reduction in the pore size. After the concrete is mixed slag reactions are practically suspended until slag becomes activated by alkalis released during Portland cement hydration. Amplitude crossover effect shows that the structure of mixtures made with CEM III at a certain age enables a better transmission of stress waves compared to mixtures made with OPC. This implies that pore sizes in mixtures made with CEM III had become smaller than in the OPC mixtures, which is caused by filing of pores with slag reaction products.

In Figure 5a-f relative compressive strength S_{rel} versus relative amplitude A_{rel} are plotted. Relative compressive strength is calculated as $S_{rel} = S(t)/S_{28}$, where $S(t)$ is compressive strength measured at age t and S_{28} is compressive strength measured at an age of 28 days. There is an obvious similarity in shape between the strength model curve and of the amplitude evolution curve presented in Figures 5a-f. In Figure 6a correlation plot of relative amplitude versus relative strength development is presented. The plot shows that there is a strong (R^2=0,85) linear correlation between these two parameters with coefficient of proportionality very close to 1 (slope = 1,033). In Figure 6 90% confidence prediction interval for regression line is also plotted. Points outside of the interval belong to mixture BI-0.4. If data for mixture

BI-0.4 is excluded from the analysis data than R^2 = 0,93 and slope is 1,04 and value of the intercept 0,01 (Figure 6b).

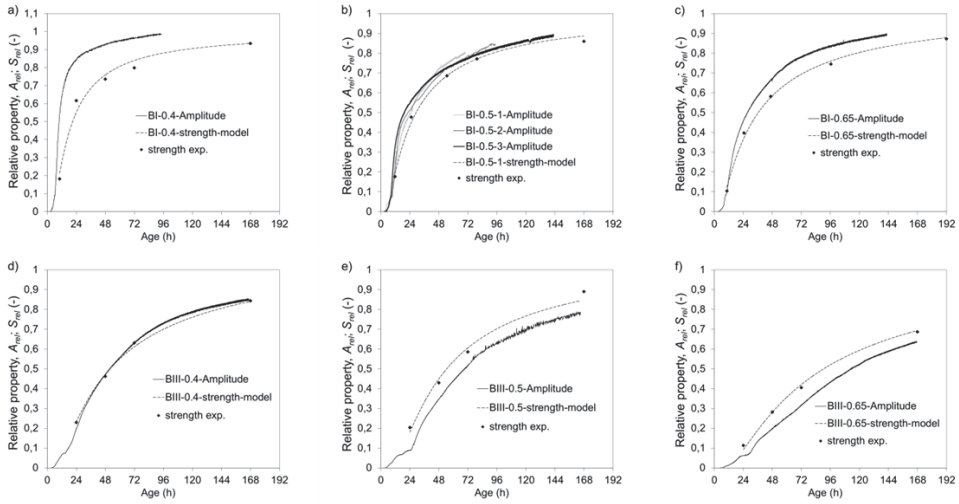

Figure 5: Relative amplitude plotted vs age of concrete compared with relative compressive strength development

Correlation between relative amplitude and relative compressive strength for each mixture can be very accurately modelled by a linear equation.

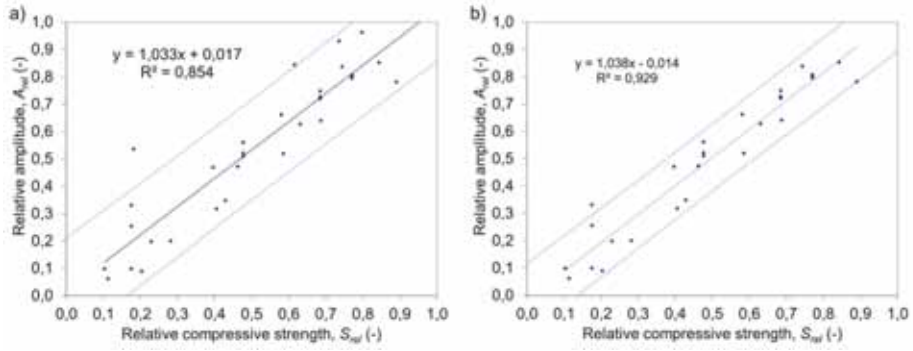

Figure 6: Correlation plots of relative amplitude vs. relative compressive strength: a) data from all mixtures; b) data with excluded mixture BI-0.4

After completion of the measurement specimens on which AU test was made were sawn and from each specimen one concrete cube with approximate dimensions 10x10x10cm^3 was prepared for compressive strength testing. This was done to evaluate actual compressive

strength on a part of the actual specimen through which ultrasonic signals were transmitted. Before compressive strength test cubes were grinded to achieve requirements for flatness of loaded surfaces given by the standard HRN EN 12390-1. Compressive strength was tested at the age of 28 days and the results are presented in Table 2. Values of the compressive strength of sawn cubes are multiplied with a strength conversion factor of 0,95 to be comparable with compressive strength on standard cubes with 15 cm edge length. In Table 2 average compressive strength measured on standard concrete for each batch are also given. Results show that compressive strength of specimens subjected to AU test was lower that compressive strength measured on standard cubes. Largest difference of 16,2 MPa is found in mixture BI-0.4. In Figure 4a it can be seen that amplitude measured on specimen from mixture BI-0.4 became lower that amplitude measured on specimen from mixture BI-0.5 at an age of approximately 96 hours. This is probably caused by the same effect that lead to reduction of compressive strength in specimen from mixture BI-0.4.

Table 2: Compressive strength measured on sawn specimens and standard concrete cubes

	BI 0.4	BI 0.5-1	BI 0.5-2	BI 0.5-3	BI 0.65	BIII 0.4	BIII 0.5	BIII 0.65
AU test (10 cm cube) (MPa)	44,1	46,8	40,5	43,6	34,9	56,8	47,7	34,0
Standard cubes (MPa)	60,3	49,8	50,9	48,5	40,1	59,5	49,4	35,8

3. CONCLUSION

Monitoring of changes in the waveform of the ultrasonic signal transmitted through the concrete during the first days of hydration was applied for analysis of strength development. From the results presented, it seems that increase of amplitude of ultrasonic wave transmitted through the concrete sample is governed by the similar mechanism as compressive strength development. Therefore amplitude of the ultrasonic signal could serve as a tool for evaluation of strength at a certain age.

References

[1] Voigt, T. The Application of an Ultrasonic Shear Wave Reflection Method for Nondestructive Testing of Cement-based Materials at Early Ages: An Experimental and Numerical Analysis, PhD thesis, University of Leipzig, 2004.
[2] RILEM Report 031 Advanced Testing of Cement-Based Materials during Setting and Hardening - Final Report of RILEM TC 185-ATC, / ed H.W. Reinhardt and C.U. Grosse, Rilem publications, 2005.
[3] Van Breugel, K. Simulation of Hydration and Formation of Structure in Hardening Cement-Based Materials, Delft Univ.Press, Delft, 1991.
[4] Schindler, A. K. Effect of Temperature on Hydration of Cementitious Materials, ACI Materials Journal, V. 101(1) (2004), str. 72-81
[5] Carino, N. J. The maturity method: From theory to application, Proceedings of the 2001 Structures Congress & Exposition, Chang, P.C. ed., Washington, D.C., May 21-23, 2001.

[6] Popovics, S. Analysis of the Concrete Strength versus Ultrasonic Pulse Velocity Relationship, American Society for Non-destructive Testing, 2001 (http://www2.asnt.org/publications/materialseval/basics/feb01basics/feb01basics.htm)
[7] Subramaniam, K. V; Mohsen, J. P.; Shaw, C. K.; Shah, S. P. Ultrasonic technique for monitorning concrete strength gain at early age, ACI Materials Journal, V. 99(5) (2002), str. 458-463.
[8] Vary, A. The acousto-ultrasonic approach, book chapter, Acousto-Ultrasonics: Theory and application, ed. Duke, J.C., Plenum, New York, 1988.
[9] Philippidis, T. P.; Aggelis, D. G. An Acousto-Ultrasonic Approach for the Determination of Water-to-Cement Ratio in Concrete, Cement and Concrete Research V. 33(4) (2003), pp 525-538. 20.
[10] Schindler, A. K. Effect of Temperature on Hydration of Cementitious Materials, ACI Materials Journal, V. 101(1) (2004), p. 72-81
[11] ACI 233R-03: Slag Cement in Concrete and Mortar, American Concrete Institute, 2003.
[12] Roy, D.M. and Idorn, G.M. Hydration, structure and properties of Blast Furnace slag cements, Mortars and Concrete, ACI Journal, Proceedings V. 79, No. 6, pp. 445-457

International RILEM Conference on Materials, Systems and Structures in Civil Engineering
Conference segment on Service Life of Cement-Based Materials and Structures
22-24 August 2016, Technical University of Denmark, Lyngby, Denmark

CRACK WIDTH CONTROL – VERIFICATION OF THE DEFORMATION COMPATIBILITY VS. COVERING THE CRACKING FORCE

Dirk Schlicke [(1)], Nguyen Viet Tue [(1)]

(1) Graz University of Technology, Institute of Structural Concrete, Graz, Austria

Abstract
According to the current design code the crack width control is provided by a minimum reinforcement covering any restraints as well as crack width verifications for the decisive load combinations, whereas the interaction of both is generally not pursued further. Almost all guidelines advise to control the crack width due to restraint by a minimum reinforcement taking up the cracking force respectively the cracking moment, e.g. [1] and [2]. However, such procedure neglects the deformation compatibility along the member length and the interaction of restraints and external loads is not pursued any further. Altogether, this can either lead to structural damage - mainly recognizable in form of leaking cracks in watertight constructions - or to inefficient constructions. A mechanical consistent crack width control under consideration of the real member behaviour can solely be achieved by the verification of the deformation compatibility since deformation compatibility is also the reason for restraints in the first place. Such procedure is shown for instance in [3] for the particular case of early age effects.

1. Introduction

The aim of this contribution is to establish the deformation based design method to enable efficient crack width control as well as the avoidance of expansion joints. For this purpose, important fundamentals on crack width control as well as their practical application are outlined at first. Following, the deformation based design method will be presented with special regard to structures with strict requirements on crack width but minor stressing due to external loads (usually retaining structures) as well as members with distinct tendency for cracking due to an interaction of restraint and external loads (usually large floors of jointless building constructions). The benefits of such procedure are highlighted in the conclusion.

2. Relevant fundamentals on crack width control

The crack width in reinforced concrete depends predominantly on the following parameters:

- applied strain,
- present reinforcement and its utilization (diameter, young's modulus and steel stress),
- bond strength and bond stress distribution in the transfer length as well as
- duration of loading (short-term or permanent stress level).

The characteristically occurring crack width w_k can be derived from the difference of steel strain ε_s and concrete strain ε_c along the crack spacing s_r. By simplifying the real strain distribution along s_r with the introduction of average values for steel strain (ε_{sm}) and concrete strain (ε_{cm}) the following correlation can be constituted:

$$w_k = \int_{x=0}^{s_r} \left(\varepsilon_s(x) - \varepsilon_c(x)\right) dx = s_r \cdot (\varepsilon_{sm} - \varepsilon_{cm}) \tag{1}$$

In the crack state of single cracks (not all possible cracks have been created along the member length), the difference of steel and concrete strain occurs only in the transfer lengths to both sides of the cracks, whereas stabilized crack patterns (all possible cracks have been created along the member length) are characterized by a difference between steel and concrete strain along the whole member length. On the safe side, the crack spacing can be determined by taking into account the cracking force of the effective concrete area ($F_{cr} = A_{c,eff} \cdot f_{ct,eff}$), the average bond strength and the reinforcement diameter d_s. It reads:

$$s_r = 2 \cdot \frac{F_{cr}}{\tau_{sm} \cdot \pi \cdot d_s} \tag{2}$$

With respect to the influence of the load duration on the strain distribution in the cack spacing (k_t = 0,6 for short-term and 0,4 for long-term) and the force to be taken by the reinforcement after cracking (F_s) the crack width can be estimated for a given reinforcement (d_s, provided area A_s, Elastic modulus E_s) by a transformation of Eq. (1) and (2) in form of:

$$w_k = \frac{F_{cr} \cdot (F_s - k_t \cdot F_{cr}) \cdot d_s}{2 \cdot \tau_{sm} \cdot E_s \cdot A_s^2} \tag{3}$$

As long as $F_s \leq F_{cr}$, only single crack patterns are to be expected and F_s is to set as F_{cr} in Eq. (3). If $F_s > F_{cr}$, all possible cracks will form along the member and a stabilized crack pattern exists. Eq. (3) considers for both crack states an undisturbed transfer length to both sides of the crack. Strictly seen, this is only correct in case of single cracks. As soon as a stabilized crack pattern has developed, the crack width might be overestimated by Eq. (3). The reason is that new cracks may form between neighbouring single cracks so that s_r decreases. Keeping in mind the transition between both crack states and statistical uncertainties of the distance between cracks in stabilized crack patterns, Eq. (3) can be seen as

justifiable for both cases. Another crucial point is the consideration of bond stresses between reinforcement and concrete which is usually simplified for conventional reinforcement with an average bond strength along the transfer lengths of $\tau_{sm} = 1.8 \cdot f_{ctm}(t)$. Further details are given e.g. in [4], [5] or [6]. Although several differences can be found in detail, Eq. (3) represents in general the EUROCODE regulations for crack width control. The direct determination of the crack width in EC2 (Sec. 7.3.4) differs only in terms of the empirical determination of the crack spacing, whereas the indirect crack width verification (Sec. 7.3.3, Table 7.2N) can be directly derived from Eq. (3). For the relation between crack width, rebar diameter and steel stress can be written according to the same assumptions in EC2 ($F_s = F_{cr}$, $k_t = 0{,}4$, $\tau_{sm} = 1.8 \cdot f_{ctm}(t)$):

$$\sigma_s(w_k) = \sqrt{6 \cdot \frac{w_k \cdot f_{ctm}(t) \cdot E_s}{d_s}} \tag{4}$$

The EC2 regulation for the minimum reinforcement (Sec. 7.3.2) bases on the same assumptions and takes up the cracking force respectively the cracking moment. The decisive stress distribution just before cracking is considered by a factor k_c (pure centric restraint $k_c = 1.0$, pure bending restraint $k_c = 0.4$), whereby the absolute size of stresses to be taken up while cracking can be modified empirically for the benefit of an efficient design. These modifications concern positively assumed influences of pre-damage due to residual stresses (factor k) and reduced stresses in case of early age cracking ($f_{ct,eff} < f_{ctm}$). Finally, it reads:

$$A_{s,min} = k_c \cdot k \cdot f_{ct,eff} \cdot \frac{A_{ct}}{\sigma_s(w_k)} \tag{5}$$

The application of Eq. (3) - Eq. (5) takes place in the context of a verification of the force equilibrium without further respect to the type of stressing. While this is very suitable for cases with external loads, such strategy has to be seen critically in cases with significant restraints. The main reason is that the restraint force depends strongly on the deformation compatibility and this includes also its decreasing by formation of any new crack. Furthermore, the crack pattern due to imposed deformations depends predominantly on the restraining condition which leads to a geometrically set patterns of cracks, as shown in Fig. 1. Only exception is to systems in which the steel force in the reinforcement is in complete equilibrium with the restraint force, e.g. end-restrained tension rods.

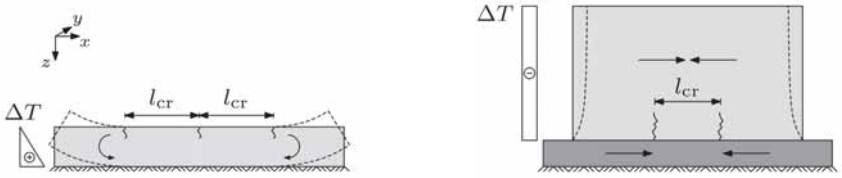

a) bending cracks due to self-weight activation of a ground slab

b) separating cracks due to external restraint of a wall on a foundation

Figure 1: Geometric set crack patterns of typical members which are predominantly restrained

Common reinforcements have no significant influence on the occurrence of these geometric set crack patterns (primary cracks). Large quantities of reinforcement would slightly reduce l_{cr}, however, the steel stress in the primary cracks is not affected by the formation of a new primary crack. Thus, these primary cracks can be assumed to be independent from each other, or in other words, the geometric set cracks separate the member in parts with a length of l_{cr} for which crack width control can be carried out independently.

The size of l_{cr} depends predominantly on the restraining situation, whereby two principal cases can be distinguished for practical design. One is the restraining of a curvature due to self-weight activation (e.g. ground slab with temperature gradient over the height), the other one is the interaction with a rigidly connected, restraining component (e.g. shortening of a wall on a foundation). For these typical member types, [3] proposes robust engineering models to determine l_{cr} on the safe side, however, a generally valid model considering the present reinforcement would require further investigations, see [7].

Besides, it needs to be said that the anchorage of the reinforcement will create secondary cracks next to the primary cracks, as shown in Fig. 2 for all cases with significant smaller effective concrete area ($A_{c,eff} < A_c$).

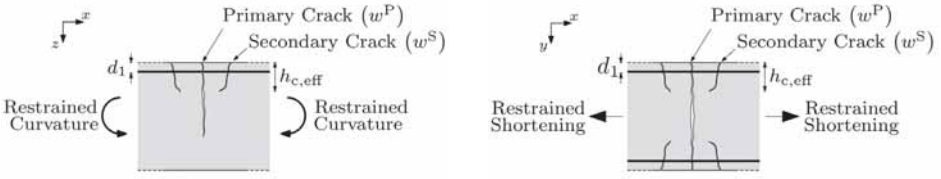

a) bending cracks (bending restraint over the thickness)

b) separating cracks (centric restraint over the thickness)

Figure 2: Crack systems consisting of a primary crack and secondary cracks, here $A_{c,eff} < A_c$

3. Crack width control on basis of deformation compatibility

3.1 General Approach

Deformation compatibility is the comparison of deformation impacts in the material with the deformation response of the system. Predominant impacts are thermal expansion ($\alpha_T \cdot \Delta T$), shrinkage due to hydration and drying ($\varepsilon_{cas} + \varepsilon_{cds}$) as well as creep ($\varepsilon_{cc}$), whereas the system response mainly consists of free deformation ($\Delta l / l$) and restrained deformation in form of restraint stresses (σ_{rest} / E_c). If the ratio between restraint stresses and real length change is expressed by a so-called restraint degree a, it can be written in the uncracked state:

$$(\alpha_T \cdot \Delta T + \varepsilon_{cas} + \varepsilon_{cds} + \varepsilon_{cc}) \cdot a = -\frac{\sigma_{rest}}{E_c} \tag{6}$$

If restraint stresses exceed a certain limit value of the tensile strength, cracking is to be expected. After cracking the deformation compatibility has to take into account the cracks with their certain width as well. As explained before, the geometric set cracks separate the member in independent parts with a length of l_{cr}, so that the deformation compatibility can be verified representatively for one primary crack in the length of l_{cr}. Besides, the stiffness of the restrained member decreases due to cracking, so that the restraint degree increases in all cases where the restraining condition is the same after cracking. With regard to the restrained deformation in the transfer length, it can be written for the cracked state:

$$(\alpha_T \cdot \Delta T + \varepsilon_{cas} + \varepsilon_{cds} + \varepsilon_{cc}) \cdot a^{II} \cdot l_{cr} = -\left[\frac{\sigma_{rest}^{II}}{E_c} \cdot l_{cr} + s_r \cdot (1 - k_t) \cdot \left(\varepsilon_{sm} - \frac{\sigma_{rest}^{II}}{E_c}\right)\right] \tag{7}$$

And on basis of the equilibrium between steel force in the primary crack and concrete force in the uncracked part between the primary cracks, the crack width amounts:

$$w = -(\alpha_T \cdot \Delta T + \varepsilon_{cas} + \varepsilon_{cds} + \varepsilon_{cc}) \cdot a^{II} \cdot l_{cr} - \frac{\sigma_s \cdot A_s}{E_c \cdot A_c} \cdot \left(l_{cr} - (1 - k_t) \cdot s_r \cdot (1 - k_t)\right) \tag{8}$$

Finally, the required reinforcement to limit the crack width under consideration of the deformation compatibility amounts:

$$A_s = \frac{-(\alpha_T \cdot \Delta T + \varepsilon_{cas} + \varepsilon_{cds} + \varepsilon_{cc}) \cdot a^{II} \cdot l_{cr} - w_k}{\left(l_{cr} - (1 - k_t) \cdot s_r \cdot (1 - k_t)\right)} \cdot \frac{E_c \cdot A_c}{\sigma_s(w_k)} \tag{9}$$

The solution of Eq. (9) is not trivial, the following are the main challenges:

- determination of the restraint degree after cracking, in particular if present reinforcement has significant influence,
- consideration of remaining concrete stresses in the uncracked part between two primary cracks, especially if these stresses vary over the height of the cross section and along the member length as in case of bottom-restrained members (e.g. walls on foundations) and
- consideration of secondary cracking.

A possible simplification is that the primary crack or the crack system consisting of primary crack and secondary cracks will have to absorb the entire restrained deformation of the uncracked state. In practical cases, this assumption is conservative because the restrained deformation in the concrete between primary cracks after cracking is neglected, even though it is bigger than the influence of any possible increase of the restraint degree after cracking. But it is also appropriate because demanding iterations due to the above listed points can be avoided. It reads:

$$w^P + \sum_{i=1}^{n} w_i^S = \frac{\sigma_{rest}}{E_c} \cdot l_{cr} \tag{10}$$

The basic idea of Eq. (10) is to create as many secondary cracks in the surrounding of the primary crack as needed to limit the crack width in the primary crack. The required number of secondary cracks can be determined with regard to the crack width criteria w_k and the simplification behind Eq. (10) by:

$$n = \left(\frac{\sigma_{\text{rest}}}{E_c} \cdot l_{cr} \cdot \frac{1}{w_k} - 1\right) \cdot 1.1 \tag{11}$$

The decreasing width of subsequently occurring secondary cracks in comparison to the width of the primary crack is expressed by the factor 1.1 which covers relevant practical situations.

The minimum reinforcement required can be derived from the number of secondary cracks n, where n is rounded up to the next integer. If $n \leq 0$ the deformation compatibility is already fulfilled with the width of the primary crack and reinforcement for crack width control is not needed. Only a skin reinforcement taking up the cracking force of the effective concrete area would be recommended. All other cases require active crack width control and the required minimum reinforcement can be determined according to [8]. Altogether, it reads:

$$n \leq 0: \quad A_{s,req} = \frac{f_{ctm}}{f_{yk}} \cdot A_{c,eff} \tag{12}$$

with: f_{ctm} ..... *number of secondary cracks required*
f_{yk} ..... *yield strength of reinforcement*
$A_{c,eff}$ ..... *effective concrete area (normally 2,5 · d_1 · b)*

$$n > 0: \quad A_{s,req} = \sqrt{\frac{d_s \cdot b^2 \cdot d_1^2 \cdot f_{ct,eff} \cdot (0.69 + 0.34 \cdot n)}{w_k \cdot E_s}} \tag{13}$$

with: d_s ..... *reinforcement diameter*
b ..... *width in direction viewed (normally 1 m)*
d_1 ..... *edge-distance of the reinforcement*
$f_{ct,eff}$ ..... *decisive tensile strength of concrete*
w_k ..... *crack width criteria*
E_s ..... *elastic modulus of reinforcement*

3.1 Application for members which are primarily restrained

In the majority of primarily restrained members, the quantification of restraint stresses respectively the restrained deformation to be absorbed requires a time discrete analysis. On the one hand, the deformation impacts appear usually by time, whereas an enormous part already occurs in the hardening phase interacting with considerable stiffness changes of the concrete. On the other hand, the size and course of time of creep deformations strongly depends on the stress history and can hardly be predicted a priori. To quantify the restrained deformation various analytical, semi-numerical or numerical approaches are available in the literature. The application of these models still require expertise beyond practical engineering knowledge. Implemented material models and their calibration to the behaviour of the

concrete used as well as considered boundary conditions (thermal and mechanical ones) can have a significant influence on the determined restrained and should be verified carefully. Some minimum standards of the latter are shown in Fig. 3 for the practical cases.

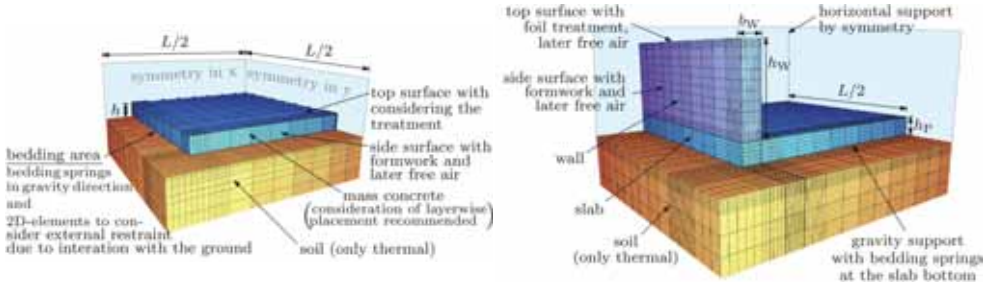

a) ground slab *b) wall on a foundation*

Figure 3: Volumetric idealizations of typical concrete members which are primarily restrained

If the restrained deformation is quantified and cracking cannot be excluded, the required minimum reinforcement can be determined with Eq. (11) - Eq. (13). It should be mentioned that residual stresses should be removed from the decisive stress distribution before applying Eq. (11). The reason is that residual stresses or so-called *Eigenstresses* are self-balanced within the cross section and will usually cause solely microcracks or small, locally restricted cracks. Of course, this pre-damage can be the starting point of a macrocrack, however, residual stresses decrease considerably in the cross section by this time and have no relevant contribution to the opening of the macrocrack. Fig. 4 illustrates these thoughts.

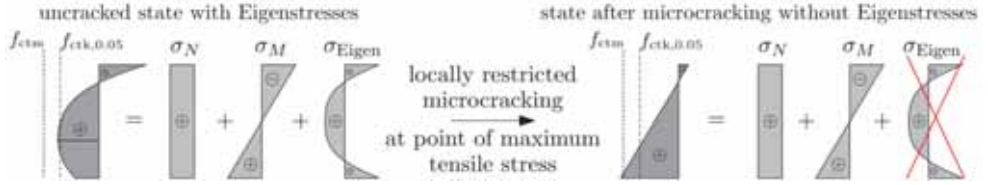

Figure 4: Role of residual stresses or so-called *Eigenstresses* on the process of macrocracking

Application examples of this approach are given in [3] and [9]. Further considerations with focus on hardening-induced stresses in very thick concrete members were presented in [10].

3.2 Application for members with significant interaction of restraint and loads

In contrast to members which are primarily restrained and which show therefore a geometric set crack pattern, the application in case of significant interaction of restraints and loads has to consider members with areas being considerably stressed respectively already showing distinct crack patterns. An illustrative example is jointless floors which are end-restrained by building cores and/or retaining walls. On the one hand, such floors are permanently subjected to bending due to loads (self-weight as well as service loads) and on the other hand, imposed deformations (early age effects as well as drying shrinkage and temperature changes during

service life) will cause a restraint force due to interaction with the restraining condition, as illustrated in Fig. 5. The size of the occurring restraint force N_{rest} depends not only on the stiffness of the restraining condition but also on the released deformation in the cracks. This means, the deformation compatibility can be complied by the elongation of the member in the cracked areas as well as the restrained deformation in the uncracked parts.

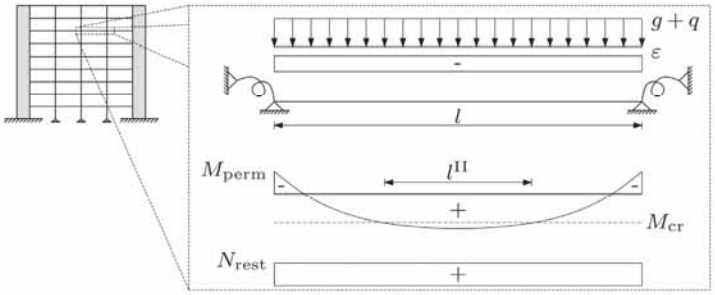

Figure 5: Interaction of restraint and loads in case of jointless floors between cores

Taking into account the imposed and remaining deformation due to hardening (ε_0), drying shrinkage and affine creep ($\varepsilon_{cds} + \varepsilon_{cc}$) as well as temperature induced shortening during service live ($\alpha_T \cdot \Delta T_N$) the deformation compatibility can be complied according to Eq. (1) and Eq. (7). In case of bending, as in the present example, it is also important to consider the decrease of released deformation between opening of the bending crack and elongation of the the member itself. By simplifying this context in the first step with a conservative assumption of a plane section in the bending crack but neglecting the concrete strain in the compression zone, this effect can be represented by a factor of 0.5. Finally it reads:

$$[\varepsilon_0 + (\varepsilon_{cds} + \varepsilon_{cc} + \alpha_T \cdot \Delta T_N) \cdot a] \cdot l = -\left[\frac{\sigma_{c,m}}{E_c} \cdot \left(l - l^{II}\right) + 0.5 \cdot \varepsilon_{sm} \cdot l^{II}\right] \quad (14)$$

Hereby, l stands for the member length (in case of the floors it would be one field) and l^{II} represents the length with a distinct crack pattern within l. With regard to the steel stress limitation under permanent loads, which may not assure a stabilized crack pattern over the full length, the required length of the floor to be in a cracked state can be determined following Eq. (14) by:

$$l^{II}_{req} = \frac{\left[\varepsilon_0 + (\varepsilon_{cds} + \varepsilon_{cc} + \alpha_T \cdot \Delta T_N) \cdot a + \frac{\sigma_{c,m}}{E_c}\right]}{\frac{\sigma_{c,m}}{E_c} - 0.5 \cdot (1 - k_t) \cdot \frac{\sigma_s(w_k)}{E_s}} \cdot l \quad (15)$$

For the solution of Eq. (15), the average concrete stress in the uncracked part ($\sigma_{c,m}$) has to be determined iteratively. In detail, all cases where the required length to be cracked is already smaller than the cracked length due to permanent loads, no restraints occur at all and $\sigma_{c,m}$ is zero anyway. In all other cases, $\sigma_{c,m}$ will increase up to a size with which the superposition of bending stresses due to permanent loads and $\sigma_{c,m}$ will have created a sufficient long cracked

length. The hereby occurring size of $\sigma_{c,m}$ can be determined with Eq. (16) whereas the location of the decisive moment under permanent loads is illustrated in Fig. 6.

$$\sigma_{c,m} = \max.\left\{0; f_{ctm} - \frac{M_{perm}(x^{II})}{W}\right\} \tag{16}$$

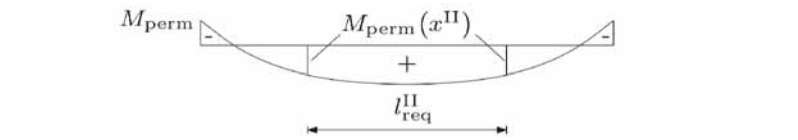

Figure 6: Interaction of restraint and loads in case of jointless floors between cores

Finally, the required reinforcement can be determined by a transformation of Eq. (3) in form of:

$$A_{s,req} = \sqrt{\frac{F_{cr} \cdot (F_s - k_t \cdot F_{cr}) \cdot d_s}{2 \cdot \tau_{sm} \cdot E_s \cdot w_k}} \tag{17}$$

The force to be taken by the reinforcement (F_s) results hereby from the moment under permanent loads as well as from the restraint force with a size of:

$$N_{rest} = \sigma_{c,m} \cdot A_c \tag{18}$$

The application of this approach in several building constructions, e.g. "*Konzernzentrale Premiere München-Unterföhring*" with an irregularly shaped 180 m long jointless floor constrained by several very stiff cores or "*Highlight Towers Parkstadt Schwabing*" with 33 levels of 80 m long floors constrained by two cores, showed, that this enables a very efficient design under avoidance of expansion joints. The most important point is hereby, that the restraint force under consideration of the stresses due to loading is much smaller than the usually considered cracking force. This provides not only efficient reinforcement amounts in the floors but also an appropriate consideration of the interaction between the floors and the building cores.

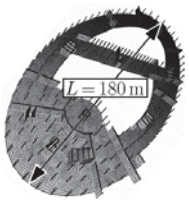

Konzernzentrale Premiere München-Unterföhring

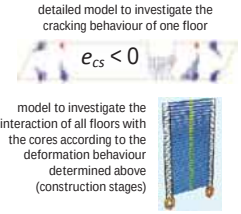

Highlight Towers Parkstadt Schwabing

Figure 7: Interaction of restraint and loads in case of jointless floors between cores

4. Discussion and conclusion

It is standard practice to determine the required minimum reinforcement for crack width control on basis of the cracking force respectively the cracking moment. However, such procedure neglects the deformation compatibility along the member length and the interaction of restraints and external loads is not considered appropriately. Altogether, this can lead to structural damage in form of leaking cracks in watertight constructions or to inefficiency.

This contribution presents fundamentals on a new design concept which bases on the verification of the deformation compatibility. The biggest improvement of this approach is the realistic consideration of the occurring restraints with respect to its decreasing by formation of any new crack. The approach can be applied for primarily restrained members as well as for members with significant interaction of restraint and loads. By taking into account the real deformation impact on the member as well as the member dimensions, the empiricism of minimum reinforcement design for crack width control due to restraint is reduced significantly. Furthermore, the flow of forces in constructions with significant interaction of restraint and loads can be taken into account realistically. Besides the benefits of mechanical proof, this concept also provides an opportunity for direct cooperation between concrete technology, structural design and construction site, offering an important contribution to the crack width control of concrete members.

References

[1] EN 1992-1-1:2004 + AC:2008: Eurocode 2: Design of concrete structures - Part 1-1: General rules and rules for buildings
[2] SIA 262:2003: Norm SIA 262 Betonbau
[3] Schlicke, D. and Tue, N.V., Minimum reinforcement for crack width control in restrained concrete members considering the deformation compatibility, Structural concrete 16 (2015), 221-232, doi: 10.1002/suco.201400058
[4] König, G. and Tue, N.V.: Grundlagen des Stahlbetonbaus. 3. Auflage. Vieweg + Teubner Verlag (2008)
[5] König, G. and Tue, N.V.: Grundlagen und Bemessungshilfen für die Rissbreiten-beschränkung im Stahlbeton und Spannbeton. DAfStb Heft 466. Beuth-Verlag, (1996).
[6] Tue, N.V. and Pierson, R. Ermittlung der Rißbreite und Nachweiskonzept nach DIN 1045. Beton- und Stahlbetonbau 96 (2001), 365–372, doi: 10.1002/best.200100390
[7] Knoppik-Wróbel, A. and Schlicke, D.: Computational prediction of restraint-induced macrocrack patterns in reinforced concrete walls. In: Proceedings of MSSCE2016 / Service Life Segment, Lyngby, Denmark (2016)
[8] Bödefeld, J.: Rissmechanik in dicken Stahlbetonbauteilen bei abfließender Hydratations-wärme, PhD thesis, University of Leipzig (2010)
[9] Schlicke, D., Mindestbewehrung für zwangbeanspruchten Beton, PhD thesis, Graz University of Technology (2014)
[10] Heinrich, J. P. and Schlicke, D.: Hardening-induced stresses in very thick concrete members – Insights from comprehensive FE-Studies. In: Proceedings of MSSCE2016 / Service Life Segment, Lyngby, Denmark (2016)

International RILEM Conference on Materials, Systems and Structures in Civil Engineering
Conference segment on Service Life of Cement-Based Materials and Structures
22-24 August 2016, Technical University of Denmark, Lyngby, Denmark

CEMRS: FAST AND EFFICIENT MODELLING PLATFORM FOR THE SIMULATION OF CEMENTITIOUS SYSTEMS

Shiju Joseph [(1)], Shashank Bishnoi [(2)], Koen Van Balen [(1)], Özlem Cizer[(1)]

(1) Building Materials and Building Technology Division, Department of Civil Engineering, KU Leuven, Belgium
(2) Department of Civil Engineering, IIT Delhi, India

Abstract
A new microstructural modelling platform, CemRS (Cementitious binders Reaction Simulator), is developed in C++ for simulating the hydration kinetics and microstructure of cementitious systems. It takes into account different materials which could be defined as a reacting material or which will act as a filler. CemRS can be used to implement several existing models such as Avarami kinetics or boundary nucleation and growth etc. or it could be used to simulate and validate original research models. It takes into account the particle size distribution of the reactant and filler so that the effect of fineness is incorporated. The statistical approach of storing particle sizes makes sure that the speed of the program is increased by several orders without the need of truncation of the particle size distribution. In this paper CemRS is used to simulate alite hydration with fillers with a new model, densified volume growth (DVG) model which is a time dependent nucleation and growth model. The paper demonstrates the ability of the modelling platform to simulate complicated models with high efficiency and accuracy.

1. Introduction

Cement hydration is a very complex process which depends on a wide range of parameters. The complexity of the system makes it very difficult to analytically predict the reaction kinetics or microstructure development. Hence different numerical microstructural models such as μic [1], CemHYD3D [2], Hymostruc [3], HydratiCA [4] etc. are being used to model different cementitious systems. One of the primary objectives of these models is to use the results from the microscale to predict the characteristics of concrete in the macro level.

Among the major parameters, the one which has a significant influence on the hydration kinetics, and which is easy to control is the fineness of the binder and partial replacement of

clinker with fillers or supplementary cementing materials. For localized applications, fineness can be easily modified by varying the discharge rate of clinker from the ball mill. At the same time modifying the clinker composition might not be practical in those cases. Hence numerical models which can predict the effect of fineness and clinker replacement has a significant effect on the practical side.

Traditionally modelling platforms truncate the particle size distribution (PSD) for reducing the computational cost. PSD are generally truncated with a maximum and minimum diameter. Truncation of maximum diameter is to reduce the computational volume as computational volume must be sufficiently large to be representative. On the other hand a minimum diameter is to reduce the total number of particles. For a multiscale application, the microscale model must be fast enough so that it can be simulated on hundreds or thousands of nodes in a macro level.

In this paper a new microstructural modelling platform is introduced, CemRS, which could model different cementitious systems such as alite, C_3A, blended cement etc. incorporating the full PSD without the need of truncation. The algorithms used to develop CemRS ensure very high computational speed without compromising the accuracy due to a truncated PSD.

2. Effect of Truncation on degree of hydration

The effect of truncation of PSD on degree of hydration depends primarily on the mechanism of hydration which is used. Assuming a uniform reactive thickness concept, a dissolution or diffusion based mechanism will hardly make significant errors on the numerical modelling scheme [5]. On the other hand, a nucleation and growth based mechanism which takes into account the surface area of the reactants and products will significantly have an effect on the degree of hydration.

Figure 1 shows the effect of truncation of alite at 0.2μm and 0.5μm. Alite of 17 μm mean diameter and 3600cm^2/g Blaine surface area is simulated using a modified boundary nucleation and growth (BNG) [6] mechanism. A deviation from the non-truncated PSD can be observed for PSD with truncation. In the modified BNG, it was assumed that individual particles that are fully hydrated will not grow further. This assumption in effect reduces the deviation from the original PSD drastically and hence this is a very modest account on the effect of truncation.

The effect of truncation on number of particles and calculated Blaine surface area is illustrated in Figure 2. It is evident that truncation of PSD can reduce the number of particles significantly and hence reduce the computational cost for traditional modelling platforms. But at the same time, this truncation is having a large effect on the surface area of the particle. As most nucleation and growth models assumes uniform growth rate on particles, the difference in the outer surface area of the products will be on a much higher scale.

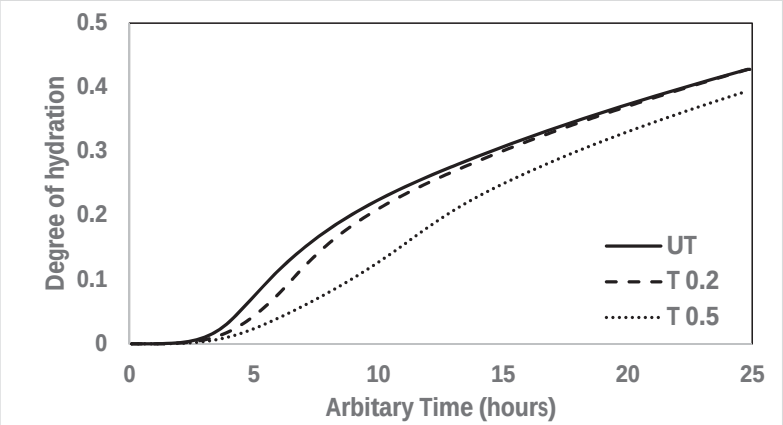

Figure 1: Effect of truncation of PSD on the degree of hydration of alite using a modified BNG model. UT - PSD without truncation, T 0.2 - PSD truncated at 0.2μm, T 0.5 - PSD truncated at 0.5μm

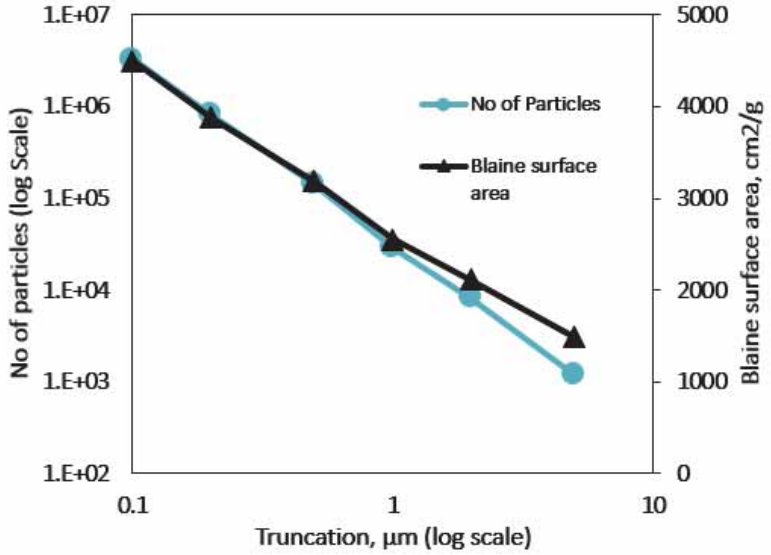

Figure 2: Effect of truncation of PSD on the number of simulated particles and numerically calculated Blaine surface area

3. Structure of CemRS

CemRS is a modelling platform which is written entirely in C++ using the object oriented approach. This program was developed based on the microstructural modelling platform μic

[1]. One of the major drawback of other modelling platforms is its rigidity of the hydration mechanism used for simulations. Depending on material, a different hydration mechanism has to be used. For eg. mechanism for hydration of C_3S cannot be used for simulating hydration of C_3A. This is not only significant for the purpose of kinetics, but also relevant on the growth and densification of outer products which has significant influence for micromechanical modelling or modelling transport properties.

3.1. Statistical modelling of PSD in CemRS

Traditionally microstructural modelling platforms model particle size distributions by randomly placing every single particle in the computational space. The computational complexity increases by adding the Cartesian coordinates of the particles along with the size into the memory. This was an absolute necessity as it was assumed that the impingements between the particles as the major reason for the deceleration period in alite. But it was later showed that impingements cannot be a reason for the deceleration as there is not a significant change in the hydration rate when the available space for hydration is changed by changing the water to cement ratio [7].

In CemRS, particles are modelled in a statistical approach along with the traditional approach. Traditional approach is used for microstructure development whereas statistical approach is used for the mathematical calculations. The statistical approach is similar to one used in Hymostruc [3]. The number of particles in range of each diameter is calculated from the PSD, and the hydration mechanism is applied on the set of particles rather than on each individual particle. This information is passed on to the PSD modelled in the traditional modelling approach to model the microstructure. This would reduce the computational requirement enormously as a few hundred particles are only required to simulate instead of billions of particles. This reduction is huge in terms of computational costs as it could reduce hours of computation to merely few seconds. Nevertheless to preserve the accuracy it is only needed to ensure that there are more sets of particles than the results from the laser diffraction experiment which is used to model the same. It must be noted that statistical approach shall be used only for the mechanisms where microstructural information such as impingements are not required. CemRS has the flexibility to choose from different particle distribution approaches.

3.2. Reaction mechanism

As the field of cement chemistry is rapidly developing over the years, CemRS is equipped with using existing and new reaction mechanisms. Each cementitious system would be required to use different reaction mechanisms. This model is equipped to handle more complicated reaction mechanisms, which is made possible due to the statistical particle modelling approach which reduces the computational time. CemRS is pre-equipped with different hydration models such a Avarami equation [8] [9] [10] [11], uniform reaction zone approach [12], BNG [6]and variations of BNG such as Reaction zone [13]. In addition to these models, a new model named densified volumetric growth (DVG) model is also developed by this authors. This model includes complicated calculations of hydrates with time dependent varying growth rate and densification of C-S-H and are calculated with concentrated layers around each particle. New models are under development for simulating

different cementitious systems. The predefined modules or classes would make it rather simple to develop new reaction.

4. Simulation in CemRS

For the purpose of demonstration of CemRS, the heat evolution from isothermal calorimeter of a triclinic C3S replaced 35% with fine quartz is modelled in Figure 3 using DVG model. Full PSD of 17μm mean diameter C3S and 18 μm mean diameter fine quartz ranging from 0.01μm to 300μm is modelled for the simulation of kinetics and traditional truncated PSD was used for modelling the microstructure. The model uses a time dependent growth rate mechanism incorporating the effect of fillers. It took around 20 seconds for this simulation on a normal computer with dual core processor.

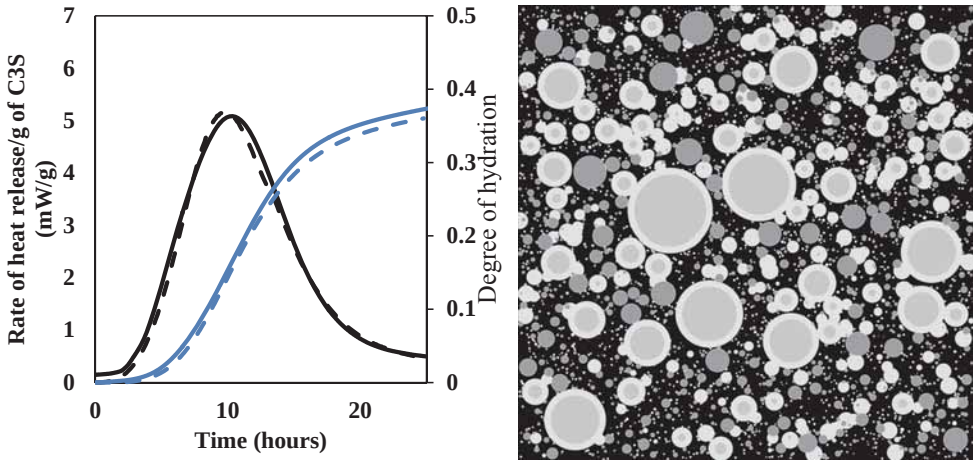

Figure 3: *(left)* Experimental(continuous line) and simulated(dashed line) heat release (black) and degree of reaction(blue) of C3S replaced with 35% fine quartz, *(right)* microstructural slice after 20 hrs of simulation. Pores are represented in black, alite in lighter shade of grey and quartz on darker shade of grey and reaction products in white.

5. Conclusions

A new microstructural modelling platform named CemRS is introduced in this paper which could simulate different cementitious systems. New hydration models can be developed and can be simulated for the mathematical validation. The modelling platform is able to simulate a full particle size distribution without the need of truncation. CemRS is computationally very efficient with a low requirement of memory space and high speeds. The high speed on the micro scale gives a future prospect for application in macro scale.

References

[1] Bishnoi S. and Scrivener K. L., mic: A new platform for modelling the hydration of cements, Cement and concrete research 39 (2009), 266-274,
[2] Bentz D., Three-dimensional computer simulation of portland cement hydration and microstructural development, Journal of the american ceramic society 80 (1997), 3-21
[3] Van Breugel K., Simulation of hydration and formation of structure in hardening Cement-Based materials, PhD Thesis, TU Delft (1991)

[4] Bullard J. W., Enjolras E., George W. L., Satterfield S. G. and Terrill J. E., A parallel reaction-transport model applied to cement hydration and microstructure development, Modelling and simulation of materials science and engineering 18 (2010), 16
[5] Joseph S. and Bishnoi S., Study on the effect of particle size distribution and Blaine fineness on the hydration of cement, CONMOD, Beijing (2014)
[6] Thomas J., A new approach to modelling the nucleation and growth kinetics of tricalcium silicate hydration, Journal of the american ceramic society 90[10] (2007) 3282-3288
[7] Kirby D. and Biernacki J. J., The effect of water to cement ratio on the hydraion kinetics of tricalcium silicate cements: testing the two step hydration hypothesis, Cement and Concrete research 42[8] (2012) ,1147-1156
[8] Avarami M., Kinetics of phase change I, Journal of chemical physics 7 (1939), 1103-1112
[9] Avarami M., Kinetics of phase change II, Journal of chemical physics 8 (1940), 212-224
[10] Johnson W. and Mehl R., Reaction kinetics in processes of nucleation and growth, Transactions of American Institute of Mining and Metallurgical Engineers 135(1939) 416-458
[11] Kolmogorov A., A statistical theory for the recrystallization of metals, Bulletin of the academy of sciences of the USSR. division of chemical sciences 3(1937) 355-359
[12] Termkhajornkit P. and Barbarulo R., Modelling the coupled effects of temperature and fineness of Portland cement on the hydration kinetics in cement paste, Cement and concrete research 42[3] (2012), 526-538

International RILEM Conference on Materials, Systems and Structures in Civil Engineering
Conference segment on Service Life of Cement-Based Materials and Structures
22-24 August 2016, Technical University of Denmark, Lyngby, Denmark

CHLORIDE ION DIFFUSION IN CONCRETE UNDER TENSILE LOAD

Ling Wang [(1)], Yan Yao[(1)], Zhendi Wang[(1)], Yin Cao[(1)], Juan Li[(1)]

(1) China Building Materials Academy, Beijing, China

Abstract
Research on chloride ion's diffusion mechanism in concrete under the situation which combines applied mechanical stress and environmental actions load is approaching the real damage process and the actual behavior of concrete in service. A modified test rig and a new test method to test the chloride ion's diffusion in concrete under tension was proposed by the RILEM TC 246-TDC through the comparative test. Test results showed that the effect caused by the combination of tensile load and environmental loads usually may turn out to be much more severe than the effect of single component. A field case in Hong Kong-Zhuhai-Macao Bridge was also included. Deep work in this field, such as service life prediction, needs to be done in the future.

1. Introduction

One dominant deteriorating process such as carbonation or chloride penetration is usually considered to predict the service life of reinforced concrete structures [1, 2]. Experimental results and observation in practice show that it is not a realistic and certainly not a conservative approach. A lot of attention have been paid to the topic of the synergistic effect of multiple factors affecting the concrete durability.[3-9]. Research indicates that the combination of mechanical and environmental loads may turn out to be much more severe consequence than a single load. This synergetic effect has been neglected so far.

Although plenty of studies have been conducted, more research is needed to obtain reliable and quantitative results. The combination of uniaxial tension and chloride penetration may be the most difficult one.Although there's limited data, it still suggested the transport behavior of chloride ion in concrete under the uniaxial tensile stress is very complicated.The measured critical stress ratio range widely [10-11].The differences in the test device, loading history and

solution concentration may result in different critical stress level and make the related results cannot be compared and analyzed [12].

All test method inevitably faces such problems, the eccentricity of tension, stress relaxation and unstable diffusion of chloride ion. The major aim of RILEM Technical Committee 246-TDC is developing the test method in order to study the behaviour of concrete under combined actions such as mechanical load and environment factors. Based on the outcome of the annotated bibliography [13], we, together with other international labs, have prepared a detailed test method for the study of chloride ion diffusion in concrete under stress recently.

2. Experiments

2.1 Test rigs

2.1.1 Test rig for tensile load

Tensile stress was applied on the dumbbell-like concrete specimens using a specially designed test rig to minimize uniaxial eccentricity (see Fig. 1).

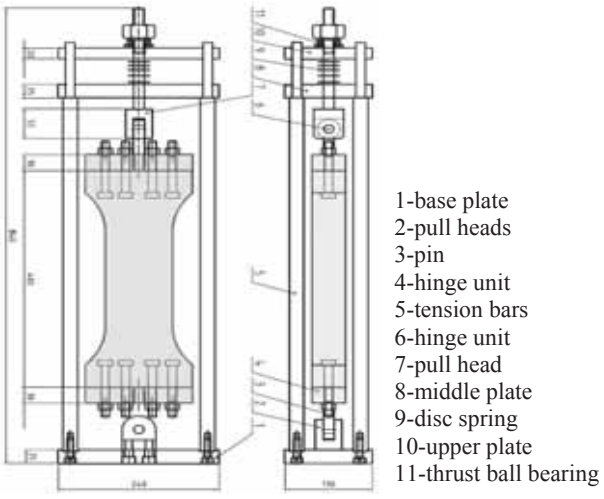

Figure 1: Schematic diagram of the test rig for tension.

Some innovations have been adopted in the design of the test rig to ensure the applied tensile stress on the specimen keeps vertical.

- **The hinge units.** The hinge units are connected to the top and bottom ends of the concrete specimen by screwing threads. They can eliminate the uniaxial eccentricity which might take place by turning in the xOz plane and the yOz plane.

- **The square hole in the middle plate.** There is a square hole in the middle plate, which locks firmly with the square portion of the pop rivet to avoid the occurrence of torque to the specimen.
- **The strain gauges on the tension bars.** The tension bars are equipped with two strain gauges in order to avoid excessive eccentricity and to control stress relaxation. If any stress value deviates from the set threshold, the adjustment is needed to keep it constant.

2.1.2 Test rig for chloride solution circulation

A chloride solution circulation setupwas applied on the open window of the prism specimens for compression and the dumbbell-like specimens for tension respectively. The solution circulation setupmainly comprises of 3 parts.

- **A saltwater tank,** which is a box made up of transparent, organic glass with one side opening. The inner dimension of the tank is 80x160x50 mm. The salt water tank was adhered to the open window of the concrete specimens using silicone. The transparent back of the tank allows easy and continuous observation of the flux of the liquid.
- **A constant flow pump,** which is adapted to circulate the 3 wt. % chloride sodium salt solution with a pre-defined speed of 5±1 ml/s.
- **A reservoir,** containing about 25 liters of aqueous salt solution (3 wt. % NaCl), which is connected to the salt water tank with tubes. The concentration of the solution was checked regularly at least once a week during the whole exposure period, and the chloride solution was isolated from the atmosphere by a cap to avoid evaporation and contamination.

2.2 Preparations of specimens

Concrete with the mix proportion of cement : water : fine aggregate : coarse aggregate =1:0.45:2.28:2.79 was prepared in this study. Type I Portland cement was used as the binder. The cement content is 368kg/m^3. Polycarboxylate superplasticizer was used to adjust the concrete slump as about 15 cm. The concrete was cast into dumbbell-like specimens. To connect with the tensile testing rig, four bolts were embedded in each end of the dumbbell-like tension specimen before casting (see Fig. 2). The ultimate tensile strength of the dumbbell-like concrete specimens at 28 d was 3.3 MPa.

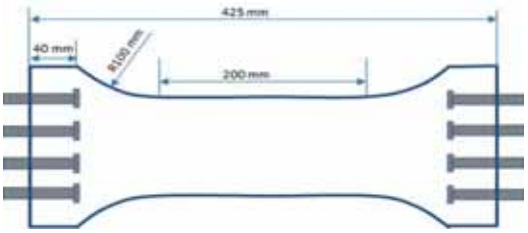

Figure 2: Dimensions of specimen for tension

A thin film of Teflon was applied to the internal faces of all the moulds in replace of the demoulding oil. After casting, the specimens were stored in a room maintained at 20°C and about 95% relative humidity (RH) for 24 h. Then, the samples were removed from the moulds and further cured in water at 20°C until testing. The tensile stress ratio, which is the ratio of

applied stress to the ultimate tensile stress, is taken at 0, 50%, and 80%. The dumbbell-like specimens were unloaded after an exposure time of 2, 6, 18 and 36 weeks, after which the specimens were ready for chloride profile determination.

2.3 Determination of chloride profiles

The plastic tank was removed from the unloaded specimens after a given exposure time. Powder from the exposure surface of all the specimens was obtained stepwise by milling layers of 1 to 2 mm thickness. The thickness of the layers was adjusted according to the expected chloride profile so that a minimum of 8 points covers the profile between the exposed surface and a depth where the chloride content reaches the initial chloride content. Chloride contents dissolved in acid were determined by chemical analysis according to EN 14629.

3. Results and discussion

3.1 Typical chloride profiles for 0,50 % and 80 % stress ratio

Fig.3 shows the chloride profile under different tensile stress ratio and different exposure duration.

It can be seen that with the increase of depth, the chloride content decreases and gradually approaching the initial chloride content. Meanwhile, the maximum chloride ion penetration depth has a direct relationship with the exposure time in all the stress ratio conditions.

When a 50% tensile stress ratio is applied, the chloride content in a certain layer is higher than the content at the same layer but without load. And when the stress ratio reaches 80%, the difference in chloride contents at the same depth is more significant. This shows that cracks inside concrete appeared and grew with the increase of stress ratio and loading time. The chloride transport in concrete under tensile stress is obviously more active than concrete without tensile stress.

3.2 Chloride's surface concentration and Diffusion coefficient

Figure 4 shows the chloride diffusion coefficient (4a) and modelled surface concentration (4b) determined by curve fitting according to EN12390-11: 2014 Annex F.

It can be seen that at the same exposure time, the diffusion coefficient of concrete under tension increases with the stress ratio. The tensile stress boosts chloride diffusion in concrete. Meanwhile, the diffusion coefficient decreases with the exposure time, no matter whether an external tensile stress is applied or not.

Due to the limited number of samples, the modelled surface concentrations of concrete under different stress ratios scatter in a relatively wide range. But it increases with exposure time and stabilize at values approaching 0.6 % for 36 weeks. The chloride profiles and the results of modelled surface concentrations also show the existence of the convection zone. However, the statistics are not very obvious. To get more reliable information on this, more tests are needed to be carried out.

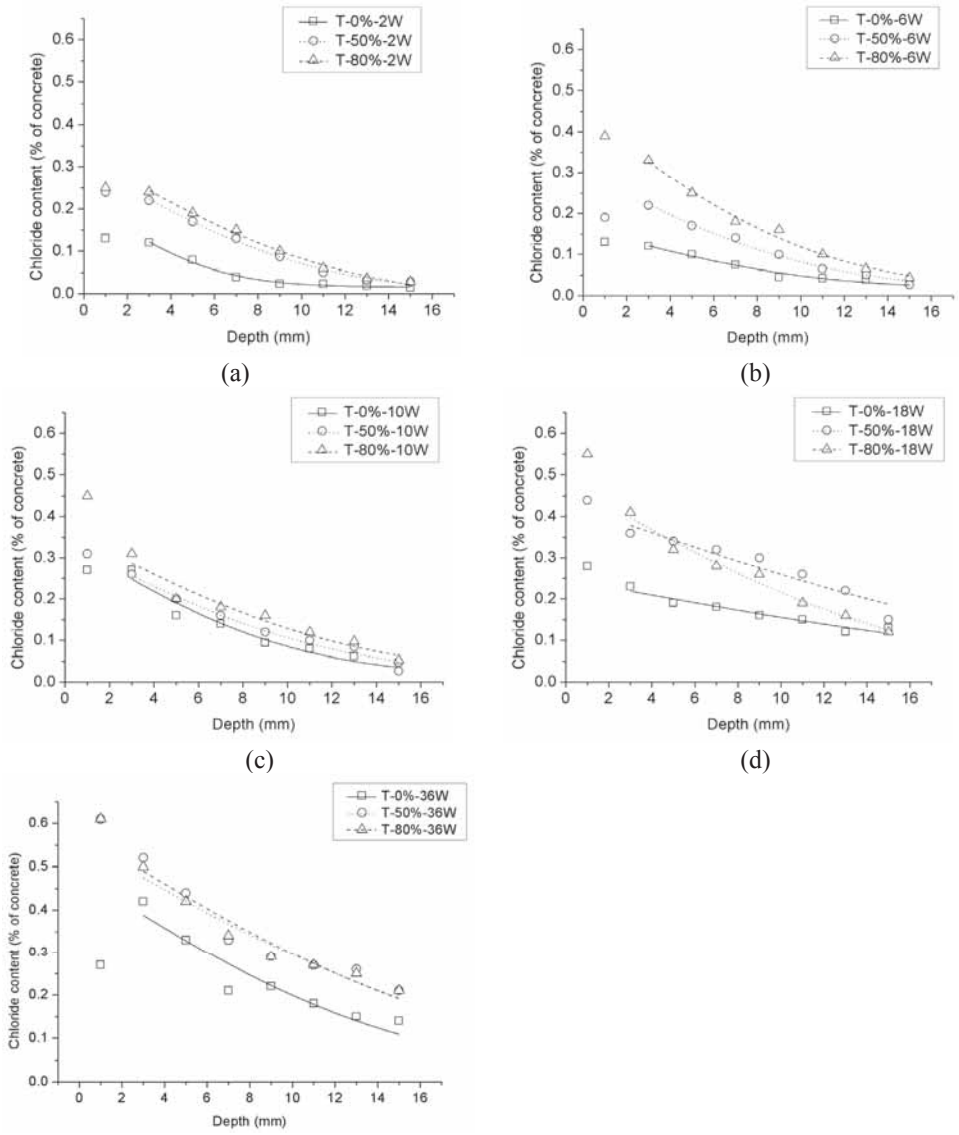

Figure 3: Chloride profiles determined after 2, 6, 10, 18 and36 weeks with 0, 50% and 80% tensile stress ratio

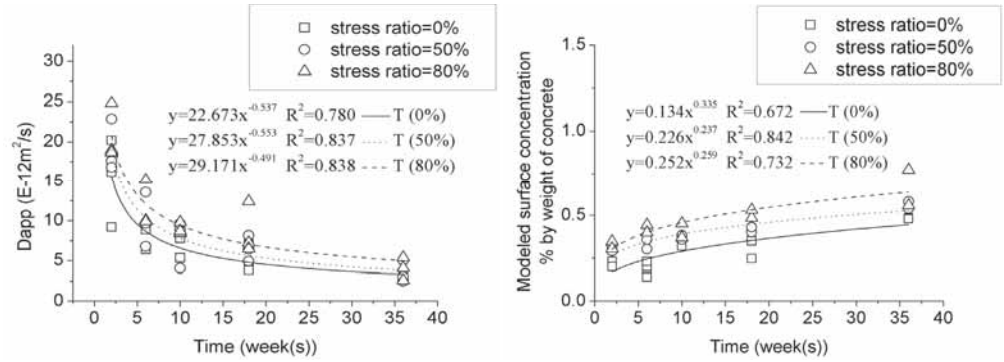

(a) (b)

Figure 4: Chloride ion diffusion coefficients and modelled surface concentrations of concrete under tension

The chloride content at the concrete surface depends on material properties, geometrical conditions, and environmental conditions. Meanwhile it may largely differ from the modelled surface concentration derived from regression analysis using the diffusion law. When a considerable convection zone is found, more points near the surface should be eliminated and then deeper layers should be drilled up. Accordingly, for the service life predictions, the content of chlorides at the substitute surface $C_{s,\Delta x}$ should be considered instead (with Δx the depth of the convection zone).

4. A case application in HZM bridge

The HongKong-Zhuhai-Macao Bridge (HZMB), crossing the Pearl River Estuary and linking HongKong to the East, and Zhuhai and Macao to the West, is a combination of several bridges, a tunnel, and some artificial islands. It is an ongoing infrastructure project. CB04 contract section of civil engineering construction of the main bridge of HZMB, is 7154m in length, refers to the mileage pile K22+083～K29+237.This section is almost in the middle of the whole bridge (see Fig.5). It consists of the north side non-navigable bridge (K22+083～K27+253, 5170m), navigable bridge (K27+253～K28+247, 5170m) and the west side non-navigable bridge (K28+247～K29+237, 990m).

The design and building task of this Section are being carried out by Guangdong Provincial Changda Highway Engineering Co. Ltd. Mixture proposition for the cast-in-site concrete which used in the connection zone between the piles and the bearing platform is shown in Table 1. The compressive strength at 28d is 57.5MPa.The concretes are strictly designed in compliance with Chinese national standard and the specification for HZMB project.

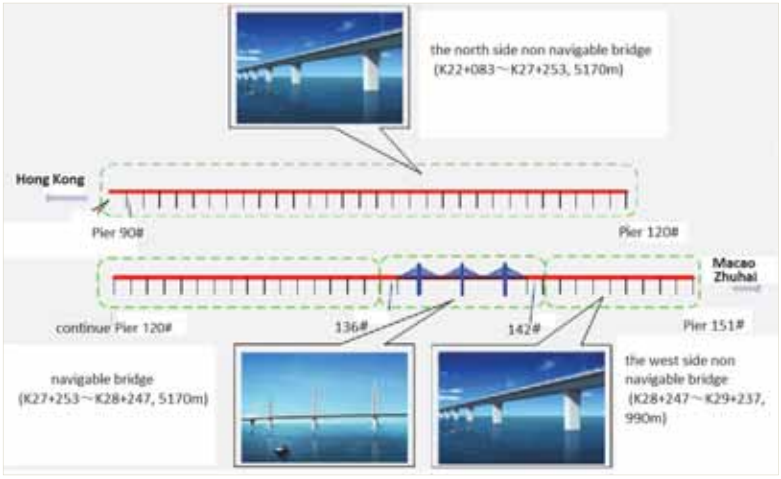

Figure 5: Bridge layout of CB04 contract section

Table 1: Mixture proportion of concrete in the connection zone in HZMB (kg/m^3).

Type	Cement	Fly ash	GGBFS	Expanding agent	Sand	Stone	water	SP
Cast-in-site	253	101	67	50	746	1054	143	7.157

The piles (Φ2m) and the gigantic concrete bearing platform（16.0m×12.0m×5.0m）will be under complicated sea conditions. The company wants to know the behavior of chloride diffusion in the immersed concrete elements under normal operating conditions and CBMA helped to carry on experiments on concrete durability under the combined action of the tensile load and the marine load according to the test method proposed by RILEM TC 246-TDC. In the experiment, we used a stress ratio (30 %) which is beyond the theoretical maximum value (18.5 %).Test results of typical chloride profiles, chloride diffusion coefficient, and chloride surface concentration and are shown in figure 6 and figure 7.

When a 30% tensile stress ratio is applied, the chloride content is higher than the matched group without load. The chloride transport in concrete under tensile stress is obviously quicker than the concrete without tensile stress.

The diffusion coefficient decreases with the exposure time, no matter whether an external tensile stress is applied or not. The diffusion coefficient of concrete under tension increases with the stress ratio at the same exposure time. The application of tensile stress speeds up chloride diffusion in concrete.

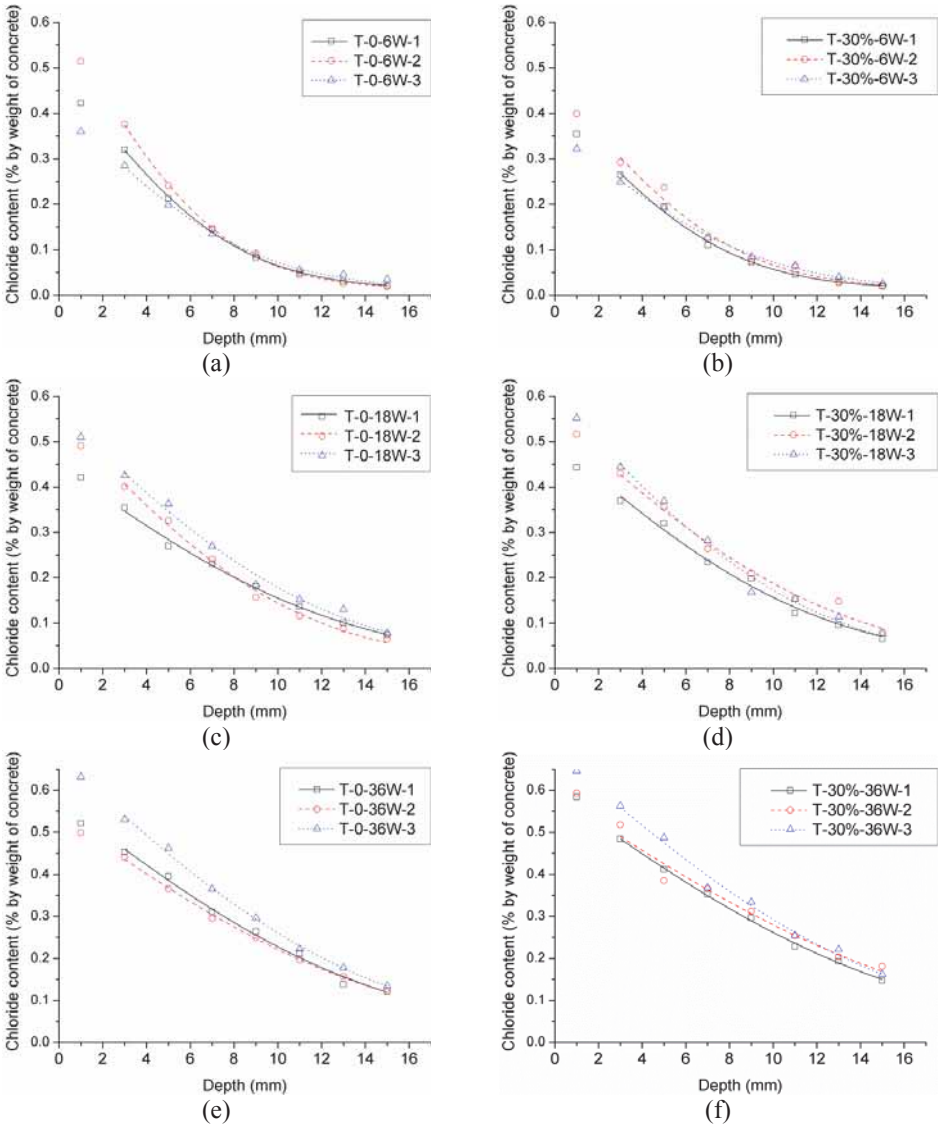

Figure 6: Chloride profiles at different exposure times at 0 % and 30% tensile stress ratio

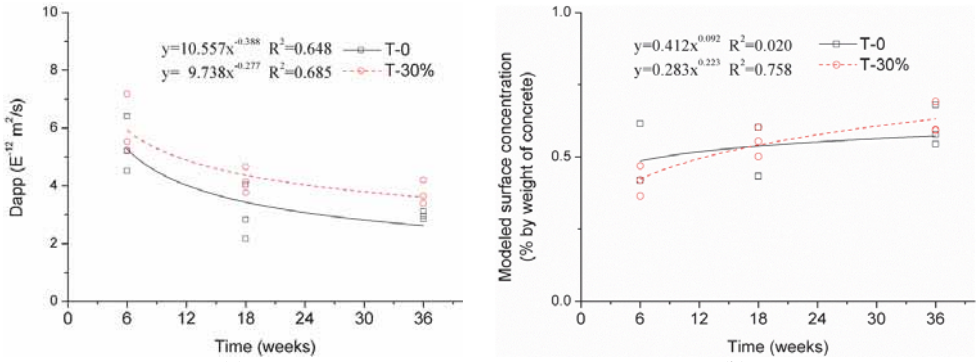

(a) (b)

Figure 7: Variation in time of the chloride ion diffusion coefficients and modelled surface concentration at 0 % and 30% tensile stress ratio

5. Conclusions

With some innovations in the design of the test rig, we construct an experiment rig ensuring tensile load keeps vertical inside the concrete specimen, which means the stress distribution in the middle part of the dumbbell-like concrete specimen homogenous. This development eliminates the influence of eccentricity, by which firstly put quantitative research on the relationship between chloride's diffusion and tension load under Ceteris Parabus Assumption (CPA). With this rig, the following conclusion was made:

1. With the new test rig, the measured statistics could be used to show quantitative relationships for the first time. The chloride profile in the specimen was firstly measured, which is shown as it decreases with the increased depth into concrete, gradually approaches the initial chloride content of the concrete. Meanwhile, the measured statistics also proved the assumption that the chloride diffusion depth increases with the exposure time, no matter the external load is applied or not.
2. With Fick's 2nd Law, a series of apparent chloride diffusion coefficients were calculated and a function was regressed. Compared with functions regressed in different tensile stresses, we concluded that the tensile stress enlarges the chloride diffusion coefficients.The effect caused by the combination of tensile load and environmental loads usually may turn out to be much more greater than the effect caused by one single component.

The regressed chloride diffusion coefficients under load may make the service life prediction of concrete structure more accurate. But deeper work in this field are still needed to be done in the future, such as the capillary absorption tests of partially pre-dried concrete specimens, influence of w/c ratio or supplementary cementitious materials, etc.

Acknowledgements

The financial support from the National Natural Science Foundation of China (Grant No.51320105016) is gratefully acknowledged.

References

[1] Gruyaert, Elke, Philip Van Den Heede, and Nele De Belie., Carbonation of slag concrete: Effect of the cement replacement level and curing on the carbonation coefficient – Effect of carbonation on the pore structure. Cement and Concrete Composites 35, no. 1(2013), 39-48. [2] Papadakis, VagelisG.,Effect of supplementary cementing materials on concrete resistance against carbonation and chloride ingress. Cement and Concrete Research 30 (2000), 291-299.
[3] Banthia N., Biparva A., and Mindess S., Permeability of concrete under stress. Cement and Concrete Research 35, no. 9 (2005), 1651-1655.
[4] Castel, A, R François, and G Arliguie., Effect of loading on carbonation penetration in reinforced concrete elements. Cement and Concrete Research 29 (1999), 561-565.
[5] Desmettre, C, and J.-P. Charron., Water permeability of reinforced concrete with and without fiber subjected to static and constant tensile loading. Cement and Concrete Research 42, no. 7 (2012), 945-952.
[6] Picandet V., Khelidj A., and G. Bastian., Effect of axial compressive damage on gas permeability of ordinary and high-performance concrete. Cement and Concrete Research 31, no. 11 (2001): 1525-1532.
[7] DjerbiTegguer, A, S Bonnet, A Khelidj, and V Baroghel-Bouny., Effect of uniaxial compressive loading on gas permeability and chloride diffusion coefficient of concrete and their relationship. Cement and Concrete Research 52, (2013), 131-139.
[8] Mu Ru, Changwen Miao, Xin Luo, and Wei Sun., Interaction between loading, freeze–thaw cycles, and chloride salt attack of concrete with and without steel fiber reinforcement. Cement and Concrete Research 32, no. 7 (2002), 1061-1066.
[9] Wang L., Yao Y., Wang Z., and Huang P., Test method to determine durability of concrete under combined environmental actions and mechanical load. Proceedings of International RILEM Conference on Concrete Repair, Rehabilitation and Retrofitting, Cape Town, South Africa (2012), 248-249.
[10] Yao, Y., Z. Wang, and L. Wang. Durability of concrete under combined mechanical load and environmental actions - a review. Journal of Sustainable Cement-Based Materials 1, no. 1-2(2012), 2-15.
[11] Yuan Y., Yang C., Water permeability of concrete under uniaxial tension. Structural Concrete 15, no. 2 (2014), 191-201.
[12] Hoseini M., V. Bindiganavile, and N. Banthia.The effect of mechanical stress on permeability of concrete : A review. Cement and Concrete Composites 31, no. 4 (2009), 213-220.
[13] Yao, Y., L. Wang, and F.H. Wittmann. Publications on durability of reinforced concrete structures under combined mechanical loads and environmental actions: an annotated bibliography. Ed. Y. Yao, L. Wang, and F.H. Wittmann. Freiburg: Aedificatio Publishers (2013).

International RILEM Conference on Materials, Systems and Structures in Civil Engineering
Conference segment on Service Life of Cement-Based Materials and Structures
22-24 August 2016, Technical University of Denmark, Lyngby, Denmark

BASIC AND DRYING SHRINKAGE OF INFRASTRUCTURE CONCRETES WITH VARIABLE FLY ASH CONTENT

Anja E. Klausen [1, 2], Gunrid Kjellmark [2], Terje Kanstad [1]

(1) Norwegian University of Science and Technology (NTNU), Trondheim, Norway
(2) SINTEF, Building and Infrastructure, Trondheim, Norway

Abstract
Studies on basic (autogenous) and drying shrinkage of infrastructure concretes with variable fly ash (FA) content have been undertaken and three different test systems have been used: (1) A simple standard test method for measurement of isothermal basic shrinkage and drying shrinkage, (2) The Dilation Rig which is a dummy rig following the Temperature-Stress Testing Machine (TSTM) and (3) The Free Deformation (FD) system which consists of several rigs of similar type as the Dilation Rig. Concretes with w/b = 0.4 and FA content in the range 0 – 33 % by total binder weight have been investigated. The experimental results show that basic shrinkage decreases with increasing FA content, while drying shrinkage is increasing with the FA content. The results are compared to the Code-type models included in the present version of Eurocode 2 and *fib* Model Code 2010, which both only indirectly account for the effect of FA through the influence of the FA content on the compressive strength. The two models give quite similar results, and the general observation is that the effect of FA is reasonably well predicted. In general, however, basic shrinkage is underestimated by the models, while drying shrinkage is overestimated.

1. Introduction

Within two Norwegian research projects denoted COIN (2007 - 2014) and DACS (2015 - 2019), research related to early age stress build-up and cracking of infrastructure concrete (w/b = 0.4 and varying fly ash (FA) content) have been carried out [1]. The work include experimental characterization of material parameters ranging from hydration heat to mechanical properties, creep and stress development in restrained situations, methods for crack width estimations, and calculation methods in general. This paper is related to experimental behaviour and modelling of basic and drying shrinkage over relatively long time durations, which both are important parameters in service limit states design, either the point

is to prevent cracking, or due to limitation of crack widths. Further details are given in [2], see also www.coinweb.no.

The influence of the concrete composition and its part materials is a rather complicated matter which is investigated in numerous projects over many decades, see e.g. [3,4]. The present research does not consider this topic generally, but is merely a qualitative investigation related solely to the replacement of cement by fly ash, which is highly relevant today for sustainability reasons, and because low-heat concretes in general have less cracking problems.

2. Materials

Two different cement types have been used: Norcem Anlegg (classified as a CEM I 52.5 N), and Norcem Anlegg FA (CEM II/A-V42.5 N), the latter including about 17 % of fly ash (FA) by weight. In addition, a varying amount of the cement was replaced by fly ash in the concrete mixing plant and 7 concretes with total fly ash content varying in the range 0 – 33 % were tested. The *w/b*-ratio was 0.4, about 5 % of silica fume was added and the total amount of binder varied slightly in the range 385 – 390 kg/m^3. The average compressive cube strength at 28 days decreased with increasing amount of fly ash in the range between 80 and 54 N/mm^2. Both the tensile strength and the E-modulus at 28 days decreased with the FA content in a similar manner. Key data for the concretes are presented in Table 1, and for further details see [1,2].

Table 1. Key data for the tested concretes

Name*	Cement type	FA-cont in cement (%)	FA added in mixer (%)	28 d cube strength (N/mm^2)
1 REF	CEM I 52.5 N	0	0	74
1 FA 19	CEM I 52.5 N	0	19	67
1 FA 33	CEM I 52.5 N	0	33	57
2 REF	CEM I 52.5 N	0	0	80
2 FA 17	CEM II/A-V42.5 N	17	0	71
2 FA 25	CEM II/A-V42.5 N	17	8	66
2 FA 33	CEM II/A-V42.5 N	17	16	54

*The 1st number refers to the test series and the 2nd to the total FA-content.
**The cube strength was adjusted to cylinder strength (multiplied by 0.8) prior to calculations

3. Test Methods

Three different test systems have been used. Firstly, a standard test method was used to measure isothermal long-term basic shrinkage (up to 8 months) and afterwards drying shrinkage (up to 5.5 years (2000 days)). In the first period, the specimens were carefully wrapped in thin plastic sheets and aluminum foil to prevent external drying (Figure 1a). The deformation was measured by a manual extensometer over the distance between steel bolts placed centrically in each end. The weight loss was recorded as part of the standard procedure

[2]. The second method is the Dilation Rig (Figure 1b), which is the dummy specimen following the Temperature-Stress Testing Machine (TSTM) for restrained stress measurements. In this case the sum of autogenous deformations and thermal dilation is measured under general temperature conditions on specimens cast directly into steel forms, carefully isolated against external drying immediately [1]. Finally, the Free Deformation (FD) system which consists of several rigs of similar type as the Dilation Rig was also used for one of the concretes. In all methods, the specimen geometry was approximately the same: prisms with dimensions 100x100x500mm.

a)

b)

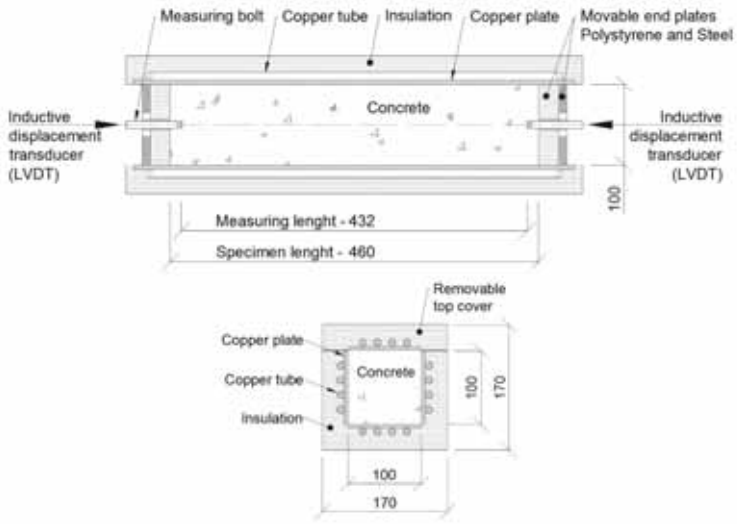

Figure 1. (a) Standard method for measurement of isothermal shrinkage [2]
(b) Dilation Rig of the TSTM System [1]

4. Code-type material models

The experimental results are compared to the Code-type models included in the present version of Eurocode 2 [5] and in *fib* Model Code 2010 [6] both briefly described below using the terminology from the latter. As seen in the formulas, the only model parameters are the compressive cylinder strength and the three parameters α_{bs}, α_{ds1} and α_{ds2} which describe the effect of the cement type. The cement classification is the same in the two models, although the full description in Model Code is replaced by letters in Eurocode 2.

Basic shrinkage:

$$\epsilon_{cbs}(t) = \epsilon_{cbs0}(f_{cm}) \cdot \beta_{bs}(t) \quad (1)$$

$$\beta_{bs}(t) = 1 - \exp(-0.2 \cdot \sqrt{t}) \quad (2)$$

- *fib Model Code 2010:*

$$\epsilon_{cbs0}(f_{cm}) = -\alpha_{bs}\left[\frac{(0.1 \cdot f_{cm})}{(6 + 0.1 \cdot f_{cm})}\right]^{2.5} \cdot 10^{-6} \quad (3)$$

Cement type 32.5N: $\alpha_{bs} = 800$
Cement type 32.5R and 42.5N: $\alpha_{bs} = 700$
Cement type 42.5R, 52.5N and 52.5R: $\alpha_{bs} = 600$

- *Eurocode 2:*

$$\epsilon_{cbs0}(f_{cm}) = 2.5(f_{ck} - 10) \cdot 10^{-6} \quad (4)$$

Drying shrinkage:

$$\epsilon_{cds}(t, t_s) = \epsilon_{cds0}(f_{cm}) \cdot \beta_{RH}(RH) \cdot \beta_{ds}(t - t_s) \quad (5)$$

$$\epsilon_{cds0}(f_{cm}) = [(220 + 110 \cdot \alpha_{ds1}) \cdot \exp(-\alpha_{ds2} \cdot f_{cm})] \cdot 10^{-6} \quad (6)$$

$$\beta_{RH}(RH) = -1.55\left[1 - \left(\frac{RH}{100}\right)^3\right] \quad (7)$$

- *fib Model Code 2010:*

$$\beta_{ds}(t - t_s) = \left(\frac{(t - t_s)}{\left(0.035 \cdot {h_o}^2 + (t - t_s)\right)}\right)^{0.5} \quad (8)$$

Cement type 32.5N: $\alpha_{ds1} = 3$, $\alpha_{ds2} = 0.013$
Cement type 32.5R and 42.5N: $\alpha_{ds1} = 4$, $\alpha_{ds2} = 0.012$
Cement type 42.5R, 52.5N and 52.5R: $\alpha_{ds1} = 6$, $\alpha_{ds2} = 0.012$

- *Eurocode 2:*

$$\beta_{ds}(t - t_s) = \left(\frac{(t - t_s)}{\left(0.04 \cdot {h_o}^{1.5} + (t - t_s)\right)}\right) \quad (9)$$

Cement type S (32.5N): $\alpha_{ds1} = 3$, $\alpha_{ds2} = 0.013$
Cement type N (32.5R and 42.5N): $\alpha_{ds1} = 4$, $\alpha_{ds2} = 0.012$
Cement type R (42.5R, 52.5N and 52.5R): $\alpha_{ds1} = 6$, $\alpha_{ds2} = 0.011$

5. Experimental and calculated results

5.1 Basic shrinkage

Figure 2a) and b) present the results from the basic shrinkage tests versus time for test series 1 and 2, which both confirm that the basic shrinkage is decreasing with increased fly ash content as expected [7,8]. For the present case, the two models give nearly similar results, which is why only *fib* Model Code 2010 is included in the figures. In general, the model in Eurocode 2 give slightly less (up to 10%) basic creep than the *fib* model. For both series, the models underestimate basic shrinkage, although they describe the effect of the increasing fly ash content reasonably well due to their strength-dependence. However, it is also seen that for the two concretes denoted 2 REF and 2 FA 17 the *fib*-model give identical results, which is clearly in disagreement with the experiments. The explanation is the different cement types and the fact that the cement type parameters elliminate the effect of the strength for these two concretes. It should also be noted that the measurements started at 1 day while the models start at t = 0. The shrinkage occurring in the model before 1 day is therefore subtracted in the figures.

It is seen that basic shrinkage continues to increase up to 6 months, and since 100 % isolation against external drying is nearly impossible to achieve the prisms were weighted also in the basic shrinkage period. The weight loss versus time is presented in Figure 1c). The weight loss is relatively small, and the corresponding error for the basic shrinkage is estimated to be less than 10 % [2].

Figure 3 presents 50 days basic shrinkage measured in the Dilation Rig and the FD-system for the concrete with 17 % fly ash grinded within the cement (2 FA 17). Corresponding results for the two models are shown in the same figure, and while the models start developing shrinkage from t = 0, the experiments develop shrinkage from the starting time for stress calculations, which for this particular concrete is determined to 9.5 hours. The results are in good agreement with the previously shown results in Figure 2b), but it is seen that the models do not describe the early time-shape of the measured curves very well. The observed resting period and expansion in the development of basic shrinkage is typical for fly ash concretes [1].

5.2 Drying shrinkage

The drying shrinkage results for the period after 6 months under isolated conditions until 5.5 years are presented in Figure 4a), b) and c) for the two test series. In general, the results show that drying shrinkage is increasing with increasing fly ash content. However, for test series 2 the highest drying shrinkage magnitude does not correspond to the highest FA content. This can presently not be explained, and it is thought casued by internal scatter. The test results are however supported by measured weigth loss due to drying as presented in Figure 6.

In general, the models underestimate drying shrinkage considerably for both test series. And, it should be noted that this overall underestimation by the models partly can be due to the late start of drying. This parameter is, however, not included in the models.

The shrinkage curves from Eurocode 2 are rather similar to *fib* Model Code (between 0 and 10 % less) as seen by comparing the calculated curves in Figure 4b) and 4c). For most cases,

the results show that the models describe the effect of fly ash content reasonably well. However, due to the cement type model parameter, 2 FA 17 gets less shrinkage than the 2 REF concrete according to both models, which is in disagreement with the test results. .

a)

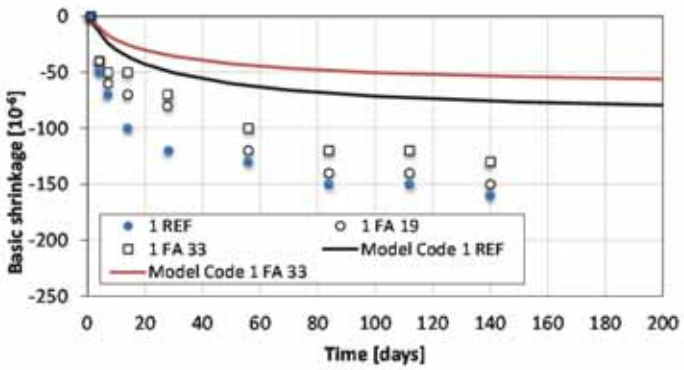

b)

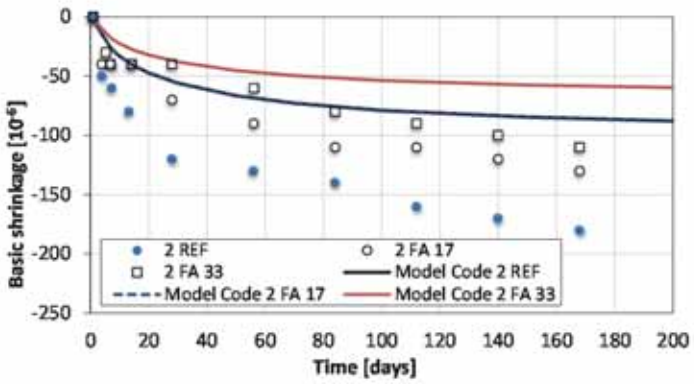

c)

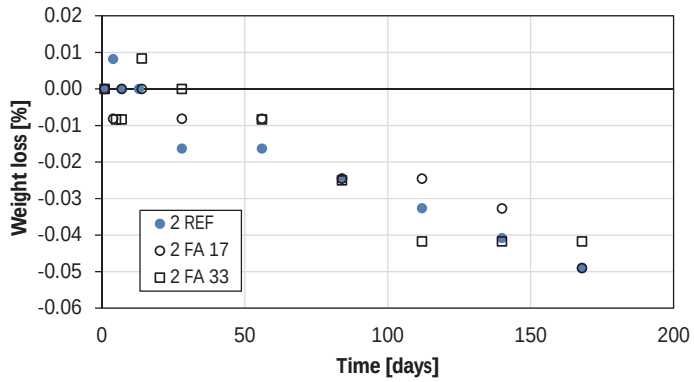

Figure 2. Basic (autogenous) shrinkage for the tested concretes. (a) 1st series, (b) 2nd series, (c) Weight loss during the isolated test.

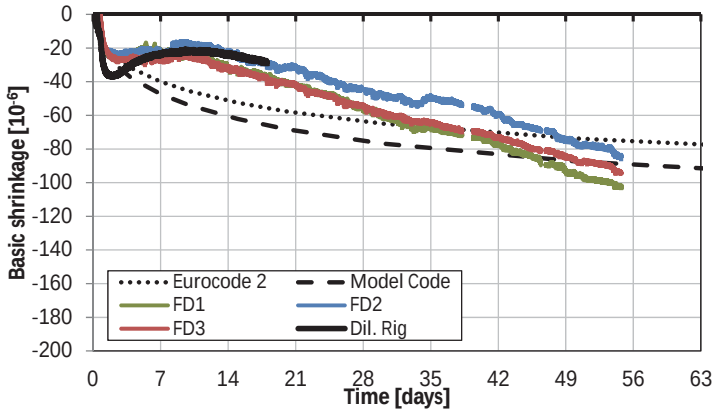

Figure 3. Basic shrinkage results for 2 FA 17 from the TSTM- and FD- systems in comparison with *fib* Model Code 2010 and Eurocode 2.

5.3 Total shrinkage

In Figure 5, the total shrinkage curves are presented and it is seen that the variation range between the investigated concretes, and thus the influence of the fly ash content, is rather small. The explanation for this is the opposite effect of fly ash on basic and drying shrinkage. Furthermore, it can also be seen that the overall agreement between the experimental results and the models is reasonably good, and thus better for total shrinkage than for the two separate parts.

6. Summary and conclusions

Experimental results for basic and drying shrinkage off infrastructure concretes with $w/b = 0.4$ and varying fly ash content (0 – 33 % by cement weight) are reported and have been compared to the code-type models in Eurocode 2 and *fib* Model Code 2010. In general, the experimental results show that basic shrinkage is decreasing, while drying shrinkage is increasing with increasing fly ash content. As a result of this, the effect of fly ash content on the total shrinkage is not significant. For most cases, the shrinkage models in Eurocode 2 and *fib* Model Code 2010 give quite similar results with deviations less than 10 %. The comparisons between experiments and calculations show that the models describe the effect of fly ash content rather well through the compressive strength parameter, while the influence of the cement type lead to confusing results. It was shown that basic shrinkage is somewhat underestimated by the models, while both models overestimate drying shrinkage considerably. On the other hand, the overall agreement between total shrinkage and the models is reasonably good.

a)

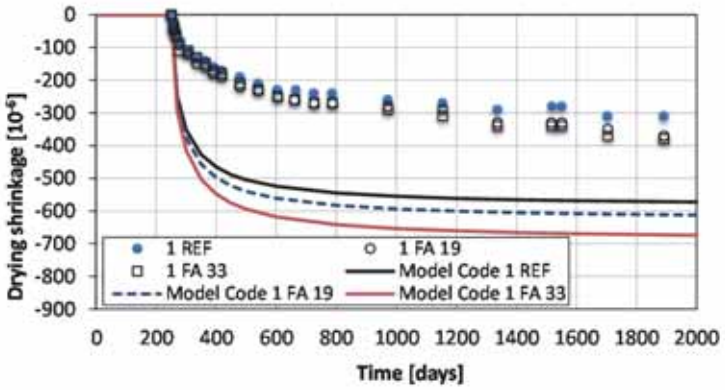

b)

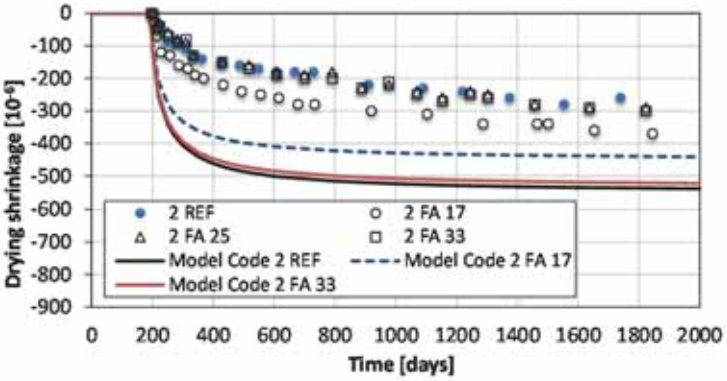

c)

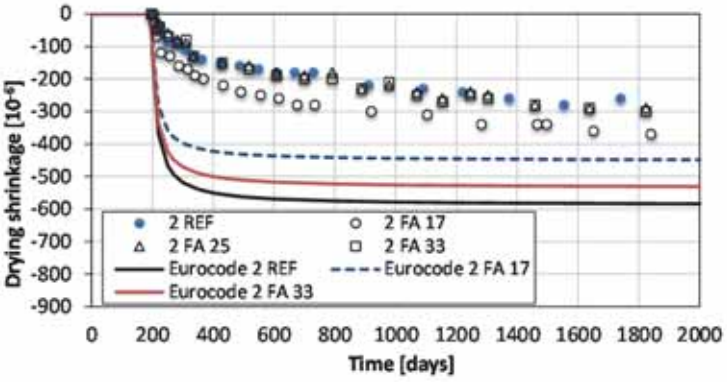

Figure 4. Drying shrinkage for the tested concretes. (a) 1st series, (b) 2nd series and Model Code models and (c) 2nd series and Eurocode models.

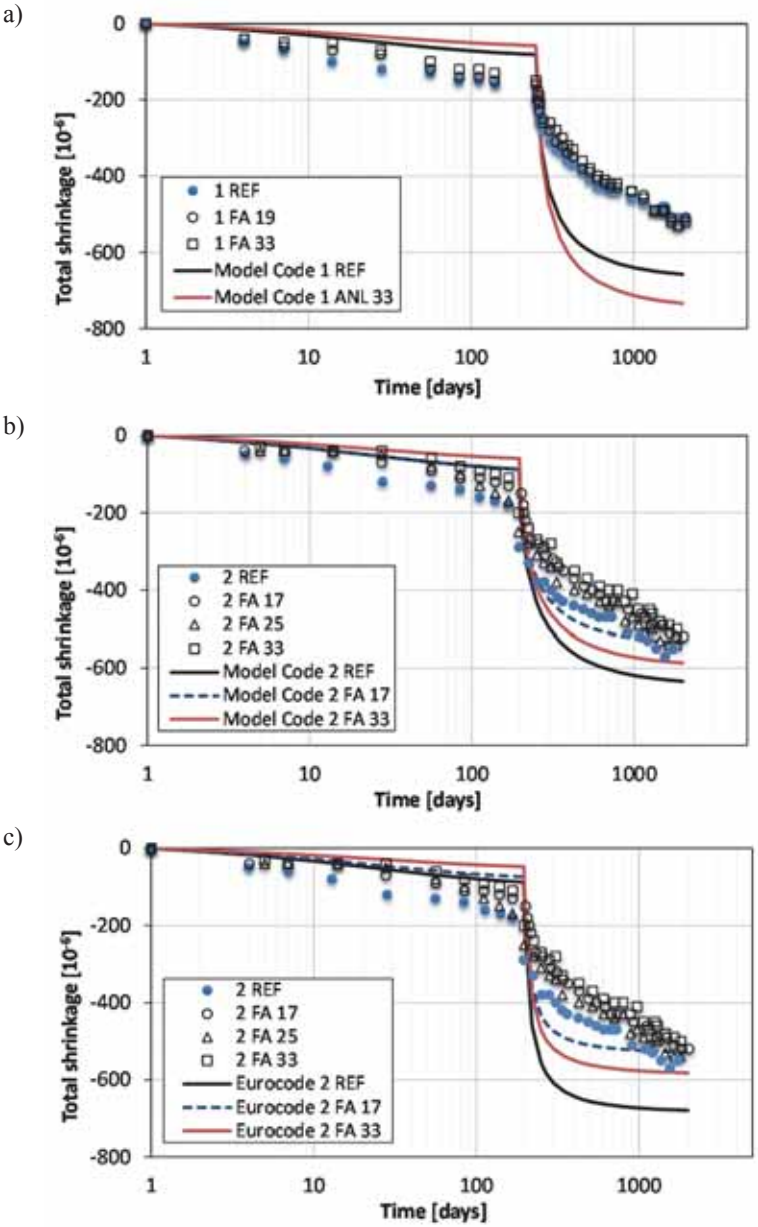

Figure 5. The sum of basic and drying shrinkage for the tested concretes. (a) 1st series, (b) 2nd series and Model Code models and (c) 2nd series and Eurocode models

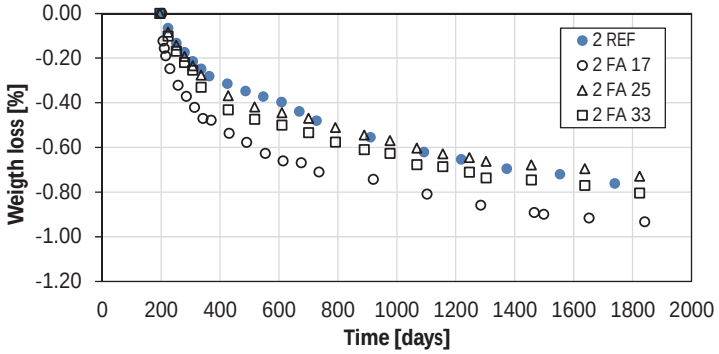

Figure 6. Weight loss due to drying

Acknowledgement

The authors acknowledge grants from COIN - Concrete Innovation Centre (www.coinweb.no) - which is a Centre for Research based Innovation, initiated by the Research Council of Norway (RCN) (2007 - 2014), and DaCS which is an industry-lead research project financed by RCN and Norwegian concrete industrial partners (2014 - 2019).

References

[1] Klausen, A.E., Early age crack assessment of concrete structures: experimental investigation of decisive parameters, PhD-thesis, Department of structural engineering, NTNU, Trondheim (2016).
[2] Kjellmark, G., Klausen. A.E., Kanstad, T., Long-term measurements of autogenous and drying shrinkage of fly ash concretes, COIN. SINTEF Report, 2016. www.coinweb.no
[3] Neville, A.M. et al., Creep of plain and structural concrete, London, (1983)
[4] Bazant, Z.P., and Panula, L., Practical prediction of timedependent deformations of concrete, Part I and II, Materials and structures (RILEM, Paris), Vol 11, (1978)
[5] EN 1992-1-1 Eurocode 2, Design of concrete structures, (2004)
[6] *fib* Model Code for concrete structures 2010, Ernst&Sohn, (2013)
[7] Lee, H. K., K. M. Lee and B. G. Kim (2003): Autogenous shrinkage of high-performance concrete containing fly ash. Magazine of concrete research 55 (2003) 507-515
[8] Bjøntegaard, Øyvind and Knut O. Kjellsen (2012): Property development and cracking tendency in hardening concrete: Effect of cement type and fly ash content. COIN Project Report 40, SINTEF Building and Infrastructure, Trondheim, Norway

International RILEM Conference on Materials, Systems and Structures in Civil Engineering
Conference segment on Service Life of Cement-Based Materials and Structures
22-24 August 2016, Technical University of Denmark, Lyngby, Denmark

AVOIDING OVERFITTING IN INVERSE MODELING OF CHLORIDE MIGRATION IN CONCRETE

Sreejith V. Nanukuttan [(1)], Neven Ukrainczyk [(2)], Des J. Robinson [(1)], and Eduardus A.B. Koenders [(2)]

(1) School of Planning, Architecture and Civil Engineering, Queen's University Belfast, United Kingdom
(2) Institute for Construction and Building Materials, Technical University Darmstadt, Germany

Abstract
Inverse analysis for reactive transport of chlorides through concrete in the presence of electric field is presented. The model is solved using MATLAB's built-in solvers "pdepe.m" and "ode15s.m". The results from the model are compared with experimental measurements from accelerated migration test and a function representing the lack of fit is formed. This function is optimised with respect to varying amount of key parameters defining the model. Levenberg-Marquardt trust-region optimisation approach is employed. The paper presents a method by which the degree of inter-dependency between parameters and sensitivity (significance) of each parameter towards model predictions can be studied on models with or without clearly defined governing equations. Eigen value analysis of the Hessian matrix was employed to investigate and avoid over-parametrisation in inverse analysis. We investigated simultaneous fitting of parameters for diffusivity, chloride binding as defined by Freundlich isotherm (thermodynamic) and binding rate (kinetic parameter). Fitting of more than 2 parameters, simultaneously, demonstrates a high degree of parameter inter-dependency. This finding is significant as mathematical models for representing chloride transport rely on several parameters for each mode of transport (i.e., diffusivity, binding, etc.), which combined may lead to unreliable simultaneous estimation of parameters.

1. Introduction

Numerous methods have been developed to determine the chloride ion diffusion coefficient, D_{ef} [1]. Conventional methods of determining the effective chloride diffusion parameter involves long test duration and hence international standards such as ASTM C1202 and Nordic Test 492, make use of an externally applied voltage to accelerate the test. The parameter determined from these tests is used either for quality control or, in conjunction with Fick's second law, to predict the chloride ingress in concrete. In contrast to the practical

development of test and predictive procedures, mathematical models for the reactive transport of ions in concrete have been developed. Recent models have become highly sophisticated taking into account the interaction of the different ionic species within the concrete [2, 3]. This has been achieved by deriving individual transport equations for each species, with the electric field resulting from any applied voltage and from the interaction of the ions themselves being calculated from the solution of a Poisson partial differential equation. In addition, supplementary equations are needed to enforce the electro-neutrality constraint and to relate the activity coefficients to the ionic strength. The mathematical model adopted here derives reactive transport equations for only the chloride ions as proposed by Spiesz et al. [1]. The goal is to bridge the gap between the experimental tests and the mathematical models. The key to achieving this is by the addition of an optimisation procedure to the numerical model, which combined is called numerical inverse modeling. This is in keeping with many mathematical modelling procedures where initially attention focuses on the direct modelling of a problem. When this can be accomplished satisfactorily, attention is then directed to accurate parameter estimation that can be achieved through established optimisation techniques, which should include sensitivity and parameter inter-dependency analysis. Spiesz et al. [1] employed inverse analysis for chloride migration in concrete using a Generalized Reduced Gradient Algorithm optimization method and a forward discretization Finite Difference numerical implementation for solving a reactive-transport model. They simultaneously fitted four parameters simultaneously characterising chloride migration, binding rate and binding capacity, but did not address the parameter estimation accuracy which may be significantly impaired due to over-parametrisation and parameter inter-dependency/correlation problem.

The work reported in this paper makes use of more advanced numerical procedures both for solving the direct model and the inverse optimisation problem. A method of lines (MOL) approach [4] is used for solving the reactive transport system of equations. Optimisation is enriched with a detailed analysis on interdependency and sensitivity of the parameters. In general, as the reactive-transport models increase in complexity, the number of parameters in a model may increase to the point where over-parameterization can result in overfitting and deterioration in prediction accuracy. This over-fit is due to a high degree of parameter inter-dependency (i.e. mutual correlation) and a lack of sensitivity where the model starts fitting the noise in the experimental data used for calibration. The result of an over-fitted model is a reduced error for the calibration data set, but larger errors in validation and prediction with other data sets, i.e. poor generalisation ability. In fact most of the inverse modeling problems are over-parameterized, particularly when prior information about the many of the parameters involved is not available. In literature there is a lack of discussion on the parameter inter-dependency, particularly in the concrete science community, where the growing interest in application of inverse modeling is generally ignoring this important aspect. This paper demonstrates a relative simple and easy procedure to quantify the level of parameter inter-dependency and sensitivity in order to decide how many parameters is possible to estimate simultaneously in a single inverse analysis. Presented procedure is general, and may be applied to parameter estimation problems of a wide variety of different processes described by models with or without clearly defined governing equations.

2. Mathematical model

The mathematical model adopted is based on the Nernst-Planck equation [1] given as:

$$\frac{\partial C_t(x,t)}{\partial t} = -D_{ef}\left(\frac{\partial^2 c}{\partial x^2} + \frac{zFE}{RT}\frac{\partial c}{\partial x}\right) - r \tag{1}$$

where D_{ef} is the effective diffusion coefficient (m^2/s), C_t is the total chloride concentration (g/dm^3 of concrete), c is the concentration of the diffusing/migrating ion (g/dm^3 in pore solution), z valence number of the ion, F Faraday constant (9.64846×104 C mol^{-1}), R ideal gas constant (8.3143 J mol^{-1} K^{-1})), T absolute temperature (K), x concrete depth (m), t time (s), E electrical field (Volt m^{-1}) and r reaction term (mol m^{-3} s^{-1}). The reaction term accounts for the ion interaction process with the solids, which leads to a binding of chlorides from the liquid phase. Reaction term (r) can be considered in two ways depending on a relative rates between chloride binding and transport (migration):

1) If a binding rate is faster than transport, an equilibrium, f.e. following Freundlich isotherm, is assured:

$$C_b = K_b\, c^n \tag{2}$$

from where the equilibrium Cl binding amount is then calculated as:

$$r = (1-p)\,\rho_s \frac{\partial C_b}{\partial t}; \qquad \frac{\partial C_b}{\partial t} = \frac{\partial C_b}{\partial c}\frac{\partial c}{\partial t} = K_b c^{(n-1)} n \frac{\partial c}{\partial t} \tag{3}$$

where ρ_s is density of solids in concrete and C_b is in units of g/g of solid, and c is in g/dm^3 of pore solution.

2) If a binding rate is slower than transport (due to acceleration by imposed voltage), equilibrium is not achieved and binding reaction kinetic process should be considered. In a simplest form the reaction kinetics can be described as [1]:

$$r = k(c - c_{eq}) = k\left(c - \left(\frac{C_b}{K_b}\right)^{1/n}\right) \tag{4}$$

where k is a kinetic constant of the binding reaction, c is the pore solution concentration and c_{eq} is equilibrium concentration following Freundlich binding isotherm eq. 2. The total chloride concentration (C_t, g/g of concrete) can be defined as a sum of free and bound chlorides, where the units are transformed by considering concrete porosity (p), density of solids in concrete (ρ_s) and saturated concrete density ρ_c:

$$C_t = \frac{p\,c + (1-p)\,\rho_s C_b}{\rho_c} \tag{5}$$

The following system of coupled partial differential is to be solved for the free chlorides (eq. 6, where c is in g/dm3 of pore solution) and bound chlorides (eq. 7, where C_b is in g/g of solid as calculated by Freundlich isotherm):

$$p\frac{\partial c\ (x,t)}{\partial t} = -D_{ef}\frac{\partial^2 c}{\partial x^2} - u\frac{\partial c}{\partial x} - k\left(c - \left(\frac{C_b}{K_b}\right)^{1/n}\right) \tag{6}$$

$$(1-p)\,\rho_s\frac{\partial C_b(x,t)}{\partial t} = k\left(c - \left(\frac{C_b}{K_b}\right)^{1/n}\right) \tag{7}$$

where $u=zFE/RT$ is the migration term (in units of m/s) induced by potential gradient ΔE, but is analogue to convective (advection) term. This set of coupled differential equations (6 and 7) is to be used to model the accelerated diffusion test where the chloride ions are driven through a concrete specimen of thickness L under the presence of an electric field caused by applying a potential difference V across the specimen. One side (x = 0) of the concrete is kept at a fixed concentration of chloride ions c_0 (64.95 g/dm^3) while the other ($x = L$ =0.05m) is assumed to have a zero concentration of chloride ions. Zero initial concentration of free and bound chlorides is set to c_i and C_{bi}. Experimental data on accelerated migration (RCM) test on mortar are taken from [1] with following experimental details: RCM applied voltage ΔU = 35V for 24h, mortar age 27 days, cement type Cem I 52.5 N (785.6 kg/m^3), w/c = 0.263, sand (0-2mm) 1382 kg/m^3, mortar saturated density 2450 g/dm^3, mortar solids density 2710 g/dm^3, c_0=70.9 g/dm^3, concrete thickness L=0.05m, porosity p=0.1511. The parameters to the problem are kinetic D_{ef}, k, and thermodynamic (binding isotherm) n and K_b. The values of these parameters are to be estimated (best fitted) to match with experimental results taken from the test. To assess the accuracy of the estimates one needs to quantify the sensitivity of each of the parameters in terms of the proximity and relative importance of each, as well as their interdependency (mutual correlation) in determining the model solution concentrations of chloride ions.

To reduce the number of parameters to be determined simultaneously with the inverse analysis we propose to use experimental data on the binding isotherm for the case of material's boundary condition (L=0). Parameter K_b can be expressed as a function of n by combining Freundlich's eq. (2) and eq. (5) for the case of concrete surface (x=0):

$$K_b = \left(\frac{\rho_c C_{t,(x=0)} - p\,c}{(1-p)\rho_s}\right) \Big/ c^n \tag{8}$$

where $C_{t,(t=0)}$ is a total chloride concentration at the concrete surface, and the fraction in a bracket represents the C_b from the Freundlich isotherm (eq 2). $C_{t,(t=0)}$ can be estimated from experimental profile data, where an equilibrium is established as observed by reaching a

maximum in the concentration profile at the near surface of the concrete. Note that the unit for free chloride is g/dm^3 of pore solution, and bound chloride is expressed in g/100g (or mas %) of concrete. For chloride binding (Freundlich) isotherm the parameters are obtained by using following units: free chloride is also in g/dm^3 of pore solution, but bound chloride is expressed in g/g of solids.

2.1 Numerical implementation

The Matlab's built-in non-linear solver "*pdepe.m*" based on Petrov-Galerkin Method Of Lines (MOL) [4] is used. The partial differential equation are first converted to ordinary differential equations using a second-order spatial discretization based on a fixed set of user defined nodes. The success of the MOL arise from its simplicity of implementation and the availability of high-quality time integrators for solving a wide range of ordinary differential equations problems. The time integration is done with the Matlab's built-in solver "*ode15s.m*" for solving stiff system of differential algebraic equations. This routine changes both the time step and the computing formula dynamically in order to minimize computational time for a desired accuracy. The setup of the analysis saw the domain divided into 500 (logarithmically spaced) cells and the time increment was automatically variable in a way to assure a numerical relative and absolute tolerance set to 10^{-4}. The second-order algorithm "*pdepe.m*" and the variable time step integration "*ode15s*" provide a good convergence rate and are robust enough to handle non-linearies and the couplings of the equations.

3. Optimisation approach (inverse model)

The optimisation package interfaces with the analysis through a user defined objective function which will return the value of squared 2-norm (i.e. a sum) of the residuals (where, residual is the difference between measured and predicted) for a specified set of design parameters. The function uses the method of lines to provide the chloride concentration at a grid of positions of depth and time. To calculate the residuals the analysis needs to find the concentrations at the same time and position as the test results. Conveniently MATLAB provides a function that will interpolate from a regular grid, as supplied from the analysis, and will estimate the concentration at the depths and time values used in the test measurements and hence allow the residuals to be determined. Cubic interpolation was used to establish the values. Minimization of an objective function, OF written in matrix notation looks like:

$$\mathrm{OF}(\mathbf{p}) = \left[\mathbf{C}_{t,measured} - \mathbf{C}_t(\mathbf{p})\right]^{\mathrm{T}} \left[\mathbf{C}_{t,measured} - \mathbf{C}_t(\mathbf{p})\right] \tag{9}$$

where $C_{t,measured}$ and $\mathbf{C}_t$ are the vectors containing the measured and simulated concentrations, respectively, and the superscript T indicates the transpose of a vector. To minimize the least squares norm given by eq. 9 the derivative of OF($\mathbf{p}$) with respect to the unknown parameter is equated to zero.

$$\mathbf{J}(\mathbf{p}) = \left[\frac{\partial \mathbf{C}_t(\mathbf{p})}{\partial \mathbf{p}}\right] = \begin{bmatrix} \frac{\partial \mathbf{C}_{t,1}}{\partial p_1} & \frac{\partial \mathbf{C}_{t,1}}{\partial p_2} & \cdots & \frac{\partial \mathbf{C}_{t,1}}{\partial p_n} \\ \vdots & \vdots & & \vdots \\ \frac{\partial \mathbf{C}_{t,m}}{\partial p_1} & \frac{\partial \mathbf{C}_{t,m}}{\partial p_2} & \cdots & \frac{\partial \mathbf{C}_{t,m}}{\partial p_n} \end{bmatrix} \tag{10}$$

The sensitivity matrix (eq. 10) has a size m by n, where m is the number of data points and n is the number of parameters. The elements of the sensitivity matrix, called the sensitivity coefficients are thus defined as the first derivative of the estimated total concentration at depth d_m with respect to the unknown parameter p_n. The estimation of the parameter for a small value of the magnitude of $J_{i,j}$ is difficult, because basically the same value for concentration would be obtained for a wide range of parameter values. The estimation problem is ill-conditioned near the initial guess used for the unknown parameter, creating difficulties in the applications of Gauss method. The Levenberg-Marquardt method alleviates such difficulties by damping oscillations and instabilities due to the ill-conditioned character of the problem, by making it large as compared to $\mathbf{J}^T\mathbf{J}$ if necessary.

The addition of constraints (Tikhonov regularization) allows the inclusion of prior information about the parameters to be estimated, including equality constraints and limits on the range of parameters. Constraints can alleviate over-parameterization by constraining the feasible region of parameters. The Levenberg-Marquardt algorithm does not handle bound constraints. Therefore, a Matlab's Trust-region-reflective algorithm was also employed, which implements the Levenberg-Marquardt algorithm using a trust-region approach to solve bound-constrained optimisation problems.

3.1 Parameter sensitivity and inter-dependency obtained by eigen value analysis

The relative roles played by parameters in achieving the fit is of extreme importance. The Hessian matrix, **H** can be used to assess the sensitivity of the solution to the value of parameters, however this can be approximated by ignoring the second-order terms in Hessian as:

$$\text{Hessian } \mathbf{H} \approx 2\mathbf{J}^T\mathbf{J} \tag{11}$$

The Hessian contains the second derivatives or curvature of the objective function with respect to the parameters. The greater the curvature the more sensitive the function will be to change in the parameters. An eigen-value analysis of the Hessian will additionally establish the principal directions where maximum sensitivity will occur. A Matlab function, [**v**, **d**] = *eig*(**H**), was used to obtain a diagonal matrix **d** of eigenvalues and matrix **v** whose columns are the corresponding right eigenvectors, so that:

$$\mathbf{H}\,\mathbf{v} = \mathbf{v}\,\mathbf{d} \tag{12}$$

Generally, if directions of the eigen vectors correspond to unit vectors, this is taken to suggest that the parameters are independent of each other. This is usually not the case as the

formulation of the differential equation would indicate that there is a connection between the parameters. With the eigen vectors being near unity the eigen value can be taken as the curvature of the objective function due to a unit change in a corresponding parameter. Care should however be taken when comparing the eigen values, as the scaling of the parameters may not be directly comparable. A scaling of a Jacobian vectors was employed here by multiplying it by a value of the estimated parameter [5: p.57].

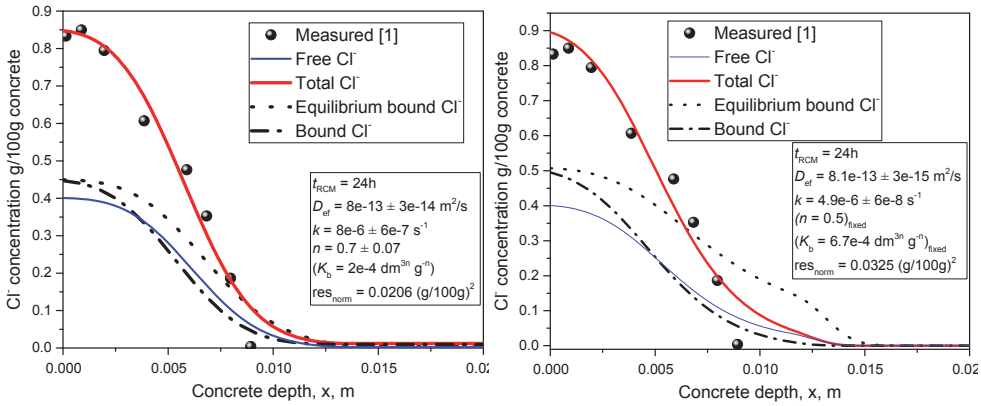

Figure 1: Chloride concentration profiles obtained after 24h RCM test: (**Left)** simultaneous estimation of three parameters : effective diffusivity (D_{ef}), binding rate constant (k) and binding parameter (n); (**Right)** simultaneous estimation of two parameters D_{ef} and k, while binding parameters were fixed to n=0.5 and K_b=6.7 10-4 dm^{3n} g^{-n} [1].

Table 1: Results of inverse analysis: estimated parameter values and eigen vectors (v_i) with corresponding eigen values.

Number of simultaneously estimated parameters	Parameters	Estimated value	v_1	v_2	v_3	R_{cond}
2	D_{ef}, 10^{-12} m^2/s	0.81	-0.998	0.059	-	1.3 10^{-6}
	k, 10^{-6} s^{-1}	4.9	-0.059	-0.998	-	
	(fixed: n=0.5; K_b=6.7 10^{-4} dm^{3n} g^{-n})	eigen value:	3.359	0.208	-	
3	D_{ef}, 10^{-12} m^2/s	8.0	-0.955	-0.234	-0.184	2.0 10^{-19}
	k, 10^{-6} s^{-1}	8.0	0.077	0.564	0.774	
	n	0.70	-0.288	-0.792	0.606	
	(K_b = f(n) via eq. 8)	eigen value:	5.403	0.156	0.001	

3.2 Results and discussion

Figure 1 shows examples of the simulated total-, actually bound- and free-chloride concentration profiles, all expressed in g/100g of concrete in order to enable their direct relative comparison. In this way, the total chloride content is a direct sum of actually bound and free chloride content. Furthermore, an equilibrium chloride content is plotted as well, which refers to the virtual case when the binding reaction would be so extremely fast, i.e. instantaneous (rate constant $k \rightarrow \infty$), that an equilibrium can be attained. However, because the binding reaction has a limited rate, i.e. significant in comparison to accelerated migration transport rate, the amount of actually bound chlorides is less than the maximally possibly achieved equilibrium values. In other words, the high velocity of ions during high-rate (non-steady state) migration transport accelerated by an electrical field, depending on the experimental conditions, hinders significantly binding compared to the equilibrium state that takes place during corresponding diffusion tests without migration acceleration. The fit (Figure 1) is very encouraging with the model being able to predict the features of the measured values, in both fitting scenarios. The implementation of the advanced (stiff) time integration and the central differencing was selected to achieve this stability and smoothness of the results. However, due to the dominance of the migration term there may be merit in considering up-winding (adaptive or solution-sensitive) approximation for the derivatives to reflect the directional nature of the ion movement.

The relative roles played by the parameters in achieving the fit is of extreme importance and to help assess this the run of the optimisation uses a set of a different number of parameters. The values of thermodynamic (binding isotherm) parameters n and K_b were fixed as obtained from [1] in agreement with independent measurement of chloride binding isotherm. However, the question arises whether, the binding parameters could be simultaneously estimated together with rate parameters D_{ef} and k, or whether the parameters are only being too sensitive to the experimental noise in the data, or too correlative with each other.

To reduce the number of parameters to be determined simultaneously with the inverse analysis we propose to use experimental data on the binding isotherm for the case of material's boundary condition (catholyte exposure solution) according to eq 8. From the surface free chloride concentration, equal to amount in catholyte exposure solution, one can obtain the corresponding equilibrated bound concentration from the measured total concentration. Fitting of 2 (D_{ef} and k) or 3 (D_{ef}, n, k) parameters took about 6 or 16 iterations, respectively, with 3 or 5 function evaluations per iteration. Optimality criteria was below 3e-4 (2 parameter fit) or below 6e-5 (for 3 parameters fit), indicating that an optimum was always possible. Comparison of values on estimated parameters (Table 1) between the different scenarios (with different amount of simultaneously fitted parameters) shows no significant variance in D_{ef}, but high variance in k and n. This indicates a confidence and robustness of the inverse analysis for the estimation of D_{ef}, which can be explained by the fact that D_{ef} exhibits the highest sensitivity and lowest interdependency with other parameters. However, this results should still be taken with care when fitting more than 2 parameters (D_{ef} and k) to other experimental data with different measurement errors. To assure accuracy simultaneous parameter estimation should always be accompanied by the eigen value analysis in order to demonstrate the degree of interdependency and sensitivity of D_{ef}. The accuracy of k, n and K_b

should be taken with care, and their estimates are only a first approximation, and fitting of 4 simultaneous parameters is definitely not recommended. Eigen values matrix is a sparse matrix with a non-zero (eigen) values positioned on its diagonal. These eigen values rate the relative contribution of eigen vectors on the objective function. The eigen vectors comprise the effect of the principal parameter together with interactions with other parameters. Therefore, the eigen values actually quantify the relative impact of the change of a principal parameter together with a combination of other inter-dependent parameters within each eigen vector. When parameters are independent (orthogonal), eigen vectors have unity values, where the position of the unity element (a v_i row in Table 1) within the vector indicates to which parameter is this vector attributed.

For example case with 2 fitting parameters in Table 1, eigen vector (column) v_1 has a maximal (-0.998) value of first element, whose vector position (first row) corresponds to the principal parameter D_{ef}. Deviation from unity absolute value of the principal parameter, and deviation from zero absolute value of the other row elements (corresponding to the other parameters, here -0.059) quantifies their correlation, i.e. the parameter inter-dependency. The dependency in v_1 is very low, 0.02, which means that only about 6% of the variance in D_{ef} is due to its interaction with the parameter n. This vector exhibits the highest eigen value (higher than for v2) indicating the highest relative sensitivity. By the values within the eigen vector v1 one can determine that this highest sensitivity corresponds predominately to D_{ef} (highest value of first row, -0.998) with very low interdependency with other parameters (close to zero values of other rows). If parameters have interdependency, eigen vectors are not ortogonal, i.e. more elements have significant deviations from non-zero values. Eigen values show the sensitivity of the eigen vector, which is a combination of the interdependent parameters. For example in simultaneous estimation of 3 parameters (Table 1), vector v_2 has a 2nd place in vector sensitivity ranking which is moreover attributed mainly to parameter n (79.2%) but also to it`s significant interdependence with k and D_{ef}. In this dependency, we see that n is more correlated to k than to D_{ef} as indicated by a difference between absolute values of 2nd (0.564) and 1st (0.234) element of v_2 vector. This is also confirmed in v_3, where the main parameter k (0.774) is more correlated to n (0.606) than to D_{ef} (0.184). The eigen vector v_3, has the least relative sensitivity to minimization of objective function, indicated by a eigen value of 0.001, compared to eigen values of v_1 (5.403) and v_2 (0.156). This means that the combined effect of (primarly) parameter k (in that eigen vector), tougether with interdependency with k and D_{ef}, has the least relative sensitivity. Likewise, the eigen vector (column) v_1 has a maximal (-0.955) absolute value of the first eigen vector element, whose vector position (first row) corresponds to the principal parameter D_{ef}. Deviation level from unity value of the principal parameter, while deviation from zero value of the other row elements corresponding to the other parameters, quantifies their correlation, i.e. the parameter inter-dependency. By reducing the number of fitting parameters, correlation/dependency and R_{cond} (inverse of a condition number for $\mathbf{J}^{\prime}\mathbf{J}$) values improve rapidly (Table 1): dependency rapidly reduces and R_{cond} rapidly increases. Simultaneous fiting of four parameters results in highly ill-conditioned system (high R_{cond}) due to overfitting and overparametrisation, where parameters show extreme degree of interdependency (results not shown in Table here). Generaly, D_{ef} was found to exhibit the highest sensitivity and and lowest interdependency, i.e. a highest eigen value for an eigen vector that indicates D_{ef} as a primarily parameter. This indicates a confidence and robustness of the inverse analysis for the estimation of D_{ef}.

However, care should be taken when fitting more than 2 parameters (D_{ef} and k) to simultaneously also estimate the binding parameters n and K_b defining the Freundlich isotherm.

4. Conclusion

Inverse modeling of the transport of chloride ions through cement based materials in the presence of an electrical field has been analysed using the MOL discretisation/integration modeling approach within the Levenberg-Marquard optimisation loop, focusing on a parameter sensitivity and interdependency. The technique is very flexible and performed well producing stable, smooth and convergent results. The parameters can readily be specified as being fixed or included as variables allowing the approach to model and optimise a range of situations. A confidence and robustness of the inverse analysis was demonstrated for the estimation of D_{ef}, by the fact that D_{ef} exhibits the highest sensitivity and lowest interdependency with the other simultaneusly parameters. However, care should be taken when fitting more than 2 parameters (D_{ef} and k) to simultaneously also estimate the binding parameters (n and K_b defining the Freundlich isotherm). The estimates of n and K_b are only a first approximation, as they are firstly highly correlated between each other, and secondly also with parameter k. In this case, the proposed eigen value and parameter interdependency analysis should be part of the inverse analysis in order to demonstrate the degree of interdependency, sensitivity and accuracy of the estimates.

An approach was proposed to reduce the number of simultaneously fited parameters from four to three, where $n=f(K_b)$ following eq. 8 considers an establishment of a binding equilibrium at the concrete surface.

References

[1] Truc O., Ollivier J.P., Nilsson L.O., Numerical simulation of multi-species transport through saturated concrete during a migration test - MsDiff code, Cem Concr Res, 30 (2000), 1581-1592
[2] Samson E., Marchand J., Modeling the transport of ions in unsaturated cement-based materials, Comp Struct, 85(2007), 1740–1756
[3] Schiesser W.E., Griffiths G.W., A Compendium of Partial Differential Equation Models, Method of Lines Analysis with MATLAB, Cambridge University Press 2009.
[4] Spiesz P., Brouwers H.J.H., Influence of the applied voltage on the Rapid Chloride Migration (RCM) test, Cem Concr Res 42 (2012), 1072–1082
[5] Steffes-Lai D., Approximation Methods for High Dimensional Simulation Results Parameter Sensitivity Analysis and Propagation of Variations for Process Chains, Logos Verlag Berlin Gmbh, 2014. ISBN 978-3-8325-3696-1, pp.233

International RILEM Conference on Materials, Systems and Structures in Civil Engineering
Conference segment on Service Life of Cement-Based Materials and Structures
22-24 August 2016, Technical University of Denmark, Lyngby, Denmark

PLASTIC SHRINKAGE CRACKING IN SELF-COMPACTING CONCRETE: A PARAMETRIC STUDY

Faez Sayahi [(1)], Mats Emborg [(1),(2)], Hans Hedlund [(1),(3)], Ingemar Löfgren [(4),(5)]

(1) Luleå University of Technology, Luleå, Sweden
(2) Betongindustri AB, Stockholm, Sweden
(3) Skanska Sverige AB, Gothenburg, Sweden
(4) Chalmers University of Technology, Gothenburg, Sweden
(5) Thomas Concrete Group, Gothenburg, Sweden

Abstract
Plastic shrinkage cracking, often the first type of cracks occurring even before initial setting, causes enormous expenses for the building industry annually. The main reason behind the phenomenon is believed to be rapid and excessive surface water evaporation of the concrete element in the plastic stage which in turn leads to the so-called plastic or capillary shrinkage. These cracks mainly occur in horizontal concrete elements with large surface to volume ratio (such as slabs, pavements, etc.). This paper reports results from experiments performed, using ring test method (NORDTEST-method NT Build 433). During the experiments, influence of water-cement (w/c) ratio, cement type, coarse aggregate content and super plasticizer dosage was investigated. Moreover, effort was made to explain the difference in cracking tendency of different concretes based on water evaporation rate and capillary pressure. It seems that various parameters have different influences on the cracking tendency, the evaporation rate, as well as the hydration rate and capillary pressure. Although, capillary pressure is local and its maximum value differs in different locations, it seems that its development rate, especially in the first few hours, is almost identical everywhere in the specimen. This may be used as a plastic shrinkage indicator.

1. Introduction

Plastic shrinkage cracking in concrete is the first type of cracks occurring within the first few hours after casting, even before the initial setting. Horizontal concrete elements with large surface to volume ratio (e.g. slabs and pavements) are prone to this type of cracking. It accelerates the ingress of harmful materials that might cause damage in future, e.g. corrosion of the reinforcement. Accordingly, cracks can dramatically impair the aesthetics, durability and serviceability of the structure [1, 2]. The main reason behind plastic shrinkage cracking is

considered to be rapid and excessive surface water evaporation in the plastic stage [3-5]. Also, the phenomenon is closely related to settlement, capillary pressure and the duration of dormant period [6]. For conventional concrete, once it is placed in the mould, its solid particles settle under the influence of the gravitational forces, forcing the water in the pore system up to the surface (i.e. bleeding). Consequently, the entire concrete surface is covered with a thin layer of water [7]. However, for self-compacting concrete (SCC) and concrete with low w/c ratio, no free water will accumulate at the surface.

As soon as the evaporation rate exceeds the rate at which water is transported to the surface, the water layer disappears, and water menisci are formed in the pores. This is the onset point of negative pressure (capillary pressure) build-up in the concrete pore system [8]. The progressive evaporation gradually decreases the radius of the menisci resulting in more negative capillary pressure build-up [8]. The capillary pressure in turn causes more settlement by pulling the solid particles down and forcing the pore water to the surface [9]. Gradually due to the consolidation and continues water loss, the solid skeleton of the concrete becomes stiffer and eventually, the settlement stops [6]. At this point, the capillary pressure, applies inward horizontal forces on the solid particles causing the concrete to shrink (i.e. plastic shrinkage). If the concrete is restrained, the plastic shrinkage can lead to tensile strain accumulation at the surface. Eventually, once the tensile strain exceeds the very low early age tensile strain capacity of the concrete, cracks start to form [10].

Many factors can influence the risk of plastic shrinkage cracking such as water-cement ratio (w/c), cement type, member size, admixtures, coarse aggregate content and ambient conditions (i.e. relative humidity, air temperature and wind velocity) [1, 11]. However, despite that many papers are dedicated to study the influence of concrete mixture constituents on plastic shrinkage cracking of SCC, it is still not possible to explain all the cracking incidents based on the current knowledge. It is also not clear why sometimes cracking tendency increases despite of reduction in the evaporation. This is where other parameters such as capillary pressure, internal temperature and/or autogenous shrinkage may offer better explanations.

Although most of the experiments in this study were already performed by other researchers [12, 13], the role of capillary pressure in particular and its relation with evaporation and duration of dormant period have not been discussed. Filling this gap is the objective of this paper. Moreover, the trend of capillary pressure development in the first few hours is especially discussed. The presented research is part of an on-going PhD project at Luleå University of Technology in Sweden which aims at gaining a comprehensive understanding about the mechanism of plastic shrinkage cracking in concrete.

2. Materials and methods

2.1 Materials and mixing process

Tables 1 and 2 show the mix design of the tested SCCs and the composition of the cements. Two reference concert mixtures (Ref.1 with 0.45 w/c ratio and Ref.2 with 0.67 w/c ratio) were produced by Portland limestone cement (CEM II/A-LL 42.5R according to EN 197-1).

Fine (0-4 mm and 0-8 mm) and coarse (8-16 mm) aggregates, respectively, constitute 60 and 40% of the total aggregates volume in both Ref.1 and Ref.2. During the experiments, superplasticizer (Sikament 56) with density of 1100 kg/m^3 and 37% by weight of dry content was used. In addition, mineral filler (Limus 40) with density of 2700 kg/m^3 was utilized to stabilize the concrete. The dry material (aggregates, cement and filler) was premixed in a pan type concrete mixer for one minute before the water and superplasticizer (SP) were added. Then the mixing process continued for another 5 minutes. To ensure reproducibility, all the concrete mixtures were produced and tested twice.

Table 1: Mix design of the different tested concretes (W/C = Water-cement ratio, Ref = Reference concrete, CC = Coarse aggregate content, SP = Superplasticizer) in kg/m^3.

Name	**W/C 0.45 (Ref.1)**	**W/C 0.67 (Ref.2)**	**W/C 0.38**	**W/C 0.55**	**Based on Ref.1**		**Based on Ref.2**	
					CC35%	**CC45%**	**SP0.6%**	**SP1.0%**
Cement	380	300	420	340	380	380	300	300
Water	171	200	160	187	171	171	200	200
Agg. 0-4	0	155	0	81	0	0	155	155
Agg. 0-8	998	771	1021	879	1089.4	921.8	771	771
Agg. 8-16	678	628	694	651	586.6	754.2	628	628
Filler	100	220	40	160	100	100	220	220
SP	5.7	2.4	4.6	4.1	5.7	5.7	1.8	3
W/C	0.45	0.67	0.38	0.55	0.45	0.45	0.67	0.67

Table 2: Composition of the utilized cements (produced by Cementa).

Name	**MgO (%)**	**SO_3 (%)**	**Cl^- (%)**	**C_3A (%)**	**Na_2O_{eqv} (%)**	**Density (kg/m^3)**	**Blaine (m^2/kg)**
CEM II/A-LL 42.5R (Bygg)	1.1-1.3	3.3-4.0	0.02-0.04	-	-	3080	430
CEM I 52.5R (SH)	1.1-1.3	3.3-4.0	0.02-0.04	-	-	3125	550
CEM I 42.5N (Anläggning)	1.2-1.5	2.3-2.5	0.01-0.03	1.3-2.7	0.48-0.58	3200	310

2.2 Testing sequence

Four concrete mixtures with different w/c ratios (W/C0.38, W/C0.45, W/C0.55 and W/C0.67) were produced and tested (Table 1). W/C0.45 (Ref.1) was used as a reference for investigating the effect of coarse aggregate content; whereas the effect of SP dosage and cement type was studied by W/C0.67 (Ref.2).

The cement used in Ref.2 (CEM II/A-LL 42.5R) was substituted by two different cements, mentioned in Table 2 in order to study the influence of cement type. To investigate the impact of coarse aggregate content, the ratio in Ref.1 was changed once from 40% to 35% (CC35%)

and once to 45% (CC45%). Moreover, the effect of SP was investigated by changing the dosage from 0.8% of cement weight in Ref.2 to 0.6% in SP0.6% and 1.0% in SP1.0%.

2.3 Method

Ring test setup (NORDTEST-method NT BUILD 433) was developed by Johansen and Dahl at NTNU (1993) [14]. The method is intended to determine the cracking tendency of young concrete (Figure 1). In this method, three identical moulds with two concentric steel rings in each are used. The dimensions of the test setup are presented in Figure 1. Steel ribs (stress raisers) are attached to the concentric rings in order to provide crack initiation points. Each mould is covered by a transparent air funnel with a suction fan. The fan produces 4.5 m/s wind velocity across the specimen surface. During these particular experiments, the room temperature and relative humidity were 20 ± 1˚C and 35 ± 3% respectively. The weight loss (i.e. weight of the evaporated water), capillary pressure and internal temperature were recorded continuously, starting at 60 minutes after the castings up to 18 hours later. One mould was placed on three load-cells (scales) in order to measure the weight of the evaporated water per second. The capillary pressure at 4 cm distance from the surface was measured and recorded in 15 s intervals using two wireless sensors. The internal temperature was recorded in 1 s intervals by using a thermo thread located at 2 cm distance from the bottom of the mould. The concrete surface was visually inspected every 30 minutes in order to determine the time of crack initiation. A digital microscope (to an accuracy of 0.05 mm) and a digital measuring wheel (to an accuracy of ±1 mm) were utilized in order to measure the crack width and the crack length, respectively. After finishing the experiments (19 hours after casting the SCC), the average crack area was calculated, as suggested by Esping and Löfgren [13], according to equation 1:

$$Average\quad crack\quad area = \frac{\sum(crack\quad length \times crack\quad width)}{3} \tag{1}$$

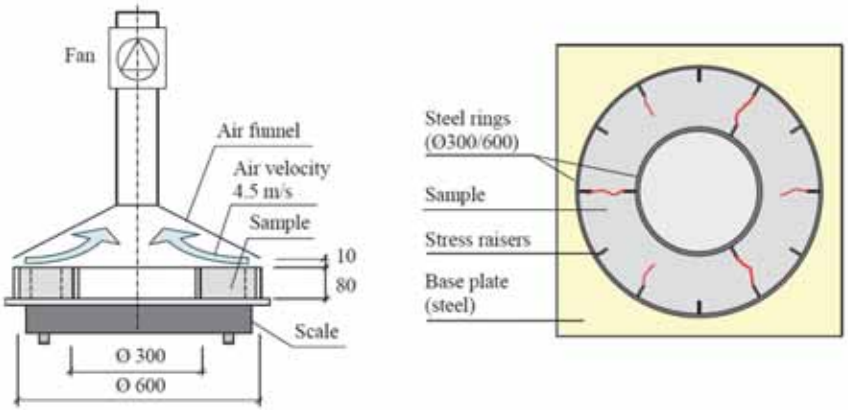

Figure 1: The ring test method setup for plastic shrinkage cracking tendency determination, from [12]. All the dimensions are in mm.

3. Results

3.1 Water-cement ratio

Evaporation: The highest total evaporation was measured in W/C 0.67, followed by W/C 0.55, W/C 0.45 and W/C 0.38 (Figure 2.a). A notable difference was observed between the evaporation of W/C 0.38 and the others. For instance, the total evaporation in its closest neighbour (W/C 0.45) was higher by 37%, while the difference between W/C 0.67 and W/C 0.45 was only 12%. However, W/C 0.38 had the highest initial evaporation rate, followed by W/C 0.45, W/C 0.55 and W/C 0.67, respectively.

Capillary pressure: According to the results, W/C 0.38, W/C 0.45 and W/C 0.55 have almost the same rate of capillary pressure build-up, whereas W/C 0.67 is totally distinguished by its higher rate (Figure 2.b).

Temperature: Increasing the w/c ratios delays the cement hydration and prolongs the dormant period. It should be noted that the temperature was measured at 2 cm distance from the bottom of the mould and thus is not the actual rate of hydration of the concrete. However, it can be considered as an indication of the effect of w/c ratio on the cement hydration.

Average crack area: W/C 0.67 had the highest average crack area, followed by W/C 0.38, W/C 0.55 and W/C 0.45 respectively (Figure 2.d). The average crack area of W/C 0.67 was almost 10 times the average crack area of W/C 0.45.

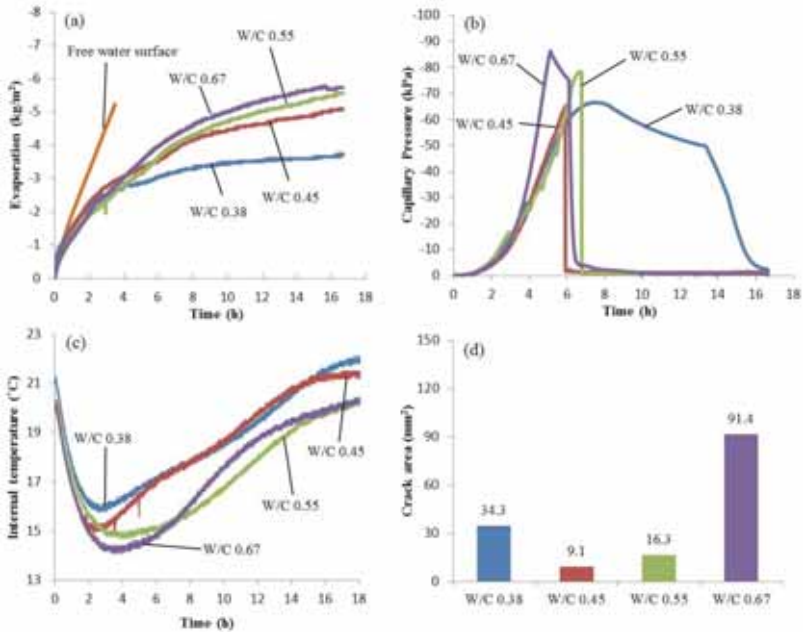

Figure 2: Influence of w/c ratio on (a) evaporation, (b) capillary pressure, (c) internal temperature and (d) average crack area.

3.2 Cement type

Evaporation: Substituting the cement used in "Ref.2" mixture (CEM II/A-LL 42.5R) with CEM I 42.5N led to 31% increase in the total evaporation, while CEM I 52.5R had an opposite impact and reduced it by 14.7% (Figure 3.a).

Capillary pressure: Cement type does not have noticeable influence on the capillary pressure build-up rate, as the slopes of the ascending part of the plotted curves in Figure 3.b are almost identical.

Temperature: The slow hydrating cement of CEM I 42.5N delayed the cement hydration to a large extent and consequently prolonged the dormant period (Figure 3.c). On the other hand CEM I 52.5R accelerated the hydration and shortened the dormant period. This cement was even the only one that reached its heat flow peak before the end of the experiment (after 15 hours).

Average crack area: While CEM I 52.5R and CEM II 42.5R show almost the same cracking tendency (although the former cracked slightly more in comparison), but a notable jump was observed in the cracking tendency of CEM I 42.5N (Figure 3.d).

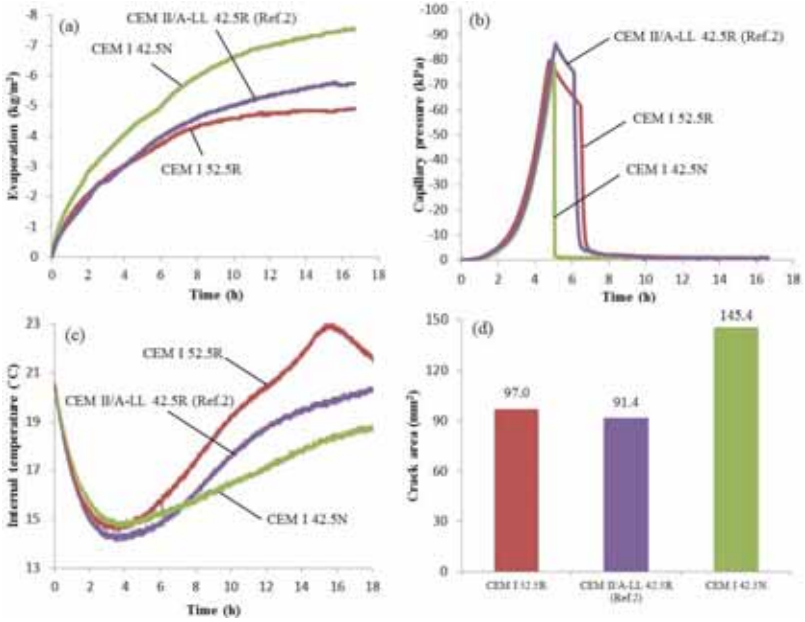

Figure 3: Influence of cement type on (a) evaporation, (b) capillary pressure, (c) internal temperature and (d) average crack area.

3.3 Coarse aggregate content

Evaporation: decreasing the coarse aggregate content from 40% to 35% decreased the total evaporation by 10%. However, the evaporation of CC35% was more than the evaporation of CC40% in the first 5 hours. The concrete was segregated to some extend when the coarse aggregate content was increased to 45%, which in turn led to even more evaporation reduction (Figure 4.a).

Capillary pressure: CC35% had a higher capillary pressure build-up rate, followed by the segregated CC45% and the reference concrete of CC40% respectively (Figure 4.b).

Temperature: Both CC35% and CC45% accelerated the cement hydration in comparison to CC40% (Figure 4.c).

Average crack area: Only 5% reduction in the coarse aggregate content of CC 40% caused an increase in the average crack area of CC 35% by 1036%. Meanwhile, increasing the coarse aggregate content by 5% resulted in 250% increase in the average crack area, which is much lower than the cracking tendency of CC 35% (Figure 4.d).

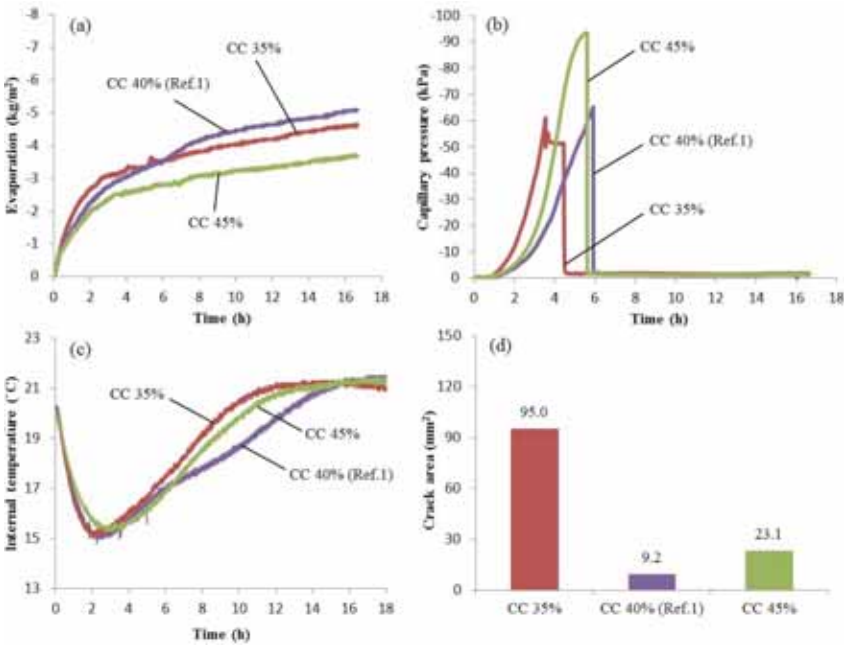

Figure 4: Influence of coarse aggregate content on (a) evaporation, (b) capillary pressure, (c) internal temperature and (d) average crack area.

3.4 Superplasticizer dosage (SP)

Evaporation: Reducing the SP dosage from 0.8% to 0.6% of the cement weight decreased the amount of the evaporated water by 18%. On the other hand the total evaporation was higher by 14% when the SP dosage was increased to 1.0% (Figure 5.a).

Capillary pressure: SP 0.6% led to a faster capillary pressure build-up, while SP1.0% delayed it in comparison to SP0.8% (Figure 5.b).

Temperature: SP0.6% accelerated the cement hydration and shortened the dormant period, while SP1.0% slightly delayed the hydration in comparison to SP0.8% (Figure 5.c).

Average crack area: SP0.6% decreased the average crack area from 91.4 mm^2 in SP0.8% to 56.8 mm^2, whereas this value was increased to 112.4 mm^2 in SP1.0% (Figure 5.d).

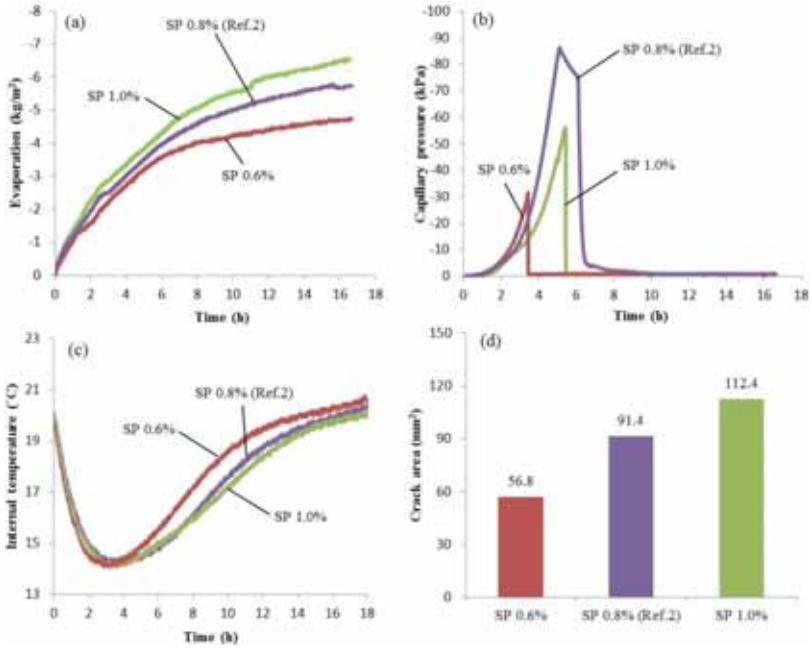

Figure 5: Influence of SP dosage on (a) evaporation, (b) capillary pressure, (c) internal temperature and (d) average crack area.

4. Discussion

Although the maximum capillary pressure value is totally local, the results show that the rate of the negative pressure build-up is almost identical everywhere in the specimen (Figure 6.a and 6.b). During the experiments, both pressure sensors showed equal capillary pressure build-up rate, despite of their different locations. This means that, regardless of the location,

the amount of the negative pressure in the pore system is almost identical, especially in the first few hours and before the air-entry point. This phenomenon was also observed in other studies [7, 15].

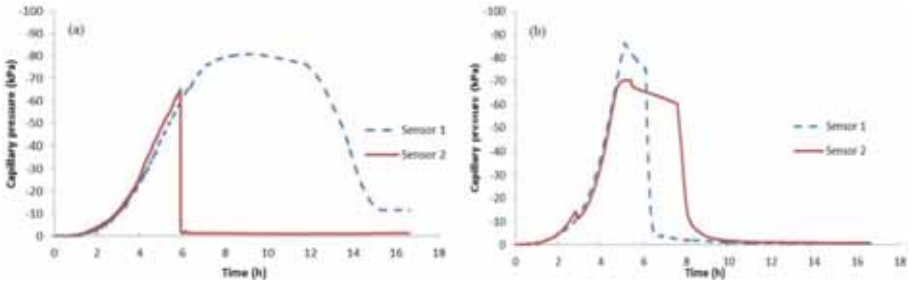

Figure 6: Capillary pressure measured at 4 cm distance from the surface in two different positions, (a) 0.45 w/c ratio and (b) 0.67 w/c ratio.

Since capillary pressure pulls the solid particles together and forces the concrete to shrink, its build-up rate can be considered as an indicator of the amount of horizontal (plastic) shrinkage. Thus, the rate of capillary pressure build-up can also be a governing mechanism of plastic shrinkage cracking alongside evaporation. For example, the concrete with 0.67 w/c ratio has the highest evaporation and crack area (Figure 2.a). It seems that the cracking in this concrete is governed by the evaporation.

However, its slightly higher evaporation (not mentioning its lowest evaporation in the first two hours) cannot justify the huge average crack area difference (Figure 2.d). In this case the higher capillary pressure build-up rate indicates that, at any particular time after capillary pressure build-up onset, W/C 0.67 experiences higher horizontal shrinkage and consequently higher tensile stresses, in comparison to the other tested concretes. Accordingly, in addition to the evaporation, the cracking tendency of concretes with high w/c ratios is amplified by the rate of capillary pressure build-up.

However, the above mentioned cannot explain the cracking behaviour of W/C 0.38. In this case, one reason can be that the concrete experiences higher autogenous shrinkage, since its dormant period is relatively short (Figure 2.c). This hypothesis is backed up with experiments performed by Esping and Löfgren [13].Meanwhile, the temperature of concretes with high w/c ratios drops faster than those with low ratios. This is probably caused by the higher cooling effect due to the higher evaporation. Moreover, delayed hydration heat development onset (longer dormant period) facilitates more temperature drop.

The main reason behind plastic shrinkage cracking differs based on the early strength gaining class of concrete (rapid or normal). As cement type seems not to affect the capillary pressure build-up rate (Figure 3.b), evaporation, may be the main cause of the cracking (Figure 3.a). It should be noted that the evaporations of the two rapid strength gaining concretes are almost identical, especially in the first 4 hours.

The segregation during CC45% production makes it hard to analyse the results. Thus, the results are not reliable enough for any conclusion to be based on. On the other hand, CC35% had lower evaporation comparing to CC40%. This can be attributed to the higher amount of fines which reduces the pores diameter and consequently decreases the bleeding. The above mentioned can also justify the higher capillary pressure build-up rate. Furthermore, the higher amount of trapped water in the concrete chemically reacts with the cement which means earlier hydration onset and shorter dormant period (Figure 4.c).

In case of the effect of SP dosage, the evaporation seems to be the main crack tendency governing mechanism. However, the relation between the evaporation and capillary pressure build-up rate cannot be fully understood without measuring the settlement and bleeding. On the other hand, SP acts like a retarder as it delays the hydration onset. Hence, at higher SP dosage the retardation will lead to a longer dormant period where water can be lost by evaporation as it's not prevented by the initial structural build-up (Figure 5.c).

5. Conclusion

Based on the results of this study the following remarks can be concluded:

- High capillary pressure build-up rate, only when accompanied with high evaporation, significantly increases the cracking tendency. This can be amplified further by a long dormant period.
- The main driving force behind plastic shrinkage cracking in concretes with high w/c ratio is evaporation alongside high capillary pressure build-up rate and long dormant period. On the other hand, autogenous shrinkage, probably, is the main reason behind crack formation in concretes with low w/c ratio.
- The optimum w/c ratio is between 0.45 and 0.55. Any concrete with w/c ratio out of this range is more prone to early age cracking.
- Reducing the evaporation or compensating the evaporated water in concretes with both low and high w/c ratios (e.g. fogging, curing membrane, wind breaker, etc.) reduces the risk of plastic shrinkage cracking.
- Concretes with normal early strength gaining cements and/or high SP dosage need to be protected against evaporation.

Acknowledgment

The authors would like to gratefully appreciate the financial support they received from the Development Fund of the Swedish Construction Industry, SBUF. Special thanks are due to the MSc students of CET 2016 and staff of Complab at Luleå University of Technology.

References

[1] Boshoff WP, Combrinck R. Modelling the severity of plastic shrinkage cracking in concrete. Cem Concr Res. 48 (2013),34-39.

[2] Sivakumar A, Santhanam M. Experimental methodology to study plastic shrinkage cracks in high strength concrete. In: Measuring, Monitoring and Modeling Concrete Properties. Springer; (2006), 291-296.
[3] Cohen MD, Olek J, Dolch WL. Mechanism of plastic shrinkage cracking in portland cement and portland cement-silica fume paste and mortar. Cem Concr Res. 20 (1990), 103-119.
[4] Radocea A. A study on the mechanism of plastic shrinkage of cement-based materials. Chalmers University of Technology (1992).
[5] ACI D. 305R-Hot Weather Concreting. American Concrete Institute International, USA (1999).
[6] Leemann A, Nygaard P, Lura P. Impact of admixtures on the plastic shrinkage cracking of self-compacting concrete. Cement and Concrete Composites, 46 (2014), 1-7.
[7] Slowik V, Schmidt M, Fritzsch R. Capillary pressure in fresh cement-based materials and identification of the air entry value. Cement and Concrete composites, 30 (2008), 557-565.
[8] Sayahi F, Emborg M, Hedlund H. Plastic Shrinkage Cracking in Concrete: State of the Art. Nordic Concrete Research. 51 (2014), 95-116.
[9] Lura P, Pease B, Mazzotta GB, Rajabipour F, Weiss J. Influence of shrinkage-reducing admixtures on development of plastic shrinkage cracks. ACI Mater J. 104 (2007), 187.
[10] Ghoddousi P, Javid AAS. Effect of reinforcement on plastic shrinkage and settlement of self-consolidating concrete as repair material. Mater Struct. 45 (2012), 41-52.
[11] Uno PJ. Plastic shrinkage cracking and evaporation formulas. ACI Mater J. 95 (1998), 365-375.
[12] Löfgren I, Esping O, Jensen O, Lura P, Kovler K. Early age cracking of self-compacting concrete. International RILEM Conference on Volume Changes of Hardening Concrete: Testing and Mitigation, Denmark (2006), 251-260.
[13] Esping O, Löfgren I, Marchand J, Bissonnette B, Gagné R, Jolin M. Investigation of early age deformation in self-compacting concrete. Proceedings of the 2nd International Symposium on Advances in Concrete Science, Quebec (2006).
[14] Johansen R, Dahl P. Control of plastic shrinkage of cement. 18th Conference on Our World in Concrete and Structures, Singapore (1993).
[15] Schmidt M, Slowik V. Capillary pressure controlled concrete curing in pavement construction. Airfield and Highway Pavement Conference, USA (2013), 295-306.

International RILEM Conference on Materials, Systems and Structures in Civil Engineering
Conference segment on Service Life of Cement-Based Materials and Structures
22-24 August 2016, Technical University of Denmark, Lyngby, Denmark

DEFINITION OF DAMAGE DISTRIBUTION DUE TO INTERNAL EXPANSIVE REACTIONS IN LONG TERM CONCRETE STRUCTURES

Esperanza Menéndez[(1)], Ricardo García-Rovés[(1)], Sergio Ruiz[(2)], José de Frutos[(3)]

(1) Institute "Eduardo Torroja" of Construction Science (CSIC), Madrid, Spain
(2) Dragados, S.A., Oviedo, Spain
(3) ETSIT – UPM, Madrid, Spain

Abstract
The long term exposition of concrete to the environmental actions can induce loss of durability properties. Some of these actions are associated with the ingress of aggressive. But also the alteration of concrete can be associated with the internal reactions of the own components of the concrete. Especially in the structures in permanent contact with the water some internal reactions can induce degradation due to expansive reactions, like alkali-silica reaction or internal sulfate attack. And, some additional factor as alkali release by aggregates can influence the increase the degradation due to expansive reactions. In this work an analysis of damage by internal expansion in field structures is done. The analysis at microstructural level of the concretes affected internal expansive reaction permits to distinguish to the origin of damage, alkali-silica reaction or internal sulfate attack. Also, a definition of the damage level of concrete could be defined for each type of degradation process. The analysis of concrete in different parts of the structures and their analysis by microstructural techniques permit to define a distribution of concrete damage in each zone.

1. Introduction

Throughout the service life of concrete structures, alterations can be produced as a result of environmental factors which could affect their functionality, compromising the safety of the structures or the structural elements, according to the degree of deterioration [1]-[15]. This deterioration might be associated with different types of factors: chemical, physical, mechanical, biological, etc. In some cases the origin of the damage is directly related to the characteristics of the concrete components (aggregates, cement, water, additives, etc.) and the interactions between them or with the environment. In the case of alterations arising from chemical reactions originating internally, in all cases water acts as a vehicle for the reaction and as a basic part of the expansive products formed. Within the expansive processes of an

internal origin it is important to highlight, given its impact and the effects produced on the concrete, the alkali-silica reaction and the sulfate attack, although there are other phenomena of a physical origin that have an impact on the freezing and thawing cycles.

The alkali-silica reaction and the sulfate attack are phenomena brought about by the chemical reaction of different components of the concrete which give rise to the neo-formation of products whose main characteristic is that they are expansive.

The formation of these expansive products in the interior of the hardened concrete makes it overcome materialist tensile strength and gives rise to the formation of cracks. Another significant characteristic is that its appearance is affected by multiple factors, both proper to the material itself and its components as well as environmental conditions. The coincidence of influential factors and the manifestation of the damage, with similar characteristics, make it essential to carry out a suitable diagnosis in order to program actions on the structure and carry out repair work where deemed necessary. For a correct diagnosis of these phenomena a micro-structural analysis of the affected concrete is essential, specifically using electronic microscopy and microanalysis techniques, together with a correct interpretation [1].

The Result of the alkali-silica reaction impact and the attack by sulphates in concrete structures has been analyzed from different points of view, although its analysis has been carried out independently, studying the mechanisms of the reaction, the impact on the properties and mechanical behaviour of the concrete affected, etc. [2]-[7].

The deterioration caused by the alkali-silica reaction and by sulfate attack can be differentiated using electronic microscopy and microanalysis techniques, considering the representativeness of the samples of the structure [16]. On the other hand, it could also be possible to observe the damage in concretes at optical microscopy level [17], [18].

The damages caused by internal expansive reactions in the concrete can be diagnosed unequivocally by using micro-structural analysis techniques based on the study electronic microscopy combined with microanalysis by X-ray [1], by applying the damage level method (DL) [19]. Also, the consequence of ASR at microstructural level are described in several papers [2], [3], [7], [9]. However, it is essential to guarantee the representation of the samples in relation to the structure to be analyzed and the experience of the technicians to have a correct results.

The suitable diagnosis allows it to be established whether the deterioration observed is related to the alkali-silica reaction, the sulphate attack or the combination of the two processes. Likewise, it is possible to establish the origin of the damage, in spite of the alteration products having the same characteristics [19].

2. Instrumental techniques

Optical microscopy: Aggregates comprising concretes of different structures are analyzed by thin section, using an optical microscope Olympus BX51.

Backscattering electron microscopy and energy dispersive X-ray (BSE-EDX): The concrete samples were prepared and analyzed by BSE-EDX identifying the different structures and the distribution of its analyzing the elemental mapping associated with the images. The samples were imbibed in low viscosity resin, cut and polished to generate appropriate observation surfaces. Microscopic analysis has been done with an electron microscopy JEOL JSM-5400 and with OXFORD Link X-ray microanalysis.

3 Concrete samples

For this study, concrete samples were extracted from different dams in operation. These dams are located in Spain, two buttress dams in the Northeast and two arch gravity dams, in the Midwest and North. The current use of the dams is hydroelectric generation.

The structures and samples names are codified with the following letters; Dam (D), Block (B), Buttress (T), Upstream (U), Center (C), Downstream (O) and sample depth level (S).

The structures analyzed are:

- D1: This structure is a 70 year-old arch gravity dam. It is located in the Northwest of Spain. It has 295 m of crest length and 115 m of height. The concrete cores selected by this research are the samples 1 to 30 coded as follows B1-C-S1, B1-C-S1, B3-C-S1, B3-C-S1, B5-C-S1, B5-C-S1, B13-C-S1, B13-C-S1, B2-C-S1, B2-C-S1, B5-O-S2, B5-O-S2, B10-O-S2, B10-O-S2, B13-O-S2, B13-O-S2, B4-O-S3, B4-O-S3, B4-U-S3, B4-U-S3, B10-O-S3, B10-O-S3, B13-U-S3, B13-U-S3, B14-O-S3, B14-O-S3, B8-O-S4, B8-O-S4, B10-U-S4, B10-U-S4.
- D2: This structure is a 40 year-old arch gravity dam with. It is located in the Midwest of Spain. It has 418 m of crest length and 66 m of height. The concrete cores selected by this research are the samples 31 to 54 coded as follows B5-U-S7, B5-O-S7, B5-U-S5, B5-O-S5, B5-U-S2, B5-O-S2, B11-U-S3, B11-O-S3, B11-U-S2, B11-O-S2, B13-C-S1, B16-C-S6, B16-C-S4, B16-U-S1, B17-U-S6, B17-O-S6, B17-U-S4, B17-O-S4, B17-U-S2, B17-O-S2, B18-C-S6, B18-C-S4, B18-U-S1, B10-C-S7.
- D3: This structure is a 60 year-old buttress dam. It is located in the North of Spain. It has 490 m of crest length and 31 m of height. The concrete cores selected by this research are the samples 55 to 83 coded as follows B5-C-S1, T11-U-S1, T11-O-S1, T11-U-S4, T11-O-S4, T11-U-S7, T11-O-S7, T11-U-S10, T11-O-S10, T15-U-S1, T15-O-S1, T15-C-S1, T15-O-S4, T15-C-S2, T16-O-S1, T16-C-S1, T16-O-S4, T16-C-S2, T17-U-S1, T17-O-S1, T17-U-S4, T17-O-S4, T17-U-S7, T17-O-S7, T17-U-S10, T17-O-S10, B24-C-S1, B24-C-S4, B24-C-S6.
- D4: This structure is a 60 year-old buttress dam. It is located in the North of Spain. It has 535 m of crest length and 37 m of height. The concrete cores selected by this research are the samples 84 to 98 coded as follows T14-U-S1, T14-C-S3, T14-O-S5, T14-O-S1, T14-C-S3, T14-U-S5, T16-U-S1, T16-O-S1, T16-U-S4, T16-O-S4, T16-U-S7, T16-O-S7, T16-U-S10, T16-O-S10, T16-O-S12.

Petrographic analysis of aggregates:

The aggregate used in the manufacture of the concrete of dam D1 is classified as a granodiorite. This aggregate is an igneous plutonic rock, associated with hercynian granites of Iberian Peninsula NW. Feldspars are more abundant than quartz. It contains more plagioclase feldspars than potassium feldspars. Dark-colored mica (biotite) is usually present, and light-colored mica (muscovite) is frequently present. Other dark-colored ferromagnesian minerals may be present in lower amounts than those of the light-colored constituents. This rock presents an intense structural deformation due to tectonic history. The Figures 1 and 2 present different mineralogical phases are observed in this aggregate as deformed quartz, altered feldspars and micas.

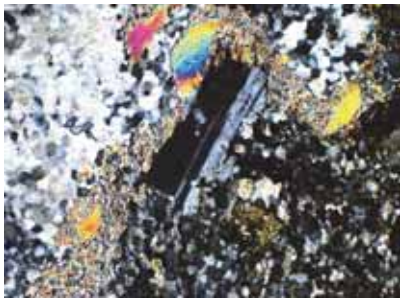

Figure 1. Quartz with undulatory extinction

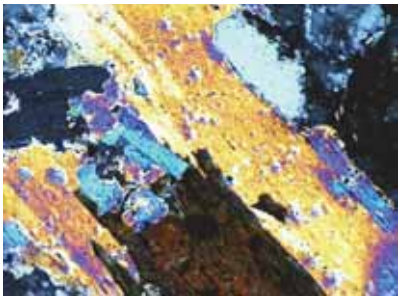

Figure 2. Biotite and muscovites

The aggregate used in the manufacture of the concrete of dam D2, is classified as a plutonic rock of the granite type. This granite is composed mainly of sodic and potasic feldspars, quartz and mica type biotite and muscovite. The Figures 3 and 4 present different mineralogical phases observed in this aggregate as deformed quartz and micas.

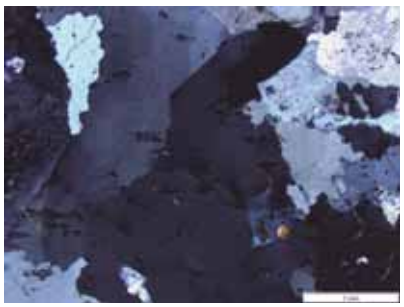

Figure 3. Quartz with undulatory extinction

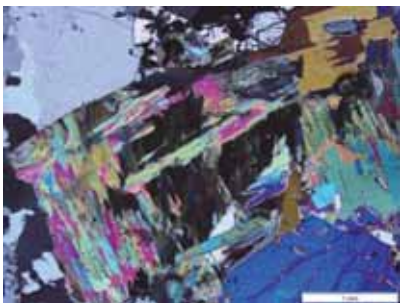

Figure 4. Biotite and muscovites

The aggregates used in the manufacture of the concretes of the two buttresses dams D3 and D4, are classified according to standard ASTM C294 [20] as arenaceous limestones. These limestones are composed mainly of calcite, also containing quartz, feldspars and mica. The Figures 5 and 6 present different mineralogical phases observed in this aggregate as micrite, sparite, bioclastic and quartz inclusions.

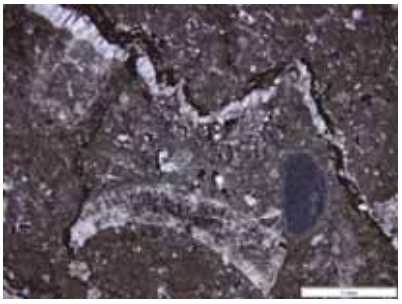

Figure 5. Micrite, sparite and bioclastic

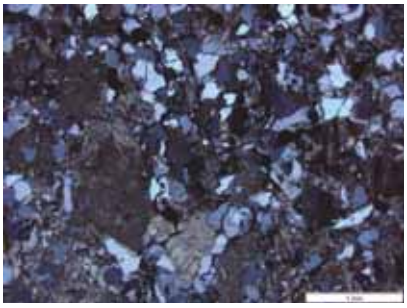

Figure 6. Detrital quartz inclusions

4 Testing methodology and results

4.1 Testing methodology

The Damage Level (DL) is a method which allows to determine the grade of damage and to assign a level of damage based on the microstructural studies, by using micro-structural analysis techniques based on the electronic microscopy study combined with X-ray microanalysis.

The application of DL method shall be done by well-formed technicians, but it is necessary to take into account the operator factor. This method is adequate to evaluate the concrete with opened and filled cracks. In the case of ASR the formation of gels produce a partial densification of the cement paste. Also, with the evolution of the reaction, cracks in aggregates, interfaces and cement paste are formed. These types of cracks are well detected by the DL method, although the evolution of SA damage produces an increase of cracks with crystallization of ettringites inside [17], [18].

The degree of damage for concretes affected by the alkali-silica reaction is set out in Table 1 and by sulphate attack is set out in Table 2, describing the degree of damage for each level, the type of product formed and their location within the material. In Figures 7 and 8 different damage degrees are seen with electron microscope.

In both types of expansive reactions five levels of damage are established, which are increased in accordance with the deterioration from 1 to 5, each level corresponding to: low (1), moderate (2), average (3), elevated (4) and extended to the total (5). For its part, the levels of damage associated to an alkali-silica reaction are named DLASR (Level of Damage caused by Alkali-silica Reaction) and DLSA (Degree of Damage by Sulfate Attack) [19].

Table 1: Definition of damage code as a function of the damage level in concretes affected by alcali-silica reaction [4].

Damage by Alkali-Silica Reaction					
Damage Code	LDASR-1	LDASR-2	LDASR-3	LDASR-4	LDASR-5
Damage degree	Low	Moderate	Average	Elevated	Extended to total
Reaction products	Vitreous gels	Vitreous gels and microcrystallines	Vitreous gels, microcrystallines and microcrystalline products	Vitreous gels, microcrystallines and microcrystalline products	Vitreous gels, microcrystallines and microcrystalline products
Location of products	Pores	Pores + aggregates	Pores + aggregates + aggregate-paste interfaces	Pores + aggregates + aggregate-paste interfaces + paste	Pores + aggregates + aggregate-paste interfaces + paste (↑fissures)

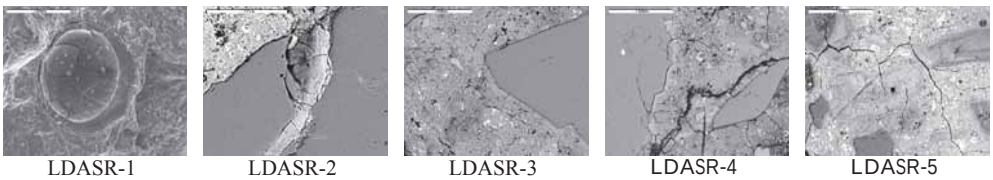

LDASR-1 LDASR-2 LDASR-3 LDASR-4 LDASR-5

Figure 7. Aspect of different damage degree by Alkali-Silica Reaction

Table 2: Definition of damage code as a function of the damage level in concretes affected by sulfate attack [4].

Damage by Sulphate Attack					
Damage Code	LDSA-1	LDSA-2	LDSA-3	LDSA-4	LDSA-5
Damage degree	Low	Moderate	Average	Elevated	Extended to total
Reaction products	Needle-shaped crystallisations	Needle-shaped crystallisations	Needle-shaped and prismatic crystallisations	Needle-shaped and prismatic crystallisations	Needle-shaped and prismatic crystallisations
Location of products	Small pores	Pores + aggregate-paste interfaces	Pores + aggregate-paste interfaces + paste	Pores + aggregate-paste interfaces + paste + small filled fissures	Pores + aggregate-paste interfaces + paste + ↑filled fissures

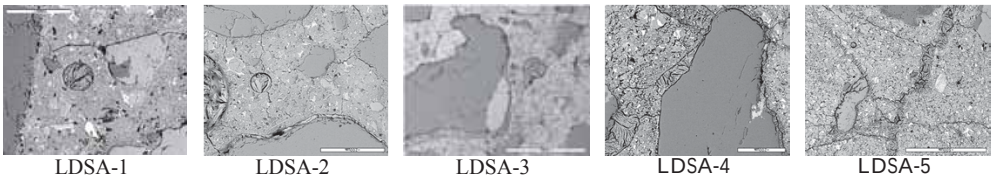

LDSA-1 LDSA-2 LDSA-3 LDSA-4 LDSA-5

Figure 8. Aspect of different damage degree by Sulfate Attack

4.2 Results and discussion

A calculation of DL, due to alkali-silica reaction and due to sulfate attack, has been done to the different cores selected.

Using the evaluation of damage by DL method it is possible to define clearly the origin of damage and qualify it, with values DL ASR (Damage Level caused by alkali-silica reaction) and values DL SA (Damage Level caused by sulfate attack).

In Figure 9 the scatter graph of distribution of damage level type is seen.

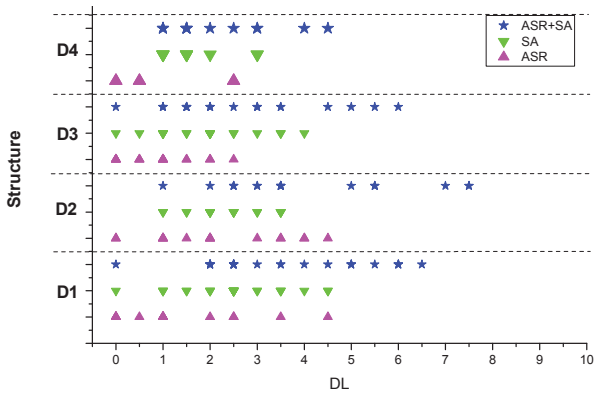

Figure 9. Scatter graph of results of the Damage Level (DL) by structure.

In Figure 10 the distribution of damage level type in structure D1 is seen.

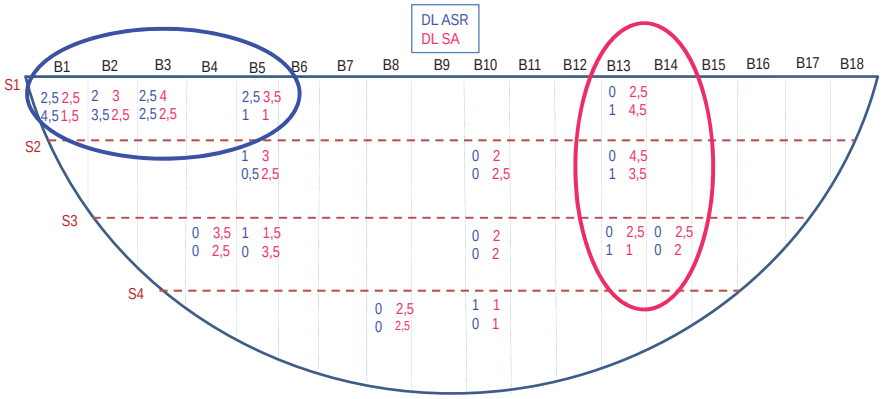

Figure 10. D1 structure damage Level (DL) graphic.

The results obtained by the application of the DL method can be seen in the Figure 11 graphic. This graphic is shows the damage level of alkali-silica reaction (DL ASR), the damage level of sulfate attack (DL SA) and the combination of both damages (DL ASR-SA).

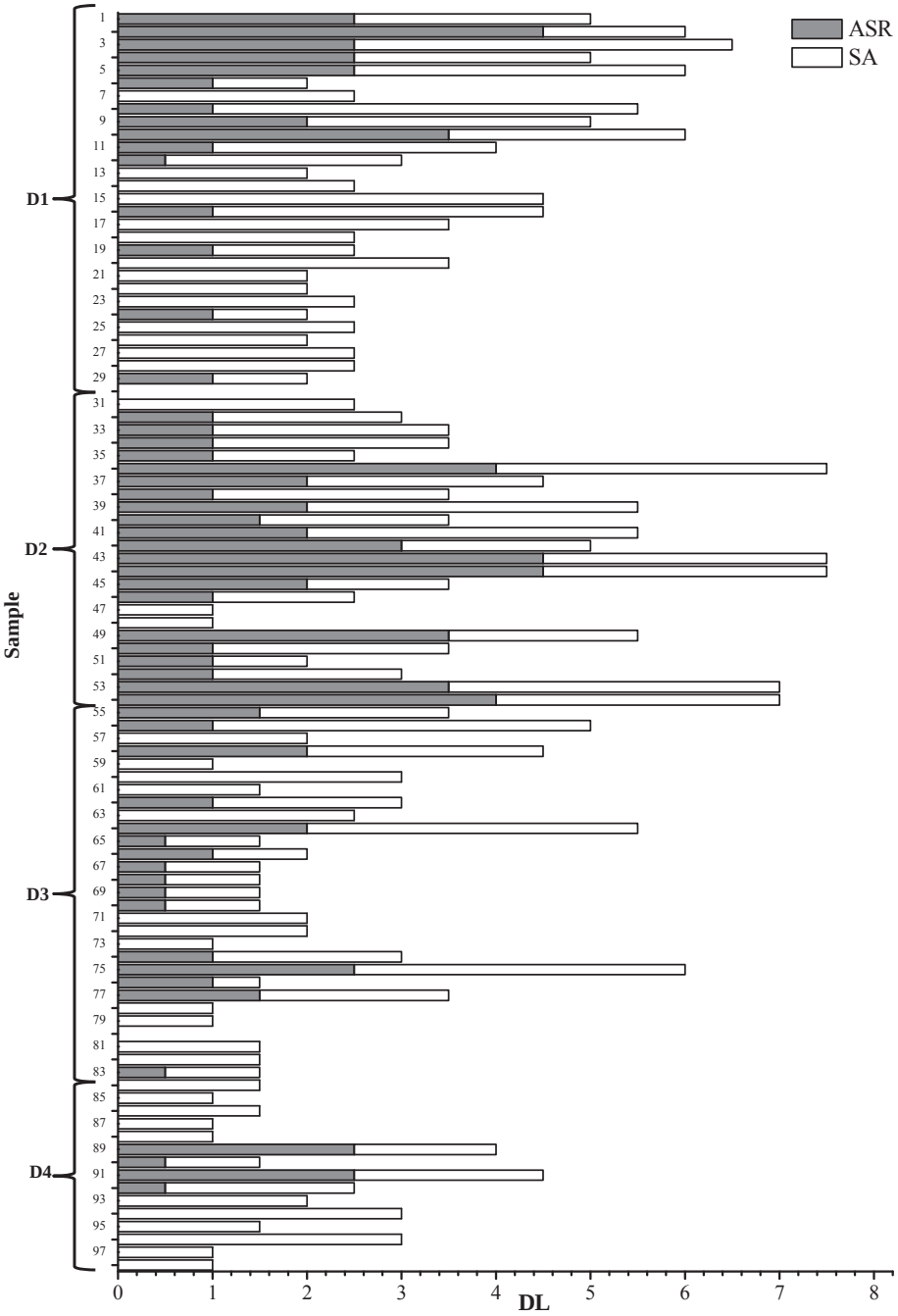

Figure 11. Damage Level (DL) graphic.

5. Conclusions

The damage level is based on microstructural observations. These observations are perfectly correlated with the damages provoked by alkali-silica reactions and sulphate attack.

This methodology can be used to determine the damage level due to alkali-silica reaction and sulfate attack of concrete structures, and determine de distribution of damage in different parts of structures, like dams. The availability of distribution of damage is a useful tool to plan the inspection, maintenance and repairs of the singular structures. Also, a prioritization of resources of different structures can be programmed.

The analysed structures have expansion problems detected in the last 40 years that have generated cracking and dimensional changes.

The experimental results show that dams D1 and D2 are more affected by ASR than the D3 and D4. The most affected dams are around 70 and 40 years old and granites aggregates have been used. While, dams D3 and D4 are 60 years old and have calcareous-siliceous type aggregates. All dams are affected by sulfate attack, although the damage is moderate to average in general.

With respect to the distribution of damage, in general higher damage level by SA is observed upstream. Also, D2 shows higher damage by ASR upstream. In D1 the distribution of damage is heterogeneous, both by ASR and by SA. In general, the damage is higher in the upper part of the structure. But the right side downstream has higher SA, while the left side has an important alteration by ASR. This distribution of damage has led to implement control instrumentation in the dams in the critical zones and to increase the maintenance actions.

Acknowledgement

This work was partially supported by the research project PIE 201460E067 related to *Analysis of diagnosis, evaluation and decision making systems of concrete structures with non-directional cracking* and by the research project BIA2013-47892-P

References

[1] Menéndez, E., Analysis of concrete structures affected by alkali silica reaction, sulfate attack and frost-drawing cycles (in spanish), IECA, (2010).
[2] British Cement Asociation, The diagnosis of alkali-silica reaction. (Report of a working party) (1988).
[3] Hobbs, D.W., Alkali-silica reaction in concrete. Thomas Telford, (1988).
[4] West, G., Alkali aggregate reaction in concrete roads and bridges, Thomas Telford, (1996).

[5] Geoffrey, G. E., Alexander, M. G., Alkali-aggregate reaction and structural damage in concrete, CRC Press, Taylor and Francis Group, (2011)
[6] Skalny, J., Marchand, J., Odler, I., Sulfate attack on concrete, Taylor and Francis Group, (2002).
[7] Scrivener, K., Skalny, J., Internal sulfate attack and delayed ettringite formation, RILEM Publications S.A.R.I, (2002).
[8] Thomas, M.D.A., Ramlocham, T., Field cases of delayed ettringite formation, RILEM Workshop on Internal Sulfate Attack and Delayed Ettringite Formation, Villars, Switzerland, (2002), pp. 85-97.
[9] Menéndez, E., Cracking and sulphate attack in field concrete in Spain, RILEM Workshop on Internal Sulfate Attack and Delayed Ettringite Formation, Villars, Switzerland, (2002), pp. 127-138.
[10] Stutzman, P.E., Deterioration of Iowa Highway Concrete Pavements. A petrographic Study, NIST, (1999).
[11] Jacobsen, S., Lindgard, L., Fritz, L., Frost dilation measurements on concrete cores from dam with ASR, Proceedings on International Congress on Alkali-Aggregate Reaction, Thondheim, Norway, (2008), pp. 131-142.
[12] Tepponen, P., Eriksson, B.E., Damages in concrete railway sleepers in Finland, Nordic Concrete Research, Vol. 6, (1987), pp. 199-209.
[13] Shayan,A., Quick, G. W., Microscopic features of cracked and uncracked concrete railway sleepers, ACI Materials Journal, vol. 89, (1992), pp. 348-361.
[14] Oberholster, R.E., Maree, H., Brand, J.H.B., Cracked prestressed concrete railway sleepers: Alkali-Silica Reaction or Delayed Ettringite Formation, Proceedings of the 9th International Conference of Alkali-Aggregate Reaction in Concrete, London, UK, (1992), pp. 739-749.
[15] Menéndez, E., Gil, A., Martín, A.B., Aldea, B., Marquez, C., Analysis of concrete dams affected by internal expansive processes. Differences and similarities between internal sulfate attack and alkali-aggregate reaction (in spanish), Advance in Security and Durability, Fundetel, (2011), 283-306.
[16] Menéndez, E. Nueva metodología de evaluación del grado de daño por reacciones expansivas internas en el hormigón mediante análisis microestructural. Conpat 2013, Cartagena de Indias, Colombia (2013).
[17] Menéndez, E., García-Rovés, R., Prendes, N., Damage assesment of dams affected expansive reactions using stereomicroscopy and electron microscopy. Relationship between the damage levels DRI and DL, Second International Dam World Conference. LNEC, Lisboa. Portugal, (2015).
[18] Menéndez, E., García-Rovés, R., Prendes, N., Damage assesment of dams affected expansive reactions using stereomicroscopy and electron microscopy. Relationship between the damage levels DRI and DL. Concrete 2015 RILEM Week, Melbourne, Australia, (2015).
[19] Menéndez, E. Evaluation and Gradation of Simultaneous Damage in Concrete Affected by Alkali-Silica Reaction and Sulfate Attack, International Review of Civil Engineering (I.R.E.C.E.), vol.2, N. 2, (2011).
[20] ASTM C 294. Standard Descriptive Nomenclature for Constituents of natural Mineral Agrgregates. (2012)

International RILEM Conference on Materials, Systems and Structures in Civil Engineering
Conference segment on Service Life of Cement-Based Materials and Structures
22-24 August 2016, Technical University of Denmark, Lyngby, Denmark

A RISK-BASED MODEL FOR DETERMINING ALLOWABLE ADMIXED CHLORIDE LIMITS IN CONCRETE

Mahmoud Shakouri, [(1)] David Trejo, [(1)] and Paolo Gardoni [(2)]

(1) Oregon State University, Corvallis, USA
(2) University of Illinois at Urbana, USA

Abstract
Chlorides can be detrimental to the corrosion of steel in concrete. As a result, many organizations limit the amount of admixed chlorides that can be included in new concrete for reinforced concrete structures. However, because chlorides are ubiquitous in most constituent materials used to make concrete, eliminating all chlorides from the constituent materials would make most concrete systems uneconomical. In addition, there is little consensus within the concrete community on how much chloride can be allowed in new concrete - a wide variety of limits are currently specified. This paper identifies variables that influence the service life of conventionally reinforced concrete systems exposed to chloride environments. It also proposes a general outline for a risk-based framework that can be used to specify allowable chloride limits in concrete. The allowable admixed chloride limit in the proposed framework is based on structure type and importance, constituent materials, exposure conditions, and risk level desired by the owner.

1. Introduction

Corrosion is a leading factor in the degradation of reinforced concrete structures in the United States. According to a study conducted by National Association of Corrosion Engineers (NACE), the annual direct cost of metallic corrosion in the United States exceeds $276 billion which represents 3.1% of the U.S. gross domestic product [1]. Moreover, the Federal Highway Administration estimates that repairing and maintaining concrete bridges in the United States costs $20.5 billion annually [2].

Chloride induced corrosion is known to be the major cause of corrosion of reinforcing steel and deterioration of concrete structures exposed to marine environments, de-icing or anti-icing salts. The transport of chlorides in concrete is a complex phenomena that often depends

on a combination of transport mechanisms, i.e., advection, convection, diffusion, migration, and permeation. However, it is commonly assumed that chloride ingress into concrete mimics diffusion and, therefore Fick's second law, as follows, is commonly used to evaluate the rate of chloride ingress:

$$\frac{dc}{dt} = \frac{d}{dx} D \frac{dc}{dx} \tag{1}$$

where c is the percent chloride concentration (% mass) at time t, D is the chloride diffusion coefficient (length^2/time), and x is the depth below the exposed surface (length.) Equation 2 gives the most common solution to the one-dimensional Fick's second law, commonly referred to as the error function, and is based on the assumptions of a constant diffusion coefficient and a constant surface chloride concentration.

$$C(x,t) = C_s - (C_s - C_i) \times erf\left(\frac{x}{\sqrt{4D_a t}}\right) \tag{2}$$

Here, $C(x,t)$ (% mass) is the chloride concentration measured at depth x and exposure time t (second), C_s (% mass) is the chloride concentration at the interface between the exposure environment and concrete, C_i (% mass) is the initial chloride concentration of the concrete mixture prior to exposure to chlorides, D_a (length^2/time) is the apparent chloride diffusion coefficient, and erf is the error function. Here D_a is an "apparent diffusion coefficient" because it accounts for all transport mechanisms and chloride binding. The time to corrosion initiation can be determined deterministically by substituting $C(x,t)$ with the critical chloride threshold, C_T, in Eq 2 and solving for t as shown in Eq 3. C_T is the chloride concentration that results in active corrosion at the steel reinforcement

$$t_i = \frac{1}{1.2614 \times 10^8 \times D_a} \times \left(\frac{x}{inverf\left(\frac{C_T - C_s}{C_i - C_s}\right)}\right)^2 \tag{3}$$

Here t_i is the time to corrosion initiation, *inverf* is the inverse error function, and the factor in the denominator converts time units from seconds to years. To reduce the likelihood of developing corrosion, several organizations in the U.S., such as American Concrete Institute (ACI) and many State Highway Agencies (SHAs), have published documents with values of the maximum amount of allowable admixed chlorides (C_A) that can be included in a new reinforced concrete structures so that $C_i \leq C_A$ [3]. However, allowable admixed chlorides limits vary from one document to another resulting in confusion for the users of such documents. While some documents base chloride limits on percent by weight of portland cement only, other documents used percent by weight of "cement" purportedly, or percent by weight of cementitious materials. An example of this wide variation of the allowable admixed

chloride limits is provided next. In this paper C_A is expressed as percent by weight of portland cement. Table 1 provides a sample mixture and typical values of the concrete properties that can be used to determine the time to corrosion.

Table 1. Mixture proportions and parameters to determine time to corrosion

Mixture Proportions		**Time to Corrosion Parameters**	
Parameter	**Kg/m^3 (lb/yd^3)**	**Parameter**	**Value**
Cement	420 (708)	x	62 mm (2.4 in.)
Water	206 (347)	D_a	2×10^{-12} m^2/sec (3.1×10^{-9} in.^{2}/sec)
Fine aggregate	683 (1151)	C_T	1.2 (% by wt of cement)
Coarse aggregate	981 (1654)	C_s	2.6 (% by wt of cement)
		C_i	0.3 (% by wt of cement)

Figure 1 shows the variability in the allowable admixed chloride limits specified by ACI and the SHAs for the concrete mixture provided in Table 1. ACI has 12 documents with four different chloride limit values for reinforced concrete ranging from 0.06 to 0.3 percent by weight of cement. Specified limits published by the SHAs vary even more significantly. In some cases these limits differ by several orders of magnitude from each other (e.g., 0.05 kg/m^3 (0.08 lb/yd^3) in Georgia vs. 0.63 kg/m^3 (1.06 lb/yd^3) in Delaware).

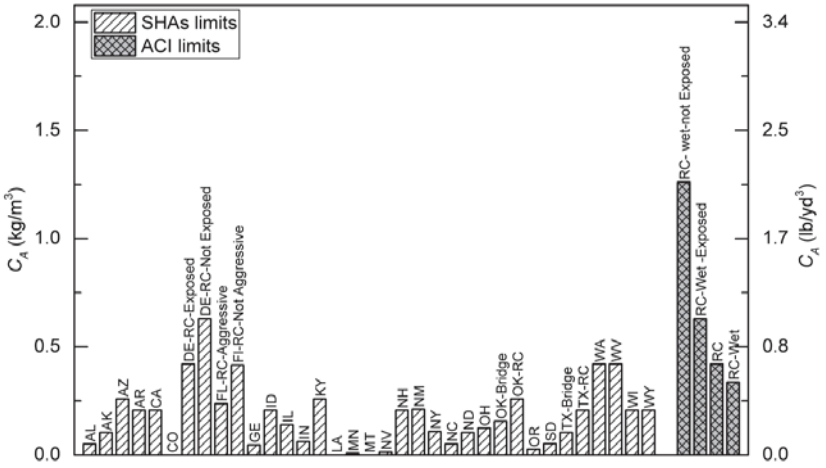

Figure 1. Specified allowable admixed chloride limits by SHAs and ACI for reinforced concrete

Using the values in Table 1, a sensitivity plot for the time to corrosion is created and shown in Figure 2. The abscissa in this figure represents the percent changes in the variables in Eq 3 and the ordinate shows the percent changes in the time to corrosion. For example, if C_i is reduced by 60 percent (i.e. from 0.3 to 0.12 percent by weight of cement) the time to corrosion increases by approximately 22 percent (from 41 years in the baseline to 50 years). Similarly, a 40 percent increase in the C_s (i.e. from 2.6 to 3.64 percent by weight of cement)

results in a 40 percent reduction in the time to corrosion. Note that the slope of the lines for each variable in Figure 2 determines how sensitive the time to corrosion is to that variable. A steeper curve for a variable indicates that the time to corrosion is more sensitive to that variable. Figure 2 shows that C_i can significantly affect the time to corrosion. Increasing admixed chlorides (C_i) can reduce the time to corrosion and vice versa. This is important as the limits on admixed chlorides vary widely.

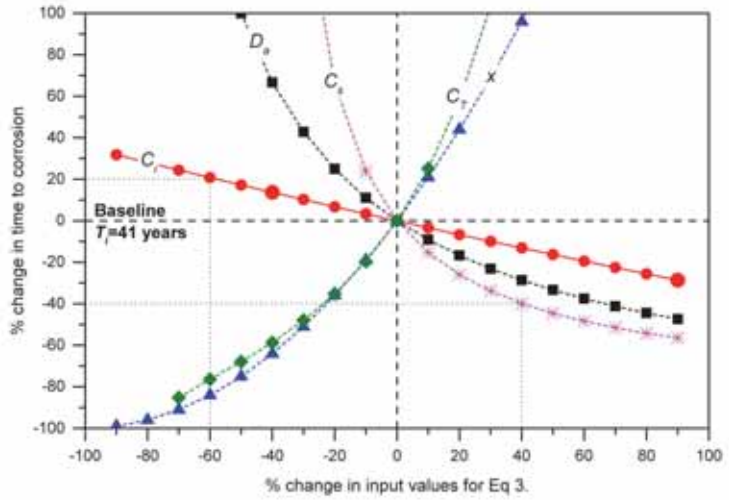

Figure 2. Sensitivity plot for time to corrosion

Lack of consensus on the allowable admixed chloride limits has created a great deal of confusion among designers and contractors [4]. The question that arises here is: *What should be the limit on the allowable admixed chloride?* This is an important question because chloride limits that are too low will make the construction of concrete structures uneconomical and high chloride limits result in shorter lifespans, possibly making the economics of the structure unfeasible. The objective of this paper is to fill this gap by developing a risk-based framework that allows owners to systematically select an appropriate allowable admixed chloride limit based on structure type and importance, exposure conditions, and risk preference of the owner.

2. **Methodology for Selecting C_A**

The proposed risk-based framework is shown in Figure 3. This framework will allow decision makers to set allowable admixed chloride limits (C_A) based on the structure type and its importance, exposure conditions, constituent materials, and the owner's risk preference. The framework presented in this paper is based on Monte Carlo simulation. In this approach, a large dataset for time to corrosion is produced by using random input values from the D_a, C_T, C_s distributions and deterministic values for C_A. Using a deterministic C_A allows for

comparing the influence of allowable admixed chloride on the time to corrosion in a controlled manner. Note that it is assumed that initial chloride concentraction C_i is equal to allowable admixed chloride limit C_A. In the first step of this process, an engineer determines the concrete mixture proportions. The constituent materials of a concrete mixture can affect D_a, C_T, and C_s [5, 6]. To account for this variability, many researchers use probabilistic methods to determine the time to corrosion [7-12]. In the probabilistic methods, a distribution is used for the variable under study. These distributions are either assumed [13, 14] or determined by fitting distributions to laboratory or field data using the goodness of fit test [15, 16].

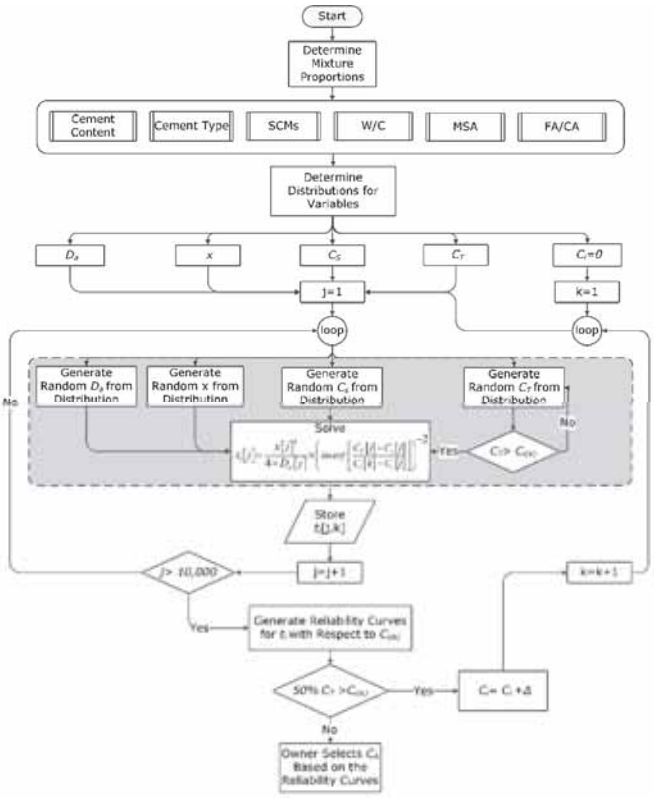

Figure 3. The proposed risk-based framework algorithm to determine allowable admixed chloride

Table 2 presents some of the distributions used by different authors reported in the literature. Note that incorrect selection of a distribution can result in an inaccurate estimate of the time to corrosion. That being said, the objective of this paper is to only demonstrate how the proposed framework can be used to specify allowable admixed chloride limits. Thus, determining the true distributions for the input parameters is left for future work. The dashed box in Figure 3 represents an iterative process to obtain a distribution for the time to corrosion

by using random values from the D_a, C_T, x, and C_s distributions, and a deterministic value for C_A. For each value of C_A, 10,000 iterations are performed and the output distribution for the time to corrosion is used to generate curves for reliability analysis. Then if C_A is less than the 50th percentile of C_T, an incremental value (e.g., Δ= 0.1) is added to C_A and the whole process is repeated again. The 50th percentile for C_T is an arbitrary value. Note that admixed chloride values that are close to critical chloride threshold will result in shorter service life. The Kaplan–Meier method [17], a non-parametric survival analysis technique is used to estimate the survival and hazard functions for the time to corrosion.

Table 2. Published distributions to determine time to corrosion, (mean, SD)

Reference	***D_a (m^2/sec)*** $\times 10^{-12}$	***x (mm)***	***C_T (varies)***	***C_s (varies)***
[12]	LN (0.0159,0.0119)	N(40, 20)	U(0.6-0.17) *(kg/m^3)*	LN(2.95, 1.47) *(kg/m^3)*
[15]	LN(1.61, 0.475)	N(36.6, 16.5)	LN(1.35, 0.135) *(kg/m^3)*	LN(4.56, 1.82) *(kg/m^3)*
[16]	N(1.29, 0.28)	N(60, 5.0)	N(0.07, 0.007) *(% wt conc.)*	N(0.63, 0.10) *(% wt conc.)*
[18]	LN(6, 1.2)	N(60, 15)	N(0.5, 0. 1) *(% wt cem.)*	N(15, 3) *(kg/m^3)*
[19]	LN(3.87, 2)	N(161, 37)	N(1.2, 0.24) *(kg/m^3)*	N(13.1, 1.35) *(kg/m^3)*
[20]	LN(30, 0.6)	N(40, 10)	N(0.5, 0.1) *(% wt cem.)*	NA
[21]	N(8.87, 0.222)	N(60, 5)	N(0.05,0.01) *(% wt conc.)*	N(1,0.3) *(% wt conc.)*

* LN= Lognormal distribution; N= Normal distribution; U= Uniform distribution

Table 3 presents the distributions of the parameters used in this study. For consistency, the mean parameters are assumed to be the same values given in Table 1.

In the context of concrete structures exposed to chlorides, the survival function denotes the probability that a concrete structure given a specified admixed chloride limit "survives" up to time *t;* that is

$$S\left(t \mid C_A\right) = 1 - P\left(t \le t_i \mid C_A\right) = 1 - F\left(t \mid C_A\right) \tag{4}$$

where S is the survival function for time t and $F\left(t \mid C_A\right)$ is the cumulative density function that is also known as failure function given the selected value of C_A. Here survive means no occurrence of corrosion in any parts of the structure. To create a hazard function, also known as a failure rate function, the ratio of the probability density function to the survival function is determined. This ratio is interpreted as the instantaneous failure rate at any point in time. The cumulative hazard function is generally used for reliability analysis and is the integral of the hazard function up to the time *t;* that is

$$H\left(t \mid C_A\right)=\int_0^t \frac{f\left(t \mid C_A\right)}{S\left(t \mid C_A\right)}=\int_0^t \frac{f\left(t \mid C_A\right)}{1-F\left(t \mid C_A\right)}=-\ln\left(1-F\left(t \mid C_A\right)\right) \tag{5}$$

Where H is the cumulative hazard function and $f(t)$ is probability mass function.

Table 3. Modeling parameters for the probabilistic time to corrosion initiation

D_a (m^2/sec) $\times 10^{-12}$	x (mm)	C_T (%wt cem.)	C_s (%wt cem.)	C_A (% wt cem.)
N(2, 0.5)	N(0.062, 0.008)	N(1.2,0.1)	N(2.6,0.22)	Deterministic range 0-0.9

The simplicity of interpreting survival and hazard plots is the main reason for the wide application of such plots in reliability analysis. These plots can help decision makers compare the effect of different admixed chloride limits on the time to corrosion and select the limit that suits their purpose based on their risk preference.

3. Results

Figure 4 summarizes the result of the Monte Carlo simulation (n=10,000) for the time to corrosion by using the probability distributions shown in Table 3. The Anderson-Darling goodness of fit was conducted on the simulated data to determine the distributions of the time to corrosion for different admixed chloride limits. Results show that the variability in the time to corrosion can be modeled using a positively skewed distribution that follows a three-parameter lognormal distribution with the location parameter μ, scale parameter σ, and shape parameter γ as shown in Figure 4. Overall, the magnitude and spread of the time to corrosion reduces as the admixed chloride limit increases. This finding corroborates with the sensitivity plot shown in Figure 1.

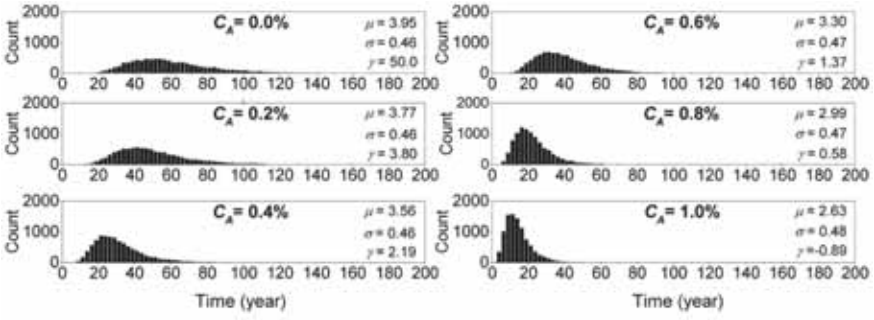

Figure 4. Histogram of time to corrosion for different C_A limits

The Kaplan-Meier survival curves for different admixed chloride limits are shown in Figure 5a. The abscissa of the graph represents the survival duration, i.e., time to corrosion, and the ordinate shows the cumulative probability of surviving up to a specified time. For example, if no chloride is included in the concrete mixture proportions (i.e., C_A =0.0%), the probability of surviving 20 years is 100%. For the concrete containing 0.6% admixed chloride by weight of

cement, the probability of surviving the same time is slightly less than 80%. The curves with lower survival durations have steeper slopes and vice versa. Figure 5b shows the cumulative hazard plot for the time to corrosion. The abscissa represents the time and the ordinate represents the cumulative probability of failure, i.e., corrosion. For example, for the concrete containing no admixed chloride, the probability of failure for the first 20 years is equal to zero, i.e., no hazard. Over time, as the concrete is exposed to chlorides, the probability of failure increases resulting in an increase in the cumulative hazard. Comparing the hazard plots of different admixed chloride concentrations reveals that the inclusion for more chlorides in a concrete mixture results in significantly higher hazard in the early years. As with the survival plot, the slopes of the curves are steeper for the concrete with more admixed chloride. The slopes of the curves eventually become parallel, demonstrating the corrosion of all concrete types at later ages.

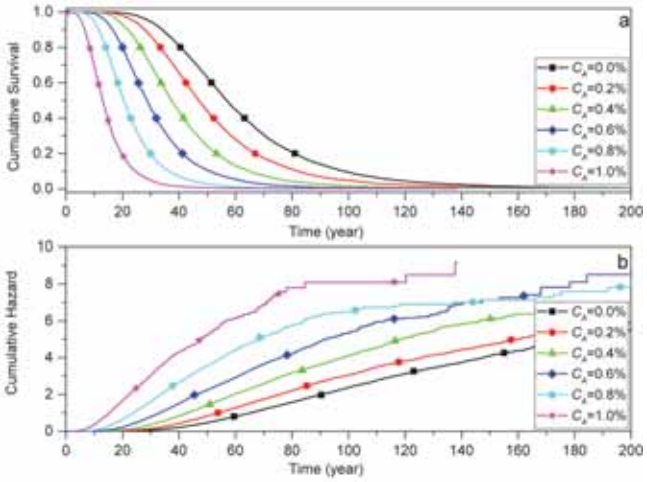

Figure 5. Reliability analysis for the time to corrosion, (a) survival plot; (b) hazard plot

Using the concrete mixture proportions in Table 1 and the allowable admixed chloride limits specified by the SHAs shown in Figure 1 reveals that, for example, in the State of Nevada (C_A=0.022 lb/yd^3÷708 lb/yd^3×100=0.003% by weight of cement) the 50-50 chance of corrosion results in the service life of approximately 56 years. In Delaware, that has a less stringent allowable admixed chloride limit (C_A=1.06 lb/yd^3÷708 lb/yd^3×100=0.14% by weight of cement), the service life for the same probability is approximately 48 years. Assuming that the specified allowable admixed chloride is followed, this means that, depending on the type of specification, the service life of a concrete in two States, can be reduced by 8 years or 14%.

4. Discussion and Conclusion

Lack of a standardized and a systematic approach to setting allowable admixed chloride limits is a major obstacle to specifying a reasonable allowable admixed chloride limit for concrete.

In fact, the wide variations of the limits currently published indicate that specifiers do not understand the influence of admixed chlorides on the time to corrosion. This paper proposed a framework to allow decision makers to set allowable admixed chloride limits based on their risk preference. The present study is based on the premise that structure type and its importance, exposure conditions, constituent materials, and an owner's risk preference are the important factors that should be taken into account when specifying allowable admixed chloride limits. Structures that are designed to last for a long time, have high importance, and are located in chloride laden environments should abide by more stringent chloride limits as opposed to structures that are designed to last only for a short period of time, have lower importance and are not exposed to chlorides.

In the proposed framework, the time to corrosion of a concrete mixture is determined by using probabilistic methods. In this regard, with respect to the type of constituent materials and exposure conditions, a probability distribution is selected for D_a, C_T, x, and C_s. Then, time to corrosion is determined for a set of deterministic values of C_A using the Monte Carlo approach. The outputs of this framework are a survival and a hazard plot. Decision makers can compare survival and hazard curves of different admixed chloride limits and based on their risk preference select the most appropriate admixed chloride limit. The selection criteria fall into the managerial domain. Several factors can be influential at this stage. The first and most important factor is cost. Obviously, using the lowest admixed chloride limit will result in the longest service life of the structure but as a trade-off, the cost of removing all chlorides or using materials with no chlorides can make the project economically unfeasible. Financial valuation for different chloride limits by considering the initial and service costs can paint a clearer picture for the decision makers. Other influential factors are, but not limited to availability of resources, time constraints, and quality.

According to the framework presented here, there is no universal allowable admixed chloride limit. Admixed chloride limits are project specific and can vary significantly from one project to another. This research is the first step in developing a systematic approach to specifying admixed chloride limits. The results of this paper should be of value to those who need to make critical decisions on setting limits for allowable admixed chlorides in concrete. To improve this framework, future research should focus on 1) determining the true distributions for the input parameters, and 2) developing a method for financial valuation of allowable admixed chloride limits.

References

[1] Koch, G.H., Brongers, M.P.H., Thompson, N.G.Y., Virmani, P., and Payer, J.H., Corrosion costs and preventive strategies in the United States. 2002, NACE International: USA.
[2] NACE International. Highways and Bridges. 2016 [cited 2016 Feb 2]; Available from: https://www.nace.org/Corrosion-Central/Industries/Highways-and-Bridges/.
[3] American Concrete Institute, Guide to durable concrete, in American Concrete Institute,. 2008, ACI 201.2R-08,: Farmington Hills, MI.

[4] Trejo, D., Isgor, B., and Weiss, J., ACI's Allowable Admixed Chloride Conundrum. Concrete International (ACI), 2016. Accepted, February 2016.
[5] Ryan, P.C. and O'Connor, A.J., Probabilistic analysis of the time to chloride induced corrosion for different Self-Compacting Concretes. Construction and Building Materials, 2013. 47: p. 1106-1116.
[6] Angst, U., Elsener, B., Larsen, C.K., and Vennesland, Ø., Critical chloride content in reinforced concrete - A review. Cement and Concrete Research, 2009. 39(12): p. 1122-1138.
[7] Vu, K.A.T. and Stewart, M.G., Structural reliability of concrete bridges including improved chloride-induced corrosion models. Structural Safety, 2000. 22(4): p. 313-333.
[8] Bastidas-Arteaga, E., Bressolette, P., Chateauneuf, A., and Sánchez-Silva, M., Probabilistic lifetime assessment of RC structures under coupled corrosion–fatigue deterioration processes. Structural Safety, 2009. 31(1): p. 84-96.
[9] Srubar Iii, W.V., Stochastic service-life modeling of chloride-induced corrosion in recycled-aggregate concrete. Cement and Concrete Composites, 2015. 55: p. 103-111.
[10] Saassouh, B. and Lounis, Z., Probabilistic modeling of chloride-induced corrosion in concrete structures using first- and second-order reliability methods. Cement and Concrete Composites, 2012. 34(9): p. 1082-1093.
[11] Papakonstantinou, K.G. and Shinozuka, M., Probabilistic model for steel corrosion in reinforced concrete structures of large dimensions considering crack effects. Engineering Structures, 2013. 57: p. 306-326.
[12] Nogueira, C.G. and Leonel, E.D., Probabilistic models applied to safety assessment of reinforced concrete structures subjected to chloride ingress. Engineering Failure Analysis, 2013. 31: p. 76-89.
[13] Kirkpatrick, T.J., Weyers, R., Anderson-Cook, C., Sprinkel, M., and Brown, M., A Model to Predict the Impact of Specification Changes on Chloride-induced Corrosion Service Life of Virginia Bridge Decks. 2002.
[14] Engelund, S. and Sørensen, J.D., A probabilistic model for chloride-ingress and initiation of corrosion in reinforced concrete structures. Structural safety, 1998. 20(1): p. 69-89.
[15] Lounis, Z., Uncertainty Modeling of Chloride Contamination and Corrosion of Concrete Bridges, in Applied Research in Uncertainty Modeling and Analysis, N. Attoh-Okine and B. Ayyub, Editors. 2005, Springer US. p. 491-511.
[16] Ferreira, M. and Jalali, S., Probabilistic assessment of the durability performance of concrete structures. Engenharia Civil, 2004. 21: p. 39-48.
[17] Kaplan, E.L. and Meier, P., Nonparametric estimation from incomplete observations. Journal of the American statistical association, 1958. 53(282): p. 457-481.
[18] Val, D.V. and Trapper, P.A., Probabilistic evaluation of initiation time of chloride-induced corrosion. Reliability Engineering & System Safety, 2008. 93(3): p. 364-372.
[19] Kwon, S.J., Na, U.J., Park, S.S., and Jung, S.H., Service life prediction of concrete wharves with early-aged crack: Probabilistic approach for chloride diffusion. Structural Safety, 2009. 31(1): p. 75-83.
[20] Bastidas-Arteaga, E., Chateauneuf, A., Sánchez-Silva, M., Bressolette, P., and Schoefs, F., A comprehensive probabilistic model of chloride ingress in unsaturated concrete. Engineering Structures, 2011. 33(3): p. 720-730.
[21] Bentz, E.C., Probabilistic modeling of service life for structures subjected to chlorides. ACI Materials journal, 2003. 100(5): p. 391-397.

International RILEM Conference on Materials, Systems and Structures in Civil Engineering
Conference segment on Service Life of Cement-Based Materials and Structures
22-24 August 2016, Technical University of Denmark, Lyngby, Denmark

INFLUENCE OF RESTRAINED SHRINKAGE IN RC BUILDUING SLABS: A CASE STUDY

Carlos Sousa [(1)], Emanuel Felisberto [(1)], Rui Faria [(1)]

(1) Faculty of Engineering of University of Porto, Porto, Portugal

Abstract
The control of cracking in reinforced concrete (RC) slabs, axially restrained by earth retaining walls or bracing systems, is a topic of practical relevance. However, even today the correct procedures to quantify the minimum steel reinforcement to ensure adequate performance under service conditions are insufficiently known. In fact, the required reinforcement is affected by several variables difficult to quantify, of which one of the most important is the axial tensile force installed on the slab due to restraints to shrinkage and thermal imposed deformations. This paper presents a procedure for serviceability analysis of cracked RC slabs, towards quantifying the required areas of steel reinforcement for controlling crack widths. The procedure is consistent with the principles of normative documents such as the Eurocode 2 (EC2) and the fib Model Code. It is based on a nonlinear finite-element (FE) analysis, in which cracking is modelled via a smeared cracking approach. A multi-fixed cracking model with strain decomposition is used to include the effects of shrinkage, creep and thermal deformations. An example involving the serviceability analysis of a restrained RC solid slab is used to demonstrate the proposed methodology potentialities, as well as the implications of the involved phenomena.

1. Introduction

This work presents a procedure for serviceability analysis of RC building structures considering the effects of applied loading and restrained shrinkage deformations. The proposed procedure can be seen as an evolution of the current analysis methodologies, based on existing design codes.

It is well known by practitioners that the required amount of steel reinforcement, in restrained RC structures, is often determined by serviceability requirements related to the limitation of

the maximum crack width. The current design codes, such as the EC2 [1], propose a procedure for estimating the maximum crack width as a function of the amount of steel reinforcement. Upgraded procedures, based on recent research [2] are proposed in the fib Model Code [3]. However, the calculated crack width depends, to a large extent, on the value of the installed axial force. And it is difficult to quantify the value of such axial force in real RC building structures because it is strongly dependent on: (i) the important redistribution of axial forces which occurs after cracking; (ii) the stiffness of the restraining elements (other parts of the structure and foundations. Advanced analytical solutions can be used to estimate the value of that axial force in simple cases. Another analysis alternative consists of carrying out a nonlinear FE analysis, considering viscoelastic and cracking effects. One of the advantages of this analysis alternative lies on the fact that it is suitable for the study of irregular and complex structures too.

The analysis procedure used in the current design practice is based on an important simplifying assumption: the axial force due to the restraint to the imposed shrinkage and thermal deformations is assumed as $N_{cr} = A_c \times f_{ctm}$, where A_c is the cross-sectional area of concrete and f_{ctm} is the average concrete tensile strength. However, such assumption can be very conservative (and therefore uneconomical). In some special circumstances the opposite may occur: it may lead to results which are not on the 'conservative' side. That may occur, for example, in RC slabs with large openings or in the region where a slab is connected to rigid bracing walls.

The procedure that is proposed in the present work is based on finite element analyses, with macro RC elements – the finite element side is approximately equal to the average crack spacing. A smeared cracking approach is employed to simulate tension stiffening effects. The results obtained so far have shown that this methodology is sufficiently robust to be applied in the analysis of real, large scale, RC structures. Therefore, it seems that it is a promising methodology to be used for:

- The analysis of special structures where it is important to accurately assess the long-term behaviour, with due account of cracking effects. An example of these type of structures is a building with a long separation between expansion joints.
- The development of parametric analyses aiming at providing guidance for the design of structures with common structural configurations.

This presentation is organized as follows: (i) firstly the structure under analysis (case study) is presented: (ii) then the methodology of analysis is described; (iii) finally, relevant results and conclusions are addressed.

2. Case study

The structure to be analysed is an RC building whose dimensions, in plan, are $60 \times 32 m^2$. The floors are made with a 0.20m thick solid slab, supported by RC beams and columns, with the layout shown in Figure 1. The interior slab spans are 7.0m long, whilst the end spans are 5.5m

long. Along the periphery the first floor slab is supported by a 0.25m thick RC wall. The walls are rigidly connected to a rock foundation and, therefore, fixed supports are adopted at the base of each wall. These walls and the respective foundations are responsible by an important restraint to the shrinkage deformations of the first floor slab. The present work focuses on the behaviour of this slab under service load conditions. The steel reinforcement in the slab consists of a quadrangular grid of 12cm^2/m near the top face and 10cm^2/m near the bottom face. The walls are reinforced with a quadrangular grid of 13.5cm^2/m on each face. A normal concrete of the grade class C25/30 is used in all the structural elements. The concrete cover is such that the distance of the exposed concrete face to the reinforcement axis is 31mm in the slab and 43mm in the walls.

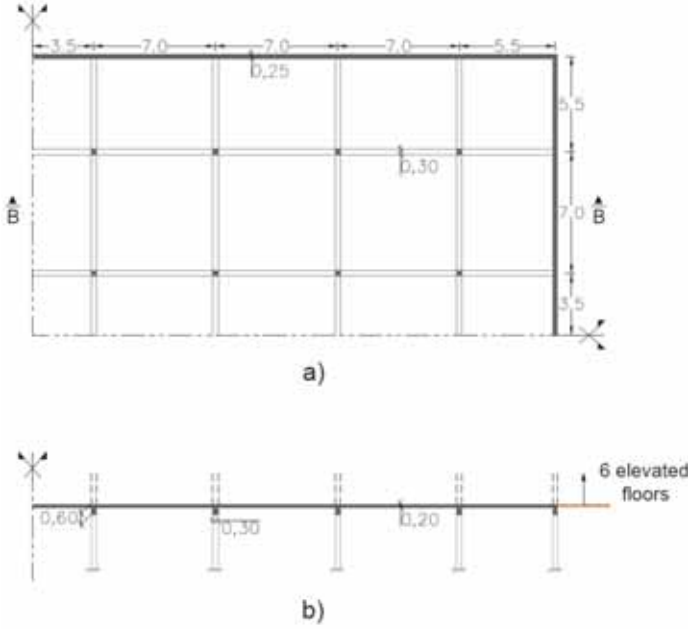

Figure 1: Scheme of the RC structure: a) floor plan; b) elevation B-B (dimensions in [m]).

For definition of the parameters that affect creep and shrinkage evolutions, an average relative humidity is taken as 60%. It is assumed that no loss of humidity occurs across the wall surface in contact with the soil. As regards the slab, shoring is assumed to be removed 28 days after casting. That is the instant of time when the slab self-weight is introduced in the analysis. The start of drying is considered to occur 14 days after casting. This is a simplifying assumption and corresponds to the average between: (i) the start of drying from the slab's top surface immediately after casting; (ii) the start of drying from the slab's bottom face at 28 days, when the formwork is removed.

The quasi-permanent loading applied to the slab is equal to the structure self-weight plus a service load of 3kN/m^2. For the purpose of quantifying the vertical loading applied to the walls, 6 elevated floors (above the one under analysis) are considered, which corresponds to a linear load on top of each wall equal to 250kN/m.

3. FE modelling

A nonlinear FE analysis is used to study the long-term structural behaviour considering the effects of creep, shrinkage and cracking. The first floor slab, beams and walls are discretized with 8-noded shell finite elements with 5 degrees of freedom per node, implemented in the FE package DIANA [4]. Each finite element is numerically integrated along the thickness through seven layers of integration points (Simpson's rule). Each layer is composed by four Gauss points. Figure 2 depicts the FE model, where one can see that only one fourth of the structure is modelled, owing to symmetry conditions.

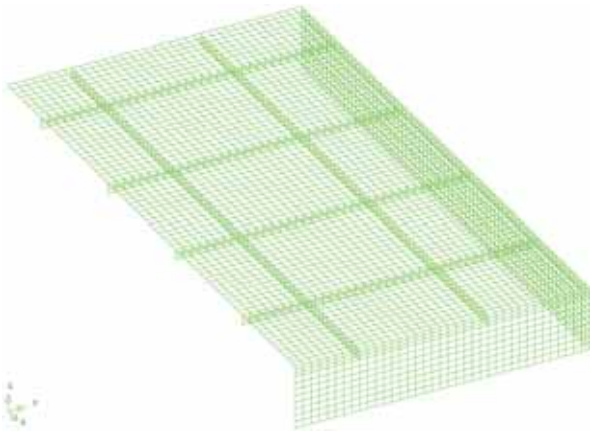

Figure 2: FE model of the RC structure.

The constitutive behaviour of concrete is simulated by a fixed crack model with a strain decomposition [5], in which the concrete strains are the summation of the stress dependent strains, the shrinkage strains and the crack strains.

The tension stiffening behaviour is simulated by using the average concrete stress-crack opening relationship described in [6]. According to this model, the average concrete stress in cracked concrete is equal to $\beta \times f_{ctm}$ if the yield stress of the reinforcement is not reached at the crack. In this smeared cracking approach the steel rebars are simulated as embedded reinforcement FEs, whose displacement fields coincide with the ones of the embedding concrete FEs (therefore, steel-concrete slip is not explicitly modelled). Instead, a macro control volume is adopted (whose dimension is approximately equal to the average distance between real concrete cracks) and the constitutive model for concrete assures that, in the FE

model, the average behaviour in that control volume is reproduced. The β value was taken as 0.4. The distance between cracks is estimated according to the fib Model Code provisions [3].

The main advantages of this approach for simulating cracking effects are: (i) it is suitable, and constitutes a robust methodology, for the analysis of large scale structures, as macro FEs are used; (ii) the adopted tension stiffening model is the one proposed by the EC2 [1] and by the fib Model Code [3], and consequently the obtained results are consistent with the approach followed in those codes.

Shrinkage is simulated by a time variation of concrete stress-independent strains according to the fib Model Code. The time variation of the concrete modulus of elasticity, as well as the creep deformations, are modelled through a Dirichlet series whose parameters are derived by curve fitting to the fib Model Code laws.

The time scale was discretized in steps whose size is progressively increasing. After the application of any action, the following sequence of time steps is considered: 0.1, 0.9, 6 and 10 days. Each individual load is applied in 10 steps of equal magnitude. The analysis ends 30 years after casting the floor slab.

4. Results and discussion

This section presents a set of results which show the structure condition at the end of the analysis (30 years). Time variations of representative results are also shown.

Figure 3 depicts the crack pattern in the slab, at the end of the analysis. The crack strains are represented by vectors normal to the cracks (one vector per cracked integration point). The results are shown for both the bottom and top slab surfaces. It can be seen that the structure is extensively cracked, owing to the stiffness of the walls rigidly connected to the foundation. The most extensively cracked region is located in the vicinity of the angle formed by the orthogonal walls. This is because the restraint action introduced by the walls is essentially of the "edge restraint" type. That is, each wall hinders the slab movement in the direction parallel to the wall.

In the bottom slab surface, the highest crack openings occur with an inclination of approximately 45º with respect to the wall directions (diagonals labelled as D_{bot1} and D_{bot2} in Figure 3a). In the top slab surface the largest crack openings are observed in the same diagonal direction. In this case, they occur above the column closest to the corner of the walls (spot labelled as D_{top} in Figure 3b).

Extensive cracking can be seen also in the walls, as shown in Figure 4. However, the crack pattern in the walls is much more uniform that the one observed in the slab. Cracking in the wall is essentially due to the uniform, fixed, restraint at the base supports.

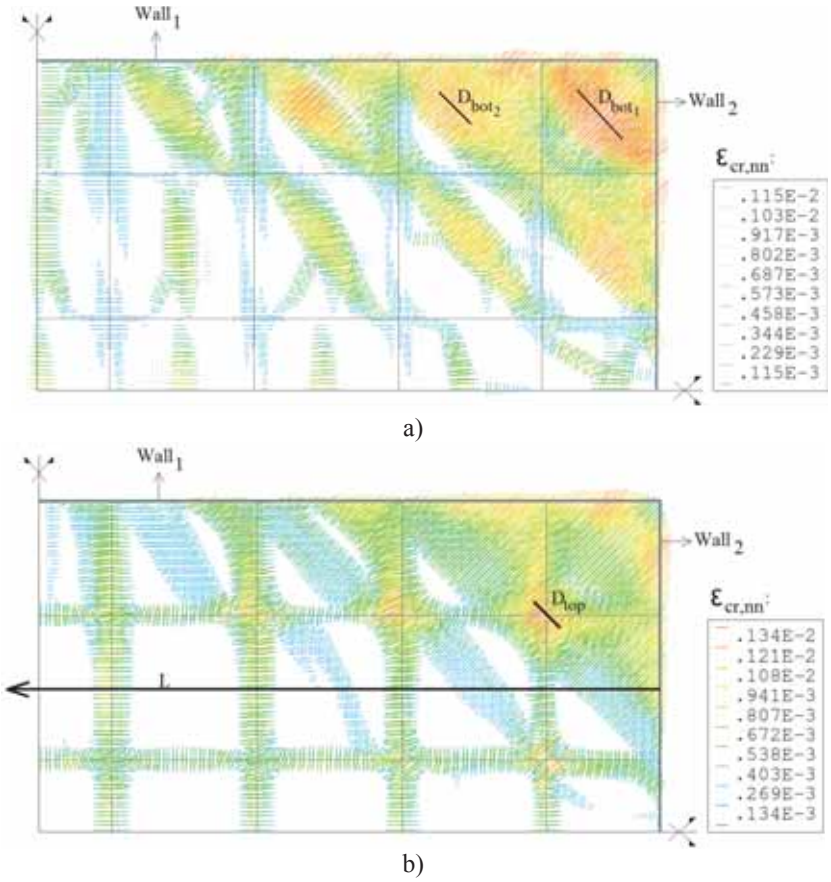

Figure 3: Crack pattern in the slab at the end of the analysis (30 years):
a) bottom slab surface; b) top slab surface.

In order to understand the magnitude of the slab restraint, Figure 5 shows the average deformation in each slab span, in the direction parallel to the side with a length of 60m (herein labelled as longitudinal direction). Such average deformation is expressed as a percentage of the deformation in a similar uncracked slab, in which no restraint exists besides the one due to its own reinforcement. For this case study, such reference deformation is equal to 606×10^{-6} at long term (30 years). Therefore, a percentage of 0% in Figure 5 would mean that the span deformation was fully restrained. The lowest deformation value shown in Figure 5 is equal to 32%. It can be seen that the deformations in the longitudinal direction increase as the distance to the wall in that direction increases too. This fact confirms that the restraint in this type of slab structure is essentially of the type "edge restraint". A wide range of variation of deformation values is observed, with a maximum deformation equal to 86% of the free slab shortening.

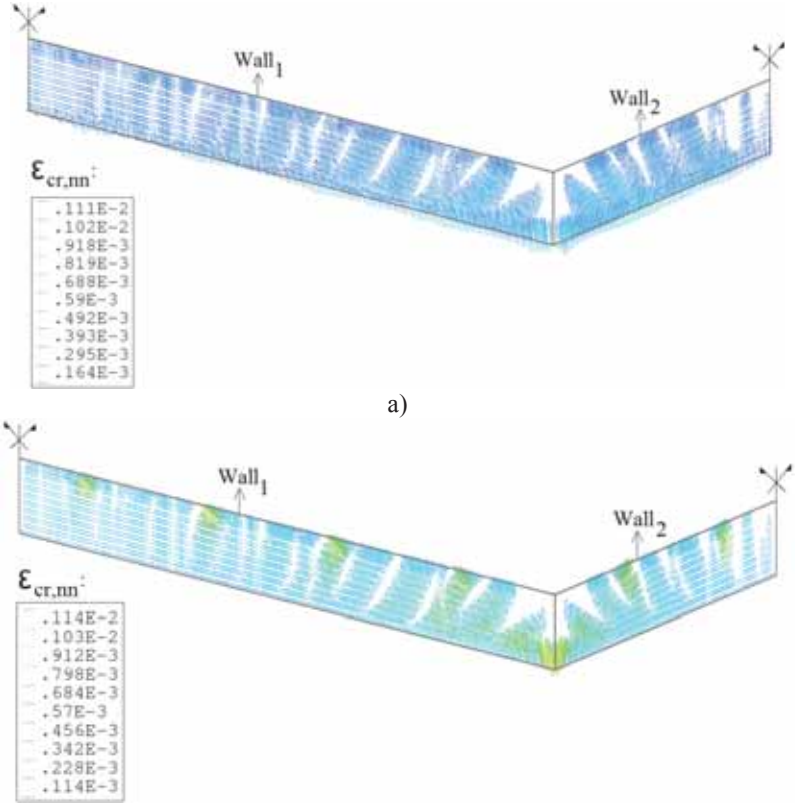

Figure 4: Crack pattern in the walls at the end of the analysis (30 years):
a) exterior wall surface; b) interior wall surface.

Figure 5: Average axial deformation of each span alignment
as a percentage of the unrestrained slab axial deformation.

It was explained before that one of the most relevant results of long-term FE analyses of these restrained structures is the axial force installed in the slab. Figure 6 shows the time variation of that force for the three critical positions identified in Figure 3: D_{bot1}, D_{bot2} and D_{top}. The axial cracking force for this slab is $N_{cr} = A_c \times f_{ctm} = 520$kN. Therefore, one can conclude that if the serviceability analysis related to the verification of the maximum crack opening was made considering an axial force of $N_{cr} = 520$kN, then an uneconomical design would be obtained, as this limit value is never attained. Figure 6 also shows that the applied axial force reaches a stable value in the first few years of the structure life. This is a consequence of the fact that, in an RC structure composed by thin members, a large percentage of creep and shrinkage deformations takes place in the first years after casting. In the structure under analysis, the concrete delayed deformations after the first 5 years are very reduced.

By looking at Figure 6 one can see that the highest axial force is reached in the first year. That value (indicated in the box in Figure 6) is significantly higher than the long-term axial force. However, it is important to note that the axial force value that is of interest for crack opening verifications is the long term one, because of the (approximately) monotonic evolution of the crack opening values (see Figure 7).

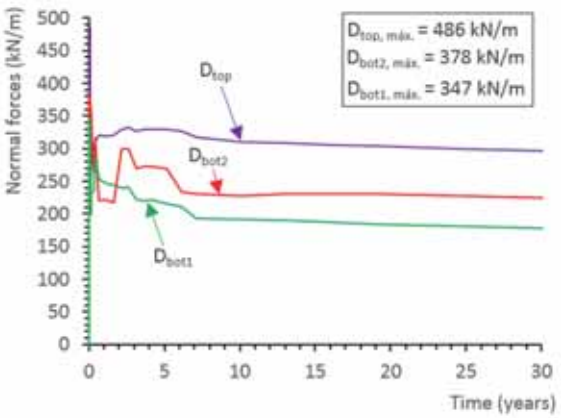

Figure 6: Time variation of axial forces in the slab, in three critical positions identified in Figure 3.

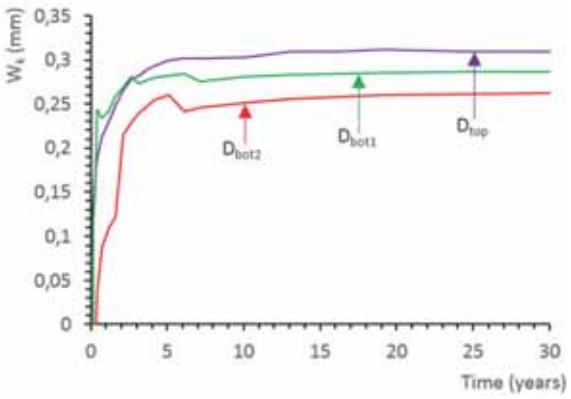

Figure 7: Time variation of maximum crack openings in the slab, in three critical positions identified in Figure 3.

Cracking plays a paramount role in decreasing the axial force value. This fact is demonstrated in Figure 8, which shows the variation of the axial force in the slab (in the longitudinal direction) along the axis L indicated in Figure 3. Figure 8 presents the results for two analyses: (i) the base analysis whose results were shown before (labelled with "with cracking" in Figure 8); (ii) a different analysis in which the only difference lies in the fact that concrete is not allowed to crack. A huge decrease of the axial force, due to cracking effects, is observed.

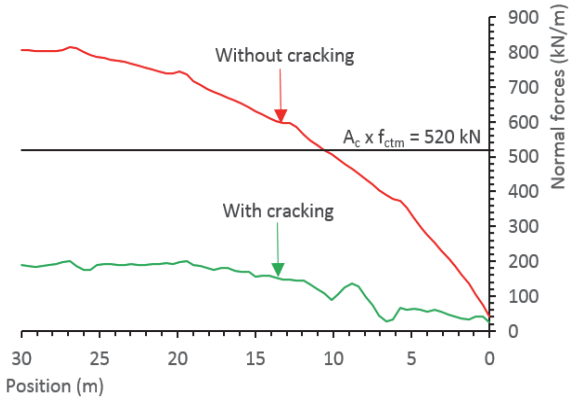

Figure 8: Axial force at the end of the analysis (30 years) along the axis L indicated in Figure 3: results considering, or not considering the effects of cracking

5. Conclusions

This communication discusses the long-term behaviour of RC building slabs, whose axial imposed shrinkage and thermal deformations are strongly restrained. A case study, which consists of a building structure with dimensions in plan of $60 \times 32 m^2$, was presented. It was shown that the long-term distribution of axial forces in the slab is strongly dependent on the influence of cracking. The numerical results indicate that the time variation of crack openings stabilizes approximately 5 years after casting, and the maximum crack openings can be calculated considering the long-term calculated efforts (at the last instant of time). The restrained deformation exhibits an important variation, and the most critical positions in terms of crack openings occur near the corner of the slab, where the restraint introduced by the walls and respective foundations is higher.

Based on the exposed results, it could be concluded that the employed procedure for nonlinear structural analysis can be a useful tool to understand the long-term behaviour of this type of structures. Besides that, in the authors' opinion, it can be a valuable instrument to assist in the serviceability design of special structures.

Acknowledgements

This work was financially supported by: Project POCI-01-0145-FEDER-007457 - CONSTRUCT - Institute of R&D In Structures and Construction funded by FEDER funds through COMPETE2020 - Programa Operacional Competitividade e Internacionalização (POCI) – and by national funds through FCT - Fundação para a Ciência e a Tecnologia; research project IntegraCrete PTDC/ECM-EST/1056/2014.

References

[1] CEN, EN 1992-1-1 - Eurocode 2: Design of concrete structures-Part 1-1: General rules and rules for buildings, Brussels (2004)
[2] Caldentey A.P., Peiretti H.C., Iribarren J.P. and Soto A.G., Cracking of RC members revisited: influence of cover, φ/ρs,ef and stirrup spacing–an experimental and theoretical study, Structural Concrete 14 (2013), 69-78
[3] *fib*, *fib* Model Code for Concrete Structures 2010, Berlin, Germany, Wilhelm Ernst & Sohn, Verlag für Architektur und technische Wissenschaften GmbH & Co. KG (2013)
[4] TNO DIANA BV, DIANA-Finite Element Analysis-Release 9.6, Delft, The Netherlands, (2015)
[5] Manie, J., Kikstra W.P., DIANA user's manual-Material Library, Delft, The Netherlands, TNO DIANA BV (2015)
[6] Azenha M., Sousa C.F., Faria R. and Serra Neves A., Thermo-hygro-mechanical modelling of self-induced stresses during the service life of RC structures, Engineering Structures 33 (2011), 3442-3453

International RILEM Conference on Materials, Systems and Structures in Civil Engineering
Conference segment on Service Life of Cement-Based Materials and Structures
22-24 August 2016, Technical University of Denmark, Lyngby, Denmark

EXTENDED ROUND ROBIN TESTING PROGRAM OF COST ACTION TU1404 – LESSONS LEARNED FROM THE INITIAL EXPERIMENTAL PHASE

Marijana Serdar [(1)], Stéphanie Staquet [(2)], Dirk Schlicke [(3)], Emmanuel Rozière [(4)], Gregor Trtnik [(5)], Sree Nanukuttan [(6)], Miguel Azenha [(7)]

(1) University of Zagreb, Faculty of Civil Engineering, Zagreb, Croatia
(2) ULB Université Libre de Bruxelles, BATir, Brussels, Belgium
(3) Graz University of Technology, Institute of Structural Concrete
(4) GeM, Ecole Centrale de Nantes, France
(5) Igmat Building Materials Institute & University of Ljubljana, Faculty of Civil and Geodetic Engineering, Slovenia
(6) Queen's University Belfast, Energy Efficient Materials & Technology cluster, UK
(7) University of Minho, ISISE, Portugal

Abstract
The extended round robin testing program (RRT^+) is used in the Working Group 1 of the COST Action TU1404 as a fundamental mechanism: i) to validate advanced, non-standardised experimental techniques for testing cement-based materials and structures, ii) to benchmark different sustainable variations of concrete mixes prepared with mineral admixtures, recycled materials and/or by-products, and iii) to obtain input data for a range of concrete properties which could serve designers and engineers to better predict lifespan, durability, and serviceability of concrete structures. With a total of 45 laboratories from Europe, Japan and Canada, performing over 50 test methods on the same concrete mix, it presents one of the most extensive initiatives for joint testing of cement-based materials. The RRT^+ is divided into two phases: the initial and main experimental phases. During the initial phase, an ordinary concrete mix is prepared using the same constituting materials and following identical preconditioning, preparation, conditioning and test procedures. Even though the framework is identical and potential external causes of deviations are limited, concrete is prepared in different laboratories and some scatter in results can be expected. This paper describes the observations during the initial experimental phase and discusses methods including statistical analysis performed to understand the scatter and results obtained.

1. Introduction

In current design standards (e.g. Eurocode, fib Model codes) design and quality control during construction are based on classification of structural materials according to strength classes, with most of the other material properties being practically dependent only on such classes. Nowadays it is clear that this approach is not sufficient and that there is a need for

performance-based approach, based on different parameters of concrete, relevant for the structural and environmental application. In order to successfully propose and deploy a performance-based approach, data on different properties of different types of concrete need to be known and validated and a database of material properties needs to be established. This is especially the case when incorporating by-products and waste materials in cement-based materials. Additionally, there are numerous advanced techniques continuously being developed, that can give answers to questions raised by modelling and limit the need for assumptions and uncertainties in current models. But to step out of the research framework and come to the wider practice, these techniques have to be validated at a pan-European level.

The main objectives of the extended Round Robin Testing (RRT^+) are twofold. The first objective is to provide better understanding of the CBM themselves (database of properties), especially high-performance and eco-concrete. This will offer new opportunities to simulation/predictive models both in terms of validation of modelling assumption/strategies and opportunities for the validation of simulation results. The second objective is the mutual validation of advanced, non-standardised experimental techniques developed in European laboratories. This will highlight the validity and added value of newly developed techniques, and lead to standardization of more precise and property targeted methods for testing CBM.

The RRT^+ is divided into two phases, the initial and main experimental phases. The initial experimental phase kick-started the RRT^+ and actually corresponds to a classical RRT. The approach employed in the RRT^+ was to ship the constituting materials from the same location in France to different participating laboratories in Europe, Canada and Japan and to ask participants to mix and test specified concrete in their laboratories. Participants received detailed guidelines on preconditioning, mixing, sampling, curing and testing of concrete. This initial experimental phase is a mandatory step for all participating laboratories to be fully included in the main phase. Even though the framework was identical and potential external causes of deviations limited, concrete was still prepared in different laboratories and some scatter in results was expected.

Results obtained by various laboratories which are presented hereafter are used to give a critical overview of the chosen approach to Round Robin Testing. The overall aim of the initial phase was to define procedures for preconditioning, mixing and curing of concrete well enough so that laboratories can create a comparable concrete. If a comparable concrete can be prepared, it will be possible to evaluate the efficiency and effectiveness of the novel and non-standardised test methods performed by different laboratories. Therefore, the statistical analysis was not performed to study the repeatability and reproducibility for each test method used in the Initial phase, since these methods are standardized and such a procedure is outside the scope of the Extended Round Robin Test. Rather, the aim was to determine if it is possible to make comparable concrete in across the different laboratories and identify the procedures that need to be defined to achieve the same.

2. Experimental program

2.1 Materials

The ordinary concrete mixture labelled OC which was used to achieve the objectives of the initial experimental phase is presented in Table 1. The mix is based on the mix used in the

context of the Vercors project [4], an experimental mock-up of a nuclear reactor containment-building at 1/3 scale which has been recently built at Renardières near Paris by Électricité de France S.A. (EDF). The mix has effective water-to-cement ratio 0.52, high-strength Portland cement and addition of chemical admixture in the form of a plasticizer. The composition presented hereafter is based on the mass of fully water saturated gravel (both 4-11 mm and 8-16 mm), dry sand and water necessary to add to the mixer.

Table 1. Composition of ordinary concrete OC mix used in the RRT program

Basic Material	Type of the material	Amount [kg/m^3]
Cement	CEM I 52.5 N-SR3 CE PM-CP2 NF HRC	320
Sand	0-4 mm, REC GSM LGP1 (13 % of CaO and 72 % of SiO2)	830
Gravel	4-11mm, R GSM LGP1 (rounded, containing silicate and limestone)	445
	8-16 mm, R Balloy (rounded, containing silicate and limestone)	550
Admixtures	Plasticizer SIKAPLAST Techno 80 (water content 80%)	2.4
Added water*	Water that needs to be added in the mixer	170.9
w_{eff}/c		0.52

* Added water = Effective water (obtained from w_{eff}/c ratio) – 0.8*amount of the Sp (80% of Sp mass is water) + water theoretically absorbed by the sand (0.77% as coefficient of absorption)

2.2 Participants, material provision and logistics

During the launching of RRT$^+$ interested participants were requested to submit a commitment letter, on which they expressed their willingness to perform specific tests during this initiative. In total 45 laboratories submitted their commitment letters, coming from 19 countries worldwide. According to the requested material, around 100 tonnes of raw material were distributed from France among the participants. With respect to efficiency, the distribution was organized over 18 national contact points. These contact points received the whole request from one country and organized a domestic redistribution. Altogether, the whole distribution process took around 4 months.

In due time to the submission deadline of this contribution, 34 out of 45 laboratories could submit their Initial phase results, and are presented in the Table 2. All listed laboratories and contact persons are the authors of experimental data presented in this paper, while the authors of the paper present managing team of RRT$^+$. Additional laboratories submitted their results after the submission deadline and are not taken into account in this publication. Delays arose in a few cases due to transport issues in terms of delivery difficulties (e.g. laboratories with restricted access possibilities), transport damages, which had to be replaced as well as challenging overseas supply chains. Besides, a few other participants were confronted with structural changes or will participate only in a very specific part of the Main phase due to the restrictions of their resources.

2.3 Preconditioning procedures

For the preparation of fully saturated gravel, it was necessary to place needed amount of gravel in a sealed tank with enough water to reach full saturation at least 7 days prior to mixing. This procedure ensured that the aggregate had sufficient time to fully absorb water.

Regardless of these sealed conditions, an additional check of absorbed water was performed on the day of mixing. If the fully saturated state had not been reached, the water needed to reach such state had to be added in the mixer. Sand had to be oven dried at 60°C for 24 hours or until constant mass was reached. After the drying, container with the sand was taken out from the oven and kept in laboratory conditions at least several hours before mixing until the temperature of the sand was 20 ± 2°C.

Table 2. Laboratories that submitted results for the Initial phase in due time

No	Institute	Country	Contact person
1	Graz University of Technology	Austria	Joachim Juhart
2	Belgian Building Research Institute (BBRI)	Belgium	Benoît Parmentier
3	KU Leuven	Belgium	Özlem Cizer
4	Ghent University	Belgium	Philip Van den Heede
5	IGH Institute Zagreb	Croatia	Dalibor Sekulić
6	Faculty of Civil Engineering Osijek	Croatia	Ivana Miličević
7	IGH Institute Split	Croatia	Elica Marušić
8	University of Zagreb	Croatia	Ivan Gabrijel
9	Czech Technical University Prague	Czech Republic	Radoslav Sovjak
10	GeM - Ecole Centrale de Nantes	France	Emmanuel Rozière
11	Nantes University, GeM Institute	France	Stéphanie Bonnet
12	Lafarge	France	Arnauld Delaplace
13	University of La Rochelle, LaSIE	France	Philippe Turcry
14	OTH Regensburg	Germany	Ivan Parić
15	TU Braunschweig iBMB/MPA	Germany	Wibke Hermerschmidt
16	TU Dresden	Germany	Egor Secrieru
17	Queen's University	Great Britain	Sree Nanukuttan
18	Democritus University of Thrace	Greece	Souzana Tastani
19	Budapest University of Technology and Economics	Hungary	Katalin Kopecsko
20	TU Delft	Netherlands	Guang Ye
21	NTNU	Norway	Anja Klausen
22	Silesian University of Technology	Poland	Jacek A. Golaszewski
23	ISEL, High Institute of Engineering	Portugal	Carla Maria Costa
24	Nat. Lab. for Civ. Eng., Dep. for Materials (LNEC)	Portugal	Maria S. Sousa Ribeiro
25	University of Minho	Portugal	Miguel Azenha
26	Teixeira Duarte, Engenharia e Construcoes	Portugal	Ivo Rosa
27	Institute for Materials Testing	Serbia	Ksenija Janković
28	University of Novi Sad	Serbia	Vlastimir Radonjanin
29	University of Ljubljana	Slovenia	Violeta B. Bosiljkov
30	Slovenian Nat. Building and Civil Eng. Institute	Slovenia	Aljoša Šajna
31	Igmat Building Materials Institute	Slovenia	Gregor Trtnik
32	ITEFI Institute (CSIC), G-CARMA	Spain	Sofia Aparicio
33	Univesitat Politechnica Madrid	Spain	Jaime C. Galvez
34	Yeditepe University	Turkey	Altug Soylev

Using the procedure described above, it was expected that the sand would not bring additional water to the mix and gravel would not absorb water from the added mixing water. Aggregates of Vercors concrete have a relatively high absorption coefficient, especially the coarse 4/11 mm aggregate (2.61 %) and the 8/16 one (2.25%), which could lead to a significant differences in effective water-to-cement ratio, if classical correction of water was performed. In fact, in a previous round robin test of early age properties [5] with 11 laboratories that prepared the same mortar mix, no requirements were set for the moisture state of the

aggregate prior to mixing, and the amount of water to be added directly into the mix was then given by a spreadsheet considering the given moisture content. Slump after mixing varied from close to 0 to well above 200 mm in these mortar batches. In the second round it was prescribed specifically that the aggregate was to be mixed with zero moisture, meaning pre-drying. In this second series, the slump after mixing varied from 150 to 255 mm. In the research performed by Cortas et al. [6] different concretes were prepared from the same concrete mixture by changing only the initial degree of saturation of limestone aggregates. Three degrees of saturation were studied, namely: 0% (dry aggregates), 50% (partially saturated aggregates) and 100% (saturated aggregates). In all mixes water content of aggregate was measured each time and the amount of added water adjusted prior to mixing. Results of autogenous and plastic shrinkage and porosity of these three mixes clearly showed that the early-age behaviour of concrete is significantly influenced by the initial water saturation of aggregates. Therefore, even though the procedure of preconditioning chosen in this RRT^{+} was somewhat complicated, time consuming and somewhat deviated from usual practice, it was crucial that all participating laboratories adhered to it, and a spreadsheet was provided to help with the procedure and collect information at all critical levels to check compliance.

2.4 Testing methods

Just after mixing, it was requested to perform following mandatory tests on fresh concrete:

1) consistency - standard slump technique according to the procedure described in standard EN 12350-2:2009 [7],
2) air content –one of the two methods described in standard EN 12350-7:2009 [8],
3) density – using methods described in standard EN 12350-6:2009 [9],
4) initial concrete temperature,
5) visual appearance of the mixture (a photograph of fresh concrete immediately after mixing and report any peculiarities, e.g. segregation of coarse aggregates, bleeding, etc.).

Consistency, air content and density had to be repeated 3 times on the same mixture within the shortest possible time window in order to adequately perform statistical analysis of the obtained results. Time of each test needed to be noted in the provided spreadsheet.

From the concrete mix, six standard specimens were taken for determining the concrete compressive strength. Most of the laboratories used standard cubes with the dimensions of 150×150×150 mm. Some laboratories used concrete cylinders with dimension Ø110/220 mm and their results are approximated to that of standard concrete cube using the procedure given in the standard EN 206-1:2000. Specimens needed to be wet cured in water at 20±2°C or in controlled humidity environment at more than 95% relative humidity and temperature of 20±2°C, as per the procedure described in standard EN 12390-2:2009 [10]. Compressive strength test needed to be performed after 7 (3 replicates) and 28 days (3 replicates), following the procedure described in standard EN 12390-3:2009/AC:2011 [11]. This paper only presents and analyses the values of slump, concrete temperature and compressive strength at 7 days. Each participating laboratory was asked to complete the above-mentioned spreadsheet for collecting results, consisting various details including preconditioning, results

of fresh and hardened state properties, as well as to provide several photographs of the concrete mix. Laboratories were required to highlight the deviations (if any) from the prescribed procedures for preconditioning, mixing and curing, as well as eventual deviations from the procedure of testing described in the required standards.

2.5 Analysis methods

For the analysis of results a basic statistical tool was utilised. Statistical analysis comprised of calculating the mean value and the standard deviation both for each participating laboratory and for the concrete properties and general mean of the group for each property, checking normality of obtained data, fitting distribution and checking for outliers using Mandel's statistics, all in accordance with the standard ISO 5725-2 [12].

Mean value, $\overline{y_{ij}}$, and standard deviation, s_{ij}, of each property were calculated for each laboratory, using following expressions:

$$\overline{y_{ij}} = \frac{1}{n_{ij}} \sum_{k=1}^{n_{ij}} y_{ijk} \quad (1)$$

$$s_{ij} = \sqrt{\frac{1}{n_{ij}-1} \sum_{k=1}^{n_{ij}} \left(y_{ijk} - \overline{y_{ij}}\right)^2} \quad (2)$$

where:

- n_{ij} – number of (replicates) test results, 3
- y_{ijk} – single result

Next, a general mean, $\overline{\overline{y_j}}$, and standard deviation, s_j, for each property was calculated, based on all mean values obtained by different laboratories, using following expressions:

$$\overline{\overline{y_j}} = \frac{\sum_{i=1}^{p} n_{ij} \overline{y_{ij}}}{\sum_{i=1}^{p} n_{ij}} \quad (3)$$

$$s_j = \sqrt{\frac{1}{p_j-1} \sum_{i=1}^{p_j} \left(\overline{y_{ij}} - \overline{\overline{y_j}}\right)^2} \quad (4)$$

where:

- p_j – number of laboratories

The relative distribution of obtained values was calculated for each tested property by grouping results in classes and determining frequency of certain obtained value. Once the relative distribution was known, it was possible to evaluate whether data was following a Normal distribution. Normality test was performed visually, by plotting Q-Q plots, showing empirical values vs theoretical values according to the Normal distribution function.

Outliers were identified using Mandel's *k* and *h* statistics. Mandel's *h* coefficient shows between-laboratory consistency statistics for each laboratory and is calculated using following equation:

$$h_{ij} = \frac{\overline{y_{ij}} - \overline{\overline{y_j}}}{\sqrt{\frac{1}{(p_j - 1)} \sum_{i=1}^{p_j} (\overline{y_{ij}} - \overline{\overline{y_j}})^2}} \quad (5)$$

For the number of laboratories involved , $p > 30$, a number of replicates within each laboratory for each property, $n = 3$, and a significance level 5%, the h coefficient for each laboratory should be lower than 1.91 [12]. If the coefficient estimated from the data is beyond 1.91, value obtained by this laboratory was considered to be an outlier. This between-laboratory consistency is of actual interest in the RRT$^+$, since it shows how consistent the results are for each laboratory, as compared to the whole group. Mandel's k coefficient shows within-laboratory consistency and it is calculated using the following equation:

$$k_{ij} = \frac{s_{ij}\sqrt{p_j}}{\sqrt{\sum s_{ij}^2}} \quad (6)$$

For number of laboratories, $p > 30$, a number of replicates within each laboratory for each property, $n = 3$, and a significance level 5%, the k coefficient for each laboratory should be lower than 1.72 [12]. If the calculated coefficient is beyond 1.72, the analysed value is considered to be an outlier. This within-laboratory consistency is potentially more of an interest for the individual laboratories, since it shows how their own deviation within one specific property is consistent with the deviation of the group.

3. Results

3.1 Consistency

Consistency using slump value was considered as one of the main parameters for determining if the participating laboratories used the same procedure and whether the same concrete was obtained. Consistency is very sensitive to even a small difference in water content, therefore it was expected that any potential difference in effective water-to-cement ratio would be evident in the slump values. The individual mean value for each participant and the standard deviation calculated from three reported values of obtained slump are presented in Figure 1.

The horizontal line in Figure 1 indicates the value of the general mean of all slump values for the entire group, calculated according to eq. (3), whereas the dotted lines correspond to the mean value ± two general standard deviations, calculated according to eq. (4), which should present 95% of all obtained values in the case behaviour follows Normal distribution. In total only 32 values of slump are presented, because the values of two laboratories were not taken into account for statistical analysis. One laboratory indicated spread value instead of slump value and the second had extremely high air content, which influenced all other properties and was at this point considered as an internal error during mixing.

Reported values of slump are between 184 to 258 mm, with general mean of the group being 219 mm and standard deviation 15.8 mm. Therefore, all concrete mixes fall into consistency class S4 or S5, with most laboratories achieving concrete consistency class S5. Concrete was found to have critical stability and some laboratories reported that it was prone to segregation.

Indeed, only after the experimental results were collected, it was realized that the cement that was shipped to participants was not the same cement used for the optimisation of the mixes. Even though they are both Ordinary Portland cement with strength class 52.5, produced in the same cement plant, they differ in the amount of C_3A. Cement used during the optimisation process was CEM I 52.5 N CE CP2 NF, with 9% of C3A and Blaine area 4400 cm^2/g, while cement actually shipped to participants ended to be CEM I 52.5 N-SR3 CE PM-CP2 NF HRC, with 2% of C3A and Blaine area 4150 cm^2/g. It is exactly this difference in the cement that caused the mix to show signs of segregation, since the amount of superplasticizer and water was not optimised for this cement. During the Main phase the mixes will again be optimised, taken into account this new type of cement.

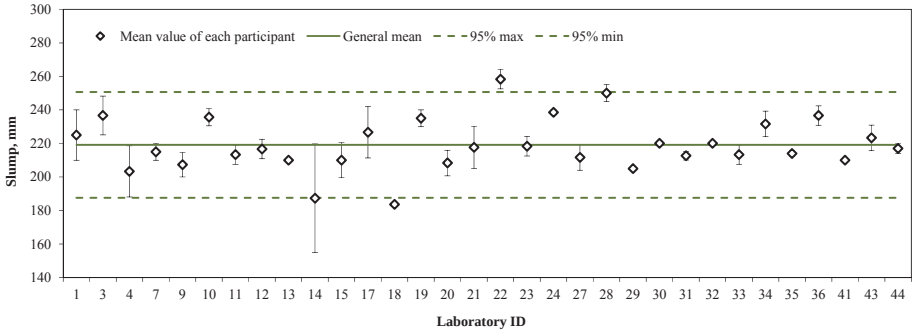

Figure 1. Individual mean values and standard deviation of obtained slump values

Figure 2. Different visual appearance of fresh concrete in different laboratories

Q-Q plot for testing normality and relative distribution of the slump values are presented in Figure 3 a) and b). It can be observed that values are normally distributed, since there is a linear relationship between the empirical value of general mean and the theoretical value according to Normal distribution. Furthermore, if relative distribution is observed, it can be concluded that the obtained values follow a Normal distribution, with the mean value having the highest frequency.

Mandel's *k* and *h* coefficients were calculated for each laboratory and are presented in Figure 4. The limiting values for both coefficients are indicated with dotted lines (significance level 5%). Since values of slump obtained by participants can be higher or lower than the general

mean, the *h* coefficient can have positive and negative value. Some participants did not report all three values of slump, or obtained the same value three times, leading to *k* coefficient equal to 0.

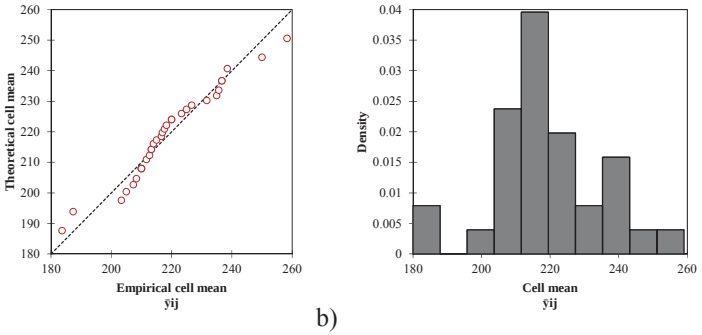

a) b)

Figure 3. a) Q-Q plot and b) relative distribution of slump values

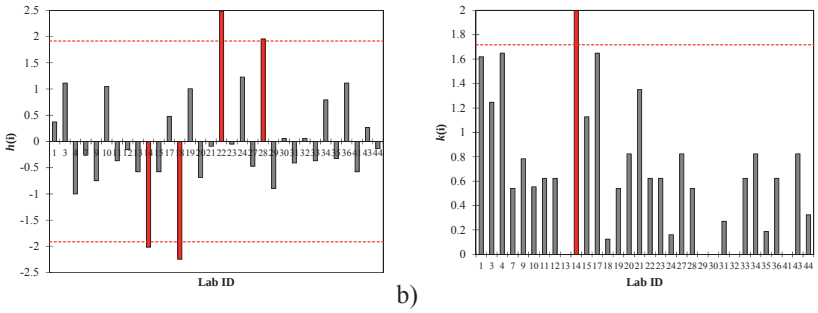

a) b)

Figure 4. a) Mandel's *h* and b) Mandel's *k* coefficients for slump values

According to Mandel's *h* coefficient, the slump values obtained by 4 laboratories are considered as outliers, since they have significantly different values (statistically) than the general mean, which led to *h* coefficients bigger than 1.91. Laboratory 18 obtained a significantly lower value of slump (184 mm) compared to other laboratories and to the general mean (219 mm). From the report obtained by this laboratory, it became obvious that the recommended procedure for preconditioning of materials was not followed, and that concrete was actually mixed with dry gravel and dry sand, instead of fully saturated gravel and dry sand. Even though the amount of water added to the mix was corrected accordingly, which led to the concrete with the same effective water-to-cement ratio, nevertheless the concrete obtained had significantly different consistency and was therefore recognised as outlier. This example strongly highlights the effect of aggregate state concerning water content and the effect it has on concrete fresh properties.

Laboratory 14 obtained slump values with significantly higher with-in laboratory deviation, which led to this value being an outlier also according to the limiting value of Mandel's *k*

coefficient. The reason for this high deviation is the loss of workability of mix during time. Mainly, laboratory 14 obtained two first values of slump similar to the general mean value. It is only the third value of slump that was lower than the general mean, which indicates that the slump testing was performed at the time when mix was starting to lose its workability. Therefore, for future testing, it should be strictly prescribed at what time certain testing needs to be performed, in relation to the instant at which cement and water were mixed.

Finally, laboratories 22 and 28 had somewhat bigger values of slump, 258 and 250 mm respectively, compared to other laboratories. Both of these laboratories followed the prescribed procedure. At the same time, in the case of both laboratories, after 7 days of preconditioning gravel, the amount of water in the gravel was higher than reported water absorption. This additional water was not subtracted, and was added to the mix together with the gravel. It is therefore possible that this additional water, added together with the gravel, caused slightly higher values of slump. However, these obtained values should be looked at from the practical point of view. Difference of 20 – 30 mm in slump value on mean slump higher than 210 mm should not be considered as significant and the slump should actually be considered as falling to the same consistency class [13].

3.2 Concrete temperature

Another important parameter, used to critically review the preconditioning procedure, was the temperature of fresh concrete. Similarly to the water content, the temperature of fresh concrete has a significant influence on its fresh state properties. The individual mean value for each participant and standard deviation calculated from three reported values of reported concrete temperature are presented in Figure 5.

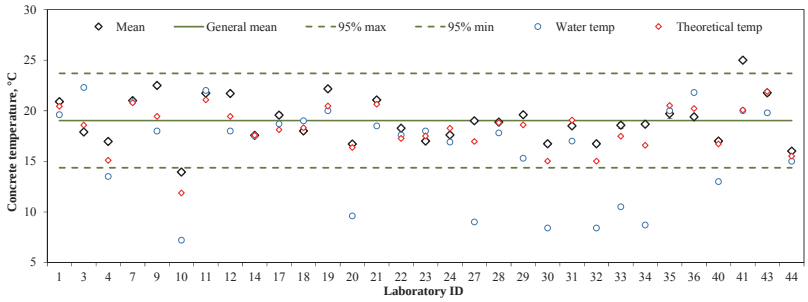

Figure 5. Individual mean values and standard deviation of obtained concrete temperature

Similar to Figure 1, the horizontal line in Figure 5 indicates the general mean of all temperature values for the entire group, calculated according to eq. (3), whereas the dotted lines represent the mean value ± two general standard deviations, calculated according to eq. (4), which should present 95% of all obtained values in the case behaviour follows Normal distribution. Figure 4 presents also temperature of water, since preconditioning of water was not strictly prescribed in the RRT$^+$ procedures. Additionally, the theoretical temperature of fresh concrete is also indicated for each laboratory, calculated using known initial temperature of each constituent, its mass in m^3 of concrete and its specific heat capacity.

In total, 31 values of fresh concrete temperature were collected. The data shows that concrete temperatures were between 13.9° and 25°C, with the general mean of the group being 19°C and standard deviation 2.3°C. The relative distribution and Q-Q plot for testing normality of obtained values are presented in Figure 6.

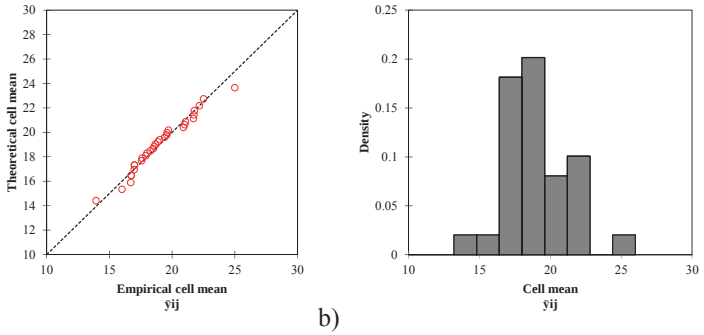

a) b)

Figure 6. a) Q-Q plot and b) relative distribution of concrete temperature

It can be observed that values are normally distributed, since there is a linear relationship between empirical value of general mean and theoretical value according to Normal distribution. Furthermore, if the relative distribution is observed, similar to slump values, it can be concluded that the temperature values follow the Normal distribution, with the mean values having the highest frequency.

When values of temperature are considered in more detail, it can be observed that several laboratories used very cold tap water (around 8°C), while the rest of the laboratories used preconditioned water at 20°C. Regardless of the fact that there is a significant difference in temperature of water, the resulting temperature of concrete is still comparable. This is highlighted using laboratories 24 and 27 as an example. In laboratory 24, water was preconditioned and had temperature similar to other constituents (17-18°C), while in the case of laboratory 27 tap water was used (9°C). Regardless of this difference of almost 10°C temperature of fresh concrete of laboratories 24 and 27 is similar (18 and 19°C respectively). But when laboratories used cold tap water and also did not precondition constituting materials to 20°C, there was an obvious difference in the achieved temperature of concrete. For example, in the case of laboratory 10, the constituting materials had temperature of 11°C and cold tap water of 7°C was used. The resulting temperature of concrete for this laboratory was 14°C, which is below 95 percentile of temperature values. This value is also recognised as outlier using Mandel's *h* statistics, Figure 7 a). Additionally to laboratory 10, the temperature value of laboratory 41 was also considered as an outlier. In the case of this laboratory, all constituents had temperature around 20°C, and the resulting concrete temperature was around 25°C, which is higher than 95 percentile of the group value. Mandel's *k* statistics indicated values of laboratories 33 and 35 as outliers, since their standard deviation had somewhat higher values compared to other laboratories. However, it should be noted that some laboratories performed only one measurement, instead of prescribed three measurements, consequently having misleadingly low standard deviation and Mandel's *k* coefficient.

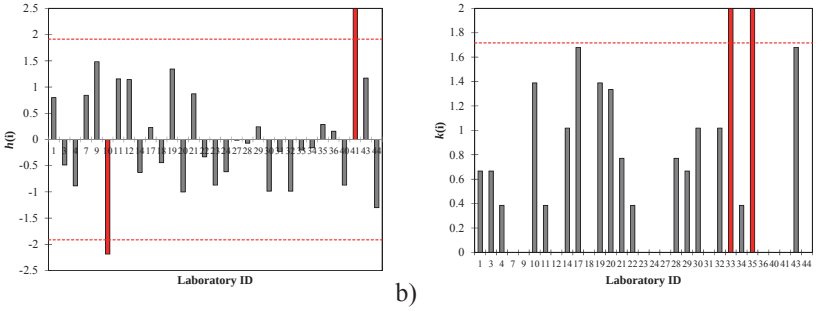

a) b)

Figure 7. a) Mandel's *h* and b) Mandel's *k* coefficients for concrete temperature

3.3 7-day compressive strength

Compressive strength is one of the most important performance indicators to assess the similarity of concrete mixes. In the frame of the Initial phase, both 7-day and 28-days strengths were requested from the participants. However, hereafter results of only 7-day strength will be presented and discussed. Figure 8 shows values of mean compressive strength for each participating laboratory, together with a general mean of all values for the entire group, calculated according to eq. (3) and two-sided 95 percentile.

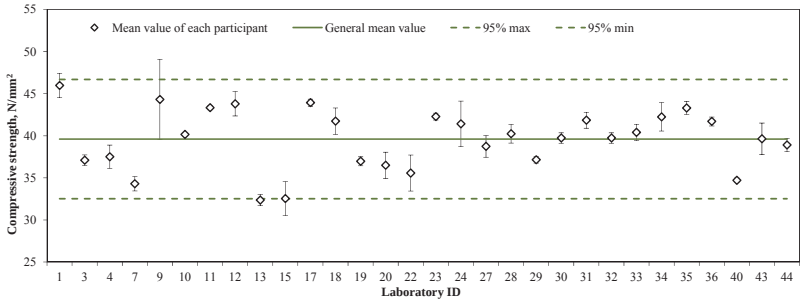

Figure 8. Individual mean values and standard deviation of obtained 7-day concrete compressive strength

In total, 30 values of 7-days compressive strength were collected. The obtained values of 7-days compressive strength are between 32 and 46 N/mm^2, with the general mean of the group being 39.6 N/mm^2 and standard deviation 3.5 N/mm^2. The coefficient of variation was 8.8%. It can be observed that most of the values reported by different laboratories fall into the range of 95 percentile. Looking at the Q-Q plot and histogram, shown in Figure 9 a) and b) respectively, it can be observed that values also follow a Normal distribution.

Even though no obvious outliers could be detected from the Q-Q plot, 4 values were identified as outliers by using Mandel's *k* and *h* coefficient, as shown in Figure 10. Both laboratory 13 and 15 obtained somewhat lower values of compressive strength (32.8 and 30.4 N/mm^2) compared to the mean value of the group (39.6 N/mm^2). The reason for this lower strength could not be found in any of the steps of procedure, since both laboratories followed

the procedure in detail. Laboratories 9 and 24 are recognised as outliers according to their Mandel's *k* coefficient, since they obtained higher standard deviation with-in their results, compared to the group.

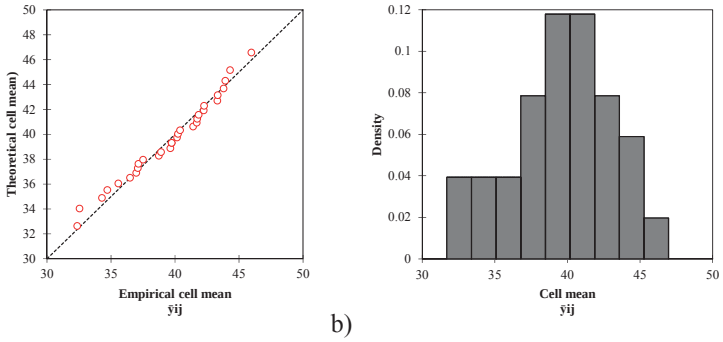

a) b)

Figure 9. a) Q-Q plot and b) relative distribution of 7-days compressive strength

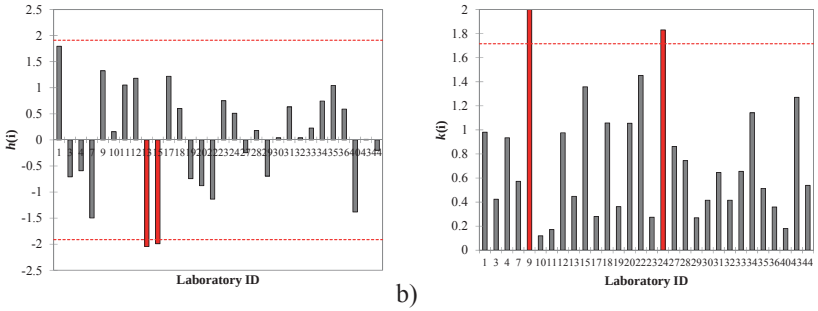

a) b)

Figure 10. a) Mandel's *h* and b) Mandel's *k* coefficients for 7-day compressive strength

Even though values of compressive strength seem to have high dispersion, data reported should be reviewed from practitioners' perspective. According to European standard EN 206-1 and conformity control procedure for acceptance of concrete during production, mean value of tested concrete should be greater or equal to characteristic compressive strength + 1.48 x standard deviation, while minimal value obtained should be greater or equal to characteristic compressive strength minus 4 N/mm^2. Taking into account that by 7 days around 70% of 28-days strength is achieved, expected general mean of 28-days strength is around 52 N/mm^2 and minimal value around 39 N/mm^2. Therefore, it can be conclude that all concrete mixes prepared in different laboratories complying with the same concrete class C30/37.

4. Conclusion

This paper presented part of the results gathered during the Initial phase of RRT$^+$, together with the statistical analysis employed to compare values obtained by different laboratories. Results during this phase were collected in predefined format, consisting of all details

concerning different steps in preparation and testing of concrete. The results and statistical analyses that were presented strongly highlight the paramount importance of detailed and rigorous preparation of the experimental campaign. The more details are prescribed, the less of a difference is obtained in the final values of different concrete properties. This is especially the case for water saturation level of aggregates and its influence on the resulting consistency of concrete. Further, it was observed that it is of crucial importance to have all information from participants over the concrete preparation. Such details become crucial when trying to explain significant differences occurring within the laboratories. Finally, it can be concluded that if all the details are prescribed and all participants follow the guidelines, the approach to RRT employed in this initiative is valid; meaning that concrete with similar properties can be prepared. Experience gathered during the Initial phase will be used in the Main phase of RRT^{+} where the focus will be on non-standardized and advance techniques for testing cementitious based materials and structures.

Acknowledgment
The research performed within the COST Action is on volunteering basis, since there is no budget foreseen for research activities. Authors would like to express their sincere gratitude to all participating laboratories for their dedicated work within this experimental campaign. Authors also acknowledge financial support of EDF, France, CEVA Logistics, Austria and Germany, OeBB Infra, Austria, Staten Vegvesen, Norway and Schleibinger Gerate, Germany. The support of the research network COST TU1404 (COST Association) is also gratefully acknowledged.

References
[1] Eurocode 2: Design of concrete structures EN1992-1-1
[2] The fib Model Code for Concrete Structures 2010
[3] Beushausen, H., Fernandez L. Performance-Based Specifications and Control of Concrete Durability, State-of-the-Art Report RILEM TC 230-PSC, RILEM, 2016
[4] http://fr.amiando.com/EDF-vercors-project.html
[5] Bjøntegaard, Ø., Martius-Hammer, T.A., Krauss, M., Budelmann, H. Recommendation for Test Methods for AD and TD of Early Age Concrete Round Robin Documentation Report: Program, Test Results and Statistical Evaluation, RILEM, 2015
[6] Cortas, R., Rozière, E., Staquet, S., Hamami, A., Loukili, A., Delplancke-Ogletre, M.-P., Effect of the water saturation of aggregates on the shrinkage induced cracking risk of concrete at early age, Cement & Concrete Composites 50 (2014) 1–9
[7] EN 12350-2:2009 Testing fresh concrete – Part 2: Slump test
[8] EN 12350-7:2009 Testing fresh concrete. Air content. Pressure methods
[9] EN 12350-6:2009 Testing fresh concrete. Density
[10] EN 12390-2:2009 Testing hardened concrete - Part 2: Making and curing specimens for strength tests
[11] EN 12390-3:2009 Testing hardened concrete -- Part 3: Compressive strength of test specimens
[12] ISO 5725-2 Accuracy (trueness and precision) of measurement methods and results -- Part 2: Basic method for the determination of repeatability and reproducibility of a standard measurement method
[13] http://www.concrete.org.uk/fingertips-nuggets.asp?cmd=display&id=800

International RILEM Conference on Materials, Systems and Structures in Civil Engineering
Conference segment on Service Life of Cement-Based Materials and Structures
22-24 August 2016, Technical University of Denmark, Lyngby, Denmark

SHORT-TERM CREEP OF CEMENT PASTE: EXPERIMENTS AND MULTISCALE MODELING

Markus Königsberger [(1)], Muhammad Irfan-ul-Hassan [(1,2)], Christian Hellmich [(1)], and Bernhard Pichler [(1)]

(1) TU Wien - Vienna University of Technology, Institute for Mechanics of Materials and Structures, Vienna, Austria
(2) University of Engineering and Technology, Civil Engineering Department, Lahore, Pakistan

Abstract
This contribution is devoted to the analysis of three minute uniaxial compressive creep tests on cement paste specimens. One such test was performed every hour and corresponding material ages were spanning from 21 hours to eight days. The material microstructure remains virtually unaltered during each individual creep test. Subsequent creep tests refer to different microstructures. The observed age- and composition-dependent creep behavior results from the viscoelastic behavior of the reaction products of cement and water, called hydrates. A single isochoric power-law creep function characterizing well-saturated Portland cement hydrates is identified through micromechanics-based downscaling of 500 different non-aging creep functions, derived in the aforementioned three minute tests. The validity of the identified hydrate creep properties is further corroborated by successful prediction of the creep evolution of a 30 years old cement paste in a 30 day creep test.

1. Introduction

Creep experiments on cementitious materials typically last for several hours [1], weeks [2], months, or even years [3], and this is of the same order of magnitude or even larger than the characteristic time of the chemical hydration reaction at early ages. Consequently, lack of separation of time-scales renders the mathematical description of early-age creep a very challenging task. In the spirit of [4-6], our experimental campaign [7] provides insight into early-age creep properties of cement pastes, separating the effect of the time-dependent deformation behavior of the hydrates from the evolution of the overall microstructure due to ongoing chemical hydration. In more detail, we report on three minute creep tests, carried out on cement pastes with three different water-to-cement ratios, at material ages ranging from 21 hours up to 8 days. The duration of our tests is short enough that the microstructure of the tested materials remains practically unchanged throughout each individual creep test. Two

subsequent creep tests already refer to different microstructures, since one creep test is performed every hour and the investigated cement pastes are younger than one week. This allows for characterizing the evolution of non-aging creep properties of specific cement pastes, throughout the first week after their production.

It is well accepted that creep of cement paste arises from the creep of the hydration products like Calcium-Silicate-Hydrate (C-S-H) [8,9]. This contribution aims at demonstrating that the aforementioned evolution of creep properties is due to the hydration process, i.e. the subsequent formation of increasingly many hydrates, while the hydrates themselves may actually exhibit time-invariant (i.e. constant, or "intrinsic") creep properties. This is done by downscaling the experimentally determined creep behavior from the cement paste scale down to the micrometer scale of hydrates. Thereby, the two-scale micromechanical representation of cement paste as developed by Pichler and Hellmich [10], in combination with the correspondence principle [11] is applied.

This paper is structured as follows. At first, we report on the three minute creep tests on cement pastes. Thereafter, we discuss the continuum micromechanical approach for homogenization of viscoelastic material properties. This allows for identification of hydrate creep constants. Finally, the predictive capabilities of the model are checked by comparing model predictions with creep strain measurements from 30 day creep tests on 30 years old cement pastes.

2. Hourly repeated minute-long quasi-static creep tests

2.1 Materials and methods

We characterize both the elastic stiffness and the creep properties of ordinary Portland cement pastes made from CEM I 42.5N. Three different compositions are investigated, defined in terms of initial water-to-cement mass ratios w/c amounting to 0.42, 0.45, and 0.50, respectively. The cylindrical cement paste specimens exhibit a diameter of 70 mm and a height of 300 mm. After demolding, they are installed in an electromechanical universal testing machine, see Fig. 1. In order to achieve a close-to-perfect central load application, metal cylinders with bottlenecks are integrated into the test setup. Length changes of the specimens are measured by five Linear Variable Differential Transducers (LVDTs). They are mounted (evenly distributed around the perimeter of the specimen) between two aluminum rings which are fixed to the specimens. The specimens are conditioned to 20 °C during the whole test period.

A series of 168 three minute uniaxial macroscopic creep tests on the aging specimens is performed, with one such test per hour and corresponding material ages spanning from 21 hours to eight days. The loading protocol is carried out under load control and consists of initial compressive loading with a stress rate amounting to 2 MPa/s, of final unloading with a stress rate amounting to 1 MPa/s, and a three minute holding period in between. During this short test period, the microstructure remains virtually unaltered, while subsequent creep tests refer to different microstructures. In order to avoid material damage, the compressive loads are restricted to at most 15% of the uniaxial compressive strength reached at the time of

testing. Tests results are combined with results from isothermal differential calorimetry [12], in order to relate material age to hydration degree ξ, the latter being defined as the hydrated clinker volume divided by the initial clinker volume.

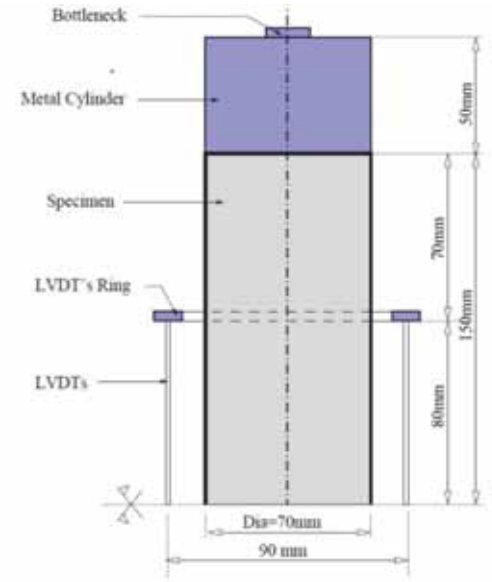

Figure 1: Schematic illustration of test setup, see also [7]

2.2 Experimental results

Considering that creep strains develop also during loading, the measured deformation histories can be almost perfectly reproduced based on the following uniaxial power-law creep function and Boltzmann's superposition principle, see also [1],

$$J_{cp}^{exp}(t-\tau) = \frac{1}{E_{cp}^{exp}} + \frac{1}{E_{c,cp}^{exp}}\left(\frac{t-\tau}{t_{ref}}\right)^{\beta_{cp}^{exp}}, \tag{1}$$

with t as chronological time, τ as time instant of loading, and $t_{ref} = 1\,\mathrm{d} = 86400\,\mathrm{s}$ as a fixed reference time [7]; with E_{cp}^{exp} denoting the elastic modulus, $E_{c,cp}^{exp}$ denoting the creep modulus, and β_{cp}^{exp} representing a dimensionless power-law creep exponent. The two creep properties and the elastic modulus are functions of the initial water-to-cement mass ratio w/c and of the (calorimetry-based) hydration degree ξ. The smaller w/c, the larger are the experimentally measured elastic and creep moduli, while the power-law exponent does not change significantly in the investigated w/c-interval. During hydration, i.e. with increasing ξ, the elastic modulus increases, in very good approximation, linearly with ξ, the creep modulus increases overlinearly, and the power-law exponent decreases slightly. Notably, the quasi-

statically determined elastic moduli agree very well with those determined ultrasonically by Karte et al. [12] on the same cement pastes [7].

3. Micromechanics Modeling

Herein, we test whether the maturity- and composition-dependent properties $E_{c,cp}^{exp}$ and β_{cp}^{exp} reported in [7] may actually be traced back to only one "universal" Portland cement-related isochoric hydrate creep tensor function [13]

$$\boldsymbol{J}_{hyd}(t-\tau) = \frac{\boldsymbol{I}_{vol}}{3\,k_{hyd}} + \frac{\boldsymbol{I}_{dev}}{2}\left[\frac{1}{\mu_{hyd}} + \frac{1}{\mu_{c,hyd}}\left(\frac{t-\tau}{t_{ref}}\right)^{\beta_{hyd}}\right], \tag{2}$$

with the (elastic) bulk and shear modulus of the hydrates denoted as k_{hyd} and μ_{hyd}, and with the shear creep modulus and the power-law creep exponent of hydrates denoted as $\mu_{c,hyd}$ and β_{hyd}. $\boldsymbol{I}_{vol}$ and $\boldsymbol{I}_{dev}$ are the volumetric and deviatoric parts of the fourth-order identity tensor $\boldsymbol{I}$. As for the downscaling from the cement paste to the hydrate level, we use the theory of viscoelastic homogenization [14–16] applied to the micromechanical representation of cement paste as developed by Pichler and Hellmich [10], described as follows.

3.1 Micromechanical representation and model input

Cement pastes are microheterogeneous materials consisting of four quasi-homogeneous constituents (or material phases), namely cement clinker, water, hydration products, and air. These four phases constitute the hierarchically organized microstructure of cement pastes, see the two-scale organogram illustrated in Fig. 2. At the scale of a few tens of microns, we envision a representative volume element (RVE) of hydrate foam, consisting of spherical water and air phases, as well as of hydrate needles oriented uniformly in all space directions. All three material phases are in direct mutual interaction, i.e. they are arranged in a so-called "polycrystalline" fashion. At the significantly larger scale of several hundreds of microns, we envision a matrix-inclusion type RVE of cement paste, consisting of a quasi-homogeneous hydrate foam matrix and a spherical cement clinker phase.

The constitutive phase properties as well as phases volume dosages are given as follows. Only the hydrates exhibit viscoelastic behavior [9], see Eq. (2), all other phases are purely elastic. Bulk modulus and shear modulus of clinker read as $k_{clin} = 116.7$ GPa and $\mu_{clin} = 53.8$ GPa [17]. The elastic properties of the hydrates were back-identified from macroscopic experiments as $k_{hyd} = 18.7$ GPa and $\mu_{hyd} = 11.8$ GPa, see [10]. Water and air exhibit vanishing solid stiffness. The phase volume fractions as functions (i) of the hydration degree and (ii) of the initial water-to-cement mass ratio are determined from the famous Powers' model [18], see [10] for details.

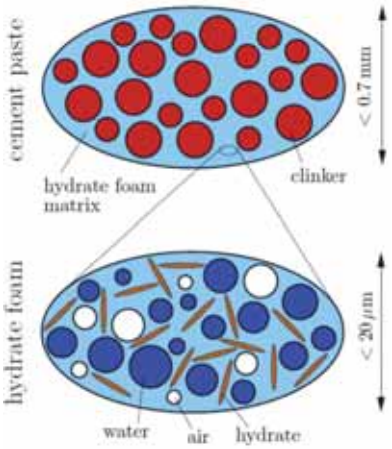

Figure 2: Two-scale representation of cement paste from [10]: RVE of matrix-inclusion composite "cement paste" where a spherical clinker phase is embedded in a hydrate foam matrix (modeled by means of a Mori-Tanaka scheme); polycrystalline RVE of "hydrate foam" built up of spherical pore phases (water and air), as well as of needle-shaped hydrate phases oriented uniformly in all space directions (modeled by means of a self-consistent scheme); both schematic 2D sketches refer to 3D representative volume elements

3.2 Homogenization of viscoelastic properties

Upscaling of the *viscoelastic properties* from the hydrate needles via the hydrate foam level to the cement paste level can be carried out by means of *quasi-elastic homogenization* in the Laplace-Carson (LC) space; this is referred to as the correspondence principle [11,14]. The viscoelastic creep behavior of hydrates according to Eq. (2), as well as the elastic behavior of water, air, and clinker are transformed into LC space. There, the polycrystalline RVE of hydrate foam is homogenized by means of the self-consistent scheme [19,20]. Subsequently, the matrix-inclusion-type RVE of cement paste is homogenized by means of the Mori-Tanaka scheme [21,22]. Details about homogenization, together with analytical formulae for the homogenized LC-transformed viscoelastic cement paste properties are provided in [13]. The homogenized creep function of cement paste is finally back-transformed from the LC domain back to the time domain, applying the numerical Gaver-Wynn-Rho algorithm [23,24], see [15] for details.

3.3 Identification of hydrate creep properties

The hydrate creep constants $\mu_{c,hyd}$ and β_{hyd} are identified by minimizing the error between the model-predicted viscous part of the uniaxial creep function of cement paste, $J_{v,cp}^{mod}$, and its experimentally measured counterpart, $J_{v,cp}^{exp}$, resulting in [13]

$$\mu_{c,hyd} = 20.7\ \text{GPa}\,, \quad \beta_{hyd} = 0.253\ \text{GPa}\,. \tag{3}$$

These two hydrate creep constants allow for satisfactory representation of the experimental results in the time domain, see Figs. 3. This underlines that the age- and composition-dependent creep behavior of cement pastes arises from the increasing volume dosage of hydrates (as predicted by the Powers hydration model), while the hydrate creep behavior is independent of material age and w/c-ratio.

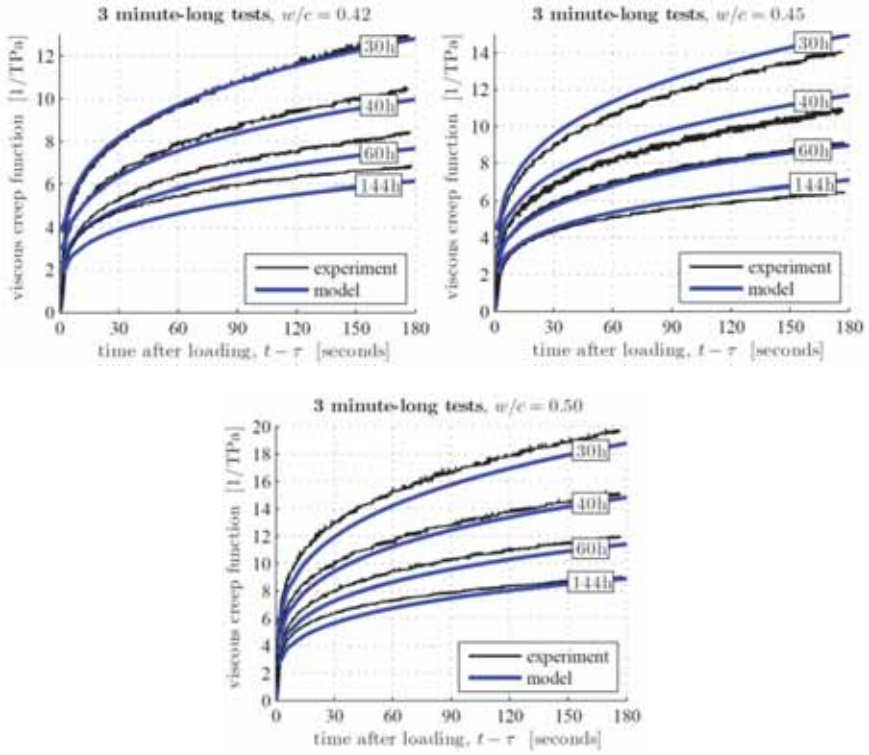

Figure 3: Comparison of experimentally determined and model-predicted viscous parts of the creep functions of cement pastes at ages amounting to 30, 40, 60, and 144 hours, respectively; after [13]

3.4 Prediction of long-term creep of mature pastes

We now check, in the sense of hypothesis testing, whether or not the hydrate creep constants (3), which were identified from 500 three minute creep tests carried out at early-ages, are also relevant for significantly longer creep durations and much more mature ages. To this end, we consider test results of Tamtsia and Beaudoin [2], who performed 30 day uniaxial compressive creep tests on 30 year-old Portland cement paste samples with $w/c = 0.5$, stored continuously under water. Given the advanced material age, the samples are practically completely hydrated, and this suggests – according to Lin and Meyer [25] – that hydration degree amounts to $\xi = 0.87$. In addition, it is appropriate to consider a constant (non-aging) microstructure throughout the creep tests. The corresponding model-predicted creep function,

i.e. the one related to $w/c = 0.50$, to $\xi = 0.87$, and to mechanical constants of hydrates according to (2) and (3), agrees remarkably well with the aforementioned experimental results, see Fig. 4.

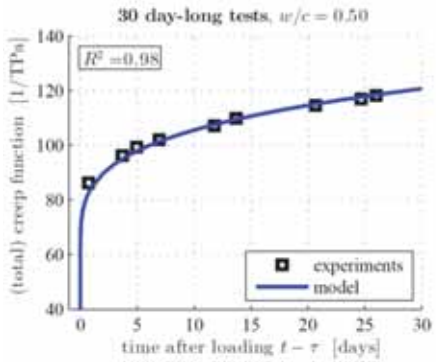

Figure 4: Comparison of experimental data [2] for (total) creep functions of 30 year-old cement paste samples with $w/c = 0.5$, with corresponding model predictions; after [13]

4. Conclusions

Based on the combination of three minute creep tests on young cement pastes and on continuum micromechanics modeling the following conclusions can be drawn:

- Hourly repeated three minute creep tests on cement pastes, with compressive force levels smaller than or equal to 15% of the compressive strength of the material, provide valuable insight into the evolution of elastic and non-aging creep properties [7].
- Ensuring that creep strains are *compressive* throughout the entire creep test, and this includes in particular the initial phase of loading, allows for identifying a static Young's modulus which is in very good approximation equal to the dynamic Young's modulus identified from ultrasonics. This underlines the fundamental characteristics of elastic properties being related to an energy potential, independently of loading paths and corresponding strain rates [7].
- The age- and composition-dependent cement paste creep behavior can be traced back to intrinsic (visco-)elastic hydrate creep constants involved in an isochoric power-law creep function. The corresponding creep function neither changes with increasing material maturity of cement paste nor with changes regarding composition of cement paste in terms of changing the w/c-ratio. Accordingly, the evolving creep properties of cement pastes result from varying volume dosages of material phases, i.e. progressively decreasing dosages of cement clinker and water as well as progressively increasing dosages of hydrates, as predicted by Powers' hydration model [13]. The described multiscale model allows for quantifying creep properties of cement pastes even at very early ages [13]. This will be beneficial for future analyses of early age cracking risk in cementitious materials.

References

[1] B.T. Tamtsia, J.J. Beaudoin, and J. Marchand. The early age short-term creep of hardening cement paste: load-induced hydration effects. Cement and Concrete Composites, 26(5):481–489, 2004.

[2] B.T. Tamtsia and J.J. Beaudoin. Basic creep of hardened cement paste: A re-examination of the role of water. Cement and Concrete Research, 30(9):1465–1475, 2000.

[3] Z.P. Bažant, M.H. Hubler, and Q. Yu. Pervasiveness of excessive segmental bridge deflections: Wake-up call for creep. ACI Structural Journal, 108(6):766, 2011.

[4] C. Boulay, M. Crespini, B. Delsaute, and S. Staquet. Monitoring of the creep and the relaxation behaviour of concrete since setting time, part 1: compression. In Strategies for Sustainable Concrete Structures, pages 1–10, France, 2012. International Conference on Numerical Modeling Strategies for Sustainable Concrete Structures (SSCS).

[5] B. Delsaute, J. Carette, and S. Staquet. Monitoring of the creep and the relaxation behaviour of concrete at very early age: complementary results on the CEOS concrete. In Proceedings, pages 1–6, Toledo, Spain, 2013. 8th International Conference on Fracture Mechanics of Concrete and Concrete Structures (Framcos VIII).

[6] B. Delsaute and S. Staquet. Monitoring of the creep and the relaxation modelling of concrete under tension and compression. In Proceedings, pages 168–175, Beijing, China, 2014. RILEM International Symposium on Concrete Modelling (CONMOD).

[7] M. Irfan-ul-Hassan, B. Pichler, R. Reihsner, and C. Hellmich. Elastic and creep properties of young cement paste, as determined from hourly repeated minute-long quasi-static tests. Cement and Concrete Research, 82:36–49, 2016.

[8] A.M. Neville. Creep of concrete as a function of its cement paste content. Magazine of Concrete Research, 16(46):21–30, 1964.

[9] P. Acker. Micromechanical analysis of creep and shrinkage mechanisms. In F.-J. Ulm, Z.P Bažant, and F.H. Wittmann, editors, Creep, shrinkage and durability mechanics of concrete and other quasi-brittle materials, 6th International Conference CONCREEP@MIT, pages 15–26, Amsterdam, 2001. Elsevier.

[10] B. Pichler and C. Hellmich. Upscaling quasi-brittle strength of cement paste and mortar: A multi-scale engineering mechanics model. Cement and Concrete Research, 41(5):467–476, 2011.

[11] W.T. Read Jr. Stress analysis for compressible viscoelastic materials. Journal of Applied Physics, 21(7):671–674, 1950.

[12] P. Karte, M. Hlobil, R. Reihsner, W. Dörner, O. Lahayne, J. Eberhardsteiner, and B. Pichler. Unloading-based stiffness characterisation of cement pastes during the second, third and fourth day after production. Strain, 51(2):156–169, 2015.

[13] M. Königsberger, M. Irfan-ul-Hassan, B. Pichler, and C. Hellmich. Downscaling-based identification of non-aging power-law creep of cement hydrates. Submitted to the Journal of Engineering Mechanics, 2016.

[14] N. Laws and R. McLaughlin. Self-consistent estimates for the viscoelastic creep compliances of composite materials. Proceedings of the Royal Society of London A: Mathematical, Physical and Engineering Sciences, 359(1697):251–273, 1978.

[15] S. Scheiner and C. Hellmich. Continuum microviscoelasticity model for aging basic creep of early-age concrete. Journal of Engineering Mechanics (ASCE), 135(4):307–323, 2009.
[16] J. Sanahuja and L. Dormieux. Creep of a C-S-H gel: a micromechanical approach. Anais da Academia Brasileira de Ciências, 82(1):25–41, 2010.
[17] K. Velez, S. Maximilien, D. Damidot, G. Fantozzi, and F. Sorrentino. Determination by nanoindentation of elastic modulus and hardness of pure constituents of Portland cement clinker. Cement and Concrete Research, 31(4):555–561, 2001.
[18] T.C. Powers and T.L. Brownyard. Studies of the physical properties of hardened Portland cement paste. American Concrete Institute Journal Proceedings, 18(2–8):101–992, 1946–1947.
[19] A.V. Hershey. The elasticity of anisotropic aggregate of anisotropic cubic crystals. Journal of Applied Mechanics Transactions (ASME), 21(3):236–240, 1954.
[20] E. Kröner. Berechnung der elastischen Konstanten des Vielkristalls aus den Konstanten des Einheitskristalls [Computation of the elastic constants of a polycrystal based on the constants of the single crystal]. Zeitschrift für Physik A: Hadrons and Nuclei, 151(4):504–518, 1958. In German.
[21] T. Mori and K. Tanaka. Average stress in matrix and average elastic energy of materials with misfitting inclusions. Acta Metallurgica, 21(5):571–574, 1973.
[22] Y. Benveniste. A new approach to the application of Mori-Tanaka's theory in composite materials. Mechanics of Materials, 6(2):147–157, 1987.
[23] J. Abate and P.P. Valkó. Multi-precision Laplace transform inversion. International Journal for Numerical Methods in Engineering, 60(5):979–993, 2004.
[24] P.P. Valkó and J. Abate. Comparison of sequence accelerators for the Gaver method of numerical Laplace transform inversion. Computers & Mathematics with Applications, 48(3):629–636, 2004.
[25] F. Lin and C. Meyer. Hydration kinetics modeling of Portland cement considering the effects of curing temperature and applied pressure. Cement and Concrete Research, 39(4):255–265, 2009.

International RILEM Conference on Materials, Systems and Structures in Civil Engineering
Conference segment on Service Life of Cement-Based Materials and Structures
22-24 August 2016, Technical University of Denmark, Lyngby, Denmark

EXPERIMENTAL AND NUMERICAL INVESTIGATION OF DRYING EFFETS ON CONCRETE'S MECHANICAL PROPERTIES

François Soleilhet [(1)], Farid Benboudjema [(1)], Fabrice Gatuingt [(1)], Xavier Jourdain [(1)]

(1) LMT-Cachan/ENS-Cachan/CNRS/Université Paris Saclay

Abstract
This paper deals with the effect of drying on concrete's mechanical properties. The study is conducted through experimental and numerical simulations with or without drying conditions. A visco-elastic model with damage for concrete provides the state of stress and damage before loading due to drying shrinkage. The mechanical behavior of specimens, with or without drying, is then compared in terms of overall behavior. This investigation will thus allow to understand and to model the effects of drying on the mechanical behaviour of cementitious materials.

1. Introduction

Concrete is one of the major materials used in construction field. Its use in numerous applications leads to different stakes. Currently, one of the major concerns for concrete structures is the long-term behaviour prediction and durability issues of the construction. Multiple kinds of solicitations combined with concrete heterogeneous mixture make it difficult to be fully defined. The purpose of the present work is to deal with the effects of drying process on mechanical properties of concrete.

Conventionally, when mechanical properties of concrete are characterized, internal stresses are assumed to be equal to zero and drying phenomena are not taken into account. However, differential drying between the surface and the core of the structure leads to a heterogeneous stresses state and can induce significant micro cracking. In some particular cases (durability and tightness issues for instance), this phenomenon could be of major importance.

The impact of drying and micro cracking on mechanical properties is not well studied whereas it seems to be significant. Regarding Young's Modulus, most authors report a

decrease of 4 to 30 % as concrete dries [1-2]. On the other hand, there is no consensus regarding the compressive and tensile strengths so far: concerning compressive strength, some authors report an increase [2,3,4,5] while others report a decrease [1,6,7]. Concerning tensile strength, a slight increase was found in a splitting test [7] while an initial decrease followed by a progressive increase up to zero percent relative humidity was observed in bending tests [8,9,10]. A decrease followed by an increase was also measured in direct tensile tests [10,11]. Relatively few studies comparing each of the methods to determine concrete's mechanical properties available today have been made. This paper presents firstly an experimental investigation of the effect of drying, on constant relative humidity, in addition to different mechanical characterization methods: flexural, splitting and compressive tests. Secondly, the results are compared to numerical simulations.

2. Experimental program

2.1 Material data

The concrete considered in this study, was the one used in the VerCors project's framework [12]. It was based on ordinary Portland cement (CEM I) with (total) water to cement ratio equal to 0.62. In addition, a plasticizer was used for a better workability. The mixing proportions and the properties of the aggregates used are given in table 1.

Its characteristic parameters were: an average compressive strength at 28 days equals to 40.75 MPa on 16x32 cm cylinders, a tensile strength equals to 3.5 MPa (using splitting test on 16x32cm cylinders) and a Young modulus equals to 32.2 GPa.

Table 1: Concrete composition.

Compound	Nature	Quantity	Unit
Cement	CEM I 52,5 R	320	kg/m^3
Sand		830	kg/m^3
Aggregate (4-11mm)	Calcareous	445	kg/m^3
Aggregate (8-16mm)	Calcareous	550	kg/m^3
Water (total)		197.6	kg/m^3
Plasticizer	SIKAPLAST Techno 80	2.75	kg/m^3

2.2 Specimens and curing conditions

In order to eliminate errors coming from mixing variability, all tested specimens were fabricated at once (one concrete mixture is used). Prismatic samples (7x7x28 cm) were casted into steel moulds, compressive and splitting samples (11x22 cm) were made in carton moulds, those dedicated for flexural (10x10x84 cm) were poured in reusable formwork specifically built for that purpose. All samples were stored in water during 28 days. At the end of the curing period, half of the samples was conserved in a humidity- and temperature-controlled room, where they were exposed to drying conditions until they reach a mass loss of about 40% with respect to the maximum one at infinite time (which has been extrapolated by

numerical simulations). The other half of the samples remains in water until the tests of all the samples were carried out.

2.3 Experimental tests

All tests were performed on three different specimens. Mean values of obtained results are presented with the associated standard variation.

2.3.1 Isothermal drying test

Isothermal drying test is conducted to monitor the drying of every specimen. Once removed from curing water, drying samples were kept into a controlled climatic chamber with an average relative humidity and temperature of 35% ± 5% and 25°C ± 1°C respectively (Figure **1**). The water in excess on the sample surface was removed with a wet cloth then each sample is weighed in open air using the same weighing device (15 kg ± 0.1 g). At the beginning (for 5 days), samples were weighed every hour and then daily.

As the study is made on multiple methods of characterisation, the drying was performed under a unique relative humidity.

Figure 1: Drying samples in the climatic chamber

2.3.2 Splitting and Compressive tests

Standard splitting and compressive tests were carried out using a 2500 kN hydraulic machine. It was composed of a lower rigid platen and an upper pivoting one. The tests were performed in accordance with NF-EN-12390 standard. The settings of the splitting test are presented in Figure **2**. It was performed under force-controlled conditions with a rate of 1.94 $kN.s^{-1}$ until failure. Special attention was paid to limit the loading eccentricity.

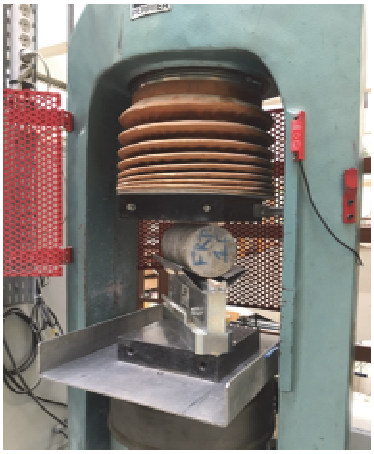

Figure 2: Settings of the splitting test

Regarding the compressive test, samples were firstly planed to obtain a good flatness and to avoid press fitting and eccentricity. The test was then performed under force-controlled conditions with a rate of 5 $kN.s^{-1}$. A cage, composed of three LVDT, was placed on the sample to measure strain. At the beginning of the test, to calculate the Young's modulus of the sample, three unloading and reloading were accomplished up to 30 percent of tensile strength. Finally, the test was conducted to completion, until the failure of the sample.

2.3.3 Flexural strength test

Flexural strength test was performed on a 10 kN hydraulic machine. It was performed under constant rate. This rate was chosen to reach the end of the elastic zone in more than 30 seconds but less that one minute. The specimen is equipped of a displacement transducer to measure the deflection of the beam.

Figure 3: Settings of the splitting test

3. Numerical modelling

3.1 Drying effects modelling

3.1.1 Drying modelling

The drying of cement-based materials is a complex phenomenon. Several, more-or-less coupled, mechanisms are involved: permeation, diffusion, adsorption-desorption and condensation-evaporation. Drying can be analysed through the resolution of liquid water, vapor and dry air mass balance equations. The use of several hypotheses [13,14] allows for considering only the mass balance equation of liquid water:

$$\frac{dS_l}{dP_c}\frac{dP_c}{dt} = div\left(k_{rl}(S_l)\frac{K}{\mu_l \phi} grad(P_c)\right) \quad (1)$$

Where S_l, P_c, ϕ, K, k_{rl} and μ_l are, respectively, the saturation degree, the capillary pressure, the porosity, the intrinsic permeability, the relative permeability and the viscosity of the liquid water.

It is shown [13,14] that this equation is sufficient for an accurate prediction of the drying of ordinary and high-performance concretes at 20°C with a relative humidity greater than 50%. The capillary pressure and the relative permeability are related to the degree of saturation through van Genuchten's relation [15]:

$$S_l = \left(1 + \frac{P_c}{P_0}\right)^{1-\gamma} \quad (2)$$

$$k_{rl}(S_l) = \sqrt{S_l}\left(1 - \left(1 - S_l^{\frac{1}{\beta}}\right)^{\beta}\right)^2 \quad (3)$$

Where P_0 and β are materials parameters.

Depending on the studied sample, the modelling was based on 2D or 3D meshes. Drying surfaces were exposed at a boundary transfer coefficient. In addition, it was found numerically that the evolution of humidity conditions in the climatic chamber did not have a significant impact on the evolution of drying, with respect to the assumption of a constant relative humidity (disregarding hysteresis effects). Therefore it was not taken into account and an average value was used. Finally, an inverse identification tool was implemented to determine K, P_0 and β values thanks to experimental mass lost results.

3.1.2 Drying shrinkage modelling

There are different ways to model drying shrinkage. Some of these are based on the theory of porous media mechanics. The development of this kind of modelling could be easily found [16]. Other models are based on phenomenological observations. Indeed, following

experimental results [17,18] found a proportional relation between water content variation and drying shrinkage rate:

$$\dot{\epsilon}_{ds} = k_{ds}\, \dot{w}\underline{\underline{1}} \tag{4}$$

Where k_{ds} is a hydrous compressibility factor and $\underline{\underline{1}}$ is the unit matrix.

It is possible to find alternative approaches but in this present work this modelling approach was chosen.

3.2 Mechanical modelling

This study is based on 3D modelling and meshing of all samples. It involves non-explicit modelling of concrete cracking using damage theory. The variable D, a scalar damage variable ranging from 0 to 1, is considered in the stress-strain relation:

$$\sigma_{ij} = (1 - D) C_{ijkl} \epsilon_{kl}^{elas} \tag{5}$$

Where σ_{ij}, C_{ijkl}, ϵ_{kl}^{elas}, are respectively stress, elastic stiffness and elastic components.

The evolution of the damage relies on an equivalent strain criterion, calculated from the equivalent strain ϵ_{eq} introduced by [19]. It was shown [20] that the evolution of damage in tension could be taken as exponentially decreasing:

$$D = 1 - \frac{\epsilon_{d0}}{\epsilon_{eq}} . \exp\left(-B_t\left(\epsilon_{eq} - \epsilon_{d0}\right)\right) \tag{6}$$

Where $\epsilon_{d0} = f_t / E_c$, with f_t the tensile strength and E_c the Young modulus, and B_t a parameter controlling the softening behaviour of the concrete. Softening behaviour of concrete may lead to non-unity of solutions and mesh dependency. Energetic regularization prevents these difficulties [21]. Regularization is based on the parameter B_t, which is a function of the size of finite element h, tensile strength f_t, fracture energy G_f and a parameter for the initiation of the damage ϵ_{d0} as described above.

$$B_t = \frac{h . f_t}{G_f - \frac{h . \epsilon_{d0} . f_t}{2}} \tag{7}$$

Finally, a random field on the tensile strength generated by the Turning Band Method [22] is used in order to take into account the variability of the material. The chosen parameters are:

- A variation coefficient equal to 10 per cent;
- A correlation length taken three times bigger than the biggest aggregate.

4. Results

4.1 Experimental results

Experimental campaign is on going. So far, only results from flexural (notched and unnotched), compressive and splitting tests are available.

Table 2: Mechanical properties obtained by experimentation (3 samples used for each test).

Tests	Characteristics	Without Drying	With Drying	Variation
Splitting test:	$f_{tm,sp}$ [MPa]	3.80 ± 0.1	3.76 ± 0.1	- 1.16 %
Compressive test:	f_{cm} [MPa]	41.2 ± 0.8	38.2 ± 0.5	- 7.42 %
	E [GPa]	32.9 ± 1	27.8 ± 0.4	- 15.5 %
Flexural test:	$f_{tm,fl}$ [MPa]	5.52 ± 0.6	5.60 ± 0.5	+ 1.41 %
	E [GPa]	32.1 ± 0.3	27.8 ± 0.4	- 19.7 %
	G_F [J.m^{-2}]	83.3 ± 0.7	98.2 ± 3.1	+ 18.2%
Notched flexural test:	$f_{tm,fl}$ [MPa]	4.65 ± 0.2	5.2 ± 0.2	+ 11.3 %
	E [GPa]	34.7 ± 0.5	26.7 ± 0.3	- 23.0 %
	G_F [J.m^{-2}]	99.3 ± 0.4	121 ± 5.0	+ 22.2%

In this table, E is the Young's modulus, f_t and f_c are respectively the tensile strength, the compressive strength and G_F is the fracture energy.

4.2 Numerical results

Numerical results presented in Table 3 show the impact of the drying process on mechanical properties. 3D FE simulations were performed with cubic linear elements. In this table, E is the Young's modulus, f_t and f_c are respectively the tensile strength and the compressive strength.

Table 3: 28-day mechanical properties estimated with numerical study.

Specimens	Characteristics	Without Drying	With Drying	Variation
Notched specimen in tension:	f_t [MPa]	3.79	3.35	-11.6 %
	E [GPa]	32.5	30.1	-7.32 %
Direct tensile test:	f_t [MPa]	3.5	1.97	-43.7 %
	E [GPa]	32.5	16.2	-50.3 %
Compression test:	f_c [MPa]	33.2	25.3	-23.9 %
	E [GPa]	32.2	20.1	-37.7 %

5. Discussion

It is noticeable that mechanical properties (measured experimentally) are not equally affected by drying effects. With regard to tensile strength, determined by flexural or splitting test, drying leads to little variation of the strength that does not seem important. Drying is an edge phenomenon, therefore we might assume that in the case of splitting test, there are no differences considering that these areas are under compression in both cases. Moreover, the localisation induced in these kinds of tests does not allow reaching the weakest link in the concrete. Finally, it was not possible, for practical reasons, to manufacture more samples and in the notched flexural test the variation seems to be due to variability of concrete and not to drying.

Significant higher differences were obtained on Young modulus. Depending on the type of the tests, we observed differences from 15.5 to 23.0 percent, which is consistent with literature, micro cracking reduces effective surface.

The fracture energy is a quantification of the energy to propagate a one square meter crack through a material. Experimentally, the real cracking pattern is rough whereas the evaluation of the energy is assumed to have a projected area. Moreover, multiple micro-cracks due to the drying leads to branching and therefore may induce an increase of the fracture energy (in a similar way, similar results can be found for concrete exposed to elevated temperatures).

From numerical point of view, each test is not similarly affected. Notched specimens seem to be less impacted than the others. This phenomenon is not in line with experimental results. In all cases, stiffness and strength are reduced if drying is taken into account. In these modelling, we observed wide variation. At this stage of modelling, numerical results were not accurate to describe the evolution of concrete's properties. They show the general tendency of the phenomena but they do not fit exactly the evolution of experimental results. The next step for the modelling is to take into account the effect of creep in the process, incompatibility of drying shrinkage between cement paste and aggregates or positive effects of capillary pressure.

6. Conclusion

Experimental tests and numerical calculations show the influence of drying phenomenon on concrete mechanical properties. Before mechanical loading, drying can lead to an important state of stress or damage the edges of the specimen and it could have an impact on stiffness or strength. This experimental campaign is almost finished and the results will be complemented by another study, subsequently carried out with only 60 days of drying. Meanwhile, a direct tensile test is being developed, it will allow extending experimental results to these tests. Besides, numerical researches will further be extended with computation of splitting and flexural tests. Finally creep (and eventually aforementioned mechanisms if necessary) will be implemented and numerical results will be averaged thanks to numerous repetitions of the simulation.

References

[1] Wittmann FH, Einfluβ des feuchtigkeitsgehaltes auf das kriechen des zementsteines. Rheologica Acta 9 (2) (1970), 282-287
[2] Yurtdas I, Peng H, Burlion N, Skoczylas F. Influences of water by cement ratio on mechanical properties of mortars submitted to drying, Cement and Concrete Research 36 (2006), 1286–1293
[3] Brooks JJ, Neville AM, A comparison of creep, elasticity and strength of concrete in tension and in compression. Magazine of Concrete Research 29 (100) (1977), 131-141
[4] Dantec P, Terme G., Séchage et comportement différé du béton : influence de la cinétique de dessiccation sur le comportement mécanique des bétons, LCPC Report 1.41.02.5 (1996)
[5] Burlion N, Bourgeois F, Shao J-F, Effects of desiccation on mechanical behaviour of concrete, Cement & Concrete Composites 27 (2007), 367–379
[6] Torrenti J-M. Comportement multiaxial du béton: Aspects expérimentaux et modélisation, PhD thesis, Marne-La-Vallée, Ecole Nationale des Ponts et Chaussées (1987)
[7] Hanson JA, Effects of curing and drying environments on splitting tensile strength of concrete, Journal of the American Concrete Institute 65(7) (1968), 535-543
[8] Kanna V, Olson RA, Jennings HM, Effect of shrinkage and moisture content on the physical characteristics of blended cement mortars, Cement and Concrete Research 18 (10) (1998), 1467-1477
[9] Philajavaara SE, A review of some of the main results of a research on the aging phenomena of concrete: effect of moisture conditions on strength, Shrinkage and creep of mature concrete, Cement and Concrete Research 4(5) (1974), 761-771
[10] Fouré B, Note sur la chute de résistance à la traction du béton léger consécutive à l'arrêt de la cure humide, Annales de l'Institut Technique du Bâtiment et des Travaux Publics 432 (1985), 3-14
[11] De Larrard F, Bostvirronois JL, On the long term losses of silica fume high strength concretes. Magazine of Concrete Research 43(155) (1991), 124-129
[12] B. Masson, Démarche industrielle de compréhension des phénomènes de transferts dans les parois en béton, 31èmes Rencontres de l'AUGC, ENS de Cachan (2013)
[13] Bažant ZP, Sener S, Kim JK, Effect of cracking on drying permeability and diffusivity of concrete. ACI Materials Journal 84 (1986), 351-357
[14] Hansen TC, Creep of concrete: the influence of variations in the humidity of ambient atmosphere, Proceedings 6th Congress of the International Association of Bridge and Structural Engineering, Stockholm (1960), 57-65
[15] Lassabatère T, Torrenti J-M, Granger L, Sur le couplage entre séchage du béton et contrainte appliqué, Proceedings Actes du Symposium Saint-Venant, Paris (1997), 331-338
[16] Thiery M, Baroghel-Bouny V, Bourneton N, Villain G, Stefani C, Modélisation du séchage des bétons : analyse des différents modes de transfert hydrique, Revue Européenne de Génie Civil 11(5) (2007), 541-577
[17] Goltermann P, Mechanical predictions of concrete deterioration – Part 2: classification of crack patterns, ACI Materials Journals 92(1) (1995), 58-63

[18]Baroghel-Bouny V, Mainguy M, Lassabatere T, Coussy O, Characterization and identification of equilibrium and transfer moisture properties for ordinary and high-performance cementitious materials, Cement and Concrete Research 29 (1999), 1225-1238
[19]Mazars J. A description of micro-and macro scale damage of concrete structures. Eng Fract Mech 25(5) (1986), 729–37
[20]Feenstra PH. Computational aspects of biaxial stress in plain and reinforced concrete, PhD thesis Technical University of Delft (1993)
[21]Hillerborg A, Modéer M, Petersson P-E. Analysis of crack formation and crack growth in concrete by means of fracture mechanics and finite elements. Cem Concr Res 6(6) (1976), 773–81
[22]Matheron, G, The intrinsic random functions and their applications, Advances inapplied probability (1973), 439-468

International RILEM Conference on Materials, Systems and Structures in Civil Engineering
Conference segment on Service Life of Cement-Based Materials and Structures
22-24 August 2016, Technical University of Denmark, Lyngby, Denmark

ON UTILISATION OF ELLIPTICAL RINGS FOR ASSESSING CRACKING TENDENCY OF CONCRETE AND OTHER CEMENT-BASED MATERIALS

Xiangming Zhou [(1)], Wei Dong [(2)], Gediminas Kastiukas [(1)]

(1) Brunel University London, Uxbridge, United Kingdom
(2) Dalian University of Technology, Dalian, P.R. China

Abstract
A new method, based on elliptical rings, was explored for assessing cracking tendency of concrete and other cement-based materials under restrained condition. The new elliptical ring test method was developed by mapping the circular ring tests recommended by AASHTO and ASTM. A series of thin and thick elliptical concrete rings were tested alongside circular ones. Cracking age and position of circular and elliptical rings were examined. It is found that thin elliptical rings with appropriate geometry can initiate crack quicker than circular ones which is desirable for accelerating the ring test. However, thick elliptical rings seem not to exhibit a desirable geometry effect of accelerating ring test. Besides, it was found that crack initiated from the inner circumferential surface and propagated toward the outer surface in thin rings. In comparison, in thick rings, crack initiated from the outer circumferential surface and propagated to the inner surface. There were multiple cracks that occurred in elliptical rings and some cracks initiated but did not propagate through the ring wall. In comparison, there was only one crack in circular rings. Finally, the features of multiple cracks in restrained elliptical rings were examined, and their impact on interpreting elliptical ring test results was elaborated.

1. Introduction

The complexities of early-age concrete cracking are yet to be fully understood. Over the years, cracking has led to premature deterioration, which effectively shortens the service life of concrete structures and presents a potential hazard to their safety and serviceability. The volume of concrete changes in response to moisture and/or temperature variation as well as the chemical reaction of cement, and if restrained, will result in stress development that may finally lead to cracking. Such undesirable phenomenon undoubtedly reduces the load carrying capacity of concrete members and accelerates deterioration hence yielding premature failure. For massive concrete structures (e.g. bridges, dams, tunnels, etc.), their serviceability

performance may be reduced due to penetration of aggressive species (such as carbon dioxide, sulphate and chloride ions) [1], leading to the corrosion of embedded reinforcement bars. Over the years, a number of test methods have been developed to assess how susceptible a given concrete mixture may be to cracking, such as the beam, plate and circular ring tests, of which the circular ring test has been proven to be the most versatile and simple to use [2]. The circular ring test method has been used by various researchers [3,4]. So far, the research has mainly concentrated on four fields, namely the effects of concrete mixture compositions [5,6], moisture gradients, drying conditions [2,6-8], and ring size and geometry [2,9]. The restrained circular ring test has become a standard method recommended by AASHTO [9] and ASTM [11] which use circular ring specimens with a concrete wall thickness of 76 and 38 mm, respectively. In both standards, strain gauges are used to measure the strain in the central restraining steel core to provide an assessment of cracking age. However, the ASTM and AASHTO circular ring test methods have been noted to have a low degree of restraint, resulting in a fairly long time before the first crack initiates [3]. They are also regarded to have a low cracking sensitivity and inefficient for evaluating large amounts of material [6]. The degree of restraint is largely dependent on the central restraining steel ring's stiffness, and geometry, so concrete in a circular ring test may not develop a visible crack at all if the steel ring is not thick enough [9]. Also, a crack can occur anywhere along the circumference of a circular concrete ring making it impossible to predict its exact position. Therefore, in a bid to overcome the above-mentioned problems from traditional circular ring tests, a novel elliptical ring geometry was first adopted by He et al. [12]. It was also discovered that the first cracking was concentrated at certain positions and largely reduced the instruments and resources needed for detecting crack initiation and propagation. More recently, the research efforts aiming to prove the capabilities of the elliptical ring test have been accomplished by Zhou et al. who developed a numerical model to analyze stress and crack initiation in concrete rings [13] and also Dong et al. who used fracture mechanics to predict the cracking of circular and elliptical concrete rings [14] and also investigated the influence of specimen size [15]. In this paper is presented the effect of concrete wall thickness on concrete cracking behaviour under restrained shrinkage and reveal how an elliptical ring specimen with a simple geometry can provide information to enable better evaluation of concrete cracking tendency.

2. Experimental

2.1. Raw materials and mix proportions

The mix proportions for the concrete in this study were: 1:1.5:1.5:0.5 (cement: sand: coarse aggregate: water) by weight. CEM II Portland cement (from LAFARGE Cement UK) conforming to EN 197-1 with a specific gravity of 2.96 and Blaine fineness of 423m^2/Kg was used. River sand with 2-mm maximum grain size and fineness modulus of 3.27 was used as fine aggregates. Gravel stone with 10-mm maximum particle size was used as coarse aggregates.

2.2. Ring Geometry

In the case of an elliptical ring, the degree of restraint largely depends on the geometrical factor *a/b*, in which *a* and *b* represent the major and minor principal semi-axes of a central

restraining steel ring's external circumference, respectively (see Fig. 1), which coincide with the major and minor principal semi-axes of the inner circumference of the concrete ring.

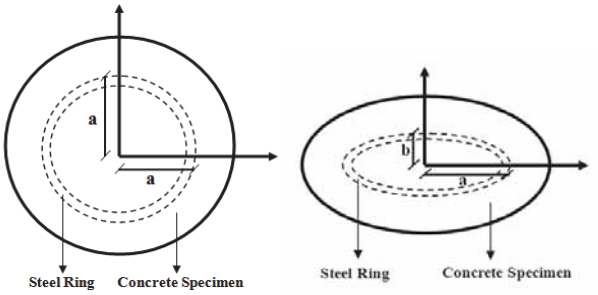

Figure 1: Notations of geometries of ring specimens (left) circular ring (right) elliptical ring

In this paper, a series of circular and elliptical rings, thin and thick with different geometries, were tested under restrained shrinkage. Table 1 summarises all the ring specimens tested and their respective crack ages for two parallel samples. All concrete rings were dried from the outer circumferential cylindrical surface with top and bottom surfaces sealed as shown in Fig. 2. All the concrete rings irrespective of their thicknesses had a height of 75 mm restrained by a 12.5 mm thick steel ring.

Table 1: Geometry and cracking age of concrete ring specimens

Thin Ring Geometry: a×b (mm×mm)	**Cracking Age (days)**	**Thick Ring Geometry: a×b (mm×mm)**	**Cracking Age (days)**
150×150	15 14		
150×125	15 14	150×125	20 21
150×100	15 14	150×100	21 22
150×75	10 10	150×75	18 18
150×60	11 15	150×60	21 19

2.3. Restrained ring test

The test setup comprises a restraining steel ring with four strain gauges, each at the vertex of the ellipse, attached at mid-height of the inner cylindrical surface of the steel ring. Strain of the inner surface of the steel ring is continuously recorded throughout the test duration. A concrete ring was then cast around the steel ring as shown in Fig. 3 and immediately covered with a plastic sheet to prevent moisture. After 24 hours of curing, the outer moulds were

stripped off, and the specimens were immediately sealed with two layers of aluminium tape on the top and bottom surfaces. The concrete ring specimen, together with the instrumented central restraining steel ring, were then moved into an environmental chamber with a temperature of 23°C and 50% relative humidity for continuous curing. Circumferential strain of the restraining steel ring was continuously monitored until a crack initiated which was captured by a sudden drop in measured strain. The concrete rings were also examined by visual observation regularly to monitor crack initiation and propagation.

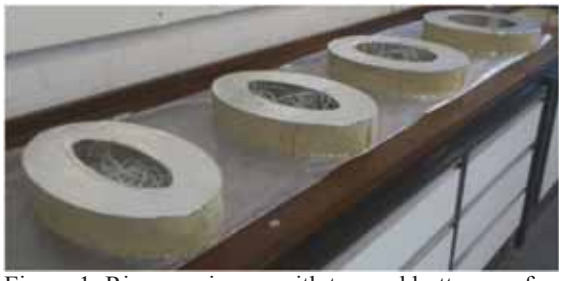

Figure 1: Ring specimens with top and bottom surfaces sealed

Figure 2: Thin circular ring (left) and thick elliptical ring (right) specimens in mould after concrete placement

3. Results and Discussion

3.1. Strain measurement and representation

As concrete dries, its shrinkage increases with age. However, the increasing concrete shrinkage is restrained by the central steel ring. Thus, an increasing pressure is imposed on the central steel ring by the surrounding concrete ring. Simultaneously, tensile stress develops in the concrete ring which also increases with age. Once the tensile stress exceeds the tensile strength of concrete, cracking initiates and the pressure imposed on the central steel ring is released resulting in the stress and thus, strain suddenly dropping in the central restraining steel ring. Cracking ages of the ring specimens determined by this technique are listed in Table 1.

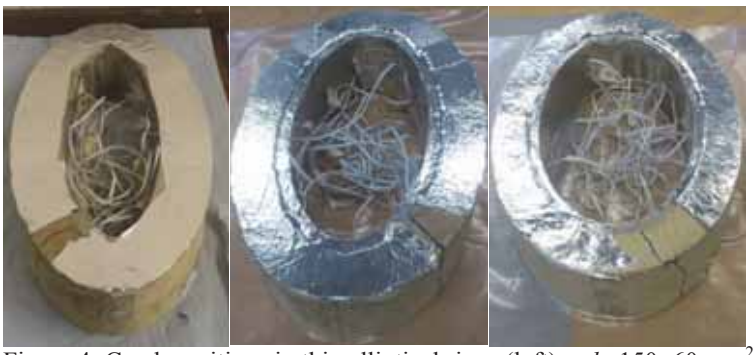

Figure 4: Crack positions in thin elliptical rings (left) $a \times b$=150×60 mm^2 (centre) $a \times b$=150×75 mm^2 (right) $a \times b$=150×100 mm^2

3.2. Effects of ring geometry on cracking in thin ring specimens

It can be found from Table 1 that thin ring specimens with shorter minor axes usually cracked earlier than those with longer minor axes. For instance, the elliptical rings with $a \times b$=150×75 mm^2 cracked at an average age of 10 days, compared to those with $a \times b$ =150×125 mm^2 and $a \times b$ =150×100 mm^2 which both cracked at an average age of 14.5 days. All the ring specimens with the geometry factor of a/b<2 cracked at the same average age i.e. 14.5 days. The latter trend suggests that the geometry factor is a contributing one affecting the maximum circumferential tensile stress, thus cracking age of concrete rings when subjected to restrained shrinkage. According to Table 1, thin elliptical rings with a geometry factor a/b>2 can cause crack initiation earlier than the circular rings. They are therefore capable of accelerating the ring test for assessing the relative likelihood of concrete cracking. The significance of the geometric factor a/b is also reflected in the cracking position. Fig. 4 shows three thin elliptical rings with b=60, 75 and 100 mm (from left to right) which all cracked in the same region of the major principal axis.

3.3. Effect of ring wall thickness on cracking age and positions

On the other hand, the thick ring specimens exhibited different cracking behaviour. Most thick ring specimens cracked at the age 20 days or more, with the exception of the elliptical $a \times b$=150×75mm^2 ring which cracked at an average age of 18 days as shown in Table 1. Fig. 5 illustrates the cracks that were observed in thick ring specimens. Cracks were observed on either side of the outer circumferential surface along the minor axis and/or the major axis for ring specimens with the geometry factor a/b between 1.5 and 2.5. From Table 1, it can be seen that ring specimens with a thicker concrete wall cracked on average almost 7 days later, under the same exposure and drying conditions. Considering that all the ring specimens have approximately the same exposed surface area-to-volume ratio (A/V) and hence equal free shrinkage, it can be deduced that an increased concrete wall thickness reduces the potential for cracking. Furthermore, thicker specimens are less sensitive to the development of a similar sized initial crack [9], implying that the crack driving energy is lower for thicker specimens which require a higher stress to cause a crack to propagate after it initiated. This further

indicates that ring wall thickness influences the behaviour of concrete under restrained condition.

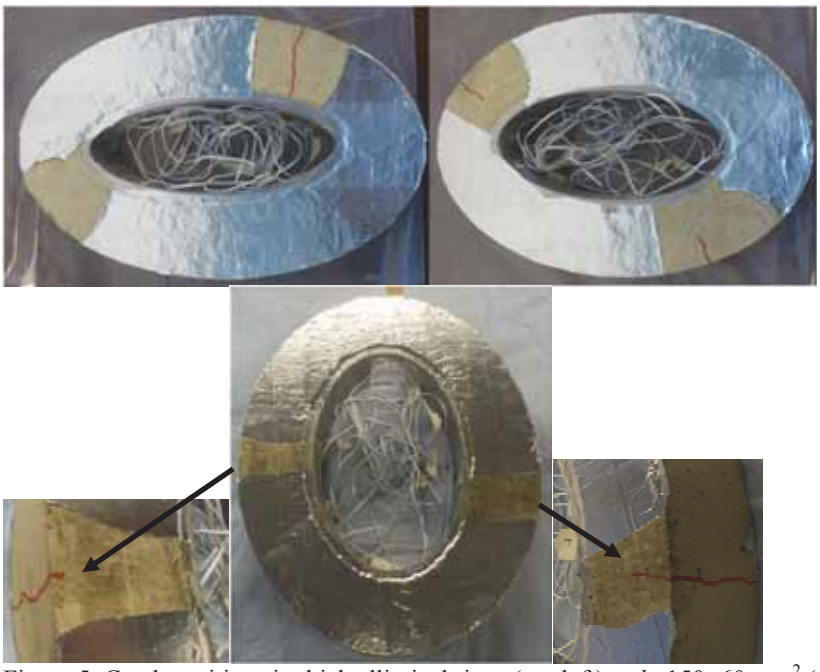

Figure 5: Crack positions in thick elliptical rings (top left) $a \times b$=150×60 mm^2 (top right) $a \times b$=150×75 mm^2 (bottom) $a \times b$=150×100 mm^2

3.4. Crack initiation and propagation

Cracks were examined after the ring test was completed and the central steel ring was removed, and the aluminium tape was stripped off. As shown in Fig. 6, there were notable cracks in the thin elliptical ring with $a \times b$=150×125 mm^2 on its inner circumferential surface along the major principal axis. In these figures, points I and II highlight the cracks that initiated without propagating through the concrete ring wall while point III illustrates more vividly a crack that eventually propagated through the concrete ring wall. Cracks were also observed in the $a \times b$=150×100 mm^2, 150×75 mm^2 and 150×60 mm^2 thin elliptical ring specimens (see Fig. 4) which occurred very close to the vertex in the region where the maximum circumferential tensile stress is expected. However, upon further observation, these cracks, seen at the inner surface along the major principal axis, did not manage to propagate through the concrete ring wall. Neither did they appear across the top surface of the concrete ring specimens. In the course of the test, cracking in thin rings could not be observed from the outer circumferential surface of the ring as they did not propagate through to that extent.

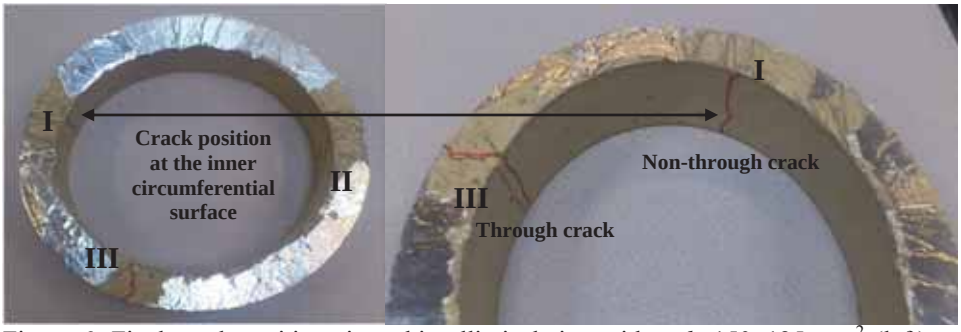

Figure 6: Final crack positions in a thin elliptical ring with $a \times b$=150×125 mm^2 (left) over view (right) through and non-through cracks

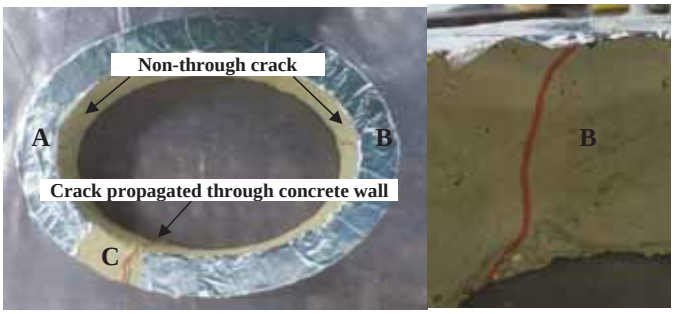

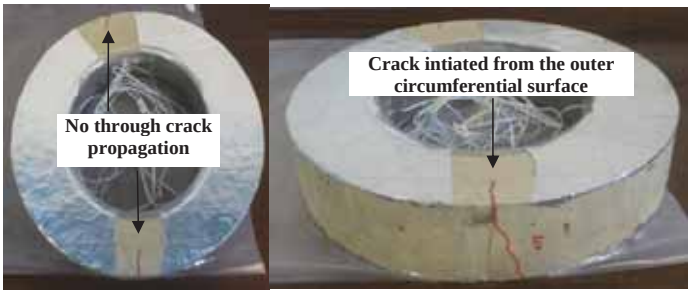

Figure 7 Crack positions in a (top) thin ring with $a \times b$=150×100 mm^2 (bottom) thick ring with $a \times b$=150×125 mm^2

It was found from this study that cracks were usually noticed by visual observation one and two days after detection by strain gauges for thin and thick rings, respectively. This further supported that the abrupt drop in measured strain detected by strain gauges indicated crack initiation rather than its propagation through the ring wall. In the case of thin rings, due to the geometric effect, stress concentration may take place at a specified position which is usually close to the vertex along the major axis at the inner circumferential surface of an elliptical concrete ring. Therefore cracks are more likely to initiate at these regions. Subsequently, other

cracks may initiate and propagate at areas along the minor axis further away from the vertex as a result of stress redistribution after initial cracks occur. Crack propagation in concrete can start in a stable or unstable stage, the former inferring that a crack can only propagate under increasing driving energy which is provided by the shrinkage that occurs in concrete. As concrete matures, shrinkage increases leading to an increased driving energy and hence continued crack propagation. As observed, cracks originally initiated at points A and B along the major axis of a thin ring but ceased to propagate due to reduced crack driving energy. However, as a result of increased circumferential tensile stress redistribution in other regions of the concrete ring, a new crack was generated and subsequently propagated at C. This behaviour may account for crack propagation throughout the complete length of the concrete wall for rings $a \times b$=150×125 mm^2 and $a \times b$=150×100 mm^2 as shown in Figs. 6 and 7. Eventually, the crack was observed visually at C becoming the only crack managing to propagate through the wall of the ring specimen while A and B on either side of the major axis initiated but failed to propagate. Conversely, as a result of the increased stress in thicker specimens which is believed to develop in the radial direction of the ring due to the presence of a moisture gradient, Weiss and Shah [8] proposed that cracks may actually initiate at the outer circumferential surface and propagate towards the inner one in thick rings. The latter hypothesis is confirmed in this study by the results of thick elliptical rings $a \times b$ =150×75 mm^2, 150×100 mm^2 and 150×125 mm^2 as shown in Figs. 6 and 7. Those rings were observed to crack at two opposite positions along their outer circumference and propagate towards the inner circumference of the rings. These cracks extended through the full height of the rings on their outer circumferential surface after which the ring test was stopped. However, the cracks were found unable to propagate through the concrete ring wall after the test was stopped and the aluminate tape at the top and bottom surfaces of the ring specimens was stripped off.

4. Conclusions

This paper explored the use of elliptical rings to assess the cracking potential of concrete, and the effect of ring geometry including ring wall thickness on the cracking behaviour of ring specimens under restrained shrinkage. Experimental efforts included using elliptical ring specimens to provide information for a simple geometry to enable an improved understanding of shrinkage cracking and better evaluation of cracking tendency of concrete. Based on the experimental results, the following conclusions were drawn:

1. Thin elliptical rings, with a wall thickness of 37.5 mm as recommended by ASTM C1581/C1581M-09a and a geometric factor $a/b \geqslant 2$, can increase the likelihood of crack initiation in concrete specimens at expected positions and are seen to crack at an earlier age with a decrease in minor principal axis.
2. The abrupt drop observed from steel strain recorded during the restrained ring test indicated crack initiation. However, visual observation of the crack was one or two days after for thin and thick ring specimens, respectively.
3. In restrained thin elliptical rings, crack initiated at the vertices on the major axis of the inner elliptical circumference and propagated from the inner circumference to the outer one. However, in restrained thick elliptical rings, crack initiated at the two vertices

either on the minor axis or on the major axis of the outer elliptical circumference and propagated to the inner one.

4. Thin elliptical rings were observed to have cracks on the inner circumferential surface of the concrete ring along the major principal axis as would have been expected but without propagating through the ring wall. As such, it is possible that some cracks initiate but do not necessarily propagate fully through the concrete ring wall.
5. For the ring specimens with a thin concrete wall, the elliptical rings with the geometry factor a/b=2 is recommended to replace circular rings for restrained shrinkage test, which can increase cracking sensitivity so that concrete ring can crack in a shorter period for faster assessment of cracking potential of a large amount of concrete mixtures.
6. Finally, it is revealed further that, as the wall thickness of a concrete ring is increased, the potential for cracking is consequently reduced since the thicker walled specimens are less sensitive to small cracks (i.e. a lower crack driving energy is experienced).

Acknowledgement

The financial support from Engineering and Physical Science Research Council (EPSRC) UK under the grant EP/I031952/1 and EPSRC Doctoral Training Account allocation to Brunel University is greatly appreciated.

References

[1] Briffaut, M., Benboudjema, F., Torrenti J.M., Nahas G.; A thermal active restrained shrinkage ring test to study the early age concrete behaviour of massive structures. *Cement and Concrete Research*, 41 (2011) 56-63.
[2] Moon J.H., Weiss J.; Estimating residual stress in the restrained ring test under circumferential drying. *Cement and Concrete Composites*, 2006;28(5):486-96.
[3] Bentur A., and Kovler K.; "Evaluation of Early Age Cracking Characteristics in Cementitious Systems," *Materials and Structures*, 36(3), (2003) pp 183-190.
[4] Benboudjema, F., Briffaut, M., Hilaire, A., Torrenti, J.M., Nahas, G.; Early age behavior of massive concrete structures: from experiments to numerical simulations from the RILEM-JCI International Workshop on Crack Control of Mass Concrete and Related Issues concerning Early-Age of Concrete Structures - CONCRACK 3, France (2012), 21–32.
[5] Li Z.J., Qi M., Li Z.L., Ma B.G.; Crack width of high-performance concrete due to restrained shrinkage. *Journal of Matererials Civil Engineering ASCE,* 1999;11(3):214-23.
[6] See, H.T., Attiogbe, E.K., and Miltenberger, M.A.; "Shrinkage Cracking Characteristics of Concrete Using Ring Specimens." *ACI Materials Journal*, 100-M28, 2003 pp 239-245
[7] Hossain A.B., Weiss J.; Assessing residual stress development and stress relaxation in restrained concrete ring specimens. *Cement and Concrete Composites*, 2004;26(5):531-40.

[8] Weiss W.J., Shah S.P., Restrained shrinkage cracking: the role of shrinkage reducing admixtures and specimen geometry. *Materials and Structures*, 2002;35(246):85-91.
[9] Hossain A.B., Weiss J.; The role of specimen geometry and boundary conditions on stress development and cracking in the restrained ring test. Cement and Concrete Research, 2006;36(1):189-99.
[10] ASSHTO, T 334-08, Standard Method of Test for Estimating the Cracking Tendency of Concrete, Washington D.C, 2012.
[11] ASTM International, "ASTM C1581 / C1581M-09a, Standard Test Method for Determining Age at Cracking and Induced Tensile Stress Characteristics of Mortar and Concrete under Restrained Shrinkage," West Conshohocken, 2009.
[12] He Z., Zhou XM., Li ZJ.; New experimental method for studying early-age cracking of cement-based materials. *ACI Materials Journal*, 2004;101(1):50-6.
[13] X. Zhou, W. Dong, and O. Oladiran, "Crack-Healing Investigation in Bituminous Materials," *J. Mater. Civ. Eng.*, vol. 25, no. January, pp. 864–870, 2013.
[14] W. Dong, X. Zhou, and Z. Wu, "A fracture mechanics-based method for prediction of cracking of circular and elliptical concrete rings under restrained shrinkage," *Eng. Fract. Mech.*, vol. 131, pp. 687–701, 2014.
[15] W. Dong, X. Zhou, Z. Wu, and G. Kastiukas, "Effects of specimen size on assessment of shrinkage cracking of concrete via elliptical rings: Thin vs. thick," *Comput. Struct.*, 2016.

International RILEM Conference on Materials, Systems and Structures in Civil Engineering
Conference segment on Service Life of Cement-Based Materials and Structures
22-24 August 2016, Technical University of Denmark, Lyngby, Denmark

MODELLING OF TRANSPORT OF CHLORIDE IONS IN CONCRETE UNDER COMPRESSIVE LOAD

Yin Cao [(1)], Yan Yao [(1)], Ling Wang [(1)], Zhendi Wang [(1)]

(1) State Key Laboratory of Green Building Materials, China Building Materials Academy, Beijing, China

Abstract
The transport behaviour of chloride ion in concrete under external compressive load was studied by using the test method and test rigs proposed by RILEM TC 246-TDC. The model of chloride diffusion based on Fick's II law was used to illustrate the chloride diffusion of concrete exposed to imposed compressive load. Further, based on the experimental results and statistical output from former research, a probabilistic analysis was conducted to illustrate the effect of external load, aging exponent and the critical chloride content on the reliability–based service life of concrete under combined mechanical load and chloride diffusion.

1. Introduction

The corrosion of reinforcing steels in concrete structures is one of the main causes of the degradation and reduction of service life of these structures, mainly when they are exposed to marine environment or de-icing salts. In these two situations, the corrosion of reinforcement is initiated when chlorides ions penetrate into concrete and reach a critical content at the surface of the rebar which disrupts the passive layer protecting the rebar. An understanding of the process of chloride transportation in concrete is of great importance for engineers to predict the service life of concrete structures and numerous studies dealing with chloride attack were carried out [1-3]. However, most of them have just focused on concrete under unloaded condition which was normally not the case in real concrete structures. Studies showed that chloride diffusivity of concrete in the compressive zone was quite different from the tensile zone when concrete beams were subjected to bending load [4-6]. In addition, filed investigations also found different corrosion status within a same concrete structure due to the different stress state. A lot of attentions have been paid on the topic of the synergistic effect of external load and environmental actions on concrete durability [7-10]. Many prediction models based on chloride-induced corrosion of reinforcement in concrete structures have been

proposed in the past decades [11]. However, most of the models did not consider the influence of imposed stress on chloride absorption and chloride diffusion.

In this contribution transport behaviour of chloride ion in concrete exposed to external compressive was investigated using the test setups developed by RILEM Technical Committee 246-TDC. The influence of imposed stress on chloride diffusion as well as the influence on the service life of unloaded concrete and concrete under compression is presented. Far more long-term laboratory tests and field investigations should be carried out in order to establish a reliable basis for taking the influence of an applied load on durability and service life into consideration.

2. Experimental

2.1 Preparation of specimens

Ordinary Portland cement Type CEM I, 42.5 R, local crushed granitic aggregates with a maximum diameter of 20 mm, and river sand with a maximum diameter of 5 mm, both from Beijing area, were mixed to produce the fresh concrete. Superplasticizer was added to the fresh concrete to make the slump to be 15 cm. The mix proportion of concrete is given in Table 1.

The concrete was cast into 100 x 100 x 400 mm^3 prisms for compression. After compaction all specimens were first cured in the concrete laboratory, covered with wet burlap for 24 hours. Then the forms were removed and the specimens were further cured in tap water with saturated $Ca(OH)_2$ at a temperature of 20 °C until they reached an age of 28 days.

Table 1: Composition of concrete

W/C	Cement (kg/m^3)	Water (kg/m^3)	Fine aggregate (kg/m^3)	Coarse aggregate (kg/m^3)	Super-plasticizer (kg/m^3)
0.45	368	165.5	840	1027.5	3.4

2.2 Test procedure

The ultimate uniaxial compressive strength was tested at 28 d using the test setups designed by RILEM TC 246-TDC, being 36.6 MPa. Water cured specimens were taken out and the free water on the surface were removed with a towel. Then the surface of the specimen were sealed with two layers of self-adhesive aluminium foil immediately, leaving an open window (80 × 160 mm) for chloride exposure on one moulded side surface. The open window was temporarily closed until a plastic tank with the inner dimension of (80 × 160 × 50) mm^3 was adhered to with silicone.

Compressive load was applied using the same test setup for ultimate uniaxial compressive strength test. The compressive stress ratio, the ratio of applied load to the ultimate compressive load, is taken as 0, 0.3 and 0.6. A constant flow pump was adopted to circulate the 3 wt. % sodium chloride solution with a pre-defined speed of 5±1 ml/s. The concentration of the solution was checked regularly at least once a week during the whole exposure period.

After exposure of 2, 6, 10, 18, and 36 weeks, the specimens were unloaded and processed for chloride profile determination. A grinding machine was used to obtain concrete powder samples layer by layer with layer depth of 2 mm at the exposure surface of concrete. The total chloride content of each layer was determined by chemical analysis in accordance with EN 14629 [12].

3. Experimental results and discussion

3.1 Chloride profiles

Figure 1 shows the influence of compressive load stress on chloride penetration under the cases of same exposure duration of 2 weeks, 6 weeks, 10 weeks, 18 weeks and 36 weeks respectively. It can be observed that the chloride content decreases with the increase of depth, gradually reaching to the initial chloride content. When a 30% of maximum compressive load is applied, the chloride content of the layer with the same depth is lower than that without load. But when the stress ratio reaches to 60%, the chloride content is higher than that without compression.

The measured chloride profile can be modelled based on the Fick's II law (Eq. (1)). Apparent diffusion coefficients and modelled surface concentrations determined by curve fitting according to EN12390-11: 2014 Annex F [13] are shown in Figure 2 and Figure 3, respectively.

$$C(x, t)=C_0+(C_s-C_0)[1-\mathrm{erf}\frac{x}{2\sqrt{D_{app}\cdot t}}] \quad (1)$$

Where x is the depth; t is the exposure time; D_{app} is the apparent chloride coefficient; C_0 is the initial chloride content of the concrete; C_s is the surface chloride content ; and $C(x,t)$ is the chloride concentration at depth x and time t.

3.2 Apparent diffusion coefficients

It can be seen from Fig. 2 that the diffusion coefficient of concrete under compression decreases first and then increases with stress ratio. Low stress ratio of compressive stress reduces the chloride diffusion in concrete, but when the stress ratio exceeds a critical value, the chloride diffusion speeds. In the meanwhile, the chloride diffusion depth increases with the exposure time and the diffusion coefficient decreases with the exposure time, no matter whether an external load is applied or not. The difference among the apparent chloride diffusion coefficients of concrete under different compressive ratios is seemingly to narrow after longer exposure time. All the values for the diffusion coefficients tend to stabilize at values approaching 3.7 E-12 m^2/s for late ages (36 weeks). In the long run, the influence of the imposed compressive load on the apparent chloride diffusion coefficients seems not so significant, but still need to be validated by longer laboratory experiments and even investigation of specimens from exposure cites or real structures.

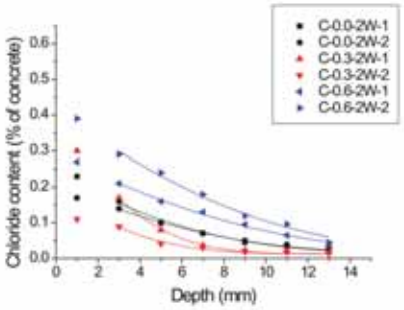

(a) Chloride profiles of concrete after 2 week's exposure

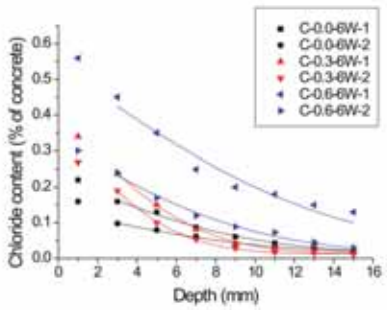

(b) Chloride profiles of concrete after 6 week's exposure

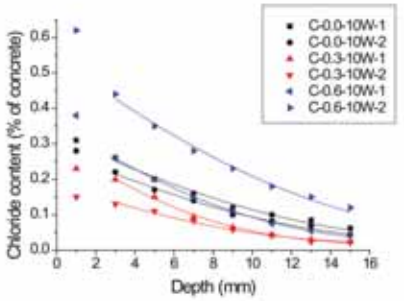

(c) Chloride profiles of concrete after 10 week's exposure

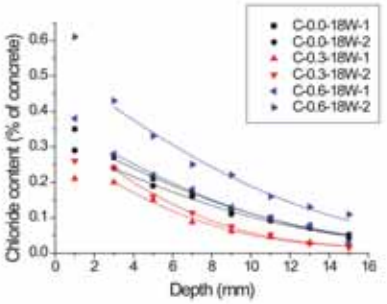

(d) Chloride profiles of concrete after 18 week's exposure

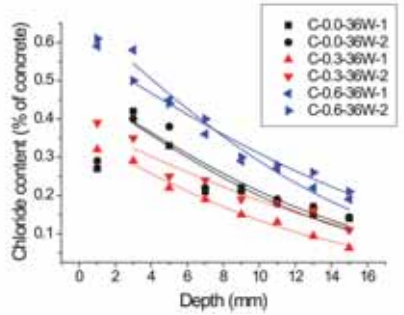

(e) Chloride profiles of concrete after 36 week's exposure

Figure 1: Chloride profiles determined after 2, 6, 10, 18 and 36 weeks with 0, 0.3 and 0.6 compressive load

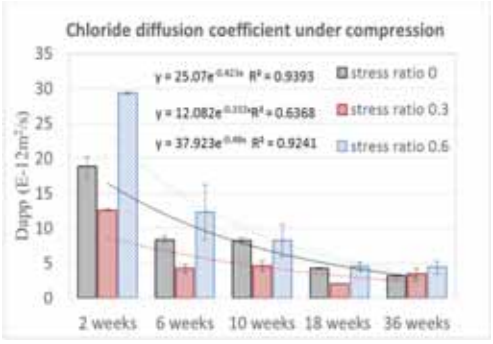

Figure 2: Apparent chloride diffusion coefficients under compressive load

3.3 Modelled surface concentrations

The modelled surface concentrations of concrete under different loading ratios scatter in a relatively wide range but tend to increase with exposure time and stabilize at values approaching around 0.6 %. Compare to the experimental results (Fig. 1), the modelled surface concentrations are slightly higher, which shows the existence of convection zone at the exposed surface.

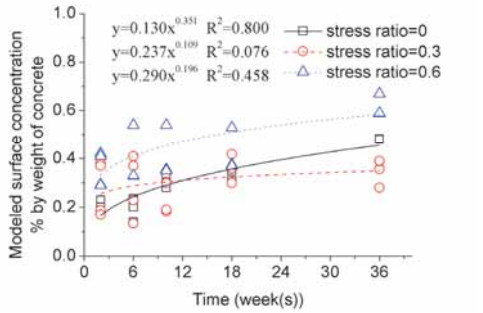

Figure 3: Modelled surface concentrations under compressive load

4. Modelling and prediction

4.1 Modelling

As diffusion is the most active mechanism in chloride transport in concrete, a widely used formula of mathematical models to estimate the initiation of chloride corrosion is based on Fick's second law. Equation (1) constitutes the mathematical description of chloride penetration in concrete without load used in [12-14]. In this equation, the input parameter which is influenced by the stress ratio most is the diffusion coefficient Dapp. If the time dependence is considered, Dapp(t) should be determined by means of Equation (2) and Equation (3).

$$D_{app}(t)=k_e \cdot D_{app}(t_0) \cdot \left(\frac{t_0}{t}\right)^{\alpha} \quad (2)$$

$$k_e = \exp\left(b_e \cdot \left(\frac{1}{T_{ref}} - \frac{1}{T_{real}}\right)\right) \quad (3)$$

Dapp(t0) is the apparent chloride diffusion coefficient at a reference time t0 determined by means of an inverse analysis from chloride profiles measured from diffusion test, is the ageing exponent indicating the decrease of apparent chloride diffusion coefficient over time. However, for a realistic determination of the ageing exponent, the long-term behaviour of *Dapp* should be considered; the exposure time should be as long as possible at least several years. According to Fig. 2, the ageing exponent of concrete unloaded (stress ratio 0) and mechanically loaded (with stress ratio 0.3 and 0.6) is 0.423 (unloaded) and 0.332 and 0.48, respectively derived by curve fitting of the average *Dapps* vs. time. But due to very limited samples and rather short-term test, the validity of derived ageing exponents should be reconsidered. So, the average aging exponent 0.412 is used to make the reliability calculation. And the other aging exponent in accordance with fib bulletin 34 [14] is also conducted in order to illustrate its influence.

Table 2 Diffusion coefficient *Dapp* and ageing exponent under different loading condition

Parameter	**Unit**	**Distribution**	**Values (m; s)**		
			0%	**30%**	**60%**
Dapp,6w	[10-12m²/s]	Normal	7.44; 1.16	5.23; 2.47	12.15; 5.50
α (1)	[-]	Constant	0.423	0.332	0.480
α (2) [14]	[-]	Beta, $0 \leqslant \alpha \leqslant 1$		0.30; 0.12	

The other input parameters are shown in Tab. 3, some of which were determined according to the investigation of real concrete structures specimens from the exposure sites in China [17] and the others in accordance with [14].

Table 3 Input parameters for the service life prediction.

Parameter	**Explanation**	**Unit**	**Distribution**	**Values (m; s)**
C_{crit} [17]	Critical chloride content	wt.-%/c	Beta $0.2 \leq C_{crit} \leq 2.0$	0.60; 0.15
C_s[17]	Surface chloride content	wt.-%/c	Lgnormal	3.8; 0.58
dc[17]	Concrete cover	mm	Normal	80; 5.3
t_0	Reference testing time (t_0 = 6w)	a	Constant	0.115
T_{ref}[14]	Reference temperature	K	Constant	293
T_{real}[14]	Real temperature	K	Normal	288; 5.0
be[14]	Regression variable	K	Normal	4800; 700

4.2 Prediction

The service life prediction for 50 years under compressive load is shown in Fig. 4. The calculations are performed with the software STRUREL provide by Centre for Building Materials, Technical University of Munich.

Figure 4 a. shows how the service life is changed by the variable aging factor and diffusion coefficient, both of which are affected by external load. Although the diffusion coefficient of concrete under stress ratio 0.3 is smaller than stress free concretes, the lower ageing factor makes less and lower *Dapp* decrement in time, resulting in less reliability in the long run. Service life prediction of concrete under stress ratio 0.6 is just the opposite. The age factor of concrete under stress ratio 0.6 is higher than stress free concrete, but the increment of diffusion coefficient by external load is big enough to make a more diffusion flux within 60 years or more.

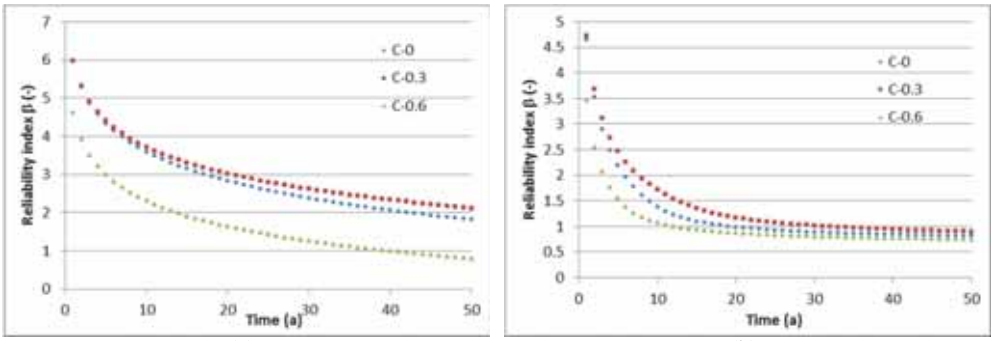

(a) (b)

Figure 4: Development of reliability index over time (a. aging exponent derived from short-term laboratory tests; b. the same aging exponent in accordance with [14].)

As is shown in Fig. 2, the diffusion coefficient of concrete under compression decreases first and then increases with stress ratio, showing the direct influence of external load on the chloride transport into concrete. Figure 4 a. and Figure 4 b. show how the external load influences the service life of concrete by its effect on apparent diffusion coefficient. Under the condition of the same distribution of the ageing exponents, the service life under compressive stress ratio 0.3 is prolonged and under compressive stress ratio 0.6 it is shortened in comparison to stress free condition. In Fig. 4 a., assuming a target reliability of 1.0 to the end of service life, the end of service life is reached more than 50 years under unloaded condition. The service life even increases when the concrete is exposed to 30 % of the ultimate compressive load and decreases to less than 40 years when loaded with 60% of the ultimate compressive load. When the aging exponent changes (Fig. 4 b), the derived service life changes significantly. But still, 30% of the ultimate compressive load prolongs the service life of concrete while 60% of the ultimate compressive load shortens the service of concrete. Aging exponent has a great effect on the calculated service life. Thus, more research should be carried out to get reliable aging exponents for concrete under different exposure conditions or reliable distribution functions.

The parametric sensitivities α_i can also be calculated by the software. α_i denotes the sensitivity of reliability index with respect to changes in the mean value or standard deviation of variable.
Figure 5 shows the sensitivity with respect to small changes in the standard deviation of variable in Fig 4 (b). The sensitivity can be defined as follows and quantifies the sensitivity of β with respect to changes in the variability of a variable [18].

$$\alpha_{\sigma,i} \approx -\beta\alpha_i^2 \tag{4}$$

$$\sum(\alpha_i)^2 = 1 \tag{5}$$

The values shown in Figure 5 are α_i^2 so that we can use a pie chart to illustrate the influence of a parameter on the reliability index thus the service life.It can be seen from Figure 5 that the age exponent and apparent chloride diffusion coefficient have a significant influence on the service life. Therefore, to get a better understanding of the impact of external compressive load on the service life prediction, the priority is to study its influence on chloride diffusion coefficient and the ageing exponent. For this purpose, further studies are needed to establish a more adequate data base containing results after long-term combined mechanical and chloride exposure, serving as the valid basis for reliability assessment and service life prediction.

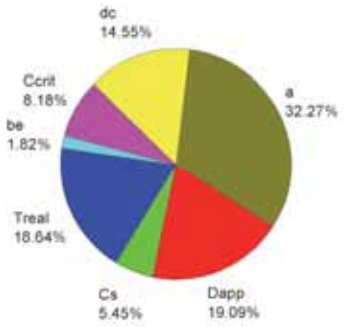

Figure 5: Sensitivity analyses of the service life prediction.

In addition, the sensitivity analysis shows the influence of critical chloride concentration in service life prediction. The critical chloride concentration that initiates pitting corrosion in concrete may also affected by the impose stress. Therefore, far more experimental and modelling research beyond this contribution is needed in order to take external load into consideration in the service life prediction and reliability assessment of concrete structure under combined mechanical load and chloride exposure.

5. Conclusions

The diffusion coefficient of concrete under compression decreases first and then increases with stress ratio. Low stress ratio of compressive stress reduces the chloride diffusion in concrete, but when the stress ratio exceeds a critical value, the chloride diffusion speeds.
The diffusion coefficient decreases with the exposure time, no matter whether an external load is applied or not. 36 weeks' exposure seems not efficient for the determination of the ageing exponent of apparent diffusion coefficient. Laboratory results show that various uncertainties in parameters of chloride diffusion under load still exist and calibration with long term field investigation is necessary.
Probabilistic analysis shows significant influence of the diffusion coefficient, aging exponent and the critical chloride concentration on the reliability–based service life of concrete under combined mechanical load and chloride diffusion. These input parameters used in the reliability calculation are affected to some extent by the external load. Thus, it is obvious that there is still an urgent need to obtain results from long-term laboratory and field studies of concrete under external load in order to improve the mathematical service life prediction and arrive at a more reasonable and practical estimation of the service life of reinforced concrete structures.

Acknowledgements
The financial support from the National Natural Science Foundation of China (Grant No.51320105016) is gratefully acknowledged. The authors thank the Centre for Building Materials, Technical University of Munich for providing the software STRUREL. The financial support from China Scholarship Council is also acknowledged.

References

[1] C. Andrade, M. Prieto, P. Tanner, F. Tavares, R. d'Andrea. Testing and modelling chloride penetration into concrete, Construction and Building Materials 39 (2013), 9–18
[2] David Conciatori , Hamid Sadouki, Eugen Brühwiler. Capillary suction and diffusion model for chloride ingress into concrete. Cement and Concrete Research 38 (2008), 1401–1408.
[3] Glass GK, Buenfeld NR. Chloride-induced corrosion of steel in concrete. Prog Struct Eng Mater 2 (2001), 448–58
[4] Kermani A. Permeability of stressed concrete. Building Research & Information19 (1991), 360–366
[5] He Shiqin, Gong Jinxin. Influence of Flexural Loading on Permeability of Chloride Ion in Concrete. Journal of building materials 8, no. 2 (2005), 134-138. (In Chinese)
[6] Saito M, Ishimori H. Chloride permeability and repeated of concrete under loading. Cement and Concrete research 25 (1995), 803–808
[7] Jaffer SJ, Hansson CM. Chloride-induced corrosion products of steel in cracked concrete subjected to different loading conditions. Cem Concr Res 39 (2009), 116–25

[8] Jin Wu, Hongming Li, Zhe Wang, Jingjing Liu. Transport model of chloride ions in concrete under loads and drying-wetting cycles. Construction and Building Materials 112 (2016), 733–738
[9] Djerbi Tegguer, A, S Bonnet, A Khelidj, and V Baroghel-Bouny., Effect of uniaxial compressive loading on gas permeability and chloride diffusion coefficient of concrete and their relationship. Cement and Concrete Research 52 (2013), 131-139
[10] Yao, Y., Z. Wang, and L. Wang. Durability of concrete under combined mechanical load and environmental actions - a review. Journal of Sustainable Cement-Based Materials 1, (2012), 2-15
[11] TANG L, NILSSON L O, BASHEER P A M. Resistance of Concrete toChloride Ingress – Testing and Modelling. London: Taylor & Francis Group (2011)
[12] BS EN 14629: Products and systems for the protection and repair of concrete structures – Test methods – Determination of chloride content in hardened concrete (2007)
[13] EN12390-11: Determination of the chloride resistance of concrete, unidirectional diffusion (2015)
[14] fib bulletin 34. Model Code for Service Life Design (2006).
[15] fib MC. Model Code for Concrete Structures (2010)
[16] ISO 16204:2012. Durability – Service life design of concrete structures (2012)
[17] Wang Shengnian, Su Quanke, Fan Zhihong, et al. Durability design principle and method for concrete structures in Hong Kong-Zhuai-Macau sea link project. China Civil Engineering Journal 47 (2014), 1-8.
[18] Hohenbichler, M., Rackwitz, R. Sensitivity and importance measures in structural reliability, Civil Engineering Systems, 3 (1986), 203-209.

International RILEM Conference on Materials, Systems and Structures in Civil Engineering
Conference segment on Service Life of Cement-Based Materials and Structures
22-24 August 2016, Technical University of Denmark, Lyngby, Denmark

MULTIDEPTH CORROSION MONITORING SYSTEM EVALUATION AND APPLICATION

Dalibor Sekulić [(1)], Ivan Gabrijel [(2)]

(1) Institut IGH d.d. Zagreb, Croatia
(2) University of Zagreb, Faculty of Civil Engineering, Zagreb, Croatia

Abstract
Deterioration of reinforced concrete structures due to aggressive influences is serious problem worldwide. It is recognized that corrosion of steel reinforcement in concrete is the major reason for serious damages and degradation of RC structures. Proactive maintenance before significant damage occurs to the structure optimizes cost and impact on the structure. To be able to perform proactive maintenance of corroding structures, continuous corrosion monitoring which is able to predict future deterioration is essential. The work presented was focused on the analysis of measurement techniques for corrosion monitoring. Based on the review of the existing test methods and criteria that methods must be non-expensive, relative simple and capable to detect corrosion at early stage three techniques were selected for additional analysis through experiments. Selected techniques are implementation of multidepth sensors for macrocell currents, corrosion potential and electrical resistivity measurements. A series of laboratory measurements and data evaluations, as well as calibration of selected techniques and sensors were carried out.

1. Introduction

Objective of this research is development of useful and improved corrosion monitoring system and their implementation to corrosion monitoring of reinforced concrete bridges. Requirements for system is cost effectiveness, possibility for corrosion indication in the early phase, accuracy, simple application to the new and existing structures and long term measurement stability, with use of self-made sensors capable to measure few different parameters. A comprehensive literature review of available measurement techniques is performed and based on proposed requirements several measurement principles are selected.
In the next stage, measurements on laboratory specimens were conducted and data were evaluated to confirm efficiency of selected sensors and also to make calibration. By the

comparison of the results measured by the sensors with the actual corrosion on test specimens, criteria for corrosion are established.

2. Reinforcement steel corrosion measurement methods

Corrosion of steel can be measured directly by the electrochemical methods or indirectly by the measuring parameters correlated with corrosion such as moisture, pH value, Cl^- ion content and cracks in concrete resulting from the corrosion process. Many testing and monitoring techniques have been developed for these purposes, and can be classified into electrochemical and non-electrochemical methods.

2.1 Electrochemical methods

Electrochemical monitoring methods can be classified as static and polarisation methods as shown in Table 1.

Table 1: Electrochemical monitoring methods for the reinforced concrete corrosion characterisation

ELECTROCHEMICAL METHODS	
STATIC METHODS	POLARISATION METHODS
Half-cell potential (reference electrodes)	Linear polarisation method
Corrosion macro cell current	Electrochemical impedance spectroscopy
Electrochemical noise	*Localised electrochemical impedance spectroscopy*
	Galvanostatic pulse method
	Scanning reference electrode method

Static methods measure corrosion potential and macro cell currents originated from corrosion process. Different reference electrodes for corrosion monitoring, which can be installed into concrete structure are developed. Pseudoreference mixed metal oxide electrodes (Figure1a) consists of mixed metal oxide activated titanium rod, cast in specially developed cementitious body [1, 2]. The ERE 20 Embeddable reference electrode, developed and manufactured by the FORCE Institute using a manganese dioxide electrode in a steel housing with an alkaline, chloride free gel (Figure 1b) [2, 3, 4]. The sensor manufactured by the Austrian Ingenierbüro Wietek (Figure 1c) [2, 5] is in the form of a wire wrapped around the steel to be monitored. A potential between the steel and electrode can be measured by using the half-cell. The advantage of the method is possibility for measurements of pitting corrosion at the large concrete structures. Figure 1d shows a measuring system consists of the steel electrodes and insulating supports developed by Schiessel and Rupach [6]. Steel electrodes are placed at different depths which makes possible depassivation front monitoring. Another configuration is a Corrowatch Multiprobe developed by FORCE institute (Figure 1e) [7, 8]. A multi-probe test unit (Figure 1f) developed by the Swedish FORCE Institute consists of 20 embedded steel electrodes, which are potentiostatically held at a fixed potential. Initiation of corrosion can be detected by a sudden rise in the anodic current [7, 8]. These test methods have an advantage in providing direct indication of electrochemical activity in the system.

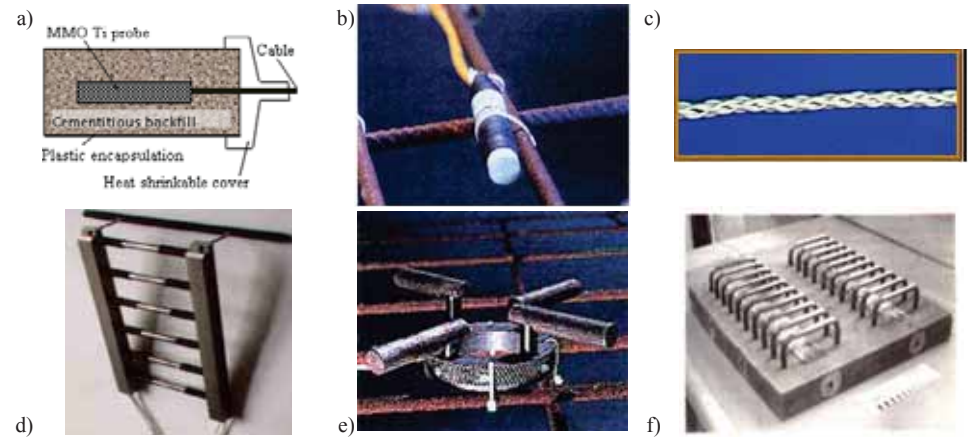

Figure 1: a) MMO Ti probe; b) ERE 20 probe; c) Wire sensor; d) Schiessel probe; e) Corrowatch probe; f) FORCE probe

Polarisation methods [9] measure response to DC or AC polarisation of reinforcement with constant or changing frequency. There are several commercially available embeddable monitoring systems. The C-probe CP100 is a combination of Silver/silver chloride reference half-cell and graphite counter electrode [10]. CORRATER 800/800T is manufactured using carbon steel measures corrosion rate of reinforcing steel in concrete [11]. General Building Research Corporation of Japan developed sensor for natural potential, polarization resistance and electrolyte resistance measurement [12]. Instrumentation is relatively expensive, measurements can be quite time consuming and methods require complex analysis.

2.2 Non-electrochemical methods

For corrosion monitoring non-electrochemical methods are also in use. Infrared thermography can detect delamination in concrete as a result of corrosion process and it is not suitable for early corrosion detection [13]. Acoustic emission method can measure stress waves from cracking of concrete, but it is difficult to distinguish are cracking originated from corrosion or from other stress sources [14]. Electrical resistivity of concrete [15, 16] and electrical resistance of steel [17] methods are not expensive, there are simple for use and measure resistivity of concrete and resistance change of corroded steel which is in good correlation with reinforcement corrosion. There are other test methods based on radiography and radiometry [18], magnetic field measurements [18], optical fibre sensors [19], but there requires expensive equipment and it is difficult to make adaptation for monitoring purposes.

3. Laboratory measurements

Based on the review of the existing test methods, it is decided to use potential measurement by reference electrodes, macrocell current and electrical resistivity measurements at various depths. All sensors for selected test methods are produced in the Institut IGH and evaluated in

laboratory measurements. In the first phase of research each sensor is tested separately and after that all three sensors is casted together into concrete specimens as shown in Figure 2, where sensors are indicated as follows:

a) Sensor for macrocell currents and electrical resistivity of concrete measurement with five electrodes made from same steel as reinforcement placed at the different depths.
b) MnO_2 sensor for corrosion potential measurement consisting of plastic tube one half filled with alkaline gel and the other half with the MnO_2, with a porous mortar plug on the sensor tip.
c) Sensor for electrical resistivity of concrete measurement consisting of two stainless steel electrodes. One electrode is also used as an anode for macrocell current measurements.
d) Reinforcement steel bars of 12 mm diameter for macrocell current measurement according to ASTM G 109 [20] for comparison purposes.

Sensors are well fixed into mould at defined depths before concrete casting. MnO_2 sensor is placed at the same depth as upper reinforcement bar (20 mm). Also, upper electrode of multidepth sensor is placed at the 20 mm depth, and other electrodes are at the depths of 30 mm, 40 mm, 50 mm and 60 mm. Prism exposure cycles were conducted according to FHWA-HRT-07-043 [21]: 4 days 3 % salt solution ponding at the top surface and 3 days drying.

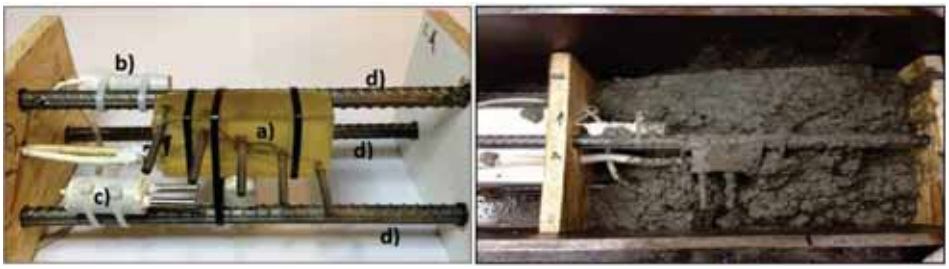

Figure 2: Sensors prepared for casting (left), concrete casting into moulds (right)

As chloride content in concrete reaches a critical level, the sensor electrode starts to corrode (corrosion initiation) and measured corrosion current between stainless steel anode and mild steel cathode decrease below the corrosion initiation current density of 0,1 μA/cm² (Figure 3 - left). Since electrodes are embedded into the concrete at different depths, corrosion initiation condition occurs at particular electrodes at different times as indicated in Figure 3 – left for one of the specimens. Figure 3 - right shows corrosion initiation times along the depth for all 6 tested specimens during cyclic salt solution exposure of 160 days. Differences between the specimens might be caused by heterogeneous concrete, or by the vertical cracks in concrete, and must be considered when performing measurement on real structures. The steel loss calculated according to Faraday law [8]. from the corrosion rates for multisensor electrodes was 1 - 6 μm, which is much lower than for the reference ASTM G109 method, where a value of 35 μm was obtained. It is supposed that multisensor electrodes interact with each other, which leads to an underestimation of steel loss by the measurements.

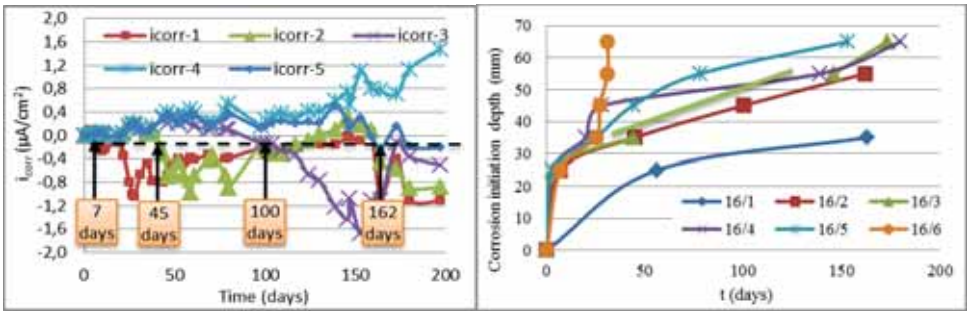

Figure 3: Measuring results of corrosion currents for specimen No. 16/2, where are indicated corrosion initiation times for reaching the condition i_{corr} = 0,1 μa/cm^2 (left). Depth of corrosion initiation according to time for all six tested specimens (right).

3.1 MnO_2 half-cell sensors

Figure 4a shows correlation between the corrosion rate (CR) measured on three reinforcement bars according to ASTM G 109 and electrical potential measured by MnO_2 sensors with indicated 95 % confidence intervals. Criteria for potentials obtained from this correlation, are shown in Figure 4b and it is in agreement with ASTM C876-09 criteria [22].

a)

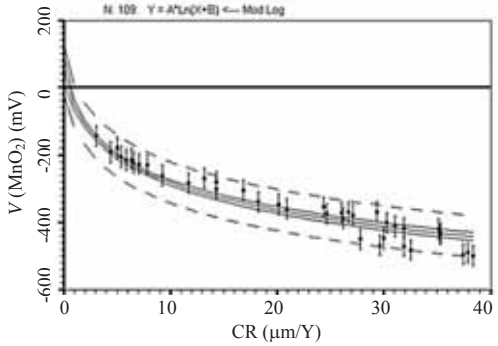

b)

CR (μm/year)	V $_{MnO2}$ (mV)
0	> -20
1	-20 -140
5	-140 - 280
15	-280 - 350
30	-350 - 500

Figure 4: a) Correlation between the CR and potential; b) criteria for potentials obtained from CR-V_{MnO2} correlation

Chloride profiles were obtained by chemical analysis of drilled concrete powder from comparative specimens exposed to same NaCl solution cycles as specimens with embedded sensors. The correlation between the corrosion rate measured by sensors and the actual Cl^- content measured by chemical analysis of drilled concrete powder is shown in Figure 5a, where 95% confidence limits are also indicated. Based on this, a correlation between the CR and Cl^- content is established as shown in Figure 5b. Critical chloride content of 0.06 %, by the weight of concrete, well known from the literature [23], is taken as a critical chloride content for initiation of corrosion. It follows that initiation if corrosion occurs for measured corrosion rate of 5 μm/Y, or for potential of -140 to -280 mV measured with MnO_2 sensors.

a)

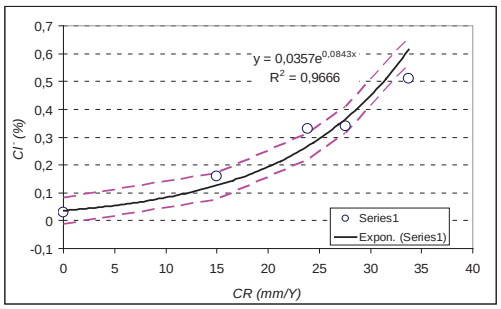

b)

CR (µm/year)	Cl^- content (%)
0	0.03
5	0.06
15	0.12
25	0.30
30	0.45

Figure 5: a) Correlation between the CR and chloride content; b) CR and corresponding Cl^- contents

3.2 Electrical resistivity sensors

The electrical resistivity technique was validated by comparison to macrocell current measurements. Figure 6 - left shows the correlation obtained between the corrosion current and concrete resistivity. During testing the specimens were exposed to 3% NaCl solution cycles which gives resistivity range from 40 Ωm to 80 Ωm (all measurements are performed in the environment which enables corrosion). Compared with the full resistivity - water saturation curve (Figure 6 - right) this range is very narrow as indicated by red area in Figure 6 - right. This is the reason why correlation between I_{corr} and concrete resistivity looks weak.

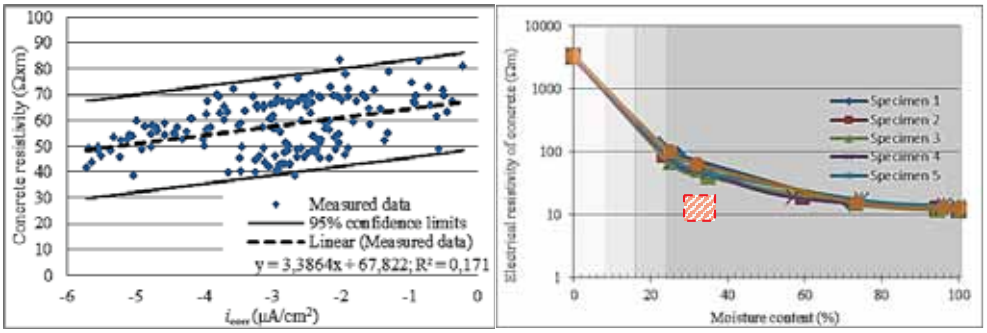

Figure 6: Resistivity of concrete measurement results (left), full resistivity - moisture content curve (right) Corrosion risk depending on concrete electrical resistivity and saturation degree.

For the correlation between the corrosion, resistivity of concrete and water saturation determination well known criteria for electrical resistivity of concrete from the first two columns of Table 2 was used [16]. A good agreement between our experimental results of corrosion current density measurement and these criteria are obtained. Also, correlation between concrete resistivity and water saturation is obtained as shown in Table 2. However, it should be taken into account that chlorides are strongly influencing concrete resistivity and in the case of chloride rich water, the limiting values of water saturation would be different.

In in-situ measurements of electrical resistivity of concrete performed on Croatian coastal bridges show that for resistivity higher than 1500 Ωm in all cases there was no corrosion

activity. For resistivity lower than 1500 Ωm corrosion rate is uncertain - it may be either low of high. This may be connected with oxygen access, because for water saturated concrete there are low resistivity, but there is no oxygen to allow corrosion process. For corrosion rates above 30 mm/Y, concrete resistivity was always lower than 500 Ωm. These considerations can be described in Table 3.

Table 2: Correlation between the resistivity of concrete and water saturation

CR (µm/year)	Concrete resistivity (Ωm)	Saturation (%)
Negligible	>1000	<8
Low	500-1000	8-15
Moderate	100-500	15-25
High	<100	>25

Table 3: Criteria for resistivity of concrete obtained from in-situ measurements

Concrete resistivity (Ωm)	Likelihood of corrosion rate
<500	High
500-1500	Moderate
>1500	Low

4 Corrosion prediction

It is important to emphasize that the multidepth sensor monitoring technique has the ability to predict future corrosion of reinforcement. As the multidepth sensors measure initiation of corrosion by anodes placed at the depths lower than reinforcement, the time for the initiation of corrosion at the reinforcement level can be predicted by the extrapolation of measurement results. For corrosion initiation according to the depth the following function is proposed (Equation 1):

$$D = A \cdot \sqrt{t} + B \cdot (1 - e^{C \cdot t}) \quad (1)$$

Where, D is the Corrosion front depth, t is the time and A, B, C are fitting parameters. In real structures (if not submerged) we have a combination of chloride diffusion and capillary absorption process. Therefore, the first part of the constructed function describes the capillary absorption process, and the second part describes the chloride diffusion process. An example of corrosion front prediction is shown in Figure 7 - left. If reinforcement is placed at the 80 mm depth it will start to corrode after 300 days, which is predicted from the measurements during the first 160 days. At the first 3 days there is significant difference between measured and predicted corrosion front depths. The reason is fast initially salt water absorption at the beginning of test, which our proposed model is not able to predict. After 25 days of testing agreement between predicted and measured values is very good. Corrosion front depth measured by sensors is checked by the chemical analysis of concrete powder drilled from the same depths as sensor electrodes as shown in Figure 7 – right.

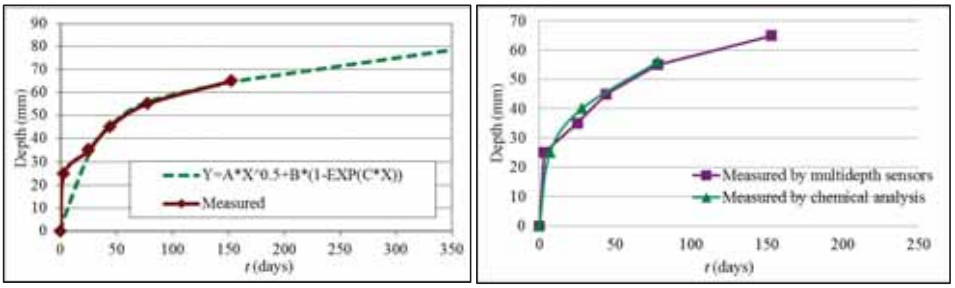

Figure 7: Corrosion front prediction (left), Corrosion front measured by chemical analysis and by sensors (right)

Figure 8 shows reinforcement cross section decrease in time obtained from measurements in the laboratory (left) and at three Croatian coastal bridges, where corrosion measurement data is available during 4 years after construction for "Cetina" bridge, at 11 years for "Krka" bridge and at 17 years for "Maslenica" bridge (right) [24]. Therefore, for prediction of reinforcement diameter decrease in the phase of corrosion propagation it is proposed to use a linear relationship. It is proved that a linear relationship is valid up to formation of the 0.3 mm wide cracks at the surface of concrete.

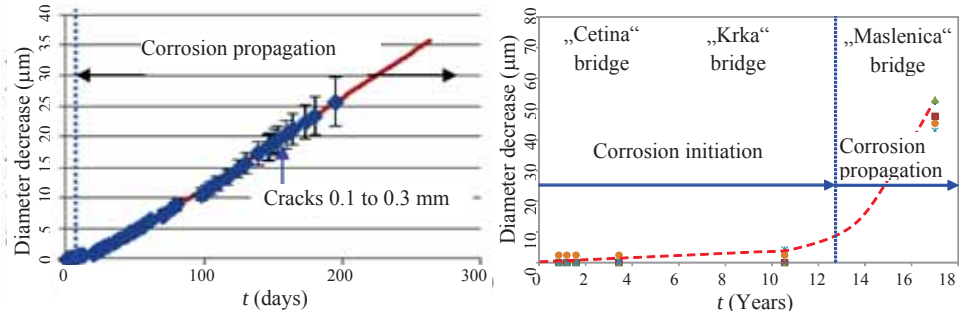

Figure 8: Reinforcement diameter decrease for corrosion initiation and corrosion propagation phases, measured in the laboratory (left) and in-situ (right)

5. Conclusion

The work was focused on developing a system for simple, accurate and cost effective monitoring of corrosion rate in RC structures exposed to chlorides. All known measurement techniques for corrosion monitoring are analysed and it is decided to use multidepth sensors for macrocell currents, corrosion potential and electrical resistivity of concrete measurements. Used sensors are able to monitor critical conditions for corrosion initiation according to depth in the concrete protective layer and for prediction of future development of corrosion.

From laboratory measurements it is obtained that multisensor electrodes interact with each other, which leads to an underestimation of steel loss by the measurements. Correlation between measured potentials and corrosion rates for our measurement system including 95% confidence limits are established, which is in agreement with well-known criteria. Also, the correlation between the corrosion rate measured by sensors and the actual Cl^- content measured by chemical analysis of drilled concrete powder is established. Based on well-known criteria for corrosion rate dependence on concrete resistivity, a correlation between corrosion rate and water saturation is established. Analysis of in-situ measurements of electrical resistivity of concrete gives different correlation between corrosion rate and resistivity, for which a reason might be in limited oxygen access and in used CEM II type of cement.

Finally simple physical model for corrosion initiation according to the depth in concrete is proposed. Model includes a combination of chloride diffusion and capillary absorption processes. It is important to emphasize that model is valid for homogenous concrete and before occurring of cracks greater of 0.3 mm.

References

[1] Ti MMO probe, brochure, http://www.cescor.net/uploads/prodotti/ti-mmo-eng.pdf
[2] Jackson Meyer, J., Bjegovic, D., Mikulic, D., Sekulic, D., Corrosion Measurement in Concrete Utilizing Different Sensor Technologies NACE paper No. 03435, NACE International, CORROSION 2003, San Diego, California, 16-20 March 2003.
[3] http://www.forcetechnology.com, Reference electrode for potential measurements in reinforced concrete, product sheet.
[4] Arup, H., Klinghoffer, O, Mietz, J. Long term performance of MnO_2 – Reference electrodes in Concrete, Corrosion 97, NACE Conference, New Orleans, 11pp. (1997)
[5] Korrosion bei Stahl- und Spannbeton, presentation, http://www.a-bau.co.at/ Publikationen_files/CMS-Praesentation.pdf
[6] Schießl, P.; Raupach, M., Monitoring System for the Corrosion Risk of Steel in Concrete Structures", Concrete International July 1992, pp. 52-55
[7] Lee, S.K., Jang B.S., Ahn, J.H., Kim, K.C., Corrosion Monitoring of a Massive Concrete Structure Exposed to Marine Environment Using Embedded Corrosion Sensors, NDE/NDT for Structural Materials Technology for Highway & Bridges, 25 August 2014
[8] Bjegović, D., Mikulić, D., Sekulić, D., Non-destructive Corrosion Rate Monitoring for Reinforced Concrete Structures, 15 th World Conference on NonDestructive Testing, Rome, 2000, Proceedings, Paper idn 642.
[9] Andrade, C., Alonso C., et. all, Test methods for on-site corrosion rate measurement of steel reinforcement in concrete by means of the polarization resistance method, RILEM TC 154-EMC: 'Electrochemical Techniques for Measuring Metallic Corrosion', Recommendations, Materials and Structures, Vol. 37, November 2004, pp 623-643
[10] Bjegovic D., Miksic, B., Stehly R., Test Protocols for Migrating Corrosion Inhibitors (MCI) in Reinforced Concrete, Emerging Trends in Corrosion Control - Evaluation, Monitoring, Solutions, Vol. 1, Akademia Books International and NACE International, India Section, New Delhi, India, 1999, pp. 3-18.

[11] Model 800 LPR Corrosion Rate Monitoring in Concrete Multiple parameter measurements with CORRATER® Probe, Brochure http://www.cosasco.com/pdfs/800_LPR_Corrosion_Rate_Monitoring%20_Concrete.pdf
[12] Nagayama, M., MCI 2020 Long Term Test Protection of Rebar in Concrete, Final Report, General Building Research Corporation of Japan, October 1999.
[13] K. Kobayashi & N. Banthia, Corrosion detection in reinforced concrete using induction heating and infrared thermography, Journal of Civil Structural Health Monitoring 1(1):25-35 · June 2011
[14] Kawasakia, Y., Wakudab T., Kobaraib, T, Ohtsu M, Corrosion mechanisms in reinforced concrete by acoustic emission, Construction and Building Materials, Volume 48, November 2013, Pages 1240–1247
[15] Hornbostel, K.; Larsen, C.K.; and Geiker, M.R., "Relationship between Concrete Resistivity and Corrosion Rate—A Literature Review," Cement and Concrete Composites, V. 39, May 2013, pp. 60-72.
[16] Polder, R., et all, Test methods for on site measurement of resistivity of concrete, Recommendations, RILEM TC 154-EMC: Electrochemnical techniques for measuring metallic corrosion, Materials and Structures, Vol. 33, December 2000, pp 603-611
[17] Legat, A., Monitoring of steel corrosion in concrete by electrode arrays and electrical resistance probes, Electrochimica Acta Volume 52, Issue 27, 10 October 2007, Pages 7590–7598
[18] Sekulić, D., Bjegović, D., Mikulić, D., Non-destructive methods for monitoring of reinforcing steel in concrete, Proceedings of 9th International Conference and Exhibition, Structural Faults and Repair - 2001 / Ford, Michael C. (ur.). - Edinburgh : Commonwealth Institute , 2001.
[19] Sekulić, D.; Veža, Damir; Bjegovic, D.; Mikulić, D. Naslov: Corrosion monitoring in concrete structures with fibre optics, Proceedings of the "Structural Faults and Repair 2003" / Fowler, D. (ur.). - London : Commonwealth Institute London W8 UK , 2003. SF:47-59.
[20] ASTM G109 - 07(2013) Standard Test Method for Determining Effects of Chemical Admixtures on Corrosion of Embedded Steel Reinforcement in Concrete Exposed to Chloride Environments
[21] Darwin, D., et. all, Multiple Corrosion Protection Systems for Reinforced Concrete Bridge Components Publication No. FHWA-HRT-07-043, Federal Highway Administration, July 2007, 92 pp.
[22] ASTM C876-09. (2009). "Standard Test Method for Corrosion Potentials of Uncoated Reinforcing Steel in Concrete," Book of Standards Volume 03.02, ASTM International, West Conshohocken, PA.
[23] Angst, U., Vennesland, Ø. (2009), Critical chloride content in reinforced concrete – State of the art, Concrete Repair, Rehabilitation and Retrofitting II – Alexander et al (eds), 2009 Taylor & Francis Group, London, ISBN 978-0-415-46850-3.
[24] Bleiziffer, J., Radić, J. (2010), Monitoring performance of large Croatian bridges ARCH'10 / Chen, Baochun ; Wei, Jiangang (ed.). Zagreb: SECON , 2010. 875-882 (ISBN: 978-953-7621-10-0). 6th International Conference on Arch Bridges, Fuzhou, China, 11-13.10.2010

International RILEM Conference on Materials, Systems and Structures in Civil Engineering
Conference segment on Service Life of Cement-Based Materials and Structures
22-24 August 2016, Technical University of Denmark, Lyngby, Denmark

MODELING OF EARLY AGE CONCRETE CREEP USING RHEOLOGICAL MODELING APPROACHES

Wibke Hermerschmidt [(1)], Farid Benboudjema [(2)]

(1) Technische Universität Braunschweig, iBMB, Germany
(2) ENS Cachan, LMT Cachan, France

Abstract
Early age concrete shows a highly marked creep behavior which decreases continuously with the progression of the hardening process. Modeling approaches for the prediction of the creep behavior at early ages are of particular importance to perform realistic calculations of the temperature and stress evolution in restrained concrete structures at early ages. This paper presents a detailed investigation of rheological modeling approaches for early age concrete creep. It aims at a better understanding and a more general description of this type of modeling approaches, particularly with regard to their validity for different stress-strain histories and the description of the influence of the hardening state and the temperature. Benchmark studies with two existing rheological modeling approaches are carried out to show differences and similarities of the approaches and to identify their ability to describe the stress-strain behavior under different boundary conditions.

1. Introduction

The viscoelastic behavior of concrete is very pronounced at early ages and influences significantly the evolution of stresses in restrained concrete structures caused by heat of hydration and shrinkage. For a realistic calculation of the stress evolution, an accurate description of the viscoelastic behavior is necessary. Existing creep models in standards and guidelines are not suitable for that kind of problem because they do not describe the influences of the hardening process and the temperature on creep properly. Therefore, special creep models for early age concrete have been proposed by several authors [1-8]. The often used definition of a creep coefficient or a compliance function is difficult to handle if a continuously changing stress history, like it usually occurs in hardening concrete structures, shall be investigated. The calculation of the creep strains under non constant stress requires a stepwise superposition of the creep curves of every former load step. This procedure leads to high computational costs when used in numerical simulations of large structures.

A good alternative to these classical creep functions are rheological modeling approaches as proposed in [5-8]. The continuously changing material properties of early age concrete can be described by spring and dashpot parameters that depend on hydration degree or equivalent concrete age. Additionally, with the definition of the constitutive behavior in the form of differential equations, the description of creep under non constant stress and an application in numerical simulations is straightforward.

This paper presents a study on rheological modeling approaches for early age concrete creep. A comprehensive comparison and benchmarking of two existing rheological model approaches for early age concrete creep is presented.

2 Existing rheological modelling approaches for early age concrete creep

Two existing rheological modelling approaches will be compared in the following sections. The first is the one proposed by Benboudjema and Torrenti in [7]. It consists of a chain of three Kelvin-Voigt bodies and is denoted as "3KV" in the following. The second modelling approach, proposed by Hermerschmidt and Budelmann in [8], consists of a Maxwell chain combined with a single spring and is denoted as "4MW" in the following.

2.1 Kelvin-Voigt chain with parameters depending on hydration degree (3KV)

The 3KV model is a chain of three Kelvin-Voigt bodies, where the spring stiffnesses and the dashpot viscosities depend on the hydration degree ξ, see fig. 1.

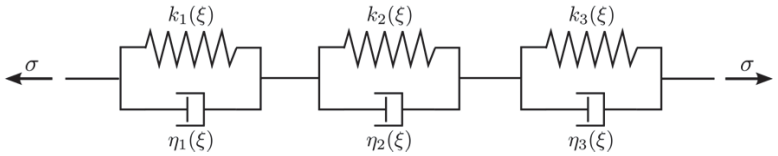

Fig. 1: Degree of hydration based Kelvin-Voigt chain (3KV) [7]

For the evolution of the spring stiffnesses, the relation

$$k_i(\xi) = k_{i,\infty} \frac{0.473}{2.081 - 1.608\bar{\xi}} \cdot \bar{\xi}^{0.62}, \text{ with } i = 1 \dots 3 \tag{1}$$

is used. In this equation, the parameter $\bar{\xi}$ is defined as

$$\bar{\xi} = \langle \frac{\xi - \xi_0}{\xi_\infty - \xi_0} \rangle_+, \tag{2}$$

where ξ_0 corresponds to the hydration degree from that on the mechanical properties of the concrete evolve and ξ_∞ is the final value of the hydration degree.

The retardation times τ_i of the Kelvin-Voigt bodies are kept constant, so that the evolution of the dashpot viscosity reads:

$$\eta_i(\xi) = \tau_i \cdot k_i(\xi), \text{ with } i = 1 \dots 3 \tag{3}$$

The retardation times τ_i are fixed parameters spaced by factor 10, where the smallest value is $\tau_1 = 0.1$ days.

The constitutive equation for one Kelvin-Voigt body with non constant spring and dashpot parameters reads:

$$\tau_i \cdot \ddot{\varepsilon}_i + \left(\tau_i \frac{\dot{k}_i}{k_i} + 1\right)\dot{\varepsilon}_i = \frac{\dot{\sigma}}{k_i} \tag{4}$$

The constitutive equation is solved stepwise using the assumption that the spring and dashpot parameters are constant within the time step. More information on this procedure is given in [7].

2.2 Maxwell chain with parameters depending on equivalent age (4MW)

The 4MW model is a parallel assembly of four Maxwell bodies and one single spring (fig. 2) where the spring stiffness of the single spring and the dashpot viscosities depend on the equivalent age of concrete t_e. The equivalent age is defined with a maturity approach based on the Arrhenius formula [8,9].

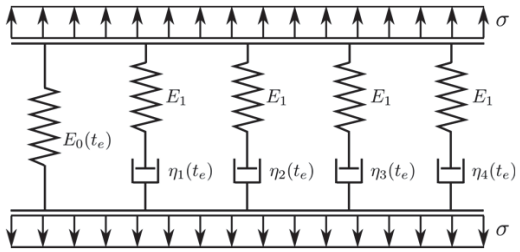

Fig. 2: Maxwell chain with parameters depending on equivalent age (4MW) [8]

The evolution of the stiffness of the single spring is given by an exponential function:

$$E_0(t_e) = f_1 \cdot \exp\left(f_2 \left(\frac{t_e}{t_k}\right)^{f_3}\right) \tag{5}$$

The stiffness of the springs in the Maxwell units is kept constant. The viscosities of the dashpots evolve with the function

$$\eta_i(t_e) = d_{1,i} \cdot \left(\frac{t_e}{t_k}\right)^{d_2}, \quad \text{with } i = 1 \dots 4. \tag{6}$$

The constitutive equation of the model is a differential equation of fourth order that reads:

$$a_0\sigma + a_1\frac{\partial\sigma}{\partial t_e} + a_2\frac{\partial^2\sigma}{\partial {t_e}^2} + a_3\frac{\partial^3\sigma}{\partial t^3} + a_4\frac{\partial^4\sigma}{\partial {t_e}^4} = b_0\sigma + b_1\frac{\partial\varepsilon}{\partial t_e} + b_2\frac{\partial^2\varepsilon}{\partial {t_e}^2} + b_3\frac{\partial^3\varepsilon}{\partial {t_e}^3} + b_4\frac{\partial^4\varepsilon}{\partial {t_e}^4} \tag{7}$$

The coefficients $a_0 \dots a_4$ and $b_0 \dots b_4$ are functions of the spring stiffnesses and dashpot viscosities, a more detailed description is given in [8] and [10]. The constitutive equation is solved numerically with the solver "ode23s" provided by MATLAB [11].

3. Benchmarking of existing approaches

To show the capability, uncertainties and limitations of the previously introduced models, a comprehensive comparison and benchmarking has been carried out. At first, the influence of the data used for the determination of the model parameters is investigated. Furthermore,

comparisons of the calculated creep behavior under different temperatures as well as under non constant stress are carried out. In addition, a simplified example of the stress evolution in a restrained beam during the hydration is investigated, to compare the behavior of the modeling approaches under realistic conditions for hardening concrete structures.

3.1 Influence of calibration data

To characterize the influence of the hardening process on the creep behavior accurately, experimental data on creep at different loading ages is required. As creep tests are time consuming and costly, it would be desirable that a model can be calibrated properly with the use of little experimental data. To describe the influence of the data used for calibration on the resulting model behavior, a study with the previously introduced models was carried out.

3.1.1 Calibration of 4MW model

In the first part of the study, the 4MW model is calibrated using different input data sets. The reference creep curves are given by the 3KV model with the parameters taken from [7]. The instantaneous elastic strain is not taken into account in this calibration. Fig. 3 shows the behavior of the 4MW model when only the creep curve(s) for the loading age(s) t_l are used as input for the calibration.

In the case that a creep curve at an early age of 1 day is used for the calibration, the model exhibits a significantly too small creep for higher loading ages than 1 day. A related behavior is observed when a creep curve for a loading age of 3 days is used for the calibration. The creep for loading ages greater than 3 days is too small and in addition the creep strains for loading ages smaller than 3 days get significantly too high. The overestimation of the creep at early ages becomes even more pronounced when the model is calibrated with a creep curve for a loading age of 7 days.

A good correlation between the 4MW model and the reference curves is observed when one creep curve for an early loading age ($t_l = 1$ day) and one for a high loading age ($t_l = 28$ days) are used together as calibration data. This indicates that a sufficient calibration of the 4MW model is possible with only two creep curves, if the loading ages are spread over a wide range to cover the phase where the main change of the creep behavior occurs.

3.1.2 Calibration of 3KV model

In the second part of the study, the 3KV model is calibrated and the reference creep curves are given by the 4MW model with the parameter set from [8]. The results from the calibration with different referent curves are shown in fig. 4.

The 3KV model shows a too large creep deformation at loading ages greater than 2 days when only the creep curve for a loading age of 2 days is used for the calibration. A better description of the creep at higher loading ages is possible when $t_l = 3$ days is used for the calibration, but in parallel it leads to a significant underestimation of the creep strain for a loading age of 2 days. For the case that $t_l = 7$ days is used for the calibration, the 3KV model fits nearly perfectly with the reference curves at higher loadings ages, but also the underestimation of creep strains for early ages becomes more pronounced.

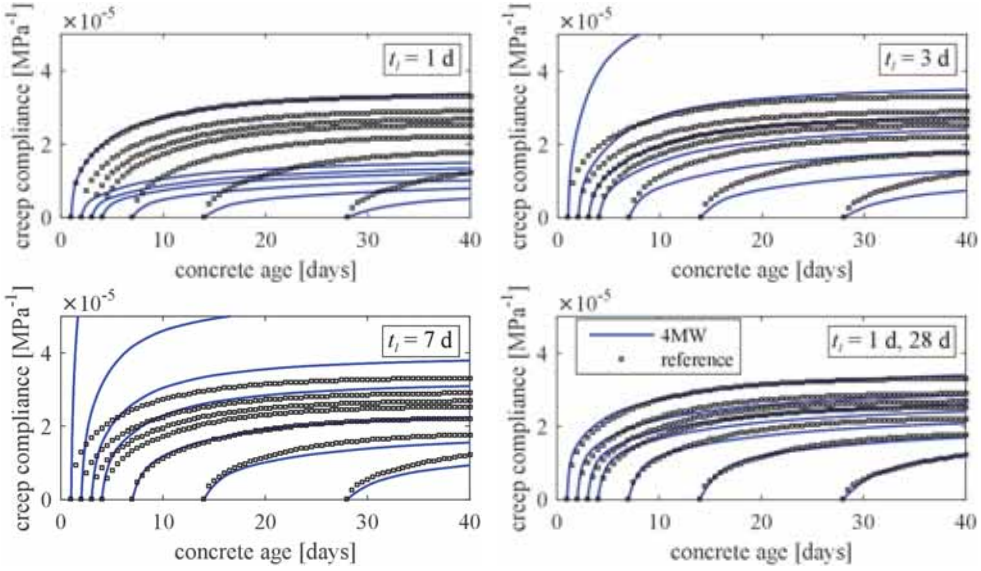

Fig. 3: Behavior of 4MW model when calibrated with different data sets

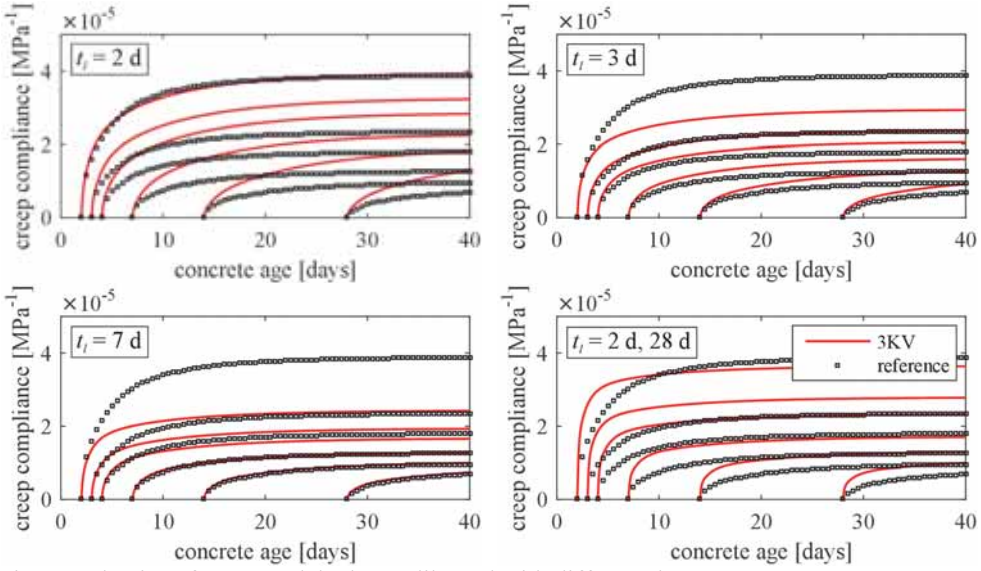

Fig. 4: Behavior of 3KV model when calibrated with different data sets

The use of two creep curves with loading ages of 2 days and 28 days respectively as calibration data does not lead to a satisfying description of the reference curves. The shape of the reference creep curves cannot be fitted well which might be due to the relatively small number of adjustable parameters in the 3KV model. In this model, only the final values of the

spring stiffnesses are adjustable parameters, while the retardation times and the relative evolution of the spring stiffnesses with hydration degree are fixed. One reason for the poor fit might be the fact that the reference creep curves describe the creep behavior of a concrete containing slag cement. The definition of the hydration degree to be proportional to the heat release might not be accurate enough in this case.

3.2 Temperature influence

The temperature influence on creep plays a significant role when thermal stresses in concrete structures shall be investigated. For hardened concrete, higher temperatures lead to an increase of creep [12,13]. Regarding early age concrete, this effect is combined with an accelerated hydration process that leads to a quicker evolution of the mechanical properties and therefore to a decrease of creep [5].

The two rheological models that are compared in this paper take into account the temperature influence with different approaches. In the 3KV model, the effect of temperature on hydration is directly included through the definition of the spring and dashpot parameters based on the hydration degree. In addition, the spring stiffnesses are reduced for temperatures higher than 20°C to take into account the more pronounced creep behavior at higher temperatures.

In the 4MW model, the temperature influence is described through the transformation of the real concrete age t into the equivalent age t_e. With the definition of the spring and dashpot parameters depending on equivalent age, the effect of temperature on the hydration process is taken into account. In addition, with the formulation of the constitutive equation depending on equivalent age, also the effect of temperature on creep is taken into account. For temperatures higher than 20°C the equivalent age is greater than the real concrete age, which leads to a longer time interval for that the equation is evaluated and thus to an increase of creep.

To compare both approaches, the parameters of both models have been adopted such that they show nearly the same creep behavior at 20°C, see fig. 5.

In fig. 5, creep curves for different temperatures are compared, assuming the same equivalent age and hydration degree at loading. The comparison shows that both approaches lead to significantly different creep curves for increased temperatures. The curves for the 3KV model are proportional to each other when regarding the same hydration degree at loading, because the reduction of the spring stiffnesses leads to a linear scale of the strain. For the 4MW model, a very pronounced increase of the creep directly after loading can be observed, while for longer loading durations the rate of creep decreases.

Because there exists only little data in the literature on creep of early age concrete at different temperatures, both modeling approaches are based on theoretical assumptions. To prove their reliability, a comparison with experimental data for different temperatures and long loading durations is necessary.

3.3 Creep under non-constant stress

The description of the stress-strain behavior under non-constant stress is realized in rheological models through an adaption of the internal variables (stresses and strains in the springs and dashpots) at each time when the stress is changed. This procedure does not require the storage of the whole stress-strain history, which is a significant advantage compared to the application of classical compliance functions or creep coefficients.

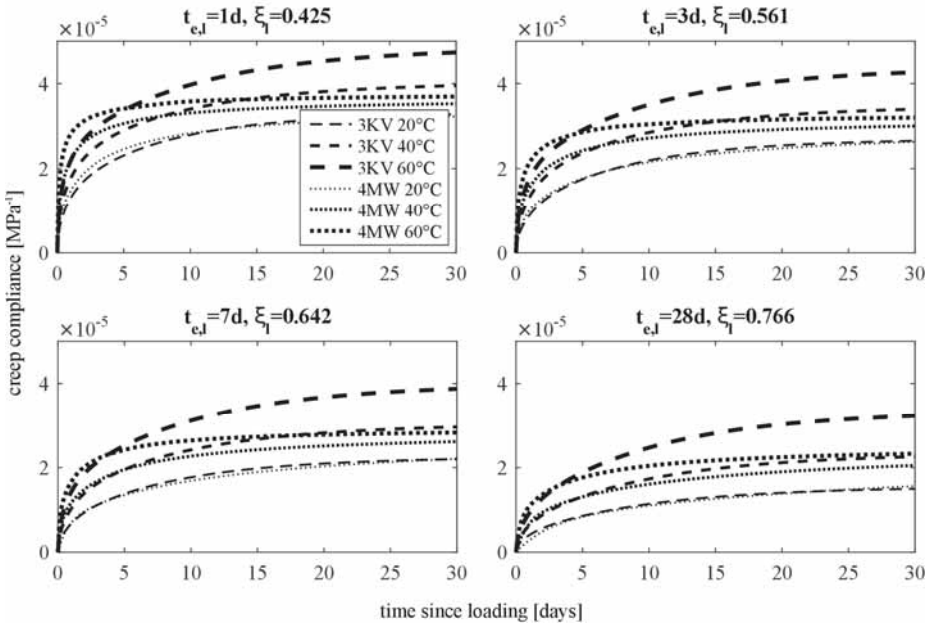

Fig. 5: Creep behavior of 3KV and 4MW model at different temperatures

To check the behavior of both rheological models under non-constant stress, a stress history with several stepped changes is investigated, see fig. 6. The same model parameters as in fig. 5 where used so that both models show nearly the same behavior for constant stress. For the calculation of the elastic strains, the evolution of the Young's modulus given in [7] is assumed. The comparison shows a nearly identical behavior for both models, because the calculation procedure leads to the same results as a superposition of the creep curves.

3.4 Stress evolution under restrained conditions

In hardening concrete structures, the release of the heat of hydration causes a continuous change of the temperatures and stresses. To show the behavior of the two rheological models under these conditions, a simplified example of a restrained concrete structure is investigated. A piecewise linear temperature history is assumed to act on a totally restrained beam, see fig. 7. To calculate the stress development, the total strain ε_{tot} – which is equal to zero due to the total restraint – is divided into three parts corresponding to the different effects of the material behavior:

$$\varepsilon_{tot} = \varepsilon_{th} + \varepsilon_{el} + \varepsilon_{ve} = 0 \quad (8)$$

The thermal strain ε_{th} is calculated using the given temperature history and a constant coefficient of thermal expansion $\alpha_T = 1{,}0 \cdot 10^{-5}\,\mathrm{K}^{-1}$. The rate of the elastic strain $\dot{\varepsilon}_{el}$ is connected to the rate of stress $\dot{\sigma}$ by the relation

$$\dot{\sigma} = E_c \cdot \dot{\varepsilon}_{el}, \quad (9)$$

where E_c is the Young's modulus that develops with time and hydration degree respectively, see fig. 7. The viscoelastic strain ε_{ve} is calculated stepwise assuming constant stress within the time step. The same model parameters as in fig. 5 and 6 were used for the rheological

models, so that both models show nearly the same creep behavior at a constant temperature of 20°C.

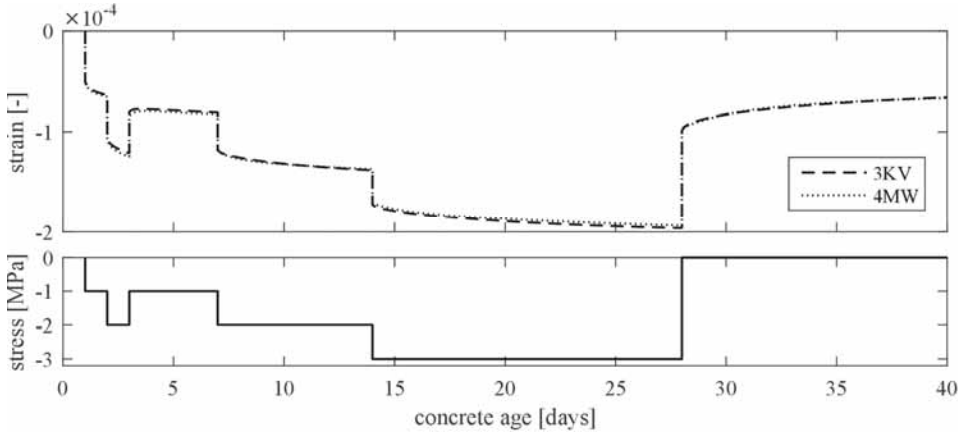

Fig. 6: Behavior of rheological models under non constant stress

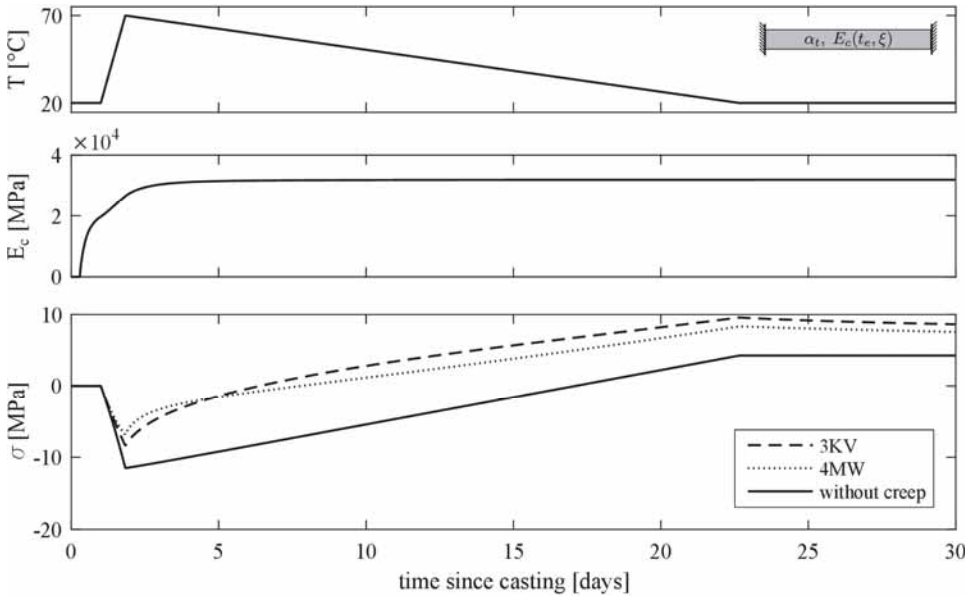

Fig. 7: Development of the temperature, Young's modulus and stress in a totally restrained concrete beam

The resulting stress evolutions in fig. 7 show the significant influence of the viscoelastic material behavior. The negligence of viscoelastic strains leads to significantly higher compressive stresses in the warming phase and lower tensile stresses after the cooling down.

If the viscoelastic behavior is taken into account, a similar behavior can be observed for both rheological models. In both cases, the maximum compressive stress is reached before the temperature maximum and the change from compressive to tensile stresses occurs much earlier than in the case of purely elastic material behavior. The exact values of the stress evolution from both models differ because of the different descriptions of the temperature influence. The 4MW model shows a lower stress level, because the very pronounced creep at elevated temperatures directly after loading becomes more important in this example. The maximum tensile stresses are ca. 13% lower for the 4MW model. Even if the difference is relatively small in this case, especially compared to the results with negligence of viscoelastic material behavior, it may become decisive in several cases, e.g. when the absence of cracks in a structure has to be guaranteed.

4. Conclusions and outlook

Comparisons and benchmarking studies of two different rheological modeling approaches for early age concrete creep have been presented in this paper.

The investigations showed that the data used for the calibration of the model parameters highly influences the reliability of the models. Because of the rapid change of the creep behavior during the hardening process, a model calibration with only one creep curve is not sufficient and can lead to a significant miscalculation of the creep behavior for not calibrated time ranges.

Benchmarking calculations of the creep behavior at different temperatures showed that both models are able to describe the general effects of temperature on hydration and creep as described in the literature. Due to the different approaches for the consideration of the temperature influence, both models produce different results, especially for very early loading ages and long loading durations. Because long term creep tests on early age concrete at elevated temperatures are very rare, additional experiments would be necessary to estimate which approach is more realistic.

The investigations on the model behavior under non-constant stress showed that the procedures to calculate the strain evolution under stepped loading are similar for both models. Thus, both models describe the same stress-strain behavior under stepped loading if their basic creep behavior is the same.

The benchmarking studies were closed with simplified calculations of the stress evolution due to restrained thermal strains in a hardening concrete beam. The calculated stress evolutions show a qualitatively similar behavior for both rheological models, but the exact values differ because of the differences in the consideration of the temperature influence.

Overall, the comparisons and benchmarking studies show that rheological models are very convenient for the use in engineering calculations and numerical simulations. The differential formulation is advantageous compared to the definition of creep by a compliance function or creep coefficient when the stress-strain behavior under non-constant conditions shall be

investigated. To get an accurate description of the real material behavior, the design of a rheological model should be based on comprehensive experimental results that allow a proper description of the main influencing parameters.

Acknowledgement

The authors thank the COST Action TU1404 for the support of the presented research within the framework of a short term scientific mission.

References

[1] Gutsch, A.-W.: Properties of early age concrete - Experiments and modelling. Materials and Structures 35 (2002), 76-79
[2] Anders, I.; Müller, H.: Material law on the time-dependent stress-strain behavior of young concretes. Proceedings of the 9th International Conference on Mechanics and Physics of Creep, Shrinkage, and Durability of Concrete (CONCREEP 9), Cambridge (2013), 467-474
[3] Schutter, G. De; Taerwe, L.: Towards a more fundamental non-linear basic creep model for early age concrete. Magazine of Concrete Research 49 (1997), 195-200
[4] Westman, G.: Concrete creep and thermal stresses. PhD thesis, Lulea University of Technology (1999)
[5] Hauggaard-Nielsen, A. B.: Mathematical modelling and experimental analysis of early age concrete. PhD thesis, Technical University of Denmark (1997)
[6] Schutter, G. De: Degree of hydration based Kelvin model for the basic creep of early age concrete. Materials and Structures 32 (1999), 260-265
[7] Benboudjema, F., Torrenti, J.M.: Early-age behaviour of concrete nuclear containments, Nuclear Engineering and Design 238 (2008) 2495-2506
[8] Hermerschmidt, W., Budelmann, H.: Creep of early age concrete under variable stress, Proceedings of the 10th International Conference on Mechanics and Physics of Creep, Shrinkage, and Durability of Concrete and Concrete Structures (CONCREEP 10), Vienna (2015), 929-937
[9] Carino, N. J.: The maturity method: theory and application. Cement, Concrete and Aggregates 6 (1984), 61–73.
[10] Findley, W. N., Lai, J. S., Onaran, K.: Creep and relaxation of nonlinear viscoelastic materials. Dover Publications (1997), 64-77
[11] Shampine, L. F., Reichelt, M. W.: The MATLAB ode suite. SIAM Journal on Scientific Computing 18 (1997), 1-22
[12] Nasser, K. W., Neville, A. M.: Creep of old concrete at normal and elevated temperatures, ACI Journal 68 (1971), 276-281
[13] Arthanari, S., Yu, C.W.: Creep of concrete under uniaxial and biaxial stresses at elevated temperatures. Magazine of Concrete Research 19 (1967), 149-156.

International RILEM Conference on Materials, Systems and Structures in Civil Engineering
Conference segment on Service Life of Cement-Based Materials and Structures
22-24 August 2016, Technical University of Denmark, Lyngby, Denmark

SIZE EFFECT ON THE DRYING SHRINKAGE

Aveline Darquennes [(1)], Mariana Vasylchenko [(1)], Farid Benboudjema [(1)]

(1) LMT (ENS Cachan, CNRS, Université Paris Saclay), 94235 Cachan, France

Abstract
When restrained, delayed deformations as the thermal, drying and autogenous shrinkages, can cause cracks in concrete structures and therefore limit their serviceability and life time. It is therefore important to correctly predict their kinetics and amplitude. For the case of massive structures, the size of the concrete structural elements and their thermal history seems to affect the evolution of the delayed deformations. Eurocode 2 for example introduces parameters to take into account the size effect in term of kinetics and final amplitude (which is quite questionable). In the present work, the size effect on drying shrinkage is studied on prismatic mortar samples to accelerate the drying process. The specimens are characterized by different average drying radius. The drying begins after a curing duration equal to 28 days to limit the effect of hydration and autogenous shrinkage on the total deformation. To separate the size and thermal history effects, some mortar samples have undergone a thermal curing similar to the thermal evolution inside a massive structure. Based on the experimental results, it appears that size effect is observed on the kinetics of drying shrinkage and that the diffusion laws are respected.

1. Introduction

During service life, different types of shrinkage affect concrete behavior at early age (deformations related to cement hydration) and at long term (deformations related to the environmental interactions). Due to the water consumption by cement, capillary depressions appear inside the cementitious matrix leading to a global contraction of the material (autogenous shrinkage). The hydration reaction being exothermal, a thermal dilation followed by contraction characterizes the behavior at early age (thermal shrinkage). In contact with the ambient air, hydric exchanges occur from concrete to the environment (drying shrinkage) amplifying the capillary depressions and generating a supplementary contraction of the cementitious material.

Several parameters affect the drying shrinkage (amplitude and kinetics), such as the Water/Cement (W/C) ratio, the curing duration, the relative humidity, cement and water content, etc. It is widely recognized [1] [2] [3] that the size of the concrete specimen has a significant effect on the drying and hence the shrinkage process. This effect is usually presented showing the different rates at which shrinkage occurs for various specimen sizes. A size increase slows down the drying kinetics as it is a diffusive process. At the same time, it is also proposed in some codes (European Code model Eurocode 2 part 1.1 [4], for example) that the ultimate shrinkage, at infinite time, is also dependent on specimen size. As the Volume/Surface (V/S) ratio increases, the final shrinkage value is reduced. Notice that for the majority of experiments, the values of the ultimate shrinkage for high V/S ratios are obtained (due to the necessary time for reaching the hydric equilibrium) by fitting curves using hyperbolic relationships [5]. However, this approach can generate errors [1]. The size effect on the ultimate value of drying shrinkage is a controversial issue. Several authors [1] [5] [6] suggest, based on analytical and experimental studies, that the ultimate shrinkage value is independent on the concrete specimen size. According to reference [1], the only factor that can produce a major size effect is the onset of cracking. Moreover, in the new fib 2010 Code Model, ACI 209 Code model and even European Code model Eurocode 2 part 2, no factor has introduced to reproduce a size effect on the ultimate value of shrinkage.

To study the size effect, the V/S ratio varies. Supplementary phenomena appear with the increase of the V/S ratio affecting the shrinkage measurement: the structural effect and the increase in the maximal temperature due to the hydration process. Indeed, the hydric exchanges begin near the drying surface in contact with the surrounding atmosphere and they develop later in the center of the specimen. In this case, the moisture distribution and the drying shrinkage are not uniform in the cross-section of the specimen [7] [8] [9] leading to the development of tensile stresses near the drying surfaces and compressive stresses in the center. When the tensile stresses reach the tensile strength, cracking appears [10]. The temperature increase inside the specimen at early age modifies its hydration kinetics and it could modify the porous network, the diffusive process and the drying kinetics. Notice that for numerous studies in the literature, the effect of drying and hydration are coupled as in the works of [6], [8] and Hansen et al. (1966) and L'Hermitte et al. (1965) taken from [11], for example. Drying begins rapidly after mixing affecting the development of the porous network and the drying process. Materials cured for 28 days contain a greater number of small pores than those cured for only one day, and retain more water at low relative humidity [10].

In the experimental project presented in this paper, 28 days old mortar specimens are tested to limit the necessary time to reach hydric equilibrium (between 1 and 2 years) and to obtain the final shrinkage value. They are characterized by various V/S ratios to analyze the size effect on the drying shrinkage as well as on the mass loss, to characterize the moisture diffusion (liquid or vapor), the drying driving mechanism. In parallel, the effect of a high temperature - similar to the thermal history in a massive structure - at early age are also studied to determine their impact on the drying shrinkage kinetics and amplitude.

2. Materials and experimental campaign

Shrinkage measurements are performed on a mortar with a W/C ratio equal to 0.5. The used materials are a Portland cement CEM I 52.5N and a normalized siliceous sand. The composition is given in Table 1. All specimens are casted at the same day to undergo the same temperature history (23°C ± 2°C) during curing. After 1 day, they are removed from the mould and protected against drying with one cellophane layer and a double aluminum tape layer. After 28 days, the layers are removed -no mass loss was observed- and the samples are placed in desiccators with a constant relative humidity (65% ± 2% R.H.) ensured by means of aqueous potassium carbonate solution. This method allows ensuring the uniformity of the relative humidity conditions around the specimen at long term (> 1 year), a major parameter to reach the hydric stability in the specimen. The desiccators are kept in a room with a temperature maintained at 23°C ± 2°C. All the measurements begin on 28th day old specimens.

Table 1: Mortar composition

	Composition (kg/m^3)
Cement	563
Water	281
Sable	1409

2.1 Size effect

The samples (40x40x160mm) used for the autogenous deformation are protected against drying by a double aluminum tape layer. The drying shrinkage is studied on specimens where the top and bottom are protected by a double aluminum tape layer to ensure only lateral drying. The longitudinal shrinkage is measured at the central axis by means of two inserts placed on each sample extremities (top and bottom) with a displacement comparator. To study size effect, prismatic specimens characterized by different effective thickness were tested. Their dimensions are (20x40x160mm), (30x40x160mm), (40x40x160mm), (50x70x350mm), (70x70x50mm) and their effective thickness h_0 is equal to 13, 17, 20, 29 and 35 mm respectively. This last parameter is defined as the ratio of the cross sectional area to the semi-perimeter of the member [1] and it is used to name each specimen (P13, P17, P20, P29 and P35) respectively. Moreover, prismatic samples (80x140x200mm) with all their surfaces sealed with a double aluminum tape layer, except the two parallel drying surfaces (80x140mm), are tested. The gauge points with stuck metallic balls are located on the top surfaces (140x200mm) at 10 and 70mm from each drying surface. The effective thickness of the specimens (named P160) is equal to 160mm. A reducing factor equal to 1.25 is added to take into account the unilateral drying [12].

For each effective thickness, three samples are tested and the average results are presented hereafter. The average standard deformation deviation is equal to 20μm/m. In parallel the mass loss is measured for all specimens and its average standard deviation is equal to 0.03%. Notice that the autogenous shrinkage is very low (equal to about 100μm/m at 250 days).

Thus, it is disregarded and only the total deformations are presented in the following results. The thermal deformation due to the temperature variation in the room is corrected.

Nevertheless, the shrinkage evolution of the larger specimens can be affected by other phenomena as the temperature increase in the specimens related to the hydration process. To take into account this parameter further experiments, described hereafter, are performed.

2.2 Thermal effect

To reproduce the temperature increase in massive structures and its effect on the porous network and the drying kinetics, two cylindrical specimens with a diameter equal to 110mm and a height equal to 220mm are placed in polystyrene cylinders directly after casting during seven days to obtain semi-adiabatic conditions. The temperature (measured with a thermocouple placed in the specimen center) reaches a value equal to 59°C at 11 hours. It reaches the ambient temperature after four days. After a week, the specimens are demolded and protected against drying with one cellophane layer and a double aluminum tape layer and stored at 23°C± 2°C. The lateral drying begins at 28 days. The stuck metallic balls are located on three straight lines. In parallel, two cylindrical specimens (named C51) are stored at 23°C± 2°C and protected against drying after 1 day. Their maximal temperature is 31.7°C at 9.4 hours. The average results are presented hereafter and the average deformation and mass loss standard deviations are equal to 10μm/m and 0.01% respectively. The effective thickness of the specimens is equal to 51mm. As the shape affects the water loss rate [5], a reducing factor equal to 1.087 is considered in the computation of the effective thickness [12].

3. Results and discussion

Figure 1 shows the evolution of the average total deformation at long term for the specimens characterized by seven different effective thicknesses. After 28 days of drying, the shrinkage value is equal to 707, 675, 506, 261, 210, 193 and 116μm/m for P13, P17, P20, P29, P35, C51 and P160 respectively. The deformation kinetics during the first months decreases with the increase in the effective thickness.

Results also show that the initial drying rate is extremely fast for the lower V/S ratio. The shrinkage for P13, P17 and P20 after 28 days of drying represents 90, 85 and 71% of its final value (at 200 days) respectively. After 90 days, the deformation reaches its maximal value for the smaller effective thicknesses (13, 17 and 20mm). The deformation evolution of these specimens is also close until about 14 days. After, it decreases for P20 and its final value is slightly inferior. However, this difference is inferior to the one (150μm/m) obtained by [14] for a mortar characterized by a W/C and a sand/cement ratio equal to 0.5 and 2 respectively, and stored at 48% of relative humidity. Thus, the final drying shrinkage does not differ much between the P13, P17 and P20 specimens.

The deformation evolution for the specimens characterized by a superior value of effective thickness is characterized by a double kinetics. This change appears at about 10 days for P160 days, 20 days for C51 and 60 days for P29 and P35. After 200 days of drying, the process is not finished for these specimens. The value of total deformation at 200 days differs for all the

effective thicknesses, except for P13 and P17. At this moment, the total deformation is three times lower for P160 in comparison with P13. This confirms that the amplitude during drying and the rate of drying shrinkage decrease with increasing specimen size before the final value of shrinkage is reached. All these results confirm a size dependence for the drying shrinkage kinetics.

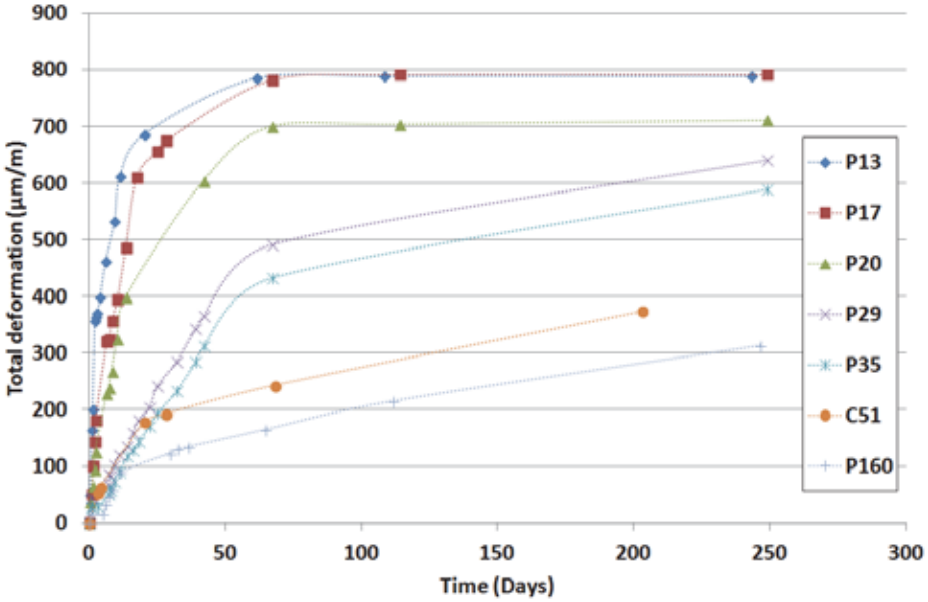

Figure 1: Total deformation for 28 days old mortar specimens as function of time

The total deformations are expressed as function of the ratio between the square roots of time and effective thickness h_0 (Figure 2). The difference between the experimental curves decreases confirming that the diffusion laws are respected. Moreover, its impact on the final value of drying shrinkage is less important. Nevertheless, more results (beyond 200 days) are necessary to confirm this last conclusion.

The mass loss is also measured for all the specimens. Figure 3 shows the evolution of the average mass loss as function of the drying time. After 28 days of drying, the mass loss value is equal to 1.8, 1.9, 1.8, 0.7, 0.6, 0.6 and 0.3% for P13, P17, P20, P29, P35, C51 and P160 respectively. The mass loss kinetics during the first months slows down with the increase in the effective thickness. A double kinetics also characterizes the mass loss evolution of the specimens presenting an effective thickness superior/equal to 29 mm. These results are concomitant to those of the total deformations. They confirm that the specimen size affects significantly the drying rate. A slight difference of behaviour is observed for P13. Its kinetics

slows down beyond 40 days and its amplitude is less important at 200 days in comparison with P17 and P20.

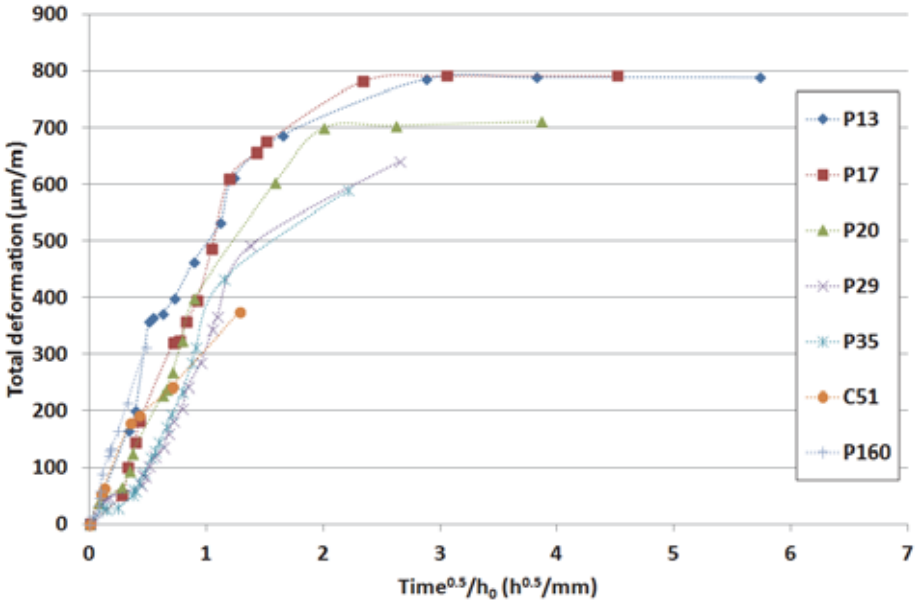

Figure 2: Total deformation for 28 days old mortar specimens as function of the ratio between the square roots of time and effective thickness

The difference between the curves tends to disappear when the mass loss is expressed as function of the ratio between square roots of time and h_0 (Figure 4) confirming that the main mechanism during drying is diffusivity. Further measurements are necessary to conclude on the influence of size effect on the final mass loss amplitude. Nevertheless, the difference of the P13 behavior appears also clearly on Figure 4. The reason for this is probably carbonation, but this hypothesis will be checked at the end of the experimental campaign (after 2 years).

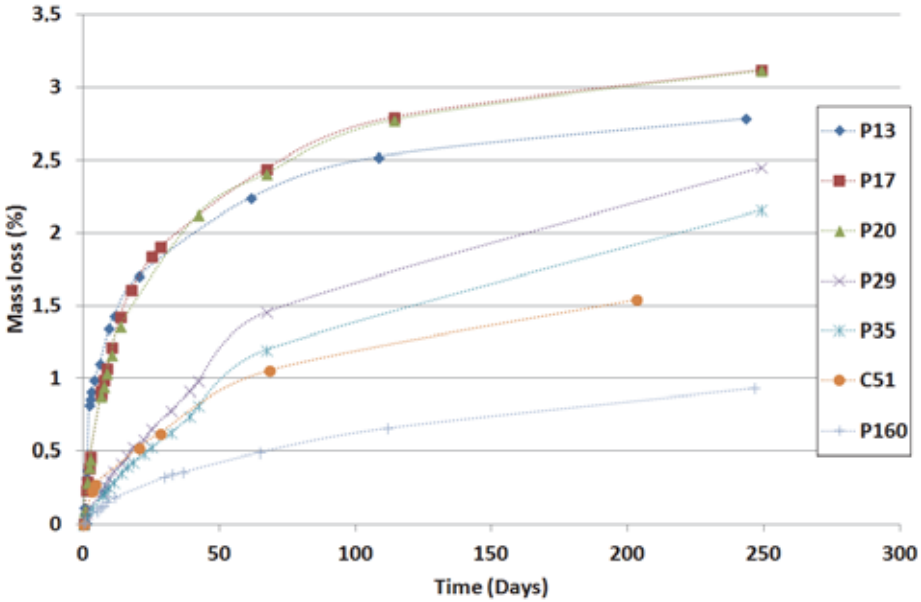

Figure 3: Mass loss for 28 days old mortar specimens as function of time

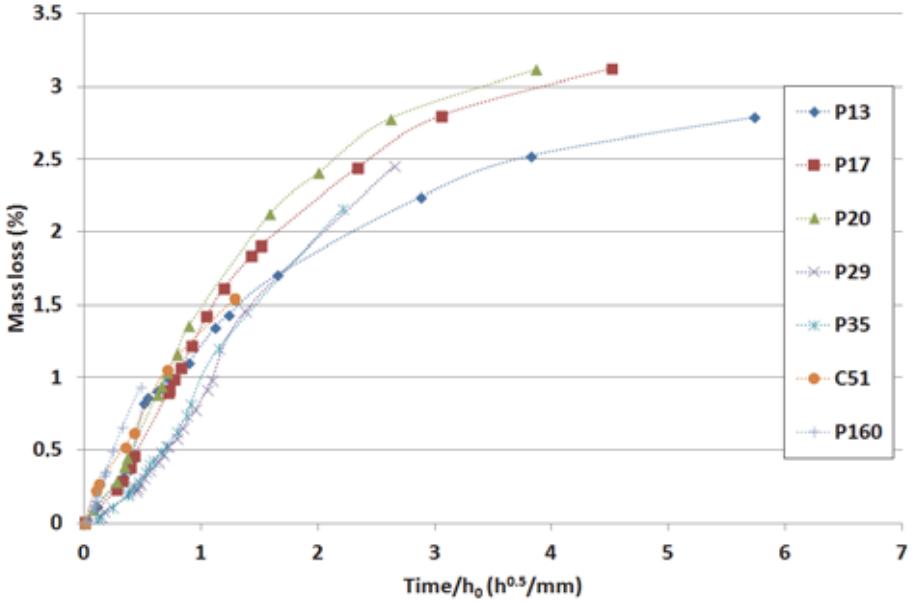

Figure 4: Mass loss for 28 days old mortar specimens as function of the ratio between the square roots of time and effective thickness

The second studied parameter is the effect of the temperature history at early age on drying and on drying shrinkage. The average results are shown in Figure 5. The mass loss and the shrinkage evolutions are similar for the two curing types (thermal and autogenous). The influence of the porous network modifications due to the temperature increase at early age on the water diffusive process is negligible. Again, further experimental tests are however necessary to characterise the porosity and the desorption isotherm to confirm these first results.

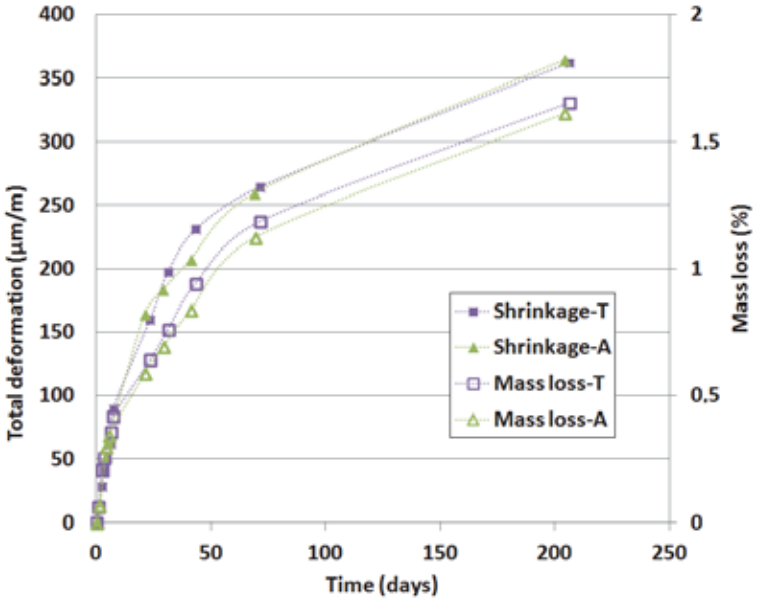

Figure 5: Evolution of shrinkage and mass loss as function of time for two types of curing : thermal (T) and autogenous (A)

4. Conclusions

The results presented in this study clearly show that the evolution of drying shrinkage is a diffusive process and thus its rate is size dependent. Characterizing the drying shrinkage kinetics on small size laboratory samples seems sufficient to predict this parameter for large concrete structural elements.

Today, only the specimens characterized by the lower effective thickness have reached their final shrinkage values, which are all quite similar. Some doubts however exist, due to the additional effects of cracking and carbonation. These two parameters will be quantified for all the specimens when their final shrinkage values will be reached. To conclude on the influence of size effect on the final shrinkage amplitude, it is necessary to wait for the total drying of the specimens characterized by a high V/S ratio.

Drying is not homogenous inside the specimens leading to deformation gradients and stresses. It is necessary to take into account this structural effect to correctly predict drying and drying shrinkage (effect of cracks). Moreover, drying is not affected by the previous thermal history (quite similar as is the case for massive structures). To confirm these first observations, desorption isotherms will be measured for materials with/without thermal curing.

The next step of this study consists in determining the ability of existing numerical models developed in our laboratory [14] to reproduce size effect on drying and on drying shrinkage and to predict accurately drying shrinkage for various concrete element sizes.

References

[1] Campbell-allen, D. And Rogers, D.F., Srinkage of concrete as affected by size, Materials and Structures 45 (1973), 193-202.
[2] Bryant, L.H. and Vadhanavikkit, C., Creep, shrinkage size, and age at loading effects, ACI materials Journal, March-April (1987), 117-123.
[3] Delaplace, A. and Noyalet, H., A simple two-stage model for simulating drying shrinkage vs. mass-loss evolution of concrete, VIII International Conference on Fracture Mechanics of Concrete and Concrete Structures (FraMCoS-8), Tolelo, Spain, (2013).
[4] Eurocode 2, Design of concrete structures – Part 1-1 : General rules and rules for buildings, EN 1992-1-1.
[5] Almudaiheem, J.A. and Hansen, W., Effect of specimen size and shape on drying shrinkage of concrete, ACI materials Journal, March-April (1987), 130-135.
[6] Samouh, H., Soive, A., Rozière, E. and Loukili, A., Experimental and numerical study of size effect on long-term drying behavior of concrete: influence of drying depth, Materials and Structures (2016).
[7] Ayano, T. And Wittmann, F.H., Drying, moisture distribution, and shrinkage of cement-based materials, Materials and Structures 35 (2002), 134-140.
[8] Al-Saleh, S.A. and Al-Zaid, R.Z., Effects of drying conditions, admixtures and specimen size on shrinkage strains, Cement and concrete research 36 (2006), 1985-1991.
[9] Granger, L., Torrenti, J.M. and Acker, P., Thoughts about drying shrinkage: Scale effects and modeling, Materials and Structures 30 (1997), 96-105.
[10] Bisschop, J., Drying shrinkage cracking at early ages, in Early age Cracking in cementitious systems, RILEM TC 181-EAS: Final Report (2002), 47-55.
[11] Torrenti, J.M., Benboudjema, F., Chauvel, D. and Barré, F., Retrait de dessiccation des bétons : résultats du PN CEOS.fr, 31èmes Rencontres de l'AUGC, Cachan, France (2013). (In French)
[12] Bažant, Z. P., Creep and shrinkage prediction model for analysis and design of concrete structures – model B3, Materials and Structures 28 (1995), 357-365.
[13] Bissonnette, B., Pierre, P. and Pigeon, M., Influence of key parameters on drying shrinkage of cementitious materials, Cement and Concrete research 29 (1999), 1655-1662.
[14] Benboudjema, F., Torrenti, J.M., Modelling desiccation shrinkage of large structures, NUCPERF Workshop, Cadarache, France (2012).

International RILEM Conference on Materials, Systems and Structures in Civil Engineering
Conference segment on Service Life of Cement-Based Materials and Structures
22-24 August 2016, Technical University of Denmark, Lyngby, Denmark

AGING TESTS FOR PERFORMANCE OF PHOTOCATALYTIC CEMENT BASED MATERIALS

František Peterka[(1)], Michaela Jakubičková[(1)], Tereza Sázavská[(1)], Elia Boonen [(2)]

(1) Technical University of Liberec, Liberec, Czech Republic
(2) Belgian Road Research Centre (BRRC), Sterrebeek, Belgium.

Abstract
Photocatalytic cementitious building materials, mainly with incorporation of TiO_2, have been shown to be a promising remediation technique for air pollutants such as NO_x and VOC's, frequently encountered in trafficked areas and the urban environment. In addition, this light-induced phenomenon can be applied for self-cleaning and disinfecting surfaces (building façades, decorative mortars, interior tiles, etc.). However, there are still doubts and questions about the durability of the photocatalytic activities (for instance the air cleaning characteristic) in time. To answer the logic question about the photocatalytic products service life, standardized testing methods have to be set up to give more reliable answers to the potential end users. First attempts have been made by Czech Republic and Belgian research groups within the European normalization efforts of CEN/TC386 "Photocatalysis". This paper presents first results of these investigations made independently in both countries, as a first step towards the evaluation of the life time of these photo-active air purifying products.

1. Introduction

Photocatalytic building materials with incorporation of titanium dioxide have been shown over the past years to be a promising technique to reduce a number of air contaminants such as nitrogen oxides (NO_x) and volatile organic compounds (VOC's), especially at sites with a high level of pollution such as highly trafficked canyon streets, road tunnels, urban environment, etc. [1-3]. In addition, the combination of TiO_2 with cement-based products offers some synergetic advantages, as the reaction products can be adsorbed at the surface and subsequently be washed away by the rain [4]. However, more recent applications have demonstrated that the durability of the air cleaning characteristic with time remains challenging, especially for the application in pavement and building materials [5-6]. Hence, there are still questions and doubts about the "life time" of these photoactive air-purifying products.

First attempts are being made by research teams in Czech Republic and Belgium, where the major objective is thus to develop standardized test procedures to be able to determine the durability of the photocatalytic efficiency in time by combining existing durability (accelerated ageing) tests with methods to determine the photocatalytic activity. In addition, the focus is initially on *cement-based* air purifying building materials in view of the large market potential. This is also connected to the normalization work being carried out for the moment within CEN Technical Committee 386 "Photocatalysis" [7], for which Czech Republic acts as the project leader.

In present paper, first results of the research conducted in Czech Republic as well as in Belgium, are presented which included a state-of-the-art on accelerated ageing testing for cement-based materials and validation of the selected ageing procedures combined with and adapted to normalized photocatalytic activity testing. In addition, results are discussed in view of recommendations for future work on the evaluation of the durability of photocatalytic cement-based building materials, where input of the COST action TU1404 could also be helpful.

2. Photocatalytic products service life time?

To answer the logic question about the photocatalytic products life time, standardized test methods need to be developed to give a clear explanation to the potential end user. Czech Republic already proposed the photocatalytic life time evaluation as a new CEN standard working item within CEN/TC 386, supported by 7 other European countries and with collaboration of Italy and Belgium. The basic idea is to specify the accelerated aging conditions for a variety of photocatalytic materials like cement-based materials, paints, thin films, etc. for different applications (e.g. horizontally on a road surface or vertically on a building façade), based on already existing durability tests in the field of application and with a possibility to define different photocatalytic durability classes.

Research teams at the Institute for Nanomaterials, Advanced Technologies and Innovations of Technical University Liberec (TUL) as well as from the Belgian Road Research Centre are working on the concept of the evaluation of the reduction in photocatalytic performance caused by different degradation processes encountered in practice such as abrasion or weathering of the photocatalytic surface (Figure 1).

Weathering for instance, is the adverse response of a material or product to the environmental conditions it is exposed to, often causing unwanted and premature product failures, where the main contributing factors are sunlight, temperature, moisture, and possible contamination by intermediate products formed during the photocatalytic process. In the case of photocatalytic materials, sunlight is needed to initiate the degradation process and drives it forward, but also leads to transformation of reaction products that can poisoned the TiO_2 catalyst embedded in the building material. In addition, temperature and humidity (RH) together with UV ageing can also change the catalyst texture and/or the matrix material, and cause adverse effects as well [1].

The objective of artificial weathering or the ageing test in general, is thus to reproduce the degradation processes and resulting damage that occurs naturally, in a laboratory under accelerated and reproducible conditions. Furthermore, the photocatalytic performance should be evaluated according to standard methods already accepted or to draft methods which are under development on international (ISO) and/or European (CEN) level, see e.g. [7].

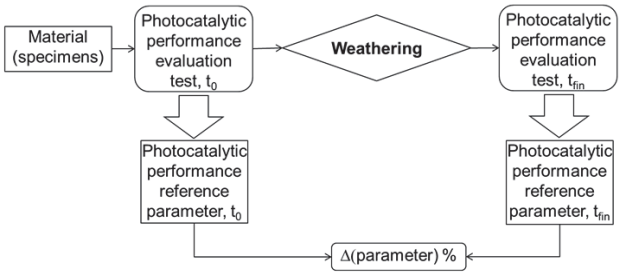

Figure 1: Concept of evaluation of photocatalytic performance reduction due to weathering.

The Institute of Nanomaterials at TUL is also designing novel composite photoactive coatings to be applied for self-cleaning activity of building façades or industrial cementitious materials while the Belgian Road Research Centre (BRRC) is working on photocatalytic materials applied in the bulk or at the surface of cement based road construction materials where abrasion might also play a significant role. Below examples of the research activities at Institute for Nanomaterials of TUL as well as at the BRRC are presented with the aim of proposing standard ageing tests for photocatalytic cement based materials.

3. Photoactive materials and testing methods, example of research at the Institute of Nanomaterials (TUL, Czech Republic)

The research team of TUL is collaborating with industrial partners on the application of patented nanocomposite materials with a photoactive function. First tests towards durability have been performed on the transparent coating called “Balclean” which is claimed to have self-cleaning and anti-microbial properties to keep building facades clean. The air purification effect of the coated surface area is in this case considered to be a beneficial side effect.

3.1 BALclean nanocomposite material

The photocatalytic composite paint consists of a photocatalyst and a binder material. The photocatalytic nanoparticles are formed by agglomerated TiO_2 in water whereas the SiO_2 binder nanoparticles are used in the form of a stabilized aqueous suspension. The combined nanocomposite was prepared in the form of an aqueous dispersion containing 1-3 % of dry matter consisting of 40 wt. % of TiO_2 and 60 wt. % of SiO_2.

3.2 Photocatalytic activity testing

First of all, the photocatalytic self-cleaning activity of the coatings was determined on the one hand according to the ISO 10678:2010 standard method based on methylene blue

decomposition [8]. Methylene blue (MB) is degraded upon contact with the photoactive surface under UV illumination and using an aqueous solution of MB.
On the other hand, the composite was also applied on the outer concrete facade of a building (Fig. 2). The effect of the photocatalytic coating on the wall was followed by visual change surface analysis. For the analysis the Flip-Pal plus mobile scanner and the DoSa software application were used to describe the colour intensity changes of the surface. This analysis was performed more than one year after the coating application.

Figure 2 Photos of the entrance of Institute for Nanomaterials at TUL consisting of concrete panels which were protected by the BALCLEAN coating. To observe the self-cleaning function, only each second stream was coated, as illustrated in the picture on the right.

Furthermore the air purification effect was measured according to the method described in ISO 22197-1:2007 [9]. A shortened version of the test was carried out using the test set-up shown in Figure 3. This consists of a metal container, in which the sample is placed, with a UV-transparent glass at the top and a free height of 5 mm between the surface of the sample and the glass. Next, air with an NO-concentration of 1 ppm is blown over the surface with a flow rate of 3 l/min. The relative humidity of the ingoing air is regulated at 50 % RH and the UV light intensity is equal to 10 W/m^2 in the range between 300 and 460 nm, with a. maximum at 365 nm. The test sample has a surface of 50 x 100 mm.

3.3 Weathering test applied to coated cementitious samples

As an example, a combined weathering cycle used for testing of coating systems for exterior use according to the standard method CSN – EN 927-6 was applied:

- 24 h condensation of water at T = 45°C
- 2,5 h UV-A irradiation at 1 W/m^2 andT = 60°C, followed by 0.5 h water spraying at 6-7 l/min. (

The second sub-cycle is repeated 48 times (48x3 = 144h) before applying the first cycle again (condensation) and the total test duration was 1000 hours.

The Balclean coating was applied on mortar (?) samples of 5x5 cm with an upper layer of acrylate, silicate or silicone paint. In addition, the Balclean coating was prepared with different amounts of photoactive nanomaterial (3% and 5%). Measurements of the photocatalytic activity were made on these samples before and after applying the artificial

weathering test described above. The corresponding changes in photocatalytic material performance (NO_x abatement) of the samples are shown in Table 1.

Figure 3 Test set-up according to ISO 221971-1:2007 [9] to determine the air purifying properties (NO_x abatement) of the products.

Table1 Reduction in photocatalytic performance of Balclean samples after 1000h of artificial weathering according to CSN EN 927-6.

Sample	**Δ in efficiency after weathering (%)**
Acrylate, 3% Photocatalyst	75
Acrylate, 5% Photocatalyst	87
silicate 3%, Photocatalyst	64
silicate 5%, Photocatalyst	77
silicone 3%, Photocatalyst	60
silicone 5%, Photocatalyst	62

3.4 Discussion and conclusion

The reduction in photocatalytic air purifying activity of coated and painted cement based materials is significant (Table 1), but regarding self-cleaning performance the material can still keep its expected function after more than one year of outdoor exposure (Figure 2). Future accelerated weathering (with changing conditions and test time for instance) in combination with the results for the naturally aged material needs to be performed to be able to develop a CEN standard for durability testing of these photocatalytic materials. In addition, the correlation between the conditions of the artificial weathering test and the expected life time (5, 10 years or even less?) of the photocatalytic activity needs to be further investigated accordingly.

4. Photoactive materials and testing methods, example of measurements in Belgium (BRRC)

4.1. Methods

In a first phase, a state-of-the-art report on accelerated ageing tests applicable to cement-based building materials was set-up. Here, a division has been made in three main areas of ageing

tests: abrasion, freeze-thaw cycles resistance, and artificial weathering with UV exposure and humidity.

Next, a first selection of applicable ageing procedures was made based on practical feasibility and compatibility with the photocatalytic evaluation test(s):

1) Abrasion tests
- PEI-test following NBN EN ISO 10545-7:1999 [10] for coatings (surface application)
- Böhme abrasion test according to NBN EN 1338:2003 [11], Annex H (concrete paving blocks) for TiO_2 applied in the bulk..

2) Freeze/thaw resistance
- *with* de-icing salt: "Slab test" following EN 1338, Annex D
- *without* de-icing salt: Slab without addition of NaCl.

3) Hygro-thermal cycles with UV-lighting
NBN EN ISO 4892-3:2006 [12] in combination with NBN EN 1871:2000 (road marking paints), paragraph 4.1.4: UV-A lamp (340 nm).

In addition, a range of commercially available test materials was also selected based on representativeness in the market, difference in type of product, in initial photocatalytic activity, and in application (horizontal-vertical): photocatalytic concrete pavement blocks (2 types), road concrete with active cement (2 types of surface finish), one cementitious skim coat and different photoactive coatings and paints. For the evaluation of all these samples before and after ageing, the air purifying activity was also determined according to ISO 22197:2007 (NO_x abatement, as described above).

Finally, part of the samples was also placed outside on the roof of the BRRC building in Sterrebeek (Fig. 4) to be able to study the natural ageing of the materials.

Figure 4 Natural ageing on the roof top of the BRRC building in Sterrebeek (Belgium).

4.2. Results

Firstly, some preliminary testing was performed to determine the applicability and compatibility of the different test methods. Concerning the **freeze-thaw testing** for instance, different products were applied on some ordinary concrete tiles and tested for their initial air purifying action (reduction of NO_x). Afterwards, the samples were subjected to the Slab test

(with de-icing salt solution ponding on the surface) during 7 freezing and thawing cycles, and then re-tested for their activity, see Fig. 5.

The results show that the substrate itself is not suitable (insufficient freeze-thaw resistance), but that the procedure (combination of NO_x-test with freeze-thaw Slab test) is well applicable. Hence, new testing was started with "better" reference concrete plates manufactured according to EN 1766 [14] which show intrinsically better resistance against freeze-thaw cycles with de-icing salts.

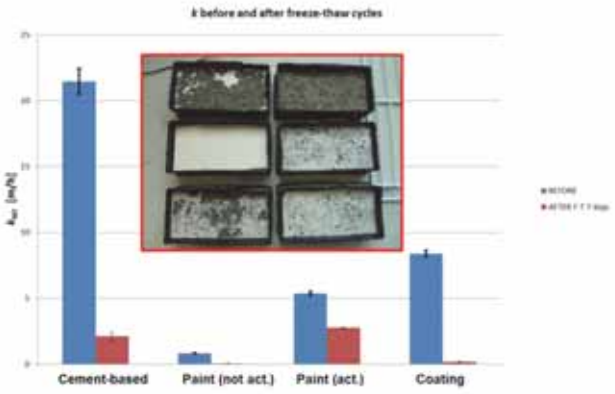

Figure 5 Photocatalytic activity in terms of k-value for NO reduction (the higher the value, the higher the activity) before and after freeze-thaw cycles with de-icing salt.

For the **abrasion experiments**, first tests were performed (Fig 6), on the one hand to determine if the PEI test intended for ceramic tiles would be a suitable simulation of the wear of coatings applied at the surface of the material; on the other hand, the Böhme abrasion test was performed for samples with TiO_2 applied in the bulk of the product (paving block and road concrete).

In the Böhme abrasion test on the other hand, the test specimens with surface area of ca. 7x7 cm² are placed on the test track of a disc abrader on which standard abrasive is strewn, the disc being rotated and the specimens subjected to an abrasive load of (294 ± 3) N for 16 cycles of each 22 rotations (standardized). The uniform abrasive wear of the surface is determined as the loss in specimen volume. Three different types of specimen were tested: a concrete paving block with TiO_2 in the mass, road concrete with exposed aggregates surface and with broomed surface finish. For this last one, the wear was limited to only 2 cycles of 12 revolutions each, in order not to abrade the top layer entirely, see Fig. 6. From Fig. 7 it is clear that for products with application of TiO_2 in the bulk, the photocatalytic activity remains intact or even increases. This is especially true for the road concrete with broomed surface for which further microscopical analysis will be performed to investigate the surface area.

Finally, concerning **artificial weathering,** first tests have started with several samples of coatings and/or paints applied on the reference concrete plates of EN 1766, which are being subjected to 40 cycles (480h in total) of:

- 8h UV-A irradiation at 60±2 °C
- 4h condensation at 50±2 °C, and in accordance with EN 1871:2000, §4.1.4.

This test procedure is thus similar to the weathering described in section 3.3 according to the Czech testing.

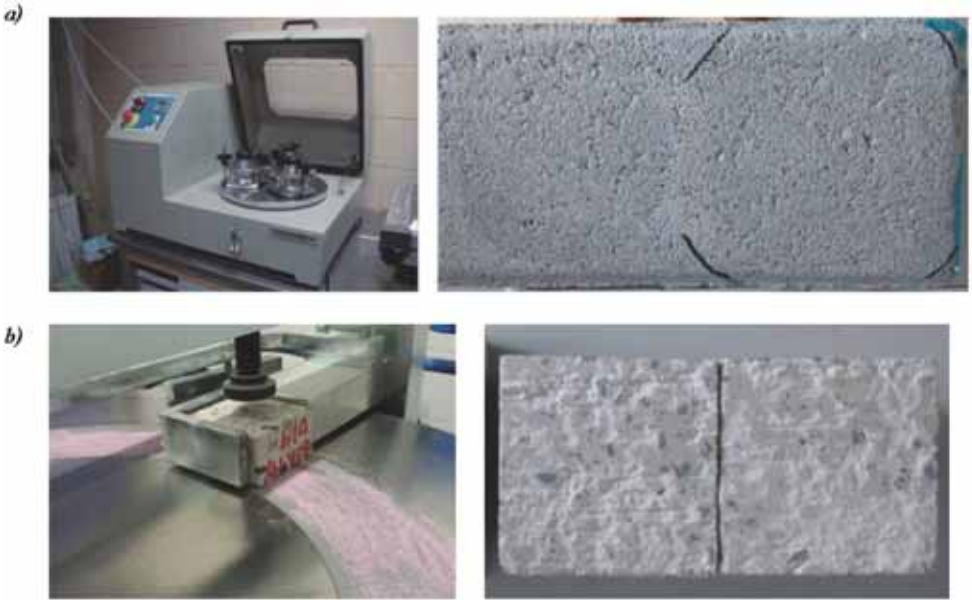

Figure 6 Abrasion tests executed in Belgium: a) superficial wear following PEI-test for coatings, b) Böhme abrasion test for application in the bulk (broomed road concrete).

For the PEI-test an abrasion of 750 revolutions applied on two circular zones with a diameter of ca. 9 cm on concrete blocks of 20x10 cm² with a photo-active coating, yielded a visual wear of the surface. This also gave rise to a strong decrease in the photocatalytic activity (Fig. 7), probably because part of the coating is lost from the surface.

4.5 Conclusions and perspectives

Based on the initial testing as explained above (Fig. 5), freeze-thaw resistance of several new samples is being tested following EN 1338, Annex D. Here, the so-called Slab test will be performed for 7 cycles with de-icing salt or for 42 cycles without de-icing salt.

Concerning simulation of abrasion, the PEI wearing test for ceramic tiles can be applied for the superficial abrasion of TiO_2 coatings applied at the surface, where it is proposed to execute the abrasive cycle until a visual wearing has appeared (for instance 750 revolutions). For products with TiO_2 applied in the bulk of the material on the other hand, the Böhme abrasion test could be performed. Here, it is proposed to execute only 1 cycle of 22 rotations

in order to not completely remove the top layer and obtain a better simulation of the abrasive wear by traffic.

Future accelerated testing with these selected procedures, in combination with the follow-up of the samples exposed to natural ageing (Fig. 4), will help to determine the repeatability of the durability testing in order to possibly set up different photocatalytic ageing classes. Finally in the end, hopefully these results and findings will also enable evaluation of the life time of photocatalytic building materials based on scientifically sound test methods and procedures established in future standards.

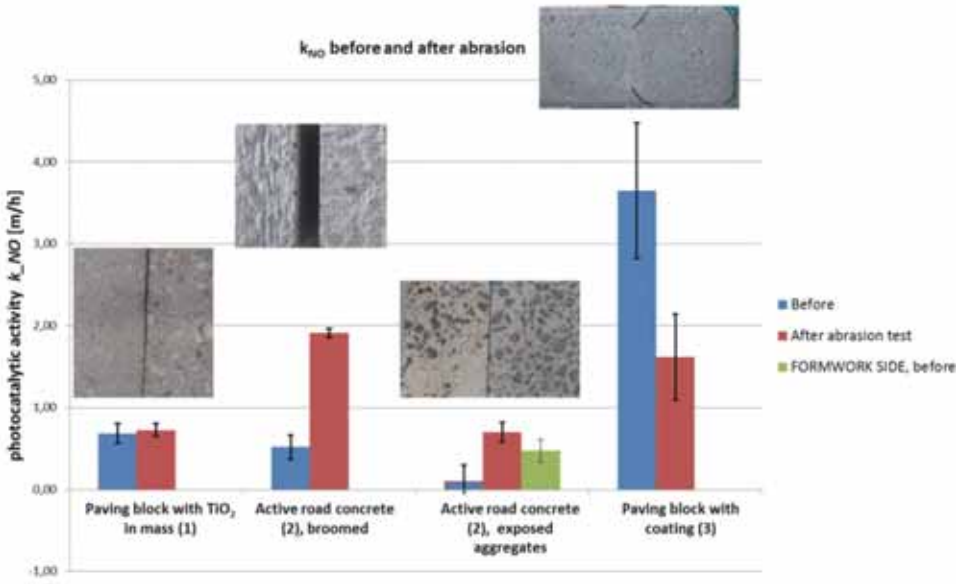

Figure 7 Photocatalytic activities before and after abrasion tests, expressed as first order k-value for NO reduction.

5. Final Conclusions

Expertise from and consultation with experts for durability issues of cementitious materials as from COST TU 1404 is very important to be able to design broadly accepted CEN standards concerning accelerated ageing of photocatalytic cement based building materials. In this respect, the first promising results of currently conducted research in Czech Republic and Belgium were presented here as a basis to start the discussion.

Acknowledgements

These topical activities of the Institute for Nanomaterials, Advanced Technologies and Innovations of Technical University Liberec (TUL) are supported by the Czech Ministry of Education, Youth and Sports in the framework of COST program and by Czech national TAČR organization.

The Belgian authors on the other hand gratefully acknowledge the FPS Economy (Federal Public Service Belgium) and NBN (Belgian Bureau for Standardisation) for the financial support of the project.

References

[1] Fujishima, A., Zhang, X. & Tryk, D.A., TiO_2 photocatalysis and related surface phenomena, Surf Sci Rep 63 (2008), 515–582.
[2] Peterka, F ,Cleaning by photoactive nanosurfaces. *Public Service Review: European Science & Technology*, Issue 11, pp. 68-69 (2011)
[3] Chen, J., Poon, C., Photocatalytic construction and building materials: from fundamentals to applications, Build Environ 44 (2009), 1899–1906.
[4] Boonen, E. And Beeldens, A., Recent Photocatalytic Applications for Air Purification in Belgium, Coatings 4 (2014), 553–573.
[5] Gallus, M., Akylas, V., Barmpas, F., Beeldens, A., Boonen, E., Boréave, A., Bottalico,L.; Cazaunau, M., Chen, H., Daële, V.; et al, Build Environ 84 (2015), 125-133.
[6] M.M. Ballari, H.J.H. Brouwers, Full scale demonstration of air purifying pavement, J Hazard Mat 254–255 (2013), 406–414.
[7] CEN Technical Committee 386 "Photocatalysis" Business Plan—(internet) Draft BUSINESS PLAN CEN/TC386 PHOTOCATALYSIS. Available online: https://standards.cen.eu/BP/653744.pdf (accessed on 16th of June 2016).
[8] ISO 10678:2010, Fine ceramics (advanced ceramics, advanced technical ceramics) - Determination of photocatalytic activity of surfaces in an aqueous medium by degradation of methylene blue, International Standards Organisation, Switzerland (2010).
[9] ISO 22197-1:2007, Fine ceramics (advanced ceramics, advanced technical ceramics) – Test method for air-purification performance of semi conducting photocatalytic materials - Part 1: Removal of nitric oxide, Int. Standards Organisation, Switzerland (2007).
[10] NBN EN ISO 10545-7:1999, Ceramic tiles - Part 7: Determination of resistance to surface abrasion for glazed tiles, ISO 10545-7:1996 +AC:1999, Switzerland (1999).
[11] NBN EN 1338:2003, Concrete paving blocks - Requirements and test methods, ANNEX D: Determination of freeze/thaw resistance with de-icing salt + ANNEX H: Measuring of abrasion according to the Böhme test, European standard (2003).
[12] NBN EN ISO 4892-3:2006, Plastics - Methods of exposure to laboratory light sources – Part 3: Fluorescent UV lamps, ISO 4892-3:2006, Switzerland (2006).
[13] NBN EN 1871:2000, Road marking materials – Physical properties, European standard (2000).
[14] NBN EN 1766:2000, Products and systems for the protection and repair of concrete structures - Test methods – Reference concretes for testing, European standard (2000).

International RILEM Conference on Materials, Systems and Structures in Civil Engineering
Conference segment on Service Life of Cement-Based Materials and Structures
22-24 August 2016, Technical University of Denmark, Lyngby, Denmark

QUANTIFICATION THE FILLING OF MICROCRACKS DUE TO AUTOGENOUS SELF-HEALING IN CEMENT PASTE

Jiayi Chen [(1)], Xian Liu [(2)], Guang Ye [(1)]

(1) Delft University of Technology, Delft, The Netherlands
(2) Tongji University, Shanghai, China

Abstract
Microcracks play vital roles in the prediction of the service life of concrete structure. Because microcracks in concrete structure are the preferential ingression channels for aggressive ions, e.g., chloride, sulphate, etc. However, microcracks have potentials to self-heal autogenously due to the continuous hydration of unhydrated cement, especially when ultra-/ high strength concrete is used. To quantify the autogenous self-healing effects of microcracks in cement paste, our experiment is designed to monitor the self-healing process of microcracks in cement paste continuously by using optical microscope. The healing products are quantified by image analysis with newly implemented software in MATLAB. The results indicate that the microcracks are not filled evenly along the crack length and most healing products are $Ca(OH)_2$, which dissolve partly from the paste matrix and re-nucleate in the microcrack, in addition to its counterpart from the continuous hydration of unhydrated cement. Furthermore, the sample cracked at earlier age shows higher potential to heal, while the sample with smaller crack width experiences greater filling efficiency. The obtained autogenous self-healing mechanism will be used in the future simulation.

1. Introduction

Microcracks (crack width below 0.1mm) are inevitable in concrete structure, especially when high thermal stresses happen in mass concrete members. Microcracks play vital roles in the prediction of the service life of concrete structure. Because they are the preferential ingression channels for ingressive ions, e.g., chloride, sulphate, etc. For instance, the chloride migration coefficients of concrete samples with microcracks caused by rapid freezing and thawing cycles experienced 2.5 to 8 times higher than that the references [1]. Fortunately, microcracks have the potentials to self-heal due to the continuous hydration of unhydrated cement, especially for ultra-/high strength concrete. Abrams [2] observed that the compressive

strength of the specimens recovered: the specimens had been tested first at 28 days, then the cracked specimens were stored outdoors and exposed to the weather for eight years before the compressive strength was measured again. The recovered strength was more than twice of the 28 day strength after 8 years [2]. However, many researchers pointed out that the recoveries of mechanical properties are less significant compared to the recoveries of transport properties and the continuity of the sample [1-3]. While the mechanical properties of concrete with microcracks recovered less than 10% after self-healing under water for 3 months at 20℃, the chloride migration coefficient reduced between 25% and 40%, and the ultrasonic pulse velocity (UPV) recovered from 50% to 100% [1]. The 40% reduced chloride migration coefficient indicates that the cracks are partly filled. The UPV recovery of 100% shows the crack space is bridged, so the continuity of the sample is rebuilt. Therefore, it can be assumed that the autogenous self-healing only happens at a few places where the microcracks are partly or completely blocked by newly formed hydration products. To confirm the assumption and to evaluate the efficiency of autogenous self-healing of the microcracks, an experimental process is designed to monitor the self-healing process of microcracks in cement paste, by which the amount of healing products are quantified.

2. Materials and methods

In this study, optical microscope is used to continuously monitor the autogenous self-healing process. Under optical microscope the water can remain in liquid form at room temperature. The reaction conditions for further hydration are similar to that in reality. The thin section sample is prepared with thickness of 100 μm. As a result, it becomes possible to distinguish the cracking space, origin paste matrix and newly formed hydration product under an optical microscope. With the polarized filters in the optical microscope, the qualification analysis can be carried out.
The general experiment process is explained as follows: the experiment started with casting cement paste samples in sealed plastic cylindrical containers with different water to cement (w/c) ratios, followed by curing them at 20 ℃. At desired ages, the samples were ground to 100 μm in thickness and cracked under microscope to specified crack widths. At last the samples were saturated with water and sealed, so the self-healing process was monitored. The specific procedures will be demonstrated in section 2.2.

2.1 Materials

In this study, Portland cement CEM I 42.5N is used. The sample series are shown in table 1. Various variables are presented, including w/c ratios, curing ages before cracking, and the average crack widths. All samples are monitored under optical microscope for 3 days after cracking.

2.2 Methods

2.2.1 Preparation of thin section samples

At the desired age, the cement paste samples were removed from the plastic containers. The samples were cut to 1 cm in thickness for thin section machine. SiC Paper is a type of coated abrasive that consists of sheets of paper with abrasive material glued to one face. Prior to gluing the sample with the working glass, SiC Paper #120 grits was used to sand one surface

in order to increase the contact area. Another surface of the sample was ground and polished to 1000±10 μm in thickness. This finished surface was glued to the object glass with acetone-dissoluble glue. Afterwards, the sample was turned over and cut again to make a new working surface. Similarly, this surface was ground and polished until the thickness of the sample is 100±10 μm. The thin section sample was ready for next procedure.

Table 1 Sample series

	w/c ratio	Age (day)	Crack width (μm)		w/c ratio	Age (day)	Crack width (μm)
A25S07W40	0.25	7	40	A25S28W80	0.25	28	80
A50S07W40	0.5	7	40	A50S28W80	0.5	28	80
A25S28W40	0.25	28	40	A25S07W120	0.25	7	120
A50S28W40	0.5	28	40	A50S07W120	0.5	7	120
A25S07W80	0.25	7	80	A25S28W120	0.25	28	120
A50S07W80	0.5	7	80	A50S28W120	0.5	28	120

2.2.2 Cracking samples under optical microscope

In order to generate the microcracks in samples many approaches were reported: 1) Microcracks were distributed randomly in the sample after rapid freezing and thawing cycles [1-4]. 2) The crack-width controlled splitting test to gain the microcracks [5-8]. 3) Huang et al obtained the microcracks of 30 μm by attaching two ground and polished samples to each other [9].For the first approach, the crack width obtained from rapid freezing and thawing cycles ranges from 1 to 10 μm; however, this range is too narrow for systematic studies of the microcracks. The second and third approaches generate artificial cracks with two characteristic shapes, i.e., V shape and flat shape, respectively. The real microcracking pattern cannot be represented by these two methods.

In this research, a new pre-crack technique was proposed to obtain specific crack width in a more realistic shape. Several steps are followed: firstly, the thin section sample was immerged in acetone solution to dissolve the glue combined the sample with the object glass. Secondly, the thin section sample was rinsed carefully with ethanol and dried in the air. Thirdly, the sample was bended and cracked into two parts, of which one part was glued again with a new object glass. Fourthly, another part of the cracked sample was placed close to the newly crack flank and adjusted subtly under the optical microscope. This part was glued to keep the crack in place when the specific crack width was measured under the optical microscope. The mode of the optical microscope is LEITZ DMRXP 301-371.010.

2.2.3 Petrographic analysis

The petrographic analysis uses the polarising and scanning electron microscopes to obtain information about the mineralogy, compositional features, etc.[10]. When the light from the bottom source goes through a polarized filter, the light is polarized at one direction. As the light goes through the thin section sample, the crystal phases reflect the light into other directions, i.e., non-polarized. Another polarized filter is used perpendicular to the first one,

so the light is polarized again. These two polarized filters are called crossed polarized filters, by this, only the crystal phases are shown in the images; therefore the amorphous calcium silicate hydrates (C-S-H) phase are not included in further analysis. From this way the general phase information of the hydration products were obtained.

2.2.4 Monitoring under optical microscope

When the micro-cracked sample was ready, the double-side tape was glued around the sample. After being saturated in water, the sample was covered with covering glass. The covering glass was sealed along the edges with transparent nail polish, to avoid the air leakage and the water evaporation; therefore the paste matrix will not be carbonated during the experiment.

The sample was then monitored under the optical microscope with the external callipers at x and y directions to control the movement of sample. A computer was connected with the optical microscope to take photos in each 30 minutes. Both images under the polarized filter and under the crossed polarized filters were taken. To improve the experiment efficiency, three different samples were placed under the optical microscope to obtain images in each 30 minutes. The total monitoring time was 3 days. The images obtained for one sample were used to conduct the image analysis with newly implemented MATLAB software.

2.2.5 Image analysis

The disturbance in the images was happened when the samples were changed regularly during the observation under optical microscope. The images could shift in x and y directions and rotation in x-y panel. As shown in Figure 1, the analysis software was implemented in MATLAB. The software could relocate the images back to their original locations, i.e., removing the disturbance in terms of the shifts in x and y directions and rotation in x-y panel. Afterwards, the images were used for further image analysis.

In Figure 1, on the left top of the Graphical User Interface (GUI), the image called origin image is the first image taken during the experiment. On the left bottom the image called target image is subjected to relocation. The image on the right in Figure 1 is the superimposed image of origin and target images to show the differences.

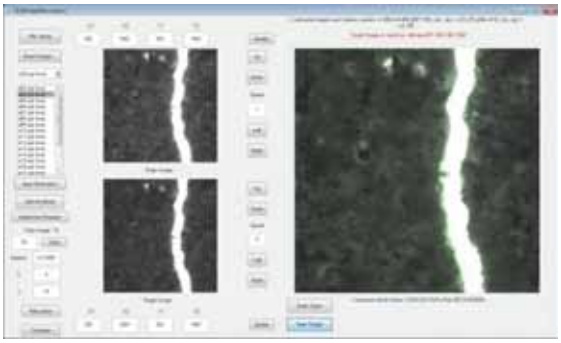

Figure 1. GUI of the analysis software

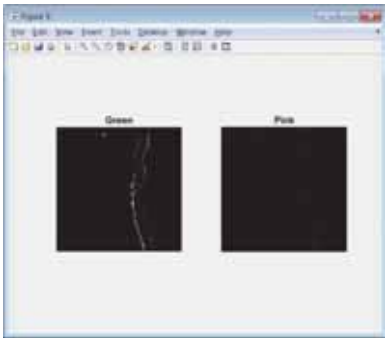

Figure 2. Example of relocation result

2.2.5.1 Relocation operation

Because the rotation centre (o_x, o_y), dx and dy (shifts in x and y direction) are 4 unknown variables, 4 points from the origin image and the counterpart points from the target image are chosen. Consequently, the rotation angle and shifts of dx and dy can be calculated. The values can be manually changed if the relocation result is not optimized.

In Figure 2, the pixels belonging to target image rather than origin image are shown on the left, which represent the hydration products. The pixels belonging to origin image rather than target image are shown on the right. These pixels are the errors that should be eliminated as much as possible. After being carefully adjusted, the amount of these pixels is reduced to less than 0.05% of total amount of pixels.

2.2.5.2 Analysis procedure

In order to quantify the hydration products, during image processing only the hydration products and the crack space are selected, other pixels are removed completely after the relocation operation.

Figure 3 gives an example of the intermediate images during the analysis. These images demonstrate the procedure how the hydration products and the crack space are selected. Firstly, the target image in Figure 3(a) is filtered with grayscale threshold, generating the crack mask given in Figure 3(b). Secondly, the crack area in Figure 3(c) is cut out from the target image with the aid of crack mask. Lastly, the hydration products are selected from the crack area with the help of grayscale threshold. From the crack mask, the crack widths are calculated along the crack from top to bottom. Similarly, the hydration products are quantified. The filling rate is calculated along the crack from top to bottom as shown in Figure 4(a). The filling rate is sorted and then grouped according to the filling efficiency, e.g., 0%, from 0% to 10%, etc. The statistical analysis is given in Figure 4(b). The x axis is the filling efficiency, the columns are the length of locations with these filling efficiencies divided by the total length of the crack in percentage (left y axis) and the curve is the cumulative curve of analysed locations in percentage (right y axis).

4. Results and discussion

The analysis results of samples with different w/c ratios, curing ages and average crack widths are compared.

4.1 Influence of w/c ratios

To demonstrate the influences of different w/c ratios on self-healing, sample A25S28W40 with w/c of 0.25 and sample A50S28W40 with w/c of 0.50 are compared. As shown in Figure 5(b), about 25% length of crack in sample A25S28W40 does not show any change in terms of crack widths. It indicates that no hydration products are formed within the crack space. 20% the length of crack is filled up to 5%, i.e., the crack width at these locations decreases by 5%.

Similarly, the filling efficiencies for the rest of the crack are shown in Figure 5(b). In sample A25S28W40, the highest filling efficiency is about 35%. In other words, there is a significant decrease in crack width at some locations.

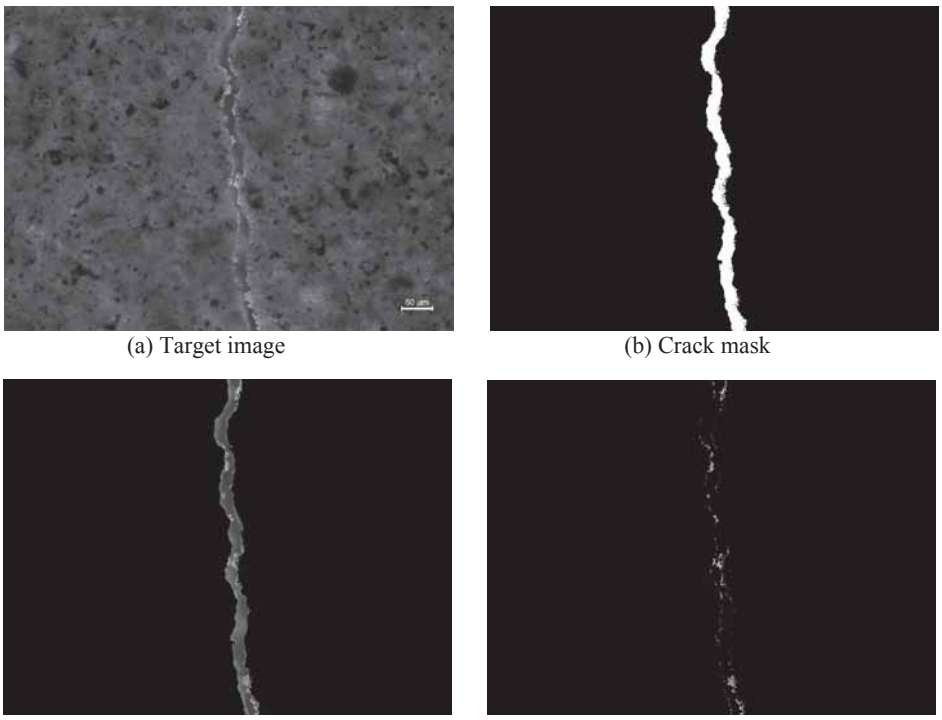

(a) Target image (b) Crack mask

(c) Crack area (d) Hydration product

Figure 3. Analysis of hydration products and crack space

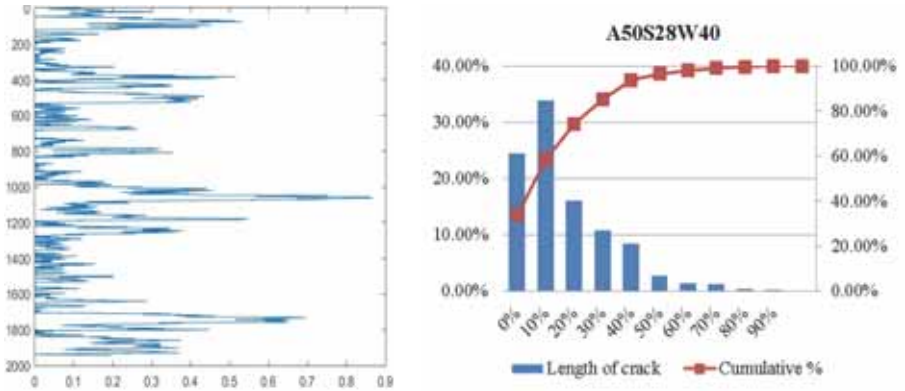

(a) Filling rate along the crack (b) Statistical analysis

Figure 4. Filling rate and statistical analysis

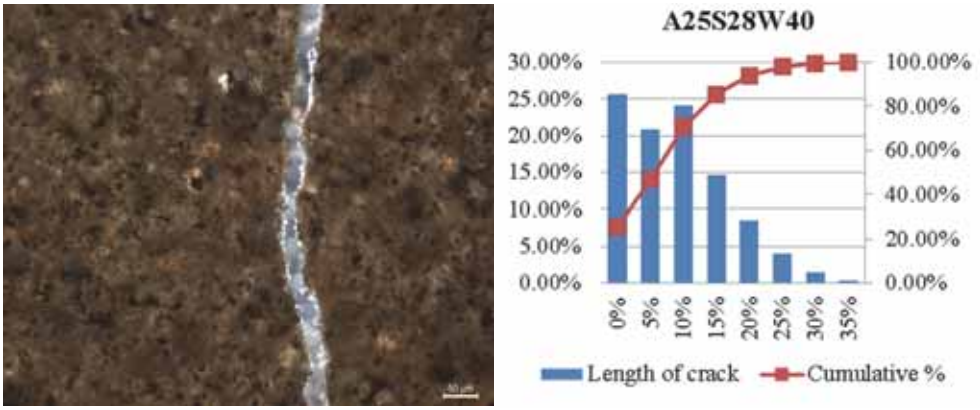

(a) Final image (b) Filling effiency

Figure 5. Quantification of hydration products in A25S28W40 after self-healing for 3 days

For A50S28W40 shown in Figure 6, about 25% the length of crack exhibits no filling effect at all. The filling efficiencies for the 35.49% length of the crack are between 20% and 40%. The rest 6.17% length of the crack is filled from 50% to 90%.

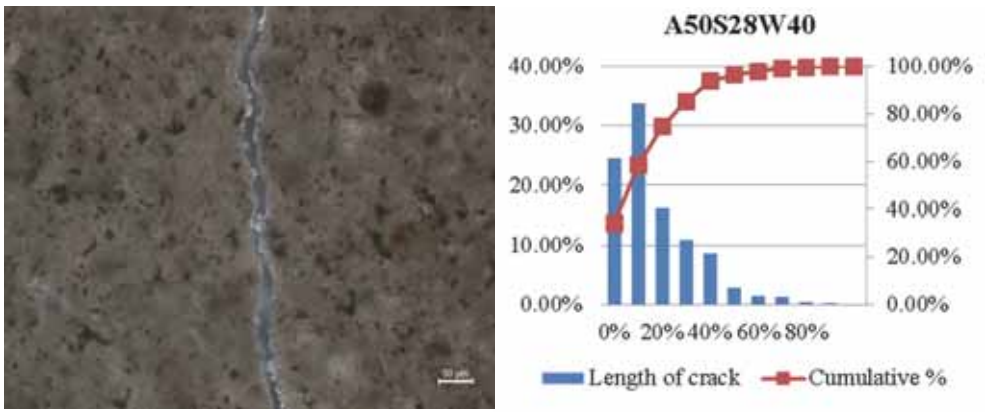

(a) Final image (b) Filling efficiency

Figure 6. Quantification of hydration products in A50S28W40 after self-healing for 3 days

It was expected that the sample with lower w/c ratios would have a higher filling efficiency due to higher amount of unhydrated cement available for further hydration. Surprisingly, the A50S28W40 with higher w/c shows much better filling effect in general. The reason is probably attributed to the dissolution of existing hydration products from the matrix of cement paste. Lauer and Slate also reported that cement phase with a higher w/c ratio experienced better healing effects, and they proposed that when the calcium hydroxide was

used during the reaction within the crack space, more calcium hydroxide ions diffused from the interior, i.e., the paste matrix [11]. This phenomenon can explain why A50S28W40 have a higher filling efficiency than A20S28W40. Furthermore, it suggests that long-term autogenous self-healing is possible even after the cement particles are completely hydrated, as long as the water is present.

Notably, the greatest filling efficiency of 90% in A50S28W40 is of significance: if the crack were the path for transporting ions, the 0.31% length of the crack in A50S28W40 would not be noticeable in terms of length, however it would be the "critical neck" in the overall transporting process. In other words, the autogenous self-healing contributes to better transport properties by partially blocking the microcracks. Further investigation is need to study the influences of the blocking of microcracks on the transport properties due to autogenous self-healing.

4.2 Influence of curing ages before cracking samples

Similarly, healing efficiency of A25S28W40 and A25S07W40, as shown in Figure 5 and Figure 7, are compared with respect to different curing ages, i.e., 28 days and 7 days before cracking.

About 25% of the length of crack in A25S28W40 with 28 days curing does not have any filling effect. The percent of the length of crack without healing in A25S07W40 with 7 days curing is less than 15%, and the greatest filling efficiency is about 80%. It is indicated that samples with micro-cracks at early age have a higher potential to heal themselves. A possible explanation for this might be that the samples with microcracks at early age have higher amount of unhydrated cement particles exposed to or near to the crack edge.

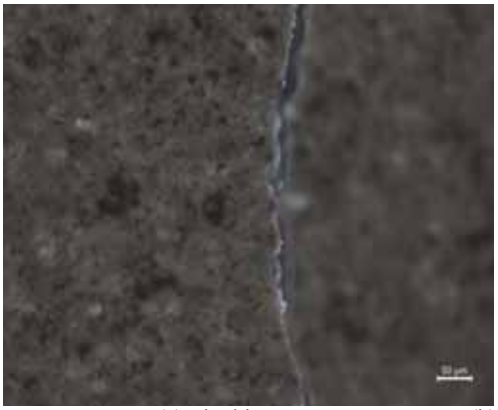

(a) Final image

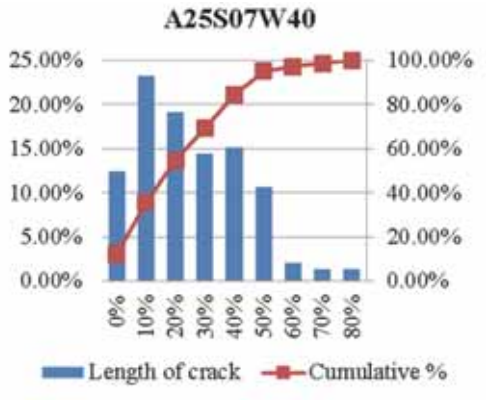

(b) Filling efficiency

Figure 7. Quantification of hydration products in A25S07W40 after self-healing for 3 days

However, it should be noticed that the experiments were carried out under the conditions avoiding any moisture and air exchanging. The carbonation is prevented explicitly. The contribution of the carbonation during the healing process is not taken into account in this

study. A general petrographic analysis was carried out to qualify the hydration products. The results from petrographic analysis indicate that most healing products within the crack space are calcium hydroxide. Neville claimed that the autogenous self-healing phenomena were attributed principally to further hydration of unhydrated cementitious materials based on his early results [12]. However, it was explained later by him that this was only applicable to young concrete, and the predominant products in the crack space was calcium carbonate [13]. Additionally, It was reported that the maximum chloride diffusivities of samples from field were more than 10 times lower than those obtained from the same concrete under laboratory condition [14]. The self-healing effect is greatly underestimated under the laboratory condition. To fully understand the influences of the self-healing on concrete with microcracks, the impacts of carbonation should be taken into account.

4.3 Influence of average crack widths

Samples with average crack widths of 40 μm (A25S07W40) and 80 μm (A25S07W80) are compared. It is observed from Figure 7 and Figure 8 that two samples show similar distributions in terms of the right-skewed shapes. This distribution shape indicates that the amount of hydration products is limited by the nature of the w/c ratio and the age before cracking [15]. It can therefore be assumed that the amount of hydration products is similar for these two samples, so the filling efficiency is only affected by the crack width. Specifically, the lengths of crack without any hydration products are 12.46% and 19.60% for A25S07W40 and A25S07W80, respectively. The crack width of 25S07W80 is twice that of the A25S07W40, and the former has almost double the length of crack without healing compared to latter. This finding suggests that in general the crack width does not influence the quantity of self-healing products, and the filling efficiency decreases with the increase of crack width.

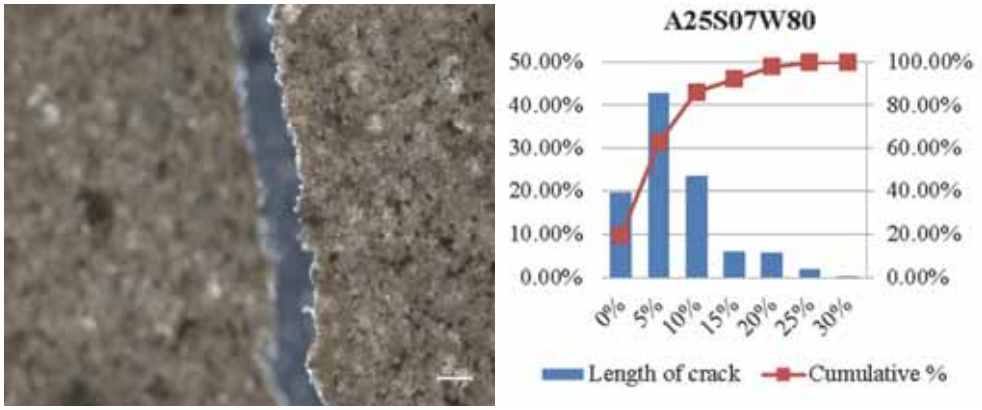

(a) Final image (b) Filling efficiency

Figure 8. Quantification of hydration products in A25S07W80 after self-healing for 3 days

5. Conclusions

In this study the autogenous self-healing process is monitored quantitatively. The influencing factors on the healing efficiency, i.e., various w/c ratios, curing ages before cracking and average crack widths are compared.

It is found that the microcracks are not filled evenly along the crack path; some locations are blocked to a greater extent than the rest. The sample of higher w/c ratio experiences better filling effect has shown that the hydration products formed in the crack space may be attributed to the dissolution of existing hydration products from the cement paste. The samples cracked at earlier age or with smaller crack widths show high self-healing potential. The presence of water may play vital roles regarding the long-term autogenous self-healing effects even after the cement particles are completely hydrated.

The condition for carbonation is avoided explicitly during the experiments for simplification. Future research should take into account the influences of carbonation on self-healing of concrete, which may further boost the autogenous self-healing effects in the long term.

References

[1] Jacobsen, S., J. Marchand and L. Boisvert, Effect of cracking and healing on chloride transport in OPC concrete, Cement and Concrete Research 26 (1996), 869-881.
[2] Jacobsen, S. and E.J. Sellevold, Self healing of high strength concrete after deterioration by freeze/thaw, Cement and Concrete Research 26 (1996), 55-62.
[3] Zhu, Y., Y. Yang and Y. Yao, Autogenous self-healing of engineered cementitious composites under freeze–thaw cycles, Constr. and Build. Materials 34 (2012), 522-530.
[4] Jacobsen, S., J. Marchand and H. Hornain, Sem observations of the microstructure of frost deteriorated and self-healed concretes, Cem. Concr. Res. 25 (1995), 1781-1790.
[5] Jang, S.Y., B.S. Kim and B.H. Oh, Effect of crack width on chloride diffusion coeffs. of concrete by steady-state migration tests, Cem. Concr. Res. 41 (2011), 9-19.
[6] Picandet, V., A. Khelidj and H. Bellegou, Crack effects on gas and water permeability of concretes, Cement and Concrete Research 39 (2009), 537-547.
[7] Park, S.-S., S.-J. Kwon and S.H. Jung, Analysis technique for chloride penetration in cracked concrete using equivalent diffusion and permeation, Construction and Building Materials 29 (2012), 183-192.
[8] Akhavan, A., S.-M.-H. Shafaatian and F. Rajabipour, Quantifying the effects of crack width, tortuosity, and roughness on water permeability of cracked mortars, Cement and Concrete Research 42 (2012), 313-320.
[9] Huang, H., G. Ye and D. Damidot, Characterization and quantification of self-healing behaviors of microcracks due to further hydration in cement paste, Cement and Concrete Research 52 (2013), 71-81.
Alan, B.P. and S. Ian, Concrete Petrography: A Handbook of Investigative Techniques, Second Edition (2015), 3.
[10] Lauer, R.K. and F.O. Slate, Autogenous Healing of Cement Paste, ACI Journal 52 (1956), 1083-1097.
[11] Neville, A., Properties of Concrete, Fourth Edition (1995), 844.
[12] Neville, A., Autogenous Healing—A Concrete Miracle?, Concr. Int. 24 (2002), 76-82.
[13] Sandberg, P. and L. Tang, Field Study of the Penetration of Chlorides and Other Ions Into a High Quality Concrete Marine Bridge Column, Proceedings of the Third International Conference SP-145 (1994), 557-571.
[14] Nancy, R.T., Typical Histogram Shapes and What They Mean, The Quality Toolbox Second Edition (2004), 292-299.

International RILEM Conference on Materials, Systems and Structures in Civil Engineering
Conference segment on Service Life of Cement-Based Materials and Structures
22-24 August 2016, Technical University of Denmark, Lyngby, Denmark

ULTRASONIC ASSESSMENT IN CURING PROCESS OF CBM USING EXPERIMENTAL MONITORING TESTS AND MICROSTRUCTURAL SIMULATION TOOLS

José Vicente Fuente [(1)], Jorge Gosalbez[(1)] , Sofía Aparicio [(2)], Margarita González [(2)], José J. Anaya [(2)]

(1) Universitat Politècnica de València
(2) ITEFI-CSIC, Instituto de Tecnologías Físicas y de la Información "Leonardo Torres Quevedo", Consejo Superior de Investigaciones Científicas

Abstract
This study comprises an approach of ultrasonic testing application to understand the influence of microstructural and constitutive components of Cement Based Materials (CBM) to the ultrasonic wave propagation. Nondestructive testing (NDT) represents a significant advance in a quality control of CBM and the concrete structures field. From NDT methodologies, the ultrasonic testing represents an important family. It is well-known the widespread application of the Son-Reb methodology to determine the level of integrity and bearing capacity of the structures. The ultrasonic monitoring allows determining the strength activity during the setting and hardening processes meanwhile the Carino's maturity method predicts the compressive strength in concrete mixed and it is used on construction sites. The combination of procedures seems to be affordable and it will contribute definitely to the universality of a unique method. With this research work, it is shown an experimental set-up based on cement pastes and mortars varying w/c ratio and aggregate proportion to obtain a discrete uniform variation of microstructures. The object is to analyse the ultrasonic parameters (velocity, wave reflection factor and centroid frequency) during the curing process and to assess them with microstructure and ultrasonic modelling (Hymostruct Lite and Wave2000 software©) and with experimental tests (nanoidentation, porosity and strength tests).

1. Introduction

The propagation, attenuation and scattering of the mechanical waves can be used to recover information about the microstructure of the material under inspection [1].
In this paper, some research has been performed combining experimental tests from:

- NDT based on ultrasounds to characterise the probes.
- Reference tests to characterise the microstructure and its evolution
- Numerical simulation of the ultrasound propagation for equivalence microstructures to know the influence of a NDT parameter to characterise the final properties of CBM.

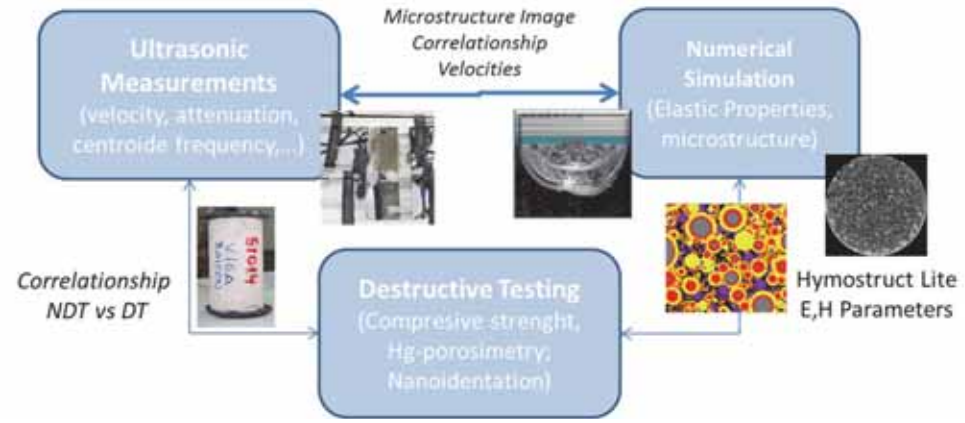

Figure 1. Flux process for the experimental research.

Figure 1 represents how the flux of information has been carried out for the correlation between NDT and destructive testing (DT) parameters. Based on this research, a prediction model can be established for final properties, as compressive strength, from the measurement of the evolution of ultrasonic parameters during the curing process (from early stages until 72 hours) on the CBM as it is described in [2].

2. Ultrasonic set-up and equipment

For this purpose, a methacrylate cell for continuous ultrasonic pulse measurement has been made. The volume of the cell volume is prepared for a small portion of fresh CBM with a reduced thickness to facilitate the propagation in transmission mode at early stages due to the high attenuation coefficient in the initial setting and hardening processes. By the other hand, elastic ethylene-vinyl acetate (*EVA*) has been interposed as each part of the methacrylate mould where the fresh concrete has to be poured. This *EVA* doesn't allow propagating the ultrasonic energy by the mould in the first stages where CBM velocity is lower than the methacrylate and its impedance is higher.

The ultrasonic signals and the internal curing temperatures were monitored with remote ultrasonic and acquisition devices and control software. The control software was programmed in Labview©® (Figure 2). In this sense, two ultrasonic equipments were programmed to work simultaneously and to measure by through-transmission and pulse/echo alternatively. The selected devices were DPR300 from JSR Instruments that which provide an effective control for the required acquisition periodicity.

An intermediate frequency was used for the transmission mode (500 kHz Olympus V101, 1'') and higher frequency (shear wave 5 MHz-Olympus V155) was used for the pulse/echo mode to estimate the Wave Reflection Factor (WRF). The WRF consists of the continuous

reflection in a steel cube to cause a repetitive wave reflection pulses. The steel cube is floating in the fresh concrete so that there is an intrinsic and slowly variation on the reflected energy between the steel bottom face and the CBM contact interface due to the *Snell law*. The reflected energy is detected and used to calculate the WRF at early stages. The centroid frequency (CF) was calculated for a specific time window [3].

Figure 2. Labview interface for advanced-users to generate the emitted pulses.

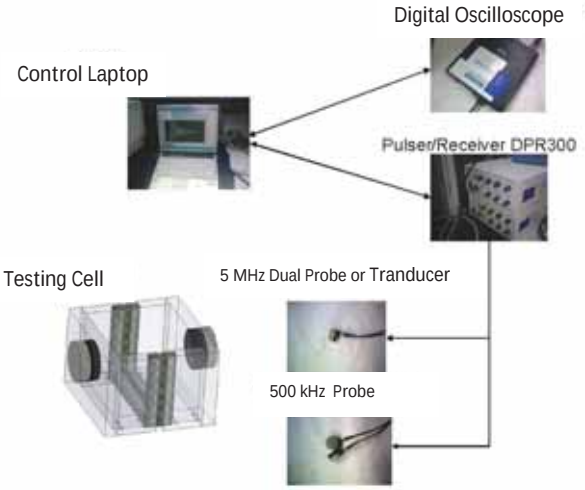

Figure 3. Test cell (left), lap-top (left-top), oscilloscope and DPR modulus (top-right) and transducers/probes for transmission and pulse/echo measurements

The inner CBM temperature, or curing temperature, is an important parameter to be monitored at fresh state where most part of exothermic hydration reactions took place. Temperature allows following the energy balance of these chemical reactions and detects properly the setting and the hardening times during the cement hydration. For this purpose a thermocouple PT100 and the TT7 of ISOTECH® device were used.

The digital signal processing (Figure 4) was developed using Labview©® and Matlab©®. Additionally, temporal filters have been applied in order to remove spare noise signals coming from industrial environment and to improve the signal to noise ratio. These algorithms estimate the centroid frequency, WRF, velocity at each curing age.

In order to check the velocity measurement procedure, water was used as reference media (1479±20 m/s) [1]. Additionally, theTB3550 steel block, the Panametrics 5058 PR ultrasonic device and a Tektronics TDS3012 oscilloscope were used for the perceptive calibration of the system according to the standards. The ultrasonic simulation was performed once the NDT

and DT were done. For this purpose, pictures of the microstructure were taken to estimate the total air void and to build the model with *Hymostruc lite*© [4]. This process is described more in depth in Section 5.

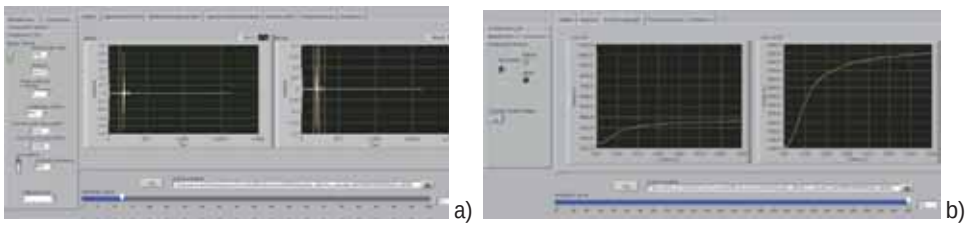

Figure 4. (a) Control windowing for reflection factor [white-red window], (b) and threshold and longitudinal velocity evolution.

3. Experimental Workplan

In order to obtain a representative range of microstructures, 2 different cement types were used with 4 water/cement (w/c) ratios for cement pastes (CP) and 4 aggregate/cement (ag/c) ratios for mortars (MC). The standardized aggregate (*germann normasand*) was used. The nomenclatures of the two different cements were CEM I 42.5 R/SR Sulphate Resistant (Cem I R/SR) and CEM II 42.5 R acting this as the reference cement (also called Cem II N). The w/c ratios for CP were 0.28, 0.30, 0.32 and 0.34 to produce a porosity increase but similar microstructure composition. The MC were dosed using an effective w/c of 0.4 and considering the adsorption water factor of 0.45% - in weight. The CP and MC were built according to EN 196-3 and the representative specimen was a cube of 4 cm size to assure stopping the hydration processes by the immersion in acetone at specific times 16, 22 & 72 hours for microstructural characterization (Figure 5).

Figure 5. Picture with specimen containers with acetone and ultrasonic equipment.

According to this plan, a wide range of microstructures (8 for CP and 8 for MC) was obtained to analyse the relationship between NDT and DT (strength/porosity) properties.

4. Destructive testing

The microstructure characterisation has been performed according EN 196-1 for 160 x 40 x 40 mm of prismatic specimen for compressive strength. The DTs were done at 16, 22 and 72 hours, the mixing time was established as zero time and the final stage was fixed after1000 hours. The machine test has a load cell of 20.000 kN from Ibertest®©. The Hg-intrusion porosity analysis (MIC) was also carried out over some samples (4.5-6 g for each sample). The equipment used was *Autopore*®© IV 9500.

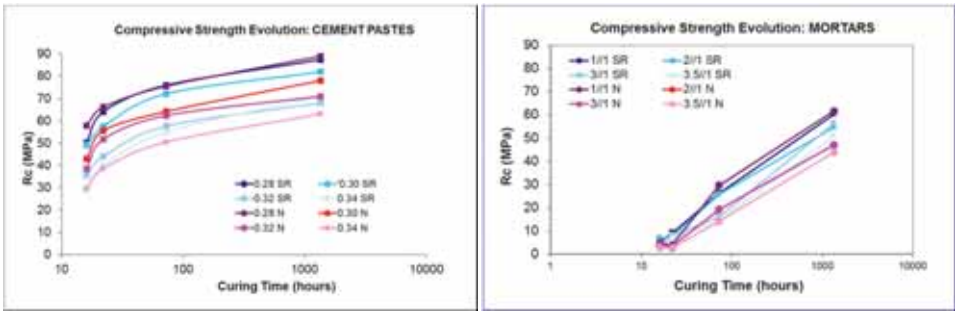

Figure 6. Evolution of the compressive strength for CBM: CP (left) and MC (right).

Some relevant differences have occurred in the strength evolution of CP respect to MC (Figure 6). It is observed that pastes (CP) achieve their final values before mortar (MC) and that mortar activates their hydration process after pastes due to the higher cement contain.

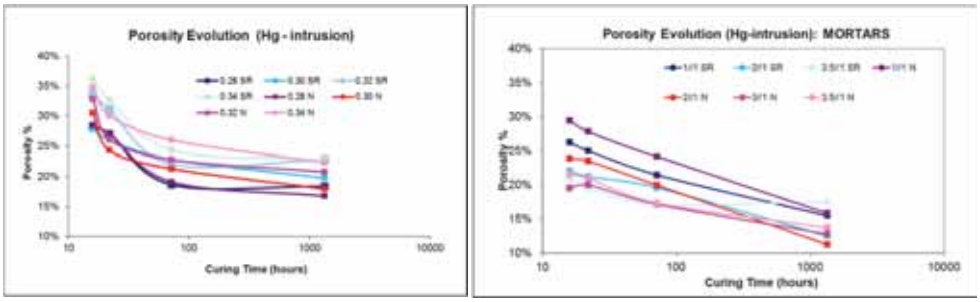

Figure 7. Global porosity evolution for a) CP *(left)* and b) MC *(right)*.

Figure 7 shows a different behaviour in the porosity evolution for CP and MC. The decreasing trend is more appreciable in CP than MC, although CP starts with high porosity at early stages [5]. It is noted that the CP reaches nearly the 85% of its final value after 22 hours, especially at lower a/c ratios. The MIP test reflects that the pore size distribution is not definitively achieved at this early time, but the matrix percolation is produced, so the hardening process is already finished. Regarding mortars evolution, it can be observed a linear decreasing trend

with a logarithmic representation of x-axis *(time)*. High ag/c ratio reflects a slightly increment of total porosity at 22 h. while lower ag/c does not reflect this trend.

Once the evolution of the porosity/strength parameters was characterised, the elastic modulus characterisation of the hydrated phases was performed at specific control times using nanoidentation. The nanoidentation is a minor destructive testing technique that requires a sample preparation of representative microstructure. The Nanoidenter XP of MTS[©®] allows performing the test with *nanovision* module to select the most suitable area [6]. Table 1 shows the referenced values for hydration phases.

Table 1. E (Young mod.), H (hardness) values for hydrated/anhydrate of CP and aggregates.

Phases	E (GPa)	H (GPa)	Phases	E (GPa)	H (GPa)
Porosity	0-12	0.13-0.24	HD-CSH	27-38	0.85-0.95
LD CSH	13-26	0.42-0.49	CH	39	1.30-1.40
C_3S/C_2S	130	-	Coarse/Fine Agg.	80/70	-

LD-CSH = Low density of Calcium silica; HD-CSH: ídem for high density; CH: Calcium hydroxide, C_3S/C_2S are the anhydrate phases.

The tests were performed on 0.28N and 0.34N CP types as examples of extreme porosities in order to quantify the elastic modulus range and volume portion of these phases. These values were the inputs for the simulation in order to match experimental velocity, measured at laboratory, with measured velocities using conventional tests at specific times (Figure 8).

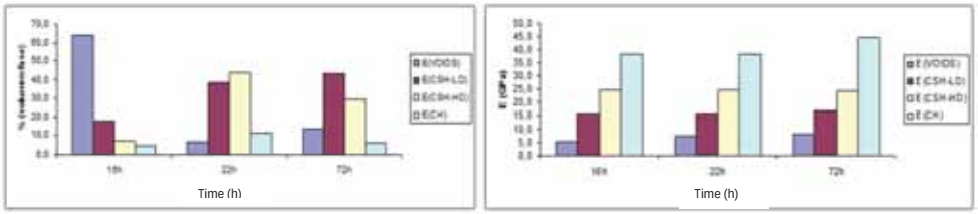

Figure 8. Elastic modulus & % volume of each phase derived from Nanoidentation at 0.28 N.

5. Ultrasonic simulation

The numerical simulation of the ultrasonic propagation reproduces how the pulse energy interacts with the microstructure of material. For this purpose, *Wave2000Plus software*[©] of *Cyberlogic* was used. To perform this analysis, it is required to build the microstructure since from the morphology, elastic modulus values and porosity/strength values. The free version of *NIST*[®], *Hymostruct Lite*[©] was used to create the specific cell image during each curing time, with the phases distribution and the E values from Table 1 for each CP type [7]. This cell size

was too small to perform a representative ultrasonic propagation; therefore, the cell was replicated to obtain a useful size, about 4-5 cm. This process is shown in Figure 9.

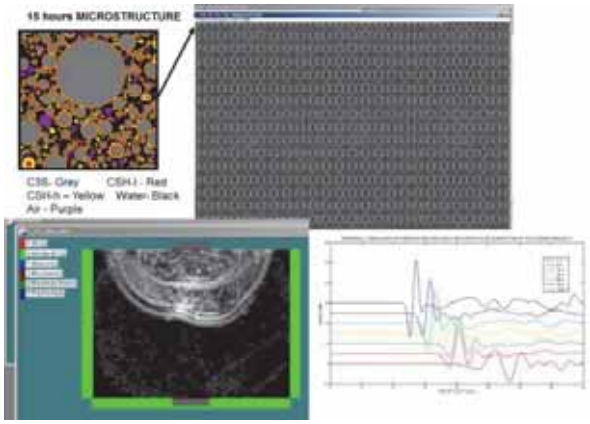

Figure 9.Numerical simulation adapting *Hymostruct* and *Wave2000* software.

It is important to note, that the ultrasonic propagation was simulated in 2D instead of 3D. A slight difference between simulated and experimental velocity was appreciated considering the 3D-scatering and the velocity group in a scattering media.

6. Ultrasonic experimental results

As it has been described in the Section 2, the ultrasonic experiments were carried out by continuos monitoring at specific times. Here, it is shown the results for CP and MC of continuos monitoring for longitudinal velocity and centroid frequency using log-time axis.

7. Correlations between NDT vs DT

For the case of CP, it can be observed that longitudinal wave can follow the decrease of the porosity except at spefic porosity region placed about 22-30% (Figure 11.a). These porosities and velocities correspond to two cases: 16 hours for lower w/c (low porosity) and 22 hours for higher w/c, depending the CP type. Out of this anomalous range, the simple longitudinal wave can predict the porosity during the hardening process. For the case of MC, the velocity reveals better relationship with compressive strength than porosity. Using velocity as NDT parameter to estime the strength, a coarse band it is consider at the experimental data (Figure 11.b).

8. Building a predictive model

Although the predictive model is not completely obtained, some of achievements from the experimental results are presented. According to the global porosity and the nanoidentation

test, E values for each phase in the CP can be assigned. The averaged results of the Young modulus (E) in the cement paste matrix were calculated and used for the simulations: a) 14.8±2.1 GPa for 16 hours, b) 18.0±1.2 GPa for 22 hours and c) 25.2±2.2 GPa for 72 hours. With the computation of the density and the elastic modulus the λ and μ (Lamé *elastic constants*) values were determined and used as a input for the Wave2000.

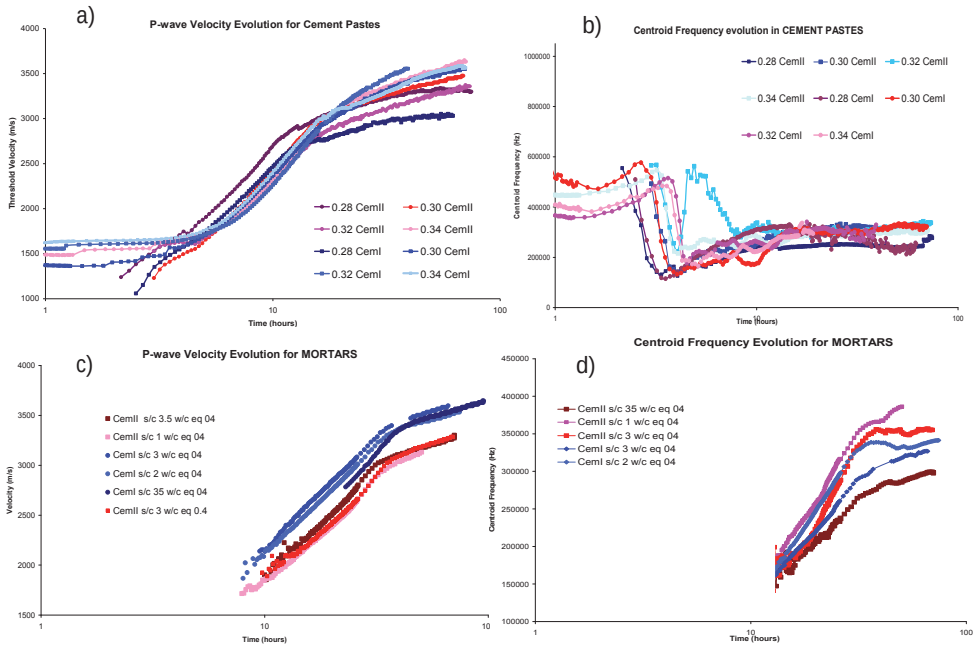

Figure 10. Experimental results: a) Vp of CP, b) CF for CP; c) Vp for MC, and d) CF for MC.

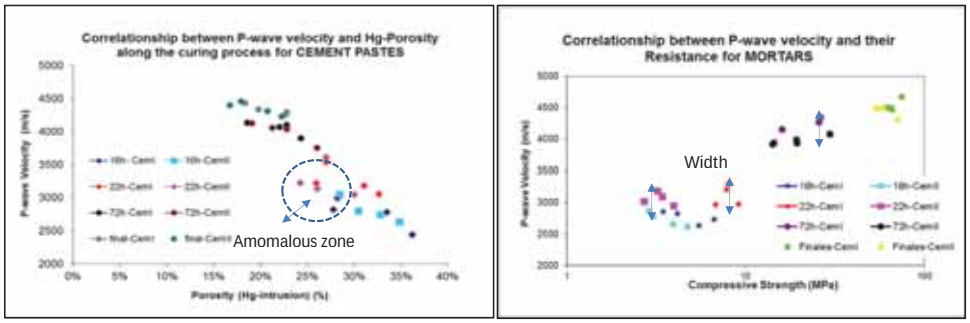

Figure 11. Correlations between NDT versus destructive tests at 16, 22, 72 h. & final stage.

According to the above average values about 15% of variation in the Young modulus (E) estimation depending on what microstruture was tested: 0.28 or 0.34. An especial wide variation range in unhydrated phases associated to high E values was found. This effect was also detected by the mismatching observed in the simulated longitudinal velocity, where it is used these values and the experimental ones. To built the predictive model, an iterative algorithm was programed in order to fit the air contain, the representative E values for each phase (air void, free water, LD-CSH, HD-CSH, CH) and the unydrated C_3S to obtain the maximum matching between numerical and experimental values of speed wave (Figure 13).

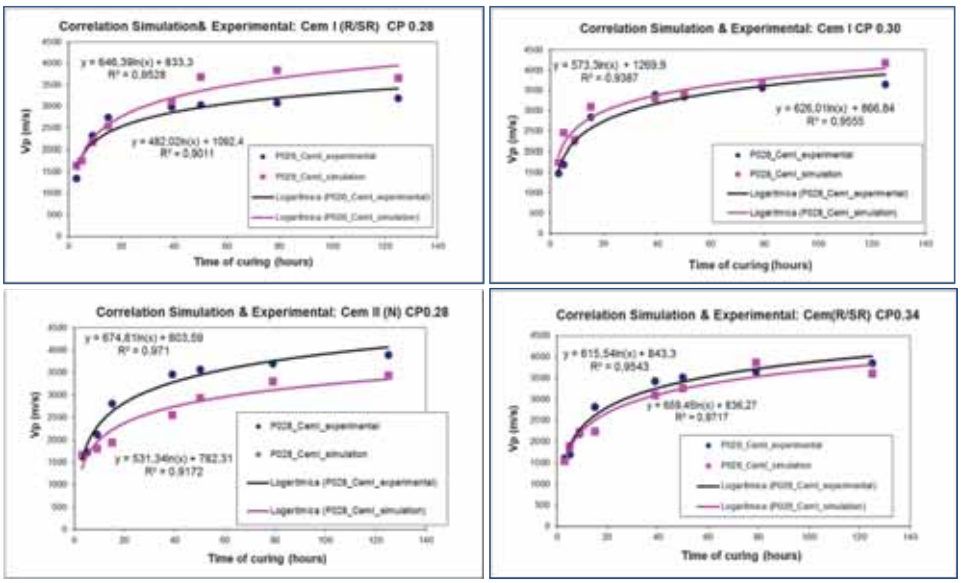

Figure 12. Velocities from numerical model (theoretical) and experimental tests.

The following achievements to obtaining the maximum correlationship can be concluded as follows:

- the model is fitted to 5% of air containt to match the curves showed at the Figure 12,
- lower w/c ratio reflects mismatch between experimental and simulated velocity. In this sense, the discrepance is shown since from 22 hours of the curing time. Also, the 5% of the air contain can be considered an expected value following the standart EN 196-3.
- The E value for C_3S should be reduced 60% respect to expected values (that are in the range of 130 GPa) in order to match experimental and numerical values. This effect can be masked by others like the use of 2D modelling instead of 3D-models and other limitations that offers different results respect to experimental ones.

9. Conclusions

It was concluded that longitudinal ultrasonic velocity can be used for MIP porosity estimation during the first 72 hours but showing an anomalous region in the hardening process at the CP. The main conclusion for the MC, equivalent their matrix to the analysed CP, is that the longitudinal ultrasonic velocity can be used to follow the acquisition of the compressive strenght at the same curing period, although the estimation is produced in a coarse band, independent of cement type or w/c ratio, as it can be shown in Figure 11.b.

Related to the predictive model, it can be concluded that the maximun matching of theoretical and experinental data for ultrasonic P-wave estimation is obtained using a 5% of air contain in the hymostruct cell and a significant reduction for unhydrated phases from the tabulated values.

Acknowledgment

This research has been supported by the references project BIA-2006-15188-C03, TEC2012-38402-C04-03 and BIA2014-55311-C2-2-P of Spanish goverment MINECO and IVACE regional administration whithin the project IMIDIC/2010/224.

References

[1] Sayers, C.M. “Ultrasonic propagation through hydrating cements”, Ultrasonics, Vol 31, nº3 pp 147-153, 1993.
[2] Aparicio S. et al.,“A Wireless Monitoring System to Study the Setting & Hardening Processes of Cementitious Materials”, *Proceedings 10th European Conf. of NDT*, Moscow, June 2010.
[3] L. Vergara, J. Gosálbez, J.V. Fuente, R. Miralles, I. Bosch “Measurement of cement porosity by centroid frequency profiles of ultrasonic grain noise”, Signal Processing, ISSN: 0165-1684, vol 82, pp 2315-2324, January 2004.
[4] G. Ye, E. Koenders, K. van Breugel, "HYMOSTRUC: An Advanced Program for Prediction of Mechanical Properties and Durability of Civil Engineering Structures", in B.H.V. Topping, (Editor), *"Proceedings of the Eleventh International Conference on Civil, Structural and Environmental Engineering Computing",* Civil-Comp Press, Stirlingshire, UK, Paper 4, 2007.
[5] D.P. Bentz et al., Early-Age Properties of Cement-Based Materials: Influence of Water-to-Cement Ratio, ASCE Journal of Materials in Civil Engineering, vol.21(9), pp 512-517, 2009.
[6] G. Constantinides, et al., The effect of two types of C-S-H on the elasticity of cement-based materials: Results from nanoindentation and micromechanical modeling. Cement and Concrete Research 34 (2004) 67–80.
[7] G. Ye, K. van Breugel, A.L.A.Fraaij “Experimental study on ultrasonic pulse velocity evaluation of the microstructure of cementitiuos material at early page”, Delft University of Technology, HERON, vol. 46, nº 3, 2001.

International RILEM Conference on Materials, Systems and Structures in Civil Engineering
Conference segment on Service Life of Cement-Based Materials and Structures
22-24 August 2016, Technical University of Denmark, Lyngby, Denmark

FINITE ELEMENT MODELS CAPABLE TO GIVE DETAILED INFORMATION ABOUT CRACKS SPACING AND OPENING IN CONCRETE STRUCTURES IN SERVICE LIFE CONDITIONS

Pierre Rossi [(1)], Jean-Louis Tailhan[(1)]

(1) Institut Français des Sciences et Technologies des Transports, de l'Aménagement et des Réseaux (IFSTTAR), Paris-Est University, France

Abstract
IFSTTAR has been developing probabilistic cracking models since 1987. The numerical model, originally developed to analyze the cracking of concrete, was more recently enhanced to take into account the presence of rebars and the bond between rebars and concrete and to model Fibre Reinforced Concretes (FRC). The concrete-rebar bond is represented by interface elements. Their behaviour is described with a simple deterministic damage model with only two parameters, cohesion and slip (i.e. relative tangential displacement between steel and concrete). Concerning FRCs, after the crack creation in the matrix, the acting of the fibres is taken into account by introducing a dissipated post-cracking energy which is randomly distributed on the mesh elements as for the matrix tensile strength (at the origin of the cracks creation). For Concrete, Reinforced Concrete (RC) and FRC Structures, the probabilistic finite elements models have been fully validated. Their specificity and their originality are based on the fact that they are capable to bring very precise and accurate information about cracks spacing and cracks opening when the service limit state of the structures is concerned.
This paper presents some examples of analysis of the cracking process of RC and FRC structures under service limit state loadings.

1. Introduction

IFSTTAR, the French Institute of Science and Technology for Transports, Development and Networks, has been developing a probabilistic explicit cracking model since 1987.

Their specificity and their originality are based on the fact that they are capable to bring very precise and accurate information about cracks spacing and cracks opening when the service limit state of the structures is concerned.
This paper is divided in two main parts:

- The first one is devoted to a synthetic presentation of the numerical models developed in the frame of probabilistic approaches.
- The second one is devoted to examples of validated applications of these numerical models.

2. Probabilistic explicit and semi-explicit cracking model for concrete

2.1 Probabilistic explicit cracking model

The model was first developed at IFSTTAR by Rossi [1, 2] and recently improved by Tailhan et al. [3]. It describes the behaviour of concrete via its two major characteristics: heterogeneity, and sensitivity to scale effects [4]. The physical basis of the model (presented in detail in [1, 2]) can be summarized as follow:

- The heterogeneity of concrete is due to its composition. The local mechanical characteristics (Young's modulus E_b, tensile strength f_t, shear strength τ_c) are randomly distributed.
- The scale effects are a consequence of the heterogeneity of the material. The mechanical response directly depends on the volume of material that is stressed.
- The cracking process is controlled by defects in the cement paste, by the heterogeneity of the material, and by the development of tensile stress gradients.

The following points specify how the numerical model accounts for these physical evidences:

- The model is developed in the framework of the finite element method, each element representing a given volume of (heterogeneous) material.
- The tensile strength is distributed randomly on all elements of the mesh using a probability distribution function whose characteristics depend on the ratio: *volume of the finite element/volume of the largest aggregate*, and the compressive strength (as it depends on the mesh, while the volume of the largest aggregate is a property of the concrete [1, 2, and 3].
- The shear strength is also distributed randomly on all elements using a distribution function: (1) its mean value is independent of the mesh size and is assumed equal to the half of the average compressive strength of the concrete and (2) its deviation depends on the element's size, and is the same (for elements of same size) as that of the tensile strength.
- In the explicit cracking model, developed, in priority, to perform 2D simulations, the cracks are explicitly represented by interface elements of zero thickness. These elements connect volume elements representing un-cracked plain concrete. Failure criteria of Rankin in tension and Tresca in shear are used. As far as tensile or shear stresses remain lower than their critical values, the interface element ensures the continuity of displacements between the nodes of the two neighboring volume elements. The material cell gathering these two volume elements and the interface element remains therefore elastic. Once one of the preceding failure criteria is reached, the interface element opens and an elementary crack is created. Its tensile and shear

strengths as well as its normal and tangential stiffness values become equal to zero [1, 2, 3]. In case of crack re-closure, the interface element recovers its normal stiffness and follows a classical Coulomb's law [5].

Note that in this model, the creation and the propagation of a crack is the result of the creation of elementary failure planes that randomly appear and can coalesce to form the macroscopic cracks (Figure 1).

Note also that, in fact, the finite element volume considered to determinate the tensile strength distribution function is, in the explicit cracking model, the total volume of two volume elements interfaced by one interface element (Figure 1).

To conclude, it can be said that this probabilistic model is in fact a deterministic one with probabilized parameters. Hence, it is necessary to perform a large number of computations to statistically validate the results following a Monte Carlo method, because only one simulation is not relevant when a probabilistic model is used. The number of numerical simulations needed is related to the structural problem concerned and the scattering of the structural response. In this way, it is easy to perform a safety analysis of the loaded structure.

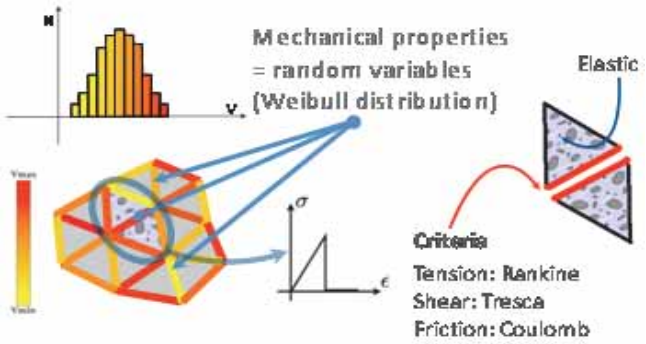

Figure 1: Probabilistic concrete cracking model

2.2 Probabilistic semi-explicit cracking model

The semi-explicit cracking model is based on the same physical assumptions than the explicit one. The main difference between the two approaches is related to the way of modeling the cracks. As a matter of fact, in the semi-explicit cracking model, cracks are not modeled by using interface elements but by using volume elements (linear triangles in 2D or linear tetrahedron in 3D).

The Failure criteria of Rankin in tension and Tresca in shear are thus applied at the gravity center of the elements. When one of these criteria is reached in one element, all the components of the matrix of rigidity of the volume element become equal to zero. It is a "kill element" approach. By this way, a crack is modeled by a hole.

Note that, in the frame of this semi-explicit cracking model, the finite element volume considered to determinate the tensile strength distribution function is the volume of the volume element itself.

3. Concrete-rebar bond model

A simple and robust model has been developed and validated at IFSTTAR [6, 7, and 8]. It takes into account the nonlinear behaviour of the concrete-rebar bond in the frame of damage mechanics. It can represent physical phenomena such as interface sliding, cracks appearance and degradation process. The concrete-rebar bond is modeled as interface elements. Their role is to:

- Ensure the displacement continuity between the concrete and the steel before the slip of the interface and before the cracking of the concrete, thus ensuring the transfer of stresses between steel and concrete.
- Represent the macroscopic mechanical effect of the rebar at the ribs – which is not explicitly represented in the mesh.
- Simulate a local failure between steel and concrete along the rebar resulting from a loss of the local adhesion due to shear cracking.
- Simulate the local friction between the concrete and the steel after the interface failure.

The model is implemented in 2D and 3D. It models the concrete-rebar bond as a material zone that progressively degrades in shear (the tensile failure is neglected). Prior to total failure, stresses are continuously transmitted through the interface.

The interface model is based on a damage model that maintains a constant level of stress when the critical shear has been reached (Figure 2). When the relative tangential displacement between the concrete and the rebar exceeds a critical value, the interface element is declared broken [9]. After failure, a Mohr-Coulomb type of friction behaviour is maintained (Figure 3). The interface model is deterministic. This is a valid approximation because the cracking process around the rebar is governed by the presence of the ribs (rather than the heterogeneity of concrete) [9].

Only the values of the maximum shear stress, C, and of the tangential critical relative displacement, δ_t^{cri}, have to be determined. This is done by numerical inverse analysis of tie-beam tests.

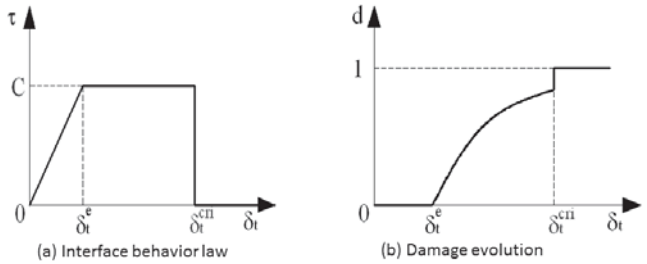

Figure 2:a) Steel-concrete interface behaviour law b) Damage evolution

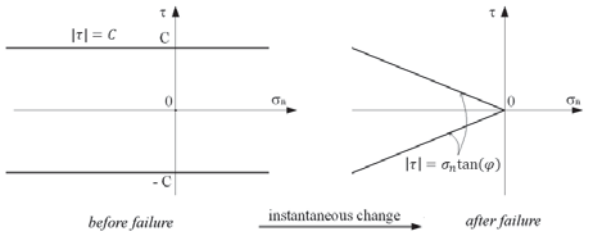

Figure 3. Mohr-Coulomb friction after failure of the steel-concrete interface

4. Probabilistic explicit cracking model for FRC

The extension of the probabilistic explicit model to analyze the cracking process of FRC structures is very simple.

The first step is to create cracks in the matrix, it means, in the concrete. It is realized by opening the interface elements as described in chapter 2.1.

Thus, after cracking, the interface element rigidity is considered different for normal and tangential displacements. In 2D, normal and tangential rigidities of the interface element are K_n' and K_t' respectively. This post-cracking elastic behaviour exists until it reaches a limit, δ_0, related to the normal displacement. Once this limit value is reached, the mechanical behaviour of the interface element changes. As a matter of fact, the normal stress is considered as ***linearly decreasing*** with the normal displacement in order to take into account the damage of the bond between the concrete and the fibre and the pullout of the fibre. The decreasing evolution is obtained with a damage model.

Finally, the interface element is considered definitely broken, and its normal and tangential rigidities are equal to zero, when the normal displacement occurring during the damage step reaches a critical value, δ_c. This value corresponds to the state where the effect of fibres is considered negligible.

The post-cracking total energy dissipated during the linear increase and followed by the linear decrease of the normal stress is considered randomly distributed on the mesh elements as for the material tensile strength. However, the random distribution results from a log-normal distribution function with a mean value independent of the mesh elements size and a standard deviation increasing with the decrease in the mesh elements size, which is physically logical (see Rossi [10]). In practice, to model a given structure, the distribution function is determined in the following manner:

- The mean value is directly obtained by performing a certain number of uniaxial tensile tests on notched specimens (the post-cracking energy is classically determined from the load-crack opening curve) or indirectly by performing an inverse approach based on numerical simulations of bending test.
- The standard deviation, which depends on the mesh elements size, is determined by an inverse analysis approach that consists of simulating uniaxial tests (on notched specimens) or bending tests with different element mesh sizes . As a matter of fact, knowing from the mean value of the post-cracking energy, several numerical simulations are realized for each mesh size and the standard deviation related to each mesh size is obtained by fitting the experimental results (in terms of mean and standard deviation of the numerical responses compared to their corresponding experimental values). By this way, it is possible to find a relation between the standard deviation and the finite element mesh size.

The numerical mechanical behaviour adopted for the post-cracking step is illustrated in Figure 4. Only the normal stress - normal displacement curve is considered in this figure.

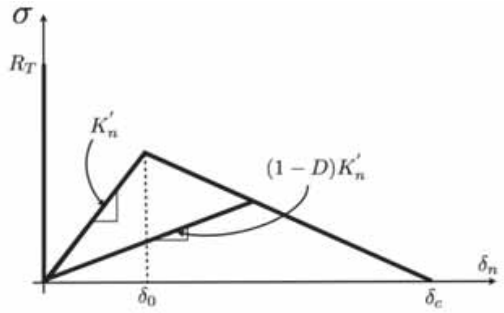

Figure 4. modelling of the post-cracking behaviour of frc

5. Example of application of the numerical model related to RC structures

This example of validation of the numerical model was published in a previous paper [7]. The structure concerned is a reinforced slab-beam submitted to three-points bending; 3.30 m long (3.00 m between supports), 0.80 m wide, and 0.15 m thick (an element must have a thickness $\leq 1/5$ of its width to be considered a slab). All details (geometry, reinforcement, loading conditions...) concerning this RC structure are given in Figure 5.

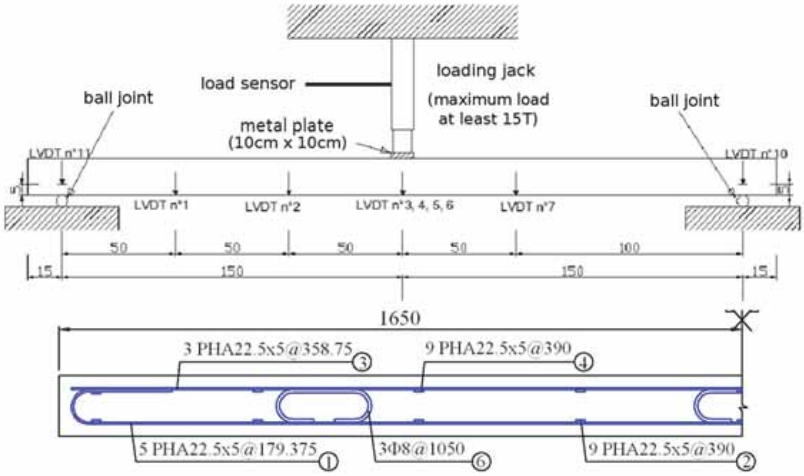

Figure 5. Slab-beam dimensions, type of reinforcement and loading conditions

The mean compressive strength of the concrete studied was 55 MPa.
The mechanical properties of the steel rebars were:

- Young modulus: 200 000 MPa
- Linear hardening modulus 1120 MPa.
- Elastic limit strength: 640 MPa,
- Ultimate limit strength: 720 MPa,
- Ultimate strain: 12 %

Tie-Beam test were performed in parallel of this structural test to get (by inverse approach, see chapter 3) the values of the parameters of the concrete-rebars bond model.
These values were the following: C = 16 MPa and δ_t^{cri} = 23 µm
3D simulation of the beam-slab was performed. The finite elements mesh used is presented in Figure 6.

Figure 6. 3D finite elements mesh of the beam-slab

The finites elements used were:

- hexahedral linear elements for the steel bar,
- 3D linear interface elements for the concrete/steel bond,
- Tetrahedral linear elements for the concrete.

In Figure 7 is shown a comparison between experience and numerical simulation concerning the global behaviour of the structure represented by the Load-Deflection curve.

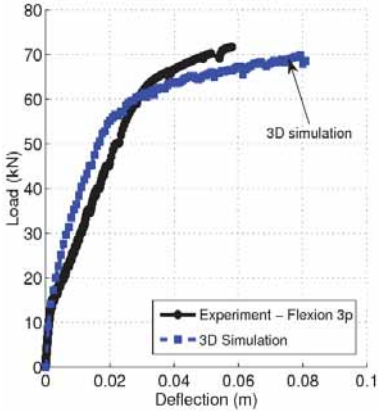

Figure7. Load-Deflection curves-Comparison between experience and numerical simulation

Figure 8 and 9 summarize comparison between numerical simulations and experimental tests in terms of mean, min and max curves related respectively to the number of cracks versus load and to the cracks opening versus load.

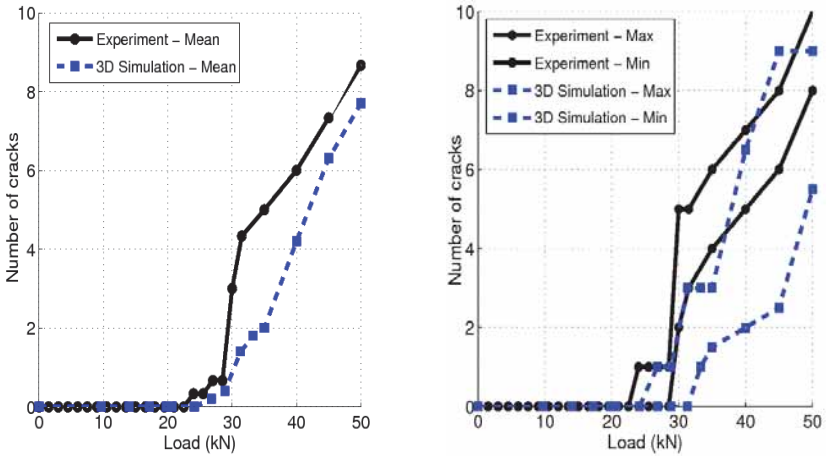

Figure 8. Slab-beam test – Number of cracks versus load – mean, min, max curves – Comparison between experience and numerical simulations

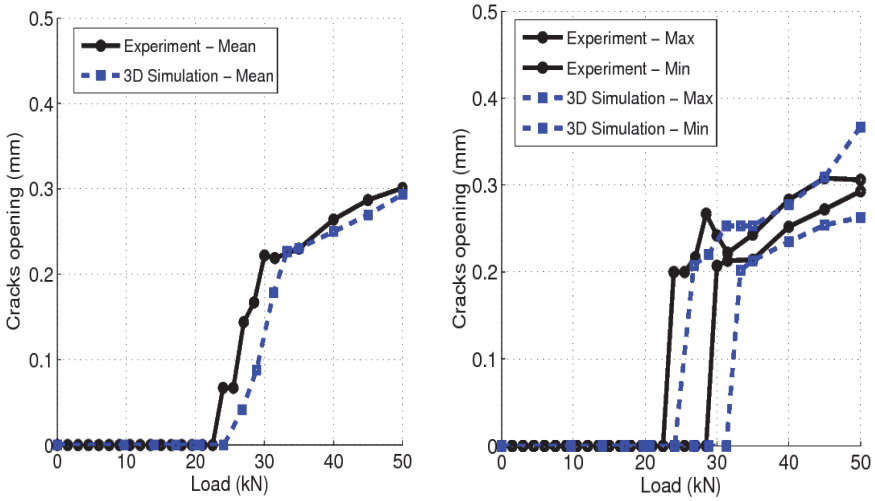

Figure 9. Slab-beam test – Cracks opening versus load – mean, min, max curves – Comparison between experience and numerical simulations

6. Example of application of the numerical model related to FRC structures

This example of validation of the numerical model has been published in a previous paper [11]. The FRC structure concerned was a Steel Fibre Reinforced Concrete (SFRC) beam submitted to 4-point bending. The experimental campaign that allows the comparison of experimental and numerical results was conducted at Ecole Polytechnique de Montréal, Canada [12]. The dimensions (length, width, height) of the beam were the following: 2600 x 400 x 300 mm. The testing apparatus used for this experimental campaign is presented in Figure 10.

The SFRC used was a self-compacting one containing 78 kg/m^3 of hooked-end steel fibres. These fibers were 35 mm long and had a diameter of 0.55 mm. This SFRC achieved an average compressive strength of approximately 60 MPa at 28 days.

In order to characterize the tensile behavior, uniaxial tension tests were performed on this SFRC. The RILEM uniaxial tension test [14] was conducted on notched core-cylinders (h = 100 mm and Ø = 85 mm). Six specimens for each mix were cored horizontally from a 500 × 600 × 400 mm block casted in addition to the beams.

These tensile tests were performed to determinate, by inverse approach, the parameters of tensile behaviour model of the SFRC (chapter 4).

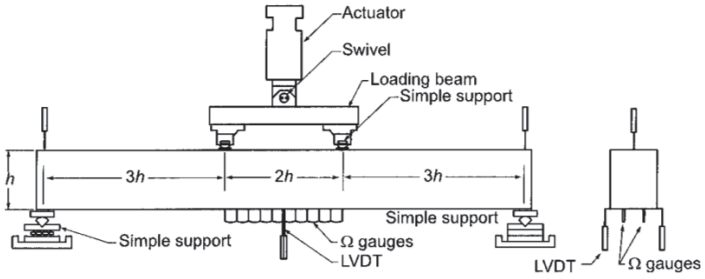

Figure 10. Beams'dimensions, testing apparatus and instrumentation related to the experimental tests

The parameters of the tensile behaviour model related to the studied SFRC were the following:

- Average tensile strength: 2.46 MPa
- Tensile strength standard deviation: 0.34 MPa
- Average post-cracking energy: 4.26 MPa.mm
- Post-cracking energy standard deviation: 0.88 MPa.mm
- δ_0: 0.05 mm
- δ_C: 4 mm

The finite elements mesh used to simulate the beam behaviour is presented in Figure 11.

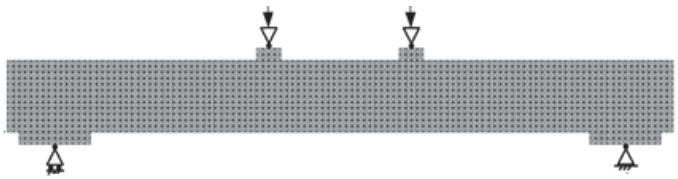

Figure 11. Finite elements mesh of the SFRC beam.

Figure 12 presents a comparison between the global behaviour of the SFRC beam obtained with the experience and with the numerical simulation. This global behaviour is considered in the frame of the Load-deflection curve of the beam.

Figure 13 presents an example of cracking pattern obtained with the numerical simulation.
Figure 14 proposes a comparison between the evolution (with the loading moment) of the maximum crack opening displacement obtained experimentally with the one obtained numerically.

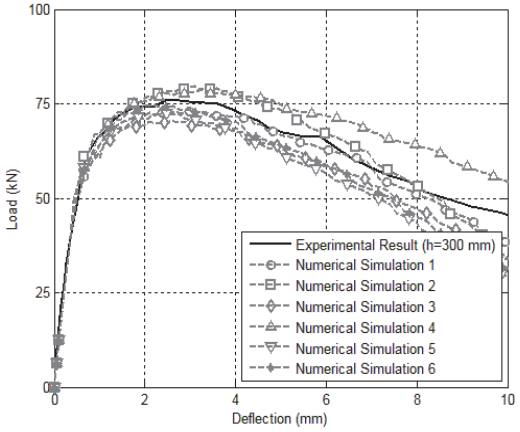

Figure 12. Load-deflection curve - Comparison between experience and numerical simulation.

Peak load: 78 kN

Figure 13. Example of cracking pattern obtained with the numerical simulation

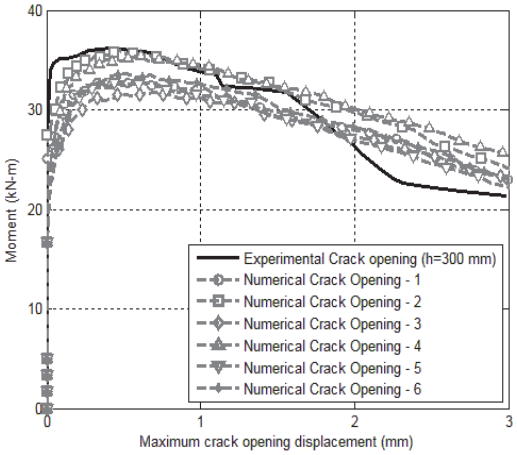

Figure 14. Maximum crack opening displacement versus loading moment - Comparison between experience and numerical simulation

7. Conclusions

This paper presents numerical models developed to get precise information on the cracking process (cracks spacing and opening) of RC and FRC structures since their service state until their ultimate state. These models are deterministic ones with probabilized parameters. They are relevant only if you use it in the frame of Monte-Carlo approach .
Two examples of validation of these models are presented: one related to the bending behaviour of a reinforced slab-beam and one related to the bending behaviour of a steel fibre reinforced beam.
These two examples show that the proposed models are relevant regarding their objectives.

References

[1] Rossi, P. and Richer S., Numerical Modelling of Concrete Cracking Based on a Stochastic Approach, *Materials and Structures*, (1987) **20**(119): 334-337.
[2] Rossi, P. and Wu, X., Probabilistic model for material behaviour analysis and appraisement of concrete, *Magazine of Concrete Research* (1992) **44**(161): 271-280.
[3] Tailhan, J.-L. et al., From Local to Global Probabilistic Modeling of Concrete Cracking, *Annals of Solid and Structural Mechanics* (2010), **1**: 103-115.
[4] Rossi, P., et al., Scale effect on concrete in tension, *Materials and Structures* (1994) **27**: 437-444.
[5] Rossi, P., Ulm, F.Jj. and Hachi, F., Compressive behaviour of concrete : physical mechanisms and modelling, *ASCE Engineering Mechanics* (1996), vol. 122 (11), pp-1038-1043.
[6] Phan, T. S. et al., Numerical modeling of the rebar/concrete interface: case of the flat steel rebars, *Materials and structures* 46.6 (2013): 1011-1025.
[7] Phan, T. S., Tailhan, J.-L. and Rossi, P., 3D numerical modelling of concrete structural element reinforced with ribbed flat steel rebars, *Structural Concrete* 14.4 (2013): 378-388.
[8] Phan, T. S., Rossi, P. and Tailhan, J.-L., Numerical modelling of the concrete/rebar bond, *Cement and Concrete Composites* 59 (2015): 1-9.
[9] Rossi, P., Comportement dynamique des bétons: du matériau à la structure, *Annales de l'Institut technique du bâtiment et des travaux publics* (1993), n°. 511, Institut technique du bâtiment et des travaux publics (in french).
[10] Rossi, P., Experimental study of scaling effect related to post-cracking behaviours of Metal Fibres Reinforced Concretes, *European Journal of Environmental and Civil Engineering* (2012), Vol.16(10), pp.1261-1268.
[11] Rossi, P. and Daviau-Desnoyers, D. and Tailhan, J.L., Analysis of Cracking in Steel Fibre Reinforced Concrete (SFRC) Structures in Bending using Probabilistic Modelling, *Structural Concrete*, (2015) n°3, pp. 381-388.
[12] de Montaignac de Chauvance, R., Analyse du comportement d'éléments fléchis en béton renforcé de fibes métalliques. Du matériau à la structure. *PhD Thesis of'Ecole Polytechnique de Montréal,* Canada (2011), p. 258 (in french).

International RILEM Conference on Materials, Systems and Structures in Civil Engineering
Conference segment on Service Life of Cement-Based Materials and Structures
22-24 August 2016, Technical University of Denmark, Lyngby, Denmark

EFFECT OF GRANULATED BLAST FURNACE SLAG ON THE DURABILITY OF SELF COMPACTING CONCRETE IN HOT ENVIRONMENT

Kenai Said [(1)], Yahiaoui Walid [(1)], Menadi Belkacem[(1)]

(1) Geomaterials laboratory, Civil engineering department, University of Blida, Algeria.

Abstract
Self-compacting concrete (SCC) is characterized by its high volume of paste and the presence of mineral additions such as ground granulated blast furnace slag (GGBFS) and natural pouzzolana. The performance of SCC in moderate climate is well investigated. However, few studies are available on the effect of hot environment. This paper reports the results of an experimental study conducted to evaluate the effect of GGBFS and initial water-curing period on the performance of SCC. Cement was substituted by blast furnace slag by weight at two different levels of substitution (15% and 25%). Concrete specimens were stored either in a water at T=20 °C, or in the open air during summer period (T= 35 to 40 C° and R.H= 50 to 60%) after an initial humid curing period of 3, 7 or 28 days. Compressive strength at 28 and 90 days, water capillary and porosity were investigated. The increase in the substitution level of slag from 15 to 25% resulted in a compressive strength at 28 days comparable to that of cement without addition, irrespective of the period of curing. The experimental results show the importance of humid curing in hot climates in particular when GGBFS is used.

1. Introduction

Self-compacting concrete is relatively a new concrete that is highly flowable and takes place without vibration and often possessing higher strength and durability properties. Self-compacting concrete is characterized by its high paste content and hence various cementitious materials such as slag, natural pouzzolana, limestone and metakaolin are added to the mix. The performance of SCC in moderate climate is well investigated [1-4]. Several studies have been conducted on the performance of vibrated concrete in hot climate [5-6]. However, few studies are available on the effect of hot and dry environment.

Hot weather conditions create several problems for both fresh and hardened concrete. Reduced durability is one of the major problems in concrete prepared under hot weather conditions. Under hot weather conditions, concrete has to be cured for an extended period of time compared to normal weather conditions in order to achieve acceptable strength and durability [7]. The characteristics of hardened self-compacting concrete made of slag depend on the nature and proportions of the constituents but also on the storage conditions that affect the hydration reactions. The ambient temperature is one of the most important environmental factors. Temperature could reach up to 40 °C in summer coupled with relatively low humidity and hence high and rapid loss of water by evaporation. The loss of water is particularly significant at concrete surfaces and hence causes uneven shrinkage creating severe thermal stresses in concrete and hence risk of cracking. The increase in the water curing duration increases the compressive strength whereas air curing decreases compressive strength [8]. Concretes that received no curing showed the poorest performance in terms of the strength development, porosity, and resistance to the chloride- ion penetration [9]. Moist cured concrete for only two days showed significant improvement in strength, and other characteristics, as compared with the concretes without any curing [10].

In this study, GGBFS was used to replace 15 and 25% of Portland cement. Two curing regimes were applied to investigate the effect of initial water-curing period and curing conditions on the properties of SCC made of local medium hydraulicity slag. Compressive strength, porosity and capillary absorption were investigated.

2. Materials

The cement used is a blended cement type CEM II/A 42.5 with a specific surface of Blaine of 304 m²/kg. A granulated blast furnace slag steel factory which was ground in the laboratory at a fineness of 350 m²/g was used as a substitution by weight of cement. This slag is known of its low to medium activity [11, 12]. The chemical composition of slag is summarized in Table 1. The sand used was a mixture of two sands: a river sand and a dune sand. Two types of gravel were used (3/8 and 8/15). A polycarboxylate superplasticizer named MEDAFLOW 30 was used.

Table 1: Chemical composition of slag

Element	SiO_2	Al_2O_3	Fe_2O_3	CaO	MgO	MnO	K_2O	SO_3	TiO_2
%	40.10	6.00	2.00	42.20	4.70	2.60	1.20	0.15	1.20

3. Methods

The water/binder ratio was kept constant at 0.40 in this study. The dosage of superplasticizer was optimized on mortar to obtain a homogeneous and stable self-compacting mortar (without bleeding). The dosage of superplasticizer was kept constant in the mixes (1.6% of cement by

weight). Concrete mix design was based on the Okamura general method [13, 14]. Three formulations were studied, namely an SCC mix without additions chosen as the reference concrete and SCC with 15 and 25% slag as cement replacement by weight. Details of the mix proportion of SCC are given in Table 2. After an initial moist curing of 0, 3, 7, or 28 days, the specimens were cured in two different environments:

- Water curing at 20 ± 2 ° C
- In the open air on the laboratory roof in summer (T=30- 45 °C, HR=65-70 %) (Figures 1 and 2)

Table 2: Mix proportions details of SCC used

Mix composition (kg/m^3)	**SCC-0S**	**SCC-15S**	**SCC-25S**
Cement	491.07	419.11	371.32
Slag	0	69.65	116.57
CA 3/8	247.39	247.39	247.39
CA 8/15	494.78	494.78	494.78
Sand	920.49	920.49	920.49
Water	197.66	197.66	197.66
SP	7.85	7.85	7.85

SCC-15S: Self-compacting concrete with 15% slag as cement replacement.

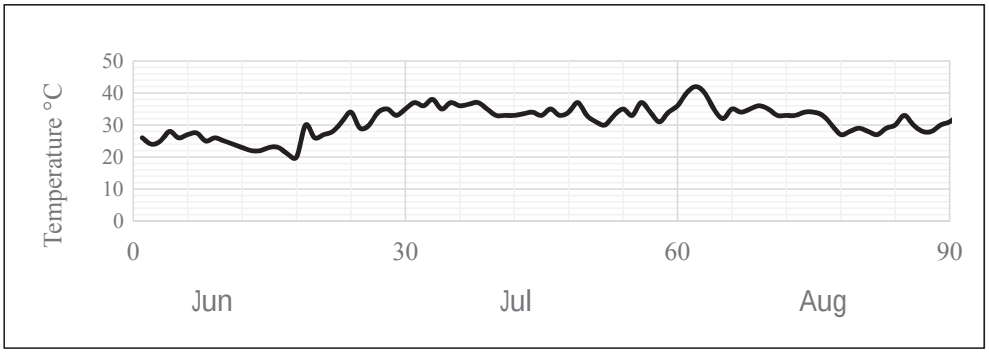

Figure 1: Variation in maximum temperatures in the region during the test period.

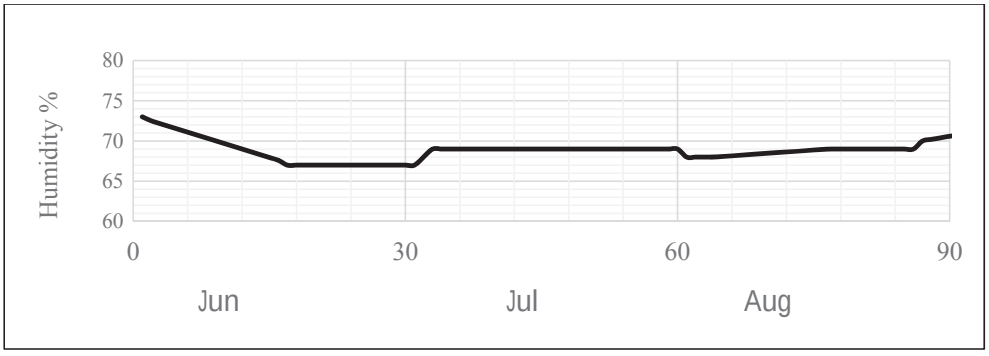

Figure 2: Variation in humidity in the region during the test period.

The slump flow test of fresh SCC was conducted according to EFNARC [15]. The initial slump flow value of fresh SCC is represented by the mean diameter (measured in two perpendicular directions) of concrete after lifting the standard slump cone.

The L-box test was performed in accordance with EFNARC standards. During the test, fresh SCC was allowed to flow upon the release of a trap door from the vertical section to the horizontal section by a few reinforcement bars of L-shape box. The height of concrete at the end of the horizontal section was compared to the height of concrete remaining in the vertical section [15].

The stability test method was used to assess the segregation resistance of fresh SCC. The method consisted of taking 4.8±0.2 liters of SCC and allowing the concrete to stand for 15 min in bucket covered with a lid to prevent evaporation, then, SCC mixture was poured on to 5 mm sieve, which sat on a sieve pan on a weighing scale. After 2 min, the mass of mortar passed through the sieve was measured and expressed as a percentage of the weight of the original sample on the sieve [15].

The compressive strength of concrete was measured on cubic specimens 100x100x100 mm^3 for each concrete mix at the age of 28 and 90 days. The compressive strength tests were performed on a 3000 kN compressive machine at a loading speed of 0.5 kN/s according to NF P 18-406 standards [16].

The capillary absorption tests were performed on molded cubic specimens (100x100x100 mm) according to ASTM C1585-04 procedure [17]. The specimens were stored in a ventilated oven at a temperature of 50-±2°C and RH of 80 ± 3 % for 3 days until constant weight. The side faces of the specimens were coated by a resin to ensure unidirectional flow and prevent the evaporation of the absorbed water. The specimens were emerged in the water container on a maximum height of 5 mm. Before each weight measurement, the specimens were removed from the container, wiped and then weighed. Measurements were taken at: 1 min, 5 min, 10 min, 20 min, 30 min, 1h, 2h, 3h, 4h, 5h and 6h.

The absorption, I, is the change in mass divided by the product of the cross-sectional area of the test specimen and the density of water. For the purpose of this test, the temperature dependence of the density of water is neglected and a value of 0.001 g/mm^3 is used. The units of I are mm.

$$I = \frac{m_t}{a * d} \quad (1)$$

Where:

I = the absorption,

m_t = the change in specimen mass in grams, at the time t,

a = the exposed area of the specimen, in mm^2,

d = the density of the water in g/mm^3.

Accessible porosity test [18] was determined by weighing a specimen of concrete after immersion in water after saturation under vacuum. The specimen was dried in an oven at a temperature of 105±5°C until the difference between two successive weightings, did not exceed 0.1%. The sample was placed in a closed chamber (dryer), under a constant pressure for 4 hours. Then the water was introduced gradually until filling and the specimen was covered by about 20 mm of water. The specimen was maintained in saturation during 18±2h. Specimens were then weighed in water and in air with a hydrostatic balance. Accessible porosity to water, ε, is expressed as percentage by volume according to the equation Eq. (1).

$$\varepsilon = \frac{M_{air} - M_{dry}}{M_{air} - M_{water}} \times 100 \quad (2)$$

M_{water} : weight in water of saturated sample
M_{air} : weight in air of saturated sample
M_{dry} : weight of oven-dried sample.

4. Results and discussion

4.1 Properties of fresh SCC

The properties of fresh SCC are presented in Table 3. For all SCCs the slump flow was between 635 and 780 mm, which is an indication of good deformability. The effect of GGBFS on the flow is remarkable. The slump flow of SCC-R is less than that of SCC containing slag. However all SCC mixes showed slump flow diameter values in the range of 550-850 mm and hence in the range required for SCC. The L-box ratio characterizes the filling and passing ability of SCC and blocking risk was observed for all mixes as the L-box blocking ratio was below 0.8. It can also be seen that the segregation ratio of SCC mixture are considered satisfactory. All the studied SCC mixes are stable (laitance < 15%).

Table 3: Results of fresh properties of SCC

Tests	SCC-0S	SCC-15S	SCC-25S
Slump flow Diameter (mm)	635	720	780
Blocking ratio (h_2/h_1) (%)	86	90	96
Segregation ratio (%)	5.50	7.90	10.95

4.2 Compressive strength

Figures 3 and 4 show the variation of the compressive strength of SCC with slag and the duration of moist curing (T = 20 ° C, RH = 100%). Compressive strength was measured at 28 and 90 days of age after a humid curing for 0, 3, 7 and 28 days and then stored on the roof of the laboratory during summer period. It can be clearly seen that the compressive strength is greatly affected by the curing period and the slag content. The compressive strength values obtained at 28 days of age for 0% slag were 84, 89 and 93% for 0, 3 and 7 days of humid curing respectively compared with standard 28 days water curing specimens. These values for 15% slag were 89, 88 and 92% for 0, 3 and 7 days of humid curing, respectively. Similar results were obtained at 90 days of age.

As expected, the longer duration of water curing the higher the compressive strength. Specimens without any water curing presented a compressive strength of only 84, 89 and 84% of the value obtained at the same age after 28 days of water curing for 0, 15 and 25% of slag. Curing in water is more effective for the short term periods of curing (3 and 7 days). As compared to specimens without water curing, seven days water curing gave an increase in compressive strength of 3.52, 1.47 and 3.01 MPa of 0, 15 and 25% slag, while 28 days curing gave only 6.44, 4.42 and 6.38 MPa for 0, 15 and 25% slag of gain in compressive strength. Hence a minimum period of humid curing of 3 to 7 days could be recommended. It should be noted that in practice duration of curing higher than 7 days is unlikely. Air curing resulted in reductions in compressive strength for all mixes.

The increase in the substitution level of slag from 15 to 25% resulted in a compressive strength at 28 days comparable to that of cement without addition, irrespective of the period of curing. For example, 28 days of curing the compressive strength values are 40.57, 39.15 and 40.21 for slag contents of 0, 15 and 25% respectively. This is due to the effect of slag which hydrates less rapidly at younger ages.

The values of compressive strength at 90 days ranged from 37 to 44, 37 to 50 and 40 to 55 MPa for slag contents of 0, 15 and 25% respectively. A slight increase of 1.5 to 13% and 9.4 to 21% in the compressive strength at 90 days is observed when slag cement is increased from 15% to 25 % respectively. Zhao et al. [19] have shown that that the initial water-curing period

has a significant effect on compressive strength of SCC. The initial water-curing period of 7 days has a maximum 28-days compressive strength.

Ferhat and Tohumcu [8] reported that the highest compressive strength values were obtained from standard cured specimens (cured in water for 28 days). The increase in the water curing duration resulted in increases in compressive strength. Air curing caused compressive strength decreases and the lowest strength values are obtained from air cured specimens. Lime-saturated cured samples were also found to give higher compressive strength than dry cured samples of concrete [20].

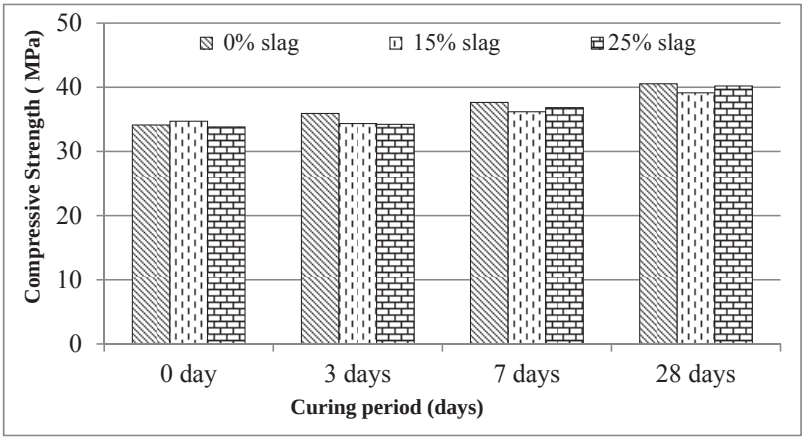

Figure 3: Effect of slag content and curing on the 28 days compressive strength of concrete.

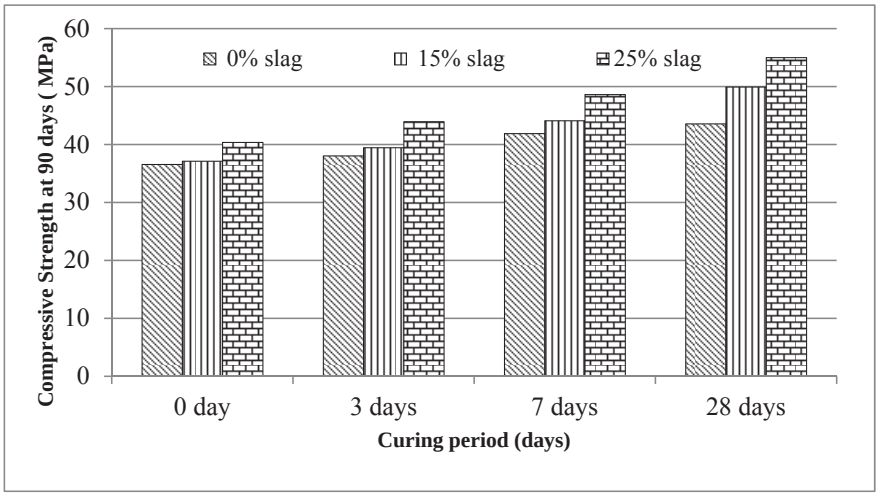

Figure 4: Effect of slag content and curing on the 90 days compressive strength of concrete

4.3 Capillary absorption

Figures 5 to 7 show that the capillary absorption decreases with the duration of water curing. It can be seen that the capillary absorption at 28 days of water curing has the lowest absorption coefficient. The longer the duration of curing in water, the lower is the absorption coefficient. The absorption coefficients obtained after 28 days of water curing is 80, 61 and 41 % of those obtained when no water curing was applied for respectively 0, 15 and 25 % of slag.

Water curing was most effective at 3 and 7 days showing the importance of a minimum period of curing. The incorporation of slag generated a slight decrease in water absorption for both SCC mixes with 15 and 25 % slag. A period of 7 days of curing reduces the water absorption coefficient by 15, 18 and 35 % for 0, 15 and 25 % slag mixes, respectively. Capillary absorption is related to the development of hydration and the filling of pores with hydration products which is slow with slag mixes.

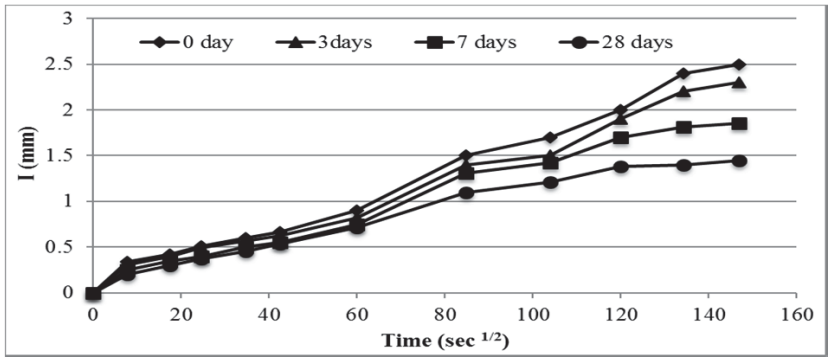

Figure 5: Capillary absorption for 0% slag

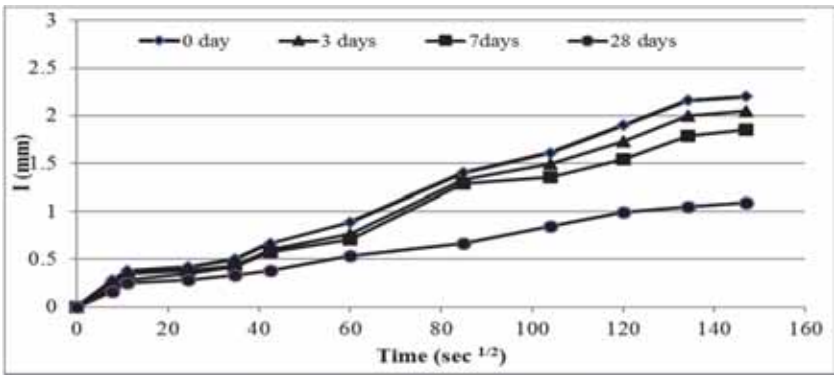

Figure 6: Capillary absorption for 15% of slag.

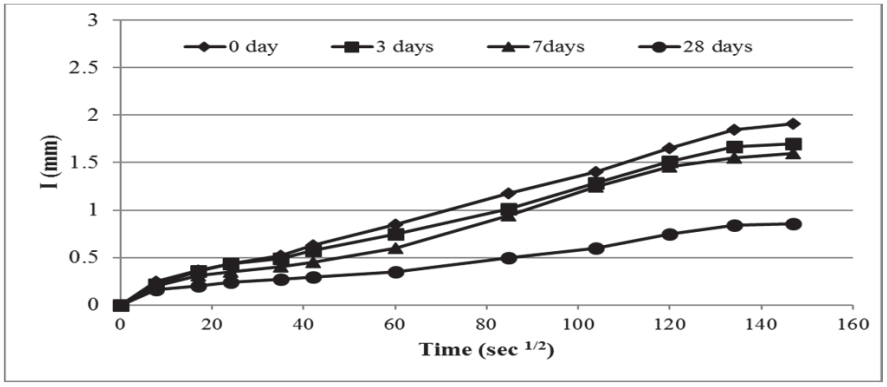

Figure 7: Capillary absorption for 25% of slag.

4.4 Porosity

Figure 8 presents the results of the porosity according to the curing time and the slag content. Concretes which have not received any curing show the worst performance in terms of porosity. It can be also observed that the initial water curing period has a significant effect on porosity of SCC, as the curing period increased; there was a reduction in the porosity in all concrete specimens. The lowest porosity was noted in the concrete specimen cured for 28 days.

Concretes containing slag have a lower porosity than that of the reference concrete. This may be explained by the refinement of capillary pores of the cement matrix of concrete cured with the progress of hydration. For example, it has been observed that substitution of 15 to 25% slag causes an average decrease of the porosity of 2.70% and 3.03% respectively.

SCC with 15% and 25% slag have fairly comparable porosity, with a slight increase in porosity for the SCC with 15% slag. Porosity decreases from 16.1% to 14.6 % and 13.8% to 11.20% and from 13.50% to 10.7% when the curing time increases from 0 to 28 days to slag content of 0, 15 and 25%, respectively.

Figure 9 illustrates the relationship between the compressive strength at 90 days and the accessible pores of the slag-based SCC at 90 days . This correlation confirms that the mechanical strength is related to the porosity accessible to water (the slope of the trend lines is identical).

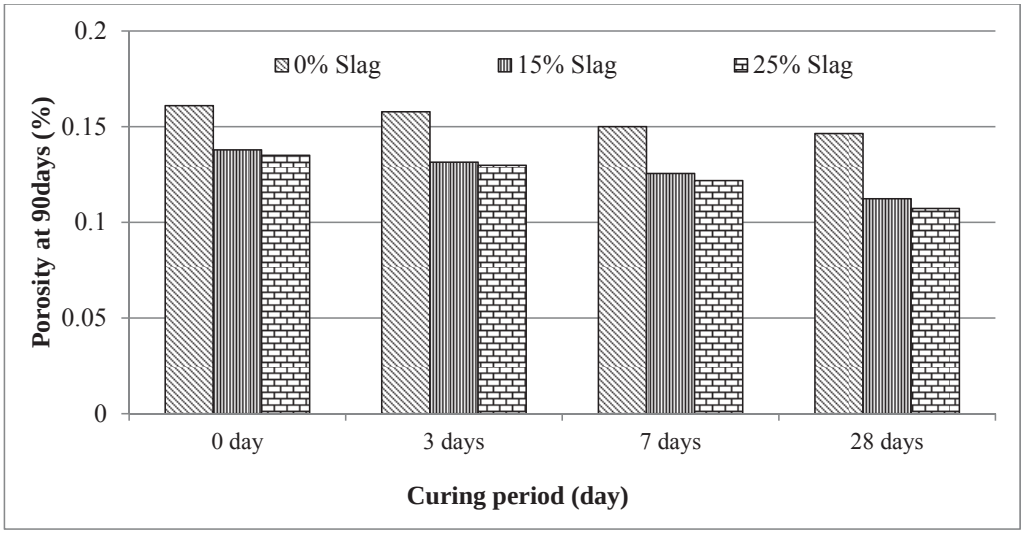

Figure 8: Effect of slag content and curing period on porosity at 90 days.

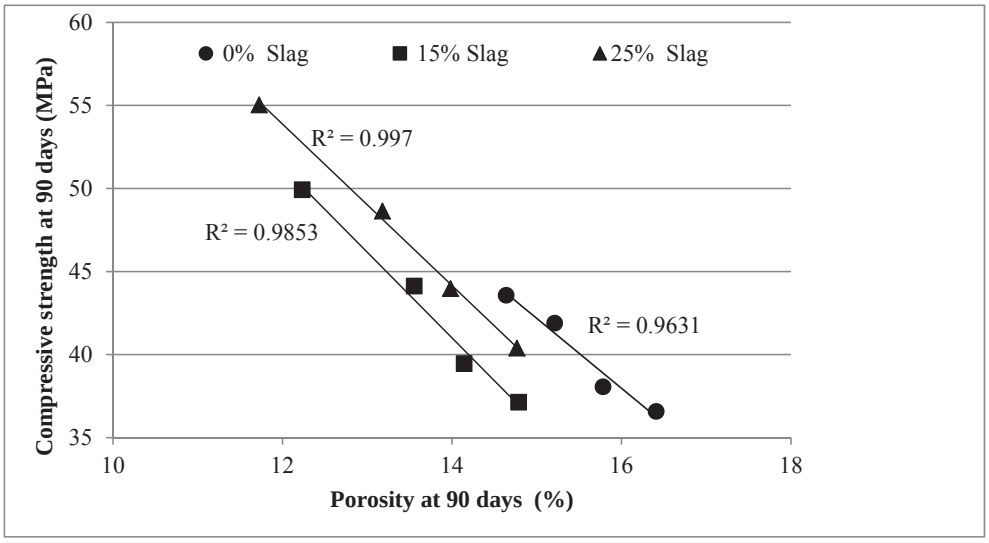

Figure 9: Correlation between compressive strength and porosity at 90 days.

5. Conclusion

This paper presents an experimental investigation to determine the effect of initial water-curing period and curing conditions on the performance of SCC with two ratios of slag replacements. The following conclusions can be drawn:

- The substitution of cement by slag leads to comparable compressive strength at 28 days of age. However, at long term increased strength was observed.
- Absorption by capillary and porosity at 90 days decrease with increasing slag content and an increase in the duration of water curing.
- Curing in hot environment conditions contributes to the physico-chemical changes which result in an increase in the porosity and capillary absorption compared to that stored in water. These two parameters are related to the increase in the size of the capillary pores but also to the deterioration of the cement matrix and appearance of microcracks.

References

[1] Boukendakdji, O., Kenai S., Kadri, H. and Rouis, F. Effect of slag on the self compacted concrete, Constr Build Mater 23 (2009), 2593-2598.
[2] Belaidi, ASE., Azzouz, L. and Kadri E., Kenai S, Effect of natural pozzolana and marble powder on the properties of self compacted concrete, Constr Build Mater 31 (2012), 251-257.
[3] Boukendakdji, O., Kadri, E.H. and Kenai, S., Effect of granulated blast furnace slag and superplasticizer type on the fresh properties and compressive strength of self compacting concrete, Cem Concr Comp 34(2012), 583-590.
[4] Benabed, B., Kadri, E., Azzouz,L. and Kenai, S., Properties of self-compacting mortar made with various types of sand; Cem Concr Comp 34 (2012), 1167-1173.
[5] Kenai, S. and Amrane, A. Mechanical properties and permeability of slag in Algerian got climate, Proceedings of Fourth Int. Conference on Concrete Technology in Developing Countries, Gazimagusa, Turkey (1996), 138-148.
[6] Kenai, S. and Lachemat, L. Effect of curing on properties of concrete in hot climate, Proceedings of sixth Arab civil engineering symposium, Damascus, Syria, 21-24 October (1995) , 991-998.
[7] Ibrahim, M. Shameem, M. Al-Mehthel, M. and Maslehuddin, M. Effect of curing methods on strength and durability of concrete under hot weather conditions; Cem Concr Comp 41 (2013) 60‑69.
[8] Ferhat B.A., and Tohumcu, I., Effects of different curing regimes on the compressive strength properties of self compacting concrete incorporating fly ash and silica fume, Mater Desig, 51 (2013) 12–18.
[9] Al-Khaiat, H. and Haque, M.N., Effect of initial curing on early strength and physical properties of a lightweight concrete, Cem Concr Res, 28(6) 1998, 859‑66.

[10] Ramezanianpour, A. A., Effect of Curing on the Compressive Strength, Resistance to Chloride-Ion Penetration and Porosity of Concretes Incorporating Slag, Fly Ash or Silica Fume, Cem Concr Comp 17 (1995), 125-133.
[11] Hadj-Sadok, A., Kenai, S. Courard, L., Michel, F and Khatib, J., Durability of mortar and concretes containing slag with low hydraulicity activity, Cem Concr Comp, 34 (2012), 671-677.
[12] Hadj-Sadok, Kenai, S., Courard, L. and Darimont, A., Microstructure and durability of mortars modified with medium active blast furnace slag , Constr Build Mater, 25 (2) (2011), 1018-1025.
[13] Okamura H. and Ouchi M., "Self-Compacting Concrete. Development, present use and future", Proceedings of the First International RILEM Symposium on Self-Compacting Concrete, 1999, Stockholm, Suède pp. 3-14.
[14] Okamura H. and Ouchi M. « Self-compacting concrete » Journal of advanced Concrete Technology, 2003, vol 1, n°1, pp. 5-15.
[15] EFNARC « The European guidelines for self compacting concrete » The European Federation of Specialist Construction Chemicals and Concrete Systems. www.efnarc.org, 2005.
[16] NF P 18-455: Testing hardened concrete -Part 3, Compressive strength of test specimens, 2003.
[17] ASTM 1585-11. Standard test method for measurement of rate of absorption of water by hydraulic cement concretes, 2012.
[18] CPC11.3, Absorption of water by concrete by immersion under vacuum, in RILEM Recommendations for the Testing and Use of Constructions Materials, RILEM, Editor (E & FN SPON, (1984) 36-37.
[19] Zhao, H. Sun, W. Wu, X. and Gao, B., Effect of initial water-curing period and curing condition on the properties of self-compacting concrete, Mater Desig, 35(2012), 194-200.
[20] Turkmen, I. and Kantarcı, A, Effects of expanded perlite aggregate and different curing conditions on the physical and mechanical properties of self-compacting concrete, Build Env, 42 (2007), 2378–2383.

International RILEM Conference on Materials, Systems and Structures in Civil Engineering
Conference segment on Service Life of Cement-Based Materials and Structures
22-24 August 2016, Technical University of Denmark, Lyngby, Denmark

EVALUATION OF THE LDPM ELASTIC AND FRACTURE PARAMETERS BY UP-SCALING PROCEDURE

G. Sherzer[(1)], Peng Gao[(2)], Guang Ye[(2)], Erez Gal[(1)]

(1) Department of Structural Engineering, Ben-Gurion University, Beer-Sheva, Israel
(2) Faculty of Civil Engineering and Geoscience, Delft University, Delft, Netherland

Abstract
The heterogeneity of the concrete may be considered on different size scales of observation, ranging from the atomistic scale ($10^{-10}m$), characterized by the behavior of crystalline particles of hydrated Portland cement, to the macroscopic scale (10^{1}m), where concrete has traditionally been considered homogeneous. The multiscale framework we are proposing in this paper is based on the following models: chemical analyses at the cement paste scale; mechanical lattice model at the cement and mortar scales; geometrical aggregate distribution models at the mortar and concrete scales; and the Lattice Discrete Particle Model (LDPM) at the concrete scale. For that purpose, a set of analysis starting from a known set of parameters of the cement paste. This input is utilized to evaluate the mechanical properties of the mortar-s (cement and sand), and then these properties are used to evaluate the mechanical properties of the mortar-a4 (mortar-s and aggregate smaller then 4mm). The upscaling in the proposed methodology involved the evaluation of the LDPM concrete parameters based on the mortar-a4 properties. Here we are suggesting a uni-axial tension "numerical experiments" on the mortar-a4 scale to evaluate the elastic and fracture LDPM mechanical parameters.

1. Introduction

Modeling the behavior of concrete structures is a challenging research task. Usually the mechanical behavior of concrete is macroscopically modeled via plastic and/or damage constitutive relations (e.g. see [1] among others). These macroscopic models are characterized by the large number of parameters needed to be calibrated in order to analyze the complex behavior of the concrete at the different stages of loading and at the different damage modes. The need of looking for alternative models for these macroscopic models is due to the fact that the concrete has a variety of microstructures. The variety of micro-structures includes: addition of fibers made up from different materials; variation of aggregate size, shape and type; water to cement ratio, cement composition, etc. The use of multi-scale analysis

evidently is the appropriate way to model the behavior of concrete structures by coupling between the concrete micro-structures and its macroscopic properties needed to analyze a structure [2-17].

The microstructure of cement paste can be imaged either experimentally [18] or numerically [19-23]. Micro x-ray computed tomography (CT) [18] offers a nondestructive experimental technique to collect microstructure information of cement paste in terms of digitized voxels. Computer modeling packages are also available to simulate cement hydration and microstructure formation processes, including, the HYMOSTRUC3D model [19, 21], the CEMHYD3D [22], and the μic model [23].

The HYMOSTRUC3D model simulates the reaction process and the formation of the microstructure in hydrating Portland cement and takes into account the hydration kinetics. In this model, the cement particles are modeled as spheres, which grow during the hydration process. The HYMOSTRUC3D is designed as a 3D model by considering the water-to-cement ratio, the amount of cement, the mineralogical composition, cement fineness measured by Blaine apparatus, the temperature of the mix for Portland and blended cements, and specimen geometry as input parameters [24]. The Rosin–Rammler sieve curve is the approach adopted for describing the particle size distribution in the cement. The HYMOSTRUC3D model provides information concerning the location, morphology, and the degree of hydration of the cement particles. More details can be found in [19, 21].

The LDPM [2-10, 17] simulates concrete meso-structure by a three-dimensional assemblage of particles that are generated randomly according to a given grain size distribution. The approach usually adopted for the size distribution of the particles is the Fuller curve. The LDPM has been extensively calibrated and validated in the last few years, and it has shown superior capabilities from both qualitative and quantitative standpoints in reproducing and predicting concrete behavior under a wide range of loading conditions. The LDPM can simulate: 1) uniaxial (unconfined and confined) compression tests including the effect of specimen slenderness and the effect of friction of the loading platens; 2) biaxial compression tests; 3) triaxial compression tests with reversal of softening into hardening for increasing confinement; 4) hydrostatic compression tests, which never show softening; 5) direct tensile tests; 6) splitting tensile (Brazilian) tests; 7) fracture tests; 8) energetic size effects; 9) cycling loading; 10) the correct ratio between compressive strength and tensile strength; and 11) the rate effect on concrete strength. This model characterizes concrete at the meso-scale level—the level considered to be that of coarse aggregate pieces. This scale level takes into account the interaction between the various components of the concrete. The LDPM is formulated in the framework of discrete models for which the unknown displacement field is not continuous, but rather defined at discrete points representing the center of discrete particles. The geometric of the particles are obtained using Delaunay triangulation that provides volume subdivision into tetrahedral. The behavior of a particle contact represents the mechanical interaction between adjacent aggregate particles, through the embedding mortar. Such interactions are governed by meso-scale constitutive equations simulating meso-scale tensile fracturing with strain-softening, cohesive and frictional shearing, and nonlinear compressive behavior with strain-hardening. The contact areas are represented by the external triangular faces which are called facets. At the facet, the vectorial stress–strain relationships are

imposed. Discrete compatibility equations are formulated through the relative displacements and rotations of adjacent aggregates (elements), where in each facet, there are two components for shear strains and a normal strain component. More details can be found in [7].

The goal of this research is to bridge between the microscopic cement paste scale and the concrete mesoscale by upscaling the cement properties in order to obtain the LDPM mechanical parameters. The proposed methodology is based on several models, as detailed in the nest sections, to provide the mechanical parameters of *mortar-4a* to obtain the input for the LDPM. As a result, the LDPM model will include information from the lower scales of the mortar constituents and might allow to reduce the number of experiments needed for the calibration process.

The LDPM was chosen to represent the concrete behavior at the meso scale level, due to its ability to capture the size, shape effects and the components influence of the concrete mix. The three lower scale models were chosen to provide the inputs of the 15 mechanical parameters of the LDPM are: The HYMOSTRUC model [19] for its capability to capture the information of mineralogical composition of cement clinker, the concrete mix proportion, and the chemical reaction of cement; The Anm material model [25] is used to simulate the concrete in meso-scale with irregular shape of aggregates and the lattice model suggested by [26] was chosen for its ability to simulate fracture process and the fact that this model has been validated with experiments [27]. This paper does not present validation study of the suggested numerical models as it already presented in [8], [30].

Finally, this paper suggests an upscaling of the elastic and fracture parameters of the LDPM using a successive analysis of three existing lower scale models.

2. Microstructure modeling of cement paste

In this research the (HYMOSTRUC3D) model suggested by [19], is used to simulate the cement hydration and microstructure of cement paste. The simulations were performed for a specific concrete mix design [28]. The microstructure of the cement paste is used for the further mechanical simulation of uniaxial compression to obtain the cement paste mechanical properties based on the specimen size, the mineralogical composition of cement, the cement fineness and the water/cement ratio. The concrete mix properties simulated in this paper are as follow: Portland cement (CEM 42.5 N/AM-SLV) with maximum cement size of $50\ \mu m$, a w/c ratio of 0.567, air content 0.6 - 1.16% and the Iso and mix temperature of 20˚C. The w/c ratio of 0.567 was used for all scales (cement paste/mortar/concrete) simulations, due to the fact that all aggregates were saturated with dry surfaces and there are no superplasticizers in the mix. The mineralogical compositions of the cement were obtained from (XRD) analysis [27].The input parameters for HYMOSTRUC3D simulation are summarized in Table 1. The microstructures at the curing age of 3 hours are shown in Figure1 (left) and 28 days is shown in Figure1 (right).

The contour colors in Figure 1 represents the porous, unhydrated cement, inner hydration product, outer hydration product and CH.

Table 1: Specification of the HYMOSTRUC3D inputs used in the simulation

	Inputs specification
Mineralogical composition	C_3S: 54.9 %, C_2S: 19.1 %, C_3A: 4 %, C_4AF: 8.8%
Minimum particle diameter	1 μm
Cement fineness (Rosin-Rammler distribution)	(n = 1.05771, b = 0.04282)
Curing temperature	20°C

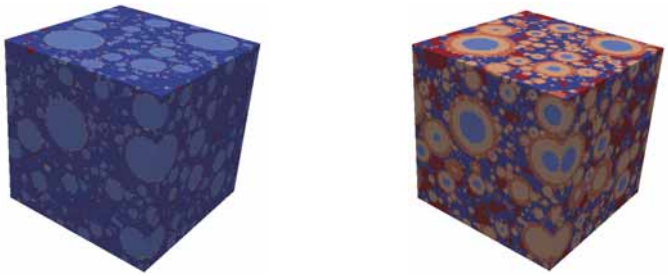

Figure 1: Microstructures of cement paste at –ages of 3 hours (left) and 28 days (right)

3. Mechanical simulation at, the microscopic scale

In order to evaluate the mechanical properties of the hydrated cement, 3D lattice model [26] is used to evaluate the mechanical properties of the cement paste at age of 28 days. The mechanical properties of each constituent of the microstructure are presented in Table 2 as published in [29]. In this scale we use a two-step homogenize presses as follow.

First homogenization step – at these step a thousand cubical specimens with size of 10μm×10μm×10μm were analyzed. Using uniaxial tensile test with (HF) – High Friction boundary condition were the lateral displacement is prevented at the boundary points and all other points are free to expand. The loading is imposing incrementally on the specimen as a unit displacement on the specimen in the longitudinal direction.

The lattice model converts the spherical particle that represents the microstructure of hydrated cement to a voxel-based digital image, where the ImgLat lattice construction method was applied, for more information see [29], in this paper the resolution is chosen to be 1 μm/Voxel. The mechanical properties required for the lattice model are the Young modulus, shear modulus, tensile strength and compression strength (the fracture energy of the cement is not included in the analysis of the used Lattice model) which are presented in Table 2.

Second homogenization step - at this step a cubical specimen size of 100μm×100μm×100μm were analyzed. The resulting stress-strain curve obtained from the simulation of the first homogenization step was approximated by a multi-linear curve. These

multi-linear curves are the local mechanical properties of each element in this step depending on the location of each cube. A uniaxial tension simulation of this scale provides us the mechanical properties of the upper Mortar-s scale.

Table 2: Specification of the lattice model inputs used in the simulation of cement paste

No	Element type	Young modulus E (GPa)	Shear modulus G (GPa)	Tensile strength f_t (GPa)	Compression strength f_c (GPa)
1	Unhydrated cement	135	52	1.8	-1.8
2	Interface- Unhydrated & Inner	49	20	0.24	-2.4
3	Inner product	30	12	0.24	-2.4
4	Interface- Inner & Outer	25	10	0.15	-1. 5
5	Outer product	22	8.9	0.15	-1.5
6	Interface- Outer & CH	26.4	10.6	0.15	-1.5
7	(CH) - Calcium hydroxides	33	13.2	0.264	-2.64
8	Interface- Unhydrated & Outer	38	15.2	0.15	-1.5
9	Interface- Inner & CH	31.5	12.6	0.24	-2.4

4. Upscaling the Mortar-s scale

The Mortar-s scale includes cement paste, sand and interface transition zone. The mechanical properties of the sand and the interface between the sand and the cement paste are given in Table 3. The mechanical properties of the cement paste are given as multi-linear curve from the results obtained in section 3 as depicted in Figure 2. The specimen size chosen as *3mm ×3mm ×3mm*, in order to account for computational time and maintain reasonable results to consider the specimen as homogeneous [30]. The resolution of this scale needs to be equal or smaller than the cement specimen which was 100 μm ×100 μm ×100 μm, therefore the resolution is chosen to be 0.1 mm/Voxel, for more information see [29]. The mechanical properties required for the lattice model simulation are the Young modulus, shear modulus, tensile strength and compression strength which are presented in Table 3.

The performed simulation test obtained in order to provide results for the Mortar-a_4 scale is the uniaxial tension analysis as presented in Figure 3.

Table 3: Table Specification of the lattice model inputs used in the simulation of mortar s

No	Element type	Young modulus E (GPa)	Shear modulus G (GPa)	Tensile strength f_t (GPa)	Compression strength f_c (GPa)
1	Sand	70000	29000	24	-240
2	Interface- sand & cement	22000	8900	0.75	-7.5

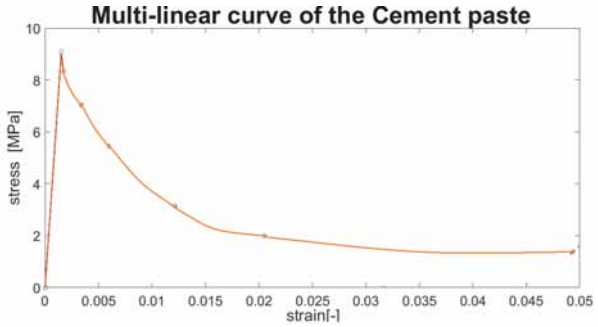

Figure 2: Cement paste stress-strain curve

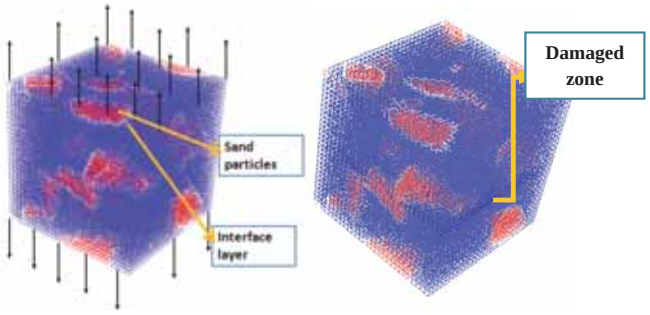

Figure 3: Uni-axial tension analysis on the Mortar-s scale and the resulted damaged zone on

5. Upscaling Mortar a_4 Scale

This scale represents the Mortar-a_4 which is the combination of Mortar-s, aggregates smaller then *4mm* and interface layer between them. From section 4 we obtain the Young modulus, shear modulus, tensile strength and compression strength of Mortar-s mechanical properties see Figure 4. To complete the mechanical information needed to analyze this scale the mechanical properties of the aggregates and the interface between the aggregates are given in Table 4. The specimen size chosen for this scale is *10mm×10mm×10mm* and the resolution

chosen to be 1 mm/Voxel. The Anm model has been applied to obtain the geometry of the mortar-a_4 unit cell. The Anm material model is used to distribute the aggregates particles into the unit cell with periodic morphology along the unit cell boundaries.

Table 4: Specification of the lattice model inputs used in the simulation of mortar a 4mm

No	Element type	Young modulus E (GPa)	Shear modulus G (GPa)	Tensile strength f_t (GPa)	Compression strength f_c (GPa)
1	aggregates	70000	29000	24	-240
2	Interface- aggregates & mortar s	41000	17000	1	-10

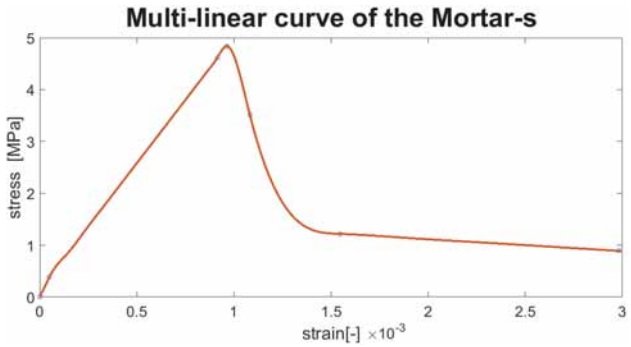

Figure 4: Mortar-s stress-strain curve

6. Evaluation of LDPM Elastic parameters

3D lattice simulations were performed at the *Mortar-a_4* scale in order to evaluate the elastic (E_0, ν), fracture (l_t, σ_t) and shear parameters for the LDPM. The LDPM constitutive parameters are representing the facet mechanical behavior where the mortar is located, therefore it can be assumed that the failure modes are characterized by the cement past up-scaled to mortar that includes aggregates smaller than *4* mm and ITZ (Interface Transition Zone). The simulation performed to evaluate these LDPM parameters are a uniaxial tensile test with High Friction (HF). HF boundary condition for the tension test were applied by preventing lateral displacement at the boundary nodes while all the other nodes were free to expand. The tensile simulation done by incrementally applying a displacement on the specimen in the longitudinal direction. As mentioned above the specimen size is *10mm×10mm×10mm* and the resolution chosen for this scale is *1mm*/Voxel.

The stress-strain curve of the Mortar-a_4 due to a tension simulation and the figures that relate the up-scaled LDPM parameters are presented in Figure 5. The pick value of the stress strain in Figure 5b is the tensile strength, σ_t, and it up-scaled directly to the LDPM as a material parameter. The fracture energy, G_t, can be calculated as the area under the stress–strain curve.

The fracture energy is calculated in order to define the characteristic length, LDPM parameter, as $l_t = \frac{2E_o G_t}{\sigma_t^2}$ see also Cusatis [7]. The normal elastic modulus, E_0, is calculated for each facet using the following expression $\frac{L}{E_0} = \frac{L_a}{E_a} + \frac{L_m}{E_m}$ where E_a and E_m are the module of elasticity and L_a and L_m are the length of the aggregate and mortar respectively, while L is the total length of the facet. The module elasticity of the mortar is evaluated from the slop of the stress-strain curve of the mortar (see Figure 5a), while the value of module elasticity of the aggregates are as published in the literature, e.g. see [29]. The Poisson ratio of the concrete is assumed as *0.18* and the LDPM α parameter is calculated as shown in Figure 5a.

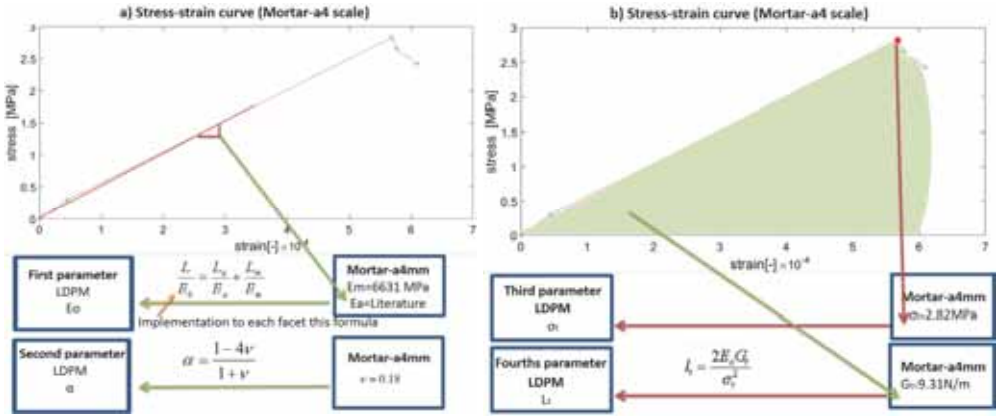

Figure 5: Mortar-a_4 stress-strain curve

7. Conclusion

The main aim of this research is to propose an upscaling procedure between the cement paste at micro-scale and the concrete at meso-scale, using existing models.

This research utilizes three models to obtain the parameters for the LDPM (concrete) model in order to obtain a full multi-scale technique that encompass all the various levels and take into account the contributory effects of lower-scale phenomena in the evaluation of the overall material properties at the macroscopic scale.

The three lower scale models that were chosen for the suggested upscaling procedure are: the HYMOSTRUC model for revealing cement hydration and microstructural formation, the Anm model for simulating the concrete in meso-scale with irregular shape of aggregates, and a lattice model based on Timoshenko beam elements for the mechanical analysis of the cement paste and the mortar scales.

The LDPM was chosen to simulate the concrete behavior at the meso-scale level, due to its ability to capture the size and shape effects and the effect of various concrete mix.

In this paper we demonstrated the suggested methodology by evaluating the elastic and fracture parameters of the LDPM.

References

[1] Riedel W., Thoma K., Hiermaier S., and Schmolinske E., Penetration of reinforced concrete by BETA-B-500 numerical analysis using a new macroscopic concrete model for hydrocodes, in 9th Int Symp Interaction of the Effects of Munitions with Structures (1999).
[2] Cusatis G., Bažant Z., and Cedolin L., 3D Lattice model for dynamic simulations of creep, fracturing and rate effect in concrete, in Creep, shrinkage and durability mechanics of concrete and other quasi-brittle materials, Proceedings of the 6th International Conference, Cambridge (MA), USA, (2001), 113-118
[3] Cusatis G., Bazant Z. P., and Cedolin L., Confinement-shear lattice model for concrete damage in tension and compression: I. Computation and validation, Journal of Engineering Mechanics, 129, (2003) 1439-1448
[4] Cusatis G., Polli M., and Cedolin L., Mesolevel analysis of fracture tests for concrete, in Fracture Mechanics of Concrete Structures, Proceedings of the Fifth International Conference on Fracture Mechanics of Concrete and Concrete Structures—FraMCoS-5, Vail Cascade Resort, Vail Colorado, Ia-FraMCos, USA (2004), 345-351
[5] Cusatis G. and Cedolin L., Two-scale study of concrete fracturing behavior, Engineering Fracture Mechanics, 74 3-17, 2007
[6] Cusatis G., Bažant Z. P., and Cedolin L., Confinement-shear lattice CSL model for fracture propagation in concrete, Computer methods in applied mechanics and engineering, 195, (2006) 7154-7171
[7] Cusatis G., Pelessone D., and Mencarelli A., Lattice Discrete Particle Model (LDPM) for failure behavior of concrete. I: Theory, Cement and Concrete Composites, 33, (2011) 881-890
[8] Cusatis G., Mencarelli A., Pelessone D., and Baylot J., Lattice Discrete Particle Model (LDPM) for failure behavior of concrete. II: Calibration and validation, Cement and Concrete composites, 33, (2011) 891-905
[9] Cusatis G., Pelessone D., Mencarelli A., and Baylot J. T., Simulation of reinforced concrete structures under blast and penetration through lattice discrete particle modeling, in ASME 2007 International Mechanical Engineering Congress and Exposition (2007) 581-584
[10] Cusatis G., Mencarelli A., Pelessone D., and Baylot J. T., Lattice discrete particle model (LDPM) for fracture dynamics and rate effect in concrete, in Structures Congress (2008)
[11] Gal E. and Kryvoruk R., Meso-scale analysis of FRC using a two-step homogenization approach, Computers & Structures, 89, (2011) 921-929
[12] Gal E., Ganz A., Hadad L., and Kryvoruk R., Development of a concrete unit cell, International Journal for Multiscale Computational Engineering, 6 (2008).
[13] Gal E., Suday E., and Waisman H., Homogenization of materials having inclusions surrounded by layers modeled by the extended finite element method, International Journal for Multiscale Computational Engineering, 11 (2013)
[14] Gal E. and Kryvoruk R., Fiber reinforced concrete properties- a multiscale approach, Computers & concrete, 8, (2011) 525-539

[15] Grigorovitch M. and Gal E., A new method for calculating local response in elastic media—the embedded unit cell approach, Computational Modelling of Concrete Structures, (2014) 471
[16] Bazant Z. P., Caner F. C., Carol I., Adley M. D., and Akers S. A., Microplane model M4 for concrete. I: Formulation with work-conjugate deviatoric stress, Journal of Engineering Mechanics, 126, (2000) 944-953
[17] Cusatis G., Bazant Z. P., and Cedolin L., Confinement-shear lattice model for concrete damage in tension and compression: II. Computation and validation, Journal of Engineering Mechanics, 129, (2003) 1449-1458
[18] Flannery B. P., Deckman H. W., Roberge W. G., and D'AMICO K. L., Three-dimensional X-ray microtomography, Science, 237, (1987) 1439-1444
[19] Ye G., Van Breugel K., and Fraaij A., Three-dimensional microstructure analysis of numerically simulated cementitious materials, Cement and Concrete Research, 33, (2003) 215-222
[20] Koster M., Hannawald J., and Brameshuber W., Simulation of water permeability and water vapor diffusion through hardened cement paste, Computational Mechanics, 37 (2006) 163-172,.
[21] Van Breugel K., Numerical simulation of hydration and microstructural development in hardening cement-based materials:(II) applications, Cement and Concrete Research, 25, (1995) 522-530
[22] Bentz D. P., CEMHYD3D: A three-dimensional cement hydration and microstructure development modelling package. Version 2.0, National Institute of Standards and Technology Interagency Report, (2000) 7232
[23] Bishnoi S. and Scrivener K. L., μic: A new platform for modelling the hydration of cements, Cement and Concrete Research, 39, (2009) 266-274
[24] N. Ukrainczyk, E. Koenders, and K. Van Breugel, "Multicomponent modelling of Portland cement hydration reactions, in Second International Conference on Microstructural-related durability of cementitious Composites, Amsterdam, The Netherlands (2012) 11-13
[25] Qian Z., Garboczi E., Ye G., and Schlangen E., Anm: a geometrical model for the composite structure of mortar and concrete using real-shape particles, Materials and Structures, 49, (2016) 149-158
[26] Qian Z., Schlangen E., Ye G., and Van Breugel K., Multiscale lattice fracture model for cement-based materials, in ICCM 2012: 4th International Conference on Computational Methods, Gold Coast, Australia (2012) 25-28.
[27] Šavija M., Luković B., and Schlangen E., Experimental and Numerical Study of Water Uptake in Strained SHCC, 10th International Conference on Mechanics and Physics of Creep, Shrinkage, and Durability of Concrete and Concrete Structures. (2015).
[28] Sherzer G., Marianchik E., Cohen R., and Gal E., Development, Calibration & Validation of Lateral Displacement for Concrete Uniaxial Compression Test, presented at the CONCREEP 10, Vienna University of Technology, Austria, (2015)
[29] Qian Z., Multiscale modeling of fracture processes in cementitious materials, PhD thesis, Technical University of Delft (2012)
[30] Garboczi E. J., and Bentz D. P., Computer simulation and percolation theory applied to concrete, Annual Reviews of Computational Physics VII, p. 85, (1999).

Author Index

Materials, Systems and Structures in Civil Engineering 2016

Service Life of Cement-Based Materials and Structures

Vol. 2

Edited by
Miguel Azenha, Ivan Gabrijel, Terje Kanstad, Dirk Schlicke and Ole Mejlhede Jensen

RILEM Proceedings PRO 109
ISBN Vol. 1: 978-2-35158-170-4
ISBN Vol. 2: 978-2-35158-171-1
ISBN Vol. 1&2: 978-2-35158-172-8
e-ISBN: 978-2-35158-173-5

This volume contains the proceedings of the MSSCE 2016 conference segment on "Service Life of Cement-Based Materials and Structures", which is organized by COST Action TU1404 (www.tu1404.eu). This COST Action is entitled: "Towards the next generation of standards for service life of cement-based materials and structures", dedicated to assist deepening knowledge regarding the service life behaviour of cement-based materials and structures. The main purpose of this Action is to bring together relevant stakeholders (experimental and numerical researchers, standardization offices, manufacturers, designers, contractors, owners and authorities) in order to reflect today's state of knowledge in new guidelines/recommendations, introduce new products and technologies to the market, and promote international and inter-speciality exchange of new information, creating avenues for new developments. The COST Action is basically divided in three main workgroups targeted to this purpose:

WG1 – Testing of cement-based materials and RRT$^+$

WG 2 – Modelling and benchmarking

WG 3 – Recommendations and products

Also, two important instruments of the Action are now under way: the Extended Round Robin Testing Program (RRT$^+$), and the numerical benchmarking. The RRT$^+$ is currently involving 43 laboratories.

The present conference segment deals with a wide breadth of topics related to the service life of concrete, comprising aspects related to the 3 Workgroups mentioned above. The conference segment is attended by 80 presenters from university, industry and practice representing more than 30 different countries. All contributions have been peer reviewed.

The event "Materials, Systems and Structures in Civil Engineering 2016", 15-29 August 2016, Lyngby, Denmark, is scientifically sponsored by RILEM. The event is hosted by the Department of Civil Engineering at the Technical University of Denmark and is financially sponsored by a number of independent foundations and organizations.

RILEM Publications S.a.r.l.
157 rue des Blains, F-92220 Bagneux - FRANCE
Tel: +33 1 45 36 10 20 Fax: +33 1 45 36 63 20
E-mail: dg@rilem.net